Diversity-promoting and Large-scale Machine Learning for Healthcare

Pengtao Xie

CMU-ML-18-106

Aug 2018

Machine Learning Department
School of Computer Science
Carnegie Mellon University
Pittsburgh, PA

Thesis Committee:
Eric P. Xing, Chair
Ruslan Salakhutdinov
Pradeep Ravikumar
Ryan Adams (Princeton & Google Brain)
David Sontag (MIT)

Submitted in partial fulfillment of the requirements for the degree of Doctor of Philosophy.

This research was sponsored by: Office of Naval Research award number N000140910758; Air Force Office of Scientific Research award FA95501010247; National Science Foundation awards IIS1115313, IIS1111142, IIS1218282 and IIS1447676; Defense Advanced Research Projects Agency award FA872105C0003; Department of the Air Force award FA870215D0002; National Institutes of Health award P30DA035778; Pennsylvania Department of Health's Big Data for Better Health (BD4BH) award; and a grant from the University of Pittsburgh Medical Center.

Keywords: Diversity-promoting Learning, Large-scale Distributed Learning, Machine Learning for Healthcare, Regularization, Bayesian Priors, Generalization Error Analysis, System and Algorithm Co-design

Dedicated to my parents
for their endless love, support, and encouragement

Abstract

In healthcare, a tsunami of medical data has emerged, including electronic health records, images, literature, etc. These data are heterogeneous and noisy, which renders clinical decision-makings time-consuming, error-prone, and suboptimal. In this thesis, we develop machine learning (ML) models and systems for distilling high-value patterns from unstructured clinical data and making informed and real-time medical predictions and recommendations, to aid physicians in improving the efficiency of workflow and the quality of patient care. When developing these models, we encounter several challenges: (1) How to better capture infrequent clinical patterns, such as rare subtypes of diseases; (2) How to make the models generalize well on unseen patients? (3) How to promote the interpretability of the decisions? (4) How to improve the timeliness of decision-making without sacrificing its quality? (5) How to efficiently discover massive clinical patterns from large-scale data?

To address challenges (1-4), we systematically study *diversity-promoting learning*, which encourages the components in ML models (1) to diversely spread out to give infrequent patterns a broader coverage, (2) to be imposed with structured constraints for better generalization performance, (3) to be mutually complementary for more compact representation of information, and (4) to be less redundant for better interpretability. The study is performed in both frequentist statistics and Bayesian statistics. In the former, we develop diversity-promoting regularizers that are empirically effective, theoretically analyzable, and computationally efficient, and propose a rich set of optimization algorithms to solve the regularized problems. In the latter, we propose Bayesian priors that can effectively entail an inductive bias of "diversity" among a finite or infinite number of components and develop efficient posterior inference algorithms. We provide theoretical analysis on why promoting diversity can better capture infrequent betters and improve generalization. The developed regularizers and priors are demonstrated to be effective in a wide range of ML models.

To address challenge (5), we study *large-scale learning*. Specifically, we design efficient distributed ML systems by exploiting a system-algorithm co-design approach. Inspired by a sufficient factor property of many ML models, we design a peer-to-peer system – Orpheus – that significantly reduces communication and fault tolerance costs. We also provide theoretical analysis showing that algorithms executed on Orpheus are guaranteed to converge. The efficiency of our system is demonstrated in several large-scale applications.

We apply the proposed diversity-promoting learning (DPL) techniques and the distributed ML system to solve healthcare problems. In a similar-patient retrieval application, DPL shows great effectiveness in improving retrieval performance on infrequent diseases, enabling fast and accurate retrieval, and reducing overfitting. In a medical-topic discovery task, our Orpheus system is able to extract tens of thousands of topics from millions of documents in a few hours. Besides these two applications, we also design effective ML models for hierarchical multi-label tagging of medical images and automated ICD coding.

Acknowledgments

First and foremost, I would like to thank my PhD advisor Professor Eric Xing for his great advice, encouragement, support, and help throughout my journey at CMU. Eric's exceptional insights and broad vision have played an instrumental role in helping me to pick impactful problems. He has consistently put in his time and energy in guiding me through every challenge in research, from designing models to diagnosing errors in experiments, from writing papers to giving presentations. I am also grateful to him for allowing me the freedom to do research in a diverse range of fields that I am passionate about. His enthusiasm for research, his passion for life, and his work ethic have been a great source of inspiration and will continue to shape me in the future.

I would like to express my deepest gratitude to my other thesis committee members: Professors Ruslan Salakhutdinov, Pradeep Ravikumar, Ryan Adams, and David Sontag, for their invaluable feedback that has helped to improve many parts of this thesis. The insightful discussions with Russ and Pradeep inspired several ideas in this thesis. Ryan's early work on priors for diversity in generative latent variable models is the motivation for systematically studying diversity-promoting learning in this thesis. David's sharp insights and invaluable comments steered me in the right direction in the study of ML for healthcare.

I have been very fortunate to collaborate with many brilliant friends: Qirong Ho, Ruslan Salakhutdinov, Wei Wu, Barnabas Poczos, Aarti Singh, James Zou, Yaoliang Yu, Jun Zhu, Jianxin Li, Jin Kyu Kim, Hongbao Zhang, Baoyu Jing, Devendra Sachan, Yuntian Deng, Yi Zhou, Haoran Shi, Yichen Zhu, Hao Zhang, Shizhen Xu, Haoyi Zhou, Shuai Zhang, Yuan Xie, Yulong Pei, among many others. It has always been a great pleasure and a valuable learning experience to brainstorm ideas, design models and algorithms, debug code, and write papers with these talented people and I am proud of the work we have done together over the last 5 years.

I am also very thankful to the Sailing Lab and Machine Learning Department for fostering a friendly and wonderful environment for research and life. I would like to thank Diane Stidle, Michelle Martin, Mallory Deptola and the entire MLD staff for their warm help and kind support. I deeply appreciate many of CMU faculties, for their wonderful courses and talks.

Lastly and most importantly, I am extremely grateful to my family. I could not have done this without the constant encouragement, unwavering support, and endless love from my parents.

Contents

List of Figures

List of Tables

Chapter 1

Introduction

1.1 Thesis Introduction and Scope

With the widespread adoption of electronic health records (EHR) systems, and the rapid development of new technologies such as high-throughput medical imaging devices, low-cost genome profiling systems, networked and even wearable sensors, mobile applications, and rich accumulation of medical knowledge/discoveries in databases, a tsunami of medical and healthcare data has emerged. It was estimated that 153 exabytes (one exabyte equals one billion gigabytes) of healthcare data were produced in 2013 [431]. In 2020, an estimated 2314 exabytes will be produced. From 2013 to 2020, an overall rate of increase is at least 48 percent annually [431]. In addition to the sheer volume, the complexity of healthcare data is also overwhelming. As shown in Figure 1.1, it includes clinical notes, medical images, lab values, vital signs, etc., coming from multiple heterogeneous modalities including texts, images, tabular data, time series, graph and so on. The rich clinical data is becoming an increasingly important source of holistic and detailed information for both healthcare providers and receivers. Collectively analyzing and digesting these rich information generated from multiple sources; uncovering the health implications, risk factors, and mechanisms underlying the heterogeneous and noisy data records at both individual patient and whole population levels; making clinical decisions including diagnosis, triage, and treatment thereupon, are now routine activities expected to be conducted by medical professionals including physicians, nurses, pharmacists and so on. As the amount and complexity of medical data are rapidly growing, these activities are becoming increasingly more difficult for human experts. The information overload makes medical analytics and decisions-making time-consuming, error-prone, suboptimal, and less-transparent. As a result, physicians, patients, and hospitals suffer a number of pain points, quality-wise and efficiency-wise. For example, in terms of quality, 250,000 Americans die each year from medical errors, which has become the third leading cause of death in the US [90]. 12 million Americans are misdiagnosed each year [305]. Preventable medication errors impact more than 7 million patients and cost almost $21 billion annually [87]. 15 to 25 percent of patients are readmitted within 30 days and readmissions are costly (e.g., $41.3 billion in 2011) [158]. In terms of inefficiency, patients wait on average 6 hours in emergency rooms [12]. Nearly 400,000 patients wait 24 hours or more. Physicians spend only 27 percent of their office day on direct clinical face time with patients [306]. The

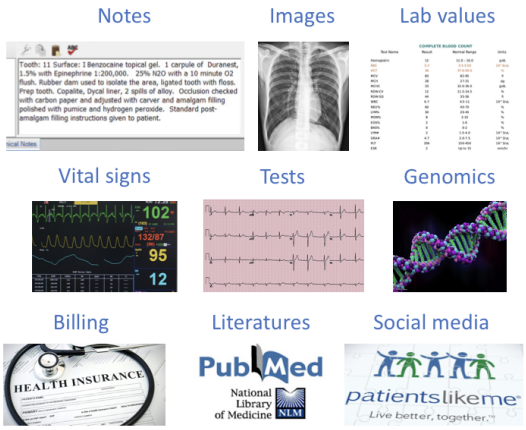

Figure 1.1: Different types of clinical data.

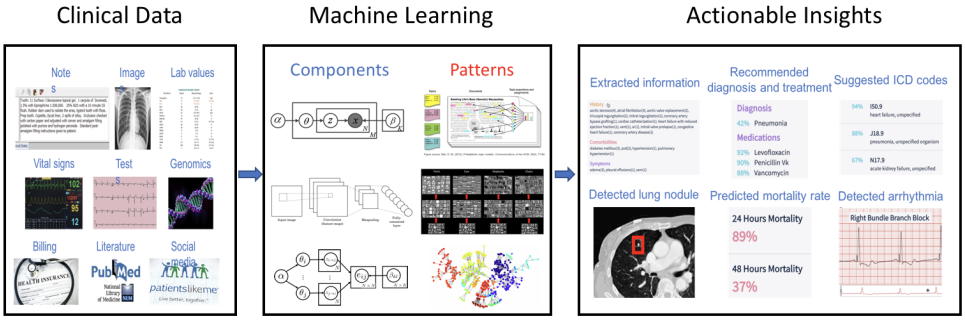

Figure 1.2: Thesis goal: develop machine learning algorithms and systems to transform the raw clinical data into actionable insights.

U.S. healthcare system wastes $750 billion annually due to unnecessary services, inefficient care delivery, excess administrative costs, etc [308].

The advancement of machine learning (ML) technology opens up opportunities for next generation computer-aided medical data analysis and data-driven clinical decision making, where machine learning algorithms and systems can be developed to automatically and collectively digest massive medical data such as electronic health records, images, behavioral data, and the genome, to make data-driven and intelligent diagnostic predictions. An ML system can automatically analyze multiple sources of information with rich structure; uncover the medically-meaningful hidden concepts from low-level records to aid medical professionals to easily and concisely understand the medical data; and create a compact set of informative diagnostic procedures and treatment courses and make healthcare recommendations thereupon.

In this thesis, we aim at leveraging the power of machine learning in automatically distilling insights from large-scale heterogeneous data for automatic smart data-driven medical predictions, recommendations, and decision-making, to assist physicians and hospitals in improving the quality and efficiency of healthcare (Figure 1.2). We develop machine learning algorithms

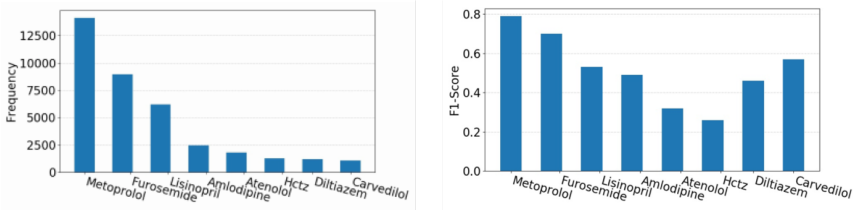

Figure 1.3: (Left) Frequencies of 8 antihypertensive medications. (Right) F1 scores on individual medications in a discharge medication prediction task.

and systems that turn the raw clinical data into actionable insights. Specifically, we focus on the following clinical applications: retrieving similar patients [376], discovering medical topics from large-scale texts, hierarchical tagging of medical images, and automatically assigning ICD codes [378].

During the development of these algorithms, we identify several fundamental issues.

- **How to better capture infrequent patterns?** At the core of ML-based healthcare is to discover the latent patterns (e.g., topics in clinical notes, disease subtypes, phenotypes) underlying the observed clinical data. Under many circumstances, the frequency of patterns is highly imbalanced [376]. Some patterns have very high frequency while others occur less frequently. For instance, Figure 1.3(Left) shows the frequencies that 8 antihypertensive medications are prescribed. Metoprolol and furosemide are used very frequently while the rest less often. Existing ML models lack the capability of capturing infrequent patterns. We applied a convolutional neural network model to classify the aforementioned 8 antihypertensive medications [393]. Figure 1.3(Right) shows the F1 scores (the higher, the better) on individual medications. As can be seen, while achieving high F1 scores on frequent medications, CNN performs less well on the infrequent ones. Such a deficiency of existing models possibly results from the design of their objective function used for training [371]. For example, a maximum likelihood estimator would reward itself by modeling the frequent patterns well as they are the major contributors to the likelihood function. On the other hand, infrequent patterns contribute much less to the likelihood, thereby it is not very rewarding to model them well and they tend to be ignored. Figure 1.4(Left) presents an illustration. Since dominant patterns denoted by these two large circles are the major contributors of the likelihood function, ML models would allocate a number of triangles to cover the large circles as best as possible. On the other hand, the infrequent patterns denoted by the small circles contribute less to the likelihood function, thereby it is not very rewarding to model them well and ML models tend to ignore them. Infrequent patterns are of crucial importance in clinical settings. For example, many infrequent diseases are life-threatening [363]. It is critical to capture them.
- **How to alleviate overfitting?** In certain clinical applications, the number of medical records available for training is limited. For example, when training a diagnostic model for an infrequent disease, we typically have no access to a sufficiently large number of patient cases due to the rareness of this disease. Under such circumstances, overfitting easily happens: the trained model works well on the training data but generalizes poorly on unseen patients. To alleviate overfitting, we need to incorporate prior beliefs of the model structure.

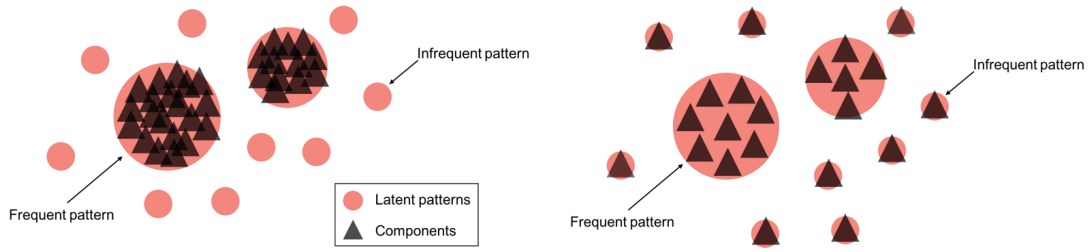

Without diversification

With diversification

Figure 1.4: In this illustration, circles denote patterns and triangles denote the components. The size of a circle is proportional to the frequency of the corresponding pattern. (Left) Without diversification, ML models allocate a lot of components to cover the frequent patterns as best as possible. For the infrequent patterns, since they are weak signals, ML models tend to ignore them. (Right) With diversification, components that are originally cluttered around the frequent patterns are pushed apart. They diversely spread out. Some components that are originally cluttered around the frequent patterns are spared to cover the infrequent patterns.

- **How to improve interpretability?** Being interpretable and transparent is a must for an ML model to be willingly used by human physicians. Oftentimes, the patterns extracted by existing ML methods have a lot of redundancy and overlap [350], which are ambiguous and difficult to interpret. For example, in computational phenotyping from EHRs, it is observed that the learned phenotypes by the standard matrix and tensor factorization [350] algorithms have much overlap, causing confusion such as two similar treatment plans are learned for the same type of disease [350]. It is necessary to make the learned patterns distinct and interpretable.
- **How to compress model size without sacrificing modeling power?** In clinical practice, making a timely decision is crucial for improving patient outcome. To achieve time efficiency, the size (specifically, the number of weight parameters) of ML models needs to be kept small. However, reducing the model size, which accordingly reduces the capacity and expressivity of this model, typically sacrifice modeling power and performance. It is technically appealing but challenging to compress model size without losing performance.
- **How to efficiently learn large-scale models?** In certain healthcare applications, both the model size and data size are large, incurring substantial computation overhead that exceeds the capacity of a single machine. It is necessary to design and build distributed systems to efficiently train such models.

To solve the first four problems, we study *diversity-promoting learning* (DPL) [223, 367, 369, 371, 372, 373, 376, 379, 380, 381]. Many ML models are equipped with *components*, each aiming at capturing a latent pattern and is parameterized by a weight vector. For instance, in a topic model [49], the components are referred to as *topics*, aiming at discovering the semantics underlying documents. Each topic is associated with a multinomial vector. In neural networks, the components are called *hidden units*. Each unit, parameterized by a weight vector, is desired to capture a latent feature. DPL aims at encouraging the component vectors to be "diverse". First,

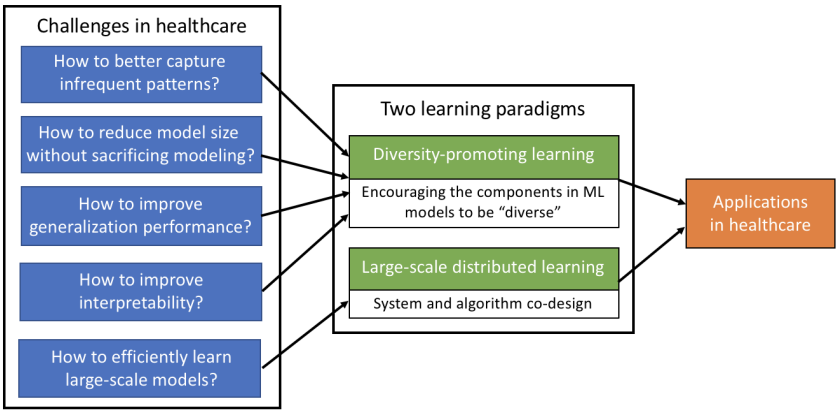

Figure 1.5: Thesis scope. To address the first four challenges, we study diversity-promoting learning, which encourages the components in ML models to be diverse. To address the fifth challenge, we study large-scale distributed learning by exploiting a system and algorithm co-design approach. Then we apply the methods developed in these two learning paradigms to solve problems in heathcare.

regarding better capturing infrequent patterns, if the model components are biased to be far apart from each other, then one would expect that such components will tend to be less overlapping and less aggregated over frequent patterns. They diversely spread out to different regions in the pattern space and give the infrequent patterns a better chance to be captured [369], as illustrated in Figure 1.4(Right). Second, regarding alleviating overfitting, promoting diversity imposes a structural constraint on model parameters, which reduces the model capacity and therefore improves generalization performance on unseen data [372]. Third, regarding interpretability, if components are encouraged to be distinct from each other and non-overlapping, then it would be cognitively easy for a human to associate each component to an object or concept in the physical world [350]. Fourth, regarding performance-lossless model-compression, "diversified" components bear less redundancy and are mutually complementary, making it possible to capture information sufficiently well with a small set of components [367]. To address the fifth problem, we design efficient distributed ML systems [370, 377, 384, 411], by exploiting a system-algorithm co-design approach: system design is tailored to the unique mathematical properties of ML algorithms, and algorithms can be re-designed to better exploit the system architecture. We apply the developed diversity-promoting learning techniques and distributed ML systems to healthcare applications. Figure 1.5 summarizes the scope of this thesis.

1.2 Contributions

Overall, the contributions of this thesis are made in three areas: diversity-promoting learning, large-scale distributed learning, and ML for healthcare.

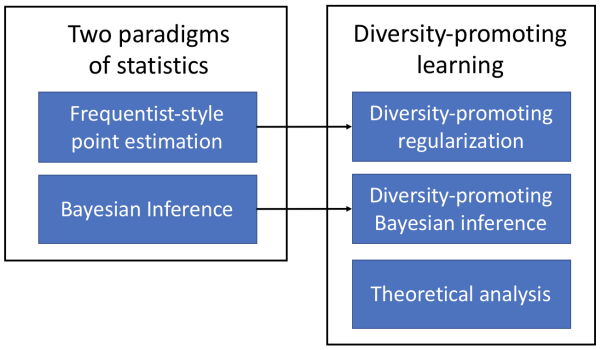

Figure 1.6: Study scope of diversity-promoting learning.

1.2.1 Diversity-promoting Learning

This thesis work represents the first one that systematically studies this new learning paradigm: diversity-promoting learning. In statistics, there are two paradigms: frequentist-style point estimation and Bayesian inference. Our study of diversity-promoting learning is tailored to these two paradigms. In frequentist-style point estimation, we develop empirically effective, theoretically analyzable, and computationally efficient regularization approaches to encourage model components to be diverse. In Bayesian inference, we design Bayesian priors that effectively entail an inductive bias of "diversity" among a finite or infinite number of components and develop efficient posterior inference algorithms. Finally, we provide theoretical analysis regarding the benefits of promoting diversity. Figure 1.6 summarizes the study scope of diversity-promoting learning.

Diversity-promoting Regularization

In diversity-promoting regularization, we made the following contributions.

- We propose to characterize "diversity" from two perspectives: uncorrelation and evenness, based on which we define a uniform eigenvalue regularizer (UER) [376]. Compared with previous diversity-promoting regularizers, the UER is able to measure "diversity" in a global way, is insensitive to vector scaling, and is amenable for computation. We apply UER to distance metric learning [383] and long short-term memory networks [163] and develop an efficient projected gradient descent algorithm. In various experiments, we demonstrate the effectiveness of UER in better capturing infrequent patterns, reducing model size without sacrificing modeling power, and improving generalization performance.
- Considering UER is nonconvex which presents great challenges for optimization, we develop a family of convex diversity-promoting regularizers [379] based on the Bregman matrix divergence (BMD) [100], where the global optimal is guaranteed to be achievable. We apply these regularizers to distance metric learning and develop an efficient proximal gradient algorithm [270]. In experiments, we demonstrate the advantages of the convex BMD (CBMD) regularizers over the nonconvex counterparts. First, because the global optimal solution is achievable, CBMD obtains better modeling performance. Second, unlike nonconvex regular-

izers that need multiple (random) restarts for a better local optimal, CBMD runs only once, hence is computationally more efficient.

- While UER and convex BMD regularizers are empirically effective in alleviating overfitting, a theoretical analysis of their effectiveness is difficult to establish. In light of this, we propose a new regularization approach: *angular constraints* (ACs) [372], that is both empirically effective and theoretically analyzable. The analysis reveals that properly manipulating the ACs can achieve the lowest generalization errors. We develop an efficient algorithm based on ADMM [52] and demonstrate the empirical effectiveness of ACs in alleviating overfitting of deep neural networks and sparse coding [266]. A connection is also made between the ACs and the log-determinant divergence regularizer [379].
- We extend the study of diversity-promoting learning from finite-dimensional vectors to infinite-dimensional functions in the reproducing kernel Hilbert space (RKHS) [374]. We define Bregman matrix divergence regularizers on RKHS functions and solve the regularized problems using functional gradient descent [89]. On two case studies – kernel sparse coding [120] and kernel distance metric learning [335] – we demonstrate the merits of promoting diversity in RKHS.
- We combine diversity-promoting regularization with sparsity-promoting regularization, which jointly bring in an effect of nonoverlapness [380], for the sake of selecting less-overlapped variables in ML problems that have multiple responses. We propose an LDD-L1 regularizer and derive efficient coordinate descent algorithms. Experiments on four ML models demonstrate the effectiveness of LDD-L1 in selecting less-overlapped variables and improving generalization performance.

Diversity-promoting Bayesian Learning

In diversity-promoting Bayesian learning, we made the following contributions.

- We define a mutual angular process (MAP) [381], which is a Bayesian prior biased towards components that have large mutual angles. This prior facilitates the development of posterior inference algorithms based on variational inference [340], which is usually more efficient than sampling-based [127] algorithms. We apply this prior to a Bayesian mixture of experts model [354] and demonstrate its effectiveness and efficiency in experiments.
- To promote diversity in Bayesian nonparametric models [111], we extend the MAP to *infinite MAP* (IMAP) which encourages infinitely many components to have large mutual angles. We apply the IMAP to an infinite latent feature model [143] and develop a posterior inference algorithm based on slicing sampling [328] and Riemann manifold Hamiltonian Monte Carlo [129]. Experiments demonstrate the effectiveness of IMAP.

Theoretical Analysis

We performed various analysis to formally understand the effectiveness of promoting diversity and made the following contributions.

- We analyze why the nonconvex Bregman matrix divergence (BMD) regularizers can better capture infrequent patterns [379]. In the context of distance metric learning, we define an

imbalance factor (the lower, the better) to characterize the performance on infrequent patterns. The analysis shows that decreasing the BMD regularizers can reduce the upper bound of the imbalance factor and hence achieve better performance on infrequent patterns.

- We analyze how the angular constraints (ACs) affect the generalization error (which is the sum of estimation error and approximation error) of neural networks [372]. The analysis reveals that a stronger regularization reduces estimation errors and increases approximation errors. Properly tuning the regularization strength can achieve the best tradeoff among these two types of errors and accordingly the optimal generalization performance on unseen data.
- We analyze how the nonconvex [374, 380] and convex [379] BMD regularizers affect the estimation error of distance metric learning. The analysis shows that decreasing these regularizers can effectively reduce the estimation error bound.

1.2.2 Large-scale Distributed Learning

The second part of this thesis studies large-scale learning. We design efficient distributed ML systems by exploiting a system-algorithm co-design approach. Specifically, inspired by a mathematical property – the sufficient factor (SF) property [370] – that is shared by many ML models parameterized by matrices, we design a peer-to-peer system [370, 377], that significantly reduces communication and fault tolerance costs. We made the following contributions.

- For efficient communication, we propose (1) *sufficient factor broadcasting* (SFB) [370] which transfers small-sized vectors among machines for the synchronization of matrix-form parameters, (2) *random multicast* [377] where each machine randomly selects a subset of machines to communicate within each clock, (3) *SF selection* [377] that selects a subset of most representative SFs to communicate. These techniques greatly reduce the number of network messages and the size of each message.
- For efficient fault tolerance, we propose to represent the parameter matrix using SFs and propose an incremental SF checkpoint (ISFC) scheme [377]. ISFC continuously saves new SFs computed at each clock to stable storage and greatly reduces disk IO, avoids compute-cycle waste, and provides fine-grained (per-clock) rollbacks.
- We provide an easy-to-use programming interface [377] which can automatically identify the computation of SFs and the transformation from SFs to update matrices.
- We conduct convergence analysis of the SFB computation model [370]. The analysis shows that though synchronized in a decentralized manner, the parameter replicas on different machines converge to the same optimal.
- We evaluate our system on three representative ML models and show that it achieves high efficiency and scales well with more machines.
- For ML models having both small-sized and large-sized update matrices, we propose a *structure-aware message passing* (SAMP) protocol [411], which is a hybrid communication approach between the centralized parameter server (PS) [226, 355] and decentralized SFB. PS and SFB are utilized to transfer small and large matrices respectively. The protocol leverages the best of these two communication schemes and significantly minimizes the communication cost. We evaluate this protocol on convolutional neural networks. Un-

der 8 GPU machines, SAMP improves the speedup from 3.9 to 5.7 on AlexNet [203] and from 3.8 to 4.8 on GoogLeNet.

1.2.3 ML for Healthcare

In the third part of this thesis, we design ML models and apply the diversity-promoting and large-scale learning techniques developed in the first two parts to address critical problems in healthcare. We made the following contributions.

- We apply our diversity-promoting distance metric learning model [379] for similar-patient retrieval and demonstrate its effectiveness on two electronic health records datasets. Thanks to the ability of our method in better capturing infrequent patterns, better retrieval performance is achieved on infrequent diseases. By promoting diversity, the dimension of latent representations (accordingly, the time complexity of retrieval) can be reduced, without sacrificing the retrieval accuracy. This enables fast and accurate retrieval, which facilitates timely and sound clinical decision-making. Besides, our diversity-promoting regularizer effectively reduces overfitting.
- We implement a distributed topic model (TM) on our Orpheus system [377] and apply it to large-scale medical-topic discovery. Leveraging the sufficient factor (SF) property of the TM, Orpheus performs SF broadcasting and incremental SF checkpoint to significantly reduce communication and fault tolerance costs. Using 34 CPU machines, the Orpheus-TM is able to learn 50K topics from 8.2M PubMed documents (vocabulary size is 141K) in 5.4 hours, which is much faster than FlexiFaCT [207] (33.9 hours) – a Hadoop-based model-parallel system, and Bosen [355] (23.5) – a parameter server based data-parallel system.
- To solve the problem that medical images are difficult to index and search due to the lack of textual tags, we study multi-label hierarchical tagging of images. We propose an adversarial learning [134] strategy to capture the correlations among medical concepts, a tree-of-sequences LSTM model [378] to explore the hierarchical structure of the concept ontology, and a contextual attention model to localize abnormal regions. Experiments on a pathology dataset and a radiology dataset demonstrate the effectiveness of our methods.
- We study the automatic assignment of ICD codes based on physicians' free-form diagnosis descriptions, to reduce coding errors and costs [378]. A neural architecture is proposed, which consists of four ingredients: (1) tree-of-sequences LSTM encoding for simultaneously capturing the semantics and hierarchical relationship of codes, (2) adversarial learning for reconciling the different writing styles of diagnosis descriptions (DDs) and code descriptions (CDs), (3) isotonic constraints for incorporating the importance order among the assigned codes, and (4) attentional matching for performing many-to-one and one-to-many mappings from DDs to CDs. We demonstrate the effectiveness of the proposed methods on a clinical datasets with 59K patient visits.

1.3 Related Works

In this section, we present a general review of related works in diversity-promoting learning, large-scale distributed learning, and machine learning for healthcare. Additional related works are reviewed in individual sections.

1.3.1 Diversity-promoting Learning

Diversity promoting regularization has been studied in ensemble learning [402], latent space modeling [365, 369, 429], and classification [242]. In ensemble learning, several studies [27, 209, 271, 402] explore how to select a diverse subset of base classifiers or regressors, with the aim to improve generalization performance. In latent space modeling, several works [29, 82, 429] encourage components to be mutually different for the sake of reducing redundancy and alleviating overfitting. In multi-way and hierarchical classification, two works [177, 242, 420] promote "diversity" among the coefficient vectors of classifiers, for the sake of ensuring model continuity and exploiting the semantic relationship embedded in the class hierarchy. In these works, various diversity-promoting regularizers have been proposed, based on determinantal point process [204, 429], cosine similarity [29, 369, 402] and matrix covariance [82]. In the sequel, we present a brief review of them.

Determinantal point process (DPP) DPP [204] was used by [246, 429] to encourage the topic vectors in latent Dirichlet allocation [49], Gaussian mean vectors in Gaussian mixture model and hidden units in neural network to be "diverse". DPP is defined over K vectors: $p(\{\mathbf{a}_i\}_{i=1}^K) \propto \det(\mathbf{L})$, where $\mathbf{L}$ is a $K \times K$ kernel matrix with $L_{ij} = k(\mathbf{a}_i, \mathbf{a}_j)$ and $k(\cdot, \cdot)$ is a kernel function. $\det(\cdot)$ denotes the determinant of a matrix. A configuration of $\{\mathbf{a}_i\}_{i=1}^K$ with larger probability is deemed to be more "diverse". The underlying intuition is that: $\det(\mathbf{L})$ represents the volume of the parallelepiped formed by vectors in the feature space associated with the kernel k. If these vectors are more mutually different, the volume is larger, which results in a larger $p(\{\mathbf{a}_i\}_{i=1}^K)$. The shortcoming of DPP is that it is sensitive to vector scaling. Enlarging the magnitudes of vectors results in larger volume, but does not essentially change the "diversity" of vectors.

Pairwise cosine similarity Several works [29, 369, 402] define diversity-promoting regularizers based on the pairwise cosine similarity among component vectors: smaller cosine similarity scores imply that the components are more different from each other, hence are more "diverse". Cosine similarity is preferred over other distances or similarity measures because of its insensitivity to geometry transformations of vectors such as scaling, translation, and rotation. Given K component vectors, the cosine similarity s_{ij} between each pair of components $\mathbf{a}_i$ and $\mathbf{a}_j$ is computed as $s_{ij} = \mathbf{a}_i \cdot \mathbf{a}_j / (\|\mathbf{a}_i\|_2 \|\mathbf{a}_j\|_2)$. Then these scores are aggregated to measure the overall "diversity" of all components. In [402], these scores are aggregated as $\sum_{1 \leq i < j \leq K} (1 - s_{ij})$. In [29], the aggregation is performed as $-\log(\frac{1}{K(K-1)} \sum_{1 \leq i < j \leq K} \beta |s_{ij}|)^{\frac{1}{\beta}}$ where $\beta > 0$. In [369], the aggregated score is defined as the mean of $\arccos(|s_{ij}|)$ minus the variance of $\arccos(|s_{ij}|)$. The variance term is utilized to encourage the vectors to evenly spread out to different directions. Xie et al. [365] define the regularizer as $\sum_{1 \leq i < j \leq m} k(\mathbf{a}_i, \mathbf{a}_j)$ where $k(\cdot, \cdot)$ is a kernel function.

These regularizers are applied to classifiers ensemble, neural networks, and restricted Boltzmann machine [369]. These approaches can only capture second-order (pairwise) relations among vectors. Representing higher-order relations such as how to measure the "diversity" of three vectors as a whole (without reducing to pairwise dissimilarity) is beyond the capability of these methods.

Covariance Two works [82, 242] defined diversity-promoting regularizers based on matrix covariance. Malkin and Bilmes [242] compute the covariance matrix $\mathbf{C}$ of the component vectors: $\mathbf{C} = \frac{1}{K}\sum_{i=1}^{K}(\mathbf{a}_i - \boldsymbol{\mu})(\mathbf{a}_i - \boldsymbol{\mu})^\top$ where $\boldsymbol{\mu} = \frac{1}{K}\sum_{i=1}^{K}\mathbf{a}_i$, then encourage diversity by maximizing the determinant of $\mathbf{C}$. Similar to the DPP, this regularizer is sensitive to vector scaling. Cogswell et al. [82] designed a regularizer to reduce the correlation among hidden units in neural networks. Given N activation vectors $\{\mathbf{h}_i\}_{i=1}^{N}$ computed over N data samples where different dimensions of each vector correspond to different hidden units, they compute the sample covariance matrix of hidden units $\mathbf{C} = \frac{1}{N}\sum_{i=1}^{N}(\mathbf{h}_i - \boldsymbol{\mu})(\mathbf{h}_i - \boldsymbol{\mu})^\top$ where $\boldsymbol{\mu} = \frac{1}{N}\sum_{i=1}^{K}\mathbf{h}_i$ and define the regularizer as $\|\mathbf{C}\|_F^2 - \|\text{diag}(\mathbf{C})\|_2^2$, which encourages the off-diagonal entries of $\mathbf{C}$, i.e., the covariance between different hidden units, to be small. This regularizer is defined over intermediate variables (which are hidden activations in the neural network case) and influences the weight parameters indirectly. The number of intermediate variables could be much larger than that of weight parameters (which is the case in convolutional neural networks). This renders this regularizer computationally inefficient.

1.3.2 Distributed Learning

Many distributed ML systems have been built recently, including (1) dataflow systems such as Hadoop-based Mahout [93] and Spark-based MLlib [407]; (2) graph computation frameworks such as Pregel [241] and GraphLab [132]; (3) parameter server (PS) architectures such as DistBelief [93], Project Adam [78], ParameterServer [226], Bosen PS [355], and GeePS [85]; (4) hybrid systems such as TensorFlow [13] and MXNet [73]. These systems explore the tradeoffs among correctness of computation, ease of programmability, and efficiency of execution. Hadoop-Mahout and Spark-MLlib provide an easy-to-use MapReduce-style programming interface and strictly guarantee computational exactness using BSP. However, their speed of execution is typically slower than ML-specialized systems, partially because (1) BSP is sensitive to stragglers [162]; (2) parameter state is immutable, which does not support fast in-place update. Frameworks based on graph abstractions [132, 241] support fine-grained scheduling of computations and flexible consistency models, which contribute to high efficiency. However, to run on these frameworks, an ML model needs to be abstracted as a graph, which is very difficult to achieve for MPMs. Parameter server architectures [78, 85, 94, 226, 355] and hybrid systems [13, 73] (partially adopting PS) offer a flexible and easy-to-use *distributed shared memory* programming abstraction and possess high efficiency by allowing mutable parameter states and in-place updates, fine-grained partitioning of computation, and flexible consistency models. However, when used to train MPMs, these systems communicate large matrices, which incur high communication overhead.

Peer-to-peer (P2P) architectures have been investigated in distributed ML [222, 353, 370, 411]. Li et al. [222] propose to synchronize parameter replicas by exchanging parameter updates

in a P2P manner to simplify fault-tolerance. Watcharapichat et al. [353] design a decentralized architecture to exchange partial gradient of deep neural networks among machines, for the sake of saturating cluster resources. These two works transmit matrices in the network and do not leverage the SVs to reduce communication cost.

1.3.3 ML for Healthcare

With the prosperity of healthcare data such as electronic health record (EHR), genomic data, patient behavior data and the growing need of extracting knowledge and insights from these data, ML-based data-driven healthcare analytics have received much attention recently.

Predictive modeling Predictive modeling in data-driven healthcare is concerned about building machine learning models to predict diagnosis, prognosis, patient risk factors, readmission, disease onset and so on. Wang et al. [344] studied disease prognosis by leveraging the information of clinically similar patient cohorts which are retrieved using a local spline regression based similarity measure. Zhou et al. [422] proposed a top-k stability selection method to select the most informative features for patient risk prediction. Chen et al. [72] developed a cloud-based predictive modeling system for pediatric asthma readmission prediction. Choi et al. [79] developed a temporal model using recurrent neural networks to predict the diagnosis and medication categories for a subsequent visit. Razavian et al. [287] developed predictive models to predict the onset and assess the risk factors of type 2 diabetes. Razavian et al. [288] used LSTM [163] networks and convolutional networks for multi-task prediction of disease onset.

Natural language processing and understanding of clinical notes Clinical notes contain rich medical information. Many studies have developed natural language processing and machine learning methods to extract useful information from free-form clinical texts. Chen et al. [75] studied word sense disambiguation using support vector machine and active learning. Tang et al. [324] developed a temporal information extraction system that can identify events, temporal expressions, and their temporal relations in clinical texts. Tang et al. [323] studied clinical entities recognition in hospital discharge summaries using structural support vector machines. Gobbel et al. [130] designed a tool to assist in the annotation of medical texts, which leverages interactive training to reduce the annotation time without introducing bias. Tang et al. [325] performed a comparison study of three types of word representations, including clustering-based representation, distributional representation, and word embeddings, for biomedical named entity recognition. Halpern et al. [150] developed a bipartite probabilistic graphical models for joint prediction of clinical conditions from the electronic medical records.

Computational phenotyping Computational phenotyping, which extracts high-level clinical concepts and patterns from EHRs, have been widely investigated. Chen et al. [75] integrated an uncertainty sampling active learning approach with support vector machine for high-throughput phenotyping. Doan et al. [103] developed an information retrieval system that consists of text processing tools to standardize phenotype variables and information retrieval tools that support

queries from users and return ranked results. Ho et al. [161] developed a non-negative tensor factorization method to derive phenotype candidates with minimal human supervision. Wang et al. [350] proposed a constrained non-negative tensor factorization and completion method for phenotyping which incorporates guidance constraints to align with existing medical knowledge, and pairwise constraints for obtaining less-overlapped phenotypes. Halpern et al. [149] developed a phenotype library that uses both structured and unstructured data from the EHRs to represent patients for real-time clinical decision support. Joshi et al. [187] proposed a non-negative matrix factorization method augmented with domain specific constraints for automated phenotyping of multiple co-occurring medical conditions.

Patient similarity measure Effectively measuring the similarity between patients can help with a number of downstream applications such as diagnosis, prognosis, and treatment. Ebadollahi et al. [106] leveraged inter-patient similarity for retrieving patients who display similar trends in their physiological time-series data. Wang et al. [343] proposed a composite distance integration approach to combine the individual distance metrics learned from different physicians into a globally consistent metric. Sun et al. [315] proposed a locally supervised metric learning approach to learn a generalized Mahalanobis distance that is tailored toward physician feedback and introduce an interactive metric learning method that can incrementally update an existing metric based on streaming feedback. Ng et al. [261] applied distance metric learning to find clinically similar patients and trained personalized predictive models on the retrieved patients.

Disease progression modeling Disease progression modeling is instrumental in early diagnosis and personalized care. Jackson et al. [173] developed a hidden Markov model for simultaneously estimating the transition rates and the probabilities of stage misclassification. Zhou et al. [421] proposed a fused group lasso approach for disease progression modeling with known biomarkers. Exarchos et al. [108] developed a dynamic Bayesian network to model the progression of coronary atherosclerosis. Wang et al. [348] proposed a probabilistic disease progression model that learns from discrete-time observations with non-equal intervals and discovers the full progression trajectory from a set of incomplete records.

Chapter 2

Diversity-promoting Learning I – Regularization

In this chapter, we study diversity-promoting learning in the context of frequentist statistics, by developing regularization techniques.

Figure 2.1 shows an overview of the studies of diversity-promoting regularization. We begin with defining a uniform eigenvalue regularizer that simultaneously encourages uncorrelation and evenness among components [376]. This regularizer is nonconvex, presenting great challenges for optimization. In light of this, we develop convex Bregman matrix divergence regularizers where the global optimal is achievable [379]. While the uniform eigenvalue regularizer and the convex Bregman matrix divergence regularizers are empirically effective, theoretically they are not amenable for the analysis of generalization errors, especially the approximation errors. Therefore, we propose a new regularization approach called angular constraints [372] which are not only empirically effective, but also theoretically analyzable. These three regularizers promote diversity among finite-dimensional vectors. In the next work, we extend the study to infinite-dimensional functions in the reproducing kernel Hilbert space (RKHS) [373]. Finally, we combine diversity-promoting regularization with sparsity-promoting regularization [380], which jointly brings in an effect of reducing overlap among the supports of vectors.

2.1 Uncorrelation and Evenness: A Diversity-promoting Regularizer

We start with formally defining "diversity" [376]. Several diversity-promoting regularizers have been proposed, based upon determinantal point process [204, 429], cosine similarity [29, 369, 402], and covariance [82, 242]. While these regularizers demonstrate notable efficacy, they have certain limitations, such as sensitivity to vector scaling [242, 429], inability to measure diversity in a global manner [29, 369, 402], and computational inefficiency [82]. To address these limitations, we propose a new diversity-promoting regularizer [376] gaining inspiration from principal component analysis [185], biological diversity [240], and information theory [83]. We characterize "diversity" by considering two factors: *uncorrelation* and *evenness*. Uncorrelation is a measure of how uncorrelated the components are. Literally, less correlation is equivalent to more

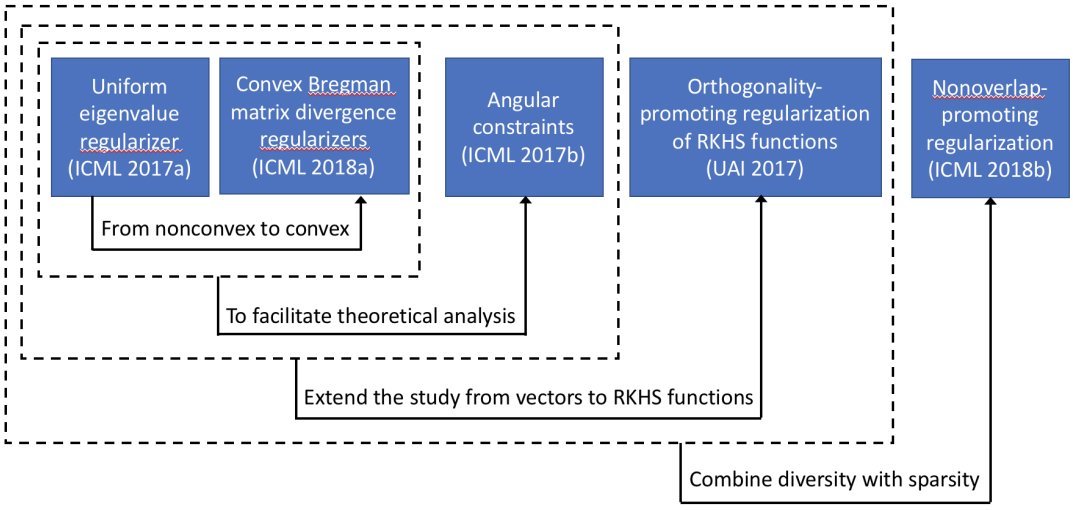

Figure 2.1: An overview of the studies of diversity-promoting regularization.

diversity. By encouraging the components to be uncorrelated, each of them can independently capture a unique pattern. Evenness is borrowed from biological diversity [240], which measures how equally important different species are in maintaining the ecological balance within an ecosystem. If no species dominates another, the ecosystem is deemed as being more diverse. Likewise, in ML, we desire the components to play equally important roles and no one dominates another, such that each component contributes significantly to the modeling of data. Specifically, we assign each component an "importance" score and encourage these scores to be even.

We study uncorrelation and evenness from a statistical perspective. The components are considered as random variables and the eigenvalues of their covariance matrix can be leveraged to characterize these two factors. First, according to the principle component analysis [185], the disparity of eigenvalues reflects the correlation among components: the more uniform the eigenvalues, the less correlated the components. Second, eigenvalues represent the variance along principal directions and can be used to measure the "importance" of components. Promoting uniform importance amounts to encouraging evenness among eigenvalues.

To promote uniformity among the eigenvalues, we encourage the discrete distribution parameterized by the normalized eigenvalues to have small Kullback-Leibler divergence with the uniform distribution, based on which, we define a *uniform eigenvalue regularizer* (UER) [376]. We apply UER to two ML models – distance metric learning (DML) [383] and long short-term memory (LSTM) network [163] – to encourage their components to be diverse and develop an efficient projected gradient descent algorithm. Experiments on healthcare, image, and text data demonstrate that UER (1) greatly improves generalization performance; (2) better captures infrequent patterns; (3) reduces model size without sacrificing modeling power; (4) outperforms other diversity-promoting regularizers.

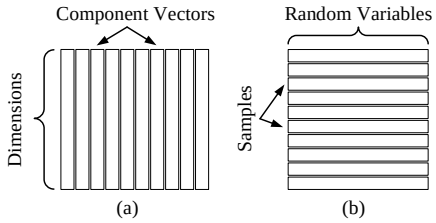

Figure 2.2: Two views of the component matrix.

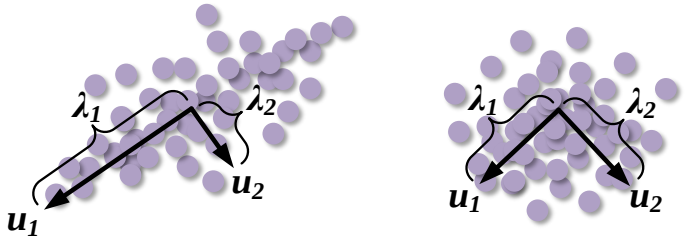

(a) $\lambda_1 > \lambda_2$ (b) $\lambda_1 \approx \lambda_2$

Figure 2.3: When the principal directions ($\mathbf{u}_1$ and $\mathbf{u}_2$) are not aligned with the coordinate axis, the level of disparity between the eigenvalues (λ_1 and λ_2) indicates the correlation between random variables (components).

2.1.1 Uniform Eigenvalue Regularizer

We start with characterizing the uncorrelation among components: treating the components as random variables and measuring their covariance which is proportional to their correlation. Let $\mathbf{A} \in \mathbb{R}^{d \times m}$ denote the component matrix where in the k-th column is the parameter vector $\mathbf{a}_k$ of component k. Alternatively, we can take a row view (Figure 2.2b) of $\mathbf{A}$: each component is treated as a random variable and each row vector $\tilde{\mathbf{a}}_i^\top$ can be seen as a sample drawn from the random vector formed by the m components. Let $\boldsymbol{\mu} = \frac{1}{d}\sum_{i=1}^{d} \tilde{\mathbf{a}}_i = \frac{1}{d}\mathbf{A}^\top \mathbf{1}$ be the sample mean, where the elements of $\mathbf{1} \in \mathbb{R}^d$ are all 1. We compute the empirical covariance matrix of the components as

$$\begin{aligned} \mathbf{G} &= \tfrac{1}{d}\textstyle\sum_{i=1}^{d}(\tilde{\mathbf{a}}_i - \boldsymbol{\mu})(\tilde{\mathbf{a}}_i - \boldsymbol{\mu})^\top \\ &= \tfrac{1}{d}\mathbf{A}^\top\mathbf{A} - (\tfrac{1}{d}\mathbf{A}^\top\mathbf{1})(\tfrac{1}{d}\mathbf{A}^\top\mathbf{1})^\top. \end{aligned} \tag{2.1}$$

Imposing the constraint $\mathbf{A}^\top\mathbf{1} = \mathbf{0}$, we have $\mathbf{G} = \frac{1}{d}\mathbf{A}^\top\mathbf{A}$. Suppose $\mathbf{A}$ is a full rank matrix and $m < d$, then $\mathbf{G}$ is a full-rank matrix with rank m.

For the next step, we show that the eigenvalues of $\mathbf{G}$ play important roles in characterizing the uncorrelation and evenness of components. We start with uncorrelation. Let $\mathbf{G} = \sum_{k=1}^{m} \lambda_k \mathbf{u}_k \mathbf{u}_k^\top$ be the eigen-decomposition where λ_k is an eigenvalue and $\mathbf{u}_k$ is the associated eigenvector. As is well known in principle component analysis [185], an eigenvector $\mathbf{u}_k$ of the covariance matrix $\mathbf{G}$ represents a principal direction of the data points and the associated eigenvalue λ_k tells the variability of points along that direction. As shown in Figure 2.3a, the larger λ_k is, the more spread out the points along the direction $\mathbf{u}_k$. When the eigenvectors (principal directions) are not

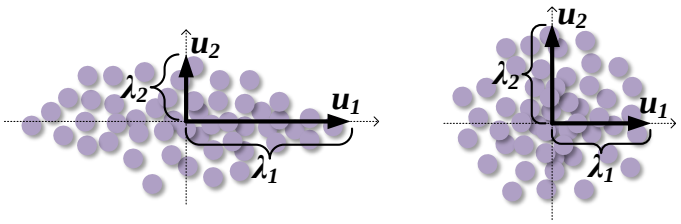

(a) $\lambda_1 > \lambda_2$ (b) $\lambda_1 \approx \lambda_2$

Figure 2.4: When the principal directions ($\mathbf{u}_1$ and $\mathbf{u}_2$) are aligned with the coordinate axis, the magnitude of eigenvalues represents the importance of components.

aligned with the coordinate axis (as shown in Figure 2.3), the level of disparity among eigenvalues indicates the level of correlation among the m components (random variables). The more different the eigenvalues are, the higher the correlation is. As shown in Figure 2.3a, λ_1 is about three times larger than λ_2 and there is a high correlation along the direction $\mathbf{u}_1$. On the other hand, in Figure 2.3b, the two eigenvalues are close to each other and the points evenly spread out in both directions with negligible correlation. In light of this, we would utilize the uniformity among eigenvalues of $\mathbf{G}$ to measure how uncorrelated the components are.

Secondly, we relate the eigenvalues with the other factor of diversity: evenness. When the eigenvectors are aligned with the coordinate axis (as shown in Figure 2.4), the components are uncorrelated. In this case, we bring in evenness to measure diversity. As stated earlier, we first need to assign each component an importance score. Since the eigenvectors are in parallel to the coordinate axis, the eigenvalues reflect the variance of components. Analogous to PCA which posits that random variables with larger variance are more important, we use variance to measure importance. As shown in Figure 2.4a, component 1 has a larger eigenvalue λ_1 and accordingly larger variability, hence is more important than component 2. According to the evenness criteria, the components are more diverse if their importance scores match, which motivates us to encourage the eigenvalues to be uniform. As shown in Figure 2.4b, the two eigenvalues are close and the two components have roughly the same variability, hence are similarly important.

To sum up, we desire to encourage the eigenvalues to be even in both cases: (1) when the eigenvectors are not aligned with the coordinate axis, they are preferred to be even to reduce the correlation of components; (2) when the eigenvectors are aligned with the coordinate axis, they are encouraged to be even such that different components contribute equally in modeling data.

Next, we discuss how to promote uniformity among eigenvalues. The basic idea is: we normalize the eigenvalues into a probability simplex and encourage the discrete distribution parameterized by the normalized eigenvalues to have small Kullback-Leibler (KL) [83] divergence with the uniform distribution. Given the eigenvalues $\{\lambda_k\}_{k=1}^m$, we first normalize them into a probability simplex $\widehat{\lambda}_k = \frac{\lambda_k}{\sum_{j=1}^m \lambda_j}$ based on which we define a distribution on a discrete random variable $X = 1, \cdots, m$ where $p(X = k) = \widehat{\lambda}_k$. In addition, to guarantee the eigenvalues are strictly positive, we require $\mathbf{A}^\top \mathbf{A}$ to be positive definite. To encourage $\{\widehat{\lambda}_k\}_{k=1}^m$ to be uniform, we encourage the distribution $p(X)$ to be "close" to a uniform distribution $q(X = k) = \frac{1}{m}$,

where the "closeness" is measured using KL divergence $KL(p||q)$:

$$\sum_{k=1}^{m} \widehat{\lambda}_k \log \frac{\widehat{\lambda}_k}{1/m} = \frac{\sum_{k=1}^{m} \lambda_k \log \lambda_k}{\sum_{j=1}^{m} \lambda_j} - \log \sum_{j=1}^{m} \lambda_j + \log m. \tag{2.2}$$

In this equation, $\sum_{k=1}^{m} \lambda_k \log \lambda_k$ is equivalent to $\text{tr}((\frac{1}{d}\mathbf{A}^\top\mathbf{A}) \log(\frac{1}{d}\mathbf{A}^\top\mathbf{A}))$, where $\log(\cdot)$ denotes matrix logarithm. To show this, note that $\log(\frac{1}{d}\mathbf{A}^\top\mathbf{A}) = \sum_{k=1}^{m} \log(\lambda_k)\mathbf{u}_k\mathbf{u}_k^\top$, according to the property of matrix logarithm. Then we have $\text{tr}((\frac{1}{d}\mathbf{A}^\top\mathbf{A}) \log(\frac{1}{d}\mathbf{A}^\top\mathbf{A}))$ equals $\text{tr}((\sum_{k=1}^{m} \lambda_k\mathbf{u}_k\mathbf{u}_k^\top)$ $(\sum_{k=1}^{m} \log(\lambda_k)\mathbf{u}_k\mathbf{u}_k^\top))$ which equals $\sum_{k=1}^{m} \lambda_k \log \lambda_k$. According to the property of matrix trace, we have $\text{tr}(\frac{1}{d}\mathbf{A}^\top\mathbf{A}) = \sum_{k=1}^{m} \lambda_k$. Then the KL divergence can be turned into a diversity-promoting uniform eigenvalue regularizer (UER):

$$\frac{\text{tr}((\frac{1}{d}\mathbf{A}^\top\mathbf{A}) \log(\frac{1}{d}\mathbf{A}^\top\mathbf{A}))}{\text{tr}(\frac{1}{d}\mathbf{A}^\top\mathbf{A})} - \log \text{tr}(\frac{1}{d}\mathbf{A}^\top\mathbf{A}), \tag{2.3}$$

subject to $\mathbf{A}^\top\mathbf{A} \succ 0$ and $\mathbf{A}^\top\mathbf{1} = 0$. In principle, the "closeness" between p and q can be measured by other distances such as the total variation distance, Hellinger distance, etc. However, the resultant formula defined on the eigenvalues (like the one in Eq.(2.2)) is very difficult (if possible) to be transformed into a formula defined on $\mathbf{A}$ (like the one in Eq.(2.3)). Consequently, it is very challenging to perform estimation of $\mathbf{A}$. In light of this, we choose to use the KL divergence.

Compared with previous diversity-promoting regularizers, UER has the following benefits: (1) It measures the diversity of all components in a holistic way, rather than reducing to pairwise dissimilarities as other regularizers [29, 369, 402] do. This enables UER to capture global relations among components. (2) Unlike determinant-based regularizers [242, 429] that are sensitive to vector scaling, UER is derived from normalized eigenvalues where the normalization effectively removes scaling. (3) UER is amenable for computation. First, unlike the decorrelation regularizer [82] that is defined over data-dependent intermediate variables and thus incurs computational inefficiency, UER is directly defined on model parameters and is independent of data. Second, unlike the regularizers proposed in [29, 369] that are non-smooth, UER is a smooth function. In general, smooth functions are more amenable for deriving optimization algorithms than non-smooth functions. The dominating computation in UER is matrix logarithm. It does not substantially increase computational overhead as long as the number of components is not too large (e.g., less than 1000).

Compared with commonly-used regularizers that are not designed for promoting diversity, such as L2, L1, and the trace norm [62], UER has the following limitations. First, it is computationally heavier. It involves eigen-decomposition that incurs $O(m^3)$ time complexity where m is the number of components. Second, in modern deep learning, most computation is conducted on GPUs. UER is not amenable for GPU implementation, which hinders its applicability. Third, it is a non-convex function, which renders the optimization of the regularized ML problems to be NP hard. Fourth, it is less amenable for theoretical analysis than L2, L1, and the trace norm.

We apply UER to promote diversity in ML models. Let $\mathcal{L}(\mathbf{A})$ denote the objective function of a model, then a UE-regularized problem can be defined as

$$\begin{array}{ll} \min_{\mathbf{A}} & \mathcal{L}(\mathbf{A}) + \lambda \left(\frac{\text{tr}((\frac{1}{d}\mathbf{A}^\top\mathbf{A}) \log(\frac{1}{d}\mathbf{A}^\top\mathbf{A}))}{\text{tr}(\frac{1}{d}\mathbf{A}^\top\mathbf{A})} - \log \text{tr}(\frac{1}{d}\mathbf{A}^\top\mathbf{A}) \right) \\ s.t. & \mathbf{A}^\top\mathbf{1} = \mathbf{0},\ \mathbf{A}^\top\mathbf{A} \succ 0. \end{array} \tag{2.4}$$

where λ is the regularization parameter. Similar to other diversity-promoting regularizers, UER is non-convex. Since $\mathcal{L}(\mathbf{A})$ in most models is non-convex, adding UER does not substantially increase difficulty for optimization.

Connection with the von Neumann entropy We make a connection between UER and the von Neumann entropy [39]. A matrix $\mathbf{M}$ is referred to as a density matrix [39] if its eigenvalues are strictly positive and sum to one, equivalently, $\mathbf{M} \succ 0$ and $\text{tr}(\mathbf{M}) = 1$. The von Neumann entropy of $\mathbf{M}$ is defined as $S(\mathbf{M}) = -\text{tr}(\mathbf{M} \log \mathbf{M})$, which is essentially the Shannon entropy [83] of its eigenvalues. If the covariance matrix $\mathbf{G}$ of components is a density matrix, then we can use its von Neumann entropy to define a UER. To encourage the eigenvalues $\{\lambda_k\}_{k=1}^m$ of $\mathbf{G}$ to be even, we directly encourage the KL divergence $\sum_{k=1}^m \lambda_k \log \frac{\lambda_k}{1/m} = \sum_{k=1}^m \lambda_k \log \lambda_k + \log m$ between the distribution parameterized by the eigenvalues (without normalization) and the uniform distribution to be small, which is equivalent to encouraging the Shannon entropy of the eigenvalues $-\sum_{k=1}^m \lambda_k \log \lambda_k$, i.e., the von Neumann entropy of $\mathbf{G}$ to be large. Then a new UER can be defined as the negative von Neumann entropy of $\mathbf{G}$: $\text{tr}((\frac{1}{d}\mathbf{A}^\top\mathbf{A}) \log(\frac{1}{d}\mathbf{A}^\top\mathbf{A}))$, subject to the constraints: (1) $\mathbf{A}^\top\mathbf{A} \succ 0$; (2) $\text{tr}(\frac{1}{d}\mathbf{A}^\top\mathbf{A}) = 1$; (3) $\mathbf{A}^\top\mathbf{1} = \mathbf{0}$. This new UER is a special case of the previous one defined in Eq.(2.3) by adding the new constraint $\text{tr}(\frac{1}{d}\mathbf{A}^\top\mathbf{A}) = 1$.

Connection with the von Neumann divergence Next we make a connection between UER and the von Neumann divergence [206]. Given two positive definite matrices $\mathbf{X}$ and $\mathbf{Y}$, their von Neumann divergence is defined as $\text{tr}(\mathbf{X}\log\mathbf{X} - \mathbf{X}\log\mathbf{Y} - \mathbf{X} + \mathbf{Y})$, which measures the closeness between the two matrices. Given two vectors $\mathbf{x}, \mathbf{y} \in \mathbb{R}^m$, their generalized KL divergence can be defined as $\sum_{k=1}^m x_k \log(\frac{x_k}{y_k}) - (x_k - y_k)$, which measures the closeness between two vectors. To encourage uniformity among the eigenvalues of the covariance matrix $\mathbf{G}$, we can decrease the generalized KL divergence between these eigenvalues and an all-1 vector:

$$\sum_{k=1}^m \lambda_k \log(\frac{\lambda_k}{1}) - (\lambda_k - 1) = \text{tr}((\frac{1}{d}\mathbf{A}^\top\mathbf{A}) \log(\frac{1}{d}\mathbf{A}^\top\mathbf{A})) - \text{tr}(\frac{1}{d}\mathbf{A}^\top\mathbf{A})) + m, \tag{2.5}$$

which is the von Neumann divergence between $\mathbf{G}$ and an identity matrix. Hence, encouraging uniformity among eigenvalues can be achieved by making $\mathbf{G}$ close to an identity matrix based on the von Neumann divergence.

2.1.2 Case Studies

In this section, we apply the uniform eigenvalue regularizer to promote diversity in two ML models: distance metric learning (DML) [383] and long short-term memory (LSTM) [163] networks.

Distance metric learning Given data pairs either labeled as "similar" or "dissimilar", DML [92, 146, 383] aims at learning a distance metric under which similar pairs would be placed close to each other and dissimilar pairs are separated apart. The learned distance can benefit a wide range of tasks, including retrieval, clustering, and classification. Following [357], we define the distance metric between $\mathbf{x}, \mathbf{y} \in \mathbb{R}^d$ as $\|\mathbf{A}^\top\mathbf{x} - \mathbf{A}^\top\mathbf{y}\|_2^2$ where $\mathbf{A} \in \mathbb{R}^{d\times m}$ is a parameter matrix

whose column vectors are called components. Built upon the DML formulation in [367], an uniform-eigenvalue regularized DML (UE-DML) problem can be formulated as

$$\begin{aligned} \min_{\mathbf{A}} \quad & \sum_{(\mathbf{x},\mathbf{y})\in\mathcal{S}} \|\mathbf{A}^\top\mathbf{x}-\mathbf{A}^\top\mathbf{y}\|_2^2 + \sum_{(\mathbf{x},\mathbf{y})\in\mathcal{D}} \max(0, 1-\|\mathbf{A}^\top\mathbf{x}-\mathbf{A}^\top\mathbf{y}\|_2^2) \\ & +\lambda\left(\frac{\mathrm{tr}((\frac{1}{d}\mathbf{A}^\top\mathbf{A})\log(\frac{1}{d}\mathbf{A}^\top\mathbf{A}))}{\mathrm{tr}(\frac{1}{d}\mathbf{A}^\top\mathbf{A})} - \log\mathrm{tr}(\tfrac{1}{d}\mathbf{A}^\top\mathbf{A})\right) \\ s.t. \quad & \mathbf{A}^\top\mathbf{1}=\mathbf{0},\ \mathbf{A}^\top\mathbf{A}\succ 0, \end{aligned} \tag{2.6}$$

where $\mathcal{S}$ and $\mathcal{D}$ are the set of similar and dissimilar pairs respectively. The first and second term in the objective function encourage similar pairs to have small distances and dissimilar pairs to have large distances respectively. The learned metrics are applied for information retrieval.

Our UE-DML method is related to the matching networks (MNs) Vinyals et al. [339] used for one shot learning. First, in matching networks, distance metrics are utilized to calculate the similarity between data examples. Second, MNs are designed to achieve accurate classification performance on infrequent classes; likewise, UE-DML aims at better capturing infrequent patterns (e.g., classes). The difference is: MNs requires the data examples to have class labels while the classes in UE-DML are latent. Though in the experiments we use the ground-truth class labels to evaluate UE-DML's performance on infrequent classes, in practice these labels are oftentimes not accessible: UE-DML can only access data pairs labeled as being similar or dissimilar, rather the class labels for individual examples.

Long short-term memory network The LSTM [163] network is a type of recurrent neural network, that is better at capturing long-term dependency in sequential modeling. At each time step t where the input is $\mathbf{x}_t$, there is an input gate $\mathbf{i}_t$, a forget gate $\mathbf{f}_t$, an output gate $\mathbf{o}_t$, a memory cell $\mathbf{c}_t$, and a hidden state $\mathbf{h}_t$. The transition equations among them are

$$\begin{aligned} \mathbf{i}_t &= \sigma(\mathbf{W}^{(i)}\mathbf{x}_t + \mathbf{U}^{(i)}\mathbf{h}_{t-1} + \mathbf{b}^{(i)}) \\ \mathbf{f}_t &= \sigma(\mathbf{W}^{(f)}\mathbf{x}_t + \mathbf{U}^{(f)}\mathbf{h}_{t-1} + \mathbf{b}^{(f)}) \\ \mathbf{o}_t &= \sigma(\mathbf{W}^{(o)}\mathbf{x}_t + \mathbf{U}^{(o)}\mathbf{h}_{t-1} + \mathbf{b}^{(o)}) \\ \mathbf{c}_t &= \mathbf{i}_t \odot \tanh(\mathbf{W}^{(c)}\mathbf{x}_t + \mathbf{U}^{(c)}\mathbf{h}_{t-1} + \mathbf{b}^{(c)}) + \mathbf{f}_t \odot \mathbf{c}_{t-1} \\ \mathbf{h}_t &= \mathbf{o}_t \odot \tanh(\mathbf{c}_t), \end{aligned} \tag{2.7}$$

where $\mathcal{W} = \{\mathbf{W}^{(s)}|s \in S = \{i, f, o, c\}\}$ and $\mathcal{U} = \{\mathbf{U}^{(s)}|s \in S\}$ are gate-specific weight matrices and $\mathcal{B} = \{\mathbf{b}^{(s)}|s \in S\}$ are bias vectors. The row vectors in $\mathbf{W}$ and $\mathbf{U}$ are treated as components. Let $\mathcal{L}(\mathcal{W}, \mathcal{U}, \mathcal{B})$ denote the loss function of an LSTM network and $\mathcal{R}(\cdot)$ denote the UER (including constraints), then a UE-regularized LSTM problem can be defined as

$$\min_{\mathcal{W},\mathcal{U},\mathcal{B}} \quad \mathcal{L}(\mathcal{W}, \mathcal{U}, \mathcal{B}) + \lambda \sum_{s\in S}(\mathcal{R}(\mathbf{W}^{(s)}) + \mathcal{R}(\mathbf{U}^{(s)})). \tag{2.8}$$

The LSTM network is applied for cloze-style reading comprehension (CSRC) [154].

2.1.3 A Projected Gradient Decent Algorithm

We develop a projected gradient descent (PGD) [53] algorithm to solve the UE-regularized problem in Eq.(2.4). The constraint $\mathbf{A}^\top\mathbf{A} \succ 0$ ensures the eigenvalues of $\mathbf{A}^\top\mathbf{A}$ are positive, such

that $\log(\mathbf{A}^\top\mathbf{A})$ is well-defined. However, it makes optimization very nasty. To address this issue, we add a small perturbation $\epsilon\mathbf{I}$ over $\mathbf{A}^\top\mathbf{A}$ where ϵ is a close-to-zero positive scalar and $\mathbf{I}$ is an identity matrix, to ensure $\log(\mathbf{A}^\top\mathbf{A}+\epsilon\mathbf{I})$ is always well-defined. Accordingly, the constraint $\mathbf{A}^\top\mathbf{A} \succ 0$ can be eliminated. The PGD algorithm iteratively performs three steps: (1) compute (sub)gradient $\triangle\mathbf{A}$ of the objective function; (2) update $\mathbf{A}$ using gradient descent: $\widetilde{\mathbf{A}} \leftarrow \mathbf{A} - \eta \triangle \mathbf{A}$; (3) project $\widetilde{\mathbf{A}}$ to the constraint set $\{\mathbf{A}|\mathbf{A}^\top\mathbf{1}=\mathbf{0}\}$.

In step (1), the derivative of $\text{tr}((\frac{1}{d}\mathbf{A}^\top\mathbf{A}+\epsilon\mathbf{I})\log(\frac{1}{d}\mathbf{A}^\top\mathbf{A}+\epsilon\mathbf{I}))$ is $\frac{2}{d}\mathbf{A}(\log(\frac{1}{d}\mathbf{A}^\top\mathbf{A}+\epsilon\mathbf{I})+\mathbf{I})$. To compute the logarithm of $\frac{1}{d}\mathbf{A}^\top\mathbf{A}+\epsilon\mathbf{I}$, we perform an eigen-decomposition of this matrix into $\mathbf{U}\mathbf{\Lambda}\mathbf{U}^\top$, transform $\mathbf{\Lambda}$ into another diagonal matrix $\widetilde{\mathbf{\Lambda}}$ where $\widetilde{\Lambda}_{jj} = \log(\Lambda_{jj})$ and then compute $\log(\frac{1}{d}\mathbf{A}^\top\mathbf{A}+\epsilon\mathbf{I})$ as $\mathbf{U}\widetilde{\mathbf{\Lambda}}\mathbf{U}^\top$. The complexity of eigen-decomposing this m-by-m matrix is $O(m^3)$. In our applications, m is no more than 500, so $O(m^3)$ is not a big bottleneck. In addition, this matrix is symmetric and the symmetry can be leveraged for fast eigen-decomposition. In implementation, we use the MAGMA [7] library that supports efficient eigen-decomposition of symmetric matrices on both CPUs and GPUs. In step (3), the projection operation amounts to solving the following problem:

$$\begin{array}{ll}\min_{\mathbf{A}} & \frac{1}{2}\|\mathbf{A}-\widetilde{\mathbf{A}}\|_F^2 \\ s.t. & \mathbf{A}^\top\mathbf{1}=\mathbf{0}.\end{array} \tag{2.9}$$

According to the KKT conditions [53], we have $\mathbf{A}-\widetilde{\mathbf{A}}+\mathbf{1}\boldsymbol{\lambda}^\top = 0$ and $\mathbf{A}^\top\mathbf{1}=\mathbf{0}$. Solving this system of equations, we get

$$\mathbf{A} = (\mathbf{I}-\frac{1}{d}\mathbf{1}\mathbf{1}^\top)\widetilde{\mathbf{A}}, \tag{2.10}$$

which centers the row vectors in $\widetilde{\mathbf{A}}$ so that they have zero mean.

2.1.4 Evaluation

In this section, we present experimental results.

Datasets We used five datasets in the experiments: an electronic health record dataset MIMIC-III [184]; two image datasets Stanford-Cars [202] and Caltech-UCSD-Birds [358]; two question answering (QA) datasets CNN and DailyMail [154]. The first three were used for DML and the last two for LSTM. Their statistics are summarized in Table 2.1.

MIMIC-III contains 58K hospital admissions of patients who stayed within the intensive care units at the Beth Israel Deaconess Medical Center between 2001 and 2012. Each admission has a primary diagnosis (a disease), which acts as the class label of this admission. There are 2833 unique diseases. We extracted 7207-dimensional features: (1) 2 dimensions from demographics, including age and gender; (2) 5300 dimensions from clinical notes, including 5000-dimensional bag-of-words (weighted using *tf-idf*) and 300-dimensional Word2Vec [256]; (3) 1905-dimensions from lab tests where the zero-order, first-order, and second-order temporal features were extracted for each of the 635 lab items. In the extraction of bag-of-words features from clinical notes, we removed stop words, then counted the document frequency (DF) of the remaining words. Then we selected 5000 words with the largest DFs to form the dictionary. Based on this dictionary, we extracted *tf-idf* features. In the extraction of Word2Vec features,

	#Train	#Test	Dimension	#Class
MIMIC	40K	18K	7207	2833
Cars	8144	8041	4096	196
Birds	9000	2788	4096	200
CNN	380K	3198	–	–
DailyMail	879K	53K	–	–

Table 2.1: Dataset statistics.

we trained a 300-dimensional embedding vector for each word using an open source tool[1]. To represent a clinical note, we averaged the embeddings of all words in this note. In lab tests, there are 635 test items in total. Each item is tested at different time points for each admission. For an item, we extracted three types of temporal features: (1) *zero-order*: averaging the values of this item measured at different time points; (2) *first-order*: taking the difference of values at every two consecutive time points t and $t-1$, and averaging these differences; (3) *second-order*: for the sequence of first-order differences generated in (2), taking the difference (called second-order difference) of values at every two consecutive time points t and $t-1$, and averaging these second-order differences. If an item is missing in an admission, we set the zero-order, first-order, and second-order feature values to 0. For the two image datasets, we used the VGG16 [303] convolutional neural network trained on the ImageNet [95] dataset to extract features, which are the 4096-dimensional outputs of the second fully-connected layer. For MIMIC-III, Stanford-Cars, and Caltech-UCSD-Birds, the features were normalized using min-max normalization along each dimension. We used PCA to reduce the feature dimension to 1000. In the two QA datasets, each data example consists of a passage, a question, and an answer. The question is a cloze-style [154] task where an entity is replaced by a placeholder and the goal is to infer this missing entity (answer) from all the possible entities appearing in the passage. For Stanford-Cars, CNN, and DailyMail, we used a single train/test split specified by the data providers; for the other two, five random splits were performed and the results were averaged over the five runs.

Experimental setup In the DML experiments, two data examples were labeled as similar if belonging to the same class and dissimilar if otherwise. The learned distance metrics were applied for retrieval whose performance was evaluated using precision@K: among the top K retrieved examples, what is the percentage of samples that share the same class label with the query example? We compared with two sets of regularizers: (1) diversity-promoting regularizers based on determinant of covariance matrix (DCM) [242], cosine similarity (CS) [402], determinantal point process (DPP) [204, 429], InCoherence (IC) [29], mutual angles (MA) [369], and decorrelation (DC) [82]; (2) regularizers that are designed for other purposes, including L2 norm for small norm, L1 norm for sparsity, low-rankness [290], and dropout [282, 313]. All these regularizers were applied to the same DML formulation (Eq.(2.6) without the UER regularizer). In addition, we compared with the vanilla Euclidean distance (EUC) and other distance learning methods including information theoretic metric learning (ITML) [92], logistic discriminant metric learning (LDML) [146], and geometric mean metric learning (GMML) [405]. We used 5-fold cross

[1]https://code.google.com/archive/p/word2vec/

	MIMIC	Cars	Birds
DML	72.5 ± 0.3	53.1 ± 0.0	55.9 ± 0.5
EUC	58.3 ± 0.1	37.8 ± 0.0	43.2 ± 0.0
ITML [92]	69.3 ± 0.4	50.1 ± 0.0	52.9 ± 0.3
LDML [146]	70.9 ± 0.9	51.3 ± 0.0	52.1 ± 0.2
GMML [405]	71.2 ± 0.3	54.2 ± 0.0	53.7 ± 0.6
L2-DML	72.9 ± 0.1	53.4 ± 0.0	57.1 ± 0.4
L1-DML	72.6 ± 0.6	53.7 ± 0.0	56.4 ± 0.2
LowRank-DML [290]	72.5 ± 0.7	53.3 ± 0.0	56.1 ± 0.6
Dropout-DML [282]	73.1 ± 0.3	53.5 ± 0.0	56.6 ± 0.3
DCM-DML [242]	73.7 ± 0.4	57.1 ± 0.0	56.5 ± 0.4
CS-DML [402]	73.5 ± 0.5	55.7 ± 0.0	57.4 ± 0.2
DPP-DML [429]	74.2 ± 0.3	55.9 ± 0.0	56.9 ± 0.7
IC-DML [29]	74.3 ± 0.2	56.3 ± 0.0	57.8 ± 0.2
MA-DML [367]	73.6 ± 0.4	55.8 ± 0.0	58.2 ± 0.1
DC-DML [82]	72.6 ± 0.1	56.2 ± 0.0	56.2 ± 0.8
UE-DML	**75.4** ± 0.3	**58.2** ± 0.0	**59.4** ± 0.2

Table 2.2: Precision@10 (%) on three datasets. The Cars dataset has a single train/test split, hence the standard error is 0. UE-DML is our method. On the second panel (EUC, etc.) are well established or state of the art distance metric learning baselines. On the the third panel (L2-DML, etc.) and the fourth panel (DCM-DML, etc.) are DML methods regularized by non-diversity regularizers and previously proposed diversity-promoting regularizers.

validation to tune the regularization parameter in $\{10^{-5}, 10^{-4}, \cdots, 10^{5}\}$ and the number of components in $\{50, 100, 200, \cdots, 500\}$. The best tuned regularization parameters of UER are: 0.001 for MIMIC, 0.01 for Cars and Birds. The best tuned component numbers are: 200 for MIMIC, 100 for Cars, and 200 for Birds. The learning rate of the PGD algorithm was set to 0.001.

In the LSTM experiments, the network architecture and experimental settings followed that in the BIDirectional Attention Flow (BIDAF) [296] model, which consists of the following layers: character embedding, word embedding, contextual embedding, attention flow, modeling, and output. The contextual and modeling layers are based on LSTM. In the character embedding based on convolutional neural networks, 100 1D filters were used, each with a width of 5. The hidden state size was set to 100. AdaDelta [409] was used for optimization with a minibatch size of 48. Dropout [313] with probability 0.2 was used for all LSTM layers. The model was trained for 8 epochs with an early stop when the validation accuracy started to drop. We compared UER with other diversity-promoting regularizers including DCM, CS, DPP, IC, MA, and DC.

Results Table 2.2 shows the retrieval precision ($K = 10$) on three datasets, where we observe: (1) UE-DML achieves much better precision than DML, proving that UER is an effective regularizer in improving generalization performance; (2) UER outperforms other diversity-promoting regularizers possibly due to its capability of capturing global relations among all components and insensitivity to vector scaling; (3) diversity-promoting regularizers perform better than other

	MIMIC	Cars	Birds	Average
DML	300	300	500	367
L2-DML	300	300	500	367
L1-DML	300	300	500	367
LowRank-DML [290]	400	300	400	367
Dropout-DML [282]	300	300	400	333
DCM-DML [242]	200	400	400	333
CS-DML [402]	300	100	300	233
DPP-DML [429]	200	300	300	267
IC-DML [29]	400	300	200	300
MA-DML [367]	300	200	300	267
DC-DML [82]	300	400	300	333
UE-DML	200	100	200	**167**

Table 2.3: Optimal number of components.

types of regularizers such as L2, L1, low rank, and dropout, demonstrating the efficacy of inducing diversity; (4) UE-DML outperforms other popular distance learning methods such as ITML, LDML, and GMML.

Table 2.3 shows the number of components that achieves the precision in Table 2.2. Compared with DML, UE-DML uses much fewer components to achieve better precision. For example, on the Cars dataset, UE-DML achieves a 58.2% precision with 100 components. In contrast, with more components (300), DML achieves a much lower precision (53.1%). This demonstrates that by encouraging the components to be diverse, UER is able to reduce model size without sacrificing modeling power. UER encourages equal "importance" among components such that each component plays a significant role in modeling data. As a result, it suffices to use a small number of components to achieve larger modeling power. Compared with other diversity-promoting regularizers, UER achieves better precision with fewer components, demonstrating its ability to better promote diversity.

Next, we verify whether "diversifying" the components in DML can better capture infrequent patterns. In the MIMIC-III dataset, we consider diseases as patterns and consider a disease as "frequent" if more than 1000 hospital admissions are diagnosed with this disease and "infrequent" if otherwise. Table 2.4 shows the retrieval precision on frequent diseases and infrequent diseases. As can be seen, compared with the baselines, UE-DML achieves more improvement on infrequent diseases than on frequent diseases. This indicates that by encouraging the components to diversely spread out, UER is able to better capture infrequent patterns (diseases in this case) without compromising the performance on frequent patterns. On infrequent diseases, UE-DML outperforms other diversity-promoting methods, showing the advantage of UER over other diversity-promoting regularizers. To further verify this, we select 3 most frequent diseases (hypertension, AFib, CAD) and randomly select 5 infrequent ones (helicobacter pylori, acute cholecystitis, joint pain-shlder, dysarthria, pressure ulcer), and show the precision@10 on each individual disease in Table 2.5. As can be seen, on the five infrequent diseases, UE-DML achieves higher precision than baselines while on the three frequent diseases UE-DML achieves

	Frequent	Infrequent
DML	77.6 ± 0.2	64.2 ± 0.3
EUC	58.7 ± 0.1	57.6 ± 0.2
ITML [92]	74.2 ± 0.6	61.3 ± 0.3
LDML [146]	76.1 ± 0.8	62.3 ± 0.9
GMML [405]	75.9 ± 0.1	63.5 ± 0.4
L2-DML	77.5 ± 0.3	65.4 ± 0.1
L1-DML	77.4 ± 0.5	64.8 ± 0.8
LowRank-DML [290]	77.7 ± 0.5	64.0 ± 0.8
Dropout-DML [282]	78.1 ± 0.2	64.9 ± 0.4
DCM-DML [242]	77.9 ± 0.4	66.8 ± 0.2
CS-DML [402]	78.0 ± 0.5	66.2 ± 0.7
DPP-DML [429]	77.3 ± 0.2	69.1 ± 0.5
IC-DML [29]	78.5 ± 0.3	67.4 ± 0.2
MA-DML [367]	76.8 ± 0.2	68.4 ± 0.4
DC-DML [82]	77.1 ± 0.1	65.3 ± 0.1
UE-DML	78.3 ± 0.3	70.7 ± 0.4

Table 2.4: Precision@10 (%) on frequent and infrequent diseases of the MIMIC-III dataset.

comparable precision.

We empirically verified whether UER can promote uncorrelation and evenness. Given m component vectors, we computed the empirical correlation (cosine similarity) of every two vectors, then averaged these pairwise correlation scores to measure the overall correlation of the m vectors. We performed the study by learning distance metrics that have 200 components, on the MIMIC-III dataset. The average correlation under unregularized DML and UE-DML is 0.73 and 0.57 respectively. This shows that UER can reduce correlation. To measure evenness, we first measured the "importance" of components. For each component with a parameter vector $\mathbf{a}$, we projected the training examples $\{\mathbf{x}_i\}_{i=1}^N$ onto $\mathbf{a}$: $\{\mathbf{x}_i^\top \mathbf{a}\}_{i=1}^N$, then used the variance of $\{\mathbf{x}_i^\top \mathbf{a}\}_{i=1}^N$ to measure the importance of this component. After that, we mapped these importance scores into a probabilistic simplex using softmax. Finally, the evenness was measured by the KL divergence between the discrete distribution parameterized by these probabilities and a uniform distribution. A smaller KL divergence indicates larger evenness. On MIMIC-III with 200 components, the KL divergence under unregularized DML and UE-DML is 3.54 and 2.92 respectively. This suggests that our regularizer is able to encourage evenness.

Table 2.6 shows the runtime taken by DML methods to reach convergence. Compared with unregularized DML, UE-DML does not increase the training time substantially. The relative increase is 11.2% on MIMIC, 15.4% on Cars, and 13.9% on Birds. The runtime of UE-DML is close to DML regularized by other diversity-promoting regularizers.

In the LSTM experiments, Table 2.7 shows state of the art accuracy on the two QA datasets. Compared with the original BIDAF [296], our method UE-BIDAF achieves better accuracy, further demonstrating UER's ability to improve generalization performance. Besides, UER outperforms other regularizers.

	1 (3566)	2 (3498)	3 (2757)	4 (204)	5 (176)	6 (148)	7 (131)	8 (121)
DML	80.2 ± 0.5	79.4 ± 0.8	80.9 ± 0.7	5.6 ± 1.6	6.1 ± 0.8	4.9 ± 0.8	4.3 ± 1.7	5.2 ± 0.6
EUC	66.4 ± 1.2	69.6 ± 1.2	61.8 ± 0.4	7.2 ± 1.0	6.9 ± 0.6	3.1 ± 1.4	6.8 ± 1.2	2.4 ± 0.7
ITML [92]	75.4 ± 1.0	76.3 ± 0.9	79.3 ± 0.9	5.3 ± 1.2	3.7 ± 1.3	6.0 ± 0.9	3.3 ± 0.9	5.0 ± 1.0
LDML [146]	77.0 ± 0.8	75.7 ± 1.0	78.1 ± 0.6	3.2 ± 1.3	5.6 ± 1.8	3.8 ± 1.1	6.7 ± 1.4	5.0 ± 1.3
GMML [405]	76.3 ± 0.4	78.7 ± 0.8	79.8 ± 0.8	3.9 ± 1.8	5.9 ± 1.5	**11.9** ± 1.4	6.1 ± 0.6	6.3 ± 1.5
L2-DML	81.0 ± 0.5	79.3 ± 0.8	77.6 ± 0.4	4.4 ± 1.1	5.6 ± 0.9	3.7 ± 0.9	4.9 ± 1.2	6.2 ± 1.1
L1-DML	78.2 ± 1.0	79.9 ± 1.1	80.8 ± 1.2	6.3 ± 1.9	4.8 ± 1.1	9.5 ± 1.0	7.7 ± 1.0	5.6 ± 1.7
LowRank-DML [290]	79.6 ± 0.4	79.7 ± 0.5	75.4 ± 0.5	3.1 ± 1.0	9.2 ± 1.2	5.5 ± 1.4	4.8 ± 0.6	4.5 ± 1.5
Dropout-DML [282]	**81.6** ± 0.5	78.7 ± 0.7	80.7 ± 0.5	3.2 ± 1.5	4.2 ± 1.9	6.1 ± 0.9	4.2 ± 0.8	6.2 ± 1.9
DCM-DML [242]	77.9 ± 1.0	77.3 ± 0.9	80.3 ± 1.2	7.1 ± 0.8	8.9 ± 0.9	9.7 ± 1.4	11.9 ± 0.7	9.0 ± 1.6
CS-DML [402]	80.0 ± 0.5	80.3 ± 0.7	80.8 ± 0.6	9.4 ± 1.3	4.8 ± 1.7	8.9 ± 1.9	9.7 ± 0.7	9.0 ± 1.0
DPP-DML [429]	79.8 ± 0.8	77.6 ± 0.2	77.4 ± 0.7	10.1 ± 1.1	10.3 ± 0.8	8.8 ± 1.7	11.7 ± 1.2	8.4 ± 1.3
IC-DML [29]	78.8 ± 1.3	79.2 ± 1.1	77.0 ± 0.8	11.8 ± 0.6	9.2 ± 1.4	5.7 ± 1.6	8.7 ± 1.4	9.6 ± 0.7
MA-DML [367]	77.3 ± 1.1	80.1 ± 1.0	**81.0** ± 0.7	11.5 ± 1.1	9.9 ± 1.1	4.9 ± 1.1	7.6 ± 1.2	10.4 ± 1.4
DC-DML [82]	80.7 ± 0.5	78.8 ± 0.7	80.5 ± 1.1	10.5 ± 0.8	**11.4** ± 1.2	9.2 ± 0.7	9.8 ± 1.2	10.4 ± 1.2
UE-DML	81.4 ± 0.9	**82.4** ± 0.8	80.5 ± 0.4	**14.3** ± 0.9	11.2 ± 1.3	10.7 ± 1.8	**15.8** ± 1.4	**13.2** ± 0.7

Table 2.5: Precision@10 (%) on three frequent and five infrequent diseases. The number next to a disease ID is its frequency.

	MIMIC	Cars	Birds
DML	20.5	9.1	10.1
DCM-DML [242]	22.3	10.9	11.7
CS-DML [402]	20.9	9.7	10.5
DPP-DML [429]	22.6	10.6	11.2
IC-DML [29]	21.1	9.7	10.5
MA-DML [367]	21.3	9.4	10.6
DC-DML [82]	21.7	10.1	10.8
UE-DML	22.8	10.5	11.5

Table 2.6: Average runtime (hours) of DML methods regularized by different diversity-promoting regularizers.

2.2 Convex Diversity-promoting Regularizers

The UE regularizer is nonconvex and is difficult to be convexified. As a result, the UE-regularized ML problems are nonconvex where achieving the global optimal is NP-hard. To achieve a better local optima, the algorithm needs to rerun multiple times, each with a different random initialization of the model, and selects the best solution among them, which incurs substantial computational overhead. Even so, the obtained optimal is a local (therefore inferior) one that might be far from the global optimal.

In this section, we design new diversity-promoting regularizers that make convex relaxation easy [379]. Similar to [74, 122, 342, 347, 367], we use near-orthogonality to represent "diversity": projection vectors are more "diverse" if they are closer to orthogonality. Near-orthogonality is promoted by encouraging the Gram matrix of vectors to be close to an identity matrix and the "closeness" is measured using the Bregman matrix divergence (BMD) [206]. As a result, a family of nonconvex BMD regularizers are defined. Then we perform convex relaxations of them by exploring the properties of eigenvalues. We apply the convex BMD regularizers to distance metric learning [383] and develop efficient proximal gradient descent [270] algorithms.

	CNN		DailyMail	
	Dev	Test	Dev	Test
Kadlec et al. [188]	68.6	69.5	75.0	73.9
Kobayashi et al. [197]	71.3	72.9	–	–
Sordoni et al. [309]	72.6	73.3	–	–
Trischler et al. [334]	73.4	74.0	–	–
Chen et al. [68]	73.8	73.6	77.6	76.6
Dhingra et al. [101]	73.0	73.8	76.7	75.7
Cui et al. [86]	73.1	74.4	–	–
Shen et al. [301]	72.9	74.7	77.6	76.6
BIDAF [296]	76.31	76.94	80.33	79.63
DCM-BIDAF [242]	76.36	76.98	80.51	79.68
CS-BIDAF [402]	76.43	77.10	80.37	79.71
DPP-BIDAF [429]	76.32	77.04	80.45	79.77
IC-BIDAF [29]	76.41	77.21	80.49	79.83
MA-BIDAF [369]	76.49	77.09	80.42	79.74
DC-BIDAF [82]	76.35	77.15	80.38	79.67
UE-BIDAF	76.58	77.27	80.63	79.86
Dhingra et al. [101]	77.9	77.9	81.5	80.9
Dhingra et al. [102]	79.2	78.6	–	–

Table 2.7: Accuracy (%) on the two QA datasets. On the second panel (BIDAF, etc.), we compare different diversity-promoting regularizers. On the first panel (Kadlec et al., etc.) and the third panel (Dhingra et al., etc) are other state-of-the-art baselines.

The algorithms only run once with a single initialization, hence are more efficient than existing nonconvex methods. Since the global optimal can be achieved, our methods can potentially yield more effective diversity-biased distance metrics. We apply the learned distance metrics for information retrieval on healthcare, texts, images, and sensory data. Compared with nonconvex baselines, our methods achieve: (1) higher computational efficiency; (2) better retrieval performance with fewer projection vectors; (3) better performance on infrequent classes.

2.2.1 Nonconvex Bregman Matrix Divergence Regularizers

We begin with defining nonconvex regularizers based on the Bregman matrix divergence, then discuss how to convexify them. We first introduce another measure of "diversity" – *near-orthogonality* [379]: the component vectors are deemed to be more diverse if they are closer to being orthogonal. To encourage near-orthogonality between two vectors $\mathbf{a}_i$ and $\mathbf{a}_j$, one way is to make their inner product $\mathbf{a}_i^\top \mathbf{a}_j$ close to zero and their ℓ_2 norm $\|\mathbf{a}_i\|_2$, $\|\mathbf{a}_j\|_2$ close to one. For m vectors $\mathbf{A} \in \mathbb{R}^{m\times d}$, their near-orthogonality can be achieved in the following manner: computing the Gram matrix $\mathbf{G}$ where $G_{ij} = \mathbf{a}_i^\top \mathbf{a}_j$, then encouraging $\mathbf{G}$ to be close to an identity matrix. Off the diagonal of $\mathbf{G}$ and $\mathbf{I}$ are $\mathbf{a}_i^\top \mathbf{a}_j$ and zero respectively. On the diagonal of $\mathbf{G}$ and $\mathbf{I}$ are $\|\mathbf{a}_i\|_2^2$ and one respectively. Making $\mathbf{G}$ close to $\mathbf{I}$ effectively encourages $\mathbf{a}_i^\top \mathbf{a}_j$ to be close to zero and $\|\mathbf{a}_i\|_2$ close to one, which therefore encourages $\mathbf{a}_i$ and $\mathbf{a}_j$ to get close to being orthogonal.

One straightforward distance between $\mathbf{G}$ and $\mathbf{I}$ is based on the squared Frobenius norm (SFN): $\|\mathbf{G}-\mathbf{I}\|_F^2$. The SFN can be factorized into pairwise inner products: $\sum_{i=1}^m \sum_{j\neq i}^m (\langle \mathbf{a}_i, \mathbf{a}_j \rangle)^2 + \sum_{i=1}^m (\|\mathbf{a}_i\|_2 - 1)^2$. As a result, it measures orthogonality of functions in a pairwise manner. We conjecture that measuring orthogonality in a global manner is more desirable (the conjecture is validated in experiments). To achieve this goal, we resort to another measure: Bregman matrix divergence (BMD) [100]. Let $\mathbf{S}^n$ denote real symmetric $n \times n$ matrices. Given a strictly convex, differentiable function $\phi : \mathbf{S}^n \rightarrow \mathbb{R}$, the BMD is defined as $D_\phi(\mathbf{X}, \mathbf{Y}) = \phi(\mathbf{X}) - \phi(\mathbf{Y}) - \text{tr}((\bigtriangledown \phi(\mathbf{Y}))^\top (\mathbf{X} - \mathbf{Y}))$, where $\text{tr}(\mathbf{A})$ denotes the trace of matrix $\mathbf{A}$. Different choices of $\phi(\mathbf{X})$ lead to different divergences. If $\phi(\mathbf{X}) = \text{tr}(\mathbf{X} \log \mathbf{X} - \mathbf{X})$, where $\log \mathbf{X}$ denotes the matrix logarithm of $\mathbf{X}$, the divergence becomes $D_{vnd}(\mathbf{X}, \mathbf{Y}) = \text{tr}(\mathbf{X} \log \mathbf{X} - \mathbf{X} \log \mathbf{Y} - \mathbf{X} + \mathbf{Y})$, which is referred to as *von Neumann divergence* (VND) [336]. If $\phi(\mathbf{X}) = -\log\det \mathbf{X}$ where $\det(\mathbf{X})$ denotes the determinant of $\mathbf{X}$, we get the *log-determinant divergence* (LDD) [206]: $D_{ldd}(\mathbf{X}, \mathbf{Y}) = \text{tr}(\mathbf{X}\mathbf{Y}^{-1}) - \log\det(\mathbf{X}\mathbf{Y}^{-1}) - n$. Interestingly, SFN is a special case of BMD when $\phi(\mathbf{X}) = \|\mathbf{X}\|_F^2$. To encourage near-orthogonality among components, we encourage the BMD between their Gram matrix $\mathbf{A}\mathbf{A}^\top$ and an identity matrix $\mathbf{I}$ to be small, which results in a family of BMD regularizers: $\Omega_\phi(\mathbf{A}) = D_\phi(\mathbf{A}\mathbf{A}^\top, \mathbf{I})$. $\Omega_\phi(\mathbf{A})$ can be specialized to different instances, according to the choices of $D_\phi(\cdot, \cdot)$. Under VND, $\Omega_\phi(\mathbf{A})$ becomes

$$\Omega_{vnd}(\mathbf{A}) = \text{tr}(\mathbf{A}\mathbf{A}^\top \log(\mathbf{A}\mathbf{A}^\top) - \mathbf{A}\mathbf{A}^\top) + m. \tag{2.11}$$

Under LDD, $\Omega_\phi(\mathbf{A})$ becomes

$$\Omega_{ldd}(\mathbf{A}) = \text{tr}(\mathbf{A}\mathbf{A}^\top) - \log\det(\mathbf{A}\mathbf{A}^\top) - m. \tag{2.12}$$

Under SFN, $\Omega_\phi(\mathbf{A})$ becomes

$$\Omega_{sfn}(\mathbf{A}) = \|\mathbf{A}\mathbf{A}^\top - \mathbf{I}\|_F^2. \tag{2.13}$$

Different from the SFN regularizer, VND and LDD do not admit a pairwise factorization, and hence allow one to measure orthogonality *globally*. Unlike DPP [204], LDD utilizes an additional term $\text{tr}(\mathbf{G}) = \sum_{i=1}^m \|\mathbf{a}_i\|_2^2$ to control the magnitude of vectors, and thus avoiding DPP's sensitivity to scaling. Similarly, VND and SFN are also insensitive to scaling since they encourage $\|\mathbf{a}\|_2$ to be close to one.

Applying these regularizers to ML models, e.g., distance metric learning (DML, Section 2.1.2), we define the following BMD-regularized DML (BMD-DML) problem:

$$\min_{\mathbf{A}} \frac{1}{|\mathcal{S}|} \sum_{(\mathbf{x},\mathbf{y})\in\mathcal{S}} \|\mathbf{A}\mathbf{x} - \mathbf{A}\mathbf{y}\|_2^2 + \frac{1}{|\mathcal{D}|} \sum_{(\mathbf{x},\mathbf{y})\in\mathcal{D}} \max(0, 1 - \|\mathbf{A}\mathbf{x} - \mathbf{A}\mathbf{y}\|_2^2) + \lambda\Omega_\phi(\mathbf{A}), \tag{2.14}$$

which is nonconvex.

2.2.2 Convex Bregman Matrix Divergence Regularizers

Next, we discuss how to relax the nonconvex BMD regularizers into convex functions. The relaxations are based on the properties of eigenvalues. Given a full-rank matrix $\mathbf{A} \in \mathbb{R}^{m\times d}$ ($m < d$), we know that $\mathbf{A}\mathbf{A}^\top \in \mathbb{R}^{m\times m}$ is a full-rank matrix with m positive eigenvalues (denoted by $\lambda_1, \cdots, \lambda_m$) and $\mathbf{A}^\top\mathbf{A} \in \mathbb{R}^{d\times d}$ is a rank-deficient matrix with $d - m$ zero eigenvalues and m positive eigenvalues that equal $\lambda_1, \cdots, \lambda_m$. For a general positive definite matrix

$\mathbf{Z} \in \mathbb{R}^{m\times m}$ whose eigenvalues are $\gamma_1, \cdots, \gamma_m$, we have $\|\mathbf{Z}\|_F^2 = \sum_{j=1}^m \gamma_j^2$, $\text{tr}(\mathbf{Z}) = \sum_{j=1}^m \gamma_j$, and $\log\det \mathbf{Z} = \sum_{j=1}^m \log\gamma_j$. Next, we leverage these facts to seek convex approximations of the BMD regularizers.

Convex SFN regularizer The eigenvalues of $\mathbf{A}\mathbf{A}^\top - \mathbf{I}_m$ are $\lambda_1 - 1, \cdots, \lambda_m - 1$ and those of $\mathbf{A}^\top\mathbf{A} - \mathbf{I}_d$ are $\lambda_1 - 1, \cdots, \lambda_m - 1, -1, \cdots, -1$. According to the fact $\|\mathbf{Z}\|_F^2 = \sum_{j=1}^m \gamma_j^2$, we have $\|\mathbf{A}^\top\mathbf{A} - \mathbf{I}_d\|_F^2 = \sum_{j=1}^m(\lambda_j - 1)^2 + \sum_{j=m+1}^d(-1)^2 = \|\mathbf{A}\mathbf{A}^\top - \mathbf{I}_m\|_F^2 + d - m$. Let $\mathbf{M}$ denote $\mathbf{A}^\top\mathbf{A}$, then the SFN regularizer $\|\mathbf{A}\mathbf{A}^\top - \mathbf{I}_m\|_F^2$ equals to $\|\mathbf{A}^\top\mathbf{A} - \mathbf{I}_d\|_F^2 - d + m = \|\mathbf{M} - \mathbf{I}_d\|_F^2 - d + m$, where $m = \text{rank}(\mathbf{A}^\top\mathbf{A}) = \text{rank}(\mathbf{M})$. It is well-known that the trace norm of a matrix is a convex envelope of its rank [311]. We use $\text{tr}(\mathbf{M})$ to approximate $\text{rank}(\mathbf{M})$ and get $\|\mathbf{A}\mathbf{A}^\top - \mathbf{I}_m\|_F^2 \approx \|\mathbf{M} - \mathbf{I}_d\|_F^2 + \text{tr}(\mathbf{M}) - d$, where the right hand side is a convex function. Dropping the constant, we get the convex SFN (CSFN) regularizer defined over $\mathbf{M}$

$$\widehat{\Omega}_{sfn}(\mathbf{M}) = \|\mathbf{M} - \mathbf{I}_d\|_F^2 + \text{tr}(\mathbf{M}). \tag{2.15}$$

Convex VND regularizer Given $\mathbf{A}\mathbf{A}^\top = \mathbf{U}\mathbf{\Lambda}\mathbf{U}^\top$ where $\Lambda_{jj} = \lambda_j$, according to the property of matrix logarithm, we have $\log(\mathbf{A}\mathbf{A}^\top) = \mathbf{U}\widehat{\mathbf{\Lambda}}\mathbf{U}^\top$ where $\widehat{\Lambda}_{jj} = \log\Lambda_{jj}$. Then $(\mathbf{A}\mathbf{A}^\top)\log(\mathbf{A}\mathbf{A}^\top) - (\mathbf{A}\mathbf{A}^\top) = \mathbf{U}(\mathbf{\Lambda}\widehat{\mathbf{\Lambda}} - \mathbf{\Lambda})\mathbf{U}^\top$, where the eigenvalues are $\{\Lambda_{jj}\log\Lambda_{jj} - \Lambda_{jj}\}_{j=1}^m$. Since $\text{tr}(\mathbf{M}) = \sum_{j=1}^m \lambda_j$, we have $\Omega_{vnd}(\mathbf{A}) = \sum_{j=1}^m(\Lambda_{jj}\log\Lambda_{jj} - \Lambda_{jj}) + m$. For $\mathbf{A}^\top\mathbf{A} + \epsilon\mathbf{I}_d$, where $\epsilon > 0$ is a small scalar and the matrix's eigenvalues are $\lambda_1 + \epsilon, \cdots, \lambda_m + \epsilon, \epsilon, \cdots, \epsilon$, we have

$$\begin{aligned}
&D_{vnd}(\mathbf{A}^\top\mathbf{A} + \epsilon\mathbf{I}_d, \mathbf{I}_d)\\
&= \text{tr}((\mathbf{A}^\top\mathbf{A} + \epsilon\mathbf{I}_d)\log(\mathbf{A}^\top\mathbf{A} + \epsilon\mathbf{I}_d) - (\mathbf{A}^\top\mathbf{A} + \epsilon\mathbf{I}_d)) + d\\
&= \textstyle\sum_{j=1}^m((\lambda_j + \epsilon)\log(\lambda_j + \epsilon) - (\lambda_j + \epsilon)) + \sum_{j=m+1}^d(\epsilon\log\epsilon - \epsilon) + d\\
&= \textstyle\sum_{j=1}^m((\lambda_j + \epsilon)(\log\lambda_j + \log(1 + \frac{\epsilon}{\lambda_j})) - (\lambda_j + \epsilon)) + (d - m)(\epsilon\log\epsilon - \epsilon) + d\\
&= \textstyle\sum_{j=1}^m(\lambda_j\log\lambda_j - \lambda_j + \lambda_j\log(1 + \frac{\epsilon}{\lambda_j}) + \epsilon(\log\lambda_j + \log(1 + \frac{\epsilon}{\lambda_j})) - \epsilon) + (d - m)(\epsilon\log\epsilon - \epsilon) + d\\
&= \Omega_{vnd}(\mathbf{A}) - m + \textstyle\sum_{j=1}^m(\lambda_j\log(1 + \frac{\epsilon}{\lambda_j}) + \epsilon(\log\lambda_j + \log(1 + \frac{\epsilon}{\lambda_j})) - \epsilon) + (d - m)(\epsilon\log\epsilon - \epsilon) + d.
\end{aligned} \tag{2.16}$$

Since ϵ is small, we have $\log(1 + \frac{\epsilon}{\lambda_j}) \approx \frac{\epsilon}{\lambda_j}$. Then $\lambda_j\log(1 + \frac{\epsilon}{\lambda_j}) \approx \epsilon$ and the last line in the above equation can be approximated with $\Omega_{vnd}(\mathbf{A}) - m + d + O(\epsilon)$, and therefore

$$\Omega_{vnd}(\mathbf{A}) \approx D_{vnd}(\mathbf{A}^\top\mathbf{A} + \epsilon\mathbf{I}_d, \mathbf{I}_d) + m - d, \tag{2.17}$$

where $O(\epsilon)$ is close to zero since ϵ is small, and can be dropped. Replacing $\mathbf{A}^\top\mathbf{A}$ with $\mathbf{M}$, approximating m with $\text{tr}(\mathbf{M})$ and dropping the constant d, we get the convex VND (CVND) regularizer:

$$\widehat{\Omega}_{vnd}(\mathbf{M}) \;=\; D_{vN}(\mathbf{M} + \epsilon\mathbf{I}_d, \mathbf{I}_d) + \text{tr}(\mathbf{M}) \propto \text{tr}((\mathbf{M} + \epsilon\mathbf{I}_d)\log(\mathbf{M} + \epsilon\mathbf{I}_d)), \tag{2.18}$$

whose convexity is shown in [264].

Convex LDD regularizer Since $\text{tr}(\mathbf{M}) = \sum_{j=1}^m \lambda_j$ and $\log\det\mathbf{M} = \sum_{j=1}^m \log\lambda_j$, we have $\Omega_{ldd}(\mathbf{A}) = \sum_{j=1}^m \lambda_j - \sum_{j=1}^m \log\lambda_j - m$ and $D_{ldd}(\mathbf{A}^\top\mathbf{A} + \epsilon\mathbf{I}_d, \mathbf{I}_d) = \sum_{j=1}^m \lambda_j + d\epsilon - (d -$

$m)\log\epsilon - \sum_{j=1}^{m}\log(\lambda_j+\epsilon)$. Further,

$$\begin{aligned}
&D_{ldd}(\mathbf{A}^\top\mathbf{A}+\epsilon\mathbf{I}_d,\mathbf{I}_d)\\
&=\sum_{j=1}^{m}\lambda_j + d\epsilon - (d-m)\log\epsilon - \sum_{j=1}^{m}\log(\lambda_j+\epsilon)\\
&=\sum_{j=1}^{m}\lambda_j + d\epsilon - (d-m)\log\epsilon - \sum_{j=1}^{m}(\log\lambda_j + \log(1+\tfrac{\epsilon}{\lambda_j}))\\
&\approx\sum_{j=1}^{m}(\lambda_j-\log\lambda_j) + m\log\epsilon - \epsilon\sum_{j=1}^{m}\tfrac{1}{\lambda_j} + d\epsilon - d\log\epsilon\\
&=\Omega_{ldd}(\mathbf{A}) + m + m\log\epsilon + O(\epsilon) - d\log\epsilon.
\end{aligned} \tag{2.19}$$

Dropping $O(\epsilon)$, we obtain

$$\Omega_{ldd}(\mathbf{A}) = D_{ldd}(\mathbf{A}^\top\mathbf{A}+\epsilon\mathbf{I}_d,\mathbf{I}_d) - (\log\epsilon+1)m + d\log\epsilon. \tag{2.20}$$

Replacing $\mathbf{A}^\top\mathbf{A}$ with $\mathbf{M}$, approximating m with $\text{tr}(\mathbf{M})$ and discarding constants, we obtain the convex LDD (CLDD) regularizer:

$$\widehat{\Omega}_{ldd}(\mathbf{M}) = D_{ldd}(\mathbf{M}+\epsilon\mathbf{I}_d,\mathbf{I}_d) - (1+\log\epsilon)\text{tr}(\mathbf{M}) \propto -\text{logdet}(\mathbf{M}+\epsilon\mathbf{I}_d) + (\log\tfrac{1}{\epsilon})\text{tr}(\mathbf{M}), \tag{2.21}$$

where the convexity of $\text{logdet}(\mathbf{M}+\epsilon\mathbf{I}_d)$ is proved in [53]. In [92, 280], an information theoretic regularizer based on the log-determinant divergence $D_{ldd}(\mathbf{M},\mathbf{I}) = -\text{logdet}(\mathbf{M}) + \text{tr}(\mathbf{M})$ is applied to encourage the Mahalanobis matrix to be close to an identity matrix. This regularizer requires $\mathbf{M}$ to be full rank while our convex LDD regularizer encourages $\mathbf{M}$ to be low-rank by associating a large weight $\log\frac{1}{\epsilon}$ to the trace norm $\text{tr}(\mathbf{M})$. Since $\mathbf{M}=\mathbf{A}^\top\mathbf{A}$, reducing the rank of $\mathbf{M}$ effectively reduces the number of components in $\mathbf{A}$.

Approximation errors We discuss the errors of convex approximation, which are generated from two sources: one is the approximation of $\Omega_\phi(\mathbf{A})$ using $D_\phi(\mathbf{A}^\top\mathbf{A}+\epsilon\mathbf{I}_d,\mathbf{I}_d)$ where the error is controlled by ϵ and can be arbitrarily small (by setting ϵ to be very small); the other is the approximation of the matrix rank using the trace norm. Though the error of the second approximation can be large, it has been both empirically and theoretically [62] demonstrated that decreasing the trace norm can effectively reduce rank. As validated in our experiments, though bearing approximation errors, these convex regularizers yield better performance than the original non-convex ones.

DML with convex BMD regularization Given these convex BMD (CBMD) regularizers (denoted by $\widehat{\Omega}_\phi(\mathbf{M})$ uniformly), we can relax the nonconvex BMD-DML problems into convex CBMD-DML formulations by replacing $\|\mathbf{A}\mathbf{x}-\mathbf{A}\mathbf{y}\|_2^2$ with $(\mathbf{x}-\mathbf{y})^\top\mathbf{M}(\mathbf{x}-\mathbf{y})$ and replacing the nonconvex BMD regularizers $\Omega_\phi(\mathbf{A})$ with $\widehat{\Omega}_\phi(\mathbf{M})$:

$$\begin{aligned}
&\min_{\mathbf{M}} \quad \tfrac{1}{|\mathcal{S}|}\sum_{(\mathbf{x},\mathbf{y})\in\mathcal{S}}(\mathbf{x}-\mathbf{y})^\top\mathbf{M}(\mathbf{x}-\mathbf{y}) + \tfrac{1}{|\mathcal{D}|}\sum_{(\mathbf{x},\mathbf{y})\in\mathcal{D}}\max(0,1-(\mathbf{x}-\mathbf{y})^\top\mathbf{M}(\mathbf{x}-\mathbf{y})) + \lambda\widehat{\Omega}_\phi(\mathbf{M})\\
&s.t. \quad \mathbf{M}\succeq 0.
\end{aligned} \tag{2.22}$$

This convex problem facilitates optimization: the global optimal is guaranteed to be achievable.

2.2.3 A Proximal Gradient Descent Algorithm

We use the stochastic proximal subgradient descent algorithm [270] to solve the CBMD-DML problems. The algorithm iteratively performs the following steps until convergence: (1) randomly sampling a mini-batch of data pairs, computing the subgradient $\triangle\mathbf{M}$ of the data-dependent loss (the first and second term in the objective function) defined on the mini-batch, then performing a subgradient descent update: $\widetilde{\mathbf{M}} = \mathbf{M} - \eta \triangle \mathbf{M}$, where η is a small stepsize; (2) applying proximal operators associated with the regularizers $\widetilde{\Omega}_\phi(\mathbf{M})$ to $\widetilde{\mathbf{M}}$. In step (1), the gradient of CBMD is $\log(\mathbf{M}+\epsilon\mathbf{I}_d)+\mathbf{I}_d$. To compute $\log(\mathbf{M}+\epsilon\mathbf{I}_d)$, we first perform an eigen-decomposition: $\mathbf{M}+\epsilon\mathbf{I}_d = \mathbf{U}\mathbf{\Lambda}\mathbf{U}^\top$; then take the log of every eigenvalue in $\mathbf{\Lambda}$, resulting in a new diagonal matrix $\widetilde{\mathbf{\Lambda}}$; finally compute $\log(\mathbf{M}+\epsilon\mathbf{I}_d)$ as $\mathbf{U}\widetilde{\mathbf{\Lambda}}\mathbf{U}^\top$. In the CLDD regularizer, the gradient of logdet$(\mathbf{M}+\epsilon\mathbf{I}_d)$ is $(\mathbf{M}+\epsilon\mathbf{I}_d)^{-1}$, which can be computed by eigen-decomposition as well. In step (2), the proximal operators associated with the regularizer $\widetilde{\Omega}_\phi(\mathbf{M})$ are derived by minimizing $\frac{1}{2\eta}\|\mathbf{M}-\widetilde{\mathbf{M}}\|_2^2 + \lambda\widetilde{\Omega}_\phi(\mathbf{M})$ subject to $\mathbf{M} \succeq 0$. Let $\{\tilde{\lambda}_j\}_{j=1}^d$ be the eigenvalues of $\widetilde{\mathbf{M}}$ and $\{x_j\}_{j=1}^d$ be the eigenvalues of $\mathbf{M}$, then this problem can be equivalently written as:

$$\begin{array}{ll} \min_{\{x_j\}_{j=1}^d} & \frac{1}{2\eta}\sum_{j=1}^d (x_j-\tilde{\lambda}_j)^2 + \lambda\sum_{j=1}^d h_\phi(x_j) \\ s.t. & \forall j = 1,\cdots,d, \quad x_j \geq 0, \end{array} \tag{2.23}$$

where $h_\phi(x_j)$ is a regularizer-specific scalar function. Further, this problem can be decomposed into d independent problems: **(a)** $\min_{x_j} f(x_j) = \frac{1}{2\eta}(x_j-\tilde{\lambda}_j)^2 + \lambda h_\phi(x_j)$ subject to $x_j \geq 0$, for $j = 1,\cdots,d$, which can be solved individually.

SFN For SFN where $\widetilde{\Omega}_\phi(\mathbf{M}) = \|\mathbf{M}-\mathbf{I}_d\|_F^2 + \text{tr}(\mathbf{M})$ and $h_\phi(x_j) = (x_j-1)^2 + x_j$, problem **(a)** is simply a quadratic programming problem. The optimal solution is $x_j^* = \max(0, \frac{\tilde{\lambda}_j+\eta\lambda}{1+2\eta\lambda})$.

VND For VND where $\widetilde{\Omega}_\phi(\mathbf{M}) = \text{tr}((\mathbf{M}+\epsilon\mathbf{I}_d)\log(\mathbf{M}+\epsilon\mathbf{I}_d))$ and $h_\phi(x_j) = (x_j+\epsilon)\log(x_j+\epsilon)$, by taking the derivative of the objective function $f(x_j)$ in problem **(a)** w.r.t x_j and setting the derivative to zero, we get $\eta\lambda\log(x_j+\epsilon) + x_j + \eta\lambda - \tilde{\lambda}_j = 0$. The root of this equation is: $\eta\lambda\omega(\frac{\epsilon-\eta\lambda+\tilde{\lambda}_j}{\eta\lambda} - \log(\eta\lambda)) - \epsilon$, where $\omega(\cdot)$ is the Wright omega function [137]. If this root is negative, then the optimal x_j is 0; if this root is positive, then the optimal x_j could be either this root or 0. We pick the one that yields the lowest $f(x_j)$. Formally, $x_j^* = \text{argmin}_{x_j} f(x_j)$, where $x \in \{\max(\eta\lambda\omega(\frac{\epsilon-\eta\lambda+\tilde{\lambda}_j}{\eta\lambda} - \log(\eta\lambda)) - \epsilon, 0), 0\}$.

LDD For LDD where $\widetilde{\Omega}_\phi(\mathbf{M}) = -\text{logdet}(\mathbf{M}+\epsilon\mathbf{I}_d) + (\log\frac{1}{\epsilon})\text{tr}(\mathbf{M})$ and $h_\phi(x_j) = -\log(x_j+\epsilon) + x_j\log\frac{1}{\epsilon}$, by taking the derivative of $f(x_j)$ w.r.t x_j and setting the derivative to zero, we get a quadratic equation: $x_j^2 + ax_j + b = 0$, where $a = \epsilon - \tilde{\lambda}_j - \eta\lambda\log\epsilon$ and $b = \eta\lambda(1-\epsilon\log\epsilon)$. The optimal solution is achieved either at the positive roots (if any) of this equation or 0. We pick the one that yields the lowest $f(x_j)$. Formally, $x_j^* = \text{argmin}_{x_j} f(x_j)$, where $x \in \{\max(\frac{-b+\sqrt{b^2-4ac}}{2a}, 0), \max(\frac{-b-\sqrt{b^2-4ac}}{2a}, 0), 0\}$.

	#Train	#Test	Dimension	#Class
MIMIC	40K	18K	1000	2833
EICU	53K	39K	1000	2175
Reuters	4152	1779	1000	49
News	11307	7538	1000	20
Cars	8144	8041	1000	196
Birds	9000	2788	1000	200
Act	7352	2947	561	6

Table 2.8: Dataset statistics.

Computational complexity In this algorithm, the major computation workload is eigen-decomposition of m-by-m matrices, with a complexity of $O(m^3)$. In our experiments, since m is no more than 1000, $O(m^3)$ is not a big bottleneck. Besides, these matrices are symmetric, the structures of which can thus be leveraged to speed up eigen-decomposition. In implementation, we use the MAGMA [7] library that supports efficient eigen-decomposition of symmetric matrices on GPUs. Note that the unregularized convex DML problem [383] also requires eigen-decomposition (of $\mathbf{M}$), hence adding these CBMD regularizes does not substantially increase additional computation cost.

2.2.4 Evaluation

In this section, we present experimental results on regularized distance metric learning, which demonstrate that compared with nonconvex BMD regularizers, the proposed convex regularizers are computationally more efficient and are more capable of capturing infrequent patterns and reducing model size without sacrificing modeling power.

Datasets We used seven datasets in the experiments: two electronic health record datasets MIMIC-III [184] and EICU (version 1.1) [131]; two text datasets Reuters [10] and 20-Newsgroups (News) [1]; two image datasets Stanford-Cars (Cars) [202] and Caltech-UCSD-Birds (Birds) [358]; and one sensory dataset 6-Activities (Act) [21]. The details of MIMIC-III, Cars, and Birds have been introduced in Section 2.1.4. The class labels in MIMIC are the primary diagnoses of patients. The EICU dataset contains hospital admissions of patients who were treated as part of the Philips eICU program across intensive care units in the United States between 2014 and 2015. Each admission has a primary diagnosis (a disease), which acts as the class label of this admission. There are 2175 unique diseases. There are 474 lab test items and 48 vital sign items. Each admission has a past medical history, which is a collection of diseases. There are 2644 unique past diseases. We extracted the following features: (1) age and gender; (2) zero, first, and second order temporal features of lab tests and vital signs; (3) past medical history: we used a binary vector to encode them; if an element in the vector is 1, then the patient had the corresponding disease in the past. The original Reuters-21578 dataset contains 21578 documents in 135 classes. We removed documents that have more than one labels, and removed classes that have less than 3 documents, which left us 5931 documents and 48 classes. Documents in Reuters and News are represented with *tf-idf* vectors where the vocabulary size is 5000. The 6-Activities

dataset contains sensory recordings of 30 subjects performing 6 activities (which are the class labels). The features are 561-dimensional sensory signals. For all the datasets except Act, the features are normalized using min-max normalization along each dimension. We used PCA to reduce the feature dimension to 1000 to reduce the computational complexity (performing eigen-decomposition of the Mahalanobis matrix bears cubic complexity in term of feature dimension). Since there is no standard split of the train/test set, we performed five random splits and averaged the results of the five runs. Dataset statistics are summarized in Table 2.8.

Experimental settings Two examples are considered as being similar if they belong to the same class and dissimilar if otherwise. The learned distance metrics were applied for retrieval (using each test example to query the rest of the test examples). For each test example, we used it to query the rest of test examples based on the learned distance metric. If the distance between $\mathbf{x}$ and $\mathbf{y}$ is smaller than a threshold s and they have the same class label, then this is a true positive. By choosing different values of s, we obtained a receiver operating characteristic (ROC) curve. The retrieval performance was evaluated using the area under (ROC) curve (AUC) [243] which is the higher, the better. For AUC on infrequent classes, we used examples belonging to infrequent classes to query the entire test set (excluding the query). AUC on frequent classes was measured in a similar way. Note that the learned distance metrics can also be applied to other tasks such as clustering and classification. In this work, we focus on retrieval.

We compared the proposed convex diversity-promoting regularizers CSFN, CVND, CLDD with two sets of baseline regularizers. The first set aims at promoting near-orthogonality ("diversity"), which are based on determinant of covariance matrix (DCM) [242], cosine similarity (CS) [402], determinantal point process (DPP) [204, 429], InCoherence (IC) [29], variational Gram function (VGF) [177, 420], decorrelation (DC) [82], mutual angles (MA) [369], squared Frobenius norm (SFN) [74, 114, 122, 347], von Neumann divergence (VND) (Section 2.2.1), log-determinant divergence (LDD) (Section 2.2.1), and orthogonal constraint (OC) $\mathbf{A}\mathbf{A}^\top = \mathbf{I}$ [233, 342]. These regularizers were applied to the nonconvex DML (NCDML) formulation in Eq.(2.14). Though VGF is convex, when it is used to regularize NCDML, the overall problem is non-convex and it is unclear how to seek a convex relaxation. The other set of regularizers are not designed particularly for promoting diversity but are commonly used, including ℓ_2 norm, ℓ_1 norm [280], $\ell_{2,1}$ norm [399], trace norm (Tr) [234], information theoretic (IT) regularizer $-\text{logdet}(\mathbf{M}) + \text{tr}(\mathbf{M})$ [92], and dropout [313]. All these regularizers were applied to the convex DML (CDML) formulation in Eq.(2.22). One common way of dealing with class-imbalance is *over-sampling* (OS) [116], which repetitively draws samples from the empirical distributions of infrequent classes until all classes have the same number of samples. In addition, we compared with the vanilla Euclidean distance (EUC) and other distance learning methods including large margin nearest neighbor (LMNN) metric learning [357], information theoretic metric learning (ITML) [92], logistic discriminant metric learning (LDML) [146], metric learning from equivalence constraints (MLEC) [200], geometric mean metric learning (GMML) [405], and independent Laplacian hashing with diversity (ILHD) [63]. In LMNN [357], there is a non-convex formulation and a convex formulation. We used the convex one. In GMML [405], the prior matrix was set to an identity matrix. ILHD [63] has several variants, among which we used ILTITF.

	MIMIC	EICU	Reuters	News	Cars	Birds	Act
NCDML	62.1	66.6	5.2	11.0	8.4	10.1	3.4
CDML	3.4	3.7	0.3	0.6	0.5	0.6	0.2
DCM-NCDML [242]	424.7	499.2	35.2	65.6	61.8	66.2	17.2
CS-NCDML [402]	263.2	284.8	22.6	47.2	34.5	42.8	14.4
DPP-NCDML [429]	411.8	479.1	36.9	61.9	64.2	70.5	16.5
IC-NCDML [29]	265.9	281.2	23.4	46.1	37.5	45.2	15.3
DC-NCDML [82]	458.5	497.5	41.8	78.2	78.9	80.7	19.9
VGF-NCDML [177]	267.3	284.1	22.3	48.9	35.8	38.7	15.4
MA-NCDML [367]	271.4	282.9	23.6	50.2	30.9	39.6	17.5
OC-NCDML [233]	104.9	118.2	9.6	14.3	14.8	17.0	3.9
SFN-NCDML [74]	261.7	277.6	22.9	46.3	36.2	38.2	15.9
VND-NCDML	401.8	488.3	33.8	62.5	67.5	73.4	17.1
LDD-NCDML	407.5	483.5	34.3	60.1	61.8	72.6	17.9
CSFN-CDML	41.1	43.9	3.3	7.3	6.5	6.9	1.8
CVND-CDML	43.8	46.2	3.6	8.1	6.9	7.8	2.0
CLDD-CDML	41.7	44.5	3.4	7.5	6.6	7.2	1.8

Table 2.9: Training time (hours) on seven datasets. On the second panel (DCM-NCDML, etc.) are NCDML methods regularized by previously proposed diversity-promoting regularizers. On the third panel (VND-NCDML, etc.) are NCDML methods regularized by our proposed nonconvex BMD regularizers. On the fourth panel (CSFN-CDML, etc.) are CDML methods regularized by our proposed convex BMD regularizers.

The NCDML-based methods except NCDML-OC were solved with stochastic subgradient descent (SSD). NCDML-OC was solved using the algorithm proposed in [359]. The CDML-based methods were solved with proximal SSD. The learning rate was set to 0.001. The mini-batch size was set to 100 (50 similar pairs and 50 dissimilar pairs). We used 5-fold cross validation to tune the regularization parameter among $\{10^{-3}, \cdots, 10^{0}\}$ and the number of components of the NCDML methods among $\{50, 100, 200, \cdots, 500\}$. In CVND and CLDD, ϵ was set to $1e-5$. The margin t was set to 1. In LMNN, the weighting parameter μ was set to 0.5. In GMML [405], the regularization parameter λ was set to 0.1. The step length t of geodesic was set to 0.3. In ILHD [63], the hash function was set to the kernel SVM [294] with a radial basis function kernel whose scale parameter was chosen to be 0.1. Each method was implemented on top of GPUs using the MAGMA [7] library. The experiments were conducted on a GPU-cluster with 40 machines.

For computational efficiency, in CDML-based methods, we do not use $(\mathbf{x}-\mathbf{y})^\top \mathbf{M}(\mathbf{x}-\mathbf{y})$ to compute distance directly. Given the learned matrix $\mathbf{M}$ (which is of rank m), we can decompose it into $\mathbf{L}^\top\mathbf{L}$ where $\mathbf{L} \in \mathbb{R}^{m\times d}$. Let $\mathbf{U}\mathbf{\Lambda}\mathbf{U}^\top$ be the eigen-decomposition of $\mathbf{M}$. Let $\lambda_1, \cdots, \lambda_m$ denote the m nonzero eigenvalues and $\mathbf{u}_i, \cdots, \mathbf{u}_m$ denote the corresponding eigenvectors. Then $\mathbf{L}$ is the transpose of $[\sqrt{\sigma_1}\mathbf{u}_1, \cdots, \sqrt{\sigma_m}\mathbf{u}_m]$. Given $\mathbf{L}$, we can use it to transform each input d-dimensional feature vector $\mathbf{x}$ into a new m-dimensional vector $\mathbf{L}\mathbf{x}$, then perform retrieval on the new vectors based on the Euclidean distance. Note that only when computing Euclidean distance

between $\mathbf{Lx}$ and $\mathbf{Ly}$, we have that $\|\mathbf{Lx}-\mathbf{Ly}\|_2^2$ is equivalent to $(\mathbf{x}-\mathbf{y})^\top\mathbf{M}(\mathbf{x}-\mathbf{y})$. For other distances or similarity measures between $\mathbf{Lx}$ and $\mathbf{Ly}$, such as L1 distance and cosine similarity, this does not hold. Performing retrieval based on $\|\mathbf{Lx}-\mathbf{Ly}\|_2^2$ is more efficient than that based on $(\mathbf{x}-\mathbf{y})^\top\mathbf{M}(\mathbf{x}-\mathbf{y})$ when m is smaller than d. Given n test examples, the computation complexity of $\|\mathbf{Lx}-\mathbf{Ly}\|_2^2$-based retrieval is $O(nmd+n^2m)$, while that of $(\mathbf{x}-\mathbf{y})^\top\mathbf{M}(\mathbf{x}-\mathbf{y})$-based retrieval is $O(n^2d^2)$.

Results The training time taken by different methods to reach convergence is shown in Table 2.9. For NCDML-based methods, we report the total time taken by the following computation: tuning the regularization parameter (4 choices) and the number of components (NCs, 6 choices) on a two-dimensional grid via 3-fold cross validation ($4 \times 6 \times 3 = 72$ experiments in total); for each of the 72 experiments, the algorithm restarted 5 times, each with a different initialization, and we picked the one yielding the lowest objective value. In total, the number of runs is $72 \times 5 = 360$. For the CDML-based methods, there is no need to restart multiple times or tune the NCs. The total number of runs is $4 \times 3 = 12$. As can be seen from the table, the proposed convex methods are much faster than the non-convex ones, due to the greatly reduced number of experimental runs, although for each single run the convex methods are less efficient than the non-convex methods due to the overhead of eigen-decomposition. The unregularized CDML takes the least time to train since it has no parameters to tune and runs only once. On average, the time of each single run in (CSFN,CVND,CLDD)-CDML is close to that in the unregularized CDML, since an eigen-decomposition is required anyway regardless of the presence of the regularizers. Unregularized NCDML runs faster that regularized NCDML methods because it has no need to tune the regularization parameter, which reduces the number of experimental runs by 4 times. Unregularized CDML runs faster than regularized CDML methods because it has no need to tune the regularization parameter or the number of projection vectors, which reduces the number of experimental runs by 12 times. (DCM,DPP,VND,LDD)-NCDML methods take longer time than other regularized NCDML methods since they need eigen-decomposition to compute the gradients. OC-NCDML has no regularization parameter to tune, hence its number of experimental runs is 4 times fewer than other regularized NCDML methods.

Next, we verify whether CSFN, CVND, and CLDD are able to better capture infrequent patterns. On three datasets MIMIC, EICU, and Reuters where the classes are imbalanced, we consider a class as being "frequent" if it contains more than 1000 examples, and "infrequent" if otherwise. We measure AUCs on all classes (AUC-All), infrequent classes (AUC-IF), and frequent classes (AUC-F). As can be seen, in most DML methods, the AUCs on infrequent classes are worse than those on frequent classes, showing that DML is sensitive to the imbalance of class-frequency and tends to be biased towards frequent classes and is less capable of capturing infrequent classes. This is in accordance with the previous findings [369]. Adding our proposed CSFN, CVND, CLDD regularizers to CDML, the AUCs on infrequent classes are greatly improved. This demonstrates that these convex regularizers can effectively capture infrequent patterns. By encouraging the components to be close to being orthogonal, our methods can reduce the redundancy among vectors. Mutually complementary vectors can achieve a broader coverage of latent features, including those associated with infrequent classes. As a result, these vectors improve the performance on infrequent classes.

Thanks to their convexity nature, our methods can achieve the global optimal solution and outperform the non-convex ones that can only achieve a local optimal and hence a sub-optimal solution. (C)VND and (C)LDD outperform (C)SFN, possibly because they measure near-orthogonality in a global way while (C)SFN conducts that in a pairwise fashion. Comparing OS-(NCDML,CDML) with the unregularized NCDML/CDML, we can see that over-sampling indeed improves performance on infrequent classes. However, this improvement is less significant than that achieved by our methods. In general, the diversity-promoting (DP) regularizers outperform the non-DP regularizers, suggesting the effectiveness of promoting diversity. The orthogonal constraint (OC) [233, 342] imposes strict orthogonality, which may be too restrictive that hurts performance. ILHD [63] learns binary hash codes, which makes retrieval more efficient. However, it achieves lower AUCs due to the quantization errors. (CSFN,CVND,CLDD)-CDML outperform popular DML approaches including LMNN, LDML, MLEC, and GMML, demonstrating their competitive standing in the DML literature.

Next we verify whether the proposed CDML methods are able to reduce model size without sacrificing modeling power. Table 2.12 shows the numbers of components that achieve the AUCs in Table 6.1 and 2.11. For CDML-based methods, the number of components (NC) is the rank of the Mahalanobis matrix since $\mathbf{M} = \mathbf{A}^\top \mathbf{A}$. We define a *compactness score* (CS) which is the ratio between AUC-All and NC. A higher CS indicates the better ability of using fewer components to achieve higher AUC. From Table 2.12, we see that the convex methods achieve larger CS than the baseline methods, demonstrating its better ability of conducting performance-lossless reduction of model size. (C)VND and (C)LDD perform better than (C)SFN, demonstrating the necessity of promoting diversity in a global manner. The proposed convex diversity-promoting (DP) regularizers outperform nonconvex DP regularizers, demonstrating their better ability in promoting diversity thanks to their convex nature. Note that the reduced component number improves the efficiency of retrieval where the computational complexity grows linearly with this number.

As can be seen from Table 6.1 and 2.11, our methods (CSFN,CVND,CLDD)-CDML achieve the best AUC-All on the test set. Table 6.3 shows the difference between training AUC and testing AUC. Our methods have the smallest gap between training and testing AUCs. This indicates that our methods are better capable of reducing overfitting and improving generalization performance.

2.3 Angular Constraints for Improving Generalization Performance

In previous two sections, we have empirically demonstrated that diversity-promoting regularization can improve generalization performance. One intuitive explanation could be: promoting diversity imposes a structural constraint on model parameters, which reduces model capacity and therefore alleviates overfitting. However, in theory why larger "diversity" results in lower generalization error (which is the sum of estimation and approximation errors) is still missing. The uniform eigenvalue regularizer and the Bregman matrix divergence (BMD) regularizers studied previously are not amenable for such analysis, especially for the approximation errors. In this

section, we aim at bridging this gap, by proposing a diversity-promoting approach that is both empirically effective and theoretically analyzable. Similar to Section 2.2, we continue to use near-orthogonality to represent "diversity", but via a different regularization approach – angular constraints (ACs) [372] where the angle between components is constrained to be close to $\frac{\pi}{2}$, which hence encourages the components to be close to being orthogonal. Using neural network as a study case, we analyze how ACs affect its generalization error (Section 4.2.1). The analysis shows that the more close to $\frac{\pi}{2}$ the angles are, the smaller the estimation error is and the larger the approximation error is. The best tradeoffs of these two errors can be explored by properly tuning the angles. We develop an algorithm based on the alternating direction method of multipliers (ADMM) [52] to solve the angle-constrained problems. In various experiments, we demonstrate that ACs improve the generalization performance and outperform other diversity-promoting regularization approaches.

2.3.1 Angular Constraints

Similar to the BMD regularizers (Section 2.2), angular constraints (ACs) use near-orthogonality to characterize "diversity" and encourage the angles between component vectors to be close to $\pi/2$. The ACs are defined as requiring the absolute value of the cosine similarity between each pair of components to be less equal to a small value τ, which leads to the following angle-constrained problem

$$\begin{array}{ll} \min\limits_{\mathcal{W}} & \mathcal{L}(\mathcal{W}) \\ s.t. & 1 \leq i < j \leq m, \frac{|\mathbf{w}_i \cdot \mathbf{w}_j|}{\|\mathbf{w}_i\|_2 \|\mathbf{w}_j\|_2} \leq \tau, \end{array} \tag{2.24}$$

where $\mathcal{W} = \{\mathbf{w}_i\}_{i=1}^m$ denotes the component vectors and $\mathcal{L}(\mathcal{W})$ is the objective function of this problem. The parameter τ controls the level of near-orthogonality (or diversity). A smaller τ indicates that the vectors are more close to being orthogonal, and hence are more diverse. As will be shown later, representing diversity using the angular constraints facilitates theoretical analysis and is empirically effective as well.

Case study I: sparse coding Given a set of data samples $\{\mathbf{x}_i\}_{i=1}^n$, where $\mathbf{x} \in \mathbb{R}^d$, sparse coding (SC) [266] aims at using a set of "basis" vectors (referred to as *dictionary*) $\mathcal{W} = \{\mathbf{w}_j\}_{j=1}^m$ to reconstruct the data samples. Each data sample $\mathbf{x}$ is reconstructed by taking a sparse linear combination of the basis vectors $\mathbf{x} \approx \sum_{j=1}^m \alpha_j \mathbf{w}_j$ where $\{\alpha_j\}_{j=1}^m$ are the linear coefficients (referred to as *sparse codes*) and most of them are zero. The reconstruction error is measured using the squared ℓ_2 norm $\|\mathbf{x} - \sum_{j=1}^m \alpha_j \mathbf{w}_j\|_2^2$. To achieve sparsity among the coefficients, ℓ_1-regularization is utilized: $\sum_{j=1}^m |\alpha_j|_1$. To avoid the degenerated case where most coefficients are zero and the basis vectors are of large magnitude, ℓ_2-regularization is applied to the basis vectors: $\|\mathbf{w}_j\|_2^2$. Putting these pieces together, we learn the basis vectors and sparse codes (denoted by $\mathcal{A}$) by minimizing the following objective function: $\mathcal{L}(\mathcal{W}, \mathcal{A}) = \frac{1}{2}\sum_{i=1}^n (\|\mathbf{x}_i - \sum_{j=1}^m \alpha_{ij}\mathbf{w}_j\|_2^2 + \lambda_1 \sum_{j=1}^m |\alpha_{ij}|_1) + \lambda_2 \sum_{j=1}^m \|\mathbf{w}_j\|_2^2$. We can use the ACs to encourage the basis vectors to be "diverse".

Case study II: neural networks In a neural network (NN) with L hidden layers, each hidden layer l is equipped with $m^{(l)}$ units and each unit i is connected with all units in layer $l-1$. Hidden unit i at layer l is parameterized by a weight vector $\mathbf{w}_i^{(l)}$. These hidden units aim at capturing latent features underlying the data. We can apply ACs to the weight vectors of hidden units (in the same layer) to encourage diversity.

Connection with the log-determinant divergence regularizer

In this section, we make a connection between the angular constraints and the log-determinant divergence (LDD) regularizer (Section 2.2.1). Let $s_{ij} = \frac{|\langle \mathbf{w}_i, \mathbf{w}_j \rangle|}{\|\mathbf{w}_i\|_2 \|\mathbf{w}_j\|_2}$ be the absolute value of the cosine similarity between $\mathbf{w}_i$ and $\mathbf{w}_j$. The angular constraints can be equivalently written as

$$s(\mathcal{W}) = (\max_{1 \leq i < j \leq m} s_{ij}) \leq \tau. \tag{2.25}$$

It can be proved that the negative gradient of the LDD regularizer $\Omega_{ldd}(\mathcal{W})$ is an descent direction of $s(\mathcal{W})$, which is formally given in the following lemma.

Lemma 1. *Let $\widehat{\mathcal{W}} = \{\widehat{\mathbf{w}}_i\}_{i=1}^m$ be a set of vectors where $\widehat{\mathbf{w}}_i = \mathbf{w}_i - \eta \mathbf{g}_i$ and $\mathbf{g}_i$ is the gradient of $\Omega_{ldd}(\mathcal{W})$ w.r.t $\mathbf{w}_i$. Then $\exists \delta > 0$ such that $\forall \eta \in (0, \delta)$, $s(\widehat{\mathcal{W}}) \leq s(\mathcal{W})$.*

This implies that $\Omega_{ldd}(\mathcal{W})$ and $s(\mathcal{W})$ are closely aligned. Decreasing $\Omega_{ldd}(\mathcal{W})$ effectively decreases $s(\mathcal{W})$ and drives the angles among components to approach $\pi/2$.

In addition, it can be showed that the variance of angles can be reduced by minimizing $\Omega_{ldd}(\mathcal{W})$. Consider a set of angles $\{\theta_{ij}\}$ where $\theta_{ij} = \arccos(s_{ij})$, for all $i \neq j$. Let $\text{var}(\{\theta_{ij}\})$ denote the variance of the angles. Then we have the following lemma.

Lemma 2. *Let $\widehat{\mathcal{W}} = \{\widehat{\mathbf{w}}_i\}_{i=1}^m$ be a set of vectors where $\widehat{\mathbf{w}}_i = \mathbf{w}_i - \eta \mathbf{g}_i$ and $\mathbf{g}_i$ is the gradient of $\Omega_{ldd}(\mathcal{W})$ w.r.t $\mathbf{w}_i$. Let $\hat{s}_{ij} = \frac{|\langle \widehat{\mathbf{w}}_i, \widehat{\mathbf{w}}_j \rangle|}{\|\widehat{\mathbf{w}}_i\|_2 \|\widehat{\mathbf{w}}_j\|_2}$ and $\hat{\theta}_{ij} = \arccos(\hat{s}_{ij})$. Then $\exists \delta > 0$ such that $\forall \eta \in (0, \delta)$, var$(\{\hat{\theta}_{ij}\}) \leq$ var$(\{\theta_{ij}\})$.*

2.3.2 An ADMM-based Algorithm

In this section, we develop an ADMM-based algorithm to solve the AC regularized problems. To make it amenable for optimization, we first factorize each weight vector $\mathbf{w}$ into its ℓ_2 norm $g = \|\mathbf{w}\|_2$ and direction $\widetilde{\mathbf{w}} = \frac{\mathbf{w}}{\|\mathbf{w}\|_2}$. Under such a factorization, $\mathbf{w}$ can be reparameterized as $\mathbf{w} = g\widetilde{\mathbf{w}}$, where $g > 0$ and $\|\widetilde{\mathbf{w}}\|_2 = 1$. Then the problem defined in Eq.(2.24) can be transformed into

$$\begin{array}{ll} \min\limits_{\widetilde{\mathcal{W}}, \mathcal{G}} & \mathcal{L}(\widetilde{\mathcal{W}}, \mathcal{G}) \\ s.t. & \forall j, g_j \geq 0, \|\widetilde{\mathbf{w}}_j\|_2 = 1 \\ & \forall i \neq j, |\widetilde{\mathbf{w}}_i \cdot \widetilde{\mathbf{w}}_j| \leq \tau, \end{array} \tag{2.26}$$

where $\widetilde{\mathcal{W}} = \{\widetilde{\mathbf{w}}_j\}_{j=1}^m$ and $\mathcal{G} = \{g_j\}_{j=1}^m$. We solve this new problem by alternating between $\widetilde{\mathcal{W}}$ and $\mathcal{G}$. With $\widetilde{\mathcal{W}}$ fixed, the problem defined over $\mathcal{G}$ is: $\min_{\mathcal{G}} \mathcal{L}(\mathcal{G})$ subject to $\forall j, g_j \geq 0$, which can be solved using projected gradient descent. With $\mathcal{G}$ fixed, the sub-problem defined over $\widetilde{\mathcal{W}}$

is

$$\begin{aligned} \min_{\widetilde{\mathcal{W}}} \quad & \mathcal{L}(\widetilde{\mathcal{W}}) \\ s.t. \quad & \forall j, \|\widetilde{\mathbf{w}}_j\|_2 = 1 \\ & \forall i \neq j, |\widetilde{\mathbf{w}}_i \cdot \widetilde{\mathbf{w}}_j| \leq \tau, \end{aligned} \tag{2.27}$$

which we solve using an ADMM-based algorithm. There are $R = m(m-1)$ pairwise constraints $|\widetilde{\mathbf{w}}_i \cdot \widetilde{\mathbf{w}}_j| \leq \tau$. For the r-th constraint, let $p(r)$ and $q(r)$ be the index of the first and second vector respectively, i.e., the r-th constraint is $|\widetilde{\mathbf{w}}_{p(r)} \cdot \widetilde{\mathbf{w}}_{q(r)}| \leq \tau$. First, we introduce auxiliary variables $\{\mathbf{v}_1^{(r)}\}_{r=1}^R$ and $\{\mathbf{v}_2^{(r)}\}_{r=1}^R$, to rewrite the problem in Eq.(2.27) into an equivalent form. For each pairwise constraint: $|\widetilde{\mathbf{w}}_{p(r)} \cdot \widetilde{\mathbf{w}}_{q(r)}| \leq \tau$, we introduce two auxiliary vectors $\mathbf{v}_1^{(r)}$ and $\mathbf{v}_2^{(r)}$, and let $\widetilde{\mathbf{w}}_{p(r)} = \mathbf{v}_1^{(r)}$, $\widetilde{\mathbf{w}}_{q(r)} = \mathbf{v}_2^{(r)}$, $\|\mathbf{v}_1^{(r)}\|_2 = 1$, $\|\mathbf{v}_2^{(r)}\|_2 = 1$, $|\mathbf{v}_1^{(r)} \cdot \mathbf{v}_2^{(r)}| \leq \tau$. To this end, we obtain the following problem

$$\begin{aligned} \min_{\widetilde{\mathcal{W}},\mathcal{V}} \quad & \mathcal{L}(\widetilde{\mathcal{W}}) \\ s.t. \quad & \forall j, \|\widetilde{\mathbf{w}}_j\|_2 = 1 \\ & \forall r, \widetilde{\mathbf{w}}_{p(r)} = \mathbf{v}_1^{(r)}, \widetilde{\mathbf{w}}_{q(r)} = \mathbf{v}_2^{(r)} \\ & \forall r, \|\mathbf{v}_1^{(r)}\|_2 = 1, \|\mathbf{v}_2^{(r)}\|_2 = 1, |\mathbf{v}_1^{(r)} \cdot \mathbf{v}_2^{(r)}| \leq \tau, \end{aligned} \tag{2.28}$$

where $\mathcal{V} = \{(\mathbf{v}_1^{(r)}, \mathbf{v}_2^{(r)})\}_{r=1}^R$. Then we define the augmented Lagrangian, with Lagrange multipliers $\mathcal{Y} = \{(\mathbf{y}_1^{(r)}, \mathbf{y}_2^{(r)})\}_{r=1}^R$ and parameter ρ

$$\begin{aligned} \min_{\widetilde{\mathcal{W}},\mathcal{V},\mathcal{Y}} \quad & \mathcal{L}(\widetilde{\mathcal{W}}) + \sum_{r=1}^R (\mathbf{y}_1^{(r)} \cdot (\widetilde{\mathbf{w}}_{p(r)} - \mathbf{v}_1^{(r)}) + \mathbf{y}_2^{(r)} \cdot (\widetilde{\mathbf{w}}_{q(r)} - \mathbf{v}_2^{(r)}) + \tfrac{\rho}{2}\|\widetilde{\mathbf{w}}_{p(r)} - \mathbf{v}_1^{(r)}\|_2^2 \\ & + \tfrac{\rho}{2}\|\widetilde{\mathbf{w}}_{q(r)} - \mathbf{v}_2^{(r)}\|_2^2) \\ s.t. \quad & \forall j, \|\widetilde{\mathbf{w}}_j\|_2 = 1 \\ & \forall r, \|\mathbf{v}_1^{(r)}\|_2 = 1, \|\mathbf{v}_2^{(r)}\|_2 = 1, |\mathbf{v}_1^{(r)} \cdot \mathbf{v}_2^{(r)}| \leq \tau, \end{aligned} \tag{2.29}$$

which can be solved by alternating between $\widetilde{\mathcal{W}}$, $\mathcal{V}$, $\mathcal{Y}$.

Solve $\widetilde{\mathcal{W}}$ The sub-problem defined over $\widetilde{\mathcal{W}}$ is

$$\begin{aligned} \min_{\widetilde{\mathcal{W}}} \quad & \mathcal{L}(\widetilde{\mathcal{W}}) + \sum_{r=1}^R (\mathbf{y}_1^{(r)} \cdot \widetilde{\mathbf{w}}_{p(r)} + \mathbf{y}_2^{(r)} \cdot \widetilde{\mathbf{w}}_{q(r)} + \tfrac{\rho}{2}\|\widetilde{\mathbf{w}}_{p(r)} - \mathbf{v}_1^{(r)}\|_2^2 + \tfrac{\rho}{2}\|\widetilde{\mathbf{w}}_{q(r)} - \mathbf{v}_2^{(r)}\|_2^2) \\ s.t. \quad & \forall j, \|\widetilde{\mathbf{w}}_j\|_2 = 1. \end{aligned} \tag{2.30}$$

For sparse coding, we solve this sub-problem using coordinate descent. At each iteration, we update $\widetilde{\mathbf{w}}_j$ by fixing the other variables. For neural network, this sub-problem can be solved using projected gradient descent which iteratively performs the following three steps: (1) compute the gradient of $\widetilde{\mathbf{w}}_j$ using backpropagation; (2) perform a gradient descent update of $\widetilde{\mathbf{w}}_j$; (3) project each vector onto the unit sphere: $\widetilde{\mathbf{w}}_j \leftarrow \widetilde{\mathbf{w}}_j / \|\widetilde{\mathbf{w}}_j\|_2$.

Solve $\mathbf{v}_1^{(r)}, \mathbf{v}_2^{(r)}$ The corresponding sub-problem is

$$\begin{aligned} \min_{\mathbf{v}_1^{(r)}, \mathbf{v}_2^{(r)}} \quad & -\mathbf{y}_1^{(r)} \cdot \mathbf{v}_1^{(r)} - \mathbf{y}_2^{(r)} \cdot \mathbf{v}_2^{(r)} + \frac{\rho}{2}\|\widetilde{\mathbf{w}}_{p(r)} - \mathbf{v}_1^{(r)}\|_2^2 + \frac{\rho}{2}\|\widetilde{\mathbf{w}}_{q(r)} - \mathbf{v}_2^{(r)}\|_2^2 \\ s.t. \quad & \|\mathbf{v}_1^{(r)}\|_2 = 1, \|\mathbf{v}_2^{(r)}\|_2 = 1, \mathbf{v}_1^{(r)} \cdot \mathbf{v}_2^{(r)} \leq \tau, -\mathbf{v}_1^{(r)} \cdot \mathbf{v}_2^{(r)} \leq \tau. \end{aligned} \tag{2.31}$$

Let γ_1, γ_2, $\lambda_1 \geq 0$, $\lambda_2 \geq 0$ be the KKT multipliers associated with the four constraints in this sub-problem. According to the KKT conditions [53], we have

$$-\mathbf{y}_1^{(r)} + \rho(\mathbf{v}_1^{(r)} - \widetilde{\mathbf{w}}_{p(r)}) + 2\gamma_1\mathbf{v}_1^{(r)} + (\lambda_1 - \lambda_2)\mathbf{v}_2^{(r)} = 0 \tag{2.32}$$

$$-\mathbf{y}_2^{(r)} + \rho(\mathbf{v}_2^{(r)} - \widetilde{\mathbf{w}}_{q(r)}) + 2\gamma_2\mathbf{v}_2^{(r)} + (\lambda_1 - \lambda_2)\mathbf{v}_1^{(r)} = 0. \tag{2.33}$$

We solve these two equations by examining four cases.

Case 1 First, we assume $\lambda_1 = 0, \lambda_2 = 0$, then $(\rho+2\gamma_1)\mathbf{v}_1^{(r)} = \mathbf{y}_1^{(r)} + \rho\widetilde{\mathbf{w}}_{p(r)}$ and $(\rho+2\gamma_2)\mathbf{v}_2^{(r)} = \mathbf{y}_2^{(r)} + \rho\widetilde{\mathbf{w}}_{q(r)}$. According to the primal feasibility [53] $\|\mathbf{v}_1^{(r)}\|_2 = 1$ and $\|\mathbf{v}_2^{(r)}\|_2 = 1$, we know

$$\mathbf{v}_1^{(r)} = \frac{\mathbf{y}_1^{(r)} + \rho\widetilde{\mathbf{w}}_{p(r)}}{\|\mathbf{y}_1^{(r)} + \rho\widetilde{\mathbf{w}}_{p(r)}\|_2}, \ \mathbf{v}_2^{(r)} = \frac{\mathbf{y}_2^{(r)} + \rho\widetilde{\mathbf{w}}_{q(r)}}{\|\mathbf{y}_2^{(r)} + \rho\widetilde{\mathbf{w}}_{q(r)}\|_2}. \tag{2.34}$$

Then we check whether the constraint $|\mathbf{v}_1^{(r)} \cdot \mathbf{v}_2^{(r)}| \leq \tau$ is satisfied. If so, then $\mathbf{v}_1^{(r)}$ and $\mathbf{v}_2^{(r)}$ are the optimal solution.

Case 2 We assume $\lambda_1 > 0$ and $\lambda_2 = 0$, then

$$(\rho + 2\gamma_1)\mathbf{v}_1^{(r)} + \lambda_1\mathbf{v}_2^{(r)} = \mathbf{y}_1^{(r)} + \rho\widetilde{\mathbf{w}}_{p(r)} \tag{2.35}$$

$$(\rho + 2\gamma_2)\mathbf{v}_2^{(r)} + \lambda_1\mathbf{v}_1^{(r)} = \mathbf{y}_2^{(r)} + \rho\widetilde{\mathbf{w}}_{q(r)}. \tag{2.36}$$

According to the complementary slackness condition [53], we know $\mathbf{v}_1^{(r)} \cdot \mathbf{v}_2^{(r)} = \tau$. For the vectors on both sides of Eq.(2.35), taking the square of their ℓ_2 norm, we get

$$(\rho + 2\gamma_1)^2 + \lambda_1^2 + 2(\rho + 2\gamma_1)\lambda_1\tau = \|\mathbf{y}_1^{(r)} + \rho\widetilde{\mathbf{w}}_{p(r)}\|_2^2. \tag{2.37}$$

Similarly, from Eq.(2.36), we get

$$(\rho + 2\gamma_2)^2 + \lambda_1^2 + 2(\rho + 2\gamma_2)\lambda_1\tau = \|\mathbf{y}_2^{(r)} + \rho\widetilde{\mathbf{w}}_{q(r)}\|_2^2. \tag{2.38}$$

Taking the inner product of the two vectors on the left hand sides of Eq.(2.35,2.36), and those on the right hand sides, we get

$$(2\rho + 2\gamma_1 + 2\gamma_2)\lambda_1 + ((\rho + 2\gamma_1)(\rho + 2\gamma_2) + \lambda_1^2)\tau = (\mathbf{y}_1^{(r)} + \rho\widetilde{\mathbf{w}}_{p(r)})^\top(\mathbf{y}_2^{(r)} + \rho\widetilde{\mathbf{w}}_{q(r)}). \tag{2.39}$$

Solving the system of equations consisting of Eq.(2.37-2.39), we obtain the optimal values of γ_1, γ_2, and λ_1. Plugging them into Eq.(2.35) and Eq.(2.36), we obtain a solution of $\mathbf{v}_1^{(r)}$ and $\mathbf{v}_2^{(r)}$. Then we check whether this solution satisfies $-\mathbf{v}_1^{(r)} \cdot \mathbf{v}_2^{(r)} \leq \tau$. If so, this is an optimal solution.

In Case 3, we discuss $\lambda_1 = 0$, $\lambda_2 > 0$. In Case 4, we discuss $\lambda_1 > 0$, $\lambda_2 > 0$. The corresponding problems can be solved in a similar way as Case 2.

Solve $\mathbf{y}_1^{(r)}, \mathbf{y}_2^{(r)}$ We simply perform the following updates:

$$\mathbf{y}_1^{(r)} = \mathbf{y}_1^{(r)} + \rho(\widetilde{\mathbf{w}}_{p(r)} - \mathbf{v}_1^{(r)}) \tag{2.40}$$

$$\mathbf{y}_2^{(r)} = \mathbf{y}_2^{(r)} + \rho(\widetilde{\mathbf{w}}_{q(r)} - \mathbf{v}_2^{(r)}). \tag{2.41}$$

Compared with a vanilla backpropagation algorithm, the major extra cost in this ADMM-based algorithm comes from solving the $R = m(m-1)$ pairs of vectors $\{\mathbf{v}_1^{(r)}, \mathbf{v}_2^{(r)}\}_{r=1}^R$. Solving each pair incurs $O(m)$ cost. The R pairs bring in a total cost of $O(m^3)$. Such a cubic cost is also incurred in other diversity-promoting methods such as [29, 213]. In practice, m is typically less than 1000. This $O(m^3)$ cost does not substantially bottleneck computation, as we will validate in experiments.

2.3.3 Evaluation

In this section, we empirically show the effectiveness of the angular constraints. The theoretical analysis is deferred to Section 4.2.1.

Sparse Coding

Following [392], we applied sparse coding for image feature learning. We used three datasets in the experiments: Scenes-15 [212], Caltech-256 [141], and UIUC-Sport [224]. For each dataset, five random train/test splits were performed and the results were averaged over the five runs. We extracted pixel-level dense SIFT [237] features with step size 8 and and patch size 16. On top of the SIFT features, we used sparse coding methods to learn a dictionary and represented each SIFT feature into a sparse code. To obtain image-level features, we applied max-pooling [392] and spatial pyramid matching [212, 392] over the pixel-level sparse codes. Then a linear SVM was applied to classify the images. We compared with other diversity-promoting regularizers including determinant of covariance matrix (DCM) [242], cosine similarity (CS) [402], determinantal point process (DPP) [204, 429], InCoherence (IC) [29], and mutual angles (MA) [369]. We used 5-fold cross validation to tune τ in $\{0.3, 0.4, \cdots, 1\}$ and the number of basis vectors in $\{50, 100, 200, \cdots, 500\}$. The parameter ρ in ADMM was set to 1.

Table 2.14 shows the classification accuracy on three datasets, from which we can see that compared with unregularized SC, AC-SC greatly improves performance. For example, on the Sports dataset, AC improves the accuracy from 87.4% to 90.9%. This suggests that AC is effective in reducing overfitting and improving generalization performance. Compared with other diversity-promoting regularizers, AC achieves better performance, demonstrating its better efficacy in promoting diversity.

Neural Networks

We evaluated AC on three types of neural networks: fully-connected NN (FNN) for phone recognition [159], CNN for image classification [203], and RNN for question answering [296]. In the main paper, we report results on four datasets: TIMIT [11], CIFAR-10 [5], CNN [154], and DailyMail [154].

FNN for phone recognition The TIMIT dataset contains a total of 6300 sentences (5.4 hours), divided into a training set (462 speakers), a validation set (50 speakers), and a core test set (24 speakers). We used the Kaldi [277] toolkit to train the monophone system which was utilized to perform forced alignment and to get labels for speech frames. The toolkit was also utilized to preprocess the data into log-filter banks. Among FNN-based methods, Karel's recipe in Kaldi achieves state of the art performance. We applied AC to the FNN in this recipe. The inputs of the FNN are the FMLLR [117] features of 21 neighboring frames, which are mean-centered and normalized to have unit variance. The number of hidden layers was 4. Each layer had 1024 hidden units. Stochastic gradient descent (SGD) was used to train the network. The learning rate was set to 0.008. We compared with four diversity-promoting regularizers: CS, IC, MA, and DeCorrelation (DC) [82]. The regularization parameter in these methods were tuned in $\{10^{-6}, 10^{-5}, \cdots, 10^{5}\}$. The β parameter in IC was set to 1.

Table 2.15 shows state of the art phone error rate (PER) on the TIMIT core test set. Methods in the first panel are mostly based on FNN, which perform less well than Kaldi. Methods in the third panel are all based on RNNs which in general perform better than FNN since they are able to capture the temporal structure in speech data. In the second panel, we compare AC with other diversity-promoting regularizers. Without regularization, the error is 18.53%. With AC, the error is reduced to 18.41%, which is very close to a strong RNN-based baseline – connectionist temporal classification (CTC) [139]. Besides, AC outperforms other regularizers.

CNN for image classification The CIFAR-10 dataset contains 32x32 color images from 10 categories, with 50,000 images for training and 10,000 for testing. We used 5000 training images as the validation set to tune hyperparameters. The data was augmented by first zero-padding the images with 4 pixels on each side, then randomly cropping the padded images to reproduce 32x32 images. We applied AC to the wide residual network (WideResNet) [406] where the depth was set to 28 and the width was set to 10. SGD was used for training, with epoch number 200, initial learning rate 0.1, minibatch size 128, Nesterov momentum 0.9, dropout probability 0.3, and weight decay 0.0005. The learning rate was dropped by 0.2 at 60, 120, and 160 epochs. The performance was the median of 5 runs. We compared with CS, IC, MA, DC, and locally constrained decorrelation (LCD) [291].

Table 2.16 shows state of the art classification error on the test set. Compared with the unregularized WideResNet which achieves an error of 3.89%, applying AC reduces the error to 3.63%. AC achieves lower error than other regularizers.

LSTM for question answering We applied AC to the long short-term memory (LSTM) [163] network (Section 2.1.2). On the row vectors of each gate-specific weight matrix, the AC was applied. The LSTM was used for a question answering (QA) task on two datasets: CNN and DailyMail [154], each containing a training, development, and test set with 300k/4k/3k and 879k/65k/53k examples respectively. Each example consists of a passage, a question, and an answer. The question is a cloze-style task where an entity is replaced by a placeholder and the goal is to infer this missing entity (answer) from all the possible entities appearing in the passage. The LSTM architecture and experimental settings followed the BIDirectional Attention Flow (BIDAF) [296] model, which consists of the following layers: character embedding, word em-

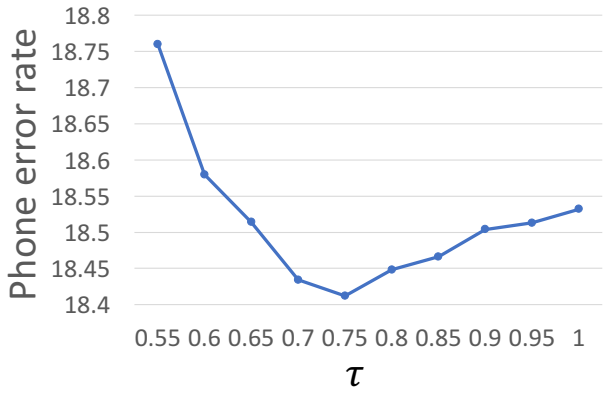

Figure 2.5: Phone error rate on TIMIT with varying τ.

bedding, contextual embedding, attention flow, modeling and output. LSTM was applied in the contextual embedding and modeling layer. Character embedding was based on one-dimensional convolutional neural network, where the number of filters was set to 100 and the width of receptive field was set to 5. In LSTM, the size of hidden state was set to 100. Optimization was based on AdaDelta [409], where the minibatch size and initial learning rate were set to 48 and 0.5. The model was trained for 8 epochs. Dropout [313] with probability 0.2 was applied. We compared with four diversity promoting regularizers: CS, IC, MA and DC.

Table 6.8 shows state of the art accuracy on the two datasets. As can be seen, after applying AC to BIDAF, the accuracy is improved from 76.94% to 77.23% on the CNN test set and from 79.63% to 79.88% on the DailyMail test set. Among the diversity-promoting regularizers, AC achieves the highest accuracy.

Sensitivity to the parameter τ Figure 2.5 shows how the phone error rates vary on the TIMIT core test set. As can be seen, the lowest test error is achieved under a moderate τ ($= 0.75$). Either a smaller or a larger τ degrades the performance. This suggests that τ effectively incurs a tradeoff between estimation and approximation errors. When τ is close to 0, the hidden units are close to being orthogonal, which yields much poorer performance. This confirms that the strict-orthogonality constraint proposed by [213] is too restrictive and is less favorable than a "soft" regularization approach.

Computational time We compare the computational time of neural networks under different regularizers. Table 2.18 shows the total runtime time of FNNs on TIMIT and CNNs on CIFAR-10 with a single GTX TITAN X GPU, and the runtime of LSTM networks on the CNN dataset with 2 TITAN X GPUs. Compared with no regularization, AC incurs a 18.2% extra time on TIMIT, 12.7% on CIFAR-10, and 14.8% on CNN. The runtime of AC is comparable to that of other diversity-promoting regularizers.

2.3.4 Appendix: Proofs and Details of Algorithms

Proof of Lemma 1

To prove Lemma 1, we need the following Lemma.

Lemma 3. *Let* $\mathbf{G}$ *be the Gram matrix defined on* $\mathcal{W} = \{\mathbf{w}_i\}_{i=1}^m$. *Let* $\mathbf{g}_i'$ *be the gradient of* $\det(\mathbf{G})$ *w.r.t* $\mathbf{w}_i$, *then* $\langle \mathbf{g}_i', \mathbf{w}_j \rangle = 0$ *for all* $j \neq i$, *and* $\langle \mathbf{g}_i', \mathbf{w}_i \rangle > 0$.

Proof. We decompose $\mathbf{w}_i$ into $\mathbf{w}_i = \mathbf{w}_i^{\parallel} + \mathbf{w}_i^{\perp}$. $\mathbf{w}_i^{\parallel}$ is in the span of $\mathcal{W}/\{\mathbf{w}_i\}$: $\mathbf{w}_i^{\parallel} = \sum_{j\neq i}^m \alpha_j \mathbf{w}_j$, where $\{\alpha_j\}_{j\neq i}^m$ are the linear coefficients. $\mathbf{w}_i^{\perp}$ is orthogonal to $\mathcal{W}/\{\mathbf{w}_i\}$: $\langle \mathbf{w}_i^{\perp}, \mathbf{w}_j \rangle = 0$ for all $j \neq i$. Let $\mathbf{c}_j$ denote the j-th column of $\mathbf{G}$. Subtracting $\sum_{j\neq i}^m \alpha_j \mathbf{c}_j$ from the i-th column, we get

$$\det(\mathbf{G}) = \begin{vmatrix} \langle \mathbf{w}_1, \mathbf{w}_1 \rangle & \cdots & 0 & \cdots & \langle \mathbf{w}_1, \mathbf{w}_m \rangle \\ \langle \mathbf{w}_2, \mathbf{w}_1 \rangle & \cdots & 0 & \cdots & \langle \mathbf{w}_2, \mathbf{w}_m \rangle \\ \vdots & \ddots & \vdots & \ddots & \vdots \\ \langle \mathbf{w}_i, \mathbf{w}_1 \rangle & \cdots & \langle \mathbf{w}_i^{\perp}, \mathbf{w}_i \rangle & \cdots & \langle \mathbf{w}_i, \mathbf{w}_m \rangle \\ \vdots & \ddots & \vdots & \ddots & \vdots \\ \langle \mathbf{w}_m, \mathbf{w}_1 \rangle & \cdots & 0 & \cdots & \langle \mathbf{w}_m, \mathbf{w}_m \rangle \end{vmatrix}. \tag{2.42}$$

Expanding the determinant according to the i-th column, we get

$$\det(\mathbf{G}) = \det(\mathbf{G}_{-i}) \langle \mathbf{w}_i^{\perp}, \mathbf{w}_i \rangle, \tag{2.43}$$

where $\mathbf{G}_{-i}$ is the Gram matrix defined on $\mathcal{W}/\{\mathbf{w}_i\}$. Then the functional gradient $\mathbf{g}_i'$ of $\det(\mathbf{G})$ w.r.t $\mathbf{w}_i$ is $\det(\mathbf{G}_{-i})\mathbf{w}_i^{\perp}$, which is orthogonal to $\mathbf{w}_j$ for all $j \neq i$. Since $\mathbf{G}$ is full rank, we know $\det(\mathbf{G}) > 0$. From Eq.(2.43) we know $\langle \mathbf{w}_i^{\perp}, \mathbf{w}_i \rangle$ is non-negative. Hence $\langle \mathbf{g}_i', \mathbf{w}_i \rangle = \det(\mathbf{G}_{-i}) \langle \mathbf{w}_i^{\perp}, \mathbf{w}_i \rangle > 0$. □

Now we are ready to prove Lemma 1. We first compute $\hat{s}_{ij}$:

$$\hat{s}_{ij} = \frac{|\langle \widehat{\mathbf{w}}_i, \widehat{\mathbf{w}}_j \rangle|}{\|\widehat{\mathbf{w}}_i\| \|\widehat{\mathbf{w}}_j\|} = \frac{|\langle \mathbf{w}_i - \eta \mathbf{g}_i, \mathbf{w}_j - \eta \mathbf{g}_j \rangle|}{\sqrt{\|\mathbf{w}_i - \eta \mathbf{g}_i\|^2} \sqrt{\|\mathbf{w}_j - \eta \mathbf{g}_j\|^2}}. \tag{2.44}$$

The functional gradient of $\log\det(\mathbf{G})$ w.r.t $\mathbf{w}_i$ is computed as $\mathbf{g}_i'' = \frac{1}{\det(\mathbf{G})} \mathbf{g}_i'$. According to Lemma 3 and the fact that $\det(\mathbf{G}) > 0$, we know $\langle \mathbf{g}_i'', \mathbf{w}_j \rangle = 0$ for all $j \neq i$, and $\langle \mathbf{g}_i'', \mathbf{w}_i \rangle > 0$. Then we have

$$\begin{aligned} & |\langle \mathbf{w}_i - \eta \mathbf{g}_i, \mathbf{w}_j - \eta \mathbf{g}_j \rangle| \\ &= |\langle \mathbf{w}_i - \eta(2\mathbf{w}_i - 2\mathbf{g}_i''), \mathbf{w}_j - \eta(2\mathbf{w}_j - 2\mathbf{g}_j'') \rangle| \\ &= |\langle (1-2\eta)\mathbf{w}_i + 2\eta \mathbf{g}_i'', (1-2\eta)\mathbf{w}_j + 2\eta \mathbf{g}_j'' \rangle| \\ &= |(1-2\eta)^2 \langle \mathbf{w}_i, \mathbf{w}_j \rangle + 4\eta^2 \langle \mathbf{g}_i'', \mathbf{g}_j'' \rangle| \\ &= |\langle \mathbf{w}_i, \mathbf{w}_j \rangle| |(1-2\eta)^2 + 4\eta^2 \langle \mathbf{g}_i'', \mathbf{g}_j'' \rangle / \langle \mathbf{w}_i, \mathbf{w}_j \rangle|, \end{aligned} \tag{2.45}$$

and

$$\begin{aligned} & \frac{1}{\sqrt{\|\mathbf{w}_i - \eta \mathbf{g}_i\|^2}} \\ &= \frac{1}{\sqrt{\|\mathbf{w}_i\|^2 - 2\eta \langle \mathbf{w}_i, \mathbf{g}_i \rangle + \eta^2 \|\mathbf{g}_i\|^2}} \\ &= \frac{1}{\sqrt{\|\mathbf{w}_i\|^2 (1 - 2\eta \langle \mathbf{w}_i, \mathbf{g}_i \rangle / \|\mathbf{w}_i\|^2 + \eta^2 \|\mathbf{g}_i\|^2 / \|\mathbf{w}_i\|^2)}} \\ &= \frac{1}{\|\mathbf{w}_i\| \sqrt{1 - \frac{2\eta \langle \mathbf{w}_i, \mathbf{g}_i \rangle}{\|\mathbf{w}_i\|^2} + \frac{\eta^2 \|\mathbf{g}_i\|^2}{\|\mathbf{w}_i\|^2}}}. \end{aligned} \tag{2.46}$$

According to the Taylor expansion, we have

$$\frac{1}{\sqrt{1+x}} = 1 - \frac{1}{2}x + o(x). \tag{2.47}$$

Then

$$\frac{1}{\sqrt{1-\frac{2\eta\langle \mathbf{w}_i,\mathbf{g}_i\rangle}{\|\mathbf{w}_i\|^2}+\frac{\eta^2\|\mathbf{g}_i\|^2}{\|\mathbf{w}_i\|^2}}} = 1 - \frac{1}{2}\left(-\frac{2\eta\langle \mathbf{w}_i,\mathbf{g}_i\rangle}{\|\mathbf{w}_i\|^2} + \frac{\eta^2\|\mathbf{g}_i\|^2}{\|\mathbf{w}_i\|^2}\right) + o\left(-\frac{2\eta\langle \mathbf{w}_i,\mathbf{g}_i\rangle}{\|\mathbf{w}_i\|^2} + \frac{\eta^2\|\mathbf{g}_i\|^2}{\|\mathbf{w}_i\|^2}\right), \tag{2.48}$$

where

$$\frac{2\eta\langle \mathbf{w}_i,\mathbf{g}_i\rangle}{\|\mathbf{w}_i\|^2} = \frac{2\eta\langle \mathbf{w}_i,2\mathbf{w}_i-2\mathbf{g}_i''\rangle}{\|\mathbf{w}_i\|^2} = 4\eta - 4\eta\frac{\langle \mathbf{w}_i,\mathbf{g}_i''\rangle}{\|\mathbf{w}_i\|^2}. \tag{2.49}$$

Hence

$$\frac{1}{\sqrt{1+\frac{2\eta\langle \mathbf{w}_i,\mathbf{g}_i\rangle}{\|\mathbf{w}_i\|^2}+\frac{\eta^2\|\mathbf{g}_i\|^2}{\|\mathbf{w}_i\|^2}}} = 1 + 2\eta - 2\eta\frac{\langle \mathbf{w}_i,\mathbf{g}_i''\rangle}{\|\mathbf{w}_i\|^2} + o(\eta), \tag{2.50}$$

and

$$\frac{1}{\sqrt{1+\frac{2\eta\langle \mathbf{w}_i,\mathbf{g}_i\rangle}{\|\mathbf{w}_i\|^2}+\frac{\eta^2\|\mathbf{g}_i\|^2}{\|\mathbf{w}_i\|^2}}}\frac{1}{\sqrt{1+\frac{2\eta\langle \mathbf{w}_j,\mathbf{g}_j\rangle}{\|\mathbf{w}_j\|^2}+\frac{\eta^2\|\mathbf{g}_j\|^2}{\|\mathbf{w}_j\|^2}}} = (1+2\eta)^2 - 2\eta\left(\frac{\langle \mathbf{w}_i,\mathbf{g}_i''\rangle}{\|\mathbf{w}_i\|^2} + \frac{\langle \mathbf{w}_j,\mathbf{g}_j''\rangle}{\|\mathbf{w}_j\|^2}\right) + o(\eta). \tag{2.51}$$

Then

$$\begin{aligned}
\hat{s}_{ij} &= \frac{|\langle \mathbf{w}_i,\mathbf{w}_j\rangle|}{\|\mathbf{w}_i\|\|\mathbf{w}_j\|}\left|(1-2\eta)^2 + \frac{4\eta^2\langle \mathbf{g}_i'',\mathbf{g}_j''\rangle}{\langle \mathbf{w}_i,\mathbf{w}_j\rangle}\right|\left((1+2\eta)^2 - 2\eta\left(\frac{\langle \mathbf{w}_i,\mathbf{g}_i''\rangle}{\|\mathbf{w}_i\|^2} + \frac{\langle \mathbf{w}_j,\mathbf{g}_j''\rangle}{\|\mathbf{w}_j\|^2}\right) + o(\eta)\right) \\
&= \frac{|\langle \mathbf{w}_i,\mathbf{w}_j\rangle|}{\|\mathbf{w}_i\|\|\mathbf{w}_j\|}\left((1-2\eta)^2 + \frac{4\eta^2\langle \mathbf{g}_i'',\mathbf{g}_j''\rangle}{\langle \mathbf{w}_i,\mathbf{w}_j\rangle}\right)\left((1+2\eta)^2 - 2\eta\left(\frac{\langle \mathbf{w}_i,\mathbf{g}_i''\rangle}{\|\mathbf{w}_i\|^2} + \frac{\langle \mathbf{w}_j,\mathbf{g}_j''\rangle}{\|\mathbf{w}_j\|^2}\right) + o(\eta)\right) \\
&= s_{ij}\left(1 - 2\eta\left(\frac{\langle \mathbf{w}_i,\mathbf{g}_i''\rangle}{\|\mathbf{w}_i\|^2} + \frac{\langle \mathbf{w}_j,\mathbf{g}_j''\rangle}{\|\mathbf{w}_j\|^2}\right) + o(\eta)\right) \\
&< s_{ij}
\end{aligned} \tag{2.52}$$

where in the second step, the absolute value can be removed because there always exists a sufficiently small η such that $(1-2\eta)^2 + \frac{4\eta^2\langle \mathbf{g}_i'',\mathbf{g}_j''\rangle}{\langle \mathbf{w}_i,\mathbf{w}_j\rangle} > 0$. Eq.(2.52) holds for all i, j, hence $s(\widehat{\mathcal{W}}) < s(\mathcal{W})$. The proof completes.

Proof of Lemma 2

To prove this lemma, we need the following lemma.

Lemma 4. *Given a nondecreasing sequence $b = (b_i)_{i=1}^n$ and a strictly decreasing function $g(x)$ which satisfies $0 \le g(b_i) \le min\{b_{i+1} - b_i : i = 1, 2, \cdots, n-1, b_{i+1} \ne b_i\}$, we define a sequence $c = (c_i)_{i=1}^n$ where $c_i = b_i + g(b_i)$. If $b_1 < b_n$, then var(c) < var(b), where $var(\cdot)$ denotes the variance of a sequence. Furthermore, let $n' = max\{j : b_j \ne b_n\}$, we define a sequence $b' = (b'_i)_{i=1}^n$ where $b'_i = b_i + g(b_n) + (g(b_{n'}) - g(b_n))\mathbb{I}(i \le n')$ and $\mathbb{I}(\cdot)$ is the indicator function, then var$(c) \le$ var(b') < var(b).*

The intuition behind the proof of Lemma 2 is: when the stepsize η is sufficiently small, we can make sure the changes of smaller angles (between consecutive iterations) are larger than the changes of larger angles, then Lemma 4 can be used to prove that the variance decreases. Let θ_{ij}

denote $\arccos(s_{ij})$. We sort θ_{ij} in nondecreasing order and denote the resultant sequence as $\theta = (\theta_k)_{k=1}^n$, then $\text{var}((\theta_{ij})) = \text{var}(\theta)$. We use the same order to index $\hat{\theta}_{ij} = \arccos(\hat{s}_{ij})$ and denote the resultant sequence as $\hat{\theta} = (\hat{\theta}_k)_{k=1}^n$, then $\text{var}((\hat{\theta}_{ij})) = \text{var}(\hat{\theta})$. Let $g(\theta_{ij}) = \frac{2\cos(\theta_{ij})}{\sqrt{1-\cos(\theta_{ij})^2}}\eta$ if $\theta_{ij} < \frac{\pi}{2}$ and 0 if $\theta_{ij} = \frac{\pi}{2}$, then $g(\theta_{ij})$ is a strictly decreasing function. Let $\tilde{\theta}_k = \theta_k + g(\theta_k)$. It is easy to see when η is sufficiently small, $0 \le g(\theta_k) \le \min\{\theta_{k+1} - \theta_k : k = 1, 2, \cdots, n-1, \theta_{k+1} \ne \theta_k\}$. According to Lemma 4, we have

$$\text{var}(\tilde{\theta}) < \text{var}(\theta),$$

where $\tilde{\theta} = (\tilde{\theta}_k)_{k=1}^n$. Furthermore, let $n' = \max\{j : \theta_j \ne \theta_n\}$, $\theta'_k = \theta_k + g(\theta_n) + (g(\theta_{n'}) - g(\theta_n))\mathbb{I}(k \le n')$, then

$$\text{var}(\tilde{\theta}) \le \text{var}(\theta') < \text{var}(\theta),$$

where $\theta' = (\theta'_k)_{k=1}^n$. $\text{var}(\theta')$ can be written as:

$$\begin{aligned}
&= \tfrac{1}{n}\textstyle\sum_{i=1}^n(\theta'_i - \tfrac{1}{n}\sum_{j=1}^n \theta'_j)^2 \\
&= \tfrac{1}{n}\textstyle\sum_{i=1}^n(\theta_i + (g(\theta_{n'}) - g(\theta_n))\mathbb{I}(i \le n') - \tfrac{1}{n}\sum_{j=1}^n \theta_j - \tfrac{n'}{n}(g(\theta_{n'}) - g(\theta_n)))^2 \\
&= \text{var}(\theta) + \tfrac{2}{n}\textstyle\sum_{i=1}^n(\theta_i - \tfrac{1}{n}\sum_{j=1}^n \theta_j)(g(\theta_{n'}) - g(\theta_n))(\mathbb{I}(i \le n') - \tfrac{n'}{n}) \\
&\quad + \tfrac{1}{n}\textstyle\sum_{i=1}^n(g(\theta_{n'}) - g(\theta_n))^2(\mathbb{I}(i \le n') - \tfrac{n'}{n})^2
\end{aligned} \tag{2.53}$$

Let $\lambda = \frac{2}{n}\sum_{i=1}^n(\theta_i - \frac{1}{n}\sum_{j=1}^n \theta_j)(\mathbb{I}(i \le n') - \frac{n'}{n})$, which can be further written as

$$\begin{aligned}
&= \tfrac{2}{n}\textstyle\sum_{i=1}^{n'}(\theta_i - \tfrac{1}{n}\sum_{j=1}^n \theta_j)(1 - \tfrac{n'}{n}) + \tfrac{2}{n}\sum_{i=n'+1}^n(\theta_i - \tfrac{1}{n}\sum_{j=1}^n \theta_j)(-\tfrac{n'}{n}) \\
&= \tfrac{2}{n}(\textstyle\sum_{i=1}^{n'}\theta_i - \tfrac{n'}{n}\sum_{j=1}^n \theta_j)(1 - \tfrac{n'}{n}) + \tfrac{2}{n}(\sum_{i=n'+1}^n \theta_i - \tfrac{n-n'}{n}\sum_{j=1}^n \theta_j)(-\tfrac{n'}{n}) \\
&= \tfrac{2n'(n-n')}{n^2}(\tfrac{1}{n'}\textstyle\sum_{i=1}^{n'}\theta_i - \tfrac{1}{n-n'}\sum_{i=n'+1}^n \theta_i)
\end{aligned} \tag{2.54}$$

As (θ_k) is nondecreasing and $\theta_n \ne \theta_{n'}$, we have $\lambda < 0$. Let $\mu = \frac{2\cos(\theta_{n'})}{\sqrt{1-\cos(\theta_{n'})^2}} - \frac{2\cos(\theta_n)}{\sqrt{1-\cos(\theta_n)^2}}$ when $\theta_n < \frac{\pi}{2}$ and $\mu = \frac{2\cos(\theta_{n'})}{\sqrt{1-\cos(\theta_{n'})^2}}$ when $\theta_n = \frac{\pi}{2}$, then $g(\theta_{n'}) - g(\theta_n) = \mu\eta$ and $\mu > 0$. Substituting λ and μ into $\text{var}(\theta')$, we can obtain:

$$\begin{aligned}
\text{var}(\theta') &= \text{var}(\theta) + \lambda\mu\eta + \tfrac{1}{n}\textstyle\sum_{i=1}^n(\mathbb{I}(i \le n') - \frac{n'}{n})^2\mu^2\eta^2 \\
&= \text{var}(\theta) + \lambda\mu\eta + o(\eta)
\end{aligned}$$

Note that $\lambda < 0$ and $\mu > 0$, so $\exists\delta_1$, such that

$$\eta < \delta_1 \Rightarrow \text{var}(\theta') < \text{var}(\theta) + \frac{\lambda\mu}{2}\eta.$$

As $\text{var}(\tilde{\theta}) < \text{var}(\theta')$, we can draw the conclusion that

$$\text{var}(\tilde{\theta}) < \text{var}(\theta) + \frac{\lambda\mu}{2}\eta.$$

Further,

$$\begin{aligned}
\text{var}(\hat{\theta}) &= \tfrac{1}{n}\textstyle\sum_{i=1}^n(\hat{\theta}_i - \tfrac{1}{n}\sum_{j=1}^n \hat{\theta}_j)^2 \\
&= \tfrac{1}{n}\textstyle\sum_{i=1}^n(\tilde{\theta}_i + o(\eta) - \tfrac{1}{n}\sum_{j=1}^n \tilde{\theta}_j + o(\eta))^2 \\
&= \tfrac{1}{n}\textstyle\sum_{i=1}^n(\tilde{\theta}_i - \tfrac{1}{n}\sum_{j=1}^n \tilde{\theta}_j)^2 + o(\eta) \\
&= \text{var}(\tilde{\theta}) + o(\eta).
\end{aligned}$$

So $\exists \delta_2 > 0$ such that $\eta < \delta_2 \Rightarrow \text{var}(\hat{\theta}) < \text{var}(\tilde{\theta}) - \frac{\lambda\mu}{4}\eta$. Let $\delta = \min\{\delta_1, \delta_2\}$, then

$$\begin{aligned} \eta < \delta &\Rightarrow \text{var}(\hat{\theta}) < \text{var}(\theta) + \tfrac{\lambda\mu}{4}\eta < \text{var}(\theta) \\ &\Rightarrow \text{var}(\hat{\theta}) < \text{var}(\theta). \end{aligned}$$

The proof completes.

Proof of Lemma 4

The intuition behind the proof is that we can view the difference between corresponding elements of the sequence b and sequence c as "updates", and we can find that the updates lead to smaller elements "catch up" larger elements. Alternatively, we can obtain the new sequence c through a set of updates. First, we update the whole sequence b by the update value of the largest elements, then the largest elements have found their correct values. Then we pick up the elements that are smaller than the largest elements, and update those by the update value of the second largest elements minus the previous update, then the second largest elements have found their correct values. In this manner, we can obtain a sequence of sequences, where the first sequence is b, the third sequence is b', the last sequence is c, and the adjacent sequences only differ by a simpler update: to the left of some element, each element is updated by the same value; and to the right of the element, each value remains unchanged. We can prove that such simpler update can guarantee to decrease the variance under certain conditions, and we can use that to prove $\text{var}(c) \leq \text{var}(b') < \text{var}(b)$.

The formal proof starts here. First, following the intuition stated above, we construct a sequence of sequences with decreasing variance, in which the variance of the first sequence is $\text{var}(b)$ and the variance of the last sequence is $\text{var}(c)$. We sort the unique values in b in ascending order and denote the resultant sequence as $d = (d_j)_{j=1}^m$. Let $l(j) = \max\{i : b_i = d_j\}$, $u(i) = \{j : d_j = b_i\}$, we construct a sequence of sequences $h^{(j)} = (h_i^{(j)})_{i=1}^n$ where $j = 1, 2, \cdots, m+1$, in the following way:

- $h_i^{(1)} = b_i$, where $i = 1, 2, \cdots, n$;
- $h_i^{(j+1)} = h_i^{(j)}$, where $j = 1, 2, \cdots, m$ and $l(m-j+1) < i \leq n$;
- $h_i^{(2)} = h_i^{(1)} + g(d_m)$, where $1 \leq i \leq l(m)$;
- $h_i^{(j+1)} = h_i^{(j)} + g(d_{m-j+1}) - g(d_{m-j+2})$, where $j = 2, 3, \cdots, m$ and $1 \leq i \leq l(m-j+1)$.

From the definition of $h^{(j)}$, we know $\text{var}(h^{(1)}) = \text{var}(b)$. As $b_1 < b_n$, we have $m \geq 2$. Now we prove that $\text{var}(h^{(m+1)}) = \text{var}(c)$ and $\forall j = 1, 2, \cdots, m$, $\text{var}(h^{(j+1)}) < \text{var}(h^{(j)})$. First, we prove $\text{var}(h^{(m+1)}) = \text{var}(c)$. Actually, we can prove $h^{(m+1)} = c$:

$$\begin{aligned} h_i^{(m+1)} &= \sum_{j=1}^{m} (h_i^{(j+1)} - h_i^{(j)}) + h_i^{(1)} \\ &= \sum_{j=1}^{m+1-u(i)} (h_i^{(j+1)} - h_i^{(j)}) + \sum_{j=m+2-u(i)}^{m} (h_i^{(j+1)} - h_i^{(j)}) + b_i. \end{aligned}$$

As $j \geq m+2-u(i) \Longleftrightarrow u(i) \leq m+2-j \Longleftrightarrow d_{m+2-j} \geq d_{u(i)} = b_i \Longleftrightarrow l(m+1-j) < i$, we know that

$$h_i^{(j+1)} = \begin{cases} h_i^{(j)}, \text{when } j \geq m+2-u(i) \\ h_i^{(j)} + g(d_{m-j+1}) - g(d_{m-j+2}), \text{when } 2 \leq j \leq m+1-u(i) \\ h_i^{(j)} + g(d_m), \text{when } j = 1. \end{cases}$$

So we have

$$\begin{aligned} h_i^{(m+1)} &= \sum_{j=1}^{m+1-u(i)} (h_i^{(j+1)} - h_i^{(j)}) + b_i \\ &= g(d_m) + \sum_{j=2}^{m+1-u(i)} (g(d_{m-j+1}) - g(d_{m-j+2})) + b_i \\ &= g(d_m) + g(d_{u(i)}) - g(d_m) + b_i \\ &= g(d_{u(i)}) + b_i \\ &= g(b_i) + b_i \\ &= c_i. \end{aligned}$$

So $\text{var}(h^{(m+1)}) = \text{var}(c)$. Then we prove that $\forall j = 1, 2, \cdots, m$, $\text{var}(h^{(j+1)}) < \text{var}(h^{(j)})$. First, we need to prove that for any j, $h_i^{(j)}$ is a non-decreasing sequence in terms of i. In order to prove that, we only need to prove $\forall j = 2, \cdots, n, h_i^{(j+1)} - h_i^{(j)} < h_{l(m-j+1)+1}^{(j)} - h_{l(m-j+1)}^{(j)}$. Then from $h^{(j+1)}$ to $h^{(j)}$, since elements before $l(m-j+1)$ are updated by the same value, and elements after $l(m-j+1)+1$ are unchanged, if the $l(m-j+1)^{th}$ element does not exceed the $l(m-j+1)+1^{th}$ element, then the order of the whole sequence remains the same during the update. The proof is as follows: $\forall j \geq 2$, $h_{l(m-j+1)+1}^{(j)} = \sum_{k=1}^{j-1} (h_{l(m-j+1)+1}^{(k+1)} - h_{l(m-j+1)+1}^{(k)}) + h_{l(m-j+1)}^{(1)}$. As $k \leq j-1 \Rightarrow l(m-k+1) \geq l(m-j+2) = l(m-j+1+1) \geq l(m-j+1)+1$, from the definition of h we know that

$$h_{l(m-j+1)+1}^{(k+1)} - h_{l(m-j+1)+1}^{(k)} = \begin{cases} g(d_{m-k+1}) - g(d_{m-k+2}), \text{when } k \geq 2 \\ g(d_m), \text{when } k = 1. \end{cases}$$

So we have

$$\begin{aligned} h_{l(m-j+1)+1}^{(j)} &= \sum_{k=1}^{j-1} (h_{l(m-j+1)+1}^{(k+1)} - h_{l(m-j+1)+1}^{(k)}) + h_{l(m-j+1)}^{(1)} \\ &= g(d_m) + \sum_{k=2}^{j-1} (g(d_{m-k+1}) - g(d_{m-k+2})) + b_{l(m-j+1)+1} \\ &= g(d_{m-j+2}) + b_{l(m-j+1)+1}. \end{aligned}$$

From the definition of $l(\cdot)$, we have that $b_{l(m-j+1)+1} = d_{m-j+2}$, so $h_{l(m-j+1)+1}^{(j)} = g(b_{l(m-j+1)}) + b_{l(m-j+1)+1}$. Similarly, $h_{l(m-j+1)}^{(j)} = b_{l(m-j+1)} + g(b_{l(m-j+2)}) = b_{l(m-j+1)} + g(b_{l(m-j+1)}) -$

$(g(d_{m-j+1}) - g(d_{m-j+2}))$. So $h^{(j)}_{l(m-j+1)+1} - h^{(j)}_{l(m-j+1)} = b_{l(m-j+1)+1} - b_{l(m-j+1)}$ $+ (g(b_{l(m-j+1)+1}) - g(b_{l(m-j+1)})) + (g(d_{m-j+1}) - g(d_{m-j+2}))$. As the function $g(x)$ is bounded between 0 and $b_{i+1} - b_i$, we have $g(b_{l(m-j+1)+1}) - g(b_{l(m-j+1)}) > -(b_{l(m-j+1)+1} - b_{l(m-j+1)})$. So

$$\begin{aligned} h^{(j)}_{l(m-j+1)+1} - h^{(j)}_{l(m-j+1)} &= b_{l(m-j+1)+1} - b_{l(m-j+1)} + (g(b_{l(m-j+1)+1}) - g(b_{l(m-j+1)})) \\ &\quad +(g(d_{m-j+1}) - g(d_{m-j+2})) \\ &> 0 + (g(d_{m-j+1}) - g(d_{m-j+2})) \\ &= g(d_{m-j+1}) - g(d_{m-j+2}). \end{aligned} \tag{2.55}$$

As $h^{(j+1)}_i - h^{(j)}_i$ is either 0 or $g(d_{m-j+1}) - g(d_{m-j+2})$ which is positive, we have proved $\forall j \geq 2$, $h^{(j+1)}_i - h^{(j)}_i < h^{(j)}_{l(m-j+1)+1} - h^{(j)}_{l(m-j+1)}$. According to the former discussion, for a fixed j, $h^{(j)}_i$ is a non-decreasing sequence.

We can prove $\text{var}(h^{(j+1)}) < \text{var}(h^{(j)})$ now. If $j = 1$, $l(m) = n$, $\forall i = 1, 2, \cdots, n$, $h^{(2)}_i - h^{(1)}_i = g(d_m)$, so $\text{var}(h^{(2)}) = \text{var}(h^{(1)})$. For $j \geq 2$, let $\Delta^{(j)} = g(d_{m-j+1}) - g(d_{m-j+2})$, let $l = l(m - j + 1)$, we first use the recursive definition of h to represent $h^{(j+1)}$ by $h^{(j)}$:

$$\begin{aligned} \text{var}(h^{(j+1)}) &= \frac{1}{n}\sum_{i=1}^{n}(h^{(j+1)}_i - \frac{1}{n}\sum_{i=1}^{n} h^{(j+1)}_i)^2 \\ &= \frac{1}{n}\sum_{i=1}^{n}(h^{(j)}_i + \mathbb{I}(i \leq l)\Delta^{(j)} - \frac{1}{n}\sum_{i=1}^{n} h^{(j)}_i - \frac{l}{n}\Delta^{(j)})^2. \end{aligned}$$

Then following simple algebra to expand the above equation, we have

$$\begin{aligned} \text{var}(h^{(j+1)}) &= \text{var}(h^{(j)}) + \frac{l\Delta^{(j)}}{n}[2(\frac{1}{l}\sum_{i=1}^{l} h^{(j)}_i - \frac{1}{n}\sum_{i=1}^{n} h^{(j)}_i) + \frac{n-l}{n}\Delta^{(j)}] \\ &= \text{var}(h^{(j)}) + \frac{l\Delta^{(j)}}{n}[2(\frac{1}{l}\sum_{i=1}^{l} h^{(j)}_i - \frac{1}{n}\sum_{i=1}^{l} h^{(j)}_i - \frac{1}{n}\sum_{i=l+1}^{n} h^{(j)}_i) + \frac{n-l}{n}\Delta^{(j)}]. \end{aligned}$$

Noting that $h^{(j)}_{l+1} - h^{(j)}_l = \Delta^{(j)}$, we can further obtain

$$\text{var}(h^{(j+1)}) = \text{var}(h^{(j)}) + \frac{l\Delta^{(j)}}{n}[2(\frac{1}{l}\sum_{i=1}^{l} h^{(j)}_i - \frac{1}{n}\sum_{i=1}^{l} h^{(j)}_i - \frac{1}{n}\sum_{i=l+1}^{n}(h^{(j)}_i - h^{(j)}_{l+1} + h^{(j)}_l)) - \frac{n-l}{n}\Delta^{(j)}].$$

Since for a fixed j, $h^{(j)}_i$ is a non-decreasing sequence, we have $\forall i \geq l+1$, $h^{(j)}_i - h^{(j)}_{l+1} + h^{(j)}_l \geq h^{(j)}_{l+1} - h^{(j)}_{l+1} + h^{(j)}_l = h^{(j)}_l$ and $\frac{1}{l}\sum_{i=1}^{l} h^{(j)}_i \leq h^{(j)}_l$. So $\frac{1}{l}\sum_{i=1}^{l} h^{(j)}_i - \frac{1}{n}\sum_{i=1}^{l} h^{(j)}_i - \frac{1}{n}\sum_{i=l+1}^{n}(h^{(j)}_i - h^{(j)}_{l+1} + h^{(j)}_l) \leq 0$ and $\text{var}(h^{(j+1)}) \leq \text{var}(h^{(j)}) - \frac{l\Delta^{(j)}}{n}\frac{n-l}{n}\Delta^{(j)} < \text{var}(h^{(j)})$.

Putting the above results together, since $\text{var}(h^{(j+1)}) < \text{var}(h^{(j)})$ and $\text{var}(h^{(m+1)}) = \text{var}(c)$, we know that $\text{var}(c) < \text{var}(h^{(1)}) = \text{var}(b)$. Furthermore, let $n' = \max\{j : b_j \neq b_n\}$, then $\forall i$, $h^{(2)}_i = h^{(1)}_i + g(d_m) = b_i + g(b_n)$, $h^{(3)}_i = h^{(2)}_i + (g(d_{m-1}) - g(d_m))\mathbb{I}(i \leq l(m-1)) = b_i + g(b_n) + (g(b_{n'}) - g(b_n))\mathbb{I}(i \leq n') = b'_i$, so $\text{var}(c) \leq \text{var}(b') < \text{var}(b)$. The proof completes.

Solve $\widetilde{\mathbf{W}}$

The sub-problem defined over $\widetilde{\mathbf{W}}$ is

$$\begin{aligned}\min_{\widetilde{\mathbf{W}}} \quad & \mathcal{L}(\widetilde{\mathbf{W}}) + \sum_{r=1}^{R}(\mathbf{y}_1^{(r)} \cdot \widetilde{\mathbf{w}}_{p(r)} + \mathbf{y}_2^{(r)} \cdot \widetilde{\mathbf{w}}_{q(r)} + \rho\|\widetilde{\mathbf{w}}_{p(r)} - \mathbf{v}_1^{(r)}\|_2^2 + \rho\|\widetilde{\mathbf{w}}_{q(r)} - \mathbf{v}_2^{(r)}\|_2^2) \\ s.t. \quad & \forall j, \|\widetilde{\mathbf{w}}_j\|_2 = 1.\end{aligned} \tag{2.56}$$

In sparse coding, this problem becomes

$$\begin{aligned}\min_{\widetilde{\mathbf{W}}} \quad & \tfrac{1}{2}\sum_{i=1}^{n}\|\mathbf{x}_i - \textstyle\sum_{j=1}^{m}\alpha_{ij}g_j\widetilde{\mathbf{w}}_j\|_2^2 + \lambda_2\sum_{j=1}^{m}\|g_j\widetilde{\mathbf{w}}_j\|_2^2 + \sum_{r=1}^{R}(\mathbf{y}_1^{(r)} \cdot \widetilde{\mathbf{w}}_{p(r)} + \mathbf{y}_2^{(r)} \cdot \widetilde{\mathbf{w}}_{q(r)} \\ & +\rho\|\widetilde{\mathbf{w}}_{p(r)} - \mathbf{v}_1^{(r)}\|_2^2 + \rho\|\widetilde{\mathbf{w}}_{q(r)} - \mathbf{v}_2^{(r)}\|_2^2) \\ s.t. \quad & \forall j, \|\widetilde{\mathbf{w}}_j\|_2 = 1.\end{aligned} \tag{2.57}$$

We solve this sub-problem using coordinate descent. At each iteration, we update $\widetilde{\mathbf{w}}_j$ by fixing the other variables. The sub-problem defined on $\widetilde{\mathbf{w}}_j$ can be written as

$$\begin{aligned}\min_{\widetilde{\mathbf{w}}} \quad & \tfrac{1}{2}\sum_{i=1}^{n}\|\mathbf{b}_i - \alpha_{ij}g_j\widetilde{\mathbf{w}}_j\|_2^2 + \lambda_2\|g_j\widetilde{\mathbf{w}}_j\|_2^2 + \sum_{r=1}^{R}(\mathbb{I}(p(r)=j)(\mathbf{y}_1^{(r)} \cdot \widetilde{\mathbf{w}}_{p(r)} + \rho\|\widetilde{\mathbf{w}}_{p(r)} - \mathbf{v}_1^{(r)}\|_2^2) \\ & +\mathbb{I}(q(r)=j)(\mathbf{y}_2^{(r)} \cdot \widetilde{\mathbf{w}}_{q(r)} + \rho\|\widetilde{\mathbf{w}}_{q(r)} - \mathbf{v}_2^{(r)}\|_2^2)) \\ s.t. \quad & \forall j, \|\widetilde{\mathbf{w}}_j\|_2 = 1,\end{aligned} \tag{2.58}$$

where $\mathbf{b}_i = \mathbf{x}_i - \sum_{k\neq j}^{m}\alpha_{ik}g_k\widetilde{\mathbf{w}}_k$. Let γ be the KKT multiplier. According to the KKT conditions, we have

$$\sum_{i=1}^{n}\alpha_{ij}g_j(\alpha_{ij}g_j\widetilde{\mathbf{w}}_j - \mathbf{b}_i) + 2\lambda_2 g_j^2\widetilde{\mathbf{w}}_j + \mathbf{y}_j + 2\rho N\widetilde{\mathbf{w}}_j - 2\rho\mathbf{v}_j + 2\gamma\widetilde{\mathbf{w}}_j = 0, \tag{2.59}$$

and

$$\|\widetilde{\mathbf{w}}_j\|_2 = 1, \tag{2.60}$$

where $\mathbf{y}_j = \sum_{r=1}^{R}(\mathbb{I}(p(r)=j)\mathbf{y}_1^{(r)} + \mathbb{I}(q(r)=j)\mathbf{y}_2^{(r)})$, $\mathbf{v}_j = \sum_{r=1}^{R}(\mathbb{I}(p(r)=j)\mathbf{v}_1^{(r)} + \mathbb{I}(q(r)=j)\mathbf{v}_2^{(r)})$, and $N = \sum_{r=1}^{R}(\mathbb{I}(p(r)=j) + \mathbb{I}(q(r)=j))$. From Eq.(2.59), we get

$$\widetilde{\mathbf{w}}_j = \frac{\sum_{i=1}^{n}\alpha_{ij}g_j\mathbf{b}_i - \mathbf{y}_j + 2\rho\mathbf{v}_j}{\sum_{i=1}^{n}\alpha_{ij}^2 g_j^2 + 2\lambda_2 g_j^2 + 2\rho N + 2\gamma}. \tag{2.61}$$

Plugging Eq.(2.61) into Eq.(2.60), we get the solution of γ. Then plugging γ back into Eq.(2.61), we get the solution of $\widetilde{\mathbf{w}}_j$.

Solve $\mathbf{v}_1^{(r)}, \mathbf{v}_2^{(r)}$ in Case 3 and 4

Case 3 We assume $\lambda_1 = 0$ and $\lambda_2 > 0$, then

$$(\rho + 2\gamma_1)\mathbf{v}_1^{(r)} - \lambda_2 \mathbf{v}_2^{(r)} = \mathbf{y}_1^{(r)} + \rho \widetilde{\mathbf{w}}_{p(r)} \tag{2.62}$$

$$(\rho + 2\gamma_2)\mathbf{v}_2^{(r)} - \lambda_2 \mathbf{v}_1^{(r)} = \mathbf{y}_2^{(r)} + \rho \widetilde{\mathbf{w}}_{q(r)}. \tag{2.63}$$

According to the complementary slackness condition, we know $\mathbf{v}_1^{(r)} \cdot \mathbf{v}_2^{(r)} = -\tau$. For the vectors on both sides of Eq.(2.62), taking the square of their ℓ_2 norm, we get

$$(\rho + 2\gamma_1)^2 + \lambda_2^2 + 2(\rho + 2\gamma_1)\lambda_2 \tau = \|\mathbf{y}_1^{(r)} + \rho \widetilde{\mathbf{w}}_{p(r)}\|_2^2. \tag{2.64}$$

Similarly, from Eq.(2.63), we get

$$(\rho + 2\gamma_2)^2 + \lambda_2^2 + 2(\rho + 2\gamma_2)\lambda_2 \tau = \|\mathbf{y}_2^{(r)} + \rho \widetilde{\mathbf{w}}_{q(r)}\|_2^2. \tag{2.65}$$

Taking the inner product of the two vectors on the left hand sides of Eq.(2.62,2.63), and those on the right hand sides, we get

$$-(2\rho + 2\gamma_1 + 2\gamma_2)\lambda_2 - ((\rho + 2\gamma_1)(\rho + 2\gamma_2) + \lambda_2^2)\tau = (\mathbf{y}_1^{(r)} + \rho \widetilde{\mathbf{w}}_{p(r)})^\top (\mathbf{y}_2^{(r)} + \rho \widetilde{\mathbf{w}}_{q(r)}). \tag{2.66}$$

Solving the system of equations consisting of Eq.(2.64-2.66), we obtain the optimal values of γ_1, γ_2, and λ_2. Plugging them into Eq.(2.62) and Eq.(2.63), we obtain a solution of $\mathbf{v}_1^{(r)}$ and $\mathbf{v}_2^{(r)}$. Then we check whether this solution satisfies $\mathbf{v}_1^{(r)} \cdot \mathbf{v}_2^{(r)} \leq \tau$. If so, this is an optimal solution.

Case 4 We assume $\lambda_1 = 0$ and $\lambda_2 = 0$, then according to the complementary slackness condition, we know $\mathbf{v}_1^{(r)} \cdot \mathbf{v}_2^{(r)} = \tau$ and $\mathbf{v}_1^{(r)} \cdot \mathbf{v}_2^{(r)} = -\tau$. This only holds when $\tau = 0$. Then the sub-problem defined on $\mathbf{v}_1^{(r)}, \mathbf{v}_2^{(r)}$ becomes

$$\min_{\mathbf{v}_1^{(r)}, \mathbf{v}_2^{(r)}} \quad -\mathbf{y}_1^{(r)} \cdot \mathbf{v}_1^{(r)} - \mathbf{y}_2^{(r)} \cdot \mathbf{v}_2^{(r)} + \tfrac{\rho}{2}\|\widetilde{\mathbf{w}}_{p(r)} - \mathbf{v}_1^{(r)}\|_2^2 + \tfrac{\rho}{2}\|\widetilde{\mathbf{w}}_{q(r)} - \mathbf{v}_2^{(r)}\|_2^2$$

$$s.t. \qquad \|\mathbf{v}_1^{(r)}\|_2 = 1, \|\mathbf{v}_2^{(r)}\|_2 = 1, \mathbf{v}_1^{(r)} \cdot \mathbf{v}_2^{(r)} = 0.$$

Let γ_1, γ_2, γ_3 be the KKT multipliers associated with the three constraints in this sub-problem. According to the KKT conditions, we have

$$(2\gamma_1 + \rho)\mathbf{v}_1^{(r)} + \gamma_3 \mathbf{v}_2^{(r)} = \mathbf{y}_1^{(r)} + \rho \widetilde{\mathbf{w}}_{p(r)} \tag{2.67}$$

$$(2\gamma_2 + \rho)\mathbf{v}_2^{(r)} + \gamma_3 \mathbf{v}_1^{(r)} = \mathbf{y}_2^{(r)} + \rho \widetilde{\mathbf{w}}_{q(r)}. \tag{2.68}$$

For the vectors on both sides of Eq.(2.67), taking the square of their ℓ_2 norm, we get

$$(2\gamma_1 + \rho)^2 + \gamma_3^2 = \|\mathbf{y}_1^{(r)} + \rho \widetilde{\mathbf{w}}_{p(r)}\|_2^2. \tag{2.69}$$

For the vectors on both sides of Eq.(2.68), taking the square of their ℓ_2 norm, we get

$$(2\gamma_2 + \rho)^2 + \gamma_3^2 = \|\mathbf{y}_2^{(r)} + \rho\widetilde{\mathbf{w}}_{q(r)}\|_2^2. \tag{2.70}$$

Taking the inner product of the two vectors on the left hand sides of Eq.(2.67,2.68), and those on the right hand sides, we get

$$(2\rho + 2\gamma_1 + 2\gamma_2)\gamma_3 = (\mathbf{y}_1^{(r)} + \rho\widetilde{\mathbf{w}}_{p(r)})^\top(\mathbf{y}_2^{(r)} + \rho\widetilde{\mathbf{w}}_{q(r)}). \tag{2.71}$$

Solving the system of equations consisting of Eq.(2.69-2.71), we obtain the optimal values of γ_1, γ_2, and γ_3. Plugging them into Eq.(2.67) and Eq.(2.68), we obtain a solution of $\mathbf{v}_1^{(r)}$ and $\mathbf{v}_2^{(r)}$. This is an optimal solution.

2.4 Diversity in the RKHS: Orthogonality-promoting Regularization of Kernel Methods

In previous sections, we study how to promote diversity among finite-dimensional vectors. In this section, we extend the study to infinite-dimensional functions [374] in the reproducing kernel Hilbert space (RKHS) [294], which is presumably more challenging.

Kernel methods perform learning in reproducing kernel Hilbert spaces (RKHSs) of functions [294]. The RKHS represents a high-dimensional feature space that can capture nonlinear patterns in the lower-dimensional observed data. This Hilbert space is associated with a kernel function k, and the inner product in the RKHS can be implicitly computed by evaluating k in the lower-dimensional input space (known as the *kernel trick*). Well-established kernel methods include support vector machine [294], kernel principal component analysis [293], kernel independent component analysis [25], to name a few. Even though their large model-capacity leads to high representational power, it also incurs substantial risk of overfitting.

One key ingredient in kernel methods is regularization, which reduces overfitting by controlling the complexity of the RKHS functions [251, 294]. Regularizers proposed previously such as RKHS norm, derivatives, green functions, and splines mostly focus on encouraging a small norm [251] and smoothness of functions [294]. Notably, the most widely-used regularizer is the squared RKHS norm.

We are interested in whether diversity-promoting regularization can outperform the existing regularizers in reducing overfitting and whether its ability of better capturing infrequent patterns and reducing model size without sacrificing modeling power holds in the RKHS. Similar to Section 2.2 and 2.3, we use near-orthogonality to characterize diversity. Similar to Section 2.2.1, to promote near-orthogonality among a set of RKHS functions $\{f_i\}_{i=1}^K$, we compute their Gram matrix $\mathbf{G}$ where $G_{ij} = \langle f_i, f_j\rangle$, and encourage $\mathbf{G}$ to be close to an identity matrix $\mathbf{I}$ where the closeness is measured using the Bregman matrix divergences [100]. We apply the proposed BMD regularizers to two kernel methods – kernel distance metric learning (KDML) [176, 335] and kernel sparse coding (KSC) [120], and develop an optimization algorithm based on the alternating direction method of multipliers (ADMM) [52] where the RKHS functions are learned using functional gradient descent (FGD) [89]. Experimental results show that the proposed near-orthogonality regularizers (1) greatly improve the generalization performance of KDML and

KSC; (2) can reduce model size without sacrificing modeling power; (3) can better capture infrequent patterns in the data; and (4) outperform other orthogonality-promoting regularizers and the squared Hilbert norm.

2.4.1 Bregman Matrix Divergence Regularized Kernel Methods

We consider kernel methods that are parameterized by a set of RKHS functions $\mathcal{F} = \{f_i\}_{i=1}^K$. Examples include kernel principal component analysis (PCA) [293], kernel independent component analysis (ICA) [25], kernel distance metric learning [176, 335] and kernel sparse coding [120], to name a few. We promote diversity among these functions by encouraging them to be close to being orthogonal. Similar to the vector case in Section 2.2.1, we compute a Gram matrix $\mathbf{G}$ where $G_{ij} = \langle f_i, f_j \rangle_{\mathcal{H}}$ and encourage $\mathbf{G}$ to be close to an identity matrix $\mathbf{I}$ by minimizing the Bregman matrix divergences (BMD) between $\mathbf{G}$ and $\mathbf{I}$. A family of BMD regularizers can be defined, based on the (1) squared Frobenius norm (SFN): $\|\mathbf{G} - \mathbf{I}\|_F^2$; (2) von Neumann divergence (VND): $\text{tr}(\mathbf{G}\log\mathbf{G} - \mathbf{G})$; (3) log determinant divergence (LDD): $\text{tr}(\mathbf{G}) - \log\det(\mathbf{G})$. To apply the VND and LDD regularizers, the Gram matrix $\mathbf{G}$ is required to be positive definite. In our experiments, this condition is always satisfied since VND and LDD encourage the RKHS functions to be close to being orthogonal (therefore linearly independent). We use these regularizers to encourage near-orthogonality among RKHS functions, and define BMD regularized kernel methods (BMD-KM):

$$\min_{\mathcal{F}} \quad \mathcal{L}(\mathcal{F}) + \lambda\Omega(\mathcal{F}), \tag{2.72}$$

where $\mathcal{L}(\mathcal{F})$ is the objective function of the kernel method, and λ is the regularization parameter. Compared to kernel PCA and ICA in which the functions are required to be strictly-orthogonal, BMD-KM can be seen as a relaxed counterpart where the functions are encouraged to be close to, but not necessarily strictly, being orthogonal. As we will demonstrate in the experiments, strict-orthogonality can compromise performance in certain applications.

We apply the BMD regularizers to two instances of kernel methods: kernel distance metric learning and kernel sparse coding.

Case study I: kernel distance metric learning (KDML) KDML [176, 335] is equipped with K RKHS functions $\mathcal{F} = \{f_i\}_{i=1}^K$ that map a data example $\mathbf{x}$ into a vector $\mathbf{h}^{(x)}$ in a K-dimensional latent space, where $\mathbf{h}_i^{(x)} = f_i(\mathbf{x})$. Given two examples $\mathbf{x}$ and $\mathbf{y}$, their distance is defined as $d_{\mathcal{F}}(\mathbf{x}, \mathbf{y}) = \|\mathbf{h}^{(x)} - \mathbf{h}^{(y)}\|_2^2$, which is parameterized by $\mathcal{F}$. Given N training examples, $\{\mathbf{x}_n, \mathbf{y}_n, t_n\}_{n=1}^N$, where $\mathbf{x}_n$ and $\mathbf{y}_n$ are similar if the label t_n equals 1 and dissimilar if $t_n = 0$, following [146], we learn the distance metric by minimizing $\sum_{n=1}^N \log(1 + \exp((2t_n - 1)d_{\mathcal{F}}(\mathbf{x}_n, \mathbf{y}_n))$. Using $\Omega(\mathcal{F})$ to promote near-orthogonality, we obtain the BMD-regularized KDML (BMD-KDML) problem:

$$\min_{\mathcal{F}} \sum_{n=1}^N \log(1 + \exp((2t_n - 1)d_{\mathcal{F}}(\mathbf{x}_n, \mathbf{y}_n)) + \lambda\Omega(\mathcal{F}). \tag{2.73}$$

Case study II: kernel sparse coding (KSC) In KSC [120], a data example $\mathbf{x}$ is mapped into $k(\mathbf{x}, \cdot)$ in an RKHS induced by the kernel function $k(\cdot, \cdot)$ and a dictionary of RKHS functions

$\mathcal{F} = \{f_i\}_{i=1}^K$ are learned to reconstruct $k(\mathbf{x}, \cdot)$. Given the training data $\{\mathbf{x}_n\}_{n=1}^N$, $\mathcal{F}$ can be learned by minimizing $\frac{1}{2}\sum_{n=1}^N \|k(\mathbf{x}_n, \cdot) - \sum_{i=1}^K a_{ni} f_i\|_{\mathcal{H}}^2 + \lambda_1 \sum_{n=1}^N \|\mathbf{a}_n\|_1 + \frac{\lambda_2}{2}\sum_{i=1}^K \|f_i\|_{\mathcal{H}}^2$, where the reconstruction error is measured by the squared Hilbert norm and $\mathbf{a}_n$ are the linear coefficients. The ℓ_1 regularizer $\|\mathbf{a}_n\|_1$ is applied to encourage the coefficients to be sparse. To avoid the degenerated case where the RKHS functions are of large norm while the coefficients are close to zero, the squared Hilbert norm regularizer $\|f_i\|_{\mathcal{H}}^2$ is applied to the RKHS functions to keep their magnitude small. By adding $\Omega(\mathcal{F})$, we obtain the BMD-regularized KSC (BMD-KSC) problem:

$$\min_{\mathcal{F},\mathcal{A}} \quad \frac{1}{2}\sum_{n=1}^N \|k(\mathbf{x}_n, \cdot) - \sum_{i=1}^K a_{ni} f_i\|_{\mathcal{H}}^2 + \lambda_1 \sum_{n=1}^N \|\mathbf{a}_n\|_1 + \frac{\lambda_2}{2}\sum_{i=1}^K \|f_i\|_{\mathcal{H}}^2 + \lambda_3 \Omega(\mathcal{F}), \tag{2.74}$$

where $\mathcal{A}$ denotes all the sparse codes.

2.4.2 A Functional Gradient Descent Algorithm

In this section, we develop an ADMM [52] based algorithm to solve the BMD-KM problem. First, by introducing auxiliary variables $\widehat{\mathcal{F}} = \{\widehat{f}_i\}_{i=1}^K$ which are a set of RKHS functions and $\mathbf{A} \in \mathbb{R}^{K\times K}$, we rewrite the BMD-KM problem into an equivalent form that is amenable for developing ADMM-based algorithms:

$$\begin{aligned} \min_{\mathcal{F},\widehat{\mathcal{F}},\mathbf{A}} \quad & \mathcal{L}(\mathcal{F}) + \lambda D_\phi(\mathbf{A}, \mathbf{I}) \\ s.t. \quad & \forall i, f_i = \widehat{f}_i \\ & \forall i, j, \langle f_i, \widehat{f}_j\rangle = A_{ij}, \langle f_i, \widehat{f}_j\rangle = A_{ji}, \end{aligned} \tag{2.75}$$

where $\mathbf{A}$ is required to be positive definite when $D_\phi(\mathbf{A}, \mathbf{I})$ is a VND or LDD regularizer. The constraints $\langle f_i, \widehat{f}_j\rangle = A_{ij}$ and $\langle f_i, \widehat{f}_j\rangle = A_{ji}$ imply that $\mathbf{A}$ is symmetric. We define the augmented Lagrangian with parameter $\rho > 0$: $\mathcal{L}(\mathcal{F}) + \lambda D_\phi(\mathbf{A}, \mathbf{I}) + \sum_{i=1}^K \langle g_i, f_i - \widehat{f}_i\rangle + \sum_{i=1}^K\sum_{j=1}^K (P_{ij}(\langle f_i, \widehat{f}_j\rangle - A_{ij}) + Q_{ij}(\langle f_i, \widehat{f}_j\rangle - A_{ji}) + \frac{\rho}{2}(\langle f_i, \widehat{f}_j\rangle - A_{ij})^2 + \frac{\rho}{2}(\langle f_i, \widehat{f}_j\rangle - A_{ji})^2)$, where $\mathcal{G} = \{g_i\}_{i=1}^K$ is another set of RKHS functions, and $\mathbf{P}, \mathbf{Q} \in \mathbb{R}^{K\times K}$ are Lagrange multipliers. Then we minimize this Lagrangian function by alternating among $\mathcal{F}$, $\widehat{\mathcal{F}}$, $\mathcal{G}$, $\mathbf{A}$, $\mathbf{P}$, $\mathbf{Q}$.

Solve A Given $\mathbf{H} \in \mathbb{R}^{K\times K}$ where $H_{ij} = \langle f_i, \hat{f}_j\rangle$, we learn $\mathbf{A}$ by minimizing $\lambda D_\phi(\mathbf{A}, \mathbf{I}) - \langle \mathbf{P}, \mathbf{A}\rangle - \langle \mathbf{Q}^\top, \mathbf{A}\rangle + \frac{\rho}{2}\|\mathbf{H} - \mathbf{A}\|_F^2 + \frac{\rho}{2}\|\mathbf{H}^\top - \mathbf{A}\|_F^2$, which is a convex problem. $D_\phi(\mathbf{A}, \mathbf{I})$ has three cases, which we discuss separately. When $D_\phi(\mathbf{A}, \mathbf{I})$ is the VND, we first perform an eigen-decomposition of $\mathbf{D} = \mathbf{P} + \mathbf{Q}^\top + \rho(\mathbf{H} + \mathbf{H}^\top)$: $\mathbf{D} = \mathbf{\Phi}\mathbf{\Sigma}\mathbf{\Phi}^{-1}$, then the optimal solution of $\mathbf{A}$ can be obtained as $\mathbf{A} = \mathbf{\Phi}\widehat{\mathbf{\Sigma}}\mathbf{\Phi}^{-1}$ where

$$\widehat{\Sigma}_{ii} = \frac{\lambda\omega\big(\frac{\Sigma_{ii}}{\lambda} - \log\big(\frac{\lambda}{2\rho}\big)\big)}{2\rho}, \tag{2.76}$$

and $\omega(\cdot)$ is the Wright omega function [137]. It can be shown that $\mathbf{A}$ is positive definite. When $D_\phi(\mathbf{A}, \mathbf{I})$ is the LDD, the optimal solution is:

$$\mathbf{A} = -\tfrac{1}{2}\mathbf{B} + \tfrac{1}{2}\sqrt{\mathbf{B}^2 - 4\mathbf{C}}, \tag{2.77}$$

where $\mathbf{B} = \frac{1}{\rho}(\lambda\mathbf{I} - \mathbf{P} - \mathbf{Q}^\top - \rho(\mathbf{H} + \mathbf{H}^\top))$ and $\mathbf{C} = -\frac{\lambda}{\rho}\mathbf{I}$. It can be verified that $\mathbf{A}$ is positive definite. When $D_\phi(\mathbf{A}, \mathbf{I})$ is the SFN, the optimal solution for $\mathbf{A}$ is:

$$\mathbf{A} = (2\lambda\mathbf{I} + \mathbf{P} + \mathbf{Q}^\top + \rho(\mathbf{H} + \mathbf{H}^\top))/(2\lambda + 2\rho). \tag{2.78}$$

Solve f_i We solve f_i by minimizing $\Upsilon = \mathcal{L}(\mathcal{F}) + \langle g_i, f_i\rangle + \sum_{j=1}^K (P_{ij}+Q_{ij})\langle f_i, \widehat{f}_j\rangle + \frac{\rho}{2}\sum_{j=1}^K((\langle f_i, \widehat{f}_j\rangle - A_{ij})^2 + (\langle f_i, \widehat{f}_j\rangle - A_{ji})^2)$. The first issue we need to address is how to represent f_i. When $f \in \mathcal{F}$ is regularized by the RKHS norm, according to the representer theorem [294], the optimal solution f^* can be expressed as a linear combination of kernel functions evaluated at the training data: $f^*(\mathbf{x}) = \sum_{n=1}^N \alpha_n k(\mathbf{x}_n, \mathbf{x})$, which we refer to as *representer theorem representation* (RTR). This endows f^* an explicit parametrization that greatly eases learning: the search space of f^* is reduced from the infinite-dimensional RKHS $\mathcal{H}$ to an N-dimensional space of coefficients $\{\alpha_n\}_{n=1}^N$. However, in Υ, due to the presence of the inner products between f_i with other functions, the representer theorem does not hold and f_i does not admit an RTR form. To address this issue, we learn f_i directly using functional gradient descent [89]. A *functional* $F : \mathcal{H} \to \mathbb{R}$ maps functions in $\mathcal{H}$ to real numbers. A *functional gradient* $\nabla F[f]$ is defined implicitly as the linear term of the change in a function due to a small perturbation ϵ in its input: $F[f + \epsilon g] = F[f] + \epsilon\langle \nabla F[f], g\rangle + O(\epsilon^2)$. Of particular interest is the *evaluation functional* $F_\mathbf{x}[f]$ which is parameterized by an input vector $\mathbf{x}$ and evaluates f at $\mathbf{x}$: $F_\mathbf{x}[f] = f(\mathbf{x})$. The functional gradient of $F_\mathbf{x}[f]$ is $k(\mathbf{x}, \cdot)$ [89] where k is the kernel associated with the RKHS. The gradient of an inner product functional $F_g[f] = \langle f, g\rangle$ is g.

The form of $\mathcal{L}(\mathcal{F})$ depends on a specific kernel method. Here, we consider KDML where $\mathcal{L}(\mathcal{F})$ is given in Eq.(2.73). In KDML, f_i appears in two types of functionals: evaluation functionals in $d_\mathcal{F}(\mathbf{x}_n, \mathbf{y}_n)$ (such as $f_i(\mathbf{x}_n)$) and inner product functionals (such as $\langle g_i, f_i\rangle$). The functional gradient of Υ is $\triangle f_i = 2\sum_{n=1}^N \sigma((2t_n - 1)d_\mathcal{F}(\mathbf{x}_n, \mathbf{y}_n))(2t_n - 1)(f_i(\mathbf{x}_n) - f_i(\mathbf{y}_n))(k(\mathbf{x}_n, \cdot) - k(\mathbf{y}_n, \cdot)) + g_i + \sum_{j=1}^K (P_{ij} + Q_{ij} + \rho(2\langle f_i, \widehat{f}_j\rangle - A_{ij} - A_{ji}))\widehat{f}_j$, where $\sigma(x) = 1/(1 + \exp(-x))$ is a sigmoid function. Given this functional gradient, we can perform gradient descent to update f_i until convergence: $f_i \leftarrow f_i - \eta\triangle f_i$, where η is the learning rate. In the algorithm, we initialize f_i, g_i, and $\widehat{f}_j$ as zero functions. Then as will be proven later on, during the algorithm execution, f_i, g_i, and $\widehat{f}_j$ are all in the form of RTR. So updating f_i amounts to updating the linear coefficients in the RTR.

Solve $\widehat{f}_j$ The sub-problem defined over $\widehat{f}_j$ is:

$$\min_{\widehat{f}_j} -\langle g_j, \widehat{f}_j\rangle + \sum_{i=1}^K((P_{ij} + Q_{ij})\langle f_i, \widehat{f}_j\rangle + \frac{\rho}{2}((\langle f_i, \widehat{f}_j\rangle - A_{ij})^2 + (\langle f_i, \widehat{f}_j\rangle - A_{ji})^2)), \tag{2.79}$$

which is a convex problem. Setting the derivative of the objective function to zero, we get an equation:

$$(2\rho\sum_{i=1}^K f_i \otimes f_i)\widehat{f}_j = \sum_{i=1}^K(\rho(A_{ij} + A_{ji}) - (P_{ij} + Q_{ij}))f_i + g_j, \tag{2.80}$$

where $\otimes$ denotes the outer product in the RKHS. As will be proven later on, $\widehat{f}_j$, g_j, and f_i are all in the form of RTR. Let $\Phi = [k(\mathbf{x}_1, \cdot), \cdots, k(\mathbf{x}_N, \cdot)]$, then $f_i = \Phi\mathbf{a}_i$, $\sum_{i=1}^K(\rho(A_{ij} + A_{ji}) -$

$(P_{ij} + Q_{ij}))f_i + g_j = \Phi\mathbf{b}$, $\widehat{f_j} = \Phi\mathbf{c}$, where $\mathbf{a}_i$, $\mathbf{b}$, $\mathbf{c}$ are coefficient vectors. $\mathbf{a}_i$ and $\mathbf{b}$ are known and $\mathbf{c}$ is to be estimated. Then Eq.(2.80) can be written as

$$(2\rho \sum_{i=1}^{K} \mathbf{a}_i \mathbf{a}_i^\top)\Phi^\top \Phi \mathbf{c} = \mathbf{b}, \tag{2.81}$$

where $(\Phi^\top \Phi)_{ij} = k(\mathbf{x}_i, \mathbf{x}_j)$ and $\mathbf{c} = ((2\rho \sum_{i=1}^{K} \mathbf{a}_i \mathbf{a}_i^\top)\Phi^\top \Phi)^{-1}\mathbf{b}$. In practice, inverting the $N \times N$ matrix $(2\rho \sum_{i=1}^{K} \mathbf{a}_i \mathbf{a}_i^\top)\Phi^\top \Phi$ is computationally prohibitive when N is large. In that case, we can switch to a stochastic FGD method to solve this problem.

The update rules for $\mathbf{P}$, $\mathbf{Q}$ and g_j are simple:

Update P $\quad \mathbf{P} = \mathbf{P} + \rho(\mathbf{H} - \mathbf{A})$

Update Q $\quad \mathbf{Q} = \mathbf{Q} + \rho(\mathbf{H} - \mathbf{A}^\top)$

Update g_j $\quad g_j = g_j + \rho(f_j - \hat{f}_j)$

RTR form of the RKHS functions Next, we present the proof that as long as the RKHS functions f_i, g_i, and $\widehat{f_j}$ are initialized to be zero, they are always in the RTR form during the entire execution of the algorithm. We prove this by induction. For the base case (iteration $t = 0$), these functions are all zero, hence admitting the RTR form. For the inductive step, assuming the statement is true at iteration $t - 1$, we prove it holds for iteration t. We begin with f_i, which is solved by functional gradient descent (FGD). At iteration t, the input of the algorithm is $f_i^{(t-1)}$ and the output is $f_i^{(t)}$. The first term of the functional gradient $\triangle f_i$ is in the RTR form, so are g_i and $\widehat{f_j}$ (according to the inductive hypothesis). Then $\triangle f_i$ is in the RTR form. Starting from $f_i^{(t-1)}$ which is in the RTR form according to the inductive hypothesis, f_i is updated iteratively in the following way: $f_i^{(s)} \leftarrow f_i^{(s-1)} - \eta \triangle f_i^{(s-1)}$ (where s indexes the FGD iterations), resulting in $f_i^{(t)}$ which is also in the RTR form.

Next, we prove that if $g_j^{(t-1)}$ and $f_i^{(t-1)}$ are in the RTR form, so will be $\widehat{f_j}$. The proof is similar to that of the representer theorem [294]. We decompose $\widehat{f_j}$ into $\widehat{f_j}^{\|}$ and $\widehat{f_j}^{\perp}$, where $\widehat{f_j}^{\|}$ is in $S = \{\sum_{n=1}^{N} \alpha_n k(\mathbf{x}_n, \mathbf{x}), \{\alpha_n\}_{n=1}^{N} \subset \mathbb{R}\}$ (i.e., in the RTR form) and $\widehat{f_j}^{\perp}$ is perpendicular to S, hence $\langle g_j, \widehat{f_j}^{\perp}\rangle = 0$, $\langle f_i, \widehat{f_j}^{\perp}\rangle = 0$. The problem defined in Eq.(2.79) can be equivalently written as:

$$\min_{\widehat{f_j}^{\|}} -\langle g_j, \widehat{f_j}^{\|}\rangle + \sum_{i=1}^{K}((P_{ij} + Q_{ij})\langle f_i, \widehat{f_j}^{\|}\rangle + \frac{\rho}{2}((\langle f_i, \widehat{f_j}^{\|}\rangle - A_{ij})^2 + (\langle f_i, \widehat{f_j}^{\|}\rangle - A_{ji})^2)). \tag{2.82}$$

Hence the optimal solution of $\widehat{f_j}$ is in the RTR form. For g_j, from its update equation $g_j = g_j + \rho(f_j - \hat{f}_j)$, it is easy to see that if $f_j^{(t-1)}$ and $\widehat{f}_j^{(t-1)}$ are in the RTR form, so will be $g_j^{(t)}$. Note that these RKHS functions are in the RTR form because of the algorithmic procedure (namely, initializing these functions as zero and using FGD to solve f) rather than the representer theorem. If we choose another way of initialization, f may not be in the RTR form.

Scalable representation of the RKHS functions based on random Fourier features When the RKHS functions are in the RTR form, $O(N^2D)$ computational cost is incurred where N is the number of training examples and D is the input feature dimension. On large-sized datasets, this is not scalable. In this section, we investigate a scalable representation of RKHS functions based on random Fourier features (RFFs) [284]. Given a shift-invariant kernel $k(\mathbf{x}, \mathbf{y}) = k(\mathbf{x} - \mathbf{y})$ such as the radial basis function (RBF) kernel, it can be approximated with RFFs: $k(\mathbf{x}, \mathbf{y}) = \langle k(\mathbf{x}, \cdot), k(\mathbf{y}, \cdot) \rangle \approx z(\mathbf{x})^\top z(\mathbf{y})$, where $z(\mathbf{x}) \in \mathbb{R}^Q$ is the RFF transformation of $\mathbf{x}$, and can be seen as an approximation of $k(\mathbf{x}, \cdot)$. $z(\mathbf{x})$ is generated in the following way: (1) compute the Fourier transform $p(\boldsymbol{\omega})$ of the kernel k; (2) draw Q i.i.d samples $\boldsymbol{\omega}_1, \cdots, \boldsymbol{\omega}_Q \in \mathbb{R}^D$ from $p(\boldsymbol{\omega})$ and Q i.i.d samples $b_1, \cdots, b_Q \in \mathbb{R}$ from the uniform distribution on $[0, 2\pi]$; (3) let $z(\mathbf{x}) = \sqrt{\frac{2}{Q}}[\cos(\boldsymbol{\omega}_1^\top \mathbf{x} + b_1), \cdots, \cos(\boldsymbol{\omega}_Q^\top \mathbf{x} + b_Q)]^\top$. For $f \in \mathcal{H}$ where $\mathcal{H}$ is an RKHS induced by a shift-invariant kernel, we know that $f(\mathbf{x}) = \langle f, k(\mathbf{x}, \cdot) \rangle$. Using $z(\mathbf{x})$ to approximate $k(\mathbf{x}, \cdot)$ and $\mathbf{w} \in \mathbb{R}^Q$ to approximate f, we get $f(\mathbf{x}) \approx \mathbf{w}^\top z(\mathbf{x})$. As such, the infinite-dimensional function f can be approximately represented as a finite-dimensional vector $\mathbf{w}$, and the BMD-KM problem defined in Eq.(2.72) can be written as:

$$\min_{\mathcal{W}} \mathcal{L}(\mathcal{W}) + \lambda \Omega(\mathcal{W}), \tag{2.83}$$

where $\mathcal{W} = \{\mathbf{w}_i\}_{i=1}^K$ and $\Omega(\mathcal{W}) = D(\mathbf{G}, \mathbf{I})$ with $G_{ij} = \mathbf{w}_i^\top \mathbf{w}_j$. Now, learning can be conducted over $\mathcal{W}$, and the computational cost is reduced from $O(N^2D)$ to $O(NQ)$, where Q is the number of RFFs and is much smaller than ND.

2.4.3 Evaluation

In this section, we present experimental results on BMD-KDML and BMD-KSC.

Datasets We used six datasets in the experiments: an electronic health record dataset MIMIC-III [184]; five image datasets including Stanford-Cars (Cars) [202], Caltech-UCSD-Birds (Birds) [358], Scenes-15 [212], Caltech-256 [141], and UIUC-Sports [224]. The first three were used for KDML and the last three for KSC. Their statistics are summarized in Table 2.19. For each dataset, five random train/test splits were performed, and the results were averaged over the five runs. For the MIMIC-III dataset, we extracted features from demographics (including age and gender), clinical notes (including bag-of-words and Word2Vec [256]), and lab tests (including zero-order, first-order, and second-order temporal features). The total feature dimension is 7207. The features for Cars and Birds datasets were extracted using the VGG16 [303] convolutional neural network trained on the ImageNet [95] dataset, which were the outputs of the second fully-connected layer with 4096 dimensions. For Scenes-15, Caltech-256, and UIUC-Sport, we extracted pixel-level dense SIFT [237] features where the step size and patch size were 8 and 16, respectively.

Experimental setup For BMD-KDML and BMD-KSC, we experimented with six combinations between three regularizers including SFN, LDD, and VND, and two representations of RKHS functions including RTR and RFF. In DML experiments, two data examples were labeled as similar if belonging to the same class and dissimilar if otherwise. The learned distance

metrics were applied for retrieval whose performance was evaluated using precision@k. Precision@k is defined as n/k where n is the number of examples (among the top k retrieved examples) that have the same class label with the query. We compared with three groups of baseline methods: (1) KDML (Eq.(2.73) without the regularizer $\Omega(\mathcal{F})$) and its variants under different regularizers including squared Hilbert norm (SHN), DPP [429] and Angle [369]; (2) other kernel DML methods including the ones proposed in [335] (Tsang) and [176] (Jain), multiple kernels DML (MK-DML) [345] and pairwise constrained component analysis (PCCA) [252]; (3) non-kernel metric learning (ML) methods, including information theoretic ML (ITML) [92], logistic discriminant ML (LDML) [146], DML with eigenvalue optimization (DML-Eig) [398], information-theoretic semi-supervised ML via entropy regularization (Seraph) [265] and geometric mean ML (GMML) [405]; (4) Euclidean distance (EUC). For methods in group (1), the RKHS functions are represented in the RTR form. In sparse coding experiments, on top of the SIFT features, we used kernel sparse coding to learn a set of RKHS functions and represented each SIFT feature into a sparse code. To obtain image-level features, we applied max-pooling [392] and spatial pyramid matching [212, 392] over the pixel-level sparse codes. The following baselines were compared with: sparse coding (SC) [392], unregularized kernel SC (KSC) [120], KSC regularized by SHN, DPP, and Angle. In these methods, the RKHS functions are represented in the RTR form. We used 5-fold cross validation to tune the regularization parameters in $\{10^{-5}, 10^{-4}, \cdots, 10^{5}\}$, the number of RKHS functions in $\{50, 100, 200, \cdots, 500\}$, and the dimension of RFF in $\{1, 2, \cdots, 10\} \times D$ where D is the feature dimension of the input data. The kernel function was chosen to be the radial basis function (RBF) $\exp(-\gamma\|\mathbf{x} - \mathbf{y}\|_2^2)$ where the scale parameter γ was tuned in $\{10^{-3}, 10^{-2}, \cdots, 10^{3}\}$. The parameter ρ in the ADMM-based algorithm was set to 1. The learning rate in functional gradient descent was set to 0.001.

Results Table 2.20 shows the retrieval precision@10 on three datasets, where we observe the following. First, BMD-KDML methods including KDML-(SFN,VND,LDD)-(RTR,RFF) greatly outperform unregularized and SHN-regularized KDML, which demonstrates that near-orthogonality regularization is an effective way to reduce overfitting. Second, BMD regularizers including SFN, VND, and LDD outperform other near-orthogonality regularizers including DPP and Angle, possibly because they are insensitive to vector scaling and amenable for optimization. Third, VND and LDD achieve comparable performance and outperform SFN, possibly because they measure near-orthogonality in a global way while SFN conducts that in a pairwise fashion. Fourth, the RFF representation of RKHS functions performs comparably to RTR, in spite of the fact that it is an approximation method. Finally, the BMD-KDML methods achieve better performance than non-kernel DML methods and other kernel DML methods, suggesting their competitive ability in learning effective distance metrics.

Table 6.2 shows the number of RKHS functions under which the precision@10 in Table 2.20 is achieved. It can be seen that the BMD-KDML methods utilize much fewer functions than KDML while achieving better precision@10. For instance, KDML-VND-RTR achieves 77.1% precision@10 with 100 functions on the MIMIC-III dataset while KDML achieves 73.8% precision@10 with 300 functions. These results demonstrate the ability of the BMD regularizers in reducing model size without sacrificing modeling power. By encouraging the functions to be near-orthogonal, the BMD regularizers decrease the redundancy among functions and make

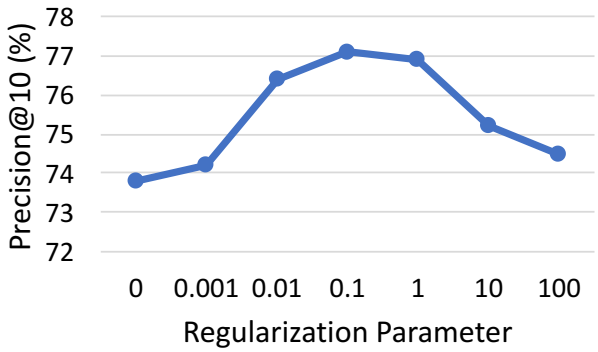

Figure 2.6: Precision@10 versus the regularization parameter λ on MIMIC-III.

the functions highly complementary. As a result, a small number of such functions are able to capture the patterns in the data sufficiently well. In addition, the BMD regularizers achieve better precision@10 with fewer functions than other near-orthogonality regularizers including DPP and Angle, suggesting their better efficacy in promoting near-orthogonality.

In the next experiment, we investigate whether near-orthogonality regularization can better capture infrequent patterns. We select 3 frequent diseases (patterns) and 5 infrequent ones from the MIMIC-III dataset. A disease is regarded as being *frequent* if the number of hospital admissions diagnosed with this disease is greater than 300. Table 2.22 shows the precision@10 on the 8 diseases, from which we observe that: (1) on the 5 infrequent diseases (labeled as D4–D8), the BMD-KDML methods achieve much higher precision@10 than the unregularized KDML, suggesting that by encouraging the functions to be close to being orthogonal, the BMD regularizers can better capture infrequent patterns; (2) on the 3 frequent diseases (labeled as D1–D3), the precision@10 achieved by the BMD-KDML methods is comparable with that achieved by the unregularized KDML, indicating that the BMD regularizers do not compromise the modeling efficacy on the frequent patterns. On the infrequent diseases, the BMD-KDML methods outperform KDML-DPP and KDML-Angle, suggesting that the BMD regularizers have better ability in promoting near-orthogonality than DPP and Angle.

Further, Figure 2.6 shows how the precision@10 on MIMIC-III varies as we increase the regularization parameter λ in KDML-VND-RTR. As can be seen, the best precision@10 is achieved under a modest λ. A very large λ would make the functions strictly orthogonal, as kernel PCA and ICA do, which would result in excessively strong regularization and therefore poor performance.

We also compare the convergence time of BMD-KDML under two representations: RTR and RFF. As shown in Table 2.23, RFF results in much faster convergence since this representation does not depend on the training data. While computationally efficient, RFF does not sacrifice much modeling power. Table 2.20 shows that RFF achieves precision@10 that is comparable to RTR.

Next, we present the kernel sparse coding results. Table 2.24 shows the classification accuracy on three datasets, from which we observe similar results as in the KDML experiments. First, KSC-(SFN,VND,LDD)-(RTR,RFF) achieve better accuracy than the unregularized and the SHN-regularized KSC. Second, the BMD regularizers outperform other near-orthogonality reg-

ularizers including DPP and Angle. Third, VND and LDD are superior to SFN. Fourth, the RFF representation of RKHS functions performs comparably to RTR. Finally, the BMD-KSC methods outperform the non-kernel SC methods and other kernel SC methods. These observations demonstrate the efficacy of the BMD regularizers in reducing overfitting and promoting near-orthogonality.

2.4.4 Appendix: Details of Algorithms

Detailed Derivation of Solving $\mathbf{A}$

Given $\mathbf{H} \in \mathbb{R}^{K\times K}$ where $H_{ij} = \langle f_i, \hat{f}_j\rangle$, the sub-problem defined over $\mathbf{A}$ is

$$\min_{\mathbf{A}} \quad \lambda D_\phi(\mathbf{A}, \mathbf{I}) - \langle \mathbf{P}, \mathbf{A}\rangle - \langle \mathbf{Q}^\top, \mathbf{A}\rangle + \tfrac{\rho}{2}\|\mathbf{H} - \mathbf{A}\|_F^2 + \tfrac{\rho}{2}\|\mathbf{H}^\top - \mathbf{A}\|_F^2. \tag{2.84}$$

$D_\phi(\mathbf{A}, \mathbf{I})$ has three cases, which we discuss separately. When $D_\phi(\mathbf{A}, \mathbf{I})$ is the squared Frobenius norm, the problem becomes

$$\min_{\mathbf{A}} \quad \lambda\|\mathbf{A} - \mathbf{I}\|_F^2 - \langle \mathbf{P}, \mathbf{A}\rangle - \langle \mathbf{Q}^\top, \mathbf{A}\rangle + \tfrac{\rho}{2}\|\mathbf{H} - \mathbf{A}\|_F^2 + \tfrac{\rho}{2}\|\mathbf{H}^\top - \mathbf{A}\|_F^2. \tag{2.85}$$

Taking the derivative and setting it to zero, we get the optimal solution for $\mathbf{A}$:

$$\mathbf{A} = (2\lambda\mathbf{I} + \mathbf{P} + \mathbf{Q}^\top + \rho(\mathbf{H} + \mathbf{H}^\top))/(2\lambda + 2\rho). \tag{2.86}$$

When $D_\phi(\mathbf{A}, \mathbf{I})$ is the log-determinant divergence, the problem is specialized to

$$\begin{array}{ll} \min_{\mathbf{A}} & \lambda(\mathrm{tr}(\mathbf{A}) - \log\det(\mathbf{A})) - \langle \mathbf{P}, \mathbf{A}\rangle - \langle \mathbf{Q}^\top, \mathbf{A}\rangle + \frac{\rho}{2}\|\mathbf{H} - \mathbf{A}\|_F^2 + \frac{\rho}{2}\|\mathbf{H}^\top - \mathbf{A}\|_F^2 \\ s.t. & \mathbf{A} \succ 0. \end{array} \tag{2.87}$$

Taking the derivative of the objective function w.r.t $\mathbf{A}$ and setting it to zero, we get

$$\mathbf{A}^2 + \tfrac{1}{\rho}(\lambda\mathbf{I} - \mathbf{P} - \mathbf{Q}^\top - \rho(\mathbf{H} + \mathbf{H}^\top))\mathbf{A} - \tfrac{\lambda}{\rho}\mathbf{I} = 0. \tag{2.88}$$

Let $\mathbf{B} = \frac{1}{\rho}(\lambda\mathbf{I} - \mathbf{P} - \mathbf{Q}^\top - \rho(\mathbf{H} + \mathbf{H}^\top))$ and $\mathbf{C} = -\frac{\lambda}{\rho}\mathbf{I}$, Eq.(2.88) can be written as

$$\mathbf{A}^2 + \mathbf{B}\mathbf{A} + \mathbf{C} = 0. \tag{2.89}$$

According to [156], since $\mathbf{B}$ and $\mathbf{C}$ commute, the solution of this equation is

$$\mathbf{A} = -\tfrac{1}{2}\mathbf{B} + \tfrac{1}{2}\sqrt{\mathbf{B}^2 - 4\mathbf{C}}. \tag{2.90}$$

Taking an eigen-decomposition of $\mathbf{B} = \mathbf{\Phi}\mathbf{\Sigma}\mathbf{\Phi}^{-1}$, we can compute $\mathbf{A}$ as $\mathbf{A} = \mathbf{\Phi}\widehat{\mathbf{\Sigma}}\mathbf{\Phi}^{-1}$, where $\widehat{\mathbf{\Sigma}}$ is a diagonal matrix with

$$\widehat{\Sigma}_{kk} = -\frac{1}{2}\Sigma_{kk} + \frac{1}{2}\sqrt{\Sigma_{kk}^2 + \frac{4\lambda}{\rho}}.$$

Since $\sqrt{\Sigma_{kk}^2 + \frac{4\lambda}{\rho}} > \Sigma_{kk}$, we know $\widehat{\Sigma}_{kk} > 0$. Hence $\mathbf{A}$ is positive definite.

When $D_\phi(\mathbf{A}, \mathbf{I})$ is the von Neumann divergence, the problem becomes

$$\begin{array}{ll} \min_{\mathbf{A}} & \lambda \text{tr}(\mathbf{A}\log\mathbf{A} - \mathbf{A}) - \langle \mathbf{P}, \mathbf{A}\rangle - \langle \mathbf{Q}^\top, \mathbf{A}\rangle + \frac{\rho}{2}\|\mathbf{H} - \mathbf{A}\|_F^2 + \frac{\rho}{2}\|\mathbf{H}^\top - \mathbf{A}\|_F^2 \\ s.t. & \mathbf{A} \succ 0. \end{array} \tag{2.91}$$

Setting the gradient of the objective function w.r.t $\mathbf{A}$ to zero, we get

$$\lambda \log \mathbf{A} + 2\rho\mathbf{A} = \mathbf{P} + \mathbf{Q}^\top + \rho(\mathbf{H} + \mathbf{H}^\top). \tag{2.92}$$

Let $\mathbf{D} = \mathbf{P} + \mathbf{Q}^\top + \rho(\mathbf{H} + \mathbf{H}^\top)$. We perform an eigen-decomposition of $\mathbf{D} = \mathbf{\Phi}\mathbf{\Sigma}\mathbf{\Phi}^{-1}$ and parameterize $\mathbf{A}$ as $\mathbf{A} = \mathbf{\Phi}\widehat{\mathbf{\Sigma}}\mathbf{\Phi}^{-1}$, then we obtain

$$\lambda \log \mathbf{A} + 2\rho\mathbf{A} = \mathbf{\Phi}(\lambda \log \widehat{\mathbf{\Sigma}} + 2\rho\widehat{\mathbf{\Sigma}})\mathbf{\Phi}^{-1}. \tag{2.93}$$

Plugging this equation into Eq.(2.92), we get the following equation

$$\lambda \log \widehat{\mathbf{\Sigma}} + 2\rho\widehat{\mathbf{\Sigma}} = \mathbf{\Sigma}, \tag{2.94}$$

which amounts to solving K independent one-variable equations taking the form

$$\lambda \log \widehat{\Sigma}_{ii} + 2\rho\widehat{\Sigma}_{ii} = \Sigma_{ii}, \tag{2.95}$$

where $i = 1, \cdots, K$. This equation has a closed-form solution

$$\widehat{\Sigma}_{ii} = \frac{\lambda\omega(\frac{\Sigma_{ii}}{\lambda} - \log(\frac{\lambda}{2\rho}))}{2\rho}, \tag{2.96}$$

where $\omega(\cdot)$ is the Wright omega function [137]. Due to the presence of $\log$, $\widehat{\Sigma}_{ii}$ is required to be positive and the solution always exists since the range of $\lambda \log \widehat{\Sigma}_{ii} + 2\rho\widehat{\Sigma}_{ii}$ and Σ_{ii} are both $(-\infty, \infty)$. Hence $\mathbf{A}$ is guaranteed to be positive definite.

An ADMM-based Algorithm for BMD-KSC

The BMD-KSC model has two set of parameters: sparse codes $\{\mathbf{a}_n\}_{n=1}^N$ and a dictionary of RKHS functions $\{f_i\}_{i=1}^K$. We use a coordinate descent algorithm to learn these two parameter sets, which iteratively performs the following two steps: (1) fixing $\{f_i\}_{i=1}^K$, solving $\{\mathbf{a}_n\}_{n=1}^N$; (2) fixing $\{\mathbf{a}_n\}_{n=1}^N$, solving $\{f_i\}_{i=1}^K$, until convergence. We first discuss step (1). The sub-problem defined over $\mathbf{a}_n$ is

$$\min_{\mathbf{a}_n} \quad \tfrac{1}{2}\|k(\mathbf{x}_n, \cdot) - \textstyle\sum_{i=1}^K a_{ni} f_i\|_{\mathcal{H}}^2 + \lambda_1\|\mathbf{a}_n\|_1. \tag{2.97}$$

$\|k(\mathbf{x}_n, \cdot) - \sum_{i=1}^K a_{ni} f_i\|_{\mathcal{H}}^2 = k(\mathbf{x}_n, \mathbf{x}_n) - 2\mathbf{a}_n^\top\mathbf{h} + \mathbf{a}_n^\top\mathbf{G}\mathbf{a}_n$ where $\mathbf{h} \in \mathbb{R}^K$, $h_i = \langle f_i, k(\mathbf{x}_n, \cdot)\rangle$, $\mathbf{G} \in \mathbb{R}^{K\times K}$ and $G_{ij} = \langle f_i, f_j\rangle$. This is a standard lasso [331] problem and can be solved using many algorithms. Next we discuss step (2), which learns $\{f_i\}_{i=1}^K$ using the ADMM-based algorithm outlined in the main paper. The updates of all variables are the same as those in BMD-KDML, except f_i. Let $b_{ni} = k(\mathbf{x}_n, \cdot) - \sum_{j\neq i}^K a_{nj} f_j$, the sub-problem defined over f_i is:

$$\begin{array}{ll} \min_{f_i} & \frac{1}{2}\sum_{n=1}^N \|b_{ni} - a_{ni} f_i\|_{\mathcal{H}}^2 + \frac{\lambda_2}{2}\|f_i\|_{\mathcal{H}}^2 + \langle g_i, f_i\rangle + \sum_{j=1}^K P_{ij}\langle f_i, \hat{f}_j\rangle + \sum_{j=1}^K Q_{ij}\langle f_i, \hat{f}_j\rangle \\ & + \frac{\rho}{2}\sum_{j=1}^K(\langle f_i, \hat{f}_j\rangle - A_{ij})^2 + \frac{\rho}{2}\sum_{j=1}^K(\langle f_i, \hat{f}_j\rangle - A_{ji})^2. \end{array} \tag{2.98}$$

This problem can be solved with functional gradient descent. The functional gradient of the objective function w.r.t f_i is

$$\sum_{n=1}^{N} a_{ni}(a_{ni}f_i - b_{ni}) + \lambda_2 f_i + g_i + \sum_{j=1}^{K}(P_{ij} + Q_{ij} + 2\rho\langle f_i, \hat{f}_j\rangle - \rho(A_{ij} + A_{ji}))\hat{f}_j. \quad (2.99)$$

2.5 Diversity and Sparsity: Nonoverlapness-promoting Regularization

In this section, we combine diversity with sparsity, which jointly bring in an effect of *nonoverlapness* [380], for the sake of selecting less-overlapped variables. Variable selection [331] is a classic problem in machine learning, widely used to find important explanatory factors, and improve generalization performance and interpretability of ML models.

Among the many criteria of evaluating model quality, two are typically considered: (1) accuracy of prediction on unseen data; (2) interpretation of the model. For (2), scientists prefer a simpler model because it puts more light on the relationship between the response and covariates. Parsimony [331] is especially an important issue when the number of predictors is large. With a large number of predictors, we often would like to determine a smaller subset that exhibits the strongest effects.

To produce accurate prediction while selecting a subset of important factors, regularization-based variable-selection methods [331, 404, 428] have been widely studied. The most notable one is ℓ_1 regularization [331], which encourages the model coefficients to be sparse. Its variants including ℓ_1/ℓ_2-norm [404] that brings in a group sparsity effect and elastic net [428] which encourages strongly correlated predictors to be in or out of the model together, among many others.

In many ML problems, multiple responses are to be predicted based on the same set of covariates. For example, in multi-task classification, the classifiers of m classes are built on top of a shared feature set and each classifier has a class-specific coefficient vector. In topic modeling [49], multiple topics are learned over the same vocabulary and each topic has a unique multinomial distribution on the words. Different responses are relevant to different subsets of covariates. For example, an education topic is relevant to words like student, university, professor while a political topic is relevant to words like government, president, election, etc. To account for the difference between different responses when performing variable selection, we desire the selected variables for different responses to be less-overlapped.

The problem is formally formulated as follows. Consider m responses sharing d covariates. Each response has a specific d-dimensional weight vector $\mathbf{w}$ where each dimension corresponds to a covariate. Let $s(\mathbf{w}) = \{k|w_k \neq 0\}$ – the support of $\mathbf{w}$ – index the selected variables for a response. For any two responses i and j, we desire their selected variables $s(\mathbf{w}_i)$ and $s(\mathbf{w}_j)$ are less overlapped, where the overlapness is measured by $\frac{|s(\mathbf{w}_i)\cap s(\mathbf{w}_j)|}{|s(\mathbf{w}_i)\cup s(\mathbf{w}_j)|}$. To achieve this effect, we propose a regularizer that simultaneously encourages different weight vectors to be close to being orthogonal and each vector to be sparse, which jointly encourage vectors' supports to have small overlap. Empirically, we verify that minimizing this regularizer reduces overlap among

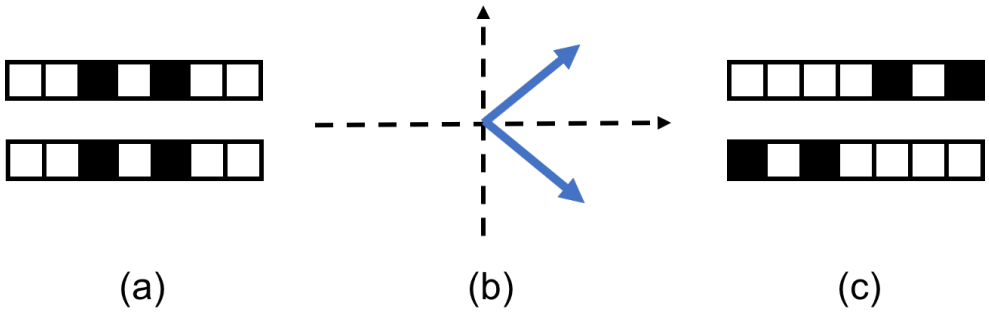

Figure 2.7: (a) Under L1 regularization, the vectors are sparse, but their supports are overlapped; (b) Under LDD regularization, the vectors are orthogonal, but their supports are overlapped; (c) Under LDD-L1 regularization, the vectors are sparse and mutually orthogonal and their supports are not overlapped.

selected variables. We apply this regularizer to four models: multiclass logistic regression, distance metric learning, sparse coding, and deep neural networks. Efficient algorithms are derived to solve these regularized problems. In particular, we develop an algorithm based on ADMM and coordinate descent for regularized sparse coding. In experiments, we demonstrate the empirical effectiveness of this regularizer in selecting non-overlap variables and improving generalization.

Related works Variable selection based on regularization has been widely studied. lasso [331] uses ℓ_1-norm to encourage the coefficient vector of the linear regression model to be sparse. The lasso is able to recover the exact support of a sparse model from data generated by this model if the covariates are not too correlated [417]. Elastic net [428] uses the weighted sum of the ℓ_1 and ℓ_2 norm to encourage strongly-correlated variables to be co-selected. Group lasso [404] uses the ℓ_1/ℓ_2 penalty, which is defined as the sum of the ℓ_2 norms of sub-weight-vectors corresponding to predefined groups, to select groups of variables. It recovers the support of a model if the support is a union of groups and if covariates of different groups are not too correlated. Zhao et al. [418] proposed composite absolute penalties for hierarchical selection of covariates, e.g., when one has a hierarchy over the covariates and wants to select covariates only if their ancestors in the hierarchy are also selected. Graphical lasso [113] uses matrix ℓ_1 norm for covariance (or neighborhood) selection.

In the context of group variable selection, several works [24, 174, 418] consider the cases where variables from different groups are (non)overlapping. Their problem settings are different from ours. In their problems, the (non)overlapping structure is with respect to groups and is known as a prior while in our problem it is with respect to different responses and is unknown.

2.5.1 Nonoverlap-promoting Regularization

We assume the model has m responses and each is parameterized by a weight vector. For a vector $\mathbf{w}$, its *support* $s(\mathbf{w})$ is defined as $\{i|w_i \neq 0\}$ – the indices of nonzero entries in $\mathbf{w}$. And the support contains indexes of the selected variables. We first define a score $\tilde{o}(\mathbf{w}_i, \mathbf{w}_j)$ to

measure the overlap between selected variables of two responses:

$$\tilde{o}(\mathbf{w}_i, \mathbf{w}_j) = \frac{|s(\mathbf{w}_i) \cap s(\mathbf{w}_j)|}{|s(\mathbf{w}_i) \cup s(\mathbf{w}_j)|}, \tag{2.100}$$

which is the Jaccard index of the supports. The smaller $\tilde{o}(\mathbf{w}_i, \mathbf{w}_j)$ is, the less overlapped the two sets of selected variables are. For m variable sets, the overlap score is defined as the sum of pairwise scores

$$o(\{\mathbf{w}_i\}_{i=1}^m) = \frac{1}{m(m-1)} \sum_{i \neq j}^{m} \tilde{o}(\mathbf{w}_i, \mathbf{w}_j). \tag{2.101}$$

This score function is not smooth, which will result in great difficulty for optimization if used as a regularizer. Instead, we propose a smooth function that is motivated from $\tilde{o}(\mathbf{w}_i, \mathbf{w}_j)$ and can achieve a similar effect as $o(\mathcal{W})$. The basic idea is: to encourage small overlap, we can encourage (1) each vector has a small number of non-zero entries and (2) the intersection of supports among vectors is small. To realize (1), we use an L1 regularizer to encourage the vectors to be sparse. To realize (2), we encourage the vectors to be close to being orthogonal. For two sparse vectors, if they are close to being orthogonal, then their supports are landed on different positions. As a result, the intersection of supports is small. To promote orthogonality, similar to Section 2.2.1, we encourage the Gram matrix $\mathbf{G}$ ($G_{ij} = \mathbf{w}_i^\top \mathbf{w}_j$) of weight vectors to be close to an identity matrix $\mathbf{I}$ and measure the "closeness" between two matrices using the log-determinant divergence (LDD), which results in the LDD regularizer $\text{tr}(\mathbf{G}) - \log\det(\mathbf{G})$. Combining the orthogonality-promoting LDD regularizer with the sparsity-promoting L1 regularizer together, we obtain the following LDD-L1 regularizer

$$\Omega(\mathcal{W}) = \text{tr}(\mathbf{G}) - \log\det(\mathbf{G}) + \gamma \sum_{i=1}^{m} |\mathbf{w}_i|_1, \tag{2.102}$$

where γ is a tradeoff parameter between these two regularizers. As verified in experiments, this regularizer can effectively promote nonoverlap. The formal analysis of the relationship between Eq.(2.102) and Eq.(2.101) will be left for future study. It is worth noting that either L1 or LDD alone is not sufficient to reduce overlap. As illustrated in Figure 2.7a where only L1 is applied, though the two vectors are sparse, their supports are completely overlapped. In Figure 2.7b where the LDD regularizer is applied, though the two vectors are very close to being orthogonal, their supports are completely overlapped since they are dense. In Figure 2.7c where the LDD-L1 regularizer is used, the two vectors are sparse and are close to being orthogonal. As a result, their supports are not overlapped.

We apply LDD-L1 to four ML models: multiclass logistic regression, distance metric learning, sparse coding, and neural networks.

- **Multiclass logistic regression (MLR)** aims at classifying a data example $\mathbf{x} \in \mathbb{R}^d$ (whose features are treated as covariates) into one of the m classes (treated as responses). It is parameterized by a coefficient matrix $\mathbf{W} \in \mathbb{R}^{d \times m}$ where the i-th column is the coefficient vector of class i and d is the feature dimension of $\mathbf{x}$. In inference, MLR calculates $\mathbf{p} = \text{softmax}(\mathbf{W}^\top \mathbf{x} + \mathbf{b}) \in \mathbb{R}^m$ where p_i denotes the probability that $\mathbf{x}$ belongs to class i and $\mathbf{b} \in \mathbb{R}^m$ is a bias vector. $\mathbf{x}$ is assigned to the class yielding the largest probability. Given

N training examples $\{\mathbf{x}_n, y_n\}_{n=1}^N$, MLR learns $\mathbf{W}$ by minimizing the cross-entropy loss between $\mathbf{p}_n$ and the ground-truth class label y_n. The LDD-L1 regularizer can be applied to encourage the coefficient vectors of different classes to have less-overlapped supports.

- **Distance metric learning (DML)** has wide applications in classification, clustering, and information retrieval [92, 146, 383]. Given data pairs labeled as similar or dissimilar, DML aims at learning a distance metric such that similar pairs would be placed close to each other and dissimilar pairs are separated apart. Following [357], we define the distance metric between $\mathbf{x}, \mathbf{y} \in \mathbb{R}^d$ as $\|\mathbf{W}^\top\mathbf{x} - \mathbf{W}^\top\mathbf{y}\|_2^2$ where $\mathbf{W} \in \mathbb{R}^{d\times m}$ contains m projection vectors which are treated as responses. The features in a data example are treated as covariates. Given N training examples, $\{\mathbf{x}_n, \mathbf{y}_n, t_n\}_{n=1}^N$, where $\mathbf{x}_n$ and $\mathbf{y}_n$ are similar if the label t_n equals 1 and dissimilar if $t_n = 0$, following [146], we learn the distance metric by minimizing $\sum_{n=1}^N \log(1 + \exp((2t_n - 1)\|\mathbf{W}^\top\mathbf{x} - \mathbf{W}^\top\mathbf{y}\|_2^2))$. Using LDD-L1 to promote nonoverlap among the projection vectors in $\mathbf{W}$, we obtain the LDD-L1 regularized DML problem:
$$\min_{\mathcal{F}} \sum_{n=1}^N \log(1 + \exp((2t_n - 1)\|\mathbf{W}^\top(\mathbf{x} - \mathbf{y})\|_2^2 + \lambda\Omega(\mathbf{W}). \tag{2.103}$$
- **Sparse Coding (SC) and Deep Neural Networks (DNNs)** have been introduced in Section 2.3.1. In SC, the features of data examples are treated as covariates and the basis vectors are treated as responses. We apply the LDD-L1 regularizer to encourage the supports of the basis vectors to have small overlap. In DNNs, hidden units in a layer l are treated as a group of responses. Their weight vectors are encouraged to have less-overlapped supports by the LDD-L1 regularizer. In the experiments, we study two popular instances of DNNs: long short-term memory (LSTM) network [163] and convolutional neural network (CNN).

2.5.2 A Coordinate Descent Algorithm

For LDD-L1-regularized MLR, NN, and DML problems, we solve them using proximal gradient descent [270]. The proximal operation is with respect to the L1 regularizer in LDD-L1. The algorithm iteratively performs the following three steps until convergence: (1) calculate gradient of $\mathcal{L}(\mathbf{W})+\lambda(\text{tr}(\mathbf{W}^\top\mathbf{W})-\text{logdet}(\mathbf{W}^\top\mathbf{W}))$ where $\mathcal{L}(\mathbf{W})$ is the loss function of the unregularized ML model and $\text{tr}(\mathbf{W}^\top\mathbf{W}) - \text{logdet}(\mathbf{W}^\top\mathbf{W})$ is the LDD regularizer in LDD-L1; (2) perform gradient descent update of $\mathbf{W}$; (3) apply the proximal operator of the L1 regularizer to $\mathbf{W}$.

For LDD-L1-SC, we solve it by alternating between $\mathbf{A}$ and $\mathbf{W}$: (1) updating $\mathbf{A}$ with $\mathbf{W}$ fixed; (2) updating $\mathbf{W}$ with $\mathbf{A}$ fixed. These two steps alternate until convergence. With $\mathbf{W}$ fixed, the sub-problem defined over $\mathbf{A}$ is $\min_{\mathbf{A}} \ \frac{1}{2}\|\mathbf{X} - \mathbf{W}\mathbf{A}\|_F^2 + \lambda_1|\mathbf{A}|_1$, which can be decomposed into n lasso problems (**P1**): for $i = 1, \cdots, n$, $\min_{\mathbf{a}_i} \ \frac{1}{2}\|\mathbf{x}_i - \mathbf{W}\mathbf{a}_i\|_2^2 + \lambda_1|\mathbf{a}_i|_1$ where $\mathbf{a}_i$ is the coefficient vector of the i-th sample. lasso can be solved by many algorithms, such as proximal gradient descent (PGD). Fixing $\mathbf{A}$, the sub-problem defined over $\mathbf{W}$ is (**P2**): $\min_{\mathbf{W}} \ \frac{1}{2}\|\mathbf{X} - \mathbf{W}\mathbf{A}\|_F^2 + \frac{\lambda_2}{2}\|\mathbf{W}\|_F^2 + \lambda_4|\mathbf{W}|_1 + \frac{\lambda_3}{2}(\text{tr}(\mathbf{W}^\top\mathbf{W}) - \log\det(\mathbf{W}^\top\mathbf{W}))$. We solve this problem using

an ADMM-based algorithm. First, we write the problem into an equivalent form:

$$\begin{array}{ll} \min_{\mathbf{W}} & \frac{1}{2}\|\mathbf{X}-\mathbf{W}\mathbf{A}\|_F^2+\frac{\lambda_2}{2}\|\mathbf{W}\|_F^2+\lambda_4|\widetilde{\mathbf{W}}|_1+\frac{\lambda_3}{2}(\text{tr}(\mathbf{W}^\top\mathbf{W})-\log\det(\mathbf{W}^\top\mathbf{W})) \\ s.t. & \mathbf{W}=\widetilde{\mathbf{W}}. \end{array} \tag{2.104}$$

Then we write down the augmented Lagrangian function (**P3**): $\frac{1}{2}\|\mathbf{X}-\mathbf{W}\mathbf{A}\|_F^2+\frac{\lambda_2}{2}\|\mathbf{W}\|_F^2+\lambda_4|\widetilde{\mathbf{W}}|_1+\langle\mathbf{U},\mathbf{W}-\widetilde{\mathbf{W}}\rangle+\frac{\rho}{2}\|\mathbf{W}-\widetilde{\mathbf{W}}\|_F^2+\frac{\lambda_3}{2}(\text{tr}(\mathbf{W}^\top\mathbf{W})-\log\det(\mathbf{W}^\top\mathbf{W}))$. We minimize this Lagrangian function by alternating among $\mathbf{W}$, $\widetilde{\mathbf{W}}$, and $\mathbf{U}$.

Update $\mathbf{W}$ The subproblem defined on $\mathbf{W}$ is (**P4**):

$$\min_{\mathbf{W}} \ \frac{1}{2}\|\mathbf{X}-\mathbf{W}\mathbf{A}\|_F^2+\frac{\lambda_2}{2}\|\mathbf{W}\|_F^2+\langle\mathbf{U},\mathbf{W}\rangle+\frac{\lambda_3}{2}(\text{tr}(\mathbf{W}^\top\mathbf{W})-\log\det(\mathbf{W}^\top\mathbf{W}))+\frac{\rho}{2}\|\mathbf{W}-\widetilde{\mathbf{W}}\|_F^2, \tag{2.105}$$

which can be solved using a coordinate descent (CD) algorithm. In each iteration of CD, one basis vector is chosen for update while the others are fixed. Without loss of generality, we assume it is $\mathbf{w}_1$. The loss function defined over $\mathbf{w}_1$ is $\frac{1}{2}\sum_{i=1}^n\|\mathbf{x}_i-\sum_{l=2}^m a_{il}\mathbf{w}_l-a_{i1}\mathbf{w}_1\|_2^2+\frac{\lambda_2+\lambda_3}{2}\|\mathbf{w}_1\|_2^2-\frac{\lambda_3}{2}\text{logdet}(\mathbf{W}^\top\mathbf{W})+\mathbf{u}^\top\mathbf{w}_1+\frac{\rho}{2}\|\mathbf{w}_1-\widetilde{\mathbf{w}}_1\|_2^2$. The optimal solution can be obtained via the following procedures: (1) calculate $\mathbf{M}=\mathbf{I}-\mathbf{W}_{\neg1}(\mathbf{W}_{\neg1}^\top\mathbf{W}_{\neg1})^{-1}\mathbf{W}_{\neg1}^\top$, where $\mathbf{W}_{\neg1}=[\mathbf{w}_2,\cdots,\mathbf{w}_m]$; (2) perform eigen-decomposition: $\mathbf{M}=\mathbf{U}\mathbf{\Sigma}\mathbf{U}^\top$; (3) solve the scalar quadratic equation $\gamma\sum_{s=m}^{d}(\mathbf{U}^\top\mathbf{b})_s^2=(\gamma c-\lambda_3)^2$ w.r.t γ, where $c=\sum_{i=1}^n a_{i1}^2+\lambda_2+\lambda_3+\rho$ and $\mathbf{b}=\sum_{i=1}^n a_{i1}(\mathbf{x}_i-\sum_{l=2}^m a_{il}\mathbf{w}_l)-\mathbf{u}+\rho\widetilde{\mathbf{w}}_j$; (4) calculate $\mathbf{w}_1$ as:

$$\mathbf{w}_1=\gamma\mathbf{U}(\gamma c\mathbf{I}-\lambda_3\mathbf{\Sigma})^{-1}\mathbf{U}^\top\mathbf{b}. \tag{2.106}$$

The detailed derivation is deferred to Section 2.5.4.

Update $\widetilde{\mathbf{W}}$ The subproblem defined on $\widetilde{\mathbf{W}}$ is (**P5**) : $\min_{\widetilde{\mathbf{W}}}\ \lambda_4|\widetilde{\mathbf{W}}|_1-\langle\mathbf{U},\widetilde{\mathbf{W}}\rangle+\frac{\rho}{2}\|\mathbf{W}-\widetilde{\mathbf{W}}\|_F^2$, which is an lasso problem and can be solved using proximal gradient descent [270].

Update $\mathbf{U}$ The update equation of $\mathbf{U}$ is simple: $\mathbf{U}=\mathbf{U}+(\mathbf{W}-\widetilde{\mathbf{W}})$.

2.5.3 Evaluation

In this section, we present experimental results.

Simulation Study

The simulation study was performed on the multiclass logistic regression model. We set the number of classes to 10. Each class is relevant to 5 variables. The variables of different classes have no overlap. We generated 1000 data samples from a multivariate Gaussian distribution with zero mean and the covariance matrix was set to an identity matrix. In the coefficient vector of each class, the entries corresponding to the relevant variables were uniformly sampled from $[-1,1]$

Algorithm 1: Algorithm for solving the LDD-L1-SC problem.

Initialize $\mathbf{W}$ and $\mathbf{A}$
repeat
  Update $\mathbf{A}$ with $\mathbf{W}$ being fixed, by solving n lasso problems (**P1**).
  repeat
    repeat
      for $i \leftarrow 1$ to m **do**
        Update the i-th column vector $\mathbf{w}_i$ of $\mathbf{W}$ using Eq.(2.106)
      end for
    until convergence of the problem (**P4**)
    Update $\widetilde{\mathbf{W}}$ by solving the lasso problem (**P5**)
    $\mathbf{U} \leftarrow \mathbf{U} + (\mathbf{W} - \widetilde{\mathbf{W}})$
  until convergence of the problem (**P3**)
until convergence of the LDD-L1-SC problem

and the rest entries were set to zero. Given a generated sample $\mathbf{x}$ and the generated coefficient matrix $\mathbf{W} \in \mathbb{R}^{10\times 50}$, the class label of sample $\mathbf{x}$ was determined as $y = \text{argmax}_k\ [\mathbf{W}\mathbf{x} + \mathbf{b}]_k$, where $\mathbf{b} \in \mathbb{R}^{10}$ was a randomly generated bias vector whose entries were sampled independently from a univariate normal distribution. We split the dataset into train/validation/test set with 600/200/200 examples respectively. The regularization parameter was tuned on the validation set to achieve the best prediction performance. We generated 50 simulated datasets. The performance was averaged over these 50 datasets. We compared our method with L1-regularization [331] and elastic net [428]. We did not compare with LDD since it is not able to select variables.

Following [193], we use sensitivity (true positive rate) and specificity (true negative rate) to measure the performance of recovering the true supports of the coefficient vectors, shown in the second and third column of Table 2.25. Our method outperforms the baselines with a large margin. LDD-L1 encourages the supports of different weight vectors to have less overlap, which makes it more suitable to select nonoverlapping variables. We also compare the performance of different methods in terms of prediction errors, shown in the fourth column of Table 2.25. LDD-L1 achieves the lowest error rate. Since the variables selected by our method are closer to the ground-truth, the predictions made by our method based upon these selected variables are more accurate.

Experiments on Real Data

We applied the LDD-L1 regularizer to three ML models and four datasets and verified whether it is able to improve generalization performance. In each experiment, the hyperparameters were tuned on the validation set.

Sparse coding for text representation learning The SC experiments were conducted on two text datasets: 20-Newsgroups (20-News) [1] and Reuters Corpus Volume 1 (RCV1) [10]. The 20-News dataset contains newsgroup documents belonging to 20 categories, where 11314, 3766,

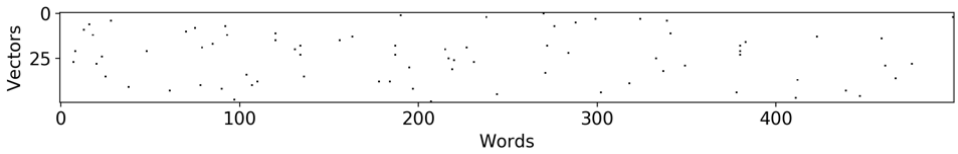

Figure 2.8: Visualization of basis vectors.

and 3766 documents were used for training, validation, and testing respectively. The original RCV1 dataset contains documents belonging to 103 categories. Following [60], we chose the largest 4 categories which contain 9625 documents, to carry out the study. The number of training, validation, and testing documents are 5775, 1925, 1925 respectively. For both datasets, stopwords were removed and all words were changed into lower-case. Top 1000 words with the highest document frequency were selected to form the vocabulary. We used tf-idf to represent documents and the feature vector of each document was normalized to have unit L2 norm. For 20-News, the number of basis vectors in LDD-L1-SC was set to 50. λ_1, λ_2, λ_3, and λ_4 were set to 1, 1, 0.1, and 0.001 respectively. For RCV1, the number of basis vectors was set to 200. λ_1, λ_2, λ_3, and λ_4 were set to 0.01, 1, 1 and 1 respectively. We compared LDD-L1 with LDD-only and L1-only.

To evaluate the model performance quantitatively, we applied the dictionary learned on the training data to infer the linear coefficients ($\mathbf{A}$ in SC) of test documents, then performed k-nearest neighbors (KNN) classification on $\mathbf{A}$. Table 2.26 shows the classification accuracy on test sets of 20-News and RCV1 and the gap between the accuracy on training and test sets. Without regularization, SC achieves a test accuracy of 0.592 on 20-News, which is lower than the training accuracy by 0.119. This suggests that an overfitting to training data occurs. With LDD-L1 regularization, the test accuracy is improved to 0.612 and the gap between training and test accuracy is reduced to 0.099, demonstrating the ability of LDD-L1 in alleviating overfitting. Though LDD alone and L1 alone improve test accuracy and reduce train/test gap, they perform less well than LDD-L1, which indicates that for overfitting reduction, encouraging nonoverlap is more effective than solely promoting orthogonality or solely promoting sparsity. Similar observations are made on the RCV1 dataset. Interestingly, the test accuracy achieved by LDD-L1-SC on RCV1 is better than the training accuracy.

Table 2.27 shows the selected variables (words that have nonzero weights) for 9 exemplar basis vectors learned by LDD-L1-SC on the 20-News dataset. From the selected words, we can see basis vector 1-9 represent the following semantics respectively: crime, faith, job, war, university, research, service, religion, and Jews. The selected words of different basis vectors have no overlap. As a result, it is easy to associate each vector with a unique concept, in other words, easy to interpret. Figure 2.8 visualizes the learned vectors where the black dots denote vectors' supports. As can be seen, the supports of different basis vectors are landed on different words and their overlap is small.

LSTM for language modeling We applied LSTM networks [163] to learn language models on the Penn Treebank (PTB) dataset [244], which consists of 923K training, 73K validation, and 82K test words. Following [254], top 10K words with the highest frequency were selected

to form the vocabulary. All other words were replaced with a special token UNK. The LSTM network architecture follows the word language model (PytorchTM) provided in Pytorch [3]. The number of hidden layers was set to 2. The embedding size was 1500. The size of hidden state was 1500. Following [279], the word embedding and softmax weights were tied. The number of training epochs was 40. Dropout with 0.65 was used. The initial learning rate was 20. Gradient clipping threshold was 0.25. The size of mini-batch was 20. In LSTM training, the network was unrolled for 35 iterations. Perplexity was used for evaluating language modeling performance (lower is better). The weight parameters were initialized uniformly between [-0.1, 0.1]. The bias parameters were initialized as 0. We compared with the following regularizers: (1) L1 regularizer; (2) orthogonality-promoting regularizers based on cosine similarity (CS) [402], incoherence (IC) [29], mutual angle (MA) [369], decorrelation (DC) [82], angular constraint (AC) (Section 2.3.1), and LDD (Section 2.2.1).

Table 2.28 shows the perplexity on the PTB test set. Without regularization, PytorchLM achieves a perplexity of 72.3. With LDD-L1 regularization, the perplexity is significantly reduced to 71.1. This shows that LDD-L1 can effectively improve generalization performance. Compared with the sparsity-promoting L1 regularizer and orthogonality-promoting regularizers, LDD-L1 – which promotes nonoverlap by simultaneously promoting sparsity and orthogonality – achieves lower perplexity. For the convenience of readers, we also list the perplexity achieved by other state of the art deep learning models. The LDD-L1 regularizer can be applied to these models as well to potentially boost their performance.

CNN for image classification The CNN experiments were performed on the CIFAR-10 dataset [5]. It consists of 32x32 color images belonging to 10 categories, where 50,000 images were used for training and 10,000 for testing. 5000 training images were used as the validation set for hyperparameter tuning. We augmented the dataset by first zero-padding the images with 4 pixels on each side, then randomly cropping the padded images to reproduce 32x32 images. The CNN architecture follows that of the wide residual network (WideResNet) [406]. The depth and width were set to 28 and 10 respectively. The networks were trained using SGD, where the epoch number was 200, the learning rate was set to 0.1 initially and was dropped by 0.2 at 60, 120, and 160 epochs, the minibatch size was 128 and the Nesterov momentum was 0.9. The dropout probability was 0.3 and the L2 weight decay was 0.0005. Model performance was measured using error rate, which was the median of 5 runs. We compared with (1) the L1 regularizer; (2) orthogonality-promoting regularizers including CS, IC, MA, DC, AC, LDD and the one based on locally constrained decorrelation (LCD) [291].

Table 2.29 shows classification errors on the CIFAR-10 test set. Compared with the unregularized WideResNet which achieves an error rate of 3.89%, the proposed LDD-L1 regularizer greatly reduces the error to 3.60%. LDD-L1 outperforms the L1 regularizer and orthogonality-promoting regularizers, demonstrating that encouraging nonoverlap is more effective than encouraging sparsity alone or orthogonality alone in improving generalization performance. The error rates achieved by other state of the art methods are also listed.

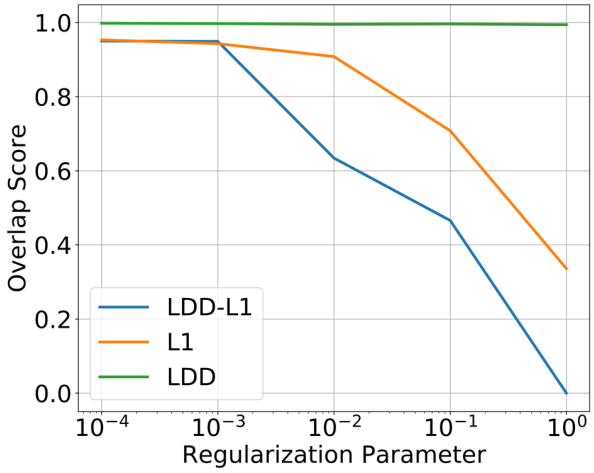

Figure 2.9: Overlap score versus the regularization parameter.

LDD-L1 and Nonoverlap

We verified whether the LDD-L1 regularizer is able to promote nonoverlap. The study was performed on the SC model and the 20-News dataset. The number of basis vectors was set to 50. For 5 choices of the regularization parameter of LDD-L1: $\{10^{-4}, 10^{-3}, \cdots, 1\}$, we ran the LDD-L1-SC model until convergence and measured the overlap score (defined in Eq.(2.101)) of the basis vectors. The tradeoff parameter γ inside LDD-L1 was set to 1. Figure 2.9 shows that the overlap score consistently decreases as the regularization parameter of LDD-L1 increases, which implies that LDD-L1 can effectively encourage nonoverlap. As a comparison, we replaced LDD-L1 with LDD-only and L1-only, and measured the overlap scores. As can be seen, for LDD-only, the overlap score remains to be 1 when the regularization parameter increases, which indicates that LDD alone is not able to reduce overlap. This is because under LDD-only, the vectors remain dense, which renders their supports to be completely overlapped. Under the same regularization parameter, LDD-L1 achieves lower overlap score than L1, which suggests that LDD-L1 is more effective in promoting nonoverlap. Given that γ – the tradeoff parameter associated with the L1 norm in LDD-L1 – was set to 1, the same regularization parameter λ imposes the same level of sparsity for both LDD-L1 and L1-only. Since LDD-L1 encourages the vectors to be mutually orthogonal, the intersection between vectors' supports is small, which consequently results in small overlap. This is not the case for L1-only, which hence is less effective in reducing overlap.

2.5.4 Appendix: Details of Algorithms

In each iteration of the CD algorithm, one basis vector is chosen for update while the others are fixed. Without loss of generality, we assume it is $\mathbf{w}_1$. The sub-problem defined over $\mathbf{w}_1$ is

$$\min_{\mathbf{w}_1} \quad \frac{1}{2}\sum_{i=1}^{n} \|\mathbf{x}_i - \sum_{l=2}^{m} a_{il}\mathbf{w}_l - a_{i1}\mathbf{w}_1\|_2^2 + \frac{\lambda_2+\lambda_3}{2}\|\mathbf{w}_1\|_2^2 - \frac{\lambda_3}{2}\text{logdet}(\mathbf{W}^\top\mathbf{W}) + \mathbf{u}^\top\mathbf{w}_1 + \frac{\rho}{2}\|\mathbf{w}_1 - \widetilde{\mathbf{w}}_1\|_2^2. \tag{2.107}$$

To obtain the optimal solution, we take the derivative of the objective function and set it to zero. First, we discuss how to compute the derivative of logdet$(\mathbf{W}^\top\mathbf{W})$ w.r.t $\mathbf{w}_1$. According to the chain rule, we have

$$\frac{\partial \text{logdet}(\mathbf{W}^\top\mathbf{W})}{\partial \mathbf{w}_1} = 2\mathbf{W}(\mathbf{W}^\top\mathbf{W})^{-1}_{:,1}, \tag{2.108}$$

where $(\mathbf{W}^\top\mathbf{W})^{-1}_{:,1}$ denotes the first column of $(\mathbf{W}^\top\mathbf{W})^{-1}$. Let $\mathbf{W}_{\neg 1} = [\mathbf{w}_2, \cdots, \mathbf{w}_m]$, then

$$\mathbf{W}^\top\mathbf{W} = \begin{bmatrix} \mathbf{w}_1^\top\mathbf{w}_1 & \mathbf{w}_1^\top\mathbf{W}_{\neg 1} \\ \mathbf{W}_{\neg 1}^\top\mathbf{w}_1 & \mathbf{W}_{\neg 1}^\top\mathbf{W}_{\neg 1}. \end{bmatrix} \tag{2.109}$$

According to the inverse of block matrix

$$\begin{bmatrix} \mathbf{A} & \mathbf{B} \\ \mathbf{C} & \mathbf{D} \end{bmatrix}^{-1} = \begin{bmatrix} \widetilde{\mathbf{A}} & \widetilde{\mathbf{B}} \\ \widetilde{\mathbf{C}} & \widetilde{\mathbf{D}} \end{bmatrix}, \tag{2.110}$$

where $\widetilde{\mathbf{A}} = (\mathbf{A} - \mathbf{B}\mathbf{D}^{-1}\mathbf{C})^{-1}$, $\widetilde{\mathbf{B}} = -(\mathbf{A} - \mathbf{B}\mathbf{D}^{-1}\mathbf{C})^{-1}\mathbf{B}\mathbf{D}^{-1}$, $\widetilde{\mathbf{C}} = -\mathbf{D}^{-1}\mathbf{C}(\mathbf{A} - \mathbf{B}\mathbf{D}^{-1}\mathbf{C})^{-1}$, $\widetilde{\mathbf{D}} = \mathbf{D}^{-1} + \mathbf{D}^{-1}\mathbf{C}(\mathbf{A} - \mathbf{B}\mathbf{D}^{-1}\mathbf{C})^{-1}\mathbf{B}\mathbf{D}^{-1}$, we have $(\mathbf{W}^\top\mathbf{W})^{-1}_{:,1}$ equals $[\mathbf{a} \quad \mathbf{b}^\top]^\top$ where

$$\mathbf{a} = (\mathbf{w}_1^\top\mathbf{w}_1 - \mathbf{w}_1^\top\mathbf{W}_{\neg 1}(\mathbf{W}_{\neg 1}^\top\mathbf{W}_{\neg 1})^{-1}\mathbf{W}_{\neg 1}^\top\mathbf{w}_1)^{-1}, \tag{2.111}$$

$$\mathbf{b} = -(\mathbf{W}_{\neg 1}^\top\mathbf{W}_{\neg 1})^{-1}\mathbf{W}_{\neg 1}^\top\mathbf{w}_1\mathbf{a}. \tag{2.112}$$

Then

$$\mathbf{W}(\mathbf{W}^\top\mathbf{W})^{-1}_{:,1} = \begin{bmatrix} \mathbf{w}_1 & \mathbf{W}_{\neg 1} \end{bmatrix} \begin{bmatrix} \mathbf{a} \\ \mathbf{b} \end{bmatrix} = \frac{\mathbf{M}\mathbf{w}_1}{\mathbf{w}_1^\top\mathbf{M}\mathbf{w}_1}, \tag{2.113}$$

where

$$\mathbf{M} = \mathbf{I} - \mathbf{W}_{\neg 1}(\mathbf{W}_{\neg 1}^\top\mathbf{W}_{\neg 1})^{-1}\mathbf{W}_{\neg 1}^\top. \tag{2.114}$$

To this end, we obtain the full gradient of the objective function in Eq.(2.107):

$$\textstyle\sum_{i=1}^n a_{i1}(a_{i1}\mathbf{w}_1 + \sum_{l=2}^m a_{il}\mathbf{w}_l - \mathbf{x}_i) + (\lambda_2 + \lambda_3)\mathbf{w}_1 - \lambda_3\frac{\mathbf{M}\mathbf{w}_1}{\mathbf{w}_1^\top\mathbf{M}\mathbf{w}_1} + \rho(\mathbf{w}_1 - \widetilde{\mathbf{w}}_1) + \mathbf{u}. \tag{2.115}$$

Setting the gradient to zero, we get

$$((\textstyle\sum_{i=1}^n a_{i1}^2 + \lambda_2 + \lambda_3 + \rho)\mathbf{I} - \lambda_3\mathbf{M}/(\mathbf{w}_1^\top\mathbf{M}\mathbf{w}_1))\mathbf{w}_1 = \sum_{i=1}^n a_{i1}(\mathbf{x}_i - \sum_{l=2}^m a_{il}\mathbf{w}_l) - \mathbf{u} + \rho\widetilde{\mathbf{w}}_1. \tag{2.116}$$

Let $\gamma = \mathbf{w}_1^\top\mathbf{M}\mathbf{w}_1$, $c = \sum_{i=1}^n a_{i1}^2 + \lambda_2 + \lambda_3 + \rho$, $\mathbf{b} = \sum_{i=1}^n a_{i1}(\mathbf{x}_i - \sum_{l=2}^m a_{il}\mathbf{w}_l) - \mathbf{u} + \rho\widetilde{\mathbf{w}}_j$, then $(c\mathbf{I} - \frac{\lambda_3}{\gamma}\mathbf{M})\mathbf{w}_1 = \mathbf{b}$ and $\mathbf{w}_1 = (c\mathbf{I} - \frac{\lambda_3}{\gamma}\mathbf{M})^{-1}\mathbf{b}$. Let $\mathbf{U}\mathbf{\Sigma}\mathbf{U}^\top$ be the eigen decomposition of $\mathbf{M}$, we have

$$\mathbf{w}_1 = \gamma\mathbf{U}(\gamma c\mathbf{I} - \lambda_3\mathbf{\Sigma})^{-1}\mathbf{U}^\top\mathbf{b}. \tag{2.117}$$

Then

$$\begin{aligned} &\mathbf{w}_1^\top\mathbf{M}\mathbf{w}_1 \\ &= \gamma^2\mathbf{b}^\top\mathbf{U}(\gamma c\mathbf{I} - \lambda_3\mathbf{\Sigma})^{-1}\mathbf{U}^\top\mathbf{U}\mathbf{\Sigma}\mathbf{U}^\top\mathbf{U}(\gamma c\mathbf{I} - \lambda_3\mathbf{\Sigma})^{-1}\mathbf{U}^\top\mathbf{b} \\ &= \gamma^2\mathbf{b}^\top\mathbf{U}(\gamma c\mathbf{I} - \lambda_3\mathbf{\Sigma})^{-1}\mathbf{\Sigma}(\gamma c\mathbf{I} - \lambda_3\mathbf{\Sigma})^{-1}\mathbf{U}^\top\mathbf{b} \\ &= \gamma^2\sum_{s=1}^d \frac{(\mathbf{U}^\top\mathbf{b})_s^2\Sigma_{ss}}{(rc - \lambda_3\Sigma_{ss})^2} = \gamma. \end{aligned} \tag{2.118}$$

The matrix $\mathbf{A} = \mathbf{W}_{\neg 1}(\mathbf{W}_{\neg 1}^\top \mathbf{W}_{\neg 1})^{-1}\mathbf{W}_{\neg 1}^\top$ is idempotent, i.e., $\mathbf{AA} = \mathbf{A}$, and its rank is $m-1$. According to the property of idempotent matrix, the first $m-1$ eigenvalues of $\mathbf{A}$ equal one and the rest equal zero. Thereafter, the first $m-1$ eigenvalues of $\mathbf{M} = \mathbf{I} - \mathbf{A}$ equal zero and the rest equal one. Based on this property, Eq.(2.118) can be simplified as

$$\gamma \sum_{s=m}^{d} \frac{(\mathbf{U}^\top \mathbf{b})_s^2}{(rc - \lambda_3)^2} = 1. \tag{2.119}$$

After simplification, it is a quadratic function where γ has a closed form solution. Then we plug the solution of γ into Eq.(2.117) to get the solution of $\mathbf{w}_1$.

	MIMIC			EICU			Reuters		
	AUC-All	AUC-F	AUC-IF	AUC-All	AUC-F	AUC-IF	AUC-All	AUC-F	AUC-IF
NCDML	0.634	0.654	0.608	0.671	0.690	0.637	0.949	0.963	0.916
CDML	0.641	0.659	0.617	0.677	0.693	0.652	0.952	0.961	0.929
EUC	0.559	0.558	0.562	0.583	0.584	0.581	0.887	0.888	0.885
LMNN [357]	0.628	0.643	0.609	0.662	0.678	0.633	0.943	0.951	0.913
LDML [146]	0.619	0.638	0.594	0.667	0.678	0.647	0.934	0.946	0.906
MLEC [200]	0.621	0.633	0.605	0.679	0.692	0.656	0.927	0.933	0.916
GMML [405]	0.607	0.621	0.588	0.668	0.679	0.648	0.931	0.938	0.905
ILHD [63]	0.577	0.590	0.560	0.637	0.652	0.610	0.905	0.919	0.893
ℓ_2-CDML	0.648	0.664	0.627	0.695	0.706	0.676	0.955	0.967	0.930
ℓ_1-CDML [280]	0.643	0.666	0.615	0.701	0.715	0.677	0.953	0.964	0.948
$\ell_{2,1}$-CDML [399]	0.646	0.658	0.630	0.703	0.727	0.661	0.963	0.970	0.936
Tr-CDML [234]	0.659	0.672	0.642	0.696	0.709	0.673	0.961	0.966	0.934
IT-CDML [92]	0.653	0.675	0.626	0.692	0.705	0.668	0.954	0.964	0.920
Dropout-CDML [282]	0.647	0.660	0.630	0.701	0.718	0.670	0.959	0.968	0.937
OS-CDML [116]	0.649	0.665	0.626	0.689	0.711	0.679	0.957	0.961	0.938
DCM-NCDML [242]	0.652	0.662	0.639	0.706	0.717	0.686	0.962	0.976	0.943
CS-NCDML [402]	0.661	0.676	0.641	0.712	0.736	0.670	0.967	0.973	0.954
DPP-NCDML [429]	0.659	**0.679**	0.632	0.714	0.725	0.695	0.958	0.971	0.937
IC-NCDML [29]	0.660	0.674	0.642	0.711	0.728	0.685	0.972	0.984	0.954
DC-NCDML [82]	0.648	0.666	0.625	0.698	0.711	0.675	0.965	0.977	0.960
VGF-NCDML [177]	0.657	0.673	0.634	0.718	0.730	0.697	0.974	0.985	0.952
MA-NCDML [367]	0.659	0.670	0.644	0.721	0.733	0.703	0.975	0.983	0.959
OC-NCDML [233]	0.651	0.663	0.636	0.705	0.716	0.685	0.955	0.966	0.931
OS-NCDML [116]	0.639	0.658	0.614	0.675	0.691	0.641	0.951	0.962	0.928
SFN-NCDML [74]	0.662	0.677	0.642	0.724	0.736	0.701	0.973	0.984	0.947
VND-NCDML	0.667	0.676	0.655	0.733	0.748	0.706	0.976	0.983	0.971
LDD-NCDML	0.664	0.674	0.651	0.731	0.743	0.711	0.973	0.981	0.964
CSFN-CDML	0.668	**0.679**	0.653	0.728	0.741	0.705	0.978	0.991	0.968
CVND-CDML	**0.672**	0.678	**0.664**	0.735	0.744	0.718	**0.984**	**0.996**	**0.982**
CLDD-CDML	0.669	0.678	0.658	**0.739**	**0.750**	**0.719**	0.981	0.993	0.980

Table 2.10: On three imbalanced datasets – MIMIC, EICU, Reuters, we show the mean AUC (averaged on 5 random train/test splits) on all classes (AUC-All), frequent classes (AUC-F), and infrequent classes (AUC-IF). On the second panel (EUC, etc.) are well established or state of the art baselines. On the third panel (ℓ_2-CDML, etc.) are CDML methods regularized by non-diversity regularizers. On the fourth panel (DCM-NCDML, etc.) are NCDML methods regularized by previously proposed diversity-promoting regularizers. On the fifth panel (VND-NCDML, etc.) are NCDML methods regularized by our proposed nonconvex BMD regularizers. On the sixth panel (CSFN-CDML, etc.) are CDML methods regularized by our proposed convex BMD regularizers.

	News	Cars	Birds	Act
NCDML	0.757	0.714	0.851	0.949
CDML	0.769	0.722	0.855	0.952
EUC	0.645	0.663	0.764	0.875
LMNN [357]	0.731	0.728	0.832	0.912
LDML [146]	0.748	0.706	0.847	0.937
MLEC [200]	0.761	0.725	0.814	0.917
GMML [405]	0.738	0.707	0.817	0.925
ILHD [63]	0.711	0.686	0.793	0.898
ℓ_2-CDML	0.774	0.728	0.872	0.958
ℓ_1-CDML [280]	0.791	0.725	0.868	0.961
$\ell_{2,1}$-CDML [399]	0.783	0.728	0.861	0.964
Tr-CDML [234]	0.785	0.731	0.875	0.955
IT-CDML [92]	0.771	0.724	0.858	0.967
Dropout-CDML [282]	0.787	0.729	0.864	0.962
OS-CDML [116]	0.779	0.732	0.869	0.963
DCM-NCDML [242]	0.773	0.736	0.882	0.964
CS-NCDML [402]	0.803	0.742	0.895	0.971
DPP-NCDML [429]	0.797	0.751	0.891	0.969
IC-NCDML [29]	0.801	0.740	0.887	0.967
DC-NCDML [82]	0.786	0.728	0.860	0.958
VGF-NCDML [177]	0.806	0.747	0.894	**0.974**
MA-NCDML [367]	0.815	0.743	0.898	0.968
OC-NCDML [233]	0.779	0.727	0.875	0.956
OS-NCDML [116]	0.764	0.716	0.855	0.950
SFN-NCDML [74]	0.808	0.749	0.896	0.970
VND-NCDML	0.814	0.754	0.902	0.972
LDD-NCDML	0.816	0.751	0.904	0.971
CSFN-CDML	0.813	0.753	0.905	0.972
CVND-CDML	**0.822**	0.755	0.908	0.973
CLDD-CDML	0.819	**0.759**	**0.913**	0.971

Table 2.11: AUC-All on 4 balanced datasets.

	MIMIC		EICU		Reuters		News		Cars		Birds		Act	
	NC	CF	NC	CF	NC	CF	NC	CF	NC	CF	NC	CF	NC	CF
NCDML	300	2.1	400	1.7	300	3.2	300	2.5	300	2.4	500	1.7	200	4.7
CDML	247	2.6	318	2.1	406	2.3	336	2.3	376	1.9	411	2.1	168	5.7
LMNN [357]	200	3.1	400	1.7	400	2.4	300	2.4	400	1.8	500	1.7	300	3.0
LDML [146]	300	2.1	400	1.7	400	2.3	200	3.7	300	2.4	400	2.1	300	3.1
MLEC [200]	487	1.3	493	1.4	276	3.4	549	1.4	624	1.2	438	1.9	327	2.8
GMML [405]	1000	0.6	1000	0.7	1000	0.9	1000	0.7	1000	0.7	1000	0.8	1000	0.9
ILHD [63]	100	5.8	100	6.4	**50**	18.1	100	7.1	100	6.9	100	7.9	**50**	18.0
ℓ_2-CDML	269	2.4	369	1.9	374	2.6	325	2.4	332	2.2	459	1.9	179	5.4
ℓ_1-CDML [280]	341	1.9	353	2.0	417	2.3	317	2.5	278	2.6	535	1.6	161	6.0
$\ell_{2,1}$-CDML [399]	196	3.3	251	2.8	288	3.3	316	2.5	293	2.5	326	2.6	135	7.1
Tr-CDML [234]	148	4.5	233	3.0	217	4.4	254	3.1	114	6.4	286	3.1	129	7.4
IT-CDML [92]	1000	0.7	1000	0.7	1000	1.0	1000	0.8	1000	0.7	1000	0.9	1000	1.0
Dropout-CDML [282]	183	3.5	284	2.5	315	3.0	251	3.1	238	3.1	304	2.8	147	6.5
DCM-NCDML [242]	100	6.5	300	2.4	100	9.6	200	3.9	200	3.7	300	2.9	100	9.6
CS-NCDML [402]	200	3.3	200	3.6	200	4.8	100	8.0	100	7.4	200	4.5	**50**	**19.4**
DPP-NCDML [429]	100	6.6	200	3.6	100	9.6	100	8.0	200	3.8	200	4.5	100	9.7
IC-NCDML [29]	200	3.3	200	3.6	200	4.9	100	8.0	200	3.7	100	8.9	100	9.7
DC-NCDML [82]	200	3.2	300	2.3	200	4.8	200	3.9	200	3.6	200	4.3	100	9.6
VGF-NCDML [177]	200	3.3	200	3.6	200	4.9	100	8.1	200	3.7	200	4.5	100	9.7
MA-NCDML [367]	200	3.3	200	3.6	100	9.8	100	8.2	100	7.4	200	4.5	**50**	**19.4**
SFN-NCDML [74]	100	6.6	200	3.6	100	9.7	100	8.1	100	7.5	200	4.5	**50**	**19.4**
OC-NCDML [233]	100	6.5	100	7.1	**50**	19.1	50	15.6	100	7.3	100	8.8	**50**	19.1
VND-NCDML	100	6.7	100	7.3	**50**	**19.5**	100	8.1	100	7.5	100	9.0	**50**	**19.4**
LDD-NCDML	100	6.6	200	3.7	100	9.7	100	8.2	100	7.5	100	9.0	**50**	**19.4**
CSFN-CDML	143	4.7	209	3.5	174	5.6	87	9.3	**62**	**12.1**	139	6.5	64	15.2
CVND-CDML	**53**	**12.7**	**65**	**11.3**	61	16.0	63	13.0	127	5.9	92	9.9	68	14.3
CLDD-CDML	76	8.8	128	5.8	85	11.5	**48**	**17.1**	91	8.3	**71**	**12.9**	55	17.7

Table 2.12: The numbers of components that achieve the AUCs in Table 6.1 and 2.11.

	MIMIC	EICU	Reuters	News	Cars	Birds	Act
NCDML	0.175	0.145	0.043	0.095	0.149	0.075	0.045
CDML	0.187	0.142	0.045	0.087	0.124	0.066	0.042
LMNN [357]	0.183	0.153	0.031	0.093	0.153	0.073	**0.013**
LDML [146]	0.159	0.139	0.034	0.079	0.131	0.072	0.068
MLEC [200]	0.162	0.131	0.042	0.088	0.151	0.039	0.043
GMML [405]	0.197	0.157	0.051	0.063	0.118	0.067	0.036
ILHD [63]	0.164	0.162	0.048	0.077	0.117	0.045	0.059
ℓ_2-CDML	0.184	0.136	0.037	0.072	0.105	0.053	0.041
ℓ_1-CDML [280]	0.173	0.131	0.042	0.064	0.113	0.061	0.026
$\ell_{2,1}$-CDML [399]	0.181	0.129	0.034	0.073	0.121	0.044	0.024
Tr-CDML [234]	0.166	0.138	0.024	0.076	0.111	0.058	0.037
IT-CDML [92]	0.174	0.134	0.033	0.061	0.109	0.036	**0.013**
Dropout-CDML [282]	0.182	0.140	0.021	0.076	0.114	0.063	0.024
OS-CDML [116]	0.166	0.133	0.032	0.063	0.108	0.057	0.031
DCM-NCDML [242]	0.159	0.131	0.035	0.069	0.127	0.064	0.035
CS-NCDML [402]	0.163	0.135	0.031	0.083	0.103	0.045	0.033
DPP-NCDML [429]	0.147	0.140	0.038	0.067	0.117	0.072	0.041
IC-NCDML [29]	0.155	0.127	0.018	0.075	0.116	0.074	0.029
DC-NCDML [82]	0.164	0.123	0.023	0.082	0.125	0.051	0.033
VGF-NCDML [177]	0.158	0.136	0.014	0.064	0.136	0.035	0.028
MA-NCDML [367]	0.143	0.128	0.023	0.078	0.102	0.031	0.042
OC-NCDML [233]	0.161	0.142	0.032	0.061	0.111	0.063	0.034
OS-NCDML [116]	0.169	0.137	0.015	0.083	0.119	0.058	0.042
SFN-NCDML [74]	0.153	0.126	0.022	0.069	0.127	0.043	0.028
VND-NCDML	0.148	0.135	0.019	0.078	0.116	0.067	0.035
LDD-NCDML	0.146	0.121	0.017	**0.054**	0.111	0.036	0.021
CSFN-CDML	0.142	0.124	0.019	0.062	0.092	0.043	0.019
CVND-CDML	0.137	**0.115**	**0.008**	0.055	0.094	0.038	**0.013**
CLDD-CDML	**0.131**	0.118	0.012	0.058	**0.089**	**0.026**	0.016

Table 2.13: The gap of training AUC and testing AUC.

	Scene	Caltech	Sports
SC [392]	83.6 ± 0.2	42.3 ± 0.4	87.4 ± 0.5
DCM-SC [242]	85.4 ± 0.5	44.7 ± 0.8	89.6 ± 0.1
CS-SC [402]	84.8 ± 0.6	45.4 ± 0.5	88.3 ± 0.3
DPP-SC [429]	84.6 ± 0.3	43.5 ± 0.3	88.1 ± 0.2
IC-SC [29]	85.5 ± 0.1	43.9 ± 0.7	90.2 ± 0.7
MA-SC [369]	86.1 ± 0.5	45.6 ± 0.4	89.7 ± 0.4
AC-SC	$\mathbf{86.5} \pm 0.7$	$\mathbf{46.1} \pm 0.3$	$\mathbf{90.9} \pm 0.3$

Table 2.14: Classification accuracy (%) on three datasets. We compare the proposed ACs with existing diversity-promoting regularizers.

Network	Error
Segmental NN [14]	21.9
MCRBM [88]	20.5
DSR [326]	19.9
Rectifier NN [332]	19.8
DBN [313]	19.7
Shallow CNN [22]	19.5
Structured DNN [391]	18.8
Posterior Modeling [278]	18.5
Kaldi [277]	18.53
CS-Kaldi [402]	18.48
IC-Kaldi [29]	18.46
MA-Kaldi [369]	18.51
DC-Kaldi [82]	18.50
AC-Kaldi	18.41
CTC [139]	18.4
RNN Transducer [139]	17.7
Attention RNN [80]	17.6
CTC+SCRF [239]	17.4
Segmental RNN [238]	17.3
RNNDrop [259]	16.9
CNN [333]	16.7

Table 2.15: Phone error rate (%) on the TIMIT test set. On the second panel (Kaldi, etc.), we compare AC with previously proposed diversity-promoting regularizers. On the first panel (Segmental NN, etc.) and the third panel (CTC, etc.) are other state of the art baselines.

Network	Error
Maxout [135]	9.38
NiN [229]	8.81
DSN [217]	7.97
Highway Network [314]	7.60
All-CNN [310]	7.25
ResNet [153]	6.61
ELU-Network [81]	6.55
LSUV [257]	5.84
Fract. Max-Pooling [138]	4.50
WideResNet [406]	3.89
CS-WideResNet [402]	3.81
IC-WideResNet [29]	3.85
MA-WideResNet [369]	3.68
DC-WideResNet [82]	3.77
LCD-WideResNet [291]	3.69
AC-WideResNet	3.63
ResNeXt [382]	3.58
PyramidNet [307]	3.48
DenseNet [169]	3.46
PyramidSepDrop [388]	3.31

Table 2.16: Classification error (%) on the CIFAR-10 test set.

	CNN		DailyMail	
	Dev	Test	Dev	Test
Hermann et al. [154]	61.6	63.0	70.5	69.0
Hill et al. [157]	63.4	6.8	-	-
Kadlec et al. [188]	68.6	69.5	75.0	73.9
Kobayashi et al. [197]	71.3	72.9	-	-
Sordoni et al. [309]	72.6	73.3	-	-
Trischler et al. [334]	73.4	74.0	-	-
Chen et al. [68]	73.8	73.6	77.6	76.6
Cui et al. [86]	73.1	74.4	-	-
Shen et al. [301]	72.9	74.7	77.6	76.6
BIDAF [296]	76.31	76.94	80.33	79.63
CS-BIDAF [402]	76.43	77.10	80.37	79.71
IC-BIDAF [29]	76.41	77.21	80.49	79.83
MA-BIDAF [369]	76.49	77.09	80.42	79.74
DC-BIDAF [82]	76.35	77.15	80.38	79.67
AC-BIDAF	76.62	77.23	80.65	79.88
Dhingra et al. [101]	77.9	77.9	81.5	80.9
Dhingra et al. [102]	79.2	78.6	–	–

Table 2.17: Accuracy (%) on two QA datasets.

	TIMIT	CIFAR-10	CNN
No regularization	1.1	6.3	69.4
CS [402]	1.2	6.8	74.8
IC [29]	1.2	6.7	76.1
MA [369]	1.3	7.0	78.6
DC [82]	1.5	7.6	82.9
LCD [291]	–	6.8	–
AC	1.3	7.1	79.7

Table 2.18: Average runtime (hours). We compare AC with existing diversity-promoting regularizers.

	#Train	#Test	Dimension	#Class
MIMIC-III	40K	18K	7207	2833
Cars	8144	8041	4096	196
Birds	9000	2788	4096	200
Scenes-15	3140	1345	–	15
Caltech-256	20846	8934	–	256
UIUC-Sports	1254	538	–	8

Table 2.19: Dataset statistics.

	MIMIC-III	Cars	Birds
EUC	58.3 $\pm$ 0.1	37.8 $\pm$ 0.0	43.2 $\pm$ 0.0
ITML [92]	69.3 $\pm$ 0.4	50.1 $\pm$ 0.0	52.9 $\pm$ 0.3
LDML [146]	70.9 $\pm$ 0.9	51.3 $\pm$ 0.0	52.1 $\pm$ 0.2
DML-Eig [398]	70.6 $\pm$ 0.7	50.7 $\pm$ 0.0	53.3 $\pm$ 0.8
Seraph [265]	71.7 $\pm$ 0.2	53.6 $\pm$ 0.0	52.9 $\pm$ 0.2
GMML [405]	71.2 $\pm$ 0.3	54.2 $\pm$ 0.0	53.7 $\pm$ 0.6
Tsang [335]	73.5 $\pm$ 0.2	55.8 $\pm$0.0	53.9 $\pm$ 0.4
MKDML [345]	75.1 $\pm$ 0.9	53.5 $\pm$0.0	54.4 $\pm$ 0.1
Jain [176]	74.9 $\pm$ 1.1	53.9 $\pm$0.0	55.9 $\pm$ 0.6
PCCA [252]	73.4 $\pm$ 0.5	56.4 $\pm$0.0	55.1 $\pm$ 0.9
KDML	73.8 $\pm$ 0.9	54.9 $\pm$0.0	54.7 $\pm$ 0.5
KDML-SHN [294]	74.2 $\pm$ 0.6	55.4 $\pm$0.0	54.8 $\pm$ 0.9
KDML-DPP [429]	75.5 $\pm$ 0.8	56.4 $\pm$0.0	57.3 $\pm$ 0.3
KDML-Angle [369]	75.9 $\pm$ 0.2	56.8 $\pm$0.0	57.1 $\pm$ 0.6
KDML-SFN-RTR	76.3 $\pm$ 0.7	56.6 $\pm$ 0.0	56.4 $\pm$ 0.1
KDML-VND-RTR	**77.1** $\pm$ 0.6	**57.7** $\pm$ 0.0	58.9 $\pm$ 0.7
KDML-LDD-RTR	76.7 $\pm$ 0.3	57.4 $\pm$ 0.0	**59.2** $\pm$ 0.3
KDML-SFN-RFF	75.9 $\pm$ 0.1	56.5 $\pm$ 0.0	56.0 $\pm$ 0.2
KDML-VND-RFF	76.9 $\pm$ 0.4	57.2 $\pm$ 0.0	58.8 $\pm$ 0.6
KDML-LDD-RFF	76.8 $\pm$ 0.8	57.1 $\pm$ 0.0	58.5 $\pm$ 0.4

Table 2.20: Retrieval precision@10 (%) on three datasets. On the first panel (EUC, etc.) are non-kernel DML methods. On the second panel (Tsang, etc.) are well established or state of the art kernel DML methods. On the third panel (KDML, etc.) are KDML methods regularized by existing regularizers. On the fourth panel (KDML-SFN-RTR, etc.) are KDML methods regularized by our proposed near-orthogonality regularizers.

	MIMIC-III	Cars	Birds	Average
KDML	300	400	300	333
KDML-SHN [294]	300	400	300	333
KDML-DPP [429]	200	300	300	267
KDML-Angle [369]	200	300	200	233
KDML-SFN-RTR	200	200	200	200
KDML-VND-RTR	100	200	200	167
KDML-LDD-RTR	100	200	200	167
KDML-SFN-RFF	100	200	200	167
KDML-VND-RFF	100	200	200	167
KDML-LDD-RFF	100	200	200	167

Table 2.21: The number of RKHS functions achieving the precision@10 in Table 2.20

	D1 (3566)	D2 (3498)	D3 (2757)	D4 (204)	D5 (176)	D6 (148)	D7 (131)	D8 (121)
Tsang [335]	80.3 ± 0.3	82.8 ± 0.7	81.9 ± 0.4	6.3 ± 0.7	3.9 ± 0.5	4.5 ± 0.5	6.7 ± 0.9	5.1 ± 0.2
MKDML [345]	83.1 ± 0.2	83.4 ± 0.7	82.3 ± 0.6	3.7 ± 1.2	5.5 ± 0.1	9.3 ± 0.8	10.0 ± 0.5	3.7 ± 0.4
Jain [176]	82.7 ± 0.7	84.6 ± 0.5	**82.9** ± 0.4	7.2 ± 0.4	8.2 ± 0.4	3.4 ± 0.9	6.2 ± 0.7	8.7 ± 0.3
PCCA [252]	82.2 ± 0.2	82.1 ± 0.6	82.1 ± 0.3	9.4 ± 0.8	7.7 ± 0.2	5.2 ± 0.4	6.1 ± 0.1	3.2 ± 0.4
KDML	82.6 ± 0.7	83.9 ± 1.2	81.7 ± 0.6	7.4 ± 1.0	5.3 ± 0.9	5.7 ± 0.3	3.8 ± 0.8	3.5 ± 0.4
KDML-SHN [294]	82.1 ± 0.5	83.6 ± 0.4	82.4 ± 0.9	8.3 ± 0.1	5.1 ± 0.8	4.7 ± 0.2	3.4 ± 0.9	3.7 ± 0.8
KDML-DPP [429]	83.4 ± 0.4	**84.7** ± 0.7	82.7 ± 1.0	11.5 ± 0.3	9.7 ± 0.5	10.4 ± 0.4	7.3 ± 0.2	7.9 ± 0.1
KDML-Angle [369]	83.7 ± 0.1	84.3 ± 0.1	81.8 ± 0.3	10.6 ± 0.2	10.2 ± 0.8	9.5 ± 0.6	8.8 ± 0.5	7.2 ± 0.3
KDML-SFN-RTR	82.5 ± 0.8	84.2 ± 1.2	82.2 ± 0.1	15.0 ± 0.3	13.4 ± 0.1	13.8 ± 0.2	12.1 ± 0.6	10.9 ± 0.5
KDML-VND-RTR	**83.9** ± 0.9	84.5 ± 0.8	82.6 ± 0.2	15.5 ± 0.9	16.2 ± 0.7	14.3 ± 0.7	12.4 ± 0.8	14.7 ± 0.8
KDML-LDD-RTR	83.7 ± 0.1	83.8 ± 0.9	82.2 ± 0.6	14.8 ± 0.4	14.2 ± 0.1	13.7 ± 0.3	10.3 ± 0.1	12.8 ± 0.2
KDML-SFN-RFF	82.3 ± 0.9	84.1 ± 0.6	81.1 ± 0.5	15.1 ± 0.2	14.9 ± 0.5	15.2 ± 0.9	13.5 ± 0.1	10.8 ± 0.3
KDML-VND-RFF	83.4 ± 0.2	83.6 ± 0.5	82.7 ± 0.4	15.2 ± 0.5	15.6 ± 0.9	10.6 ± 0.8	12.0 ± 1.1	10.3 ± 0.7
KDML-LDD-RFF	82.9 ± 0.2	84.0 ± 1.0	82.5 ± 0.9	14.4 ± 0.9	13.9 ± 1.2	15.4 ± 0.5	13.9 ± 0.2	14.4 ± 0.1

Table 2.22: Retrieval precision@10 (%) on three frequent and five infrequent diseases in the MIMIC-III dataset. The number next to a disease ID is its frequency. Note that diseases D1–D3 are frequent diseases, while that D4–D8 are infrequent ones.

	MIMIC-III	Cars	Birds
KDML-SFN-RTR	69.4	17.2	18.6
KDML-VND-RTR	69.8	17.4	18.9
KDML-LDD-RTR	69.9	17.5	18.9
KDML-SFN-RFF	12.6	2.7	2.9
KDML-VND-RFF	12.9	2.8	3.1
KDML-LDD-RFF	12.8	2.8	3.1

Table 2.23: Convergence time (hours) on three datasets.

	Scenes-15	Caltech-256	UIUC-Sports
SC [266]	83.6 ± 0.2	42.3 ± 0.4	87.4 ± 0.5
KSC [120]	85.4 ± 0.5	44.7 ± 0.8	88.2 ± 0.1
KSC-SHN [294]	85.8 ± 0.6	45.4 ± 0.5	88.3 ± 0.3
KSC-DPP [429]	86.3 ± 0.3	47.3 ± 0.8	89.3 ± 0.2
KSC-Angle [369]	86.8 ± 0.1	46.1 ± 0.8	89.5 ± 0.5
KSC-SFN-RTR	87.1 ± 0.5	47.2 ± 0.5	89.9 ± 0.3
KSC-VND-RTR	**87.9** ± 0.7	**48.6** ± 0.3	**91.3** ± 0.5
KSC-LDD-RTR	87.4 ± 0.4	48.1 ± 0.6	90.7 ± 0.2
KSC-SFN-RFF	86.8 ± 0.6	46.5 ± 0.1	89.5 ± 0.7
KSC-VND-RFF	87.5 ± 0.5	48.2 ± 0.4	90.4 ± 0.8
KSC-LDD-RFF	87.2 ± 0.1	47.8 ± 0.2	90.2 ± 0.4

Table 2.24: Classification accuracy (%) on three datasets.

	Sensitivity	Specificity	Error rate
L1 [331]	0.76	0.71	0.31
Elastic Net [428]	0.74	0.72	0.30
LDD-L1	0.82	0.75	0.24

Table 2.25: Sensitivity and specificity for support recovery and error rate for prediction.

Method	20-News		RCV1	
	Test	Gap	Test	Gap
SC [266]	0.592	0.119	0.872	0.009
LDD-SC	0.605	0.108	0.886	0.005
L1-SC [331]	0.606	0.105	0.897	0.005
LDD-L1-SC	**0.612**	0.099	**0.909**	-0.015

Table 2.26: Classification accuracy on the test sets of 20-News and RCV1, and the gap between training and test accuracy.

Basis Vector	Selected Words
1	crime, guns
2	faith, trust
3	worked, manager
4	weapons, citizens
5	board, uiuc
6	application, performance, ideas
7	service, quality
8	bible, moral
9	christ, jews, land, faq

Table 2.27: Selected words of 9 exemplar basis vectors.

Network	Test
RNN [253]	124.7
RNN+LDA [253]	113.7
Deep RNN [273]	107.5
Sum-Product Network [76]	100.0
RNN+LDA+KN-5+Cache [253]	92.0
LSTM (medium) [408]	82.7
CharCNN [194]	78.9
LSTM (large) [408]	78.4
Variational LSTM [115]	73.4
PytorchLM [3]	72.3
CS-PytorchLM [402]	71.8
IC-PytorchLM [29]	71.9
MA-PytorchLM [369]	72.0
DC-PytorchLM [82]	72.2
AC-PytorchLM	71.5
LDD-PytorchLM	71.6
L1-PytorchLM [331]	71.8
LDD-L1-PytorchLM	71.1
Pointer Sentinel LSTM [250]	70.9
Ensemble of 38 Large LSTMs [408]	68.7
Variat. LSTM Ensem. [115]	68.7
Variational RHN [426]	68.5
Variational LSTM + REAL [170]	68.5
Neural Architecture Search [427]	67.9
Variational RHN + RE [170]	66.0
Variational RHN + WT [426]	65.4
Variational RHN+WT+Dropout [426]	64.4
Architecture Search + WT V1 [427]	64.0
Architecture Search + WT V2 [427]	62.4

Table 2.28: Word-level perplexities on the PTB test set. On the second panel (PytorchLM, etc.), we compare LDD-L1 with the L1 regularizer and orthogonality-promoting regularizers. On the first panel (RNN, etc.) and the third panel (Pointer Sentinel LSTM, etc.) are other state of the art baselines.

Network	Error
Maxout [135]	9.38
NiN [229]	8.81
DSN [217]	7.97
Highway Network [314]	7.60
All-CNN [310]	7.25
ResNet [153]	6.61
ELU-Network [81]	6.55
LSUV [257]	5.84
Fract. Max-Pooling [138]	4.50
WideResNet [406]	3.89
CS-WideResNet [402]	3.81
IC-WideResNet [29]	3.85
MA-WideResNet [369]	3.68
DC-WideResNet [82]	3.77
LCD-WideResNet [291]	3.69
AC-WideResNet	3.63
LDD-WideResNet	3.65
L1-WideResNet [331]	3.81
LDD-L1-WideResNet	3.60
ResNeXt [382]	3.58
PyramidNet [307]	3.48
DenseNet [169]	3.46
PyramidSepDrop [388]	3.31

Table 2.29: Classification error (%) on the CIFAR-10 test set.

Chapter 3

Diversity-promoting Learning II – Bayesian Inference

In the last chapter, we have studied diversity-promoting learning under a frequentist-style regularized optimization framework, where the component vectors are deterministic and are learned via point estimation [352]. In this chapter, we study how to promote diversity under an alternative learning paradigm: Bayesian inference [46, 172, 260], where the components are considered as random variables of which a posterior distribution shall be computed from data under certain priors. Compared with point estimation, Bayesian learning offers complementary benefits. First, it offers a "model-averaging" [46, 172] effect for ML models when they are used for decision-making and prediction because the parameters shall be integrated under a posterior distribution, thus can potentially alleviate overfitting on training data. Second, it provides a natural way to quantify uncertainties of model parameters, and downstream decisions and predictions made thereupon [46, 172, 260]. Affandi et al. [16] investigated the "diversification" of Bayesian models using the determinantal point process (DPP) [204] prior. DPP has two drawbacks. First, it is not applicable to Bayesian nonparametric models where the number of components is infinite. Second, it is not amenable to developing variational-inference [340] based posterior inference algorithms which are usually more efficient than sampling-based [127] methods. In this chapter, we develop new diversity-promoting priors to address these limitations. Bayesian models can be classified into parametric models where the number of components is finite and nonparametric [111] models where the number of components is infinite in principle and can dynamically grow with data. To promote diversity among a finite number of components in parametric models, we propose a prior called mutual angular process [371] that encourage the components to have large mutual angles. In nonparametric models, we study an infinite mutual angular process [381] which encourages infinitely many components to be diverse.

3.1 Diversity-promoting Learning of Bayesian Parametric Models

We start with promoting diversity in Bayesian parametric models where the number of components is finite and fixed. We investigate two approaches: (1) *prior control*, which defines

diversity-promoting priors and uses them to affect the posterior via the Bayes rule; (2) *posterior regularization*, which directly performs diversity-promoting regularization over post-data distributions [424]. These two approaches have complementary advantages which will be discussed in detail below.

Following Section 2.3, we adopt a notion of diversity that component vectors are more diverse provided the pairwise angles between them are larger. In the prior control method, we define a mutual angular process (MAP) [371], which assigns higher probability density to components that have larger mutual angles. Specifically, we build a Bayesian network [198] where the nodes represent the directional vectors of the components and the local probabilities are parameterized by von Mises-Fisher [245] distributions that entail an inductive bias towards vectors with larger mutual angles. The MAP is amenable for approximate posterior inference of model components. In particular, they facilitate variational inference (VI) [340], which is usually more efficient than sampling-based [127] methods. In contrast, it is difficult to derive VI-based algorithms for the determinant point process (DPP) [204] prior. Bardenet and Titsias [30] derived bounds on the likelihood of a DPP and use these bounds for variational inference. This method is applicable when DPP is used to define the likelihood. However, when DPP is applied as a prior of components in Bayesian models, it is unclear how to apply this method for variational inference of components' posterior.

It is not always the case that a Bayesian prior can be defined to capture a certain desired effect. For example, Xie et al. [369] posit that one ingredient of diversity is evenness: the vectors are desired to uniformly spread out to different directions and each vector is evenly different from all other vectors. To achieve this, they defined a regularizer to encourage the variance of angles between vectors to be small. However, it is very difficult to define a Bayesian prior to achieve such an effect. The major technical difficulty lies in how to ensure the prior integrates to one. To address this issue, we adopt a posterior regularization approach [424], in which a diversity-promoting regularizer is directly imposed over the post-data distributions to encourage diversity and the regularizer can be flexibly defined to accommodate various desired diversity-promoting goals.

We apply these two approaches to "diversify" the "experts" (components) in the Bayesian mixture of experts model [354]. Posterior inference algorithms based on both variational inference and Markov chain Monte Carlo sampling are developed. Experiments demonstrate the effectiveness and efficiency of our methods.

3.1.1 Mutual Angular Process

We start with defining diversity-promoting Bayesian priors. We desire the priors to have two traits. First, to favor diversity, they assign a higher density to components having larger mutual angles. Second, the priors should facilitate posterior inference. In Bayesian learning, the easiness of posterior inference relies heavily on the prior [47, 341]. One possible solution is to turn a diversity-promoting regularizer $\Omega(\mathbf{A})$ (e.g., the uniform eigenvalue regularizer in Section 2.1) into a distribution $p(\mathbf{A}) = \frac{1}{Z}\exp(\Omega(\mathbf{A}))$ based on the Gibbs measure [195], where Z is the partition function guaranteeing $p(\mathbf{A})$ integrates to one. However, it is not sure whether $Z = \int_{\mathbf{A}} \exp(\Omega(\mathbf{A}))\mathrm{d}\mathbf{A}$ is finite, i.e., whether $p(\mathbf{A})$ is proper. When an improper prior is utilized in Bayesian learning, the posterior is also highly likely to be improper, except in a few special cases

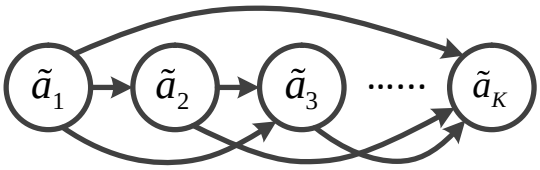

Figure 3.1: A Bayesian network representation of the mutual angular process.

[352]. Performing inference on improper posteriors is problematic.

At a high-level, we define such a prior in a sequential manner: each time we add one component to the component pool and encourage the new component to be different from the existing ones. This sequential manner has two benefits. First, it can easily define both parametric and nonparametric priors by controlling the number of components to be added. Repeating the adding process K times, we obtain a parametric prior defined on K components. Likewise, a nonparametric prior on an infinite set of components can be obtained by repeating the adding process infinitely many times. Second, priors defined in this sequential manner can be naturally decomposed into a sequence of "simpler" distributions, which makes the derivation of variational-inference-based algorithms relatively easier.

Following [369], we adopt a notion of diversity that component vectors are more diverse provided the pairwise angles between them are larger. Given a component vector $\mathbf{a}$, let $g = \|\mathbf{a}\|_2$ be its magnitude and $\tilde{\mathbf{a}}$ be the directional vector ($\|\tilde{\mathbf{a}}\|_2 = 1$), where $\mathbf{a} = g\tilde{\mathbf{a}}$. Noting that the angle between two vectors is invariant to their magnitudes, we can construct the angle-based prior by sequentially adding the directional vectors (DVs) and encouraging the new DV to have large angles with the existing ones. We use a Bayesian network (BNs) (shown in Figure 3.1) to model this adding process, where nodes represent the DVs and the parents of $\tilde{\mathbf{a}}_i$ are $\tilde{\mathbf{a}}_1, \cdots, \tilde{\mathbf{a}}_{i-1}$. To encourage large angles between $\tilde{\mathbf{a}}_i$ and $\tilde{\mathbf{a}}_1, \cdots, \tilde{\mathbf{a}}_{i-1}$, we define a local probability based on the von Mises-Fisher (vMF) [245] distribution. The probability density function of the vMF distribution is $f(\mathbf{x}) = C_p(\kappa)\exp(\kappa\boldsymbol{\mu}^\top\mathbf{x})$, where the random variable $\mathbf{x} \in \mathbb{R}^p$ lies on a $p-1$ dimensional sphere ($\|\mathbf{x}\|_2 = 1$), $\boldsymbol{\mu}$ is the mean direction with $\|\boldsymbol{\mu}\|_2 = 1$, $\kappa > 0$ is the concentration parameter, and $C_p(\kappa)$ is the normalization constant. The vMF-based local probability $p(\tilde{\mathbf{a}}_i|\text{pa}(\tilde{\mathbf{a}}_i))$ is defined as

$$p(\tilde{\mathbf{a}}_i|\text{pa}(\tilde{\mathbf{a}}_i)) = C_p(\kappa)\exp\left(\kappa\left(-\frac{\sum_{j=1}^{i-1}\tilde{\mathbf{a}}_j}{\|\sum_{j=1}^{i-1}\tilde{\mathbf{a}}_j\|_2}\right)^\top\tilde{\mathbf{a}}_i\right), \tag{3.1}$$

which encourages large angles: $\tilde{\mathbf{a}}_j^\top\tilde{\mathbf{a}}_i$ is the cosine of the angle between $\tilde{\mathbf{a}}_i$ and $\tilde{\mathbf{a}}_j$; if $\tilde{\mathbf{a}}_i$ has larger angles with $\{\tilde{\mathbf{a}}_j\}_{j=1}^{i-1}$, then the average negative cosine similarity $(-\sum_{j=1}^{i-1}\tilde{\mathbf{a}}_j)^\top\tilde{\mathbf{a}}_i$ would be larger; accordingly $p(\tilde{\mathbf{a}}_i|\text{pa}(\tilde{\mathbf{a}}_i))$ would be larger. For the magnitudes $\{g_i\}_{i=1}^K$ of the components, we sample them independently from a gamma distribution with shape parameter α_1 and rate parameter α_2. The generative process of $\mathbf{A}$ is summarized as follows:

- Draw $\tilde{\mathbf{a}}_1 \sim \text{vMF}(\boldsymbol{\mu}_0, \kappa)$
- For $i = 2, \cdots, K$, draw $\tilde{\mathbf{a}}_i \sim \text{vMF}(-\frac{\sum_{j=1}^{i-1}\tilde{\mathbf{a}}_j}{\|\sum_{j=1}^{i-1}\tilde{\mathbf{a}}_j\|_2}, \kappa)$
- For $i = 1, \cdots, K$, draw $g_i \sim \text{Gamma}(\alpha_1, \alpha_2)$

- For $i = 1, \cdots, K$, $\mathbf{a}_i = \tilde{\mathbf{a}}_i g_i$

The probability distribution over $\mathbf{A}$ can be written as

$$p(\mathbf{A}) = C_p(\kappa)\exp(\kappa\mu_0^\top \tilde{\mathbf{a}}_1)\prod_{i=2}^{K} C_p(\kappa)\exp\left(\kappa\left(-\frac{\sum_{j=1}^{i-1}\tilde{\mathbf{a}}_j}{\|\sum_{j=1}^{i-1}\tilde{\mathbf{a}}_j\|_2}\right)^\top \tilde{\mathbf{a}}_i\right)\prod_{i=1}^{K}\frac{\alpha_2^{\alpha_1} g_i^{\alpha_1-1} e^{-g_i\alpha_2}}{\Gamma(\alpha_1)}. \tag{3.2}$$

According to the factorization theorem [198] of Bayesian networks, it is easy to verify $\int_{\mathbf{A}} p(\mathbf{A})\mathrm{d}\mathbf{A} = 1$, thus $p(\mathbf{A})$ is a proper prior.

When inferring the posterior of model components using a variational inference method, we need to compute the expectation of $1/\|\sum_{j=1}^{i-1}\tilde{\mathbf{a}}_j\|_2$ appearing in the local probability $p(\tilde{\mathbf{a}}_i|\mathrm{pa}(\tilde{\mathbf{a}}_i))$, which is extremely difficult. To address this issue, we define an alternative local probability that achieves similar modeling effect as $p(\tilde{\mathbf{a}}_i|\mathrm{pa}(\tilde{\mathbf{a}}_i))$, but greatly facilitates variational inference:

$$\begin{aligned}
&\hat{p}(\tilde{\mathbf{a}}_i|\mathrm{pa}(\tilde{\mathbf{a}}_i)) \propto \exp(\kappa(-\textstyle\sum_{j=1}^{i-1}\tilde{\mathbf{a}}_j)^\top\tilde{\mathbf{a}}_i)\\
&\propto \exp\left(\kappa\|\textstyle\sum_{j=1}^{i-1}\tilde{\mathbf{a}}_j\|_2\left(-\frac{\sum_{j=1}^{i-1}\tilde{\mathbf{a}}_j}{\|\sum_{j=1}^{i-1}\tilde{\mathbf{a}}_j\|_2}\right)^\top\tilde{\mathbf{a}}_i\right)\\
&= C_p(\kappa\|\textstyle\sum_{j=1}^{i-1}\tilde{\mathbf{a}}_j\|_2)\exp\left(\kappa\|\textstyle\sum_{j=1}^{i-1}\tilde{\mathbf{a}}_j\|_2\left(-\frac{\sum_{j=1}^{i-1}\tilde{\mathbf{a}}_j}{\|\sum_{j=1}^{i-1}\tilde{\mathbf{a}}_j\|_2}\right)^\top\tilde{\mathbf{a}}_i\right)\\
&= C_p(\kappa\|\textstyle\sum_{j=1}^{i-1}\tilde{\mathbf{a}}_j\|_2)\exp(\kappa(-\textstyle\sum_{j=1}^{i-1}\tilde{\mathbf{a}}_j)^\top\tilde{\mathbf{a}}_i),
\end{aligned} \tag{3.3}$$

which is another vMF distribution with mean direction $-\sum_{j=1}^{i-1}\tilde{\mathbf{a}}_j/\|\sum_{j=1}^{i-1}\tilde{\mathbf{a}}_j\|_2$ and concentration parameter $\kappa\|\sum_{j=1}^{i-1}\tilde{\mathbf{a}}_j\|_2$. This local probability is proportional to $(-\sum_{j=1}^{i-1}\tilde{\mathbf{a}}_j)^\top\tilde{\mathbf{a}}_i$, which measures the negative cosine similarity between $\tilde{\mathbf{a}}_i$ and its parents. Thereby, $\hat{p}(\tilde{\mathbf{a}}_i|\mathrm{pa}(\tilde{\mathbf{a}}_i))$ still encourages large mutual angles. The difference between $\hat{p}(\tilde{\mathbf{a}}_i|\mathrm{pa}(\tilde{\mathbf{a}}_i))$ and $p(\tilde{\mathbf{a}}_i|\mathrm{pa}(\tilde{\mathbf{a}}_i))$ is that in $\hat{p}(\tilde{\mathbf{a}}_i|\mathrm{pa}(\tilde{\mathbf{a}}_i))$ the term $\|\sum_{j=1}^{i-1}\tilde{a}_j\|_2$ is moved from the denominator to the normalizer, thus we can avoid computing the expectation of $1/\|\sum_{j=1}^{i-1}\tilde{a}_j\|_2$. Though it incurs a new problem that we need to compute the expectation of $\log C_p(\kappa\|\sum_{j=1}^{i-1}\tilde{\mathbf{a}}_j\|_2)$, which is also difficult due to the complex form of the $C_p(\cdot)$ function, we managed to resolve this problem as detailed in Section 3.1.2. We refer to the mutual angular process defined in Eq.(3.2) as type-I MAP and that with local probability defined in Eq.(3.3) as type-II MAP.

3.1.2 Approximate Inference Algorithms

We develop algorithms to infer the posteriors of components under the MAP priors. Since exact posteriors are intractable, we resort to approximate inference techniques. Two main paradigms of approximate inference methods are: (1) variational inference (VI) [340]; (2) Markov chain Monte Carlo (MCMC) sampling [127]. These two approaches possess benefits that are mutually complementary. MCMC can achieve a better approximation of the posterior than VI since it generates samples from the true posterior while VI seeks an approximation of the posterior. However, VI can be computationally more efficient [164]. In this section, we focus on deriving the VI-based algorithm and leave the details of MCMC-based algorithms (which is relatively straightforward) to the appendix.

The basic idea of VI [340] is to use a "simpler" variational distribution $q(\mathbf{A})$ to approximate the true posterior by minimizing the Kullback-Leibler divergence between these two distributions, which is equivalent to maximizing the following variational lower bound w.r.t $q(\mathbf{A})$:

$$\mathbb{E}_{q(\mathbf{A})}[\log p(\mathcal{D}|\mathbf{A})] + \mathbb{E}_{q(\mathbf{A})}[\log p(\mathbf{A})] - \mathbb{E}_{q(\mathbf{A})}[\log q(\mathbf{A})], \tag{3.4}$$

where $p(\mathbf{A})$ is the MAP prior and $p(\mathcal{D}|\mathbf{A})$ is the data likelihood. Here we choose $q(\mathbf{A})$ to be a mean field variational distribution $q(\mathbf{A}) = \prod_{k=1}^{K} q(\tilde{\mathbf{a}}_k)q(g_k)$, where $q(\tilde{\mathbf{a}}_k) = \text{vMF}(\tilde{\mathbf{a}}_k|\hat{\mathbf{a}}_k, \hat{\kappa})$ and $q(g_k) = \text{Gamma}(g_k|r_k, s_k)$. Given the variational distribution, we first compute the analytical expression of the variational lower bound, in which we particularly discuss how to compute $\mathbb{E}_{q(\mathbf{A})}[\log p(\mathbf{A})]$. If choosing $p(\mathbf{A})$ to be the type-I MAP prior (Eq.(3.2)), we need to compute $\mathbb{E}[(-\frac{\sum_{j=1}^{i-1}\tilde{\mathbf{a}}_j}{\|\sum_{j=1}^{i-1}\tilde{\mathbf{a}}_j\|_2})^\top\tilde{\mathbf{a}}_i]$ which is very difficult to deal with due to the presence of $1/\|\sum_{j=1}^{i-1}\tilde{\mathbf{a}}_j\|_2$. Instead we choose the type-II MAP prior. Under type-II MAP, we need to compute $\mathbb{E}_{q(\mathbf{A})}[\log Z_i]$ for all i, where $Z_i = 1/C_p(\kappa\|\sum_{j=1}^{i-1}\tilde{\mathbf{a}}_j\|_2)$ is the partition function of $p(\tilde{\mathbf{a}}_i|\text{pa}(\tilde{\mathbf{a}}_i))$. The analytical form of this expectation is difficult to derive as well due to the complexity of the $C_p(x)$ function: $C_p(x) = \frac{x^{p/2-1}}{(2\pi)^{p/2}I_{p/2-1}(x)}$ where $I_{p/2-1}(x)$ is the modified Bessel function of the first kind at order $p/2-1$ [245]. To address this issue, we derive an upper bound of $\log Z_i$ and compute the expectation of the upper bound, which is relatively easy to do. Consequently, we obtain a further lower bound of the variational lower bound and learn the variational and model parameters w.r.t the new lower bound. Now we proceed to derive the upper bound of $\log Z_i$, which equals $\log\int\exp(\kappa(-\sum_{j=1}^{i-1}\tilde{\mathbf{a}}_j)\cdot\tilde{\mathbf{a}}_i)\mathrm{d}\tilde{\mathbf{a}}_i$. Applying the inequality $\log\int\exp(x)\mathrm{d}x \leq \gamma + \int\log(1+\exp(x-\gamma))\mathrm{d}x$ [50], where γ is a variational parameter, we have

$$\log Z_i \leq \gamma + \int\log(1+\exp(\kappa(-\textstyle\sum_{j=1}^{i-1}\tilde{\mathbf{a}}_j)\cdot\tilde{\mathbf{a}}_i - \gamma)\mathrm{d}\tilde{\mathbf{a}}_i. \tag{3.5}$$

Then applying the inequality $\log(1+e^{-x}) \leq \log(1+e^{-\xi}) - \frac{x-\xi}{2} - \frac{1/2-g(\xi)}{2\xi}(x^2-\xi^2)$ [50], where ξ is another variational parameter and $g(\xi) = 1/(1+\exp(-\xi))$, we have

$$\begin{aligned}&\log Z_i\\ &\leq \gamma + \int[\log(1+e^{-\xi}) - (\kappa(\textstyle\sum_{j=1}^{i-1}\tilde{\mathbf{a}}_j)\cdot\tilde{\mathbf{a}}_i + \gamma - \xi)/2 - \frac{1/2-g(\xi)}{2\xi}((\kappa(\sum_{j=1}^{i-1}\tilde{\mathbf{a}}_j)\cdot\tilde{\mathbf{a}}_i+\gamma)^2 - \xi^2)]\mathrm{d}\tilde{\mathbf{a}}_i.\end{aligned} \tag{3.6}$$

Finally applying the following integrals on a high-dimensional sphere: (1) $\int_{\|\mathbf{y}\|_2=1} 1\mathrm{d}\mathbf{y} = \frac{2\pi^{(p+1)/2}}{\Gamma(\frac{p+1}{2})}$, (2) $\int_{\|\mathbf{y}\|_2=1}\mathbf{x}^\top\mathbf{y}\mathrm{d}\mathbf{y} = 0$, (3) $\int_{\|\mathbf{y}\|_2=1}(\mathbf{x}^\top\mathbf{y})^2\mathrm{d}\mathbf{y} \leq \|\mathbf{x}\|_2^2\frac{2\pi^{(p+1)/2}}{\Gamma(\frac{p+1}{2})}$, we get

$$\begin{aligned}&\log Z_i\\ &\leq -\tfrac{1/2-g(\xi)}{2\xi}\kappa^2\|\textstyle\sum_{j=1}^{i-1}\tilde{\mathbf{a}}_j\|_2^2\frac{2\pi^{(p+1)/2}}{\Gamma(\frac{p+1}{2})} + \gamma + [\log(1+e^{-\xi}) + \tfrac{\xi-\gamma}{2} + \tfrac{1/2-g(\xi)}{2\xi}(\xi^2-\gamma^2)]\tfrac{2\pi^{(p+1)/2}}{\Gamma(\frac{p+1}{2})}.\end{aligned} \tag{3.7}$$

The expectation of this upper bound is much easier to compute. Specifically, we need to tackle $\mathbb{E}_{q(\mathbf{A})}[\|\sum_{j=1}^{i-1}\tilde{\mathbf{a}}_j\|_2^2]$, which can be computed as

$$\begin{aligned}&\mathbb{E}_{q(\mathbf{A})}[\|\textstyle\sum_{j=1}^{i-1}\tilde{\mathbf{a}}_j\|_2^2]\\ &= \mathbb{E}_{q(\mathbf{A})}[\textstyle\sum_{j=1}^{i-1}\tilde{\mathbf{a}}_j^\top\tilde{\mathbf{a}}_j + \sum_{j=1}^{i-1}\sum_{k\neq j}^{i-1}\tilde{\mathbf{a}}_j^\top\tilde{\mathbf{a}}_k]\\ &= \textstyle\sum_{j=1}^{i-1}\mathrm{tr}(\mathbb{E}_{q(\tilde{\mathbf{a}}_j)}[\tilde{\mathbf{a}}_j\tilde{\mathbf{a}}_j^\top]) + \sum_{j=1}^{i-1}\sum_{k\neq j}^{i-1}\mathbb{E}_{q(\tilde{\mathbf{a}}_j)}[\tilde{\mathbf{a}}_j]^\top\mathbb{E}_{q(\tilde{\mathbf{a}}_k)}[\tilde{\mathbf{a}}_k]\\ &= \textstyle\sum_{j=1}^{i-1}\mathrm{tr}(\mathrm{cov}(\tilde{\mathbf{a}}_j)) + \sum_{j=1}^{i-1}\sum_{k=1}^{i-1}\mathbb{E}_{q(\tilde{\mathbf{a}}_j)}[\tilde{\mathbf{a}}_j]^\top\mathbb{E}_{q(\tilde{\mathbf{a}}_k)}[\tilde{\mathbf{a}}_k],\end{aligned} \tag{3.8}$$

where $\mathbb{E}_{q(\tilde{\mathbf{a}}_j)}[\tilde{\mathbf{a}}_j] = A_p(\hat{\kappa})\hat{\mathbf{a}}_j$, $\text{cov}(\tilde{\mathbf{a}}_j) = \frac{h(\hat{\kappa})}{\hat{\kappa}}\mathbf{I} + (1 - 2\frac{\nu+1}{\hat{\kappa}}h(\hat{\kappa}) - h^2(\hat{\kappa}))\hat{\mathbf{a}}_j\hat{\mathbf{a}}_j^\top$, $h(\hat{\kappa}) = \frac{I_{\nu+1}(\hat{\kappa})}{I_\nu(\hat{\kappa})}$, $A_p(\hat{\kappa}) = \frac{I_{p/2}(\hat{\kappa})}{I_{p/2-1}(\hat{\kappa})}$ and $\nu = p/2 - 1$.

3.1.3 Diversity-promoting Posterior Regularization

In practice, one may desire to achieve more than one diversity-promoting effects. For example, the mutual angular regularizer [369] aims at encouraging the pairwise angles between components to have not only large mean, but also small variance such that the components are uniformly "different" from each other and evenly spread out to different directions in the space. It would be extremely difficult, if ever possible, to define a proper prior that can accommodate all desired effects. To overcome such inflexibility of the prior control method, we resort to a *posterior regularization* approach [424]. Instead of designing a Bayesian prior to encode the diversification desideratum and indirectly influencing the posterior, posterior regularization directly imposes a control over the post-data distributions to achieve diversity.

The basic idea of posterior regularization [424] is: formulate the posterior estimation problem as an optimization problem defined over a family of distributions; add a regularizer, which encodes the desideratum, on the distributions to be optimized. In general, designing a regularizer is much easier than designing a proper prior. Giving the prior $\pi(\mathbf{A})$ and the data likelihood $p(\mathcal{D}|\mathbf{A})$, computing the posterior $p(\mathbf{A}|\mathcal{D})$ is equivalent to solving the following optimization problem [424]

$$\sup_{q(\mathbf{A})} \ \mathbb{E}_{q(\mathbf{A})}[\log p(\mathcal{D}|\mathbf{A})\pi(\mathbf{A})] - \mathbb{E}_{q(\mathbf{A})}[\log q(\mathbf{A})], \tag{3.9}$$

where $q(\mathbf{A})$ is any valid probability distribution. To bring in diversity into the posterior, we impose a diversity-promoting regularizer $\mathcal{R}(q(\mathbf{A}))$ over $q(\mathbf{A})$ and solve the following regularized problem:

$$\sup_{q(\mathbf{A})} \ \mathbb{E}_{q(\mathbf{A})}[\log p(\mathcal{D}|\mathbf{A})\pi(\mathbf{A})] - \mathbb{E}_{q(\mathbf{A})}[\log q(\mathbf{A})] + \lambda\mathcal{R}(q(\mathbf{A})), \tag{3.10}$$

where λ is a tradeoff parameter.

Here we present a specific example of $\mathcal{R}(q(\mathbf{A}))$ while noting that many other choices are applicable. Gaining insight from [369], we define $\mathcal{R}(q(\mathbf{A}))$ as

$$\Omega(\{\mathbb{E}_{q(\mathbf{a}_i)}[\mathbf{a}_i]\}_{i=1}^K) = \frac{1}{K(K-1)}\sum_{i=1}^K\sum_{j\neq i}^K \theta_{ij} - \gamma\frac{1}{K(K-1)}\sum_{i=1}^K\sum_{j\neq i}^K\left(\theta_{ij} - \frac{1}{K(K-1)}\sum_{p=1}^K\sum_{q\neq p}^K\theta_{pq}\right)^2, \tag{3.11}$$

where $\theta_{ij} = \arccos(\frac{|\mathbb{E}[\mathbf{a}_i]\cdot\mathbb{E}[\mathbf{a}_j]|}{\|\mathbb{E}[\mathbf{a}_i]\|_2\|\mathbb{E}[\mathbf{a}_j]\|_2})$ is the angle measuring the dissimilarity between $\mathbb{E}[\mathbf{a}_i]$ and $\mathbb{E}[\mathbf{a}_j]$, and the regularizer is defined as the mean of pairwise angles minus their variance. The intuition behind this regularizer is: if the mean of angles is larger (indicating these vectors are more different from each other on the whole) and the variance of the angles is smaller (indicating these vectors evenly spread out to different directions), then these vectors are more diverse.

While posterior regularization is more flexible, it lacks some strengths possessed by the prior control method. First, prior control is a more natural way of incorporating prior knowledge, with solid theoretical foundation. Second, prior control can facilitate sampling-based algorithms that are not applicable in posterior regularization.

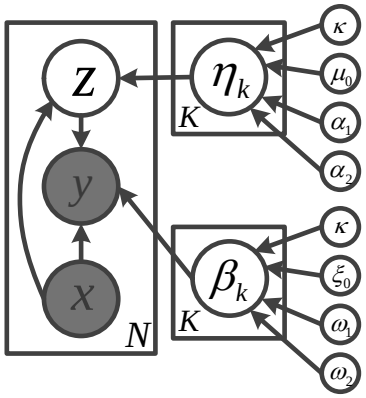

Figure 3.2: Bayesian mixture of experts with mutual angular process.

3.1.4 Case Study: Bayesian Mixture of Experts Model

In this section, we apply the two approaches developed above to "diversify" the Bayesian mixture of experts model (BMEM) [354].

BMEM with mutual angular process The mixture of experts model (MEM) [186] has been widely used for machine learning tasks where the distribution of input data is so complicated that a single model ("expert") cannot be effective for all the data. The MEM model assumes that the input data inherently belongs to multiple latent groups and one single "expert" is allocated to each group to handle the data therein. Here we consider a binary classification task. Let $\mathcal{D} = \{(\mathbf{x}_i, y_i)\}_{i=1}^N$ be the training data where $\mathbf{x}$ is the input feature vector and $y_i \in \{1, 0\}$ is the class label. MEM assumes there are K latent experts where each expert is a classifier with a coefficient vector $\boldsymbol{\beta}$. Given a test sample $\mathbf{x}$, it first goes through a gate function that decides which expert is best suitable to classify this sample and the decision is made in a probabilistic way. A discrete variable z is utilized to indicate the selected expert and the probability of assigning sample $\mathbf{x}$ to expert k ($z = k$) is $\exp(\boldsymbol{\eta}_k^\top \mathbf{x}) / \sum_{j=1}^K \exp(\boldsymbol{\eta}_j^\top \mathbf{x})$ where $\boldsymbol{\eta}_k$ is a coefficient vector characterizing the selection of expert k. Given the selected expert, the sample is classified using the coefficient vector $\boldsymbol{\beta}$ corresponding to that expert. As described in Figure 3.2, the generative process of $\{(\mathbf{x}_i, y_i)\}_{i=1}^N$ is as follows

- For $i = 1, \cdots, N$
  - Draw $z_i \sim \text{Multi}(\boldsymbol{\zeta})$, $\zeta_k = \frac{\exp(\boldsymbol{\eta}_k^\top \mathbf{x}_i)}{\sum_{j=1}^K \exp(\boldsymbol{\eta}_j^\top \mathbf{x}_i)}$
  - Draw $y_i \sim \text{Bernoulli}(\frac{1}{1+\exp(-\boldsymbol{\beta}_{z_i}^\top \mathbf{x}_i)})$

As of now, the model parameters $\mathbf{B} = \{\boldsymbol{\beta}_k\}_{k=1}^K$ and $\mathbf{H} = \{\boldsymbol{\eta}_k\}_{k=1}^K$ are deterministic variables. Next we place a prior over them to enable Bayesian learning [354] and desire this prior to be able to promote diversity among the experts to retain the advantages of "diversification" as stated

before. The mutual angular processes can be applied to achieve this goal

$$p(\mathbf{B}) = C_p(\kappa)\exp(\kappa\mu_0^\top\tilde{\boldsymbol{\beta}}_1)\prod_{i=2}^K C_p(\kappa)\exp\left(\kappa\left(-\frac{\sum_{j=1}^{i-1}\tilde{\boldsymbol{\beta}}_j}{||\sum_{j=1}^{i-1}\tilde{\boldsymbol{\beta}}_j||_2}\right)^\top\tilde{\boldsymbol{\beta}}_i\right)\prod_{i=1}^K\frac{\alpha_2^{\alpha_1}g_i^{\alpha_1-1}e^{-g_i\alpha_2}}{\Gamma(\alpha_1)}, \tag{3.12}$$

$$p(\mathbf{H}) = C_p(\kappa)\exp(\kappa\xi_0^\top\tilde{\boldsymbol{\eta}}_1)\prod_{i=2}^K C_p(\kappa)\exp\left(\kappa\left(-\frac{\sum_{j=1}^{i-1}\tilde{\boldsymbol{\eta}}_j}{||\sum_{j=1}^{i-1}\tilde{\boldsymbol{\eta}}_j||_2}\right)^\top\tilde{\boldsymbol{\eta}}_i\right)\prod_{i=1}^K\frac{\omega_2^{\omega_1}h_i^{\omega_1-1}e^{-h_i\omega_2}}{\Gamma(\omega_1)}, \tag{3.13}$$

where $\boldsymbol{\beta}_k = g_k\tilde{\boldsymbol{\beta}}_k$ and $\boldsymbol{\eta}_k = h_k\tilde{\boldsymbol{\eta}}_k$.

BMEM with diversity-promoting posterior regularization As an alternative approach, the diversity among the experts can be imposed by placing the mutual angular regularizer (Eq.(3.11)) over the post-data posteriors. The latent variables in BMEM include $\mathbf{B}$, $\mathbf{H}$, $\mathbf{z} = \{z_i\}_{i=1}^N$. The post-data distribution over them is defined as $q(\mathbf{B},\mathbf{H},\mathbf{z}) = q(\mathbf{B})q(\mathbf{H})q(\mathbf{z})$. For computational tractability, we define $q(\mathbf{B})$ and $q(\mathbf{H})$ to be: $q(\mathbf{B}) = \prod_{k=1}^K q(\tilde{\boldsymbol{\beta}}_k)q(g_k)$ and $q(\mathbf{H}) = \prod_{k=1}^K q(\tilde{\boldsymbol{\eta}}_k)q(h_k)$ where $q(\tilde{\boldsymbol{\beta}}_k)$, $q(\tilde{\boldsymbol{\eta}}_k)$ are von Mises-Fisher distributions and $q(g_k)$, $q(h_k)$ are gamma distributions, and define $q(\mathbf{z})$ to be multinomial distributions: $q(\mathbf{z}) = \prod_{i=1}^N q(z_i|\boldsymbol{\phi}_i)$ where $\boldsymbol{\phi}_i$ is a multinomial vector. The priors over $\mathbf{B}$ and $\mathbf{H}$ are specified to be: $\pi(\mathbf{B}) = \prod_{k=1}^K p(\tilde{\boldsymbol{\beta}}_k)p(g_k)$ and $\pi(\mathbf{H}) = \prod_{k=1}^K p(\tilde{\boldsymbol{\eta}}_k)p(h_k)$ where $p(\tilde{\boldsymbol{\beta}}_k)$, $p(\tilde{\boldsymbol{\eta}}_k)$ are vMF distributions and $p(g_k)$, $p(h_k)$ are gamma distributions. Under such a parameterization, we solve the following diversity-promoting posterior regularization problem

$$\begin{aligned}\sup_{q(\mathbf{B},\mathbf{H},\mathbf{z})}\ &\mathbb{E}_{q(\mathbf{B},\mathbf{H},\mathbf{z})}[\log p(\{y_i\}_{i=1}^N,\mathbf{z}|\mathbf{B},\mathbf{H})\pi(\mathbf{B},\mathbf{H})] - \mathbb{E}_{q(\mathbf{B},\mathbf{H},\mathbf{z})}[\log q(\mathbf{B},\mathbf{H},\mathbf{z})]\\ &+\lambda_1\Omega(\{\mathbb{E}_{q(\tilde{\boldsymbol{\beta}}_k)}[\tilde{\boldsymbol{\beta}}_k]\}_{k=1}^K) + \lambda_2\Omega(\{\mathbb{E}_{q(\tilde{\boldsymbol{\eta}}_k)}[\tilde{\boldsymbol{\eta}}_k]\}_{k=1}^K).\end{aligned} \tag{3.14}$$

Note that other parameterizations are also valid, such as placing Gaussian priors over $\mathbf{B}$ and $\mathbf{H}$ and setting $q(\mathbf{B})$, $q(\mathbf{H})$ to be Gaussian.

3.1.5 Evaluation

Using the Bayesian mixture of experts model as an instance, we conducted experiments to verify the effectiveness and efficiency of our proposed approaches.

Datasets We used two binary-classification datasets. The first one is the Adult-9 [275] dataset, which has ∼33K training instances and ∼16K testing instances. The feature dimension is 123. The other dataset is SUN-Building compiled from the SUN [364] dataset, which contains ∼6K building images and 7K non-building images randomly sampled from other categories, where 70% of images were used for training and the rest for testing. We used SIFT-based [236] bag-of-words to represent the images with a dimension of 1000.

Experimental settings To understand the effects of diversification in Bayesian learning, we compared with the following methods: (1) mixture of experts model (MEM) with L2 regularization (MEM-L2) where the L2 regularizer is imposed over "experts" independently; (2) MEM

K	5	10	20	30
MEM-L2	82.6	83.8	84.3	84.7
MEM-MAR [369]	85.3	86.4	86.6	87.1
BMEM-G	83.4	84.2	84.9	84.9
BMEM-DPP [429]	85.1	85.8	86.5	86.1
BMEM-MAP-I	**87.1**	**88.3**	88.6	**88.9**
BMEM-MAP-II	86.4	87.8	88.1	88.4
BMEM-PR	86.2	87.9	**88.7**	88.1

Table 3.1: Classification accuracy (%) on the Adult-9 dataset.

K	5	10	20	30
MEM-L2	76.2	78.8	79.4	79.7
MEM-MAR [369]	81.3	82.1	82.7	82.3
BMEM-G	76.5	78.6	80.2	80.4
BMEM-DPP [429]	80.4	81.6	83.7	84.5
BMEM-MAP-I	**82.1**	83.6	**85.3**	**85.2**
BMEM-MAP-II	80.9	82.8	84.9	84.1
BMEM-PR	81.7	**84.1**	83.8	84.9

Table 3.2: Classification accuracy (%) on the SUN-Building dataset.

with diversity-promoting mutual angular regularization [369] (MEM-MAR); (3) Bayesian MEM with a Gaussian prior (BMEM-G) where the "experts" are independently drawn from a Gaussian prior; (4) BMEM with a diversity-promoting determinantal point process [429] prior (BMEM-DPP); (5) BMEM with type-(I,II) mutual angular process priors (BMEM-MAP-I, BMEM-MAP-II); (6) BMEM with posterior regularization (BMEM-PR). BMEM-MAP-I was inferred with MCMC sampling and BMEM-MAP-II was inferred with variational inference. In BMEM-DPP [204], a Metropolis-Hastings sampling algorithm was adopted (variational inference and Gibbs sampling [16] are not applicable). The key parameters involved in the above methods are: (1) the regularization parameter λ in MEM-L2, MEM-MAR, and BMEM-PR; (2) the concentration parameter κ in the mutual angular processes and variational distributions; (3) the scale parameter of the radial basis function kernel in DPP. All parameters were tuned using 5-fold cross validation. Besides internal comparison, we also compared with 5 well-established classification methods achieving state of the art performance. They are: (1) kernel support vector machine (KSVM) [58]; (2) random forest (RF) [55]; (3) deep neural network (DNN) [160]; (4) infinite SVM (ISVM) [423].

Results Table 3.1 and 3.2 show the classification accuracy under different number of "experts" on the Adult-9 and SUN-Building dataset respectively. From these two tables, we observe that: (1) MAP-(I,II) outperform Gaussian, demonstrating the effectiveness of promoting diversity in Bayesian models. (2) MAP-(I,II) outperform DPP, showing their better capability in promoting diversity than DPP. (3) Bayesian learning achieves better performance than point estimation, which is manifested by comparing BMEM-G with MEM-L2, and comparing BMEM-MAP-

	Adult-9	SUN-Building
BMEM-DPP	8.2	11.7
BMEM-MAP-I	7.5	10.5
BMEM-MAP-II	2.9	4.1
BMEM-PR	3.3	4.9

Table 3.3: Training time (hours) of different methods with $K = 30$.

Category ID	C18	C17	C12	C14	C22	C34	C23	C32	C16
Number of Documents	5281	4125	1194	741	611	483	262	208	192
BMEM-G Accuracy (%)	87.3	88.5	75.7	70.1	71.6	64.2	55.9	57.4	51.3
BMEM-MAP-I Accuracy (%)	88.1	86.9	74.7	72.2	70.5	67.3	68.9	70.1	65.5
Relative Improvement (%)	1.0	-1.8	-1.3	2.9	-1.6	4.6	18.9	18.1	21.7

Table 3.4: Accuracy on 9 subcategories of the CCAT category in the RCV1.Binary dataset.

(I,II)/BMEM-PR with MEM-MAR. (4) BMEM-MAP-I works better than BMEM-MAP-II and BMEM-PR. The possible reason is that BMEM-MAP-I inferred with MCMC draws samples from the true posterior while BMEM-MAP-II and BMEM-PR inferred with variational inference (VI) seek an approximation of the posterior.

However, BMEM-MAP-II is computationally more efficient than BMEM-MAP-I. Table 3.3 compares the time (hours) taken by each method to achieve convergence, with K set to 30. BMEM-MAP-II is more efficient than BMEM-MAP-I, due to the higher efficiency of VI than MCMC. Since VI is not applicable for DPP, BMEM-DPP is inferred using MCMC sampling, hence is less efficient than BMEM-MAP-II.

To verify whether our methods can better capture infrequent patterns, from the RCV1 [220] dataset we picked up a subset of documents such that the frequencies of categories have a power-law distribution. Specifically, we chose documents from 9 subcategories (shown in the 1st row of Table 3.4) of the CCAT category as the positive instances, and randomly sampled 15K documents from non-CCAT categories as negative instances. The 2nd row shows the number of documents in each of the 9 categories. The distribution of these document frequencies is in a power-law fashion, where frequent categories (such as C18 and C17) have a lot of documents while infrequent categories (such as C32 and C16) have a small number of documents. The 3rd and 4th row show the accuracy achieved by BMEM-G and BMEM-MAP-I on each category. The 5th row shows the relative improvement of BMEM-MAP-I over BMEM-G, which is defined as $\frac{A_{map}-A_g}{A_g}$, where A_{map} and A_g denote the accuracy achieved by BMEM-MAP-I and BMEM-G respectively. While achieving accuracy comparable to BMEM-G on the frequent categories, BMEM-MAP-I obtains much better performance on the infrequent categories. For example, the relative improvements on infrequent categories C32 and C16 are 18.1% and 21.7%. This demonstrates that BMEM-MAP-I can effectively capture infrequent patterns.

Our proposed diversity-promoting methods can reduce model size without sacrificing modeling power. As can be seen from Table 3.1 and 3.2, using a smaller number of components, BMEM-MAP-(I,II) and BMEM-PR achieve accuracy that is comparable to or even better than the non-diversified BMEM-G model. For example, on the Adult-9 dataset (Table 3.2), with 5

	Adult-9	SUN-Building
KSVM [58]	85.2	84.2
RF [55]	87.7	85.1
DNN [160]	87.1	84.8
ISVM [423]	85.8	82.3
BMEM-MAP-I	**88.9**	**85.3**
BMEM-MAP-II	88.4	84.9
BMEM-PR	88.7	84.9

Table 3.5: Classification accuracy (%) on two datasets.

experts BMEM-MAP-I is able to achieve an accuracy of 87.1%, which cannot be achieved by BMEM-G with even 30 experts.

Table 3.5 presents the comparison with state of the art classification methods. Our methods outperform the baselines.

3.1.6 Appendix: Details of Algorithms

Variational Inference for Type I MAP

In this section, we present details on how to derive the variational lower bound

$$\mathbb{E}_{q(\mathbf{A})}[\log p(\mathcal{D}|\mathbf{A})] + \mathbb{E}_{q(\mathbf{A})}[\log p(\mathbf{A})] - \mathbb{E}_{q(\mathbf{A})}[\log q(\mathbf{A})], \tag{3.15}$$

where the variational distribution $q(\mathbf{A})$ is chosen to be

$$q(\mathbf{A}) = \textstyle\prod_{k=1}^{K} q(\tilde{\mathbf{a}}_k)q(g_k) = \prod_{k=1}^{K} \text{vMF}(\tilde{\mathbf{a}}_k|\hat{\mathbf{a}}_k, \hat{\kappa})\text{Gamma}(g_k|r_k, s_k). \tag{3.16}$$

Among the three expectation terms, $\mathbb{E}_{q(\mathbf{A})}[\log p(\mathbf{A})]$ and $\mathbb{E}_{q(\mathbf{A})}[\log q(\mathbf{A})]$ are model-independent and we discuss how to compute them in this section. $\mathbb{E}_{q(\mathbf{A})}[\log p(\mathcal{D}|\mathbf{A})]$ depends on the specific model and a concrete example will be given later on.

First we introduce some equalities and inequalities. Let $\mathbf{a} \sim \text{vMF}(\boldsymbol{\mu}, \kappa)$, then
(I) $\mathbb{E}[\mathbf{a}] = A_p(\kappa)\boldsymbol{\mu}$ where $A_p(\kappa) = \frac{I_{p/2}(\kappa)}{I_{p/2-1}(\kappa)}$, and $I_v(\cdot)$ denotes the modified Bessel function of the first kind at order v.
(II) $\text{cov}(\mathbf{a}) = \frac{h(\kappa)}{\kappa}\mathbf{I} + (1 - 2\frac{\nu+1}{\kappa}h(\kappa) - h^2(\kappa))\boldsymbol{\mu}\boldsymbol{\mu}^T$, where $h(\kappa) = \frac{I_{\nu+1}(\kappa)}{I_\nu(\kappa)}$ and $\nu = p/2 - 1$.
Please refer to [15] for the derivation of $\mathbb{E}[\mathbf{a}]$ and $\text{cov}(\mathbf{a})$.
(III) $\mathbb{E}[\mathbf{a}^T\mathbf{a}] = \text{tr}(\text{cov}(\mathbf{a})) + A_p^2(\kappa)\boldsymbol{\mu}^T\boldsymbol{\mu}$.

Proof

$$\begin{aligned} &\mathbb{E}[\text{tr}(\mathbf{a}^T\mathbf{a})] = \mathbb{E}[\text{tr}(\mathbf{a}\mathbf{a}^T)] = \text{tr}(\mathbb{E}[\mathbf{a}\mathbf{a}^T]) \\ &= \text{tr}(\text{cov}(\mathbf{a}) + \mathbb{E}[\mathbf{a}]\mathbb{E}[\mathbf{a}]^T) = \text{tr}(\text{cov}(\mathbf{a})) + \text{tr}(\mathbb{E}[\mathbf{a}]\mathbb{E}[\mathbf{a}]^T) \\ &= \text{tr}(\text{cov}(\mathbf{a})) + A_p^2(\kappa)\boldsymbol{\mu}^T\boldsymbol{\mu} \end{aligned} \tag{3.17}$$

Let $g \sim \text{Gamma}(\alpha, \beta)$, then
(IV) $\mathbb{E}[g] = \frac{\alpha}{\beta}$.

(V) $\mathbb{E}[\log g] = \psi(\alpha) - \log\beta$.
(VI) $\log\sum_{k=1}^{K}\exp(x_k) \leq \gamma + \sum_{k=1}^{K}\log(1+\exp(x_k-\gamma))$ and $\log\int\exp(x)\mathrm{d}x \leq \gamma + \int\log(1+\exp(x-\gamma))\mathrm{d}x$, where γ is a variational parameter. See [50] for the proof.
(VII) $\log(1+e^{-x}) \leq \log(1+e^{-\xi}) - \frac{x-\xi}{2} - \frac{1/2-g(\xi)}{2\xi}(x^2-\xi^2)$, $\log(1+e^x) \leq \log(1+e^{\xi}) + \frac{x-\xi}{2} - \frac{1/2-g(\xi)}{2\xi}(x^2-\xi^2)$, where ξ is a variational parameter and $g(\xi) = 1/(1+\exp(-\xi))$. See [50] for the proof.
(VIII) $\int_{\|\mathbf{y}\|_2=1} 1\mathrm{d}\mathbf{y} = \frac{2\pi^{(p+1)/2}}{\Gamma(\frac{p+1}{2})}$, which is the surface area of the p-dimensional unit sphere. $\Gamma(\cdot)$ is the gamma function.
(IX) $\int_{\|\mathbf{y}\|_2=1}\mathbf{x}^T\mathbf{y}\mathrm{d}\mathbf{y} = 0$, which can be shown according to the symmetry of the unit sphere.
(X) $\int_{\|\mathbf{y}\|_2=1}(\mathbf{x}^T\mathbf{y})^2\mathrm{d}\mathbf{y} \leq \|\mathbf{x}\|_2^2\frac{2\pi^{(p+1)/2}}{\Gamma(\frac{p+1}{2})}$.

Proof

$$\begin{aligned}
&\int_{\|\mathbf{y}\|_2=1}(\mathbf{x}^T\mathbf{y})^2\mathrm{d}\mathbf{y}\\
&= \|\mathbf{x}\|_2^2\int_{\|\mathbf{y}\|_2=1}((\tfrac{\mathbf{x}}{\|\mathbf{x}\|_2})^T\mathbf{y})^2\mathrm{d}\mathbf{y}\\
&= \|\mathbf{x}\|_2^2\int_{\|\mathbf{y}\|_2=1}(\mathbf{e}_1^T\mathbf{y})^2\mathrm{d}\mathbf{y}\\
&\quad \text{(according to the symmetry of unit sphere)}\\
&\leq \|\mathbf{x}\|_2^2\int_{\|\mathbf{y}\|_2=1}1\mathrm{d}\mathbf{y}\\
&= \|\mathbf{x}\|_2^2\frac{2\pi^{(p+1)/2}}{\Gamma(\frac{p+1}{2})}
\end{aligned} \tag{3.18}$$

Given these equalities and inequalities, we can upper bound $\log Z_i$ and use this upper bound to lower-bound $\mathbb{E}_{q(\mathbf{A})}[\log p(\mathbf{A})]$

$$\begin{aligned}
&\mathbb{E}_{q(\mathbf{A})}[\log p(\mathbf{A})]\\
&= \mathbb{E}_{q(\mathbf{A})}[\log p(\tilde{\mathbf{a}}_1)\textstyle\prod_{i=2}^{K}p(\tilde{\mathbf{a}}_i|\{\tilde{\mathbf{a}}_j\}_{j=1}^{i-1})\prod_{i=1}^{K}q(g_i)]\\
&= \mathbb{E}_{q(\mathbf{A})}[\log p(\tilde{\mathbf{a}}_1)\prod_{i=2}^{K}\tfrac{\exp(\kappa(-\sum_{j=1}^{i-1}\tilde{\mathbf{a}}_j)\cdot\tilde{\mathbf{a}}_i)}{Z_i}\prod_{i=1}^{K}\tfrac{\alpha_2^{\alpha_1}g_i^{\alpha_1-1}e^{-g_i\alpha_2}}{\Gamma(\alpha_1)}]\\
&\geq \kappa\mu_0^{\mathsf{T}}\mathbb{E}_{q(\tilde{\mathbf{a}}_1)}[\tilde{\mathbf{a}}_1] + \textstyle\sum_{i=2}^{K}(-\kappa\sum_{j=1}^{i-1}\mathbb{E}_{q(\tilde{\mathbf{a}}_j)}[\tilde{\mathbf{a}}_j]\cdot\mathbb{E}_{q(\tilde{\mathbf{a}}_i)}[\tilde{\mathbf{a}}_i] \quad - \gamma_i - (\log(1+e^{-\xi_i}) + \tfrac{\xi_i-\gamma_i}{2}\\
&\quad + \tfrac{1/2-g(\xi_i)}{2\xi_i}(\xi_i^2-\gamma_i^2))\tfrac{2\pi^{(p+1)/2}}{\Gamma(\frac{p+1}{2})} + \tfrac{1/2-g(\xi_i)}{2\xi_i}\kappa^2\mathbb{E}_{q(\mathbf{A})}[\|\textstyle\sum_{j=1}^{i-1}\tilde{\mathbf{a}}_j\|_2^2]\tfrac{2\pi^{(p+1)/2}}{\Gamma(\frac{p+1}{2})}) + K(\alpha_1\log\alpha_2\\
&\quad - \log\Gamma(\alpha_1)) + \sum_{i=1}^{K}(\alpha_1-1)\mathbb{E}_{q(g_i)}[\log g_i] - \alpha_2\mathbb{E}_{q(g_i)}[g_i] + \text{const}\\
&\geq \kappa A_p(\hat{\kappa})\mu_0^{\mathsf{T}}\hat{\mathbf{a}}_1 + \textstyle\sum_{i=2}^{K}(-\kappa A_p(\hat{\kappa})^2\sum_{j=1}^{i-1}\hat{\mathbf{a}}_j\cdot\hat{\mathbf{a}}_i - \gamma_i - (\log(1+e^{-\xi_i}) + \tfrac{\xi_i-\gamma_i}{2}\\
&\quad + \tfrac{1/2-g(\xi_i)}{2\xi_i}(\xi_i^2-\gamma_i^2))\tfrac{2\pi^{(p+1)/2}}{\Gamma(\frac{p+1}{2})} + \tfrac{1/2-g(\xi_i)}{2\xi_i}\kappa^2(A_p^2(\hat{\kappa})\textstyle\sum_{j=1}^{i-1}\sum_{k\neq j}^{i-1}\hat{\mathbf{a}}_j\cdot\hat{\mathbf{a}}_k + \sum_{j=1}^{i-1}(\mathrm{tr}(\Lambda_j)\\
&\quad + A_p^2(\hat{\kappa})\hat{\mathbf{a}}_j^T\hat{\mathbf{a}}_j))\tfrac{2\pi^{(p+1)/2}}{\Gamma(\frac{p+1}{2})}) + K(\alpha_1\log\alpha_2 - \log\Gamma(\alpha_1)) + \textstyle\sum_{i=1}^{K}(\alpha_1-1)(\psi(r_i)-\log(s_i)) - \alpha_2\frac{r_i}{s_i} + \text{const},
\end{aligned} \tag{3.19}$$

where $\Lambda_j = \frac{h(\hat{\kappa})}{\hat{\kappa}}\mathbf{I} + (1 - 2\frac{\nu+1}{\hat{\kappa}}h(\hat{\kappa}) - h^2(\hat{\kappa}))\hat{\mathbf{a}}_j\hat{\mathbf{a}}_j^T$.

The other expectation term $\mathbb{E}_{q(\mathbf{A})}[\log q(\mathbf{A})]$ can be computed as

$$\begin{aligned}
&\mathbb{E}_{q(\mathbf{A})}[\log q(\mathbf{A})]\\
&= \mathbb{E}_{q(\mathbf{A})}[\log\prod_{k=1}^{K}\text{vMF}(\tilde{\mathbf{a}}_k|\hat{\mathbf{a}}_k,\hat{\kappa})\text{Gamma}(g_k|r_k,s_k)]\\
&= \sum_{k=1}^{K}\hat{\kappa}A_p(\hat{\kappa})\|\hat{\alpha}_k\|_2^2 + r_k\log s_k - \log\Gamma(r_k) + (r_k-1)(\psi(r_k)-\log(s_k)) - r_k.
\end{aligned} \tag{3.20}$$

Variational Inference for BMEM-MAP-II

In this section, we discuss how to derive the variational lower bound for BMEM-MAP-II. The latent variables are $\{\boldsymbol{\beta}_k\}_{k=1}^K$, $\{\boldsymbol{\eta}_k\}_{k=1}^K$, and $\{z_n\}_{n=1}^N$. The joint distribution of all variables is

$$\begin{aligned}&p(\{\boldsymbol{\beta}_k\}_{k=1}^K, \{\boldsymbol{\eta}_k\}_{k=1}^K, \{\mathbf{x}_n, y_n, z_n\}_{n=1}^N)\\&= p(\{y_n\}_{n=1}^N|\{\mathbf{x}_n\}_{n=1}^N, \{z_n\}_{n=1}^N, \{\boldsymbol{\beta}_k\}_{k=1}^K)p(\{z_n\}_{n=1}^N|\{\mathbf{x}_n\}_{n=1}^N, \{\boldsymbol{\eta}_k\}_{k=1}^K)p(\{\boldsymbol{\beta}_k\}_{k=1}^K)p(\{\boldsymbol{\eta}_k\}_{k=1}^K).\end{aligned} \tag{3.21}$$

To perform variational inference, we employ a mean field variational distribution

$$\begin{aligned}Q &= q(\{\boldsymbol{\beta}_k\}_{k=1}^K, \{\boldsymbol{\eta}_k\}_{k=1}^K, \{z_n\}_{n=1}^N)\\&= \prod_{k=1}^K q(\boldsymbol{\beta}_k)q(\boldsymbol{\eta}_k) \prod_{n=1}^N q(z_n)\\&= \prod_{k=1}^K \text{vMF}(\tilde{\boldsymbol{\beta}}_k|\hat{\boldsymbol{\beta}}_k, \hat{\kappa})\text{Gamma}(g_k|r_k, s_k)\text{vMF}(\tilde{\boldsymbol{\eta}}_k|\hat{\boldsymbol{\eta}}_k, \hat{\kappa})\text{Gamma}(h_k|t_k, u_k) \prod_{n=1}^N q(z_n|\boldsymbol{\phi}_n).\end{aligned} \tag{3.22}$$

Accordingly, the variational lower bound is

$$\begin{aligned}&\mathbb{E}_Q[\log p(\{\boldsymbol{\beta}_k\}_{k=1}^K, \{\boldsymbol{\eta}_k\}_{k=1}^K, \{\mathbf{x}_n, y_n, z_n\}_{n=1}^N)] - \mathbb{E}_Q[\log q(\{\boldsymbol{\beta}_k\}_{k=1}^K, \{\boldsymbol{\eta}_k\}_{k=1}^K, \{z_n\}_{n=1}^N)]\\&= \mathbb{E}_Q[\log p(\{y_n\}_{n=1}^N|\{\mathbf{x}_n\}_{n=1}^N, \{z_n\}_{n=1}^N, \{\boldsymbol{\beta}_k\}_{k=1}^K)] + \mathbb{E}_Q[\log p(\{z_n\}_{n=1}^N|\{\mathbf{x}_n\}_{n=1}^N, \{\boldsymbol{\eta}_k\}_{k=1}^K)]\\&+\mathbb{E}_Q[\log p(\{\boldsymbol{\beta}_k\}_{k=1}^K)]) + \mathbb{E}_Q[\log p(\{\boldsymbol{\eta}_k\}_{k=1}^K)]) - \mathbb{E}_Q[\log q(\{\boldsymbol{\beta}_k\}_{k=1}^K)] - \mathbb{E}_Q[\log q(\{\boldsymbol{\eta}_k\}_{k=1}^K)]\\&-\mathbb{E}_Q[\log q(\{z_n\}_{n=1}^N)],\end{aligned} \tag{3.23}$$

where $\mathbb{E}_Q[\log p(\{\boldsymbol{\beta}_k\}_{k=1}^K)]$ and $\mathbb{E}_Q[\log p(\{\boldsymbol{\eta}_k\}_{k=1}^K)]$ can be lower bounded in a similar way as that in Eq.(3.19). $\mathbb{E}_Q[\log q(\{\boldsymbol{\beta}_k\}_{k=1}^K)]$ and $\mathbb{E}_Q[\log q(\{\boldsymbol{\eta}_k\}_{k=1}^K)]$ can be computed in a similar manner as that in Eq.(3.20). Next we discuss how to compute the remaining expectation terms.

Compute $\mathbb{E}_Q[\log p(\{z_n\}_{n=1}^N|\{\boldsymbol{\eta}_k\}_{k=1}^K, \{\mathbf{x}_n\}_{n=1}^N)]$ First, $p(\{z_n\}_{n=1}^N|\{\boldsymbol{\eta}_k\}_{k=1}^K, \{\mathbf{x}_n\}_{n=1}^N)$ is defined as

$$\begin{aligned}&p(\{z_n\}_{n=1}^N|\{\boldsymbol{\eta}_k\}_{k=1}^K, \{\mathbf{x}_n\}_{n=1}^N)\\&= \prod_{n=1}^N p(z_n|\mathbf{x}_n, \{\boldsymbol{\eta}_k\}_{k=1}^K)\\&= \prod_{n=1}^N \frac{\prod_{k=1}^K [\exp(\boldsymbol{\eta}_k^\intercal \mathbf{x}_n)]^{z_{nk}}}{\sum_{j=1}^K \exp(\boldsymbol{\eta}_j^\intercal \mathbf{x}_n)}.\end{aligned} \tag{3.24}$$

$\log p(\{z_n\}_{n=1}^N|\{\boldsymbol{\eta}_k\}_{k=1}^K, \{\mathbf{x}_n\}_{n=1}^N)$ can be lower bounded as

$$\begin{aligned}
&\log p(\{z_n\}_{n=1}^N|\{\boldsymbol{\eta}_k\}_{k=1}^K, \{\mathbf{x}_n\}_{n=1}^N) \\
&= \sum_{n=1}^N \sum_{k=1}^K z_{nk}\boldsymbol{\eta}_k^\mathsf{T}\mathbf{x}_n - \log(\textstyle\sum_{j=1}^K \exp(\boldsymbol{\eta}_j^\mathsf{T}\mathbf{x}_n)) \\
&= \sum_{n=1}^N \sum_{k=1}^K z_{nk}h_k\tilde{\boldsymbol{\eta}}_k^\mathsf{T}\mathbf{x}_n - \log(\textstyle\sum_{j=1}^K \exp(\boldsymbol{\eta}_j^\mathsf{T}\mathbf{x}_n)) \\
&\geq \sum_{n=1}^N \sum_{k=1}^K z_{nk}h_k\tilde{\boldsymbol{\eta}}_k^\mathsf{T}\mathbf{x}_n - c_n - \textstyle\sum_{j=1}^K \quad \log(1+\exp(\boldsymbol{\eta}_j^\mathsf{T}\mathbf{x}_n - c_n)) \text{(Using Inequality VI)} \\
&\geq \sum_{n=1}^N \sum_{k=1}^K z_{nk}h_k\tilde{\boldsymbol{\eta}}_k^\mathsf{T}\mathbf{x}_n - c_n - \textstyle\sum_{j=1}^K [\log(1+e^{-d_{nj}}) - \frac{c_n - \boldsymbol{\eta}_j^\mathsf{T}\mathbf{x}_n - d_{nj}}{2} - \frac{1/2-g(d_{nj})}{2d_{nj}}((\boldsymbol{\eta}_j^\mathsf{T}\mathbf{x}_n - c_n)^2 - d_{nj}^2)] \\
&\quad \text{(Using Inequality VII)}
\end{aligned} \tag{3.25}$$

The expectation of $\log p(\{z_n\}_{n=1}^N|\{\boldsymbol{\eta}_k\}_{k=1}^K, \{\mathbf{x}_n\}_{n=1}^N)$ can be lower bounded as

$$\begin{aligned}
&\mathbb{E}[\log p(\{z_n\}_{n=1}^N|\{\boldsymbol{\eta}_k\}_{k=1}^K, \{\mathbf{x}_n\}_{n=1}^N)] \\
&= A_p(\hat{\kappa}) \sum_{n=1}^N \sum_{k=1}^K \phi_{nk}\tfrac{t_k}{u_k}\hat{\boldsymbol{\eta}}_k^\mathsf{T}\mathbf{x}_n - c_n - \textstyle\sum_{j=1}^K [\log(1+e^{-d_{nj}}) - (c_n - A_p(\hat{\kappa})\tfrac{t_j}{u_j}\hat{\boldsymbol{\eta}}_j^\mathsf{T}\mathbf{x}_n - d_{nj})/2 \\
&- \tfrac{1/2-g(d_{nj})}{2d_{nj}}(\tfrac{t_j+t_j^2}{u_j^2}\mathbb{E}[\tilde{\boldsymbol{\eta}}_j^\mathsf{T}\mathbf{x}_n\mathbf{x}_n^\mathsf{T}\tilde{\boldsymbol{\eta}}_j] - 2c_nA_p(\hat{\kappa})\tfrac{t_j}{u_j}\hat{\boldsymbol{\eta}}_j^\mathsf{T}\mathbf{x}_n + c_n^2 - d_{nj}^2)],
\end{aligned} \tag{3.26}$$

where

$$\begin{aligned}
&\mathbb{E}[\tilde{\boldsymbol{\eta}}_k^\mathsf{T}\mathbf{x}_n\mathbf{x}_n^\mathsf{T}\tilde{\boldsymbol{\eta}}_k] \\
&= \mathbb{E}[\mathrm{tr}(\tilde{\boldsymbol{\eta}}_k^\mathsf{T}\mathbf{x}_n\mathbf{x}_n^\mathsf{T}\tilde{\boldsymbol{\eta}}_k)] \\
&= \mathbb{E}[\mathrm{tr}(\mathbf{x}_n\mathbf{x}_n^\mathsf{T}\tilde{\boldsymbol{\eta}}_k\tilde{\boldsymbol{\eta}}_k^\mathsf{T})] \\
&= \mathrm{tr}(\mathbf{x}_n\mathbf{x}_n^\mathsf{T}\mathbb{E}[\tilde{\boldsymbol{\eta}}_k\tilde{\boldsymbol{\eta}}_k^\mathsf{T}]) \\
&= \mathrm{tr}(\mathbf{x}_n\mathbf{x}_n^\mathsf{T}(\mathbb{E}[\tilde{\boldsymbol{\eta}}_k]\mathbb{E}[\tilde{\boldsymbol{\eta}}_k]^T + \mathrm{cov}(\tilde{\boldsymbol{\eta}}_k))).
\end{aligned} \tag{3.27}$$

Compute $\mathbb{E}[\log p(\{y_n\}_{n=1}^N|\{\boldsymbol{\beta}_k\}_{k=1}^K, \{\mathbf{z}_n\}_{n=1}^N)]$ $p(\{y_n\}_{n=1}^N|\{\boldsymbol{\beta}_k\}_{k=1}^K, \{\mathbf{z}_n\}_{n=1}^N)$ is defined as

$$\begin{aligned}
&p(\{y_n\}_{n=1}^N|\{\boldsymbol{\beta}_k\}_{k=1}^K, \{\mathbf{z}_n\}_{n=1}^N) \\
&= \prod_{n=1}^N p(y_n|\mathbf{z}_n, \{\boldsymbol{\beta}_k\}_{k=1}^K) \\
&= \prod_{n=1}^N \frac{1}{\prod_{k=1}^K [1+\exp(-(2y_n-1)\boldsymbol{\beta}_k^\mathsf{T}\mathbf{x}_n)]^{z_{nk}}}.
\end{aligned} \tag{3.28}$$

$\log p(\{y_n\}_{n=1}^N|\{\boldsymbol{\beta}_k\}_{k=1}^K, \{\mathbf{z}_n\}_{n=1}^N)$ can be lower bounded by

$$\begin{aligned}
&\log p(\{y_n\}_{n=1}^N|\{\boldsymbol{\beta}_k\}_{k=1}^K, \{\mathbf{z}_n\}_{n=1}^N) \\
&= -\sum_{n=1}^N \sum_{k=1}^K z_{nk}\log(1+\exp(-(2y_n-1)\boldsymbol{\beta}_k^\mathsf{T}\mathbf{x}_n)) \\
&\geq \sum_{n=1}^N \sum_{k=1}^K z_{nk}[-\log(1+e^{-e_{nk}}) + ((2y_n-1)\boldsymbol{\beta}_k^\mathsf{T}\mathbf{x}_n - e_{nk})/2 + \tfrac{1/2-g(e_{nk})}{2e_{nk}}((\boldsymbol{\beta}_k^\mathsf{T}\mathbf{x}_n)^2 - e_{nk}^2)].
\end{aligned} \tag{3.29}$$

$\mathbb{E}[\log p(\{y_n\}_{n=1}^N|\{\boldsymbol{\beta}_k\}_{k=1}^K, \{\mathbf{z}_n\}_{n=1}^N)]$ can be lower bounded by

$$\begin{aligned}&\mathbb{E}[\log p(\{y_n\}_{n=1}^N|\{\boldsymbol{\beta}_k\}_{k=1}^K, \{\mathbf{z}_n\}_{n=1}^N)]\\&\geq \sum_{n=1}^{N}\sum_{k=1}^{K}\phi_{nk}[-\log(1+e^{-e_{nk}}) + (A_p(\hat{\kappa})\frac{r_k}{s_k}\hat{\boldsymbol{\beta}}_k^\mathsf{T}\mathbf{x}_n - e_{nk})/2 + \frac{1/2-\sigma(e_{nk})}{2e_{nk}}(\frac{r_k+r_k^2}{s_k^2}\mathbb{E}[\tilde{\boldsymbol{\beta}}_k^\mathsf{T}\mathbf{x}_n\mathbf{x}_n^\mathsf{T}\tilde{\boldsymbol{\beta}}_k] - e_{nk}^2)]\\&\text{(Using Inequality VII)}\end{aligned} \tag{3.30}$$

where $\mathbb{E}[\tilde{\boldsymbol{\beta}}_k^\mathsf{T}\mathbf{x}_n\mathbf{x}_n^\mathsf{T}\tilde{\boldsymbol{\beta}}_k]$ can be computed in a similar way as that in Eq.(3.27).

Compute $\mathbb{E}[\log q(z_i)]$

$$\mathbb{E}[\log q(z_i)] = \sum_{k=1}^{K}\phi_{ik}\log\phi_{ik}. \tag{3.31}$$

In the end, we can get a lower bound of the variational lower bound, then learn all the parameters by optimizing the lower bound via coordinate ascent. In each iteration, we select one parameter x and fix all other parameters, which leads to a sub-problem defined over x. Then we optimize the sub-problem w.r.t x. For some parameters, the optimal solution of the sub-problem is in closed form. If not the case, we optimize x using the gradient ascent method. This process iterates until convergence. We omit the detailed derivation here since it only involves basic algebra and calculus, which can be done straightforwardly.

MCMC Sampling for Type-I MAP

The type-I MAP prior is not amenable for variational inference. Instead, we use an alternative approximation inference method — Markov chain Monte Carlo (MCMC) [127] sampling, which draws samples directly from the true posterior distribution and uses the samples to represent the posterior. Specifically we choose the Metropolis-Hastings (MH) algorithm [127] which generates samples from an adaptive proposal distribution, computes acceptance probabilities based on the unnormalized true posterior, and uses the acceptance probabilities to decide whether a sample should be accepted or rejected. The most commonly used proposal distribution is based on the random walk: the newly proposed sample $t+1$ comes from a random perturbation around the previous sample t. For the directional variables $\{\tilde{\mathbf{a}}_i\}_{i=1}^K$ and magnitude variables $\{g_i\}_{i=1}^K$, we define the proposal distributions to be a von Mises-Fisher distribution and a normal distribution respectively:

$$\begin{aligned}q(\tilde{\mathbf{a}}_i^{(t+1)}|\tilde{\mathbf{a}}_i^{(t)}) &= C_p(\hat{\kappa})\exp\left(\hat{\kappa}\tilde{\mathbf{a}}_i^{(t+1)}\cdot\tilde{\mathbf{a}}_i^{(t)}\right)\\q(g_i^{(t+1)}|g_i^{(t)}) &= \frac{1}{\sigma\sqrt{2\pi}}\exp\left\{-\frac{(g_i^{(t+1)}-g_i^{(t)})^2}{2\sigma^2}\right\}.\end{aligned} \tag{3.32}$$

$g_i^{(t+1)}$ is required to be positive, but the Gaussian distribution may generate non-positive samples. To address this problem, we adopt a truncated sampler [360] which repeatedly draws samples until a positive value is obtained. Under such a truncated sampling scheme, the MH acceptance ratio needs to be modified accordingly.

The MAP is parameterized by several deterministic parameters including κ, $\boldsymbol{\mu}_0$, α_1, α_2. Among them, we tune κ manually via cross validation and learn the others via an expectation

maximization (EM) framework. Let $\mathbf{x}$ denote the observed data, $\mathbf{z}$ denote all random variables, and $\boldsymbol{\theta}$ denote the deterministic parameters $\{\boldsymbol{\mu}_0, \alpha_1, \alpha_2\}$. EM is an algorithm aiming at learning $\boldsymbol{\theta}$ by maximizing the log-likelihood $p(\mathbf{x}; \boldsymbol{\theta})$ of data. It iteratively performs two steps until convergence. In the E step, $\boldsymbol{\theta}$ is fixed and the posterior $p(\mathbf{z}|\mathbf{x})$ is inferred using the aforementioned Metropolis-Hastings algorithm. In the M step, $\boldsymbol{\theta}$ is learned by optimizing a lower bound of the log-likelihood $\mathbb{E}_{p(\mathbf{z}|\mathbf{x})}[\log p(\mathbf{x}, \mathbf{z}; \boldsymbol{\theta})]$, where the expectation is computed w.r.t the posterior $p(\mathbf{z}|\mathbf{x})$ inferred in the E step. The parameters $\hat{\kappa}$ and σ in the proposal distributions are tuned manually.

Algorithm for Posterior-Regularized BMEM

In this section, we present the algorithm details of the posterior-regularized BMEM. Recall that the problem is

$$\begin{aligned}\sup_{q(\mathbf{B},\mathbf{H},\mathbf{z})} \mathbb{E}_{q(\mathbf{B},\mathbf{H},\mathbf{z})}[\log p(\{y_i\}_{i=1}^N, \mathbf{z}|\mathbf{B}, \mathbf{H})\pi(\mathbf{B}, \mathbf{H})] - \mathbb{E}_{q(\mathbf{B},\mathbf{H},\mathbf{z})}[\log q(\mathbf{B}, \mathbf{H}, \mathbf{z})] \\ +\lambda_1 \Omega(\{\mathbb{E}_{q(\tilde{\boldsymbol{\beta}}_k)}[\tilde{\boldsymbol{\beta}}_k]\}_{k=1}^K) + \lambda_2 \Omega(\{\mathbb{E}_{q(\tilde{\boldsymbol{\eta}}_k)}[\tilde{\boldsymbol{\eta}}_k]\}_{k=1}^K),\end{aligned} \tag{3.33}$$

where $\mathbf{B} = \{\boldsymbol{\beta}_k\}_{k=1}^K$, $\mathbf{H} = \{\boldsymbol{\eta}_k\}_{k=1}^K$, and $\mathbf{z} = \{z_i\}_{i=1}^N$ are latent variables and the post-data distribution over them is defined as $q(\mathbf{B}, \mathbf{H}, \mathbf{z}) = q(\mathbf{B})q(\mathbf{H})q(\mathbf{z})$. For computational tractability, we define $q(\mathbf{B})$ and $q(\mathbf{H})$ to be: $q(\mathbf{B}) = \prod_{k=1}^K q(\tilde{\boldsymbol{\beta}}_k)q(g_k)$ and $q(\mathbf{H}) = \prod_{k=1}^K q(\tilde{\boldsymbol{\eta}}_k)q(h_k)$ where $q(\tilde{\boldsymbol{\beta}}_k)$, $q(\tilde{\boldsymbol{\eta}}_k)$ are von-Mises Fisher distributions and $q(g_k)$, $q(h_k)$ are gamma distributions, and define $q(\mathbf{z})$ to be multinomial distributions: $q(\mathbf{z}) = \prod_{i=1}^N q(z_i|\boldsymbol{\phi}_i)$ where $\boldsymbol{\phi}_i$ is a multinomial vector. The priors over $\mathbf{B}$ and $\mathbf{H}$ are specified to be: $\pi(\mathbf{B}) = \prod_{k=1}^K p(\tilde{\boldsymbol{\beta}}_k)p(g_k)$ and $\pi(\mathbf{H}) = \prod_{k=1}^K p(\tilde{\boldsymbol{\eta}}_k)p(h_k)$ where $p(\tilde{\boldsymbol{\beta}}_k)$, $p(\tilde{\boldsymbol{\eta}}_k)$ are von-Mises Fisher distributions and $p(g_k)$, $p(h_k)$ are gamma distributions.

The objective in Eq.(3.33) can be further written as

$$\begin{aligned}&\mathbb{E}_{q(\mathbf{B},\mathbf{H},\mathbf{z})}[\log p(\{y_i\}_{i=1}^N, \mathbf{z}|\mathbf{B}, \mathbf{H})\pi(\mathbf{B}, \mathbf{H})] - \mathbb{E}_{q(\mathbf{B},\mathbf{H},\mathbf{z})}[\log q(\mathbf{B}, \mathbf{H}, \mathbf{z})] + \lambda_1 \Omega(\{\mathbb{E}_{q(\tilde{\boldsymbol{\beta}}_k)}[\tilde{\boldsymbol{\beta}}_k]\}_{k=1}^K) \\ &+\lambda_2 \Omega(\{\mathbb{E}_{q(\tilde{\boldsymbol{\eta}}_k)}[\tilde{\boldsymbol{\eta}}_k]\}_{k=1}^K) \\ =&\mathbb{E}_{q(\mathbf{B},\mathbf{z})}[\log p(\{y_i\}_{i=1}^N|\mathbf{z}, \mathbf{B})] + \mathbb{E}_{q(\mathbf{H},\mathbf{z})}[\log p(\mathbf{z}|\mathbf{H})] + \mathbb{E}_{q(\mathbf{H})}[\log \pi(\mathbf{H})] + \mathbb{E}_{q(\mathbf{B})}[\log \pi(\mathbf{B})] \\ &-\mathbb{E}_{q(\mathbf{B})}[\log q(\mathbf{B})] - \mathbb{E}_{q(\mathbf{H})}[\log q(\mathbf{H})] - \mathbb{E}_{q(\mathbf{z})}[\log q(\mathbf{z})] + \lambda_1 \Omega(\{\mathbb{E}_{q(\tilde{\boldsymbol{\beta}}_k)}[\tilde{\boldsymbol{\beta}}_k]\}_{k=1}^K) \\ &+\lambda_2 \Omega(\{\mathbb{E}_{q(\tilde{\boldsymbol{\eta}}_k)}[\tilde{\boldsymbol{\eta}}_k]\}_{k=1}^K).\end{aligned} \tag{3.34}$$

Among these expectation terms, $\mathbb{E}_{q(\mathbf{B},\mathbf{z})}[\log p(\{y_i\}_{i=1}^N|\mathbf{z}, \mathbf{B})]$ can be computed via Eq.(3.28-3.30) and $\mathbb{E}_{q(\mathbf{H},\mathbf{z})}[\log p(\mathbf{z}|\mathbf{H})]$ can be computed via Eq.(3.24-3.27). $\mathbb{E}_{q(\mathbf{H})}[\log \pi(\mathbf{H})]$, $\mathbb{E}_{q(\mathbf{B})}[\log \pi(\mathbf{B})]$, $\mathbb{E}_{q(\mathbf{B})}[\log q(\mathbf{B})]$, $\mathbb{E}_{q(\mathbf{H})}[\log q(\mathbf{H})]$ can be computed in a way similar to that in Eq.(3.20). $\mathbb{E}_{q(\mathbf{z})}[\log q(\mathbf{z})]$ can be computed via Eq.(3.31). Given all these expectations, we can get an analytical expression of the objective in Eq.(3.33) and learn the parameters by optimizing this objective. Regarding how to optimize the mutual angular regularizers $\Omega(\{\mathbb{E}_{q(\tilde{\boldsymbol{\beta}}_k)}[\tilde{\boldsymbol{\beta}}_k]\}_{k=1}^K)$ and $\Omega(\{\mathbb{E}_{q(\tilde{\boldsymbol{\eta}}_k)}[\tilde{\boldsymbol{\eta}}_k]\}_{k=1}^K)$, please refer to [369] for details.

3.2 Diversity-promoting Learning of Bayesian Nonparametric Models

In the last section, we study how to promote diversity among a finite number of components in parametric models. In this section, we investigate how to achieve this goal in Bayesian nonparametric (BNP) [111] models where the component number is infinite in principle, by extending the mutual angular process (Section 3.1.1) to an *infinite MAP* (IMAP).

Different from parametric models where the component number is set to an finite value and does not change throughout the entire execution of algorithm, in BNP models the number of components is unlimited and can reach infinite in principle. As more data accumulates, new components are dynamically added. Compared with parametric models, BNP models possess the following advantages: (1) they are highly flexible and adaptive: if new data cannot be well modeled by existing components, new components are automatically invoked; (2) in BNP models, the "best" number of components is determined according to the fitness to data, rather than being manually set which is a challenging task even for domain experts.

A BNP model consists of an infinite number of components, each parameterized by a vector. For example, in the Dirichlet process Gaussian mixture model (DP-GMM) [48, 286], the components are called *clusters*, each parameterized with a Gaussian mean vector. In the Indian buffet process latent feature model (IBP-LFM) [143], the components are called *features*, each parameterized by a weight vector. Given infinitely many components, BNP models design some proper mechanism to select one or a finite subset of components to model each observed data example. For example, in DP-GMM, a Chinese restaurant process (CRP) [18] is designed to assign each data example to one of the infinitely many clusters. In IBP-LFM, an Indian buffet process (IBP) [143] is utilized to select a finite set of features from the infinite feature pool to reconstruct each data example. A BNP model typically consists of two priors. One is a base distribution from which the parameter vectors of components are drawn. The other is a stochastic process – such as CRP and IBP – which designates how to select components to model data. The IMAP prior proposed in this section belongs to the first regime. It is commonly assumed that the parameter vectors of components are *independently* drawn from the same base distribution. For example, in both DP-GMM and IBP-LFM, the mean vectors and weight vectors are independently drawn from a Gaussian distribution. In our work, we aim at designing a prior that encourages the component vectors to be mutually different and "diverse", under which the component vectors are not independent anymore, which presents great challenges for posterior inference.

To "diversify" BNP models, we extend the mutual angular process to an infinite MAP (IMAP) that encourages infinitely many components to have large angles. In this prior, the components are mutually dependent, which is challenging to perform posterior inference. We develop an efficient posterior inference algorithm based on slice sampling [329] and Riemann manifold Hamiltonian Monte Carlo [129]. We apply the IMAP to induce diversity in the infinite latent feature model (ILFM) [142] and experiments on various datasets demonstrate that the IMAP is able to (1) achieve better performance with fewer components, (2) better capture infrequent patterns, and (3) reduce overfitting.

Related works Several works studied how to promote diversity in Bayesian nonparametric models. In Xu et al. [386], the component number is treated as a random variable. To obtain a unknown number of "diverse" components, they first sample a component number K from a prior, then generate K "diverse" component vectors using DPP. They apply this approach to "diversify" the cluster centers in the Dirichlet process mixture model (DPMM) [111] and feature allocation vectors in the infinite latent feature model (ILFM). However, it is unclear how to apply this method to "diversify" the weight vectors of the latent features in ILFM when it is coupled with the Indian buffet process [142]. They use a reversible jump MCMC algorithm for posterior inference, which is not scalable for high-dimensional problems. Xie and Xu [366] proposed a Bayesian repulsive Gaussian mixture model where the cluster centers in DPMM are encouraged to be "diverse". Their approach for inducing diversity is not applicable to the ILFM model.

3.2.1 Infinite Mutual Angular Process

In this section, we aim at designing a Bayesian nonparametric prior to promote diversity among infinitely many components, which is very challenging and presumably much more difficult than inducing diversity among a finite set of components. Taking the determinantal point process (DPP) [204] as example, in the finite case, a kernel matrix is computed over the component vectors and the determinant of this matrix is employed as a measure of diversity. In the infinite case, the kernel matrix would have an infinite number of rows and columns, whose determinant cannot be defined.

One possible reason that renders DPP fails to be extended to the infinite case is that DPP measures the diversity of components in a *batch* mode: the similarity between each pair of components is measured in one shot, then these similarity scores is aggregated into a diversity score (via the determinant). In the infinite case, the number of similarity scores is infinite. How to aggregate infinitely many scores into one single score and meanwhile guarantee the prior distribution derived thereafter is proper (integrating to one) is a highly challenging issue. As discussed in Section 3.1.1, one way to solve this problem is to bring in diversity in a *sequential* mode: each time we add one component to the component pool and encourage the new component to be different from the existing ones. The number of existing components is always finite, hence the (dis)similarity measurement always occurs between one component (the new one) and a finite set of components (the existing ones), which stands in contrast with the batch mode where each component is measured against infinitely many components. This adding process can be repeated infinitely many times, providing a natural way to accommodate an infinite number of components into the BNP models.

Similar to the mutual angular process in Section 3.1.1, we use a Bayesian network (BN) [198] to model the adding process of components and design local probability at each node of the BN to encourage the components to have large mutual angles. Repeating the adding process infinitely many times, we end up with a prior that encourages an infinite number of components to have large mutual angles

$$p(\{\widetilde{\mathbf{a}}_i\}_{i=1}^{\infty}) = p(\widetilde{\mathbf{a}}_1)\prod_{i=2}^{\infty} p(\widetilde{\mathbf{a}}_i|\text{pa}(\widetilde{\mathbf{a}}_i)), \tag{3.35}$$

where $\{\widetilde{\mathbf{a}}_i\}_{i=1}^{\infty}$ are the directional vectors of components. The factorization theorem [198] of Bayesian networks ensures that $p(\{\widetilde{\mathbf{a}}_i\}_{i=1}^{\infty})$ integrates to one. The magnitudes $\{g_i\}_{i=1}^{\infty}$ do not affect angles, which can be generated independently from a gamma distribution.

The generative process of components $\{\mathbf{a}_i\}_{i=1}^{\infty}$ can be summarized as follows:

- Sample $\widetilde{\mathbf{a}}_1 \sim \text{vMF}(\boldsymbol{\mu}_0, \kappa)$
- For $i = 2, \cdots, \infty$, sample $\widetilde{\mathbf{a}}_i \sim \text{vMF}(-\frac{\sum_{j=1}^{i-1} \widetilde{\mathbf{a}}_j}{\|\sum_{j=1}^{i-1} \widetilde{\mathbf{a}}_j\|_2}, \kappa)$
- For $i = 1, \cdots, \infty$, sample $g_i \sim \text{Gamma}(\alpha_1, \alpha_2)$
- For $i = 1, \cdots, \infty$, $\mathbf{a}_i = \widetilde{\mathbf{a}}_i g_i$

The probability distribution of $\{\mathbf{a}_i\}_{i=1}^{\infty}$ can be written as

$$p(\{\mathbf{a}_i\}_{i=1}^{\infty}) = C_p(\kappa) \exp(\kappa \boldsymbol{\mu}_0^{\top} \widetilde{\mathbf{a}}_1) \prod_{i=2}^{\infty} C_p(\kappa) \exp\left(\kappa \left(-\frac{\sum_{j=1}^{i-1} \widetilde{\mathbf{a}}_j}{\|\sum_{j=1}^{i-1} \widetilde{\mathbf{a}}_j\|_2}\right)^{\top} \widetilde{\mathbf{a}}_i\right) \prod_{i=1}^{\infty} \frac{\alpha_2^{\alpha_1} g_i^{\alpha_1 - 1} e^{-g_i \alpha_2}}{\Gamma(\alpha_1)}. \tag{3.36}$$

3.2.2 Case Study: Infinite Latent Feature Model

In this section, using the infinite latent feature model (ILFM) [142] as a study case, we show how to promote diversity among the components therein with the IMAP prior. Given a set of data examples $\mathcal{X} = \{\mathbf{x}_n\}_{n=1}^{N}$ where $\mathbf{x}_n \in \mathbb{R}^D$, ILFM aims at invoking a finite subset of features from an infinite feature collection $\mathcal{A} = \{\mathbf{a}_k\}_{k=1}^{\infty}$ to construct these data examples. Each feature (which is a component in this BNP model) is parameterized by a vector $\mathbf{a}_k \in \mathbb{R}^D$. For each data example $\mathbf{x}_n$, a subset of features are selected to construct it. The selection is denoted by a binary vector $\mathbf{z}_n \in \{0, 1\}^{\infty}$ where $z_{nk} = 1$ denotes the k-th feature is invoked to construct the n-th example and $z_{nk} = 0$ otherwise. Given the parameter vectors of features $\{\mathbf{a}_k\}_{k=1}^{\infty}$ and the selection vector $\mathbf{z}_n$, the example $\mathbf{x}_n$ can be represented as: $\mathbf{x}_n \sim \mathcal{N}(\sum_{k=1}^{\infty} z_{nk}\mathbf{a}_k, \sigma^2\mathbf{I})$. The binary selection vectors $\mathcal{Z} = \{\mathbf{z}_n\}_{n=1}^{N}$ can be either drawn from an Indian buffet process (IBP) [143] or a stick-breaking construction [329]. Let μ_k be the prior probability that feature k is present in a data example and the features are permuted such that their prior probabilities are in a decreasing ordering: $\mu_{(1)} > \mu_{(2)} > \cdots$. According to the stick-breaking construction, these prior probabilities can be generated in the following way: $\nu_k \sim \text{Beta}(\alpha, 1)$, $\mu_{(k)} = \nu_k \mu_{(k-1)} = \prod_{l=1}^{k} \nu_l$. Given $\mu_{(k)}$, the binary indicator z_{nk} is generated as $z_{nk}|\mu_{(k)} \sim \text{Bernoulli}(\mu_{(k)})$. To reduce the redundancy among the features, we impose the IMAP over their parameter vectors $\mathcal{A}$ to encourage them to be mutually different, which results in an IMAP-LFM model.

3.2.3 A Sampling-based Inference Algorithm

In this section, we develop a sampling algorithm to infer the posteriors of $\mathcal{A}$ and $\mathcal{Z}$ in the IMAP-LFM model. Two major challenges need to be addressed. First, the prior over $\mathcal{A}$ is not conjugate to the likelihood function $p(\mathbf{x})$. Second, the parameter vectors $\mathcal{A}$ are usually high-dimensional, rendering slow mixing. To address the first challenge, we adopt a slicing sampling algorithm [329]. This algorithm introduces an auxiliary slice variable $s|\mathcal{Z}, \mu_{(1:\infty)} \sim \text{uniform}[0, \mu^*]$, where $\mu^* = \min\{1, \min_{k:\exists n, z_{nk}=1} \mu_k\}$ is the prior probability of the last active feature. A feature k is active

Algorithm 2: A manifold Hamiltonian Monte Carlo algorithm for sampling $\widetilde{\mathbf{a}}$.

01. $\mathbf{v} \sim \mathcal{N}(0, \mathbf{I})$
02. $\mathbf{v} \leftarrow \mathbf{v} - (\mathbf{I} - \widetilde{\mathbf{a}}\widetilde{\mathbf{a}}^\top)\mathbf{v}$
03. $h \leftarrow \log p(\widetilde{\mathbf{a}}|rest) - \frac{1}{2}\mathbf{v}^\top\mathbf{v}$
04. $\widetilde{\mathbf{a}}^* \leftarrow \widetilde{\mathbf{a}}$
05. **for** $\tau = 1, \cdots, T$ **do**
06. $\quad \mathbf{v} \leftarrow \mathbf{v} + \frac{\epsilon}{2}\nabla_{\widetilde{\mathbf{a}}^*} \log p(\widetilde{\mathbf{a}}^*|rest)$
07. $\quad \mathbf{v} \leftarrow \mathbf{v} - \widetilde{\mathbf{a}}\widetilde{\mathbf{a}}^\top\mathbf{v}$
08. $\quad \widetilde{\mathbf{a}}^* \leftarrow \cos(\epsilon\|\mathbf{v}\|_2)\widetilde{\mathbf{a}}^* + \|\mathbf{v}\|_2^{-1}\sin(\epsilon\|\mathbf{v}\|_2)\mathbf{v}$
09. $\quad \mathbf{v} \leftarrow -\|\mathbf{v}\|_2\sin(\epsilon\|\mathbf{v}\|_2)\widetilde{\mathbf{a}}^* + \cos(\epsilon\|\mathbf{v}\|_2)\mathbf{v}$
10. $\quad \mathbf{v} \leftarrow \mathbf{v} + \frac{\epsilon}{2}\nabla_{\widetilde{\mathbf{a}}^*} \log p(\widetilde{\mathbf{a}}^*|rest)$
11. $\quad \mathbf{v} \leftarrow \mathbf{v} - \widetilde{\mathbf{a}}\widetilde{\mathbf{a}}^\top\mathbf{v}$
12. **end for**
13. $h^* \leftarrow \log p(\widetilde{\mathbf{a}}^*|rest) - \frac{1}{2}\mathbf{v}^\top\mathbf{v}$
14. $u \sim \text{uniform}(0, 1)$
15. **if** $u < \exp(h^* - h)$
16. $\quad \widetilde{\mathbf{a}} \leftarrow \widetilde{\mathbf{a}}^*$
17. **end if**

if there exists an example n such that $z_{nk} = 1$ and is inactive otherwise. In the sequel, we discuss the sampling of other variables.

Sample new features Let K^* be the maximal feature index with $\mu_{(K^*)} > s$ and K^+ be the index such that all active features have index $k < K^+$ (K^+ itself would be an inactive feature). If the new value of s makes $K^* \geq K^+$, then we draw $K^* - K^+ + 1$ new (inactive) features, including the parameter vectors and prior probabilities. The prior probabilities $\{\mu_{(k)}\}$ are drawn sequentially from $p(\mu_{(k)}|\mu_{(k-1)}) \propto \exp(\alpha\sum_{n=1}^N \frac{1}{n}(1-\mu_{(k)})^n)\mu_{(k)}^{\alpha-1}(1-\mu_{(k)})^N\mathbb{I}(0 \leq \mu_{(k)} \leq \mu_{(k-1)})$ using the adaptive rejection sampling (ARS) [128] method. The parameter vectors are drawn sequentially from

$$p(\mathbf{a}_k|\{\mathbf{a}_j\}_{j=1}^{k-1}) = p(\widetilde{\mathbf{a}}_k|\{\widetilde{\mathbf{a}}_j\}_{j=1}^{k-1})p(g_k) = C_p(\kappa)\exp\left(\kappa\left(-\frac{\sum_{j=1}^{k-1}\widetilde{\mathbf{a}}_j}{\|\sum_{j=1}^{k-1}\widetilde{\mathbf{a}}_j\|_2}\right)^\top\widetilde{\mathbf{a}}_k\right)\frac{\alpha_2^{\alpha_1}g_i^{\alpha_1-1}e^{-g_i\alpha_2}}{\Gamma(\alpha_1)}, \tag{3.37}$$

where we draw $\widetilde{\mathbf{a}}_k$ from $p(\widetilde{\mathbf{a}}_k|\{\widetilde{\mathbf{a}}_j\}_{j=1}^{k-1})$ which is a von Mises-Fisher distribution and draw g_k from a gamma distribution, then multiply $\widetilde{\mathbf{a}}_k$ and g_k together since they are independent. For each new feature k, the corresponding binary selection variables $z_{:,k}$ are initialized to zero.

Sample existing $\mu_{(k)}$ $(1 \leq k \leq K^+ - 1)$ We sample $\mu_{(k)}$ from $p(\mu_{(k)}|\text{rest}) \propto \mu_{(k)}^{m_k-1}(1-\mu_{(k)})^{N-m_k}\mathbb{I}(\mu_{(k+1)} \leq \mu_{(k)} \leq \mu_{(k-1)})$, where $m_k = \sum_{n=1}^N z_{nk}$.

Sample z_{nk} $(1 \leq n \leq N, 1 \leq k \leq K^*)$ Given s, we only need to sample z_{nk} for $k \leq K^*$ from $p(z_{nk} = 1|\text{rest}) \propto \frac{\mu_{(k)}}{\mu^*}p(\mathbf{x}_n|z_{n,\neg k}, z_{nk} = 1, \{\mathbf{a}_j\}_{j=1}^{K^+})$, where $p(\mathbf{x}_n|z_{n,\neg k}, z_{nk} = 1, \{\mathbf{a}_j\}_{j=1}^{K^+}) =$

Dataset	IBP-LFM	PYP-LFM	IMAP-LFM
Yale	447±7	432±3	**419**±4
Block ($\times 10^{-2}$)	6.3±0.4	5.8±0.1	**4.4**±0.2
AR	926±4	939±11	**871**±7
EEG (+2.1 $\times$ 10^6)	5382±34	3731±15	**575**±21
Piano ($\times 10^{-4}$)	5.3±0.1	5.7±0.2	**4.2**±0.2

Table 3.6: L2 test error.

Dataset	IBP-LFM	PYP-LFM	IMAP-LFM
Yale	-16.4±0.3	-14.9 ±0.4	**-12.7**±0.1
Block-Image	-2.1±0.2	-1.8±0.1	**-1.4**±0.1
AR	-13.9±0.3	-14.6±0.7	**-8.5**±0.4
EEG	-14133±54	-12893 ±73	**-9735**±32
Piano	-6.8±0.6	-6.9±0.2	**-4.2**±0.5

Table 3.7: Test log-likelihood.

$\mathcal{N}(\mathbf{x}_n|\mathbf{a}_k + \sum_{j\neq k}^{K^+} z_{nj}\mathbf{a}_j, \sigma\mathbf{I})$ and $z_{n,\neg k}$ denotes all other elements in $\mathbf{z}$ except the k-th one and $\mathbf{a}_j = \widetilde{\mathbf{a}}_j g_j$.

Sample $\mathbf{a}_k$ $(k = 1, \cdots, K^+)$ We draw $\mathbf{a}_k = \widetilde{\mathbf{a}}_k g_k$ from the following conditional probability

$$p(\widetilde{\mathbf{a}}_k g_k|\text{rest}) \propto p(\widetilde{\mathbf{a}}_k g_k|\{\mathbf{a}_j\}_{j\neq k}^{K^+}) \prod_{n=1}^{N} p(\mathbf{x}_n|z_{n,1:K^+}, \{\mathbf{a}_j\}_{j\neq k}^{K^+}, \widetilde{\mathbf{a}}_k g_k), \tag{3.38}$$

where $p(\widetilde{\mathbf{a}}_k g_k|\{\mathbf{a}_j\}_{j\neq k}^{K^+}) \propto p(\widetilde{\mathbf{a}}_k g_k|\{\mathbf{a}_i\}_{i=1}^{k-1}) \prod_{j=k+1}^{K^+} p(\mathbf{a}_j|\{\mathbf{a}_i\}_{i\neq k}^{j-1}, \widetilde{\mathbf{a}}_k g_k)$ and $p(\mathbf{x}_n|z_{n,1:K^+}, \{\mathbf{a}_j\}_{j\neq k}^{K^+}, \widetilde{\mathbf{a}}_k g_k) = \mathcal{N}(\mathbf{x}_n|\widetilde{\mathbf{a}}_k g_k + \sum_{j\neq k}^{K^+} z_{nj}\mathbf{a}_j, \sigma\mathbf{I})$. In the vanilla IBP latent feature model [143], the prior over $\mathbf{a}_k$ is a Gaussian distribution, which is conjugate to the Gaussian likelihood function. In that case, the posterior $p(\mathbf{a}_k|\text{rest})$ is again a Gaussian, from which samples can be easily drawn. But in Eq.(3.38), the posterior does not have a closed form expression since the prior $p(\widetilde{\mathbf{a}}_k g_k|\{\mathbf{a}_j\}_{j\neq k}^{K^+})$ is no longer a conjugate prior, making the sampling very challenging.

We sample $\widetilde{\mathbf{a}}_k$ and g_k separately. g_k can be efficiently sampled using the Metropolis-Hastings (MH) [152] algorithm. For $\widetilde{\mathbf{a}}_k$ which is a random vector, the sampling is much more difficult. The random walk based MH algorithm suffers slow mixing when the dimension of $\widetilde{\mathbf{a}}_k$ is large (which is typically the case). In addition, $\widetilde{\mathbf{a}}_k$ lies on a unit sphere. The sampling algorithm should preserve this geometric constraint. To address these two issues, we study a Riemann manifold Hamiltonian Monte Carlo (RM-HMC) method [59, 129]. HMC leverages the Hamiltonian dynamics to produce distant proposals for the Metropolis-Hastings algorithm, enabling a faster exploration of the state space and faster mixing. The RM-HMC algorithm introduces an auxiliary vector $\mathbf{v}$ and defines a Hamiltonian function $H(\widetilde{\mathbf{a}}_k, \mathbf{v}) = -\log p(\widetilde{\mathbf{a}}_k|\text{rest}) + \log|G(\widetilde{\mathbf{a}}_k)| + \frac{1}{2}\mathbf{v}^\top G(\widetilde{\mathbf{a}}_k)^{-1}\mathbf{v}$, where G is the metric tensor associated with the Riemann manifold, which in our case is a unit sphere. After a transformation of the coordi-

Dataset	IBP-LFM	PYP-LFM	IMAP-LFM
Reuters	45.4±0.3	43.1±0.4	**48.2**±0.6
TDT	48.3±0.7	47.5±0.3	**53.2**±0.4
20-News	21.5±0.1	23.7±0.2	**25.2**±0.1
15-Scenes	22.7±0.2	21.9±0.4	**25.3**±0.2
Caltech-101	11.6±0.4	12.1±0.1	**14.7**±0.2

Table 3.8: Clustering accuracy (%).

Dataset	IBP-LFM	PYP-LFM	IMAP-LFM
Reuters	41.7±0.5	38.6±0.2	**45.4**±0.4
TDT	44.2±0.1	46.7±0.3	**49.6**±0.6
20-News	38.9±0.8	35.2±0.5	**44.6**±0.9
15-Scenes	42.1±0.7	44.9±0.8	**47.5**±0.2
Caltech-101	34.2±0.4	36.8±0.4	**40.3**±0.3

Table 3.9: Normalized mutual information (%).

nate system, $H(\widetilde{\mathbf{a}}_k, \mathbf{v})$ can be re-written as

$$H(\widetilde{\mathbf{a}}_k, \mathbf{v}) = -\log p(\widetilde{\mathbf{a}}|rest) + \frac{1}{2}\mathbf{v}^\top \mathbf{v}. \tag{3.39}$$

$p(\widetilde{\mathbf{a}}_k|\text{rest})$ needs not to be normalized and $\log p(\widetilde{\mathbf{a}}_k|\text{rest}) \propto \kappa(-\frac{\sum_{j=1}^{k-1}\widetilde{\mathbf{a}}_j}{\|\sum_{j=1}^{k-1}\widetilde{\mathbf{a}}_j\|_2})^\top \widetilde{\mathbf{a}}_k + \sum_{j=k+1}^{K^+}$ $\kappa(-\frac{\sum_{i\neq k}^{j-1}\widetilde{\mathbf{a}}_i + \widetilde{\mathbf{a}}_k g_k}{\|\sum_{i\neq k}^{j-1}\widetilde{\mathbf{a}}_i + \widetilde{\mathbf{a}}_k g_k\|_2})^\top \widetilde{\mathbf{a}}_j + \sum_{n=1}^{N}\frac{1}{\sigma}(\mathbf{x}_n - \sum_{j\neq k}^{K^+} z_{nj}\mathbf{a}_j)^\top \widetilde{\mathbf{a}}_k g_k - \frac{1}{2\sigma}\|\widetilde{\mathbf{a}}_k g_k\|_2^2$. A new sample of $\widetilde{\mathbf{a}}_k$ can be generated by approximately solving a system of differential equations characterizing the Hamiltonian dynamics on the manifold [129]. Following [59], we solve this problem based upon geodesic flow, which is shown in Line 6-11 in Algorithm 2. Line 6 performs an update of $\mathbf{v}$ according to the Hamiltonian dynamics, where $\nabla_{\widetilde{\mathbf{a}}^*}\log p(\widetilde{\mathbf{a}}^*|rest)$ denotes the gradient of $\log p(\widetilde{\mathbf{a}}^*|rest)$ w.r.t $\widetilde{\mathbf{a}}^*$. Line 7 performs the transformation of the coordinate system. Line 8-9 calculate the geodesic flow on the unit sphere. Line 10-11 repeat the update of $\mathbf{v}$ as done in Line 6-7. These procedures are repeated T times to generate a new sample $\widetilde{\mathbf{a}}^*$, which then goes through an acceptance/rejection procedure (Line 3, 13-17).

3.2.4 Evaluation

We evaluated the effectiveness of the IMAP prior in alleviate overfitting, reducing model size without sacrificing modeling power, and capturing infrequent patterns, on a wide range of datasets.

Datasets We used ten datasets from different domains including texts, images, audio, and EEG signals: Yale [125], Block-Images [361], AR [249], EEG [165], Piano [276], Reuters [10], TDT [4], 20-News [1], 15-Scenes [212], and Caltech-101 [110]. The first five datasets were represented as raw data without feature extraction. The documents in Reuters, TDT, and 20-News were represented with bag-of-words vectors, weighted using tf-idf. The images in 15-

Method	Yale		AR	
	Train	Test	Train	Test
IBP-LFM [142]	-9.2	-16.4	-6.7	-13.9
IMAP-LFM	-9.8	-12.7	-7.2	-8.5

Table 3.10: Log-likelihood on the training and testing sets of Yale and AR.

	Yale		AR	
	# Features	L2 Error	# Features	L2 Error
IBP-LFM [142]	162	445	175	922
IMAP-LFM	165	419	176	871

Table 3.11: Number of latent features and L2 test errors.

Scenes [212] and Caltech-101 [110] were represented with visual bag-of-words vectors based on the SIFT [237] features. The train/test split of each dataset was 70%/30%. The results were averaged over five random splits.

Experimental setup For each dataset, we used the IMAP-LFM model to learn the latent features $\mathcal{A}$ on the training set, then used $\mathcal{A}$ to reconstruct the test data. The reconstruction performance was measured using log-likelihood (the larger, the better). Meanwhile, we used $\mathcal{A}$ to infer the representations $\mathcal{Z}$ of test data and performed data clustering on $\mathcal{Z}$. Clustering performance was measured using accuracy and normalized mutual information (NMI) (the higher, the better) [61]. We compared with two baselines: the Indian buffet process LFM (IBP-LFM) [142] and the Pitman-Yor process LFM (PYP-LFM) [327]. In IBP-LFM, posterior inference was performed with the slice sampling algorithm [329]. For PYP-LFM inference, we used the algorithm proposed in [327]. To attain a better local optimal, for each experiment run, we performed 5 random restarts and chose the best solution. The initialization for all models were the same. Following [105], all datasets were centered to have zero mean. We used grid search and 5-fold cross-validation to tune the hyper-parameters for all methods. In our method, κ in Eq.(3.36) was set to 1. σ^2 was set to $0.25\hat{\sigma}$ where $\hat{\sigma}$ is the standard deviation of data across all dimensions. α was set to 2. The hyper-parameters of the RM-HMC algorithm followed those in [59].

Results We first verify whether the features learned by IMAP-LFM are diverse. We computed the average of the cosine similarities between each pair of latent features. Features with smaller average cosine similarity (ACS) are considered to be more diverse. On the Reuters dataset, the ACS for IBP-LFM, PYP-LFM, and IMAP-LFM are 0.72, 0.69, 0.61, respectively. IMAP-LFM also achieves smaller ACS on other datasets. This shows that IMAP effectively promotes diversity.

Table 3.6 and 3.7 present the L2 error and log-likelihood (mean$\pm$standard error) on the test set of the first five datasets. The standard errors were computed from the 5 random train/test splits for each dataset. As can be seen, IMAP-LFM achieves much lower L2 error and higher log-likelihood than IBP-LFM and PYP-LFM. Table 3.8 and 3.9 show the clustering accuracy and NMI (mean$\pm$standard error) on the last 5 datasets which have class labels. IMAP-LFM

Dataset	IBP-LFM [142]	PYP-LFM [327]	IMAP-LFM
Yale	201±5	220±8	**165**±4
Block-Image	**8**±2	9±4	11±4
AR	257±11	193±5	**176**±8
EEG	14±2	**9**±2	12±1
Piano	37±4	34±6	**28**±3
Reuters	354±12	326±5	**294**±7
TDT	297±6	311±9	**274**±3
20-News	442±8	408±3	**369**±5
15-Scenes	192±3	218±5	**171**±8
Caltech-101	127±7	113±6	**96**±6

Table 3.12: Number of features.

outperforms the two baseline methods with a large margin.

Regarding why IMAP-LFM outperforms the baselines, we conjecture the reasons are two-fold. First, IMAP is more capable of alleviating overfitting. To verify this, we show the log-likelihood on the training and testing sets of Yale and AR in Table 3.10. Compared with IBP-LFM, IMAP-LFM achieves lower training log-likelihood and higher test log-likelihood. In IMAP-LFM, the gap between training and testing log-likelihood is smaller than that in IBP-LFM. This demonstrates that IMAP can better reduce overfitting. In both IBP-LFM and PYP-LFM, the weight vectors of latent features are drawn independently from a Gaussian distribution, which is unable to characterize the relations among features. In contrast, IMAP-LFM imposes a structure over the features, encouraging them to be "diverse" and less redundant. This diversity-biased structural constraint reduces model complexity of LFM, thus alleviating overfitting on the training data and achieving better reconstruction of the test data. Second, "diversified" features presumably have higher representational power and are able to capture richer information and subtle aspects of data, thus achieving a better modeling effect.

The L2 error and log-likelihood depend on two major factors: (1) model size, which is proportional to the number of latent features; (2) the level of "diversity" among the latent features. To clearly see the effect of (2), we removed the impact of (1) by tuning the hyperparameters of IBP-LFM and IMAP-LFM so that they have roughly the same feature number. Table 3.11 shows the number of features learned on the training set and the L2 error on the test set of Yale and AR. IMAP-LFM has almost the same feature number as IBP-LFM, but achieves significantly lower L2 error on the test set. This indicates that diversified features are better than non-diversified features.

Table 3.12 shows the number of features (mean±standard error) obtained by each model when the algorithm converges. Analyzing Table 3.6-3.9 and 3.12 simultaneously, we see that IMAP-LFM uses much fewer features to achieve better performance than the baselines. For instance, on the Reuters dataset, with 294 features, IMAP-LFM achieves a 48.2% clustering accuracy. In contrast, IBP-LFM uses 60 more features, but achieves 2.8% (absolute) lower accuracy. This suggests that IMAP is able to reduce the size of LFM (the number of features) without sacrificing modeling power. Because of IMAP's diversity-promoting mechanism, the learned features bear less redundancy and are highly complementary to each other. Each feature captures

Categories	1	2	3	4	5	6	7	8	9
Frequencies of categories	3713	2055	321	298	245	197	142	114	110
Precision@100 (%) of IBP	73.7	45.1	7.5	8.3	6.9	7.2	2.6	3.8	3.4
Precision@100 (%) of IMAP	81.5	78.4	36.2	37.8	29.1	20.4	8.3	13.8	11.6
Relative improvement (%)	11	74	382	355	321	183	219	263	241

Table 3.13: Per-category precision@100 on the Reuters dataset.

IBP-LFM [142]					IMAP-LFM				
Feature 1	Feature 2	Feature 3	Feature 4	Feature 5	Feature 1	Feature 2	Feature 3	Feature 4	Feature 5
government	saddam	nuclear	turkish	game	president	clinton	olympic	school	space
house	white	iraqi	soviet	gold	clinton	government	team	great	operation
baghdad	clinton	weapons	government	team	legal	lewinsky	hockey	institute	shuttle
weapons	united	united	weapons	season	years	nuclear	good	program	research
tax	time	work	number	april	state	work	baseball	study	life
years	president	spkr	enemy	man	baghdad	minister	gold	japanese	satellite
white	baghdad	president	good	number	church	weapons	ball	office	launch
united	iraq	people	don	work	white	india	medal	reading	lunar
state	un	baghdad	citizens	baseball	united	years	april	level	device
bill	lewinsky	state	due	years	iraqi	white	winter	number	program

Table 3.14: Visualization of features learned on the 20-News dataset.

a significant amount of information. As a result, a small number of such features are sufficient to model data well. In contrast, the features in IBP-LFM and PYP-LFM are drawn independently from a base distribution, which lacks the mechanism to reduce redundancy. IMAP achieves more significant reduction of feature numbers on datasets that have larger feature dimensions. This is possibly because higher-dimensional data contains more redundancy, giving IMAP a larger room to improve.

To verify whether IMAP helps to better capture infrequent patterns, on the learned features of the Reuters dataset we performed a retrieval task and measured the precision@100 on each category. For each test document, we retrieved 100 documents from the training set based on the Euclidean distance. Precision@100 is defined as n/100, where n is the number of retrieved documents that share the same category label with the query document. We treat each category as a pattern and define its frequency as the number of documents belonging to it. A category with more than 1000 documents is labeled as being frequent. Table 3.13 shows the per-category precision. The last row shows the relative improvement of IMAP-LFM over IBP-LFM, defined as $(P_{imap} - P_{ibp})/P_{ibp}$. As can be seen, on the infrequent categories 3-9, IMAP-LFM achieves much better precision than IBP-LFM, while on the frequent categories 1 and 2, their performance are comparable. This demonstrates that IMAP is able to better capture infrequent patterns without losing the modeling power on frequent patterns.

On the 20-News dataset, we visualized the learned features. For a latent feature with parameter vector $\mathbf{a}$, we picked up the top 10 words corresponding to the largest values in $\mathbf{a}$. Table 3.14 shows 5 exemplar features learned by IBP-LFM and IMAP-LFM. As can be seen, the features learned by IBP-LFM have much overlap and redundancy and are hard to distinguish, whereas those learned by IMAP-LFM are more diverse.

Figure 3.3 shows how the L2 reconstruction error on the Yale test dataset varies as the parameter κ increases. κ controls the level of "diversity". A larger κ results in more "diversity".

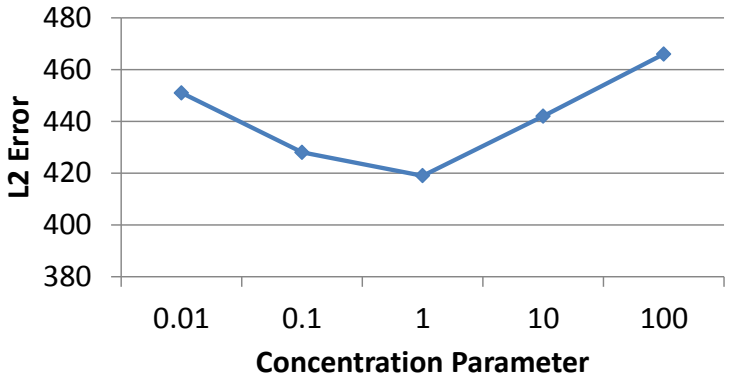

Figure 3.3: L2 error on the Yale test set versus the concentration parameter κ.

	Block-Images	20-News
RW-MH	7.6	93.7
RM-HMC	4.4	58.7

Table 3.15: Runtime (hours) of RM-HMC and RW-MH.

As can be seen from this figure, the L2 error decreases as κ increases from 0.01 to 1, which suggests that increasing the "diversity" among latent features is beneficial. This is possibly because the "diversity" effect acts as a type of inductive bias that controls the complexity of the model class, which thereby improves the generalization performance on unseen data. However, further increasing κ from 1 to 100 causes the L2 error to increase. A possible explanation is: if κ is too large, the diversity-promoting inductive bias is excessively strong, which compromises the quality of data-fitting.

We compared the convergence speed of the RM-HMC algorithm (Algorithm 2) with a random-walk based Metropolis Hastings (RW-MH) algorithm. The runtime is given in Table 3.15. As can be seen, RM-HMC is much more efficient than RW-MH, since it leverages the gradient information of $p(\widetilde{\mathbf{a}}_k|\text{rest})$ to search for "better" proposals of $\widetilde{\mathbf{a}}_k$. Compared with IBP-LFM, IMAP-LFM has an additional overhead of running the RM-HMC algorithm to sample $\widetilde{\mathbf{a}}$. Fortunately, RM-HMC converges very quickly, therefore this extra overhead is not substantial. For example, on the Block-Images dataset, the runtime of IBP-LFM and IMAP-LFM is 3.6 and 4.4 hours, respectively. On the 20-News dataset, the runtime of IBP-LFM and IMAP-LFM is 43.3 and 58.1 hours, respectively.

Chapter 4

Diversity-promoting Learning III – Analysis

In the previous two chapters, we have demonstrated the effectiveness of the proposed regularizers and Bayesian priors in (1) better capturing infrequent patterns, (2) achieving better generalization performance, and (3) reducing model size without sacrificing modeling power, via empirical studies. In this chapter, we provide theoretical analysis on why these regularizers/priors can achieve such effects.

4.1 Analysis of Better Capturing of Infrequent Patterns

On the distance metric learning model, we analyze why encouraging diversity using the nonconvex Bregman matrix divergence (NCBMD) regularizers [379] (Section 2.2.1) can better capture infrequent patterns [379]. In the analysis, we first define a score (the lower, the better) to quantify how well the infrequent patterns are captured. Then we upper bound this score using increasing functions of the NCBMD regularizers. Putting the two pieces together, we can conclude that reducing the NCBMD regularizers leads to better capturing of the infrequent patterns.

The analysis focuses on the following projection matrix:

$$\mathbf{A}^* = \arg\min_{\mathbf{A}} \ \mathrm{E}_{\mathcal{S},\mathcal{D}} \left[\frac{1}{|\mathcal{S}|} \sum_{(\mathbf{x},\mathbf{y})\in\mathcal{S}} \|\mathbf{A}\mathbf{x}-\mathbf{A}\mathbf{y}\|_2^2 + \frac{1}{|\mathcal{D}|} \sum_{(\mathbf{x},\mathbf{y})\in\mathcal{D}} \max(0, \tau - \|\mathbf{A}\mathbf{x}-\mathbf{A}\mathbf{y}\|_2^2) + \gamma\Omega_\phi(\mathbf{A}) \right]. \tag{4.1}$$

We assume the data examples in $\mathcal{S}$ and $\mathcal{D}$ are from K classes (which are considered as patterns), where class k has a distribution π_k and the corresponding expectation is $\boldsymbol{\mu}_k$. Let p_k denote the prior probability of drawing a data example from class k. We assume these classes are "imbalanced" in the sense that the variance of prior probabilities $\{p_k\}_{k=1}^K$ is large. A class is considered as being "frequent" if it has a large p and "infrequent" if otherwise. We use $\boldsymbol{\mu}_k$ to represent class k and define the Mahalanobis distance between two classes j and k as: $d_{jk} = (\boldsymbol{\mu}_j - \boldsymbol{\mu}_k)^\top \mathbf{A}^{*\top}\mathbf{A}^*(\boldsymbol{\mu}_j - \boldsymbol{\mu}_k)$.

An *imbalance factor* (IF; the lower, the better) is defined to quantify how well the infrequent

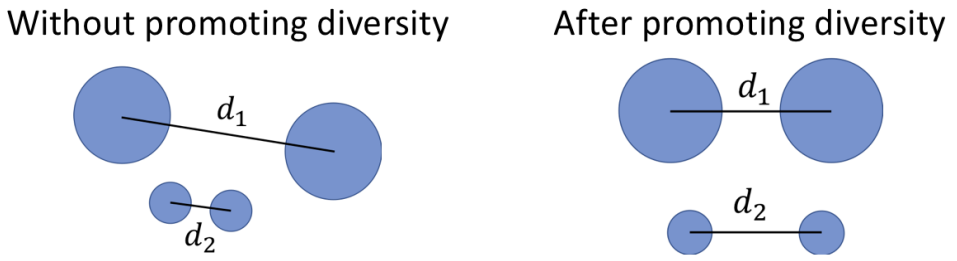

Figure 4.1: Large and small circles denote frequent and infrequent classes respectively. The objective function of DML tends to make the inter-class distance to be large. (Left) The frequent classes are dominant in the training objective of DML, and hence are given higher priority for being pushed far away from each other. The infrequent classes are paid less attention to. Their distance ends up being small since DML is constrained by inner-class data pairs which need to have small distances. (Right) By promoting diversity, the infrequent classes are paid more attention to and their distance d_2 is enlarged. As a result, the ratio between d_1 and d_2 decreases.

classes are captured:

$$\eta = \frac{\max_{j \neq k} d_{jk}}{\min_{j \neq k} d_{jk}}, \tag{4.2}$$

which is the ratio between the largest and smallest inter-class distance. Figure 4.1 illustrates why η can reflect how well the infrequent classes are captured. For two frequent classes (denoted by large circles), since they have more training examples and hence contributing more in learning $\mathbf{A}^*$, DML intends to make their distance (d_1) large; whereas for two infrequent classes (denoted by small circles), since they contribute less in learning (and DML is constrained by similar pairs which need to have small distances), their distance (d_2) may end up being small. Consequently, if classes are imbalanced, some between-class distances can be large while others small, resulting in a large IF (the ratio between d_1 and d_2), as shown in Figure 4.1(left). By promoting-diversity, the DML model pays more attention to infrequent classes and tries to make their inter-class distance (d_2) large, as shown Figure 4.1(right). As a result, the IF decreases. To sum up, if the infrequent patterns are better captured, the imbalance factor is smaller.

Next, we upper bound the IF using increasing functions of the NCBMD regularizers. We define $\xi_k = \mathbb{E}_{\mathbf{x} \sim \pi_k}[\sup_{\|\mathbf{v}\|_2=1} |\mathbf{v}^\top(\mathbf{x} - \boldsymbol{\mu}_k)|]$ and $\xi = \max_k \xi_k$. Further, we assume $\mathbf{A}^*$ has full rank R (which is the number of the projection vectors), and let $\mathbf{U}\boldsymbol{\Lambda}\mathbf{U}^\top$ denote the eigen-decomposition of $\mathbf{A}^*\mathbf{A}^{*\top}$, where $\boldsymbol{\Lambda} = \mathrm{diag}(\lambda_1, \lambda_2, \cdots \lambda_R)$ with $\lambda_1 \geq \lambda_2 \geq \cdots \geq \lambda_R$. The basic idea of deriving the upper bounds is as follows. First, we define $\mathcal{G} = \mathrm{span}\{\boldsymbol{\mu}_j - \boldsymbol{\mu}_k : j \neq k\}$ and prove that $\mathcal{G} \subset \mathrm{span}(\mathbf{A}^{*\top})$ under certain conditions where $\mathrm{span}(\mathbf{A}^{*\top})$ denotes the column space of matrix $\mathbf{A}^{*\top}$. Next, we show that if $\mathcal{G} \subset \mathrm{span}(\mathbf{A}^{*\top})$ holds, we can bound η with the condition number of $\mathbf{A}^*\mathbf{A}^{*\top}$. Finally, we bound this condition number with the NCBMD regularizers, including the von Neumann divergence (VND) regularizer and the log-determinant divergence (LDD) regularizer. Putting the pieces together, we obtain NCBMD-based upper bounds of the IF.

Theorem 1. *Let C denote the ratio between $\max_{j \neq k} \|\boldsymbol{\mu}_j - \boldsymbol{\mu}_k\|_2^2$ and $\min_{j \neq k} \|\boldsymbol{\mu}_j - \boldsymbol{\mu}_k\|_2^2$ and*

assume $\max_{j,k} \|\boldsymbol{\mu}_j - \boldsymbol{\mu}_k\|_2 \leq B_0$. *Suppose the regularization parameter* γ *and distance margin* τ *are sufficiently large:* $\gamma \geq \gamma_0$ *and* $\tau \geq \tau_0$, *where* γ_0 *and* τ_0 *depend on* $\{p_k\}_{k=1}^K$ *and* $\{\boldsymbol{\mu}_k\}_{k=1}^K$. *If* $R \geq K-1$ *and* $\xi \leq (-B_0 + \sqrt{B_0^2 + \lambda_{K-1}\beta_{K-1}/(2tr(\boldsymbol{\Lambda}))})/4$, *then we have the following bounds for the IF.*

- *For the VND regularizer* $\Omega_{vnd}(\mathbf{A}^*)$, *if* $\Omega_{vnd}(\mathbf{A}^*) \leq 1$, *the following bound of the IF* η *holds:*

$$\eta \leq Cg(\Omega_{vnd}(\mathbf{A}^*)),$$

  where $g(\cdot)$ *is an increasing function defined in the following way. Let* $f(c) = c^{1/(c+1)}(1+1/c)$, *which is strictly increasing on* $(0, 1]$ *and strictly decreasing on* $[1, \infty)$ *and let* $f^{-1}(c)$ *be the inverse function of* $f(c)$ *on* $[1, \infty)$, *then* $g(c) = f^{-1}(2-c)$ *for* $c < 1$.
- *For the LDD regularizer* $\Omega_{ldd}(\mathbf{A}^*)$, *we have*

$$\eta \leq 4Ce^{\Omega_{ldd}(\mathbf{A}^*)}.$$

As can be seen, the bounds are increasing functions of the NCBMD regularizers $\Omega_{vnd}(\mathbf{A}^*)$ and $\Omega_{ldd}(\mathbf{A}^*)$. Decreasing these regularizers would reduce the upper bounds of the imbalance factor, hence abridging the gap between infrequent and frequent classes. For the squared Frobenius norm (SFN) regularizer which is also an instance of the NCBMD regularizers, such a bound cannot be derived.

4.2 Analysis of Generalization Errors

In this section, we analyze why diversity-promoting regularization can improve the generalization performance on unseen data.

4.2.1 Generalization Error Analysis for the Angular Constraints

Using neural networks as a study case, we analyze how the angular constraints [372] (Section 2.3) affect the generalization performance. The generalization error of a hypothesis f represented with a neural network is defined as $L(f) = \mathbb{E}_{(\mathbf{x},y)\sim p^*}[\ell(f(\mathbf{x}), y)]$, where p^* is the distribution of the input-output pair $(\mathbf{x}, y)$ and $\ell(\cdot,\cdot)$ is the loss function. The training error is $\widehat{L}(f) = \frac{1}{n}\sum_{i=1}^n \ell(f(\mathbf{x}^{(i)}), y^{(i)})$, where n is the number of training samples. Let $f^* \in \text{argmin}_{f\in\mathcal{F}} L(f)$ be the true risk minimizer and $\hat{f} \in \text{argmin}_{f\in\mathcal{F}} \widehat{L}(f)$ be the empirical risk minimizer. We aim at analyzing the generalization error $L(\hat{f})$ of the empirical risk minimizer $\hat{f}$. $L(\hat{f})$ can be decomposed into $L(\hat{f}) = L(\hat{f}) - L(f^*) + L(f^*)$, where $L(\hat{f}) - L(f^*)$ is the estimation error and $L(f^*)$ is the approximation error.

For simplicity, we start with a "simple" fully connected network with one hidden layer of m units, used for univariate regression (one output unit) with squared loss. Analysis for more complicated NNs with multiple hidden layers can be achieved in a straightforward way by cascading our analysis for this "simple" NN. Let $\mathbf{x} \in \mathbb{R}^d$ be the input vector and y be the response value. For simplicity, we assume $\max\{\|\mathbf{x}\|_2, |y|\} \leq 1$. Let $\mathbf{w}_j \in \mathbb{R}^d$ be the weights connecting the j-th hidden unit with the input units, with $\|\mathbf{w}_j\|_2 \leq C$. Let $\boldsymbol{\alpha}$ be a vector where α_j is the weight

connecting the hidden unit j to the output unit, with $\|\boldsymbol{\alpha}\|_2 \leq B$. We assume the activation function $h(t)$ applied on the hidden units is Lipschitz continuous with a constant L. Commonly used activation functions such as rectified linear $h(t) = \max(0, t)$, tanh $h(t) = (e^t - e^{-t})/(e^t + e^{-t})$, and sigmoid $h(t) = 1/(1 + e^{-t})$ are all Lipschitz continuous with $L = 1, 1, 0.25$, respectively. Consider the hypothesis set

$$\mathcal{F} = \{\mathbf{x} \mapsto \sum_{j=1}^{m} \alpha_j h(\mathbf{w}_j^\top \mathbf{x}) \mid \|\boldsymbol{\alpha}\|_2 \leq B, \|\mathbf{w}_j\|_2 \leq C, \forall i \neq j, |\mathbf{w}_i \cdot \mathbf{w}_j| \leq \tau \|\mathbf{w}_i\|_2 \|\mathbf{w}_j\|_2\}.$$

The estimation error represents how well the algorithm is able to learn. We bound it in the following way. We first upper bound the estimation error using the Rademacher complexity (RC) [32] $\mathcal{R}(\mathcal{F})$ of $\mathcal{F}$, then further bound $\mathcal{R}(\mathcal{F})$ using the hyperparameter τ in the angular constraints. When bounding the RC, we leverage the composition property [32]: if a scalar function ϕ is Lipschitz with constant L_ϕ and satisfies $\phi(0) = 0$, then $R(\phi \circ \mathcal{F}) \leq 2L_\phi R(\mathcal{F})$. L_ϕ involves pairwise interactions between the weight vectors of hidden units, thus can be upper bounded using τ. Putting the pieces together, we obtain the following estimation error bound.

Theorem 2. *Let the activation function h be L-Lipschitz continuous and the loss $\ell(\hat{y}, y) = \frac{1}{2}(\hat{y} - y)^2$. Then, with probability at least $1 - \delta$:*

$$L(\hat{f}) - L(f^*) \leq \frac{\gamma^2 \sqrt{2 \ln(4/\delta)} + 4\gamma B(2CL + |h(0)|)\sqrt{m}}{\sqrt{n}}, \tag{4.3}$$

where $\gamma = 1 + BCL\sqrt{(m-1)\tau + 1} + \sqrt{m}B|h(0)|$.

Note that γ, hence the above bound on estimation error, decreases as τ becomes smaller. The bound goes to zero as n (sample size) goes to infinite. The inverse square root dependence on n matches existing results [32]. We note that it is straightforward to extend our bound to any bounded Lipschitz continuous loss ℓ.

The approximation error indicates how capable the hypothesis set $\mathcal{F}$ is to approximate a target function $g = \mathbb{E}[y|\mathbf{x}]$, where the error is measured by $\min_{f \in \mathcal{F}} \|f - g\|_{L^2}$ and $\|f - g\|_{L^2}^2 = \int (f(\mathbf{x}) - g(\mathbf{x}))^2 P(\mathrm{d}\mathbf{x})$. Following [31], we assume the target function g satisfies certain smoothness condition that is expressed in the first moment of its Fourier representation: $\int \|\boldsymbol{\omega}\|_2 |\tilde{g}(\boldsymbol{\omega})| \mathrm{d}\boldsymbol{\omega} \leq B/2$ where $\tilde{g}(\boldsymbol{\omega})$ is the Fourier representation of $g(\mathbf{x})$. To study the approximation error, we first define an auxiliary function class $\bar{\mathcal{F}} = \{\mathbf{x} \mapsto \sum_{j=1}^{m} \alpha_j h(\mathbf{w}_j^\top \mathbf{x}) \mid \|\boldsymbol{\alpha}\|_2 \leq B, \|\mathbf{w}_j\|_2 \leq C\}$. $\bar{\mathcal{F}}$ differs from $\mathcal{F}$ in that the angular constraints $\forall i \neq j, |\mathbf{w}_i \cdot \mathbf{w}_j| \leq \tau \|\mathbf{w}_i\|_2 \|\mathbf{w}_j\|_2$ are removed. Note that for $f \in \mathcal{F}$ and $\bar{f} \in \bar{\mathcal{F}}$, we have $\|g - f\|_{L^2} \leq \|g - \bar{f}\|_{L^2} + \|\bar{f} - f\|_{L^2}$. For $\|\bar{f} - f\|_{L^2}$, we derive an upper bound which is a quantity involving τ. For $\|g - \bar{f}\|_{L^2}$, its upper bound has been derived in [31]. Consequently, we obtain the upper bound of $\|g - f\|_{L^2}$, which is given in the following theorem. In order to derive explicit constants we restrict h to be the sigmoid function, but other Lipschitz continuous activation function can be similarly handled.

Theorem 3. *Let $C > 1$, $m \leq 2(\lfloor \frac{\frac{\pi}{2} - \theta}{\theta} \rfloor + 1)$, where $\theta = \arccos(\tau)$, and $h(t) = 1/(1 + e^{-t})$. Then, there is a function $f \in \mathcal{F}$ such that*

$$\|f - g\|_{L^2} \leq B(\tfrac{1}{\sqrt{m}} + \tfrac{1 + 2\ln C}{C}) + 2\sqrt{m}BC \sin(\tfrac{\min(3m\theta, \pi)}{2}).$$

This theorem implies that whether to use the angular constraint (AC) or not has a significant influence on the approximate error bound: without using AC ($\tau = 1$), the bound is a decreasing function of m (the number of hidden units); using AC ($\tau < 1$), the bound increases with m. This striking phrase-change indicates the impact of AC. Given a fixed m, the bound decreases with τ, implying that a stronger regularization (smaller τ) incurs larger approximation error. When $\tau = 1$, the second term in the bound vanishes and the bound is reduced to the one in [31], which is a decreasing function of m (and C, the upper bound on the weights). When $\tau < 1$, the second term increases with m up to the upper bound $2(\lfloor \frac{\frac{\pi}{2}-\theta}{\theta} \rfloor + 1)$. This is because a larger number of hidden units bear a larger difficulty in satisfying the pairwise ACs, which causes the function space $\mathcal{F}$ to shrink rapidly; accordingly, the approximation power of $\mathcal{F}$ decreases quickly.

The analysis in the two theorems shows that τ incurs a tradeoff between the estimation error and the approximation error: decreasing τ reduces the estimation error and enlarges the approximation error. Since the generalization error is the sum of the two errors, τ has an optimal value to yield the minimal generalization error.

4.2.2 Estimation Error Analysis for the Nonconvex Bregman Matrix Divergence Regularizers

In this section, we analyze how the nonconvex Bregman matrix divergence (BMD) regularizers [379] (Section 2.2.1) affect the estimation error of ML models. We use the distance metric learning (DML) model to perform the study. In DML, the hypothesis function is $u(\mathbf{x}, \mathbf{y}) = \|\mathbf{W}^\top(\mathbf{x} - \mathbf{y})\|_2^2$ and the loss function ℓ is the logistic loss $\ell(u(\mathbf{x}, \mathbf{y}), t) = \log(1 + \exp((2t - 1)u(\mathbf{x}, \mathbf{y})))$. Let $\mathcal{U} = \{u : (\mathbf{x}, \mathbf{y}) \mapsto \|\mathbf{W}^\top(\mathbf{x} - \mathbf{y})\|_2^2, \Omega(\mathbf{W}) \leq \tau\}$ denote the hypothesis set and $\mathcal{A} = \{\ell : (\mathbf{x}, \mathbf{y}, t) \mapsto \ell(u(\mathbf{x}, \mathbf{y}), t), u \in \mathcal{U}\}$ denote the loss class, which is the composition of the loss function with each of the hypotheses. In $\mathcal{U}$, we add the constraint $\Omega(\mathbf{W}) \leq \tau$ to incorporate the impact of the BMD regularizers $\Omega(\mathbf{W})$. τ controls the strength of regularization. A smaller τ entails stronger promotion of diversity. τ is controlled by the regularization parameter λ in Eq.(2.14). Increasing λ reduces τ. Given the joint distribution p^* of the input data pair $(\mathbf{x}, \mathbf{y})$ and the binary label t indicating whether this data pair is similar or dissimilar, the risk of the hypothesis u is $L(u) = \mathbb{E}_{(\mathbf{x},\mathbf{y},t)\sim p^*}[\ell(u(\mathbf{x}, \mathbf{y}), t)]$. Its empirical counterpart (training error) can be defined as $\widehat{L}(u) = \frac{1}{N}\sum_{n=1}^{N} \ell(u(\mathbf{x}_n, \mathbf{y}_n), t_n)$. The estimation error of a hypothesis u is defined as $L(u) - \widehat{L}(u)$, which represents how well the algorithm can learn and usually depends on the complexity of the hypothesis class and the number of training examples.

To upper bound the estimation error, we define a *capacity variable* on $\mathbf{W}$.

Definition 1 (Capacity Variable)**.** *Let $\pi_1, \cdots, \pi_m$ be the eigenvalues of $\mathbf{W}^\top\mathbf{W}$. Then the capacity variable is defined as:*

$$\mathcal{C}(\mathbf{W}) = \sum_{j=1}^{m} |\pi_j - 1|.$$

The following inequality helps us to understand the intuitive meaning of $\mathcal{C}(\mathbf{W})$:

$$\frac{1}{m}\|\mathbf{W}^\top\mathbf{W} - \mathbf{I}_m\|_1 \leq \mathcal{C}(\mathbf{W}). \tag{4.4}$$

$\frac{1}{m}\|\mathbf{W}^\top\mathbf{W} - \mathbf{I}_m\|_1$ measures the closeness between the Gram matrix $\mathbf{W}^\top\mathbf{W}$ and an identity matrix using L1 norm. The smaller this quantity is, the closer to being orthogonal the vectors in $\mathbf{W}$ are. Being an upper bound of this quantity, $\mathcal{C}(\mathbf{W})$ essentially determines the level of near-orthogonality among vectors.

We first prove that the estimation error can be upper bounded by an increasing function of the capacity variable. Then we show that the capacity variable can be upper bounded by an increasing function of the nonconvex BMD regularizers, including the log-determinant divergence (LDD) regularizer, the von Neumann divergence (VND) regularizer, and the squared Frobenius norm (SFN) regularizer. Combining these two steps we reveal the relationship between the estimation errors and the BMD regularizers, which is given in the following theorem.

Theorem 4. *Suppose* $\sup_{(\mathbf{x},\mathbf{y})}\|\mathbf{x}-\mathbf{y}\|_2 \leq B_0$ *and any column vector* $\mathbf{w}$ *of* $\mathbf{W}$ *satisfies* $\|\mathbf{w}\|_2 \leq D$. *With probability at least* $1-\delta$, *we have:*

- *For the LDD regularizer,*

$$L(u) - \widehat{L}(u) \leq 4B_0^2 D\sqrt{\frac{m(g_{ldd}^{-1}(\tau/m)m+1)}{N}} + [B_0^2 m(g_{ldd}^{-1}(\tau/m)+1)+1]\sqrt{\frac{2\log(1/\delta)}{N}}, \quad (4.5)$$

  where $g_{ldd}(x) = x - \log(x+1)$.
- *For the VND regularizer,*

$$L(u) - \widehat{L}(u) \leq 4B_0^2 D\sqrt{\frac{m(g_{vnd}^{-1}(\tau/m)m+1)}{N}} + [B_0^2 m(g_{vnd}^{-1}(\tau/m)+1)+1]\sqrt{\frac{2\log(1/\delta)}{N}}, \quad (4.6)$$

  where $g_{vnd}(x) = (x+1)\log(x+1) - x$.
- *For the SFN regularizer,*

$$L(u) - \widehat{L}(u) \leq (4+\sqrt{2\log(1/\delta)})B^2\sqrt{\frac{\tau m}{N}} + \frac{4B^2 m + (B^2 m+1)\sqrt{2\log(1/\delta)}}{\sqrt{N}}. \quad (4.7)$$

From these estimation error bounds (EEBs), we can see two major implications. First, BMD regularizers can effectively control the EEBs. Increasing the strength of BMD regularization (by enlarging λ) reduces τ, which decreases the EEBs since they are increasing functions of τ. Second, the EEBs converge with rate $O(1/\sqrt{N})$, where N is the number of training data pairs. This rate matches with that in [37, 338].

4.2.3 Estimation Error Analysis for the Convex Bregman Matrix Divergence Regularizers

In this section, we analyze how the convex BMD (CBMD) regularizers [379] (Section 2.2.2) affect the estimation error of CBMD-regularized distance metric learning problem (Eq.(2.22)). Following [338], we use *distance-based error* to measure the quality of a Mahalanobis distance matrix $\mathbf{M}$. Given the sample $\mathcal{S}$ and $\mathcal{D}$ where the total number of data pairs is $m = |S| + |D|$, the empirical error is defined as $\widehat{L}(\mathbf{M}) = \frac{1}{|\mathcal{S}|}\sum_{(\mathbf{x},\mathbf{y})\in\mathcal{S}}(\mathbf{x}-\mathbf{y})^\top\mathbf{M}(\mathbf{x}-\mathbf{y}) + \frac{1}{|\mathcal{D}|}\sum_{(\mathbf{x},\mathbf{y})\in\mathcal{D}}\max(0,\tau - (\mathbf{x}-\mathbf{y})^\top\mathbf{M}(\mathbf{x}-\mathbf{y}))$ and the expected error is $L(\mathbf{M}) = \mathrm{E}_{\mathcal{S},\mathcal{D}}[\widehat{L}(\mathbf{M})]$. Let $\widehat{\mathbf{M}}^*$ be the optimal matrix learned by minimizing the empirical error: $\widehat{\mathbf{M}}^* = \mathrm{argmin}_{\mathbf{M}}\widehat{L}(\mathbf{M})$. We are interested in

how well $\widehat{\mathbf{M}}^*$ performs on unseen data. The performance is measured using the estimation error: $\mathcal{E} = L(\widehat{\mathbf{M}}^*) - \widehat{L}(\widehat{\mathbf{M}}^*)$. To incorporate the impact of the CBMD regularizers $\Omega_\phi(\mathbf{M})$, we define the hypothesis class of $\mathbf{M}$ to be $\mathcal{M} = \{\mathbf{M} \succeq 0 : \Omega_\phi(\mathbf{M}) \leq C\}$. The upper bound C controls the strength of regularization. A smaller C entails stronger promotion of orthogonality. C is controlled by the regularization parameter γ in Eq.(4.1). Increasing γ reduces C. We perform the estimation error analysis as follows. We first establish an upper bound of the estimation error based on the Rademacher complexity $\mathcal{R}(\mathcal{M})$ of $\mathcal{M}$. Then we upper bound $\mathcal{R}(\mathcal{M})$ using the trace of $\mathbf{M}$. Finally, we derive upper bound of the trace based on the CBMD regularizers. Combining the three steps together, we establish upper bounds of the estimation error based on the CBMD regularizers, including the convex von Neumann divergence (CVND) regularizer, the convex log-determinant divergence (CLDD) regularizer, and the convex squared Frobenius norm (CSFN) regularizer:

Theorem 5. *Suppose* $\sup_{\|\mathbf{v}\|_2 \leq 1, (\mathbf{x},\mathbf{y}) \in \mathcal{S}} |\mathbf{v}^\top(\mathbf{x} - \mathbf{y})| \leq B$*, then with probability at least* $1 - \delta$*, we have:*

- *For the CVND regularizer,*

$$\mathcal{E} \leq (4B^2C + \max(\tau, B^2C)\sqrt{2\log(1/\delta)})\tfrac{1}{\sqrt{m}}.$$

- *For the CLDD regularizer,*

$$\mathcal{E} \leq (\tfrac{4B^2C}{\log(1/\epsilon)-1} + \max(\tau, \tfrac{C - D\epsilon}{\log(1/\epsilon)-1})\sqrt{2\log(1/\delta)})\tfrac{1}{\sqrt{m}}.$$

- *For the CSFN regularizer,*

$$\mathcal{E} \leq (2B^2\min(2C, \sqrt{C}) + \max(\tau, C)\sqrt{2\log(1/\delta)})\tfrac{1}{\sqrt{m}}.$$

From these estimation error bounds (EEBs), we can see two major implications. First, CBMD regularizers can effectively control the EEBs. Increasing the strength of CBMD regularization (by enlarging γ) reduces C, which decreases the EEBs since they are all increasing functions of C. Second, the EEBs converge with rate $O(1/\sqrt{m})$, where m is the number of training data pairs. This rate matches with that in [37, 338].

4.3 Appendix: Proofs

4.3.1 Proof of Theorem 1

Proof Sketch

We make the following two assumptions.

- The size of the similar and dissimilar set $|\mathcal{S}|$ and $|\mathcal{D}|$ are fixed.
- $\mathbf{A}^*$ has full row rank R.

Denote the K classes as $\mathcal{C}_1, \mathcal{C}_2, \cdots \mathcal{C}_K$. The probability that a sample is drawn from the k-th class is p_k, and $\sum_{k=1}^K p_k = 1$. Denote the class membership of an example $\mathbf{x}$ as $c(\mathbf{x})$. Denote the probability that $\mathbf{x} \in \mathcal{C}_j, \mathbf{y} \in \mathcal{C}_k$ where $(\mathbf{x}, \mathbf{y}) \in \mathcal{D}$ as $p_{jk} = p_j p_k / (1 - \sum_{l=1}^K p_l^2)$. Define

the singular value decomposition (SVD) of the matrix $\mathbf{A}^*$ as $\mathbf{U}\sqrt{\mathbf{\Lambda}}\mathbf{V}^\top$ where $\mathbf{U} \in \mathbb{R}^{R\times R}$, $\mathbf{\Lambda} \in \mathbb{R}^{R\times R}$, and $\mathbf{V} \in \mathbb{R}^{D\times R}$. $\mathbf{\Lambda} = \mathrm{diag}(\lambda_1, \lambda_2, \cdots \lambda_R)$. Then $\mathbf{A}^{*\top}\mathbf{A}^* = \mathbf{V}\mathbf{\Lambda}\mathbf{V}^\top$. Denote $\mathbf{V} = [\mathbf{v}_1, \mathbf{v}_2, \cdots \mathbf{v}_R]$. Then $\forall \mathbf{z} = \mathbf{x} - \mathbf{y}$, we have $\mathbf{z}^\top\mathbf{A}^{*\top}\mathbf{A}^*\mathbf{z} = \sum_{r=1}^R \lambda_r(\mathbf{v}_r^\top\mathbf{z})^2$. We see $\mathbf{z}^\top\mathbf{A}^{*\top}\mathbf{A}^*\mathbf{z}$ can be written as a sum of R terms. Inspired by this, we define a vector function $\alpha(\cdot)$ as $\alpha(\mathbf{u}) = \sum_{j,k=1}^K p_{jk}(\mathbf{u}^\top(\boldsymbol{\mu}_j - \boldsymbol{\mu}_k))^2$. This function measures the weighted sum of $(\mathbf{u}^\top(\boldsymbol{\mu}_j - \boldsymbol{\mu}_k))^2$ across all classes. Define $\mathcal{G} = \mathrm{span}\{\boldsymbol{\mu}_j - \boldsymbol{\mu}_k : j \neq k\}$.

Definition 2 (feature values and feature vectors)**.** *For a linear space $\mathcal{G}$, define vectors $\mathbf{w}_1, \mathbf{w}_2, \cdots, \mathbf{w}_{K-1}$ and positive real numbers $\beta_1, \beta_2, \cdots, \beta_{K-1}$ as*

$$\mathbf{w}_1 = \arg\min_{\|\mathbf{u}\|=1, \mathbf{u}\in\mathcal{G}} \alpha(\mathbf{u}), \;\; \beta_1 = \alpha(\mathbf{w}_1),$$

$$\mathbf{w}_r = \arg\min_{\substack{\|\mathbf{u}\|=1, \mathbf{u}\in\mathcal{G} \\ \mathbf{u}\perp \mathbf{w}_j, \forall j < r}} \alpha(\mathbf{u}), \;\; \beta_r = \alpha(\mathbf{w}_r), \;\; \forall r > 1$$

$\forall r > K-1$, define $\beta_r = 0$, and $\mathbf{w}_r$ as an arbitrary vector which has norm 1 and is orthogonal to $\mathbf{w}_1, \mathbf{w}_2, \cdots, \mathbf{w}_{r-1}$. $\mathbf{w}_1, \mathbf{w}_2, \cdots, \mathbf{w}_{K-1}$ are called feature vectors of $\mathcal{G}$, and $\beta_1, \beta_2, \cdots, \beta_{K-1}$ are called feature values of $\mathcal{G}$.

We give a condition on the regularizers.

Condition 1. *For a regularizer $\Omega_\phi(\cdot)$, there exists a unique matrix function $\varphi(\cdot)$ such that for any $\mathbf{A}^*$,*

$$\Omega_\phi(\mathbf{A}^*) = \varphi(\mathbf{A}^*\mathbf{A}^{*\top}) = \varphi(\mathbf{\Lambda}).$$

The VND and LDD regularizer satisfy this condition. For the VND regularizer, $\varphi(\mathbf{\Lambda}) = \mathrm{tr}(\mathbf{\Lambda}\log\mathbf{\Lambda} - \mathbf{\Lambda}) + R$; for the LDD regularizer, $\varphi(\mathbf{\Lambda}) = \mathrm{tr}(\mathbf{\Lambda}) - \log\det(\mathbf{\Lambda}) - R$. The SFN regularizer does not satisfy this condition.

Now we have enough preparation to give the following lemma. It shows that the linear space $\mathcal{G}$ can be recovered if the second moment of noise is smaller than a certain value.

Lemma 5. *Suppose $R \geq K-1$, $\max_{j\in k}\|\boldsymbol{\mu}_j - \boldsymbol{\mu}_k\|_2 \leq B_0$, and the regularization parameter γ and distance margin τ satisfy $\gamma \geq \gamma_0, \tau \geq \tau_0$. If $\xi \leq \frac{-B_0+\sqrt{B_0^2+\gamma_{K-1}\beta_{K-1}/(2\mathrm{tr}(\mathbf{\Lambda}))}}{4}$, then*

$$\mathcal{G} \subset \mathrm{span}(\mathbf{A}^{*\top}). \tag{4.8}$$

Here $\mathrm{span}(\mathbf{A}^{*\top})$ denotes the column space of matrix $\mathbf{A}^{*\top}$. Both λ_0 and τ_0 depend on $\boldsymbol{\mu}_1, \boldsymbol{\mu}_2, \cdots, \boldsymbol{\mu}_K$ and $p_1, p_2, \cdots, p_K$.

The next lemma shows that if Eq.(4.8) holds, we can bound the imbalance factor η with the condition number of $\mathbf{A}^*\mathbf{A}^{*\top}$ (denoted by $\mathrm{cond}(\mathbf{A}^*\mathbf{A}^{*\top})$). Note that the BMD regularizers $\Omega_\phi(\mathbf{A}^*)$ encourage $\mathbf{A}^*\mathbf{A}^{*\top}$ to be close to an identity matrix, i.e., encouraging the condition number to be close to 1.

Lemma 6. *If Eq.(4.8) holds, and there exists a real function g such that*

$$\mathrm{cond}(\mathbf{A}^*\mathbf{A}^{*\top}) \leq g(\Omega_\phi(\mathbf{A}^*)),$$

then we have the following bound for the imbalance factor

$$\eta \leq g(\Omega_\phi(\mathbf{A}^*))\frac{\max_{j\neq k}\|\boldsymbol{\mu}_j - \boldsymbol{\mu}_k\|^2}{\min_{j\neq k}\|\boldsymbol{\mu}_j - \boldsymbol{\mu}_k\|^2}.$$

Next, we derive the explicit forms of g for the VND and LDD regularizers.

Lemma 7. *For the VND regularizer $\Omega_{vnd}(\mathbf{A}^*)$, define $f(c) = c^{1/(c+1)}(1+1/c)$, then $f(c)$ is strictly increasing on $(0,1]$ and strictly decreasing on $[1,\infty)$. Define the inverse function of $f(\cdot)$ on $[1,\infty)$ as $f^{-1}(\cdot)$. Then if $\Omega_{vnd}(\mathbf{A}^*) < 1$, we have*

$$\mathrm{cond}(\mathbf{A}^*\mathbf{A}^{*\top}) \leq f^{-1}(2 - \Omega_{vnd}(\mathbf{A}^*)).$$

For the LDD regularizer $\Omega_{ldd}(\mathbf{A}^*)$, we have

$$\mathrm{cond}(\mathbf{A}^*\mathbf{A}^{*\top}) \leq 4e^{\Omega_{ldd}(\mathbf{A}^*)}.$$

Combining Lemma 5, 6, and 7, we finish the proof of Theorem 1.

Proof of Lemma 5

In order to prove Lemma 5, we first need some auxiliary lemmas on the properties of the function $\alpha(\cdot)$. Denote $\boldsymbol{\mu}_{jk} = \boldsymbol{\mu}_j - \boldsymbol{\mu}_k, \forall j \neq k$.

Lemma 8. *Suppose $\mathbf{u}_1, \mathbf{u}_2, \cdots \mathbf{u}_r$ and $\mathbf{v}_1, \mathbf{v}_2, \cdots \mathbf{v}_r$ are two sets of standard orthogonal vectors in $\mathbb{R}^d$, and $\mathrm{span}(\mathbf{u}_1, \mathbf{u}_2, \cdots \mathbf{u}_r) = \mathrm{span}(\mathbf{v}_1, \mathbf{v}_2, \cdots \mathbf{v}_r)$, then we have*

$$\sum_{l=1}^{r} \alpha(\mathbf{u}_l) = \sum_{l=1}^{r} \alpha(\mathbf{v}_l).$$

Proof. By the definition of these two sets of vectors, there exists a $r \times r$ standard orthogonal matrix $\mathbf{B} = (b_{jk})$, such that $(\mathbf{u}_1, \mathbf{u}_2, \cdots \mathbf{u}_r) = (\mathbf{v}_1, \mathbf{v}_2, \cdots \mathbf{v}_r)\mathbf{B}$. Then we have

$$\begin{aligned}
\sum_{l=1}^{r} \alpha(\mathbf{u}_l) &= \sum_{l=1}^{r} \sum_{j \neq k} p_{jk} ((\sum_{s=1}^{r} b_{ls}\mathbf{v}_s)^\top \boldsymbol{\mu}_{jk})^2 \\
&= \sum_{l=1}^{r} \sum_{j \neq k} p_{jk} \sum_{s,t=1}^{r} b_{ls} b_{lt} \mathbf{v}_s^\top \boldsymbol{\mu}_{jk} \mathbf{v}_t^\top \boldsymbol{\mu}_{jk} \\
&= \sum_{s=1}^{r} \sum_{j \neq k} p_{jk} (\mathbf{v}_s^\top \boldsymbol{\mu}_{jk})^2 \sum_{l=1}^{r} b_{ls}^2 + \sum_{j \neq k} p_{jk} \sum_{s,t=1}^{r} \mathbf{v}_s^\top \boldsymbol{\mu}_{jk} \mathbf{v}_t^\top \boldsymbol{\mu}_{jk} \sum_{l=1}^{r} b_{ls} b_{lt}.
\end{aligned}$$

Since $\mathbf{B}$ is a standard orthogonal matrix, we have $\forall s$, $\sum_{l=1}^{r} b_{ls}^2 = 1$ and $\forall s \neq t$, $\sum_{l=1}^{r} b_{ls} b_{lt} = 0$. Further, we have

$$\sum_{l=1}^{r} \alpha(\mathbf{u}_l) = \sum_{l=1}^{r} \alpha(\mathbf{v}_l).$$

□

Lemma 9. *For any positive integer r, any set of standard orthogonal vectors $\mathbf{u}_1, \mathbf{u}_2, \cdots \mathbf{u}_r \in \mathbb{R}^d$, and real numbers $\gamma_1 \geq \gamma_2 \geq \cdots \geq \gamma_r \geq 0$, we have*

$$\sum_{l=1}^{r} \gamma_l \alpha(\mathbf{u}_l) \leq \sum_{l=1}^{r} \gamma_l \beta_l, \tag{4.9}$$

where β_l is the l-th feature value.

Proof. We first prove the situation that $\gamma_1 = \gamma_2 = \cdots = \gamma_r = 1$, i.e.,

$$\sum_{l=1}^{r} \alpha(\mathbf{u}_l) \leq \sum_{l=1}^{r} \beta_l. \tag{4.10}$$

We prove it by induction on r. For $r = 1$, by the definition of feature values and feature vectors, Eq.(4.10) holds. Now supposing Eq.(4.10) holds for $r = s$, we prove it holds for $r = s + 1$ by contradiction. If Eq.(4.10) does not hold, then there exist standard orthogonal vectors $\mathbf{u}_1, \mathbf{u}_2, \cdots \mathbf{u}_{s+1} \in \mathbb{R}^d$, such that

$$\sum_{l=1}^{s+1} \alpha(\mathbf{u}_l) > \sum_{l=1}^{s+1} \alpha(\mathbf{w}_l), \tag{4.11}$$

where $\mathbf{w}_l$ are feature vectors. Since the dimension of $\mathrm{span}(\mathbf{u}_1, \mathbf{u}_2, \cdots \mathbf{u}_{s+1})$ is $s+1$, there exists $\widetilde{\mathbf{w}}_{s+1} \in \mathrm{span}(\mathbf{u}_1, \mathbf{u}_2, \cdots \mathbf{u}_{s+1})$, such that $\widetilde{\mathbf{w}}_{s+1} \perp \mathbf{w}_l, \forall 1 \leq l \leq s$. By the definition of the feature vector $\mathbf{w}_{s+1}$, we have

$$\sum_{l=1}^{s+1} \alpha(\mathbf{w}_l) \geq \sum_{l=1}^{s} \alpha(\mathbf{w}_l) + \alpha(\widetilde{\mathbf{w}}_{s+1}). \tag{4.12}$$

Let $\widetilde{\mathbf{w}}_1, \widetilde{\mathbf{w}}_2, \cdots \widetilde{\mathbf{w}}_{s+1}$ be a set of standard orthogonal basis of $\mathrm{span}(\mathbf{u}_1, \mathbf{u}_2, \cdots \mathbf{u}_{s+1})$, by Lemma 8, we have

$$\sum_{l=1}^{s+1} \alpha(\mathbf{u}_l) = \sum_{l=1}^{s+1} \alpha(\widetilde{\mathbf{w}}_l). \tag{4.13}$$

Combining equation (4.11), (4.12) and (4.13) we get

$$\sum_{l=1}^{s+1} \alpha(\widetilde{\mathbf{w}}_l) > \sum_{l=1}^{s} \alpha(\mathbf{w}_l) + \alpha(\widetilde{\mathbf{w}}_{s+1}).$$

Thus we have

$$\sum_{l=1}^{s} \alpha(\widetilde{\mathbf{w}}_l) > \sum_{l=1}^{s} \alpha(\mathbf{w}_l).$$

This contradicts with our induction assumption. The proof for the $\gamma_1 = \gamma_2 = \cdots = \gamma_r = 1$ case completes.

Next, we prove the situation that γ_l are not all equal to 1, by utilizing Eq.(4.10).

$$\begin{aligned}
\sum_{l=1}^{r} \gamma_l \alpha(\mathbf{u}_l) &= \sum_{l=1}^{r-1} [(\gamma_l - \gamma_{l+1}) \sum_{t=1}^{l} \alpha(\mathbf{u}_t)] + \gamma_r \sum_{t=1}^{r} \alpha(\mathbf{u}_t) \\
&\leq \sum_{l=1}^{r-1} [(\gamma_l - \gamma_{l+1}) \sum_{t=1}^{l} \beta_t] + \gamma_r \sum_{t=1}^{r} \beta_t \\
&\leq \sum_{l=1}^{r} \gamma_l \beta_l
\end{aligned}$$

The proof completes. □

Note that in Lemma 9, r can be larger than the number of nonzero feature values $K-1$. This will be used in the proof of Lemma 5 later on.

Another auxiliary lemma needed to prove Lemma 5 is given below.

Lemma 10. *Suppose $\mathbf{w}_0 \in \mathcal{G}$, define a linear space $\mathcal{H} = \{\mathbf{v} \in \mathcal{G} : \mathbf{v} \perp \mathbf{w}_0\}$. Then there are $K-2$ nonzero feature values of $\mathcal{H}$. Denote them as $\beta'_1, \beta'_2, \cdots \beta'_{K-2}$, then $\forall\ r \leq K-2$, $\forall\ \gamma_1 \geq \gamma_2 \geq \cdots \geq \gamma_r \geq 0$,*

$$\sum_{l=1}^{r} \gamma_l \beta'_l \leq \sum_{l=1}^{r} \gamma_l \beta_l.$$

Proof. Note that the dimension of $\mathcal{H}$ is $K-2$, then there are $K-2$ nonzero feature values. The feature vectors of $\mathcal{H}$ are also standard orthogonal vectors of the linear space $\mathcal{G}$. By Lemma 9, we have $\sum_{l=1}^{r} \gamma_l \beta'_l \leq \sum_{l=1}^{r} \gamma_l \beta_l,\ \forall\ r \leq K-2$. □

Now we are ready to prove Lemma 5.

Proof. (of Lemma 5) We conduct the proof by contradiction. Assuming Eq.(4.8) does not hold, we prove $\mathbf{A}^*$ can not be the global optimal solution. Let $\mathbf{U}\sqrt{\mathbf{\Lambda}}\mathbf{V}^\top$ be the SVD of $\mathbf{A}^*$. Define $\mathbf{W} = (\mathbf{w}_1, \mathbf{w}_2, \cdots \mathbf{w}_R)$ as a matrix whose columns contain the feature vectors. Let $\widetilde{\mathbf{A}} = \mathbf{U}\sqrt{\mathbf{\Lambda}}\mathbf{W}^\top$. Then by Condition 1, we have $\Omega_\phi(\mathbf{A}^*) = \Omega_\phi(\widetilde{\mathbf{A}})$. Define

$$L(\mathbf{A}) = \mathrm{E}\Big[\frac{1}{|\mathcal{S}|}\sum_{(\mathbf{x},\mathbf{y})\in\mathcal{S}} \|\mathbf{A}\mathbf{x} - \mathbf{A}\mathbf{y}\|_2^2 + \frac{1}{|\mathcal{D}|}\sum_{(\mathbf{x},\mathbf{y})\in\mathcal{D}} \max(0, \tau - \|\mathbf{A}\mathbf{x} - \mathbf{A}\mathbf{y}\|_2^2)\Big].$$

Assuming Eq.(4.8) does not hold, we prove $L(\mathbf{A}^*) > L(\widetilde{\mathbf{A}})$, i.e., $\mathbf{A}^*$ is not the optimal solution. We consider two cases: $\xi = 0$ and $\xi \neq 0$. Define $h(\mathbf{A}^*, \xi) = L(\mathbf{A}^*)$ and $h(\widetilde{\mathbf{A}}, \xi) = L(\widetilde{\mathbf{A}})$. When $\xi = 0$, we have:

$$\begin{aligned} h(\mathbf{A}^*, 0) &= \mathrm{E}\Big[\frac{1}{|\mathcal{S}|}\sum_{(\mathbf{x},\mathbf{y})\in\mathcal{S}} \|\mathbf{A}^*\boldsymbol{\mu}_{c(\mathbf{x})} - \mathbf{A}^*\boldsymbol{\mu}_{c(\mathbf{y})}\|_2^2 + \frac{1}{|\mathcal{D}|}\sum_{(\mathbf{x},\mathbf{y})\in\mathcal{D}} \max(0, \tau - \|\mathbf{A}^*\boldsymbol{\mu}_{c(\mathbf{x})} - \mathbf{A}^*\boldsymbol{\mu}_{c(\mathbf{y})}\|_2^2)\Big] \\ &= \sum_{j\neq k} p_{jk} \max(0, \tau - \|\mathbf{A}^*(\boldsymbol{\mu}_j - \boldsymbol{\mu}_k)\|_2^2), \end{aligned}$$

and

$$h(\widetilde{\mathbf{A}}, 0) = \sum_{j\neq k} p_{jk} \max(0, \tau - \|\widetilde{\mathbf{A}}(\boldsymbol{\mu}_j - \boldsymbol{\mu}_k)\|_2^2).$$

Since Eq.(4.8) does not hold by assumption, there exists a $\mathbf{w}_0$ satisfying $\mathbf{w}_0 \in \mathcal{G}$ and $\mathbf{w}_0 \notin \mathrm{span}(\mathbf{A}^*)$. Denote $\mathcal{H} = \{\mathbf{v} \in \mathcal{G} : \mathbf{v} \perp \mathbf{w}_0\}$ and its $K-2$ nonzero feature values as $\beta'_1, \beta'_2, \cdots \beta'_{K-2}$. $\forall \mathbf{u} \in \mathrm{span}(\mathbf{A}^*)$, let $\mathbf{u}'$ be the projection of $\mathbf{u}$ to the space $\mathcal{H}$ and $\mathbf{u}'$ is rescaled to have norm 1. Then $\alpha(\mathbf{u}') \geq \alpha(\mathbf{u})$. Thus, $\forall r$, the r-th feature value of $\mathrm{span}(\mathbf{A}^*)$ is no larger than the r-th feature value of $\mathcal{G}$. By Lemma 10, we have $\sum_{l=1}^{r} \gamma_l \beta'_l \leq \sum_{l=1}^{r} \gamma_l \beta_l$. By the definition of feature values, we have

$$\sum_{j\neq k} p_{jk} \|\mathbf{A}^*(\boldsymbol{\mu}_j - \boldsymbol{\mu}_k)\|_2^2 = \sum_{l=1}^{R} \gamma_l \alpha(\mathbf{a}_l) \leq \sum_{l=1}^{R} \gamma_l \beta'_l.$$

Since $\mathcal{H}$ has only $K-2$ nonzero feature values, we have

$$\sum_{l=1}^{R}\gamma_l\beta'_l=\sum_{l=1}^{K-2}\gamma_l\beta'_l\leq\sum_{l=1}^{K-2}\gamma_l\beta_l=\sum_{l=1}^{K-1}\gamma_l\alpha(\mathbf{w}_l)-\gamma_{K-1}\beta_{K-1}=\sum_{j\neq k}p_{jk}\|\widetilde{\mathbf{A}}(\boldsymbol{\mu}_j-\boldsymbol{\mu}_k)\|_2^2-\gamma_{K-1}\beta_{K-1}.$$

So we have

$$\sum_{j\neq k}p_{jk}\|\widetilde{\mathbf{A}}(\boldsymbol{\mu}_j-\boldsymbol{\mu}_k)\|_2^2\geq\sum_{j\neq k}p_{jk}\|\mathbf{A}^*(\boldsymbol{\mu}_j-\boldsymbol{\mu}_k)\|_2^2+\gamma_{K-1}\beta_{K-1}.$$

Next, we establish a relationship between $h(\mathbf{A}^*,0)$ and $h(\widetilde{\mathbf{A}},0)$, which is given in the following lemma.

Lemma 11. *There exist constants τ_0,γ_0 which are determined by $p_1,p_2,\cdots p_K$ and $\boldsymbol{\mu}_1,\boldsymbol{\mu}_2,\cdots,\boldsymbol{\mu}_K$, such that if $\tau\geq\tau_0,\gamma\geq\gamma_0$, then we have*

$$h(\mathbf{A}^*,0)-h(\widetilde{\mathbf{A}},0)>\frac{1}{2}\gamma_{K-1}\beta_{K-1}.$$

Proof. If $\|\widetilde{\mathbf{A}}(\boldsymbol{\mu}_j-\boldsymbol{\mu}_k)\|_2^2\leq\tau$ and $\|\mathbf{A}^*(\boldsymbol{\mu}_j-\boldsymbol{\mu}_k)\|_2^2\leq\tau$ for all $j\neq k$, we have $h(\mathbf{A}^*,0)-h(\widetilde{\mathbf{A}},0)=\gamma_{K-1}\beta_{K-1}$. Since $\max_{j\neq k}\|\boldsymbol{\mu}_j-\boldsymbol{\mu}_k\|_2=B_0$, we have

$$\|\mathbf{A}^*(\boldsymbol{\mu}_j-\boldsymbol{\mu}_k)\|_2^2\leq\mathrm{tr}(\boldsymbol{\Lambda})B_0^2,\ \|\widetilde{\mathbf{A}}(\boldsymbol{\mu}_j-\boldsymbol{\mu}_k)\|_2^2\leq\mathrm{tr}(\boldsymbol{\Lambda})B_0^2,\ \forall j\neq k.\tag{4.14}$$

Select τ_0 such that $\tau_0\geq K(1+\epsilon_0)B_0^2$, where ϵ_0 is any positive constant. For the VND and LDD regularizers, as $\gamma\to\infty$, $\boldsymbol{\Lambda}\to\mathbf{I}_R$. Thereby, there exists γ_0, such that if $\gamma\geq\gamma_0$, $\forall j,\ |\lambda_j-1|\leq\epsilon$. Hence, if $\gamma\geq\gamma_0,\tau\geq\tau_0$,

$$\mathrm{tr}(\boldsymbol{\Lambda})B_0^2\leq K(1+\epsilon_0)B_0^2\leq\tau_0.$$

Combining this inequality with Eq.(4.14), we finish the proof. □

Now we continue to prove Lemma 5. In Lemma 11, we have already proved that $h(\mathbf{A}^*,0)$ is strictly larger than $h(\widetilde{\mathbf{A}},0)$. We then prove that if the noise is smaller than a certain value, $h(\mathbf{A}^*,\xi)$ is strictly larger than $h(\widetilde{\mathbf{A}},\xi)$. By the definition of ξ, we have

$$\begin{aligned}
&|h(\mathbf{A}^*,\xi)-h(\mathbf{A}^*,0)|\\
\leq&\mathrm{E}\frac{1}{|\mathcal{S}|}\sum_{(x,y)\in\mathcal{S}}\|\mathbf{A}^*(\mathbf{x}-\mathbf{y})\|_2^2+\mathrm{E}\frac{1}{|\mathcal{D}|}\sum_{(x,y)\in\mathcal{D}}[\|\mathbf{A}^*(\mathbf{x}-\mathbf{y})\|_2^2-\|\mathbf{A}^*(\boldsymbol{\mu}_{c(\mathbf{x})}-\boldsymbol{\mu}_{c(\mathbf{y})})\|_2^2]\\
\leq&4\mathrm{tr}(\boldsymbol{\Lambda})\xi^2+(4B_0\xi+4\xi^2)\mathrm{tr}(\boldsymbol{\Lambda})\\
=&8\xi^2\mathrm{tr}(\boldsymbol{\Lambda})+4B_0\xi\mathrm{tr}(\boldsymbol{\Lambda}).
\end{aligned}\tag{4.15}$$

Similarly, we have

$$|h(\mathbf{A}^*,\xi)-h(\mathbf{A}^*,0)|\leq8\xi^2\mathrm{tr}(\boldsymbol{\Lambda})+4B_0\xi\mathrm{tr}(\boldsymbol{\Lambda}).\tag{4.16}$$

Combining Lemma 11 with Eq.(4.15) and Eq.(4.16), we have if $\xi\leq\frac{-B_0+\sqrt{B_0^2+\gamma_{K-1}\beta_{K-1}/(2\mathrm{tr}(\boldsymbol{\Lambda}))}}{4}$, then $L(\mathbf{A}^*)>L(\widetilde{\mathbf{A}})$, i.e., $\mathbf{A}^*$ is not the global optimal solution. By contradiction, Eq.(4.8) holds. The proof completes. □

Proof of Lemma 6

Proof. For any vector $\mathbf{u} \in \mathcal{G}$, since the condition of Lemma 5 is satisfied, we have $\mathbf{u} \in \text{span}(\mathbf{A}^*)$. Recall $\mathbf{A}^{*\top}\mathbf{A}^* = \mathbf{V}\mathbf{\Gamma}\mathbf{V}^\top$ and $\mathbf{V} = [\mathbf{v}_1, \mathbf{v}_2, \cdots \mathbf{v}_R]$. We can denote $\mathbf{u}$ as $\mathbf{u} = \|\mathbf{u}\| \sum_{j=1}^R t_j \mathbf{v}_j$, where $\sum_{j=1}^R t_j^2 = 1$. Then we have $\forall \mathbf{u} \in \mathcal{G}$,

$$\mathbf{u}^\top \mathbf{A}^{*\top}\mathbf{A}^*\mathbf{u} = \sum_{j=1}^R \langle \mathbf{v}_j, \mathbf{u}\rangle^2 \lambda_j = \sum_{j=1}^R \|\mathbf{u}\|^2 t_j^2 \lambda_j \leq \|\mathbf{u}\|^2 \lambda_1.$$

Similarly, we have $\mathbf{u}^\top \mathbf{A}^{*\top}\mathbf{A}^*\mathbf{u} \geq \|\mathbf{u}\|^2 \lambda_R$. Noting $\forall j \neq k$, $\boldsymbol{\mu}_j - \boldsymbol{\mu}_k \in \mathcal{G}$, we have

$$\eta \leq \text{cond}(\mathbf{A}^*\mathbf{A}^{*\top}) \frac{\max_{j\neq k} \|\boldsymbol{\mu}_j - \boldsymbol{\mu}_k\|^2}{\min_{j\neq k} \|\boldsymbol{\mu}_j - \boldsymbol{\mu}_k\|^2}.$$

Combining this inequality with $\text{cond}(\mathbf{A}^*\mathbf{A}^{*\top}) \leq g(\Omega_\phi(\mathbf{A}^*))$, we complete the proof. □

Proof of Lemma 7

Proof. We first prove the result about the VND regularizer. Define a scalar function $s(x) = x \log x - x + 1$ and denote $\text{cond}(\mathbf{A}^*\mathbf{A}^{*\top}) = c$. Since $s'(x) = \log x$, and $s(1) = 0$, we have

$$\begin{aligned}
\Omega_{vnd}(\mathbf{A}^*) &= \sum_{j=1}^R s(\lambda_j) \\
&\geq s(\lambda_1) + s(\lambda_R) \\
&= \lambda_1 \log \lambda_1 - \lambda_1 + \frac{\lambda_1}{c} \log \frac{\lambda_1}{c} - \frac{\lambda_1}{c} + 2.
\end{aligned}$$

Define $F(\lambda_1, c) = \lambda_1 \log \lambda_1 - \lambda_1 + \frac{\lambda_1}{c} \log \frac{\lambda_1}{c} - \frac{\lambda_1}{c} + 2$. We aim at maximizing c, so

$$\frac{\partial}{\partial \lambda_1} F(\lambda_1, c) = 0.$$

This equation has a unique solution: $\log \lambda_1 = \frac{\log c}{c+1}$. Therefore we have

$$c^{1/(c+1)}(1 + \frac{1}{c}) \geq 2 - \Omega_{vnd}(\mathbf{A}^*).$$

Define $f(c) = c^{1/(c+1)}(1 + \frac{1}{c})$. Its derivative is: $f'(c) = -\frac{\log c}{c(c+1)} c^{1/(c+1)}$. Analyzing $f'(c)$, we know that $f(c)$ increases on $(0, 1]$, decreases on $[1, \infty)$, and $f(1) = 2$. Also we have the following limits:

$$\lim_{c\to 0} f(c) = 0, \ \lim_{c\to\infty} f(c) = 1.$$

We denote the inverse function of $f(\cdot)$ on $[1, \infty)$ as $f^{-1}(\cdot)$. Then for any $\Omega_{vnd}(\mathbf{A}^*) < 1$, we have

$$\text{cond}(\mathbf{A}^*\mathbf{A}^{*\top}) \leq f^{-1}(2 - \Omega_{vnd}(\mathbf{A}^*)).$$

Next we prove the result for the LDD regularizer $\Omega_{ldd}(\mathbf{A}^*)$. Define a scalar function $s(x) = x - \log x - 1$ and denote $\mathrm{cond}(\mathbf{A}^*\mathbf{A}^{*\top}) = c$. Since $s'(x) = 1 - \frac{1}{x}$ and $s(1) = 0$, we have

$$\begin{aligned}\Omega_{ldd}(\mathbf{A}^*) &= \sum_{j=1}^{R} s(\lambda_j) \\ &\geq s(\lambda_1) + s(\lambda_R) \\ &= \lambda_1 - \log \lambda_1 + \frac{\lambda_1}{c} - \log \frac{\lambda_1}{c} - 2.\end{aligned}$$

Therefore we have

$$\begin{aligned}\log c &\leq \Omega_{ldd}(\mathbf{A}^*) + 2\log \lambda_1 - \lambda_1(1 + \frac{1}{c}) + 2 \\ &\leq \Omega_{ldd}(\mathbf{A}^*) + 2\log \lambda_1 - \lambda_1 + 2 \\ &\leq \Omega_{ldd}(\mathbf{A}^*) + 2\log 2 - 2 + 2 \\ &= \Omega_{ldd}(\mathbf{A}^*) + 2\log 2.\end{aligned}$$

The third inequality is obtained from the following fact: the scalar function $\log x - x$ gets its maximum when $x = 2$. Further, we have

$$c \leq 4e^{\Omega_{ldd}(\mathbf{A}^*)}.$$

The proof completes.

□

4.3.2 Proof of Theorem 2

A well established result in learning theory is that the estimation error can be upper bounded by the Rademacher complexity [32]. We start from the Rademacher complexity, seek a further upper bound of it, and show how the diversity of the hidden units affects this upper bound. The Rademacher complexity $\mathcal{R}_n(\ell \circ \mathcal{F})$ of the function class $\mathcal{F}$ composed with the loss function ℓ is defined as

$$\mathcal{R}_n(\ell \circ \mathcal{F}) = \mathbb{E} \sup_{f \in \mathcal{F}} \frac{1}{n} \left| \sum_{i=1}^{n} \sigma_i \ell(f(\mathbf{x}^{(i)}), y^{(i)}) \right|, \tag{4.17}$$

where $\{\sigma_i\}$ are independent and uniform over $\{-1, 1\}$ and $\{(\mathbf{x}^{(i)}, y^{(i)})\}_{i=1}^n$ are i.i.d samples drawn from p^*. Note that for later convenience, we take the absolute value in the above definition.

We can use the Rademacher complexity to upper bound the estimation error, as shown in Lemma 12.

Lemma 12 ([298, Theorem 26.5])**.** *With probability at least* $1 - \delta$*:*

$$L(\hat{f}) - L(f^*) \leq 4\mathcal{R}_n(\ell \circ \mathcal{F}) + 2\gamma\sqrt{\frac{2\log(4/\delta)}{n}}, \tag{4.18}$$

for $\gamma \geq \sup_{\mathbf{x},y,f} |\ell(f(\mathbf{x}), y)|$.

Our analysis starts from this lemma and we seek a further upper bound on $\mathcal{R}_n(\ell \circ \mathcal{F})$. The analysis needs an upper bound of the Rademacher complexity of the hypothesis set $\mathcal{F}$, which is given in Lemma 13.

Lemma 13. *Let $\mathcal{R}_n(\bar{\mathcal{F}})$ denote the Rademacher complexity of the hypothesis set $\bar{\mathcal{F}} = \{f(\mathbf{x}) = \sum_{j=1}^{m} \alpha_j h(\mathbf{w}_j^\top \mathbf{x}) \mid \|\boldsymbol{\alpha}\|_2 \le B, \|\mathbf{w}_j\|_2 \le C, \|\mathbf{x}\|_2 \le 1\}$, and h be L-Lipschitz, then*

$$\mathcal{R}_n(\bar{\mathcal{F}}) \le B(2CL + |h(0)|)\sqrt{\frac{m}{n}}. \tag{4.19}$$

Proof. The proof is analogous to that of [32, Theorem 18]. First, we have from [298, Lemma 26.11] that the Rademacher complexity of the class of linear functions $\mathcal{L} = \{\mathbf{x} \mapsto \mathbf{w}^\top \mathbf{x} : \|\mathbf{w}\|_2 \le C, \mathbf{w} \in \mathbb{R}^d\}$ is

$$\mathcal{R}_n(\mathcal{L}) \le C/\sqrt{n}. \tag{4.20}$$

Since composing with a 1-Lipschitz function h that vanishes at 0 can only increase the Rademacher complexity by a factor of two [216, Theorem 4.12], we have

$$\begin{aligned} \mathcal{R}_n(h \circ \mathcal{L}) &\le \mathcal{R}_n((h - h(0)) \circ \mathcal{L}) + |h(0)|/\sqrt{n} && (4.21)\\ &\le (2CL + |h(0)|)/\sqrt{n}. && (4.22) \end{aligned}$$

Lastly, since taking the (absolute) convex hull of a set of functions does not increase the Rademacher complexity [32, Theorem 12.2], we have

$$\mathcal{R}_n(\bar{\mathcal{F}}) \le \mathcal{R}_n(\sqrt{m}B \cdot \mathrm{absconv}(h \circ \mathcal{L})) \le B(2CL + |h(0)|)\sqrt{\frac{m}{n}}. \tag{4.23}$$

We note that if instead we consider

$$\mathcal{F}' = \{f(\mathbf{x}) = \sum_{j=1}^{m} \alpha_j h(\mathbf{w}_j^T \mathbf{x}) \mid \|\boldsymbol{\alpha}\|_1 \le B, \|\mathbf{w}_j\|_1 \le C, \|\mathbf{x}\|_2 \le 1\},$$

then a similar argument confirms that $\mathcal{R}_n(\mathcal{F}') \le B(2CL + |h(0)|)\sqrt{\frac{2\ln(2d)}{n}}$. □

In addition, we need the following uniform bound on the output of the network.

Lemma 14. *For any $\|\mathbf{x}\|_2 \le 1, \|\boldsymbol{\alpha}\|_2 \le B$ and L-Lipschitz continuous h, we have*

$$\sup_{\|\mathbf{w}_j\|_2 \le C, \forall i \ne j, \frac{|\mathbf{w}_i^\top \mathbf{w}_j|}{\|\mathbf{w}_i\|_2 \|\mathbf{w}_j\|_2} \le \tau} \left| \sum_{j=1}^{m} \alpha_j h(\mathbf{w}_j^\top \mathbf{x}) \right| \le BCL\sqrt{1 - \tau + m\tau} + \sqrt{m}B|h(0)|. \tag{4.24}$$

Proof. Indeed, let $u_j = h(\mathbf{w}_j^\top \mathbf{x}) - h(0)$. Then, $|u_j| \le L|\mathbf{w}_j^\top \mathbf{x}|$, hence

$$\begin{aligned} \left| \sum_{j=1}^{m} \alpha_j [h(\mathbf{w}_j^\top \mathbf{x}) - h(0)] \right| &\le \|\boldsymbol{\alpha}\|_2 \|\mathbf{u}\|_2 && (4.25)\\ &\le BL\|W^\top \mathbf{x}\|_2 && (4.26)\\ &\le BL\|W\|_{\mathrm{sp}}, && (4.27) \end{aligned}$$

where $W = [\mathbf{w}_1, \ldots, \mathbf{w}_m]$, and $\|W\|_{\text{sp}}$ is the spectral norm, which we bound as follows:

$$\|W\|_{\text{sp}}^2 = \max_{\|\mathbf{x}\|_2 \leq 1} \mathbf{x}^\top W^\top W \mathbf{x} \tag{4.28}$$

$$\leq \max_{\|\mathbf{x}\|_2 \leq 1} \sum_{i,j} |x_i||x_j||\mathbf{w}_i^\top \mathbf{w}_j| \tag{4.29}$$

$$\leq \max_{\|\mathbf{x}\|_2 \leq 1} (1-\tau) \sum_i x_i^2 \|\mathbf{w}_i\|_2^2 + \tau \sum_{i,j} |x_i||x_j| \|\mathbf{w}_i\|_2 \|\mathbf{w}_j\|_2 \tag{4.30}$$

$$\leq C^2[(1-\tau) + m\tau]. \tag{4.31}$$

Plugging the bound on $\|W\|_{\text{sp}}$ into (4.27) and applying the triangle inequality completes the proof. □

We are now ready to prove Theorem 2. The square loss function $\ell_y(t) = \ell(t, y) = \frac{1}{2}(t-y)^2$ is Lipschitz continuous with constant

$$\gamma = \sup_{\|\mathbf{x}\|_2 \leq 1, |y| \leq 1, f \in \mathcal{F}} |f(\mathbf{x}) - y| \leq \sup_{\mathbf{x}, y, f} (|f(\mathbf{x})| + |y|) \tag{4.32}$$

$$\leq 1 + BCL\sqrt{1 - \tau + m\tau} + \sqrt{m}B|h(0)|, \tag{4.33}$$

where the last inequality follows from Lemma 14. Applying the contraction property [298, Lemma 26.9] of the Rademacher complexity, we have

$$\mathcal{R}_n(\ell \circ \mathcal{F}) \leq (1 + BCL\sqrt{1 - \tau + m\tau} + \sqrt{m}B|h(0)|)\mathcal{R}_n(\mathcal{F}) \tag{4.34}$$

$$\leq (1 + BCL\sqrt{1 - \tau + m\tau} + \sqrt{m}B|h(0)|)\mathcal{R}_n(\bar{\mathcal{F}}). \tag{4.35}$$

Using Lemma 13 and Lemma 12 the claim follows.

In our proof we bound the Rademacher complexity of $\mathcal{F}$ using that of $\bar{\mathcal{F}}$ which simply ignores the pairwise correlation constraints. This step is likely very loose and it would be interesting to refine the bound so that it enjoys a reasonable dependence on τ.

4.3.3 Proof of Theorem 3

We need the following approximation error bound due to [31]:

Lemma 15 ([31, Theorem 3])**.** *Consider the function class*

$$\bar{\mathcal{F}} = \{\mathbf{x} \mapsto \sum_{j=1}^m \alpha_j h(\bar{\mathbf{w}}_j^T \mathbf{x}) \mid \|\boldsymbol{\alpha}\|_2 \leq B, \|\bar{\mathbf{w}}_j\|_2 \leq C, \|\mathbf{x}\|_2 \leq 1\}, \tag{4.36}$$

where the activation function $h(t) = 1/(1+e^{-t})$. Then, for any square integratable function g with

$$\int_{\boldsymbol{\omega}} \|\boldsymbol{\omega}\|_2 |\tilde{g}(\boldsymbol{\omega})| \mathrm{d}\boldsymbol{\omega} \leq B/2,$$

where $\tilde{g}(\boldsymbol{\omega})$ is the Fourier representation of $g(\mathbf{x})$, there exists $\bar{f} \in \bar{\mathcal{F}}$ such that

$$\|g - \bar{f}\|_{L^2} \leq B\left(\frac{1}{\sqrt{m}} + \frac{1 + 2\ln C}{C}\right). \tag{4.37}$$

We remark that [31] used instead the ℓ_1 constraint $\|\boldsymbol{\alpha}\|_1 \leq B$ in the definition of the function class $\bar{\mathcal{F}}$. For our purpose the ℓ_2 constraint on $\boldsymbol{\alpha}$ is more natural, and it is clear that we can only increase the function class $\bar{\mathcal{F}}$ by using the ℓ_2 constraint. As C and m tend to infinity, the above bound indicates that any square integratable function g can be approximated (under the L_2 metric) by the function class $\bar{\mathcal{F}}$. This is the well-known universal approximation property of neural networks. Moreover, if we choose $C \geq \sqrt{m} \ln m$, then the approximation error decreases at the usual rate $1/\sqrt{m}$.

Our key idea is to approximate the function class $\bar{\mathcal{F}}$ by the function class $\mathcal{F}$, where the pairwise angle constraint $\theta_{jk} \geq \theta$ is enforced. Of course, this is possible only when m is not too large.

Lemma 16. *Let $\theta = \arccos(\tau) \in (0, \frac{\pi}{2})$ and $m \leq 2(\lfloor \frac{\frac{\pi}{2}-\theta}{\theta} \rfloor + 1)$. For any unit vectors $(\bar{\mathbf{w}}_j)_{j=1}^m$, there exist unit vectors $(\mathbf{w}_j)_{j=1}^m$ such that*

$$\forall j \neq k \in \{1, \cdots, m\}, \ \ |\mathbf{w}_j \cdot \mathbf{w}_k| \leq \tau, \tag{4.38}$$

$$\forall j \in \{1, \cdots, m\}, \ \ \mathbf{w}_j \cdot \bar{\mathbf{w}}_j \geq \cos[\min(3m\theta, \pi)]. \tag{4.39}$$

Assuming Lemma 16 holds for now we can proceed to prove Theorem 3. According to Lemma 15, there exists some $\bar{f} = \sum_{j=1}^m \alpha_j h(\bar{\mathbf{w}}_j^\top \mathbf{x}) \in \bar{\mathcal{F}}$ such that

$$\|g - \bar{f}\|_{L^2} \leq B(\frac{1}{\sqrt{m}} + \frac{1 + 2\ln C}{C}). \tag{4.40}$$

Since

$$\|g - f\|_{L^2} \leq \|g - \bar{f}\|_{L^2} + \|\bar{f} - f\|_{L^2}, \tag{4.41}$$

we need only bound the last term as follows. Let us define $f = \sum_{j=1}^m \alpha_j h(\mathbf{w}_j^\top \mathbf{x})$, where $(\mathbf{w}_j)_{j=1}^m$ are given in Lemma 16 and scaled so that $\|\mathbf{w}_j\|_2 = \|\bar{\mathbf{w}}_j\|_2$. Straightforward calculation shows:

$$\|f - \bar{f}\|_{L^2}^2 = \int_{\|\mathbf{x}\|_2 \leq 1} (f(\mathbf{x}) - \bar{f}(\mathbf{x}))^2 \mathrm{d}\mu(\mathbf{x}) \tag{4.42}$$

$$= \int_{\|\mathbf{x}\|_2 \leq 1} \left(\sum_j \alpha_j \Big(h(\mathbf{w}_j^\top \mathbf{x}) - h(\bar{\mathbf{w}}_j^\top \mathbf{x}) \Big) \right)^2 \mathrm{d}\mu(\mathbf{x}) \tag{4.43}$$

$$\leq \int_{\|\mathbf{x}\|_2 \leq 1} \|\boldsymbol{\alpha}\|_2^2 \sum_j |\mathbf{w}_j^\top \mathbf{x} - \bar{\mathbf{w}}_j^\top \mathbf{x}|^2 \mathrm{d}\mu(\mathbf{x}) \tag{4.44}$$

$$\leq B^2 \sum_j \|\mathbf{w}_j - \bar{\mathbf{w}}_j\|_2^2 \tag{4.45}$$

$$= 2B^2 \sum_j \|\mathbf{w}_j\|_2^2 - \mathbf{w}_j^\top \bar{\mathbf{w}}_j \tag{4.46}$$

$$\leq 2B^2 (1 - \cos[\min(3m\theta, \pi)]) \sum_j \|\mathbf{w}_j\|_2^2 \tag{4.47}$$

$$\leq 4mB^2C^2 \sin^2 \frac{\min(3m\theta, \pi)}{2}. \tag{4.48}$$

Substituting back to (4.41) we have

$$\|g - f\|_{L^2} \leq \|g - \bar{f}\|_{L^2} + \|\bar{f} - f\|_{L^2} \tag{4.49}$$

$$\leq B(\frac{1}{\sqrt{m}} + \frac{1 + 2\ln C}{C}) + 2\sqrt{m}BC \sin\frac{\min(3m\theta, \pi)}{2}, \tag{4.50}$$

which was to be proved.

Proof of Lemma 16

The following simple lemma will be useful in our proof.

Lemma 17. *For any three unit vectors* $\mathbf{u}_1$*,* $\mathbf{u}_2$*, and* $\mathbf{u}_3$*:*

$$\angle(\mathbf{u}_1, \mathbf{u}_3) \leq \angle(\mathbf{u}_1, \mathbf{u}_2) + \angle(\mathbf{u}_2, \mathbf{u}_3), \tag{4.51}$$

with the convention $\angle(\mathbf{x}, \mathbf{y}) \in [0, \pi)$.

Proof. Without loss of generality, let $\mathbf{u}_2 = \mathbf{e}_1$. Let $\theta_{12} = \angle(\mathbf{u}_1, \mathbf{u}_2)$, $\theta_{23} = \angle(\mathbf{u}_2, \mathbf{u}_3)$, and $\theta_{13} = \angle(\mathbf{u}_1, \mathbf{u}_3)$. Then, $\mathbf{u}_1 = \cos\theta_{12} \cdot \mathbf{u}_2 + \sin\theta_{12} \cdot \mathbf{v}$ where the first element of the unit vector $\mathbf{v}$ equals 0. Similarly, $\mathbf{u}_3 = \cos\theta_{23} \cdot \mathbf{u}_2 + \sin\theta_{23} \cdot \mathbf{w}$ where the first element in the unit vector $\mathbf{w}$ equals 0. Therefore,

$$\cos\theta_{13} = \mathbf{u}_1^\top \mathbf{u}_3 \tag{4.52}$$

$$= (\cos\theta_{12} \cdot \mathbf{u}_2 + \sin\theta_{12} \cdot \mathbf{v})^\top (\cos\theta_{23} \cdot \mathbf{u}_2 + \sin\theta_{23} \cdot \mathbf{w}) \tag{4.53}$$

$$= \cos\theta_{12}\cos\theta_{23} + \sin\theta_{12}\sin\theta_{23}\mathbf{v}^\top\mathbf{w} \tag{4.54}$$

$$\geq \cos\theta_{12}\cos\theta_{23} - \sin\theta_{12}\sin\theta_{23} \tag{4.55}$$

$$= \cos(\theta_{12} + \theta_{23}). \tag{4.56}$$

If $\theta_{12} + \theta_{23} < \pi$, $\arccos(\cos(\theta_{12} + \theta_{23})) = \theta_{12} + \theta_{23}$. As $\arccos(\cdot)$ is monotonically decreasing, we have $\theta_{13} \leq \theta_{12} + \theta_{23}$. Otherwise, $\theta_{13} < \pi \leq \theta_{12} + \theta_{23}$. □

We now begin to prove Lemma 16. Let $\phi(\mathbf{a}, \mathbf{b}) = \arccos(\frac{\mathbf{a}\cdot\mathbf{b}}{\|\mathbf{a}\|_2\|\mathbf{b}\|_2})$, $\rho(\mathbf{a}, \mathbf{b}) = \arccos(\frac{|\mathbf{a}\cdot\mathbf{b}|}{\|\mathbf{a}\|_2\|\mathbf{b}\|_2})$. We begin our proof by considering a 2-dimensional case ($d = 2$). Let $k = \lfloor\frac{\frac{\pi}{2} - \theta}{\theta}\rfloor$. Define an index set $\mathcal{I} = \{-(k+1), -k, \cdots, -1, 1, 2, \cdots, k+1\}$. We define a set of vectors $(\mathbf{e}_i)_{i\in\mathcal{I}}$: $\mathbf{e}_i = (\sin\theta_i, \cos\theta_i)$, where $\theta_i \in (-\frac{\pi}{2}, \frac{\pi}{2})$ is defined as follows:

$$\theta_i = \mathrm{sgn}(i)(\frac{\theta}{2} + (|i| - 1)\theta). \tag{4.57}$$

From the definition we have:

$$\begin{array}{l} \forall i \neq j \in \mathcal{I}, \rho(\mathbf{e}_i, \mathbf{e}_j) \geq \theta, \\ -\frac{\pi}{2} + \frac{\theta}{2} \leq \theta_{-(k+1)} < -\frac{\pi}{2} + \frac{3}{2}\theta, \\ \frac{\pi}{2} - \frac{3}{2}\theta < \theta_{k+1} \leq \frac{\pi}{2} - \frac{\theta}{2}. \end{array} \tag{4.58}$$

And we can further verify that $\forall i \in \mathcal{I}$, there exist different $i_1, \cdots, i_{2k+1} \in \mathcal{I}\backslash i$ such that $\phi(\mathbf{e}_i, \mathbf{e}_{i_j}) \leq j\theta$. For any $\mathbf{e} = (\sin\beta, \cos\beta)$ with $\beta \in [-\frac{\pi}{2}, \frac{\pi}{2}]$, we can find an $i \in \mathcal{I}$ such that $\phi(\mathbf{e}_i, \mathbf{e}) \leq \frac{3}{2}\theta$:

- If $\beta \geq \theta_{k+1}$, taking $i = k+1$, we have $\phi(\mathbf{e}_i, \mathbf{e}) \leq \frac{\pi}{2} - \theta_{k+1} < \frac{3}{2}\theta$.
- If $\beta \leq \theta_{-(k+1)}$, taking $i = -(k+1)$, we also have $\phi(\mathbf{e}_i, \mathbf{e}) \leq \frac{3}{2}\theta$.
- Otherwise, taking $i = \text{sgn}(\beta)\lceil \frac{\beta - \frac{\theta}{2}}{\theta} \rceil$, we also have $\phi(\mathbf{e}_i, \mathbf{e}) \leq \theta < \frac{3}{2}\theta$.

Recall that for any i, there exist different $i_1, \cdots, i_{2k+1} \in \mathcal{I} \backslash i$ such that $\phi(\mathbf{e}_i, \mathbf{e}_{i_j}) \leq j\theta$, and using Lemma 17, we can draw the conclusion that for any $\mathbf{e} = (\sin\beta, \cos\beta)$ with $\beta \in [-\frac{\pi}{2}, \frac{\pi}{2}]$, there exist different $i_1, \cdots, i_{2k+2}$ such that $\phi(\mathbf{e}_i, \mathbf{e}_{i_j}) \leq \frac{3}{2}\theta + (j-1)\theta = (j + \frac{1}{2})\theta$. For any $(\mathbf{w}'_j)_{j=1}^m$, assume $\mathbf{w}'_j = \|\mathbf{w}'_j\|_2(\sin\beta_j, \cos\beta_j)$, and assume $\beta_j \in [-\frac{\pi}{2}, \frac{\pi}{2}]$. Using the above conclusion, for $\mathbf{w}'_1$, we can find some r_1 such that $\phi(\mathbf{w}'_1, \mathbf{e}_{r_1}) \leq \frac{3}{2}\theta$. For $\mathbf{w}'_2$, we can find different i_1, i_2 such that $\phi(\mathbf{w}'_2, \mathbf{e}_{i_1}) \leq \frac{3}{2}\theta < (\frac{3}{2}+1)\theta$ and $\phi(\mathbf{w}'_2, \mathbf{e}_{i_2}) \leq (\frac{3}{2}+1)\theta$. So we can find $r_2 \neq r_1$ such that $\phi(\mathbf{w}'_2, \mathbf{e}_{r_2}) \leq (\frac{3}{2}+1)\theta$. Following this scheme, we can find $r_j \notin \{r_1, \cdots, r_{j-1}\}$ and $\phi(\mathbf{w}'_j, \mathbf{e}_{r_j}) \leq (j + \frac{1}{2})\theta < 3m\theta$ for $j = 1, \cdots, m$, as we have assumed that $m \leq 2(k+1)$. Let $\mathbf{w}_j = \|\mathbf{w}'_j\|_2 \mathbf{e}_{r_j}$, then we have constructed $(\mathbf{w}_j)_{j=1}^m$ such that

$$\forall j \in \{1, \cdots, m\}, \phi(\mathbf{w}'_j, \mathbf{w}_j) \leq 3m\theta, \tag{4.59}$$

$$\forall j \in \{1, \cdots, m\}, \|\mathbf{w}'_j\|_2 = \|\mathbf{w}_j\|_2, \tag{4.60}$$

$$\forall j \neq k, \rho(\mathbf{w}_j, \mathbf{w}_k) \geq \theta. \tag{4.61}$$

Note that we have assumed $\forall j = 1, \cdots, m$, $\beta_j \in [-\frac{\pi}{2}, \frac{\pi}{2}]$. In order to show that the conclusion holds for general $\mathbf{w}'_j$, we need to consider the cases where $\beta_j \in [-\frac{3}{2}\pi, -\frac{\pi}{2}]$. For those cases, we can let $\beta'_j = \beta_j + \pi$, then $\beta'_j \in [-\frac{\pi}{2}, \frac{\pi}{2}]$. Let $\mathbf{w}''_j = \|\mathbf{w}'_j\|_2(\sin\beta'_j, \cos\beta'_j)$, we can find an $\mathbf{e}_{r_j}$ such that $\phi(\mathbf{w}''_j, \mathbf{e}_{r_j}) \leq m\theta$ following the same procedure. Let $\mathbf{w}_j = -\|\mathbf{w}'_j\|_2 \mathbf{e}_{r_j}$, then $\phi(\mathbf{w}'_j, \mathbf{w}_j) = \phi(\mathbf{w}''_j, \mathbf{e}_{r_j}) \leq 2m\theta$. Since $\rho(-\mathbf{e}_{r_j}, \mathbf{e}_k) = \rho(\mathbf{e}_{r_j}, \mathbf{e}_k)$, the $\rho(\mathbf{w}_j, \mathbf{w}_k) \geq \theta$ condition is still satisfied. Also noting that $\phi(\mathbf{a}, \mathbf{b}) \leq \pi$ for any a, b, we complete the proof for the 2-dimensional case.

Now we consider a general d-dimensional case. Similar to the 2-dimensional case, we construct a set of vectors with unit L_2 norm such that the pairwise angles $\rho(\mathbf{w}_j, \mathbf{w}_k) \geq \theta$ for $j \neq k$. We perform the construction in two phases. In the first phase, we construct a sequence of unit vector sets indexed by $\mathcal{I} = \{-(k+1), \cdots, -1, 1, \cdots, k+1\}$:

$$\forall i \in \mathcal{I}, \mathcal{E}_i = \{\mathbf{e} \in \mathbb{R}^d | \|\mathbf{e}\|_2 = 1, \mathbf{e} \cdot (1, 0, \cdots, 0) = \cos\theta_i\}, \tag{4.62}$$

where $\theta_i = \text{sgn}(i)(\frac{\theta}{2} + (|i|-1)\theta)$ is defined in Eq.(4.57). It can be shown that $\forall i \neq j$, $\forall \mathbf{e}_i \in \mathcal{E}_i, \mathbf{e}_j \in \mathcal{E}_j$,

$$\rho(\mathbf{e}_i, \mathbf{e}_j) \geq \theta. \tag{4.63}$$

The proof is as follows. First, we write $\mathbf{e}_i$ as $\mathbf{e}_i = (\cos\theta_i, 0, \cdots, 0) + \mathbf{r}_i$, where $\|\mathbf{r}_i\|_2 = |\sin\theta_i|$. Similarly, $\mathbf{e}_j = (\cos\theta_j, 0, \cdots, 0) + \mathbf{r}_j$, where $\|\mathbf{r}_j\|_2 = |\sin\theta_j|$. Hence we have

$$\mathbf{e}_i \cdot \mathbf{e}_j = \cos\theta_i \cos\theta_j + \mathbf{r}_i \cdot \mathbf{r}_j. \tag{4.64}$$

Hence

$$\cos(\rho(\mathbf{e}_i, \mathbf{e}_j)) = |\mathbf{e}_i \cdot \mathbf{e}_j| \tag{4.65}$$

$$\leq \cos\theta_i \cos\theta_j + |\sin\theta_i \sin\theta_j| \tag{4.66}$$

$$= \max(\cos(\theta_i + \theta_j), \cos(\theta_i - \theta_j)). \tag{4.67}$$

We have shown in the 2-dimensional case that $\cos(\theta_i + \theta_j) \geq \cos\theta$ and $\cos(\theta_i - \theta_j) \geq \cos\theta$, hence $\rho(\mathbf{e}_i, \mathbf{e}_j) \geq \theta$. In other words, we have proved that for any two vectors from $\mathcal{E}_i$ and $\mathcal{E}_j$, their pairwise angle is lower bounded by θ. Now we proceed to construct a set of vectors for each $\mathcal{E}_i$ such that the pairwise angles can also be lower bounded by θ. The construction is as follows. First, we claim that for any $\mathcal{E}_i$, if $\mathcal{W} \subset \mathcal{E}$ satisfies

$$\forall \mathbf{w}_j \neq \mathbf{w}_k \in \mathcal{W}, \phi(\mathbf{w}_j, \mathbf{w}_k) \geq \theta, \tag{4.68}$$

then $|W|$ is finite. In order to prove that, we first define $B(\mathbf{x}, r) = \{\mathbf{y} \in \mathbb{R}^n : \|\mathbf{y} - \mathbf{x}\|_2 < r\}$. Then $\mathcal{E}_i \subset \cup_{\mathbf{e}\in\mathcal{E}_i} B(\mathbf{e}, \frac{1-\cos\frac{\theta}{2}}{1+\cos\frac{\theta}{2}})$. According to the definition of $\mathcal{E}_i$, it is a compact set. Therefore the open cover has a finite subcover. Therefore we have $\exists V \subset \mathcal{E}_i$ with $|V|$ being finite and

$$\mathcal{E}_i \subset \cup_{\mathbf{v}\in V}\ B\left(\mathbf{v}, \frac{1-\cos\frac{\theta}{2}}{1+\cos\frac{\theta}{2}}\right). \tag{4.69}$$

Furthermore, we can verify that $\forall \mathbf{v} \in V, \forall \mathbf{e}_1, \mathbf{e}_2 \in B(\mathbf{v}, \frac{1-\cos\frac{\theta}{2}}{1+\cos\frac{\theta}{2}})$, $\phi(\mathbf{e}_1, \mathbf{e}_2) \leq \theta$. So if $\mathcal{W} \subset \mathcal{E}_i$ satisfies $\forall \mathbf{w}_j \neq \mathbf{w}_k \in \mathcal{W}, \phi(\mathbf{w}_j, \mathbf{w}_k) \geq \theta$, then for each $\mathbf{v} \in V$, $|B(\mathbf{v}, \frac{1-\cos\frac{\theta}{2}}{1+\cos\frac{\theta}{2}}) \cap \mathcal{W}| = 1$. As $\mathcal{W} \subset \mathcal{E}_i$, we have

$$\begin{aligned}
|W| &= |W \cap \mathcal{E}_i| && (4.70)\\
&= \left|W \cap \left(\cup_{\mathbf{v}\in V} B\left(\mathbf{v}, \frac{1-\cos\frac{\theta}{2}}{1+\cos\frac{\theta}{2}}\right)\right)\right| && (4.71)\\
&= \left|\cup_{\mathbf{v}\in V} W \cap B\left(\mathbf{v}, \frac{1-\cos\frac{\theta}{2}}{1+\cos\frac{\theta}{2}}\right)\right| && (4.72)\\
&\leq \sum_{\mathbf{v}\in V}\left|W \cap B\left(\mathbf{v}, \frac{1-\cos\frac{\theta}{2}}{1+\cos\frac{\theta}{2}}\right)\right| && (4.73)\\
&\leq \sum_{\mathbf{v}\in V} 1 && (4.74)\\
&= |V|. && (4.75)
\end{aligned}$$

Therefore, we have proved that $|W|$ is finite. Using this fact, we can construct a sequence of vectors $\mathbf{w}_j \in \mathcal{E}_i (j = 1, \cdots, l)$ in the following way:

1. Let $\mathbf{w}_1 \in \mathcal{E}_i$ be any vector in $\mathcal{E}_i$.
2. For $j \geq 2$, let $\mathbf{w}_j \in \mathcal{E}_i$ be any vector satisfying

$$\begin{aligned}
&\forall k = 1, \cdots, j-1, \phi(\mathbf{w}_j, \mathbf{w}_k) \geq \theta, && (4.76)\\
&\exists k \in \{1, \cdots, j-1\}, \phi(\mathbf{w}_j, \mathbf{w}_k) = \theta, && (4.77)
\end{aligned}$$

   until we cannot find such vectors any more.
3. As we have proved that $|W|$ is finite, the above process will end in finite steps. Assume that the last vector we found is indexed by l.

We will verify that such constructed vectors satisfy

$$\forall j \neq k \in \{1, \cdots, l\}, \rho(\mathbf{w}_j, \mathbf{w}_k) \geq \theta. \tag{4.78}$$

According to the construction, $\phi(\mathbf{w}_j, \mathbf{w}_k) \geq \theta$. As $\rho(\mathbf{w}_j, \mathbf{w}_k) = \min(\phi(\mathbf{w}_j, \mathbf{w}_k), \pi - \phi(\mathbf{w}_j, \mathbf{w}_k))$, we only need to show that $\pi - \phi(\mathbf{w}_j, \mathbf{w}_k) \geq \theta$. To show this is true, we use the definition of $\mathcal{E}_i$ to write $\mathbf{w}_j$ as $\mathbf{w}_j = (\cos\theta_i, 0, \cdots, 0) + \mathbf{r}_j$, where $\|\mathbf{r}_j\|_2 = |\sin\theta_i|$. Similarly, $\mathbf{w}_k = (\cos\theta_i, 0, \cdots, 0) + \mathbf{r}_k$, where $\|\mathbf{r}_k\|_2 = |\sin\theta_i|$. Therefore $\cos(\phi(\mathbf{w}_j, \mathbf{w}_k)) = \mathbf{w}_j \cdot \mathbf{w}_k \geq \cos^2\theta_i - \sin^2\theta_i = \cos(2\theta_i) \geq \cos(\pi - \theta)$, where the last inequality follows from the construction of θ_i. So $\pi - \phi(\mathbf{w}_j, \mathbf{w}_k) \geq \theta$, the proof for $\rho(\mathbf{w}_j, \mathbf{w}_k) \geq \theta$ is completed.

Now we will show that $\forall \mathbf{e} \in \mathcal{E}_i$, we can find $j \in \{1, \cdots, l\}$ such that $\phi(\mathbf{e}, \mathbf{w}_j) \leq \theta$. We prove it by contradiction: assume that there exists $\mathbf{e}$ such that $\min_{j\in\{1,\cdots,l\}} \phi(\mathbf{e}, \mathbf{w}_j) > \theta$, then as $\mathcal{E}_j$ is a connected set, there is a path $q : t \in [0, 1] \to \mathcal{E}_j$ connecting $\mathbf{e}$ to $\mathbf{w}_1$. When $t = 0$, the path starts at $q(0) = \mathbf{e}$; when $t = 1$, the path ends at $q(1) = \mathbf{w}_1$. We define functions $r_j(t) = \phi(q(t), \mathbf{w}_j)$ for $t \in [0, 1]$ and $j = 1, \cdots, l$. It is straightforward to see that $r_j(t)$ is continuous, hence $\min_j(r_j(t))$ is also continuous. As $\min_j(r_j(0)) > \theta$ and $\min_j(r_j(0)) = 0 < \theta$, there exists $t^* \in (0, 1)$ such that $\min_j(r_j(0)) = \theta$. Then $q(t^*)$ satisfies Condition 4.76, which contradicts the construction in W as the construction only ends when we cannot find such vectors. Hence we have proved that

$$\forall \mathbf{e} \in \mathcal{E}_i, \exists j \in \{1, \cdots, l\}, \phi(\mathbf{e}, \mathbf{w}_j) \leq \theta. \tag{4.79}$$

Now we can proceed to prove the main lemma. For each $i \in \mathcal{I}$, we use Condition 4.76 to construct a sequence of vectors $\mathbf{w}_{ij}$. Then such constructed vectors have pairwise angles greater than or equal to θ. Then for any $\mathbf{e} \in \mathcal{R}^d$ with $\|\mathbf{e}\|_2 = 1$, we write $\mathbf{e}$ in sphere coordinates as $\mathbf{e} = (\cos r_1, \sin r_1 \cos r_2, \cdots, \prod_{j=1}^{d} \sin r_j)$. Use the same method as we did for the 2-dimensional case, we can find θ_i such that $|\theta_i - r| \leq \frac{3}{2}\theta$. Then $\mathbf{e}' = (\cos\theta_i, \sin\theta_i \cos r_2, \cdots, \sin\theta_i \prod_{j=2}^{d} \sin r_j) \in \mathcal{E}_i$. It is easy to verify that $\phi(\mathbf{e}, \mathbf{e}') = |\theta_i - r| \leq \frac{3}{2}\theta$. As $\mathbf{e}' \in \mathcal{E}_i$, there exists $\mathbf{w}_{ij}$ as we constructed such that $\phi(\mathbf{e}', \mathbf{w}_{ij}) \leq \theta$. So $\phi(\mathbf{e}, \mathbf{w}_{ij}) \leq \phi(\mathbf{e}, \mathbf{e}') + \phi(\mathbf{e}', \mathbf{w}_{ij}) \leq \frac{5}{2}\theta < 3\theta$. So we have proved that for any $\mathbf{e} \in \mathbb{R}^d$ with $\|\mathbf{e}\|_2 = 1$, we can find $\mathbf{w}_{ij}$ such that $\phi(\mathbf{e}, \mathbf{w}_{ij}) < 3\theta$.

For any $\mathbf{w}_{ij}$, assume $i + 1 \in \mathcal{I}$, we first project $\mathbf{w}_{ij}$ to $\mathbf{w}^* \in \mathcal{E}_{i+1}$. We have proved that $\phi(\mathbf{w}_{ij}, \mathbf{w}^*) \leq \frac{3}{2}\theta$ and also proved that we can find $\mathbf{w}_{i+1,j'} \in \mathcal{E}_{i+1}$ such that $\phi(\mathbf{w}_{i+1,j'}, \mathbf{w}^*) \leq \theta$. So we have found $\mathbf{w}_{i+1,j'}$ such that $\phi(\mathbf{w}_{ij}, \mathbf{w}_{i+1,j'}) \leq \frac{5}{2}\theta < 3\theta$. We can use similar scheme to prove that $\forall \mathbf{w}_{ij}$, there exist different $\mathbf{w}_{i_1,j_1} \cdots, \mathbf{w}_{i_{2k+1},j_{2k+1}}$ such that $(i_r, j_r) \neq (i, j)$ and $\phi(\mathbf{w}_{ij}, \mathbf{w}_{i_r,j_r}) \leq 3r\theta$. Following the same proof as the 2-dimensional case, we can prove that if $m \leq 2k + 1$, then we can find a set of vectors $(\mathbf{w}_j)_{j=1}^m$ such that

$$\forall j \in \{1, \cdots, m\}, \phi(\mathbf{w}'_j, \mathbf{w}_j) \leq \min(3m\theta, \pi), \tag{4.80}$$

$$\forall j \in \{1, \cdots, m\}, \|\mathbf{w}'_j\|_2 = \|\mathbf{w}_j\|_2, \tag{4.81}$$

$$\forall j \neq k, \rho(\mathbf{w}_j, \mathbf{w}_k) \geq \theta. \tag{4.82}$$

The proof completes.

4.3.4 Proof of Theorem 4

Proof Sketch

Define $\mathcal{W} = \{\mathbf{W} \in \mathbb{R}^{d\times m} | \Omega(\mathbf{W}) \leq \tau\}$ and $\widetilde{\mathcal{C}}(\mathcal{W}) = \sup_{\mathbf{W}\in\mathcal{W}} \mathcal{C}(\mathbf{W})$. The following lemma shows that the estimation error can be upper bounded using $\mathcal{C}(\mathcal{W})$.

Lemma 18. *Suppose* $\sup_{(\mathbf{x},\mathbf{y})} \|\mathbf{x}-\mathbf{y}\|_2 \leq B_0$ *and* $\|\mathbf{w}\|_2 \leq D$*, then with probability at least* $1-\delta$*, we have*

$$L(u) - \widehat{L}(u) \leq 4B_0^2 D\sqrt{\frac{(\widetilde{\mathcal{C}}(\mathcal{W})+1)m}{N}} + [B_0^2(\widetilde{\mathcal{C}}(\mathcal{W})+m)+1]\sqrt{\frac{2\log(1/\delta)}{N}}. \tag{4.83}$$

The upper bound is an increasing function of $\widetilde{\mathcal{C}}(\mathcal{W})$. The following lemma shows that $\mathcal{C}(\mathbf{W})$ can be upper bounded by an increasing function of the LDD regularizer $\Omega_{ldd}(\mathbf{W})$.

Lemma 19. *Let* $g(x) = x - \log(x+1)$*. Then we have*

$$\mathcal{C}(\mathbf{W}) \leq g^{-1}(\Omega_{ldd}(\mathbf{W})/m)m.$$

where $g^{-1}(\cdot)$ *is the inverse function of* g *on* $[0,\infty)$ *and is an increasing function.*

Since $\Omega_{ldd}(\mathbf{W}) \leq \tau$, we have $\mathcal{C}(\mathbf{W}) \leq g^{-1}(\tau/m)m$ for any $\mathbf{W} \in \mathcal{W}$, i.e., $\widetilde{\mathcal{C}}(\mathcal{W}) \leq g^{-1}(\tau/m)m$. Substituting this inequality into Lemma 18, we obtain the bound in Eq.(4.5) in Theorem 4.

Proof of Lemma 18

Proof. Let $\mathcal{U} = \{u : (\mathbf{x},\mathbf{y}) \to \|\mathbf{W}(\mathbf{x}-\mathbf{y})\|_2^2\}$ be the set of hypothesis $u(\mathbf{x},\mathbf{y}) = \|\mathbf{W}(\mathbf{x}-\mathbf{y})\|_2^2$, and $\mathcal{R}(\mathcal{U})$ be the Rademacher complexity [32] of $\mathcal{U}$ which is defined as:

$$\mathcal{R}(\mathcal{U}) = \mathrm{E}_{S_N,\sigma} \sup_{u\in\mathcal{U}} \frac{1}{n}\sum_{n=1}^{N} \sigma_n \|\mathbf{W}(\mathbf{x}_n - \mathbf{y}_n)\|_2^2,$$

where $S_N = ((\mathbf{x}_1,\mathbf{y}_1,t_1),(\mathbf{x}_2,\mathbf{y}_2,t_2)\cdots(\mathbf{x}_n,\mathbf{y}_n,t_N))$ are the training examples, $\sigma_n \in \{-1,1\}$ are the Rademacher variables, and $\sigma = (\sigma_1,\sigma_2,\cdots\sigma_N)$.

Lemma 20 shows that the estimation error can be bounded using the Rademacher complexity. Its proof is adapted from [32]. Readers only need to notice $x+1$ is an upper bound of $\log(1+\exp(\mathbf{x}))$ for $x > 0$.

Lemma 20. *With probability at least* $1-\delta$*, we have*

$$L(u) - \widehat{L}(u) \leq 2\mathcal{R}(\mathcal{U}) + \sup_{\mathbf{x},\mathbf{y},\mathbf{W}'\in\mathcal{W}} (\|\mathbf{W}'(\mathbf{x}-\mathbf{y})\|_2^2 + 1)\sqrt{\frac{2\log(1/\delta)}{N}}. \tag{4.84}$$

We then bound $\mathcal{R}(\mathcal{U})$ and $\sup_{\mathbf{x},\mathbf{y},\mathbf{W}'\in\mathcal{W}} \|\mathbf{W}'(\mathbf{x}-\mathbf{y})\|_2^2$. The result is in the following lemma.

Lemma 21. *Suppose* $\sup_{(\mathbf{x},\mathbf{y})} \|\mathbf{x}-\mathbf{y}\|_2 \leq B_0$ *and* $\|\mathbf{w}\|_2 \leq D$*, then we have*

$$\mathcal{R}(\mathcal{U}) \leq \frac{2B_0^2 D\sqrt{m}}{\sqrt{N}}\sqrt{\widetilde{\mathcal{C}}(\mathcal{W})+1},$$

and

$$\sup_{\mathbf{x},\mathbf{y},\mathbf{W}'\in\mathcal{W}} \|\mathbf{W}'(\mathbf{x}-\mathbf{y})\|_2^2 \leq B_0^2(\widetilde{\mathcal{C}}(\mathcal{W})+m).$$

Proof. We first give bound on $\mathcal{R}(\mathcal{U})$. Let $\mathcal{R}(\mathcal{S}) = \{s : (\mathbf{x},\mathbf{y}) \to \sum_{j=1}^m |\langle \mathbf{w}_j, \mathbf{x}-\mathbf{y}\rangle|, \mathbf{W}\in\mathcal{W}\}$ be the set of hypothesis $s(\mathbf{x},\mathbf{y}) = \sum_{j=1}^m |\langle \mathbf{w}_j, \mathbf{x}-\mathbf{y}\rangle|$. Denote $|\langle \mathbf{w}_j, \mathbf{x}_n-\mathbf{y}_n\rangle| = \langle \mathbf{w}_j, a_{n,j}(\mathbf{x}_n-\mathbf{y}_n)\rangle$, where $a_{n,j}\in\{-1,1\}$. Then

$$\mathcal{R}(\mathcal{S}) = \mathrm{E}_{S_N,\sigma} \sup_{\mathbf{W}\in\mathcal{W}} \frac{1}{N}\sum_{n=1}^N \sigma_n \sum_{j=1}^m \langle \mathbf{w}_j, a_{n,j}(\mathbf{x}_n-\mathbf{y}_n)\rangle. \tag{4.85}$$

We first bound $\mathcal{R}(\mathcal{S})$.

$$\begin{aligned}
\mathcal{R}(\mathcal{S}) &= \mathrm{E}_{S_N,\sigma} \sup_{\mathbf{W}\in\mathcal{W}} \frac{1}{N}\sum_{j=1}^m \langle \mathbf{w}_j, \sum_{n=1}^N \sigma_n a_{n,j}(\mathbf{x}_n-\mathbf{y}_n)\rangle \\
&= \mathrm{E}_{S_N,\sigma} \sup_{\mathbf{W}\in\mathcal{W}} \frac{1}{N}\langle \sum_{j=1}^m \mathbf{w}_j, \sum_{n=1}^N \sigma_n a_{n,j}(\mathbf{x}_n-\mathbf{y}_n)\rangle \\
&\leq \mathrm{E}_{S_N,\sigma} \sup_{\mathbf{W}\in\mathcal{W}} \frac{1}{N}\|\sum_{j=1}^m \mathbf{w}_j\|_2 \|\sum_{n=1}^N \sigma_n a_{n,j}(\mathbf{x}_n-\mathbf{y}_n)\|_2 \\
&= \mathrm{E}_{S_N,\sigma} \sup_{\mathbf{W}\in\mathcal{W}} \frac{1}{N}\sqrt{\langle \sum_{j=1}^m \mathbf{w}_j, \sum_{j=1}^m \mathbf{w}_j\rangle}\sqrt{\langle \sum_{n=1}^N \sigma_n a_{n,j}(\mathbf{x}_n-\mathbf{y}_n), \sum_{n=1}^N \sigma_n a_{n,j}(\mathbf{x}_n-\mathbf{y}_n)\rangle}.
\end{aligned} \tag{4.86}$$

Applying Jensen's inequality to Eq.(4.86), we have

$$\mathcal{R}(\mathcal{S}) \leq \mathrm{E}_{S_N} \sup_{\mathbf{W}\in\mathcal{W}} \frac{1}{N}\sqrt{\sum_{j,k=1}^m |\langle \mathbf{w}_j, \mathbf{w}_k\rangle|}\sqrt{\mathrm{E}_\sigma\langle \sum_{n=1}^N \sigma_n a_{n,j}(\mathbf{x}_n-\mathbf{y}_n), \sum_{n=1}^N \sigma_n a_{n,j}(\mathbf{x}_n-\mathbf{y}_n)\rangle}. \tag{4.87}$$

Combining Eq.(4.87) with the inequality $\sum_{j,k=1}^m |\langle \mathbf{w}_j, \mathbf{w}_k\rangle - \delta_{j,k}| \leq m\mathcal{C}(\mathbf{W})$, we have

$$\begin{aligned}
\mathcal{R}(\mathcal{S}) &\leq \mathrm{E}_{S_N} \sup_{\mathbf{W}\in\mathcal{W}} \frac{1}{N}\sqrt{m\mathcal{C}(\mathbf{W})+m}\sqrt{\sum_{n=1}^N \|\mathbf{x}_n-\mathbf{y}_n\|_2} \\
&\leq \frac{\sqrt{m}}{\sqrt{N}} \sup_{\mathbf{W}\in\mathcal{W}} \sqrt{(\mathcal{C}(\mathbf{W})+1)}B_0.
\end{aligned}$$

Let $\mathbf{w}$ denote any column vector of $\mathbf{W}\in\mathcal{W}$ and $\mathbf{x}$ denote any data example. According to the

composition property of Rademacher complexity (Theorem 12 in [32]), we have

$$\begin{aligned}\mathcal{R}(\mathcal{U}) &\leq 2\sup_{\mathbf{w},\mathbf{x}}\langle \mathbf{w},\mathbf{x}\rangle \mathcal{R}(\mathcal{S}) \\ &\leq 2\sup_{\mathbf{w}}\|\mathbf{w}\|_2 B_0 \mathcal{R}(\mathcal{S}) \\ &\leq \frac{2B_0^2 D\sqrt{m}}{\sqrt{N}}\sqrt{\widetilde{\mathcal{C}}(\mathcal{W})+1}.\end{aligned}$$

Next we give bound on $\sup_{\mathbf{x},\mathbf{y},\mathbf{W}'\in\mathcal{W}}\|\mathbf{W}'(\mathbf{x}-\mathbf{y})\|_2^2$.

$$\begin{aligned}\sup_{\mathbf{x},\mathbf{y},\mathbf{W}'\in\mathcal{W}}\|\mathbf{W}'(\mathbf{x}-\mathbf{y})\|_2^2 &\leq \sup_{\mathbf{W}'\in\mathcal{W}}\sum_{j=1}^{m}\langle \mathbf{w}'_j,\mathbf{w}'_j\rangle \sup_{(\mathbf{x},\mathbf{y})}\|\mathbf{x}-\mathbf{y}\|_2^2 \\ &= \sup_{\mathbf{W}'\in\mathcal{W}}\mathrm{tr}(\mathbf{W}'^{\top}\mathbf{W}')\sup_{(\mathbf{x},\mathbf{y})}\|\mathbf{x}-\mathbf{y}\|_2^2 \\ &\leq (\widetilde{\mathcal{C}}(\mathcal{W})+m)B_0^2\end{aligned}$$

□

Combining Lemma 21 with Lemma 20, we complete the proof of Lemma 18. □

Proof of Lemma 19

Proof. The function $g(x)=x-\log(x+1)$ is decreasing on$(-1,0]$, increasing on $[0,\infty)$, $g(0)=0$, and $g(-t)>g(t)$ for $\forall 0\leq t<1$. We have

$$\begin{aligned}\Omega_{ldd}(\mathbf{W}) &= \mathrm{tr}(\mathbf{W}^{\top}\mathbf{W})-\log\det(\mathbf{W}^{\top}\mathbf{W})-m \\ &= \sum_{j=1}^{m} g(\pi_j-1) \\ &\geq \sum_{j=1}^{m} g(|\pi_j-1|) \\ &\geq g(\frac{1}{m}\sum_{j=1}^{m}|\pi_j-1|)m \\ &= g(\mathcal{C}(\mathbf{W})/m)m.\end{aligned}$$

The first inequality is due to $g(-t)>g(t)$, and the second inequality can be attained by Jensen's inequality. Finally we have

$$g(\mathcal{C}(\mathbf{W})/m)m \leq \Omega_{ldd}(\mathbf{W}).$$

Thus, we have

$$\mathcal{C}(\mathbf{W}) \leq g^{-1}(\Omega_{ldd}(\mathbf{W})/m)m.$$

□

Extend the Analysis to the VND Regularizer

Next, we extend the estimation error analysis to the VND regularizer. The following lemma shows that $\mathcal{C}(\mathbf{W})$ can be upper bounded by an increasing function of the VND regularizer $\Omega_{vnd}(\mathbf{W})$.

Lemma 22. *Define a real function $g = (x+1)\log(x+1) - x$, which is increasing on $[0, \infty)$. Then we have:*

$$\mathcal{C}(\mathbf{W}) \leq m g^{-1}(\Omega_{vnd}(\mathbf{W})/m),$$

where g^{-1} is the inverse function of g.

Proof. g is decreasing on $(-1, 0]$ and increasing on $[0, \infty)$. $g(0) = 0$, $g(-t) > g(t)$ for $\forall 0 \leq t < 1$. We have

$$\begin{aligned}
\Omega_{vnd}(\mathbf{W}) &= \mathrm{tr}(\mathbf{G}\log\mathbf{G}) - \mathrm{tr}(\mathbf{G}) + m \\
&= \sum_{j=1}^{m} g(\pi_j - 1) \\
&\geq \sum_{j=1}^{m} g(|\pi_j - 1|) \\
&\geq m g(\frac{1}{m}\sum_{j=1}^{m} |\pi_j - 1|) \\
&= m g(\mathcal{C}(\mathbf{W})/m),
\end{aligned}$$

where $\mathbf{G} = \mathbf{W}^\top\mathbf{W}$ and $\{\pi_j\}_{j=1}^m$ are the eigenvalues of $\mathbf{G}$. The first inequality is due to $g(-t) > g(t)$, and the second inequality can be attained by Jensen's inequality. Finally we have

$$g(\mathcal{C}(\mathbf{W})/m) \leq \Omega_{vnd}(\mathbf{W}).$$

Thus, we have

$$\mathcal{C}(\mathbf{W}) \leq m g^{-1}(\Omega_{vnd}(\mathbf{W})/m).$$

□

Combining Lemma 22 with Lemma 18, we obtain the bound in Eq.(4.6) in Theorem 4.

Analysis of the SFN Regularizer

For SFN, the analysis approach is different. Instead of leveraging the intermediate capacity variable, we directly bound the estimation error with SFN. The following lemma gives an upper bound of the Rademacher complexity.

Lemma 23. *Suppose $\sup_{(\mathbf{x},\mathbf{y})}\|\mathbf{x} - \mathbf{y}\| \leq B$, then we have*

$$\mathcal{R}(\mathcal{U}) \leq \frac{2B^2\sqrt{m}}{\sqrt{N}}(\|\mathbf{W}^\top\mathbf{W} - \mathbf{I}\|_F + \sqrt{m}),$$

and

$$\sup_{\mathbf{x},\mathbf{y},\mathbf{W}'\in\mathcal{W}} \|\mathbf{W}'(\mathbf{x} - \mathbf{y})\|_2^2 \leq \sup_{\mathbf{W}'\in\mathcal{W}} (\sqrt{m}\|\mathbf{W}^\top\mathbf{W} - \mathbf{I}\|_F + m)B^2.$$

Proof. We first prove the bound of $\mathcal{R}(\mathcal{U})$. Recall the definition of $\mathcal{R}(\mathcal{S})$ in Eq.(4.85). By the proof of Lemma 21, we have

$$\mathcal{R}(\mathcal{S}) \leq \frac{B}{\sqrt{N}} \mathrm{E}_{S_N} \sup_{\mathbf{W} \in \mathcal{W}} \sqrt{\sum_{j,k=1}^{m} |\langle \mathbf{w}_j, \mathbf{w}_k \rangle|}, \tag{4.88}$$

$$\mathcal{R}(\mathcal{U}) \leq 2 \sup_{\mathbf{W} \in \mathcal{W}} \|\mathbf{w}_j\|_2 B \mathcal{R}(\mathcal{S}). \tag{4.89}$$

By the properties of matrix norm, we have $\|\mathbf{W}^\top \mathbf{W}\|_F \leq \|\mathbf{W}^\top \mathbf{W} - \mathbf{I}\|_F + \|\mathbf{I}\|_F \leq \|\mathbf{W}^\top \mathbf{W} - \mathbf{I}\|_F + \sqrt{m}$. Further, by Jensen's inequality, we have

$$\sup_{\mathbf{W} \in \mathcal{W}} \sqrt{\sum_{j,k=1}^{m} |\langle \mathbf{w}_j, \mathbf{w}_k \rangle|} \leq \sqrt[4]{m^2 \|\mathbf{W}^\top \mathbf{W}\|_F^2} \leq \sqrt{m} \sqrt{\|\mathbf{W}^\top \mathbf{W} - \mathbf{I}\|_F + \sqrt{m}}. \tag{4.90}$$

Also note that

$$\sup_{\mathbf{W} \in \mathcal{W}} \|\mathbf{w}_j\|_2 = \sqrt{\langle \mathbf{w}_j, \mathbf{w}_j \rangle} \leq \sqrt{\|\mathbf{W}^\top \mathbf{W}\|_F} \leq \sqrt{\|\mathbf{W}^\top \mathbf{W} - \mathbf{I}\|_F + \sqrt{m}}. \tag{4.91}$$

Combining Eq.(4.88) and Eq.(4.91), we have

$$\mathcal{R}(\mathcal{U}) \leq \frac{2B^2 \sqrt{m}}{\sqrt{N}} (\|\mathbf{W}^\top \mathbf{W} - \mathbf{I}\|_F + \sqrt{m}).$$

We then drive the bound on $\sup_{\mathbf{x},\mathbf{y},\mathbf{W}' \in \mathcal{W}} \|\mathbf{W}'(\mathbf{x} - \mathbf{y})\|_2^2$.

$$\begin{aligned}
\sup_{\mathbf{x},\mathbf{y},\mathbf{W}' \in \mathcal{W}} \|\mathbf{W}'(\mathbf{x} - \mathbf{y})\|_2^2 &\leq \sup_{\mathbf{W} \in \mathcal{W}} \mathrm{tr}(\mathbf{W}^\top \mathbf{W}) \sup_{(\mathbf{x},\mathbf{y})} \|\mathbf{x} - \mathbf{y}\|^2 \\
&\leq \sqrt{m \|\mathbf{W}^\top \mathbf{W}\|_F^2} B^2 \\
&\leq (\sqrt{m} \|\mathbf{W}^\top \mathbf{W} - \mathbf{I}\|_F + m) B^2
\end{aligned}$$

□

Combining Lemma 23 with Lemma 20 and noting that $\|\mathbf{W} - \mathbf{I}\|_F^2 \leq \tau$, we complete the proof of the estimation error bound w.r.t SFN given in Eq.(4.7).

4.3.5 Proof of Theorem 5

Proof Sketch

Part of the proof is tailored to the CVND regularizer. Extensions to CSFN and CLDD are given later. The proof is based on the Rademacher complexity (RC) [32], which measures the complexity of a hypothesis class. The Rademacher complexity $\mathcal{R}(\mathcal{M})$ of the function class $\mathcal{M}$ is defined as:

$$\mathcal{R}(\mathcal{M}) = \mathrm{E}_{\mathcal{S},\mathcal{D},\sigma} \sup_{\mathbf{M}\in\mathcal{M}} \frac{1}{m}\sum_{i=1}^{m} \sigma_i(\mathbf{x}_i - \mathbf{y}_i)^\top \mathbf{M}(\mathbf{x}_i - \mathbf{y}_i),$$

where m is the number of data pairs in the training data ($m = |\mathcal{S}| + |\mathcal{D}|$), $\sigma_i \in \{-1, 1\}$ is the Rademacher variable, and $\sigma = (\sigma_1, \sigma_2, \cdots \sigma_m)$.

We first establish an upper bound of the estimation error based on RC. Intuitively, a less-complicated hypothesis class generalizes better on unseen data. Then we upper bound the RC based on the CBMD regularizers. Combining the two steps together, we establish upper bounds of the estimation error based on the CBMD regularizers. The following lemma presents the RC-based upper bound of the estimation error. Its proof is adapted from [32].

Lemma 24. *With probability at least $1 - \delta$, we have*

$$\sup_{\mathbf{M}\in\mathcal{M}} (L(\mathbf{M}) - \widehat{L}(\mathbf{M})) \leq 2\mathcal{R}(\mathcal{M}) + \max(\tau, \sup_{\substack{(\mathbf{x},\mathbf{y})\in\mathcal{S} \\ \mathbf{M}\in\mathcal{M}}} (\mathbf{x}-\mathbf{y})^\top \mathbf{M}(\mathbf{x}-\mathbf{y}))\sqrt{\frac{2\log(1/\delta)}{m}}. \tag{4.92}$$

For the second term in the bound, it is easy to verify

$$\sup_{\substack{(\mathbf{x},\mathbf{y})\in\mathcal{S} \\ \mathbf{M}\in\mathcal{M}}} (x-y)^\top \mathbf{M}(\mathbf{x}-\mathbf{y}) \leq \sup_{\mathbf{M}\in\mathcal{M}} \mathrm{tr}(\mathbf{M}) \sup_{(\mathbf{x},\mathbf{y})\in\mathcal{S}} \|\mathbf{x}-\mathbf{y}\|_2^2. \tag{4.93}$$

Now we focus on the first term. We denote $\mathbf{z} = \mathbf{x} - \mathbf{y}$, $\mathbf{z}_i = \mathbf{x}_i - \mathbf{y}_i$.

Lemma 25. *Suppose $\sup_{\|\mathbf{v}\|_2\leq 1,\mathbf{z}} |\mathbf{v}^\top \mathbf{z}| \leq B$, then we have*

$$\mathcal{R}(\mathcal{M}) \leq \frac{2B^2}{\sqrt{m}} \sup_{\mathbf{M}\in\mathcal{M}} \mathrm{tr}(\mathbf{M}). \tag{4.94}$$

We next show that $\mathrm{tr}(\mathbf{M})$ can be bounded by the CVND regularizer $\widehat{\Omega}_{vnd}(\mathbf{M})$.

Lemma 26. *For the convex VND regularizer $\widehat{\Omega}_{vnd}(\mathbf{M})$, for any positive semidefinite matrix $\mathbf{M}$, we have*

$$\mathrm{tr}(\mathbf{M}) \leq \widehat{\Omega}_{vnd}(\mathbf{M}).$$

Combining Lemma 24, 25, 26 and Eq.(4.93) and noting that $\mathcal{E} = L(\widehat{\mathbf{M}}^*) - \widehat{L}(\widehat{\mathbf{M}}^*) \leq \sup_{\mathbf{M}\in\mathcal{M}}(L(\mathbf{M}) - \widehat{L}(\mathbf{M}))$ and $\widehat{\Omega}_{vnd}(\mathbf{M}) \leq C$ (C is the upper bound in the hypothesis class $\mathcal{M}$), we complete the proof of the first bound in Theorem 5. In the sequel, we present detailed proofs of these lemmas and extend the results to CSNF and CLDD.

Proof of Lemma 25

Proof. For any $\mathbf{M} \in \mathcal{M}$, denote its spectral decomposition as $\mathbf{M} = \mathbf{V}\mathbf{\Pi}\mathbf{V}^\top$, where $\mathbf{V}$ is a standard orthogonal matrix and $\mathbf{\Pi}$ is a diagonal matrix. Denote $\mathbf{V} = (\mathbf{v}_1, \mathbf{v}_2, \cdots \mathbf{v}_D)$, $\mathbf{\Pi} =$

$\mathrm{diag}(\pi_1, \pi_2, \cdots \pi_D)$, then we have

$$\begin{aligned}
\mathcal{R}(\mathcal{M}) &= \mathrm{E}_{\mathcal{S},\mathcal{D},\sigma} \sup_{\mathbf{M}\in\mathcal{M}} \left[\frac{1}{m}\sum_{i=1}^{m}\sigma_i \mathbf{z}_i^T \mathbf{M}\mathbf{z}_i\right] \\
&= \frac{1}{m}\mathrm{E}_{\mathcal{S},\mathcal{D},\sigma} \sup_{\mathbf{M}\in\mathcal{M}} \left[\sum_{i=1}^{m}\sigma_i \sum_{j=1}^{D}\pi_j (\mathbf{v}_j^\top \mathbf{z}_i)^2\right] \\
&= \frac{1}{m}\mathrm{E}_{\mathcal{S},\mathcal{D},\sigma} \sup_{\mathbf{M}\in\mathcal{M}} \left[\sum_{j=1}^{D}\pi_j \sum_{i=1}^{m}\sigma_i (\mathbf{v}_j^\top \mathbf{z}_i)^2\right] \\
&= \frac{1}{m}\mathrm{E}_{\mathcal{S},\mathcal{D},\sigma} \sup_{\mathbf{M}\in\mathcal{M}} \left[\sum_{j=1}^{D}\pi_j \sup_{\|\mathbf{v}\|_2\leq 1}\sum_{i=1}^{m}\sigma_i (\mathbf{v}^\top \mathbf{z}_i)^2\right] \\
&= \frac{1}{m}\mathrm{E}_{\mathcal{S},\mathcal{D},\sigma} \sup_{\mathbf{\Pi}} \sum_{j=1}^{D}\pi_j \sup_{\|\mathbf{v}\|_2\leq 1}\sum_{i=1}^{m}\sigma_i (\mathbf{v}^\top \mathbf{z}_i)^2 \\
&\leq \frac{1}{m}\sup_{\mathbf{M}\in\mathcal{M}} \mathrm{tr}(\mathbf{M})\mathrm{E}_{\mathcal{S},\mathcal{D},\sigma} \sup_{\|\mathbf{v}\|_2\leq 1}\sum_{i=1}^{m}\sigma_i (\mathbf{v}^\top \mathbf{z}_i)^2.
\end{aligned}$$

Since $(\mathbf{v}^\top \mathbf{z})^2$ is Lipschitz continuous w.r.t $\mathbf{v}^\top \mathbf{z}$ with constant $2\sup_{\|\mathbf{v}\|_2\leq 1,\mathbf{z}} \mathbf{v}^\top \mathbf{z}$, according to the composition property [32] of Rademacher complexity on Lipschitz continuous functions, we have

$$\begin{aligned}
\mathcal{R}(\mathcal{M}) &\leq \frac{1}{m} 2 \sup_{\|\mathbf{v}\|_2\leq 1,\mathbf{z}} (\mathbf{v}^\top \mathbf{z}) \sup_{\mathbf{M}\in\mathcal{M}} \mathrm{tr}(\mathbf{M})\mathrm{E}_{\mathcal{S},\mathcal{D},\sigma} \sup_{\|\mathbf{v}\|_2\leq 1}\sum_{i=1}^{m}\sigma_i \mathbf{v}^\top \mathbf{z}_i \\
&= 2\frac{B}{m}\sup_{\mathbf{M}\in\mathcal{M}} \mathrm{tr}(\mathbf{M})\mathrm{E}_{\mathcal{S},\mathcal{D},\sigma} \sup_{\|\mathbf{v}\|_2\leq 1}\sum_{i=1}^{m}\sigma_i \mathbf{v}^\top \mathbf{z}_i \\
&\leq 2\frac{B}{m}\sup_{\mathbf{M}\in\mathcal{M}} \mathrm{tr}(\mathbf{M})\mathrm{E}_{\mathcal{S},\mathcal{D},\sigma} \sup_{\|\mathbf{v}\|_2\leq 1}\|\mathbf{v}\|_2\|\sum_{i=1}^{m}\sigma_i \mathbf{z}_i\|_2 \\
&= 2\frac{B}{m}\sup_{\mathbf{M}\in\mathcal{M}} \mathrm{tr}(\mathbf{M})\mathrm{E}_{\mathcal{S},\mathcal{D},\sigma}\sqrt{(\sum_{i=1}^{m}\sigma_i \mathbf{z}_i)^2}.
\end{aligned}$$

By Jensen's inequality, we have

$$\begin{aligned}
\mathcal{R}(\mathcal{M}) &\leq 2\frac{B}{m}\sup_{\mathbf{M}\in\mathcal{M}} \mathrm{tr}(\mathbf{M})\mathrm{E}_{\mathcal{S},\mathcal{D}}\sqrt{\mathrm{E}_\sigma(\sum_{i=1}^{m}\sigma_i \mathbf{z}_i)^2} \\
&=\leq 2\frac{B}{m}\sup_{\mathbf{M}\in\mathcal{M}} \mathrm{tr}(\mathbf{M})\mathrm{E}_{\mathcal{S},\mathcal{D}}\sqrt{\sum_{i=1}^{m}\mathbf{z}_i^2} \\
&\leq \frac{2B^2}{\sqrt{m}}\sup_{\mathbf{M}\in\mathcal{M}} \mathrm{tr}(\mathbf{M}).
\end{aligned}$$

□

Proof of lemma 26

Proof. By the definition of the convex VND regularizer, we have

$$\begin{aligned}\widehat{\Omega}_{vnd}(\mathbf{M}) =&\Gamma_{vnd}(\mathbf{M}+\epsilon\mathbf{I}_D,\mathbf{I}_D)+\operatorname{tr}(\mathbf{M})\\ =&\operatorname{tr}[(\mathbf{M}+\epsilon\mathbf{I}_D)\log(\mathbf{M}+\epsilon\mathbf{I}_D)-(\mathbf{M}+\epsilon\mathbf{I}_D)\log\mathbf{I}_D-(\mathbf{M}+\epsilon)+\mathbf{I}_D]+\operatorname{tr}(\mathbf{M})\\ =&\sum_{j=1}^{D}[(\pi_j+\epsilon)\log(\pi_j+\epsilon)-(\pi_j+\epsilon)+1]+\sum_{j=1}^{D}\pi_j\\ =&\sum_{j=1}^{D}[(\lambda_j+\epsilon)\log(\lambda_j+\epsilon)-\epsilon+1].\end{aligned}$$

Denote $\bar{\pi}=(\sum_{j=1}^{D}\pi_j)/D=\operatorname{tr}(\mathbf{M})/D$, then by Jensen's inequality, we have

$$\sum_{j=1}^{D}(\lambda_j+\epsilon)\log(\lambda_j+\epsilon)\geq D(\bar{\pi}+\epsilon)\log(\bar{\pi}+\epsilon).$$

Since $\forall x\in\mathbb{R}_+, x-1\leq x\log x$, we have

$$\begin{aligned}\bar{\pi}+\epsilon-1&\leq(\bar{\pi}+\epsilon)\log(\bar{\pi}+\epsilon)\\ &\leq\frac{1}{D}\sum_{j=1}^{D}(\lambda_j+\epsilon)\log(\lambda_j+\epsilon)\\ &\leq\frac{1}{D}\widehat{\Omega}_{vnd}(\mathbf{M})+\epsilon-1.\end{aligned}$$

Therefore we have

$$\operatorname{tr}(\mathbf{M})\leq\widehat{\Omega}_{vnd}(\mathbf{M}).$$

□

Estimation Error Bound for the Convex SFN Regularizer

In this section we prove estimation error bounds for the convex SFN regularizer. The CSFN is composed of two parts. One is the squared Frobenius norm of $\mathbf{M}-\mathbf{I}_D$ and the other is the trace of $\mathbf{M}$. We have already established a relationship between $\operatorname{tr}(\mathbf{M})$ and $\mathcal{R}(\mathcal{M})$. Now we analyze the relationship between $\|\mathbf{M}-\mathbf{I}_D\|_F$ and $\mathcal{R}(\mathcal{M})$, which is given in the following lemma.

Lemma 27. *Suppose* $\sup_{\|\mathbf{v}\|_2\leq1,\mathbf{z}}|\mathbf{v}^\top\mathbf{z}|\leq B$*, then we have*

$$\mathcal{R}(\mathcal{M})\leq\frac{B^2}{\sqrt{m}}\sup_{\mathbf{M}\in\mathcal{M}}\|\mathbf{M}-\mathbf{I}_D\|_F. \tag{4.95}$$

Proof. Denote $M(j,k) = a_{jk}$, and $\delta_{jk} = \mathrm{I}_{\{j=k\}}$, $\mathbf{z}_i = (z_{i1}, z_{i2}, \cdots z_{id})$, then we have

$$\begin{aligned}
\mathcal{R}(\mathcal{M}) =& \frac{1}{m}\mathrm{E}_{\mathcal{S},\mathcal{D},\sigma} \sup_{\mathbf{M}\in\mathcal{M}} \left[\sum_{j,k} a_{jk} \sum_{i=1}^{m} \sigma_i z_{ij} z_{ik} \right] \\
=& \frac{1}{m}\mathrm{E}_{\mathcal{S},\mathcal{D},\sigma} \sup_{\mathbf{M}\in\mathcal{M}} \left[\sum_{j,k} (a_{jk} - \delta_{jk}) \sum_{i=1}^{m} \sigma_i z_{ij} z_{ik} + \sum_{j,k} \delta_{jk} \sum_{i=1}^{m} \sigma_i z_{ij} z_{ik} \right] \\
\leq& \frac{1}{m}\mathrm{E}_{\mathcal{S},\mathcal{D},\sigma} \sup_{\mathbf{M}\in\mathcal{M}} \left[\|\mathbf{M} - \mathbf{I}_D\|_F \sqrt{\sum_{j,k} (\sum_{i=1}^{m} \sigma_i z_{ij} z_{ik})^2} \right].
\end{aligned}$$

Here the inequality is attained by Cauchy's inequality. Applying Jensen's inequality, we have

$$\begin{aligned}
\mathcal{R}(\mathcal{M}) &\leq \frac{1}{m} \sup_{\mathbf{M}\in\mathcal{M}} \|\mathbf{M} - \mathbf{I}_D\|_F \, \mathrm{E}_{\mathcal{S},\mathcal{D}} \left[\sqrt{\mathrm{E}_\sigma \sum_{j,k} (\sum_{i=1}^{m} \sigma_i z_{ij} z_{ik})^2} \right] \\
&= \frac{1}{\sqrt{m}} \sup_{\mathbf{M}\in\mathcal{M}} \|\mathbf{M} - \mathbf{I}_D\|_F \, \mathrm{E}_{\mathcal{S},\mathcal{D}} \left[\sqrt{\sum_{j,k} z_{ij}^2 z_{ik}^2} \right].
\end{aligned}$$

Recalling the definition of B, we have

$$\mathcal{R}(\mathcal{M}) \leq \frac{B^2}{\sqrt{m}} \sup_{\mathbf{M}\in\mathcal{M}} \|\mathbf{M} - \mathbf{I}_D\|_F.$$

□

We now bound the estimation error with the convex SFN regularizer, which is given in the following lemma.

Lemma 28. *Suppose* $\sup_{\|\mathbf{v}\|_2\leq 1,\mathbf{z}} |\mathbf{v}^\top \mathbf{z}| \leq B$*, then with probability at least* $1-\delta$*, we have*

$$\sup_{\mathbf{M}\in\mathcal{M}} (L(\mathbf{M}) - \widehat{L}(\mathbf{M})) \leq \frac{2B^2}{\sqrt{m}} \min(2\widehat{\Omega}_{sfn}(\mathbf{M}), \sqrt{\widehat{\Omega}_{sfn}(\mathbf{M})}) + \max(\tau, \widehat{\Omega}_{sfn}(\mathbf{M})) \sqrt{\frac{2\log(1/\delta)}{m}}.$$

Proof. For the convex SFN regularizer $\widehat{\Omega}_{sfn}(\mathbf{M})$, we have $\mathrm{tr}(\mathbf{M}) \leq \widehat{\Omega}_{sfn}(\mathbf{M})$ and $\|\mathbf{M} - \mathbf{I}_D\| \leq \widehat{\Omega}_{sfn}(\mathbf{M})$. By Eq.(4.93), we have

$$\sup_{\substack{(\mathbf{x},\mathbf{y})\in\mathcal{S} \\ \mathbf{M}\in\mathcal{M}}} (x-y)^\top \mathbf{M}(\mathbf{x}-\mathbf{y}) \leq \sup_{\mathbf{M}\in\mathcal{M}} \widehat{\Omega}_{sfn}(\mathbf{M}) B^2. \tag{4.96}$$

By Lemma 25 and 27, we have

$$\mathcal{R}(\mathcal{M}) \leq \frac{B^2}{\sqrt{m}} \min(2\widehat{\Omega}_{sfn}(\mathbf{M}), \sqrt{\widehat{\Omega}_{sfn}(\mathbf{M})}). \tag{4.97}$$

Substituting Eq.(4.97) and Eq.(4.96) into Lemma 24, we have

$$\sup_{\mathbf{M}\in\mathcal{M}}(L(\mathbf{M})-\widehat{L}(\mathbf{M}))\leq\frac{2B^2}{\sqrt{m}}\min(2\widehat{\Omega}_{sfn}(\mathbf{M}),\sqrt{\widehat{\Omega}_{sfn}(\mathbf{M})})+\max(\tau,\widehat{\Omega}_{sfn}(\mathbf{M}))\sqrt{\frac{2\log(1/\delta)}{m}}.$$

□

Noting that $\mathcal{E}=L(\widehat{\mathbf{M}}^*)-\widehat{L}(\widehat{\mathbf{M}}^*)\leq\sup_{\mathbf{M}\in\mathcal{M}}(L(\mathbf{M})-\widehat{L}(\mathbf{M}))$ and $\widehat{\Omega}_{sfn}(\mathbf{M})\leq C$, we conclude $\mathcal{E}\leq\frac{2B^2}{\sqrt{m}}\min(2C,\sqrt{C})+\max(\tau,C)\sqrt{\frac{2\log(1/\delta)}{m}}$.

Estimation Error Bound for the Convex LDD Regularizer

Starting from Lemma 24, we bound $\mathcal{R}(\mathcal{M})$ and $\sup_{\mathbf{M}\in\mathcal{M}}\mathrm{tr}(\mathbf{M})$ which are given in the following two lemmas.

Lemma 29. *Suppose* $\sup_{\|\mathbf{v}\|_2\leq1,\mathbf{z}}|\mathbf{v}^\top\mathbf{z}|\leq B$*, then we have*

$$\mathcal{R}(\mathcal{M})\leq\frac{B}{\sqrt{m}}\frac{\widehat{\Omega}_{ldd}(\mathbf{M})}{\log(1/\epsilon)-1}.$$

Proof. We first perform some calculation on the convex LDD regularizer.

$$\begin{aligned}\widehat{\Omega}_{ldd}(\mathbf{M})&=\Gamma_{ldd}(\mathbf{M}+\epsilon\mathbf{I}_D,\mathbf{I}_D)-(1+\log\epsilon)\mathrm{tr}(\mathbf{M})\\&=\mathrm{tr}((\mathbf{M}+\epsilon\mathbf{I}_D)\mathbf{I}_D^{-1})-\log\det((\mathbf{M}+\epsilon\mathbf{I}_D)\mathbf{I}_D^{-1})-D-(1+\log\epsilon)\mathrm{tr}(\mathbf{M})\\&=\textstyle\sum_{j=1}^D(\pi_j+\epsilon)-\sum_{j=1}^D\log(\pi_j+\epsilon)-D-(1+\log\epsilon)\sum_{j=1}^D\pi_j\\&=\log(\tfrac{1}{\epsilon})\textstyle\sum_{j=1}^D\pi_j-\sum_{j=1}^D\log(\pi_j+\epsilon)-D(1-\epsilon).\end{aligned}\tag{4.98}$$

Now we upper bound the Rademacher complexity using the CLDD regularizer.

$$\begin{aligned}\log(\frac{1}{\epsilon})\mathcal{R}(\mathcal{M})=&\frac{\log(\frac{1}{\epsilon})}{m}\mathrm{E}_{\mathcal{S},\mathcal{D},\sigma}\sup_{\mathbf{M}\in\mathcal{M}}\left[\sum_{j=1}^D\pi_j\sum_{i=1}^m\sigma_i(\mathbf{v}_j^\top\mathbf{z}_i)^2\right]\\\leq&\frac{1}{m}\mathrm{E}_{\mathcal{S},\mathcal{D},\sigma}\sup_{\mathbf{\Pi}}\sum_{j=1}^D[(\log(\frac{1}{\epsilon})\pi_j-\log(\pi_j+\epsilon))+\log(\pi_j+\epsilon)]\sup_{\|\mathbf{v}\|_2\leq1}\sum_{i=1}^m\sigma_i(\mathbf{v}^\top\mathbf{z}_i)^2.\end{aligned}$$

Similar to the proof of Lemma 25, we have

$$\begin{aligned}\log(\tfrac{1}{\epsilon})\mathcal{R}(\mathcal{M})&\leq\tfrac{2B^2}{\sqrt{m}}\sup_{\mathbf{\Pi}}\textstyle\sum_{j=1}^D[(\log(\frac{1}{\epsilon})\pi_j-\log(\pi_j+\epsilon))+\log(\pi_j+\epsilon)]\\&\leq\tfrac{2B^2}{\sqrt{m}}[\sup_{\mathbf{M}\in\mathcal{M}}\widehat{\Omega}_{ldd}(\mathbf{M})+\sup_{\mathbf{M}\in\mathcal{M}}\textstyle\sum_{j=1}^D\log(\pi_j+\epsilon)].\end{aligned}\tag{4.99}$$

Denoting $A=\sum_{j=1}^D\log(\pi_j+\epsilon)$, we bound A with $\widehat{\Omega}_{ldd}(\mathbf{M})$. Denoting $\bar{\pi}=(\sum_{j=1}^D\pi_j)/D=\mathrm{tr}(\mathbf{M})/D$, by Jensen's inequality, we have

$$A\leq D\log(\bar{\pi}+\epsilon),\tag{4.100}$$

then $\bar{\pi} \geq e^{A/D} - \epsilon$. Replacing $\bar{\pi}$ with A in Eq.(4.98), we have

$$\begin{aligned}\widehat{\Omega}_{ldd}(\mathbf{M}) \geq & D\log(1/\epsilon)(e^{A/D} - \epsilon) - A - D(1-\epsilon) \\ \geq & D\log(1/\epsilon)(\frac{A}{D} + 1 - \epsilon) - A - D(1-\epsilon) \\ = & (\log(1/\epsilon) - 1)A + [\log(\frac{1}{\epsilon}) - 1]D(1-\epsilon).\end{aligned}$$

Further,

$$A \leq \frac{\widehat{\Omega}_{ldd}(\mathbf{M})}{\log(\frac{1}{\epsilon}) - 1} - D(1-\epsilon). \tag{4.101}$$

Substituting this upper bound of A into Eq.(4.99), we have

$$\mathcal{R}(\mathcal{M}) \leq \frac{2B^2}{\sqrt{m}} \frac{\sup_{\mathbf{M}\in\mathcal{M}} \widehat{\Omega}_{ldd}(\mathbf{M})}{\log(1/\epsilon) - 1}.$$

□

The next lemma shows the bound of $\mathrm{tr}(\mathbf{M})$.

Lemma 30. *For any positive semidefinite matrix* $\mathbf{M}$*, we have*

$$\mathrm{tr}(\mathbf{M}) \leq \frac{\widehat{\Omega}_{ldd}(\mathbf{M}) - D\epsilon}{\log(\frac{1}{\epsilon}) - 1}.$$

Proof.

$$\begin{aligned}\widehat{\Omega}_{ldd}(\mathbf{M}) \geq & D\log(1/\epsilon)\bar{\pi} - D\log(\bar{\pi} + \epsilon) - D(1-\epsilon) \\ \geq & D\log(1/\epsilon)\bar{\pi} + D(1-\bar{\pi}) - D(1-\epsilon) \\ = & D[\log(1/\epsilon) - 1]\bar{\pi} + D\epsilon.\end{aligned}$$

Then

$$\mathrm{tr}(\mathbf{M}) = D\bar{\pi} \leq \frac{\widehat{\Omega}_{ldd}(\mathbf{M}) - D\epsilon}{\log(\frac{1}{\epsilon}) - 1}.$$

□

Combining Lemma 29, 30, and 24, we get the following estimation error bound w.r.t the convex LDD regularizer.

Lemma 31. *Suppose* $\sup_{\|\mathbf{v}\|_2\leq 1, \mathbf{z}} |\mathbf{v}^\top \mathbf{z}| \leq B$*, then with probability at least* $1-\delta$*, we have*

$$\sup_{\mathbf{M}\in\mathcal{M}} (L(\mathbf{M}) - \widehat{L}(\mathbf{M})) \leq \frac{4B^2\, \widehat{\Omega}_{ldd}(\mathbf{M})}{\sqrt{m}\,[\log(1/\epsilon) - 1]} + \max\Big(\tau, \frac{\widehat{\Omega}_{ldd}(\mathbf{M}) - D\epsilon}{\log(\frac{1}{\epsilon}) - 1}\Big)\sqrt{\frac{2\log(1/\delta)}{m}}.$$

Chapter 5

Large-scale Learning via System and Algorithm Co-design

In this chapter, we present another line of research in this thesis: large-scale machine learning, where we design efficient distributed systems [370, 377] for healthcare applications at scale.

To execute ML algorithms efficiently on a distributed system, it is important to perform *system and algorithm co-design*. On one hand, ML algorithms possess unique properties such as iterativeness and error tolerance [162], which can be leveraged to design efficient systems. On the other hand, based on the features of the system such as parallelism and (a)synchronicity, ML algorithms can be adjusted for more efficient execution.

Through a principled system and algorithm co-design, we build the Orpheus system for training matrix-parameterized models (MPMs), a very general class of ML models including multiclass logistic regression (MLR), deep neural networks, sparse coding [266], collaborative filtering [54], topic models [49], etc. In MPMs, model parameters can be represented by a matrix $\mathbf{W}$. For example, in MLR, rows of $\mathbf{W}$ represent the classification coefficient vectors corresponding to different classes; whereas in SC rows of $\mathbf{W}$ correspond to the basis vectors used for reconstructing the observed data. A learning algorithm, such as stochastic gradient descent (SGD), would iteratively compute an update $\Delta\mathbf{W}$ from data, to be aggregated with the current version of $\mathbf{W}$.

Learning MPMs in large scale ML problems is challenging: ML application scales have risen dramatically, a good example being the ImageNet [95] compendium with millions of images grouped into tens of thousands of classes. To ensure fast running times when scaling up MPMs to such large problems, it is desirable to turn to distributed computation; however, a unique challenge to MPMs is that the parameter matrix grows rapidly with problem size, causing straightforward parallelization strategies to perform less ideally. Consider a data-parallel algorithm, in which every worker uses a subset of the data to update the parameters — a common paradigm is to synchronize the full parameter matrix and update matrices amongst all workers [78, 93, 94, 136, 222, 304]. However, this synchronization can quickly become a bottleneck: take MLR for example, in which the parameter matrix $\mathbf{W}$ is of size $J \times D$, where J is the number of classes and D is the feature dimensionality. In one application of MLR to Wikipedia [272], $J = 325\text{k}$ and $D > 10,000$, thus $\mathbf{W}$ contains several billion entries (tens of GBs of memory). Because typical computer cluster networks can only transfer a few GBs per second at the

most, inter-machine synchronization of $\mathbf{W}$ can dominate and bottleneck the actual algorithmic computation. In addition to the communication overhead, checkpointing these matrices for fault tolerance purposes incurs substantial disk IO.

In recent years, many distributed frameworks have been developed for large scale machine learning, including bulk synchronous parallel (BSP) systems such as Hadoop [93] and Spark [407], graph computation frameworks such as GraphLab [132], and bounded-asynchronous key-value stores such as TensorFlow [13], Bosen [162, 355], Project Adam [78], and [226]. When using these systems to learn MPMs, it is common to transmit the full parameter matrices $\mathbf{W}$ and/or matrix updates $\Delta\mathbf{W}$ between machines, usually in a server-client style [78, 93, 94, 136, 222, 304]. As the matrices become larger due to increasing problem sizes, so do communication costs and synchronization delays — hence, reducing such costs is a key priority when using these frameworks.

To facilitate system-algorithm co-design, we begin by investigating the structure of matrix parameterized models. Many MPMs bear the following property: when the parameter matrix $\mathbf{W}$ is optimized with SGD [78, 94, 162] or stochastic dual coordinate ascent (SDCA) [167, 299], the update $\triangle\mathbf{W}$ computed over one (or a few) data sample(s) is of low-rank, *e.g*. it can be written as the outer product of two vectors $\mathbf{u}$ and $\mathbf{v}$: $\triangle\mathbf{W} = \mathbf{u}\mathbf{v}^\top$. The vectors $\mathbf{u}$ and $\mathbf{v}$ are *sufficient factors* (SF, meaning that they are sufficient to reconstruct the update matrix $\triangle\mathbf{W}$). A rich set of models [78, 218, 266, 383] fall into this family: for instance, when solving an MLR problem using SGD, the stochastic gradient is $\triangle\mathbf{W} = \mathbf{u}\mathbf{v}^\top$, where $\mathbf{u}$ is the prediction probability vector and $\mathbf{v}$ is the feature vector. Similarly, when solving an ℓ_2 regularized MLR problem using SDCA, the update matrix $\triangle\mathbf{W}$ also admits such as a structure, where $\mathbf{u}$ is the update vector of a dual variable and $\mathbf{v}$ is the feature vector. Other models include neural networks [78], distance metric learning [383], sparse coding [266], non-negative matrix factorization [218], and principal component analysis, to name a few.

Leveraging this property, we propose a computation model called sufficient factor broadcasting (SFB). The basic idea is to send sufficient factors (SFs) between workers, which then reconstruct matrix updates $\triangle\mathbf{W}$ locally, thus greatly reducing inter-machine parameter communication. This stands in contrast to the well-established parameter server idiom [78, 226], a centralized design where workers maintain a "local" image of the parameters $\mathbf{W}$, which are synchronized with a central parameter image $\mathbf{W}$ (stored on the "parameter servers"). In existing parameter server designs, the (small, low-rank) updates $\triangle\mathbf{W}$ are accumulated into the central parameter server's $\mathbf{W}$, and the low-rank structure of each update $\triangle\mathbf{W}$ is lost in the process. Thus, the parameter server can only transmit the (large, full-rank) matrix $\mathbf{W}$ to the workers, inducing extra communication that could be avoided. We address this issue by a *decentralized, peer-to-peer architecture* that performs SFB, where each worker keeps its own image of the parameters $\mathbf{W}$ (either in memory or on local disk), and sends sufficient factors to other workers for parameter synchronization. SFB is highly communication-efficient; transmission costs are linear in the dimensions of the parameter matrix, and the resulting faster communication greatly reduces waiting time in synchronous systems (e.g. Hadoop and Spark), or improves parameter freshness in (bounded) asynchronous systems (e.g. GraphLab, Petuum-PS and [226]). Most importantly, such savings are achieved without compromising the mathematical equivalence of the new ML solution to the original one. SFs have been used to speed up some (but not all) network communication in deep learning [78]; our work differs primarily in that we always transmit SFs,

never full matrices.

In addition to the SFB computation model, we propose a battery of system designs (SD) and algorithm designs (ADs) for efficient communication, light-weight fault tolerance and recovery, and easiness of programming. In communication, an AD – *SF selection* and a SD – *random multicast* are used to further reduce the size of each network message and the number of messages. In fault tolerance, based on an AD – *using SFs to represent parameter states*, an SD – *incremental SF checkpoint* (ISFC) – is used, which continuously saves new SFs computed at each clock to stable storage. Compared with checkpointing parameter matrices, ISFC greatly reduces disk IO, avoids compute-cycle waste, and provides fine-grained (per-clock) rollbacks. In addition, we provide an easy-to-use programming model where the generation of SFs is automatically identified rather than being specified by users, which reduces users' programming efforts.

We provide theoretical analysis which shows that the algorithms executed using SFB are guaranteed to converge. We also extend SFB to a hybrid communication model where decentralized SFB and centralized parameter server are used together to train convolutional neural networks. Evaluations on a wide range of ML applications demonstrate the efficiency and scalability of our systems.

5.1 Sufficient Factor Property

The core goal of sufficient factor broadcasting (SFB) is to reduce network communication costs for matrix-parameterized models; specifically, those that follow an optimization formulation

$$\textbf{(P)} \quad \min_{\mathbf{W}} \frac{1}{N} \sum_{i=1}^{N} f_i(\mathbf{W}\mathbf{a}_i) + h(\mathbf{W}), \tag{5.1}$$

where the model is parametrized by a matrix $\mathbf{W} \in \mathbb{R}^{J \times D}$. The loss function $f_i(\cdot)$ is typically defined over a set of training samples $\{(\mathbf{a}_i, \mathbf{b}_i)\}_{i=1}^N$, with the dependence on $\mathbf{b}_i$ being suppressed. We allow $f_i(\cdot)$ to be either convex or nonconvex, smooth or nonsmooth (with subgradient everywhere); examples include ℓ_2 loss and multiclass logistic loss, amongst others. The regularizer $h(\mathbf{W})$ is assumed to admit an efficient proximal operator $\text{prox}_h(\cdot)$. For example, $h(\cdot)$ could be an indicator function of convex constraints, ℓ_1-, ℓ_2-, trace-norm, to name a few. The vectors $\mathbf{a}_i$ and $\mathbf{b}_i$ can represent observed features, supervised information (e.g., class labels in classification, response values in regression), or even unobserved auxiliary information (such as sparse codes in sparse coding [266]) associated with data sample i. The key property we exploit below ranges from the matrix-vector multiplication $\mathbf{W}\mathbf{a}_i$. This optimization problem **(P)** can be used to represent a rich set of ML models [78, 218, 266, 383], such as the following:

- Distance metric learning (DML) [383] improves the performance of other ML algorithms, by learning a new distance function that correctly represents similar and dissimilar pairs of data samples; this distance function is a matrix $\mathbf{W}$ that can have billions of parameters or more, depending on the data sample dimensionality. The vector $\mathbf{a}_i$ is the difference of the feature vectors in the i-th data pair and $f_i(\cdot)$ can be either a quadratic function or a hinge loss function, depending on the similarity/dissimilarity label $\mathbf{b}_i$ of the data pair. In both cases, $h(\cdot)$ can be an ℓ_1-, ℓ_2-, trace-norm regularizer or simply $h(\cdot) = 0$ (no regularization).

- Sparse coding (SC) [266] learns a dictionary of basis from data, so that the data can be re-represented sparsely (and thus efficiently) in terms of the dictionary. In SC, $\mathbf{W}$ is the dictionary matrix, $\mathbf{a}_i$ are the sparse codes, $\mathbf{b}_i$ is the input feature vector, and $f_i(\cdot)$ is a quadratic function [266]. To prevent the entries in $\mathbf{W}$ from becoming too large, each column $\mathbf{W}_k$ must satisfy $\|\mathbf{W}_k\|_2 \leq 1$. In this case, $h(\mathbf{W})$ is an indicator function which equals 0 if $\mathbf{W}$ satisfies the constraints and equals ∞ otherwise.

To solve the optimization problem **(P)**, it is common to employ either (proximal) stochastic gradient descent (SGD) [78, 94, 162, 222] or stochastic dual coordinate ascent (SDCA) [167, 299], both of which are popular and well-established parallel optimization techniques.

Proximal SGD In proximal SGD, a stochastic estimate of the gradient, $\triangle\mathbf{W}$, is first computed over one data sample (or a mini-batch of samples), in order to update $\mathbf{W}$ via $\mathbf{W} \leftarrow \mathbf{W} - \eta \triangle \mathbf{W}$ (where η is the learning rate). Following this, the proximal operator $\text{prox}_{\eta h}(\cdot)$ is applied to $\mathbf{W}$. Notably, the stochastic gradient $\triangle\mathbf{W}$ in **(P)** can be written as the outer product of two vectors $\triangle\mathbf{W} = \mathbf{u}\mathbf{v}^\top$, where $\mathbf{u} = \frac{\partial f(\mathbf{W}\mathbf{a}_i, \mathbf{b}_i)}{\partial(\mathbf{W}\mathbf{a}_i)}$, $\mathbf{v} = \mathbf{a}_i$, according to the chain rule. Later, we will show that this low rank structure of $\triangle\mathbf{W}$ can greatly reduce inter-worker communication.

Stochastic DCA SDCA applies to problems **(P)** where $f_i(\cdot)$ is convex and $h(\cdot)$ is strongly convex (*e.g.* when $h(\cdot)$ contains the squared ℓ_2 norm); it solves the dual problem of **(P)**, via stochastic coordinate ascent on the dual variables. Introducing the dual matrix $\mathbf{U} = [\mathbf{u}_1, \ldots, \mathbf{u}_N] \in \mathbb{R}^{J \times N}$ and the data matrix $\mathbf{A} = [\mathbf{a}_1, \ldots, \mathbf{a}_N] \in \mathbb{R}^{D \times N}$, the dual problem of **(P)** can be written as

$$\textbf{(D)} \quad \min_{\mathbf{U}} \frac{1}{N} \sum_{i=1}^{N} f_i^*(-\mathbf{u}_i) + h^*(\frac{1}{N}\mathbf{U}\mathbf{A}^\top), \tag{5.2}$$

where $f_i^*(\cdot)$ and $h^*(\cdot)$ are the Fenchel conjugate functions of $f_i(\cdot)$ and $h(\cdot)$, respectively. The primal-dual matrices $\mathbf{W}$ and $\mathbf{U}$ are connected by $\mathbf{W} = \nabla h^*(\mathbf{Z})$, where the auxiliary matrix $\mathbf{Z} := \frac{1}{N}\mathbf{U}\mathbf{A}^\top$. Algorithmically, we need to update the dual matrix $\mathbf{U}$, the primal matrix $\mathbf{W}$, and the auxiliary matrix $\mathbf{Z}$: every iteration, we pick a random data sample i, and compute the stochastic update $\triangle\mathbf{u}_i$ by minimizing **(D)** while holding $\{\mathbf{u}_j\}_{j \neq i}$ fixed. The dual variable is updated via $\mathbf{u}_i \leftarrow \mathbf{u}_i - \triangle\mathbf{u}_i$, the auxiliary variable via $\mathbf{Z} \leftarrow \mathbf{Z} - \triangle\mathbf{u}_i\mathbf{a}_i^\top$, and the primal variable via $\mathbf{W} \leftarrow \nabla h^*(\mathbf{Z})$. Similar to SGD, the update of $\mathbf{Z}$ is also the outer product of two vectors: $\triangle\mathbf{u}_i$ and $\mathbf{a}_i$, which can be exploited to reduce communication cost.

Sufficient factor property in SGD and SDCA In both SGD and SDCA, the parameter matrix update can be computed as the outer product of two vectors — we call these sufficient factors (SFs). This property can be leveraged to improve the communication efficiency of distributed ML systems: instead of communicating parameter/update matrices among machines, we can communicate the SFs and reconstruct the update matrices locally at each machine. Because the SFs are much smaller in size, synchronization costs can be dramatically reduced.

More generally, the update matrix $\triangle\mathbf{W}$ may not be exactly rank-1, but still of very low rank. For example, when each machine uses a mini-batch of size K, $\triangle\mathbf{W}$ is of rank at most K; in restricted Boltzmann machines, the update of the weight matrix is computed from four vectors

$\mathbf{u}_1, \mathbf{v}_1, \mathbf{u}_2, \mathbf{v}_2$ as $\mathbf{u}_1\mathbf{v}_1^\top - \mathbf{u}_2\mathbf{v}_2^\top$, *i.e.* rank-2; for the BFGS algorithm [40], the update of the inverse Hessian is computed from two vectors $\mathbf{u}, \mathbf{v}$ as $\alpha\mathbf{u}\mathbf{u}^\top - \beta(\mathbf{u}\mathbf{v}^\top + \mathbf{v}\mathbf{u}^\top)$, *i.e.* rank-3. Even when the update matrix $\triangle\mathbf{W}$ is not genuinely low-rank, to reduce communication cost, it might still make sense to send only a certain low-rank *approximation*. We intend to investigate these possibilities in future work.

5.2 Orpheus: A Light-weight Peer-to-peer System

In this section, we present a peer-to-peer framework Orpheus where the system design is driven by the sufficient factor property. Orpheus is a decentralized system that executes data-parallel [78, 85, 94, 226, 355] distributed training of matrix-parameterized ML models. Orpheus runs on a group of worker machines connected via a peer-to-peer (P2P) network. Unlike the client-server architectures including the parameter server [78, 85, 94, 162, 226, 355], machines in Orpheus play equal roles without server/client asymmetry and every pair of machines can communicate. Each machine holds one shard of the data and a replica of the model parameters. Machines synchronize their model replicas to ensure consistency, by exchanging parameter-(pre)updates via network communication. Under this general framework, Orpheus applies a battery of system-algorithm co-designs to achieve efficiency in communication and fault tolerance.

For efficient communication, the main idea is to represent the parameter update matrices by their corresponding SFs, which can be understood as "pre-updates", meaning that the actual update matrices must be computed on each client upon receiving fresh SFs, and the update matrices themselves are never transmitted. Since the size of SFs is much smaller than matrices, the communication cost can be substantially reduced. Under a P2P architecture, in addition to void transmitting update matrices, Orpheus can also avoid transmitting parameter matrices, while still achieving synchrony. Besides, *random multicast*, under which each machine sends SFs to a randomly-chosen subset of machines, is leveraged to reduce the number of messages. *SF selection*, which chooses a subset of representative SFs to communicate, is used to further reduce the size of each message.

Orpheus uses *incremental SF checkpoint* for fault tolerance, motivated by the fact that the parameter states can be represented as a dynamically growing set of SFs. Machines continuously save the new SFs computed in each logical time onto stable storage. To recover a parameter state, Orpheus transforms the saved SFs into a matrix. Compared with checkpointing parameter matrices [13, 407], saving vectors requires much less disk IO and does not require the application program to halt. Besides, the parameters can be rollbacked to the state in any logical time.

In programming abstraction, the SFs are explicitly exposed such that system-level optimizations based on SFs can be exploited. Orpheus is able to automatically identify the symbolic expressions representing SFs and updates, relieving users' burden to manually specify them.

Orpheus supports two consistency models: bulk synchronous parallel (BSP) [42] and staleness synchronous parallel (SSP) [162]. BSP sets a global barrier at each clock. A worker cannot proceed to the next clock until all workers reach this barrier. SSP allows workers to have different paces as long as their difference in clock is no more than a user-defined *staleness* threshold.

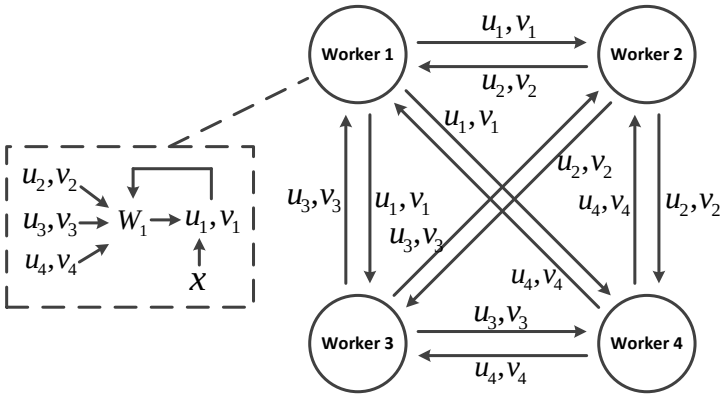

Figure 5.1: Sufficient factor broadcasting.

5.2.1 Communication: Sufficient Factor Broadcasting (SFB)

Orpheus explores system-algorithm co-design to perform efficient communication. To ensure the consistency among different parameter replicas, the updates computed at different machines need to be exchanged. One popular system architecture that enables this is *parameter server* (PS) [78, 85, 94, 226, 355], which conceptually consists of a server machine that maintains shared state of the parameters and a set of worker machines each having a local cache of the parameters. In PS, the updates computed at worker machines are aggregated at the server and applied to the shared state. The shared state is subsequently sent back to workers to refresh their local caches. When PS is used to train MPMs, the update and parameter matrices – which could contain billions of elements [214] – are transferred, incurring substantial communication overhead.

Sufficient Factor Broadcasting

Leveraging the SF property of the update matrix in problems **(P)** and **(D)**, we propose a *sufficient factor broadcasting* (SFB) computation model that supports efficient (low-communication) distributed learning of the parameter matrix $\mathbf{W}$. We assume a setting with P workers, each of which holds a data shard and a copy of the parameter matrix[1] $\mathbf{W}$. Stochastic updates to $\mathbf{W}$ are generated via proximal SGD or SDCA, and communicated between machines to ensure parameter consistency. In proximal SGD, on every iteration, each worker p computes SFs $(\mathbf{u}_p, \mathbf{v}_p)$, based on one data sample $\mathbf{x}_i = (\mathbf{a}_i, \mathbf{b}_i)$ in the worker's data shard. The worker then broadcasts $(\mathbf{u}_p, \mathbf{v}_p)$ to all other workers; once all P workers have performed their broadcast (and have thus received all SFs), they re-construct the P update matrices (one per data sample) from the P SFs, and apply them to update their local copy of $\mathbf{W}$. Finally, each worker applies the proximal operator $\text{prox}_h(\cdot)$. When using SDCA, the above procedure is instead used to broadcast SFs for the auxiliary matrix $\mathbf{Z}$, which is then used to obtain the primal matrix $\mathbf{W} = \nabla h^*(\mathbf{Z})$. Figure 5.1 illustrates the SFB operation: 4 workers compute their respective SFs $(\mathbf{u}_1, \mathbf{v}_1), \ldots, (\mathbf{u}_4, \mathbf{v}_4)$, which are then

[1]For simplicity, we assume each worker has enough memory to hold a full copy of the parameter matrix $\mathbf{W}$. If $\mathbf{W}$ is too large, one can either partition it across multiple machines [94, 226], or use local disk storage (*i.e.* out of core operation). We plan to investigate these strategies as future work.

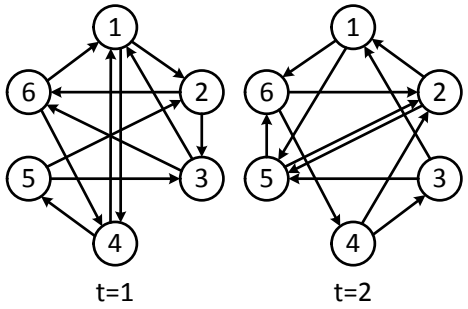

Figure 5.2: Random multicast.

broadcast to the other 3 workers. Each worker p uses all 4 SFs $(\mathbf{u}_1, \mathbf{v}_1), \ldots, (\mathbf{u}_4, \mathbf{v}_4)$ to exactly reconstruct the update matrices $\triangle \mathbf{W}_p = \mathbf{u}_p \mathbf{v}_p^\top$, and update their local copy of the parameter matrix: $\mathbf{W}_p \leftarrow \mathbf{W}_p - \sum_{q=1}^{4} \mathbf{u}_q \mathbf{v}_q^\top$. While the above description reflects synchronous execution, it is easy to extend to (bounded) asynchronous execution.

The communication cost of transmitting SFs is $O(J + D)$ which is linear in matrix dimensions while that of transmitting update matrices (UMs) is $O(JD)$ which is quadratic in matrix dimensions. Hence SF-transfer can greatly reduce communication overhead. The transformation from SFs to a UM is mathematically exact, without compromising computational correctness.

In PS, the one-sided communication cost from workers to the server can be reduced by transmitting SFs [78]: each worker sends the new SFs to the server, where the received SFs are transformed to UMs to update the shared parameter state. However, since the parameter matrix cannot be computed from a few SFs, from server to workers the newly-updated parameters needs to be sent as a matrix, which still incurs high communication overhead. To avoid transmitting parameter matrices, Orpheus adopts a decentralized peer-to-peer architecture where worker machines synchronize their parameter replicas by exchanging updates in the form of SFs. Unlike PS, the P2P architecture does not maintain the shared parameter state and can completely avoid transmitting any type of matrices.

While SF-transfer greatly reduces communication cost, it increases computation overhead. Each group of SFs are transformed into the same update multiple times (on different receivers). However, in-memory computation is usually much more efficient than inter-machine network communication, especially with the advent of GPU computing, hence the reduction in communication cost overshadows the increase of computation overhead.

Random Multicast

While P2P transfer of SFs greatly reduces the size of each message (from a matrix to a few vectors), its limitation is SFs need to be sent from each machine to every other machine, which renders the number of messages per clock to be quadratic in the number of machines P. To address this issue, Orpheus adopts *random multicast*: in each clock, each machine *randomly* selects $Q (Q < P - 1)$ machines to send SFs to. This cuts messages per clock from $\mathcal{O}(P^2)$ to $\mathcal{O}(PQ)$. Figure 5.2 shows an example. In each iteration t, an update U_p^t generated by machine p is sent only to machines that are directly connected with p (and the update U_p^t takes effect at

iteration $t+1$). The effect of U_p^t is *indirectly and eventually* transmitted to every other machine q, via the updates generated by machines sitting between p and q in the topology. This happens at iteration $t+\tau$, for some delay $\tau > 1$ that depends on Q and the location of p and q in the network topology. Consequently, the P machines will not have the exact same parameter image $\mathbf{W}$, even under bulk synchronous parallel execution — yet this does not empirically (Section 5.2.5) compromise algorithm accuracy as long as Q is not too small. We hypothesize that this property is related to the tolerance of ML algorithms to bounded-asynchronous execution and random error, and we provide a theoretical analysis in Section 5.4.

Two random selection methods are provided. One is *uniform selection*: each machine has the same probability to be selected. The other is *prioritized selection* for load-balancing purpose. Each machine is assigned a priority score based on its progress (measured by clock). A machine with faster progress (higher priority) is selected with higher probability and receives more SFs from slower machines. It spends more compute cycles to consume these remote SFs and slows down the computation of new SFs, giving the slower machines a grace time to catch up.

Unlike a deterministic multicast topology [222] where each machine communicates with a fixed set of machines throughout the application run, random multicast provides several benefits. First, dynamically changing the topology in each clock gives every two machines a chance to communicate directly, which facilitates more symmetric synchronization. Second, random multicast is more robust to network connection failures since the failure of a network connection between two machines will not affect their communication with other one. Third, random multicast makes resource elasticity simpler to implement: adding and removing machines require minimal coordination with existing ones, unlike a deterministic topology which must be modified every time a worker joins or leaves.

SF Selection

In ML practice, parameter updates are usually computed over a small batch (whose size typically ranges from tens to hundreds) of examples. At each clock, a batch of K training examples are selected and an update is generated with respect to each example. When represented as matrices, these K updates can be aggregated into a single matrix to communicate. Hence the communication cost is independent of K. However, this is not the case in sufficient factors transfer: the K SFGs cannot be aggregated into one single SFG; they must be transferred individually. Therefore, communication cost grows linearly with K. To alleviate this cost, Orpheus provides *SF selection* (SFS), which chooses a subset of C SFGs (where $C < K$) – that best represent the entire batch – to communicate.

We design an efficient sampling-based algorithm called *joint matrix column subset selection* (JMCSS) to perform SFS. Given the P matrices $X^{(1)}, \cdots, X^{(P)}$ where $X^{(p)}$ stores the p-th SF of all SFGs, JMCSS selects a subset of non-redundant column vectors from each matrix to approximate the entire matrix. The selection of columns in different matrices are tied together, i.e., if the i-th column is selected in one matrix, for all other matrices their i-th column must be selected as well to atomically form an SFG. Let $I = \{i_1, \cdots, i_C\}$ index the selected SFGs and $S_I^{(p)}$ be a matrix whose columns are from $X^{(p)}$ and indexed by I. The goal is to find out the optimal selection I such that the following approximation error is minimized: $\sum_{p=1}^{P} \|X^{(p)} - S_I^{(p)}(S_I^{(p)})^\dagger X^{(p)}\|_2$,

Algorithm 3: Joint matrix column subset selection.

Input: $\{X^{(p)}\}_{p=1}^{P}$
Initialize: $\forall\, p,\, X_0^{(p)} = X^{(p)},\, S_0^{(p)} = []$
for $t \in \{1, \ldots, C\}$ **do**
  Compute the squared L2 norm of column vectors in $\{X_{t-1}^{(p)}\}_{p=1}^{P}$
  Sample a column index i_t
  $\forall\, p,\, X_t^{(p)} \leftarrow X_{t-1}^{(p)} / \{x_{i_t}^{(p)}\},\, S_t^{(p)} \leftarrow S_{t-1}^{(p)} \cup \{x_{i_t}^{(p)}\}$
  $\forall\, p,\, X_t^{(p)} \leftarrow X_t^{(p)} - S_t^{(p)} (S_t^{(p)})^{\dagger} X_t^{(p)}$
end for
Output: $\{S^{(p)}\}_{p=1}^{P}$

where $(S_I^{(p)})^{\dagger}$ is the pseudo-inverse of $S_I^{(p)}$.

Finding the exact solution of this problem is NP-hard. To address this issue, we develop a sampling-based method (Algorithm 3), which is an adaptation of the iterative norm sampling algorithm [99]. Let $S^{(p)}$ be a dynamically growing matrix that stores the column vectors to be selected from $X^{(p)}$ and $S_t^{(p)}$ denote the state of $S^{(p)}$ at iteration t. Accordingly, $X^{(p)}$ is dynamically shrinking and its state is denoted by $X_t^{(p)}$. At the t-th iteration, an index i_t is sampled and the i_t-th column vectors are taken out from $\{X^{(p)}\}_{p=1}^{P}$ and added to $\{S^{(p)}\}_{p=1}^{P}$. i_t is sampled in the following way. First, we compute the squared L2 norm of each column vector in $\{X_{t-1}^{(p)}\}_{p=1}^{P}$. Then sample i_t ($1 \leq i_t \leq K+1-t$) with probability proportional to $\prod_{p=1}^{P} \|x_{i_t}^{(p)}\|_2^2$, where $x_{i_t}^{(p)}$ denotes the i_t-th column vector in $X_{t-1}^{(p)}$. The selected column vector is removed from $X_{t-1}^{(p)}$ and added to $S_{t-1}^{(p)}$. Then a back projection is utilized to transform $X_t^{(p)}$: $X_t^{(p)} \leftarrow X_t^{(p)} - S_t^{(p)} (S_t^{(p)})^{\dagger} X_t^{(p)}$. After C iterations, we obtain the selected SFs contained in $\{S^{(p)}\}_{p=1}^{P}$ and pack them into SFGs, which are subsequently sent to other machines. Under JMCSS, the aggregated update generated from the C SFGs is close to that computed from the entire batch. Hence SFS does not compromise parameter-synchronization quality.

The selection of SFs is pipelined with their computation and communication to increase throughput. Two FIFO queues (denoted by A and B) containing SFs are utilized for coordination. The computation thread adds newly-computed SFs into queue A. The selection thread dequeues SFs from A, executes the selection and adds the selected SFs to queue B. The communication thread dequeues SFs from B and sends them to other machines. The three modules operate asynchronously: for each one, as long as its input queue is not empty and output queue is not full, the operation continues. The two queues can be concurrently accessed by their producer and consumer.

Cost Analysis

Figure 5.3 compares the communications, space and time (to apply updates to $\mathbf{W}$) costs of peer-to-peer SFB, against parameter server (PS) architectures [94, 226, 355]. For SFB with a broadcasting scheme, in each mini-batch, every worker broadcasts K SF pairs $(\mathbf{u}, \mathbf{v})$ to $P-1$ other workers, i.e. $O(P^2K(J+D))$ values are sent per iteration — linear in matrix dimensions J, D,

Computational Model	Total comms, per iter	$\mathbf{W}$ storage per machine	$\mathbf{W}$ update time, per iter
SFB (peer-to-peer, broadcast)	$O(P^2K(J+D))$	$O(JD)$	$O(P^2KJD)$
SFB (peer-to-peer, multicast)	$O(PQK(J+D))$	$O(JD)$	$O(PQKJD)$
PS (client-server)	$O(PJD)$	$O(JD)$	$O(PJD)$ at server, $O(PKJD)$ at clients

Figure 5.3: Cost of using SFB versus PS. K is the mini-batch size, J, D are the dimensions of $\mathbf{W}$, and P is the number of workers.

and quadratic in P. For SFB with a multicast scheme, every worker communicates SF pairs with $Q < P$ peers, hence the communication cost is reduced to $O(PQK(J+D))$. Because SF pairs cannot be aggregated before transmission, the cost has a dependency on K. In contrast, the communication cost in PS is $O(PJD)$, linear in P, quadratic in matrix dimensions, and independent of K. For both SFB and PS, the cost of storing $\mathbf{W}$ is $O(JD)$ on every machine. As for the time taken to update $\mathbf{W}$ per iteration, PS costs $O(PJD)$ at the server (to aggregate P client update matrices) and $O(PKJD)$ at the P clients (to aggregate K updates into one update matrix). By comparison, SFB bears a cost of $O(P^2KJD)$ under broadcasting and $O(PQKJD)$ under multicast due to the additional overhead of reconstructing each update matrix P or Q times.

Compared with PS, SFB achieves communication savings by paying an extra computation cost. In a number of practical scenarios, such a tradeoff is worthwhile. Consider large problem scales where $\min(J, D) \geq 10000$, and moderate mini-batch sizes $1 \leq K \leq 100$ (as studied in this work); when using a moderate number of machines (around 10-100), the $O(P^2K(J+D))$ communications cost of SFB is lower than the $O(PJD)$ cost for PS, and the relative benefit of SFB improves as the dimensions J, D of $\mathbf{W}$ grow. In data center scale computing environments with thousands of machines, we can adopt the multicast scheme. As for the time needed to apply updates to $\mathbf{W}$, it turns out that the additional cost of reconstructing each update matrix P or Q times in SFB is negligible in practice — we have observed in our experiments that the time spent computing SFs, as well as communicating SFs over the network, greatly dominates the cost of reconstructing update matrices using SFs. Overall, the communication savings dominate the added computational overhead, which we validated in experiments.

5.2.2 Fault Tolerance

In this section, further exploring the SF update property, we propose to represent the parameter matrix using SFs. Based on such a representation, a light-weight fault tolerance approach is developed.

SF-based Representation of Parameters

We first show the parameter matrix can be represented as a set of SFs. At clock T, the parameter state W_T is mathematically equal to $W_0 + \sum_{t=1}^{T} \triangle W_t$ where $\triangle W_t$ is the update matrix computed

at clock t and W_0 is the initialization of the parameters. As noted earlier, $\triangle W_t$ can be computed from an SFG G_t: $\triangle W_t = h(G_t)$, using a transformation h. Following the standard practice of initializing ML models using randomization, we randomly generate an SFG G_0, then let $W_0 = h(G_0)$. To this end, the parameter state can be represented as $W_T = \sum_{t=0}^{T} h(G_t)$, using a set of SFGs.

Incremental SF Checkpoint

Based on the SF-representation (SFR) of parameters and inspired by the asynchronous and incremental checkpointing methods [17, 263], Orpheus provides an *incremental SF checkpoint* (ISFC) mechanism for fault tolerance and recovery: each machine continuously saves the new SFGs computed in each clock to stable storage and restores the parameters from the saved SFGs when machine failure happens. Unlike existing systems [13, 407] which checkpoint large matrices, saving small vectors consume much less disk bandwidth. To reduce the frequency of disk write, the SFGs generated after each clock are not immediately written onto the disk, but staged in the host memory. When a large batch of SFGs are accumulated, Orpheus writes them together.

ISFC does not require the application program to halt while checkpointing the SFs. The IO thread reads the SFs and the computing thread writes the parameter matrix. There is no read/write conflict. In contrast, in matrix-based checkpointing, the IO thread reads the parameter matrix, which requires the computation thread to halt to ensure consistency, incurring waste of compute cycles.

ISFC is able to rollback the parameters to the state at any clock. To obtain the state at clock T, Orpheus collects the SFGs computed up to T and transforms them into a parameter matrix. This granularity is much more fine-grained than checkpointing parameter matrices. Since saving large-sized matrices to disk is time-consuming, the system can only afford to perform a checkpoint periodically and the parameter states between two checkpoints are lost. The `restore(T)` API is used for recovery where T is a user-specified clock which the parameters are to be rollbacked to. The default T is the latest clock.

5.2.3 Programming Model

The Orpheus programming model provides a data abstraction called sufficient factor group (SFG) and two user-defined functions that generate and consume SFGs to update model parameters. Each SFG contains a set of SFs that are generated with respect to one data example and atomically produces a parameter update. The SFs are immutable and dense, and their default type is `float`. Inside an SFG, each SF has an index. To program an Orpheus application, users specify two functions: (1) `compute_svg` which takes the current parameter state and one data example as inputs and computes vectors that collectively form an SFG; (2) `compute_update` which takes an SFG and produces a parameter update. These two functions are invoked by the Orpheus engine to perform *data-parallel* distributed ML: each of the P machines holds one shard of the training data and a replica of parameters; different parameter replicas are synchronized across machines to retain consistency (consistency means different replicas are encouraged to be as close as possible). Every machine executes a sequence of operations iteratively: in each clock, a small batch of training examples are randomly selected from the data shard and `compute_svg`

Algorithm 4: Execution semantics.

Allocate an empty SFG set $\mathcal{S} = \{\}$
Select a small batch of training examples $\mathcal{X}$
for each $x \in \mathcal{X}$
  Compute an SFG s = `compute_svg` $(W^{(\text{old})}, x)$
  Add s to $\mathcal{S}$
end for
Send $\mathcal{S}$ to other machines
Receive the SFG set $\mathcal{T}$ from other machines
for each $s \in \mathcal{S} \cup \mathcal{T}$
  Compute an update u = `compute_update`(s)
  Update parameters $W^{(\text{new})} \leftarrow W^{(\text{old})} + u$
end for

is invoked to compute an SFG with respect to each example; the SFGs are then sent to other machines for parameter synchronization; `compute_update` is invoked to transform locally-generated SFGs and remotely-received SFGs into updates which are subsequently added to the parameter replica. The execution semantics (per-clock) of the Orpheus engine is shown in Algorithm 4. Unlike existing systems which directly compute parameter updates from training data, Orpheus breaks this computation into two steps and explicitly exposes the intermediate SFs to users, which enables SF-based system-level optimizations to be exploited.

Below shows how these two functions are implemented in MLR. The inputs of the `compute_svg` function include the parameter replica `Parameters` and a data example `Data` and the output is a `SFG`. A SFG is declared via `SFG([`$d_1, \cdots, d_J$`])` where d_j is the length of the j-th SF. In MLR, an SFG contains two SFs: the first one is the difference between the prediction vector `softmax(W*smp.feats)` and the label vector `smp.label`; the second one is the feature vector `smp.feats`. The update matrix is computed as the outer product between the two SFs.

```
def compute_svg(Parameters W, Data smp):
  svg=SFG([W.nrows, W.ncols])
  x=softmax(W*smp.feats)-smp.label
  svg.sv[0]=x
  svg.sv[1]=smp.feats
  return svg
def compute_update(SFG svg):
  return outproduct(svg.sv[0],svg.sv[1])
```

Automatic Identification of SFs and Updates

When ML models are trained using gradient descent or quasi-Newton algorithms, the computation of SFGs and updates can be automatically identified by the Orpheus engine, which relieves users from writing the two functions `compute_svg` and `compute_update`. The only input required from users is a symbolic expression of the loss function, which is in general much easier

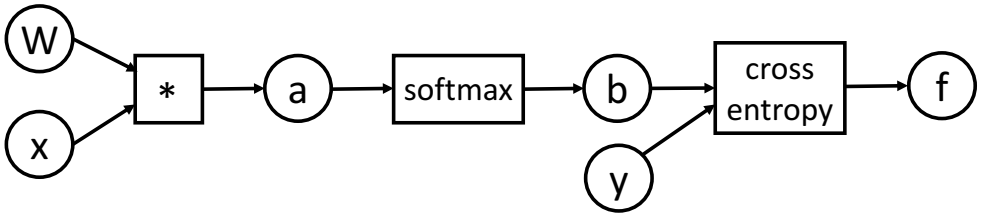

Figure 5.4: Expression graph.

Type	Inputs	Outputs	Examples
1	vector	scalar	L2 norm
2	vector	vector	softmax
3	vector, vector	scalar	cross entropy
4	vector, vector	vector	addition, subtraction
5	matrix, vector	vector	matrix-vector product

Table 5.1: Different types of operators.

to program compared with the two functions. Note that this is not an extra burden: in most ML applications, users need to specify this loss function to measure the progress of execution.

The identification procedure of SFs depends on the optimization algorithm – either gradient descent or quasi-Newton – specified by the users for minimizing the loss function. For both algorithms, automatic differentiation techniques [13, 34] are needed to compute the gradient of variables. Given the symbolic expression of the loss function, such as `f=cross_entropy(softmax(W*x),y)` in MLR, the Orpheus engine first parses it into an expression graph [43] as shown in Figure 5.4. In the graph, circles denote variables including terminals such as `W`, `x`, `y` and intermediate ones such as `a=W*x`, `b=softmax(a)`; boxes denote operators applied to variables. According to their inputs and outputs, operators can be categorized into different types, shown in Table 5.1. Given the expression graph, Orpheus uses automatic differentiation to compute the symbolic expressions of the gradient $\partial f/\partial z$ of f w.r.t to each unknown variable z (either a terminal or an intermediate one). The computation is executed recursively in the backward direction of the graph. For example, in Figure 5.4, to obtain $\partial f/\partial a$, we first compute $\partial f/\partial b$, then transform it into $\partial f/\partial a$ using an operator-specific matrix A. For a type-2 operator (e.g., softmax) in Table 5.1, $A_{ij} = \partial b_j/\partial a_i$.

If W is involved in a type-5 operator (Table 5.1) which takes W and a vector x as inputs and produces a vector a and the gradient descent algorithm is used to minimize the loss function, then the SFG contains two SFs which can be automatically identified: one is $\partial f/\partial a$ and the other is x. Accordingly, the update of W can be automatically identified as the outer product of the two SFs.

If quasi-Newton methods are used to learn ML models parameterized by a vector x, Orpheus can automatically identify the SFs of the update of the approximated Hessian matrix W. First of all, automatic differentiation is applied to compute the symbolic expression of the gradient $g(x) = \partial f/\partial x$. To identify the SFs at clock k, we plug in the states x_{k+1} and x_k of the parameter vector in clock $k+1$ and k into $g(x)$ and calculate a vector $y_k = g(x_{k+1}) - g(x_k)$. We also

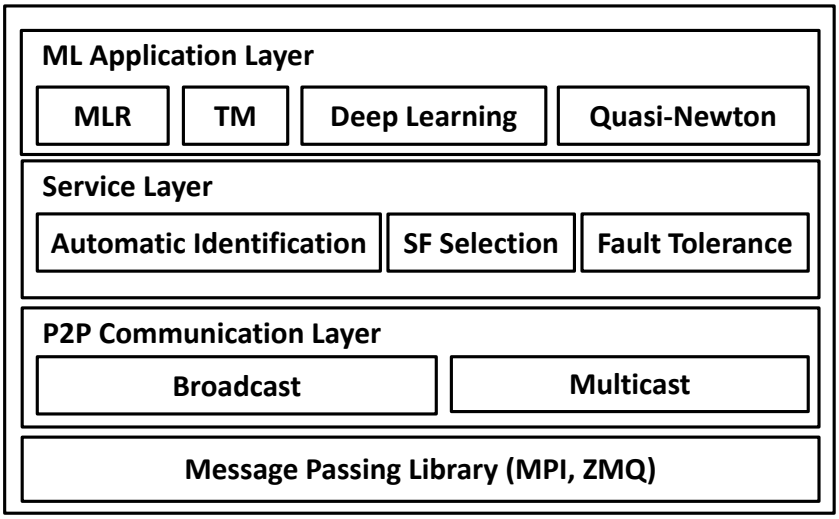

Figure 5.5: Software stack.

compute another vector $s_k = x_{k+1} - x_k$. Then based on s_k, y_k, and W_k (the state of W at clock k), we can identify the SFs which depend on the specific quasi-Newton algorithm instance. For BFGS, the procedures are: (1) set $y_k \leftarrow y_k / \sqrt{y_k^\top s_k}$; (2) compute $v_k = W_k s_k$; (3) set $y_k \leftarrow y_k / \sqrt{s_k^\top v_k}$. Then the SFs are identified as y_k and v_k and the update of W_k is computed as $y_k y_k^\top - v_k v_k^\top$. For DFP, the procedures are: (1) set $s_k \leftarrow s_k / \sqrt{y_k^\top s_k}$; (2) compute $v_k = W_k y_k$; (2) set $v_k \leftarrow v_k / \sqrt{y_k^\top v_k}$. Then the SFs are identified as s_k and v_k and the update of W_k is computed as $s_k s_k^\top - v_k^\top v_k$.

5.2.4 Implementation

Orpheus is a decentralized system, where workers are symmetric, running the same software stack, which is conceptually divided into three layers (Figure 5.5): (1) an *ML application layer* including ML programs implemented on top of Orpheus, such as multiclass logistic regression, topic models, deep learning models, etc.; (2) a *service layer* for automatic identification of SFs, SF selection, fault tolerance, etc.; (3) a *P2P communication layer* for sufficient factor transfer and random multicast.

The major modules in the Orpheus engine include: (1) an *interpreter* that automatically identifies the symbolic expressions of SFs and parameter updates; (2) a *SF generator* that selects training examples from local data shard and computes an SFG for each example using the symbolic expressions of SFs produced by the interpreter; (3) an *SF selector* that chooses a small subset of most representative SFs out of those computed by the generator for communication; (4) a *communication manager* that transfers the SFs chosen by the selector using broadcast or random multicast and receives remote SFs; (5) an *update generator* which computes update matrices from locally-generated and remotely-received SFs and updates the parameter matrix; (6) a *central coordinator* for periodic centralized synchronization, parameter-replicas rotation, and elasticity.

Heterogeneous computing The Orpheus programming interface exposes a rich set of *operators*, such as matrix multiplication, vector addition, and softmax, through which users write their ML programs. To support heterogeneous computing, each operator has a CPU implementation and a GPU implementation built upon highly optimized libraries such as Eigen, cuBLAS, and cuDNN. In the GPU implementation, Orpheus performs *kernel fusion* which combines a sequence of kernels into a single one, to reduce the number of kernel lunches that bear large overhead. The Orpheus engine generates a dependency graph of operators by parsing users' program and traverses the graph to fuse consecutive operators into one CUDA kernel.

Elasticity Orpheus is elastic to resource adjustment. Adding new machines and preempting existing machines do not interrupt the current execution. To add a new machine, the central coordinator executes the following steps: (1) launching the Orpheus engine and application program on the new machine; (2) averaging the parameter replicas of existing machines and placing the averaged parameters on the new machine; (3) taking a chunk of training data from each existing machine and assigning the data to the new machine; (4) adding the new machine into the P2P network. When an existing machine is preempted, it is taken off from the P2P network and its data shard is re-distributed to other machines.

Periodic centralized synchronization Complementary to the P2P decentralized parameter synchronization, Orpheus performs a centralized synchronization periodically. The centralized coordinator sets a global barrier every R clocks. When all workers reach this barrier, the coordinator calls the `AllReduce(average)` interface to average the parameter replicas and set each replica to the average. After that, workers perform decentralized synchronization until the next barrier. Centralized synchronization effectively removes parameter-replicas' discrepancy accumulated during decentralized execution and it will not incur substantial communication cost since it is invoked periodically.

Rotation of parameter replicas Orpheus adopts data parallelism, where each worker has access to one shard of the data. Since computation is usually much faster than communication, the updates computed locally are much more frequent than those received remotely. This would render imbalanced updating of parameters: a parameter replica is more frequently updated based on the local data residing in the same machine than data shards on other machines. This is another cause of out-of-synchronization. To address this issue, Orpheus performs *parameter-replica rotation*, which enables each parameter replica to explore all data shards on different machines. Logically, the machines are connected via a ring network. Parameter-replicas rotate along the ring periodically (every S iterations) while each data shard sits still on the same machine during the entire execution. We choose to rotate the parameters rather than data since the size of parameters is much smaller than data. A centralized coordinator sets a barrier every S iterations. When all workers reach the barrier, it invokes the `Rotate` API which triggers the rotation of parameter replicas.

Data prefetching The loading of training data from CPU to GPU is overlapped with the SF generator via a *data queue*. The next batches of training examples are prefetched into the queue

while the generator is processing the current one. In certain applications, each training example is associated with a *data-dependent variable* (DDV). For instance, in topic model, each document has a topic proportion vector. The states of DDVs need to be maintained throughout execution. Training examples and their DDVs are stored in consecutive host/device memory for locality and are prefetched together. At the end of a clock, GPU buffer storing examples is immediately ready for overwriting. The DDVs are swapped from GPU memory to host memory, which is pipelined using a DDV queue.

Hardware/software-aware SF Transfer

Orpheus provides a communication library for efficient message broadcasting. It contains a collection of broadcast methods designed for different hardware and software configurations, including (1) whether the communication is CPU-to-CPU or GPU-to-GPU; (2) whether InfiniBand [6] is available; (3) whether the consistency model is BSP or SSP.

- **CPU-to-CPU, BSP** In this case, we use the MPI_Allgather [8] routine to perform *all-to-all* broadcast. In each clock, it gathers the SFs computed by each machine and distributes them to all machines. MPI_Allgather is a blocking operation (i.e. the control does not return to the application until the receiving buffer is ready to receive SFs from all machines). This is in accordance with the BSP consistency model where the execution cannot proceed to the next clock until all machines reach the global barrier.
- **CPU-to-CPU, SSP** Under SSP, each machine is allowed to have a different pace to compute and broadcast SFs. To enable this, the all-to-all broadcast is decomposed into multiple *one-to-all* broadcast. Each machine separately invokes the MPI_Bcast routine to broadcast its messages to others. MPI_Bcast is a blocking operation: the next message cannot be sent until the current one finishes. This guarantees the SFs are received in order: SFs generated at clock t arrive early than those at $t+1$. This order is important for the correctness of ML applications: the updates generated earlier should be applied first.
- **CPU-to-CPU, BSP, InfiniBand** An all-gather operation is executed by leveraging the Remote Direct Memory Access (RDMA) feature [318] provided by InfiniBand, which supports zero-copy networking by enabling the network adapter to transfer data directly to or from application memory, without going through the operating system. The recursive doubling (RD) [145] algorithm is used to implement all-gather, where pairs of processes exchange their SFs via point-to-point communication. In each iteration, the SFs collected during all previous iterations are included in the exchange. RDMA is used for the point-to-point transfer during the execution of RD.
- **CPU-to-CPU, SSP, InfiniBand** Each machine performs one-to-all broadcast separately, using the hardware supported broadcast (HSB) in InfiniBand. HSB is topology-aware: packets are duplicated by the switches only when necessary; therefore network traffic is reduced by avoiding the cases that multiple identical packets travel through the same physical link. The limitation of HSB is that messages can be dropped or arrive out of order, which degrades the correctness of ML execution. To retain reliability and in-order delivery, on top of HSB another layer of network protocol [232] is added, where (1) receivers send ACKs back to the root machine to confirm message delivery; (2) a message is re-transmitted using point-to-point

reliable communication if no ACK is received before timeout; (3) receivers use a continuous clock counter to detect out-of-order messages and put them in order.

- **GPU-to-GPU** To reduce the latency of inter-machine SF transfer between two GPUs, we use the GPUDirect RDMA [2] provided by CUDA, which allows network adapters to directly read from or write to GPU device memory, without staging through host memory. Between two network adaptors, the SFs are communicated using the methods listed above.

Similar to broadcast, several multicast methods tailored to different system configurations are provided.

- **CPU-to-CPU** We use MPI group communication primitives for CPU-to-CPU multicast. In each clock, `MPI_Comm_split` is invoked to split the communicator `MPI_COMM_WORLD` into a target group (containing the selected machines) and a non-target group. Then the message is broadcast to the target group.
- **CPU-to-CPU, InfiniBand** The efficient but unreliable multicast method supported by InfiniBand at hardware level and a reliable point-to-point network protocol are used together. InfiniBand combines the selected machines into a single *multicast address* and sends the message to it. Point-to-point re-transmission is issued if no ACK is received before timeout. Since the selection of receivers is random, any machine does not receive messages in continuous clocks from another machine, making it difficult to detect out-of-order messages. We adopt a simple approach: a message is discarded if it arrives late.
- **GPU-to-GPU** GPUDirect RDMA is used to copy buffers from GPU memory to network adaptor. Then the communication between network adaptors is handled using the two methods given above.

5.2.5 Evaluation

We evaluate Orpheus on three ML applications: multiclass logistic regression (MLR), topic model (TM) [207], and long short-term memory (LSTM) [163] network.

Experimental Setup

Cluster setup We used two clusters: (1) a CPU cluster having 34 machines each with 64 cores and 128 GB memory, connected by FDR10 Infiniband; (2) a GPU cluster having 40 machines each with one TitanX GPU and 64GB memory, connected by 40Gbps Ethernet. We trained MLR and TM on the CPU cluster and trained LSTM on the GPU cluster. Unless otherwise noted, the experiments were performed using all machines in each cluster.

Baseline systems We compared with (1) Spark-MLR from Spark MLlib-2.0.0, which is based on an L-BFGS algorithm (Spark-MLR has an SGD-based implementation, which converges slower than L-BFGS); (2) Bosen-MLR and Bosen-TM: MLR and TM implemented using a recent parameter server (PS) Bosen [355], with additional system features (e.g., parameter-update filtering) borrowed from another PS [226]; (3) TensorFlow-MLR and TensorFlow-LSTM: TensorFlow-1.0 implementation of MLR and TensorFlow-1.7 implementation of LSTM, which

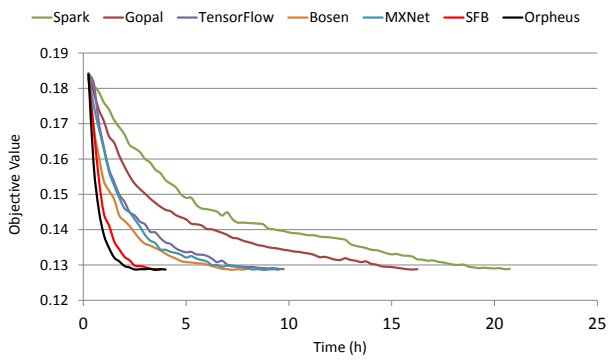

Figure 5.6: Convergence curves in the MLR experiments.

are partially based on PS; (4) MXNet-MLR and MXNet-LSTM: MXNet-0.7 [73] implementation of MLR and MXNet-1.1 implementation of LSTM, using PS-based data parallelism; (5) Gopal-MLR [136]: a model-parallel MLR based on Hadoop; (6) FlexiFaCT-TM [207]: a Hadoop implementation of TM. Note that Spark and Tensorflow implement a probabilistic topic model – latent Dirichlet allocation [49], which is different from the non-probabilistic TM in Orpheus.

Utilization of system features All system features except elasticity were used in the experiments. Most broadcast and multicast methods were utilized since our experiments span various hardware-level configurations (CPU, GPU, InfiniBand, Ethernet) and software-level settings (broadcast, multicast, BSP, SSP).

Datasets Three datasets were used in the experiments: Wikipedia [272], PubMed [9], and 1B-Word [67]. The Wikipedia dataset contains ∼2.4 million documents from 325K classes. Documents are represented with 20K-dimensional bag-of-words vectors. The PubMed dataset contains 8.2M documents and ∼0.74B words. The vocabulary size is 141K. The 1B-Word dataset contains ∼0.8B words with a vocabulary size of ∼0.8M. The MLR, TM, and LSTM experiments were conducted on the Wikipedia, PubMed, and 1B-Word dataset respectively.

ML and system hyper-parameter setup The topic number in TM and the state-vector dimension in LSTM was set to 50K and 40K respectively. As a result, the parameter matrix in MLR, TM, and LSTM has a size of 325K×20K, 50K×141K, 40K×40K, containing ∼6.5B, ∼7.1B, ∼1.6B entries respectively. The parameters in all applications were trained using the SGD algorithm with a mini-batch size of 100. In SF selection, the number of selected SFs was set to 25. In random multicast, the number of destinations each machine sends message to was set to 4. The consistency model was set to SSP with a staleness value of 4.

Overall Results

Comparison with other systems We first compare the convergence speed of these systems. In this comparison, no system uses fault tolerance. By *convergence*, it means the loss function

MLR			
# CPU Machines	12	34	Speedup
Spark	37.3	19.6	1.9
Gopal	31.7	15.1	2.1
TensorFlow-1.0	16.9	8.9	1.9
Bosen	15.7	7.1	2.2
MXNet-0.7	12.8	8.4	1.5
SFB	5.1	2.7	1.9
Orpheus	**4.4**	**1.9**	**2.3**
TM			
# CPU Machines	12	34	Speedup
FlexiFaCT	61.1	33.9	1.8
Bosen	49.4	23.5	2.1
SFB	20.1	9.7	2.1
Orpheus	**13.2**	**5.4**	**2.4**
LSTM			
# GPU Machines	12	40	Speedup
TensorFlow-1.7	14.2	5.9	2.4
MXNet-1.1	12.5	4.6	2.7
Orpheus	**11.9**	**4.1**	**2.9**

Table 5.2: The second and third columns show the convergence time (hours) of each system, under a different number of machines. The third column shows the speedup of each system when the number of machines is increased from 12 to 34 (in MLR and TM), or from 12 to 40 (in LSTM).

value (e.g., cross-entropy loss in MLR, negative log-likelihood in TM and LSTM) on the training set levels off. A better system takes less time to converge. In each of our experiments, different systems converged to the same loss value. Figure 5.6 shows the convergence curves for MLR (34 machines). The second and third columns of Table 5.2 shows the convergence time of each system, under a different number of machines. On all three models, Orpheus converges faster than the baseline systems.

We first compare Orpheus with parameter server (PS) based systems including Bosen [355], TensorFlow-1.0 [13], and MXNet-0.7 [73]. On MLR, with 34 CPU machines, the speedup of Orpheus over Bosen, TensorFlow-1.0, MXNet-0.7 and SFB is 3.7x, 4.7x, 4.4x and 1.4x respectively. On TM, with 34 CPU machines, Orpheus is 4.4x and 1.8x faster than Bosen and SFB respectively. On LSTM, with 40 GPU machines, Orpheus is 1.4x faster than TensorFlow-1.7 and 1.1x faster than MXNet-1.1. As we will further show later, these speedups are achieved mainly because Orpheus is more efficient in communication. Compared with SFB, Orpheus reduces the number of sent SFs using SF selection and provides a random multicast scheme which works better than the deterministic multicast scheme utilized in SFB. Similar to SFB, Orpheus transmits small-sized vectors instead of large-sized matrices, which greatly reduces network traffic, compared with PS-based systems.

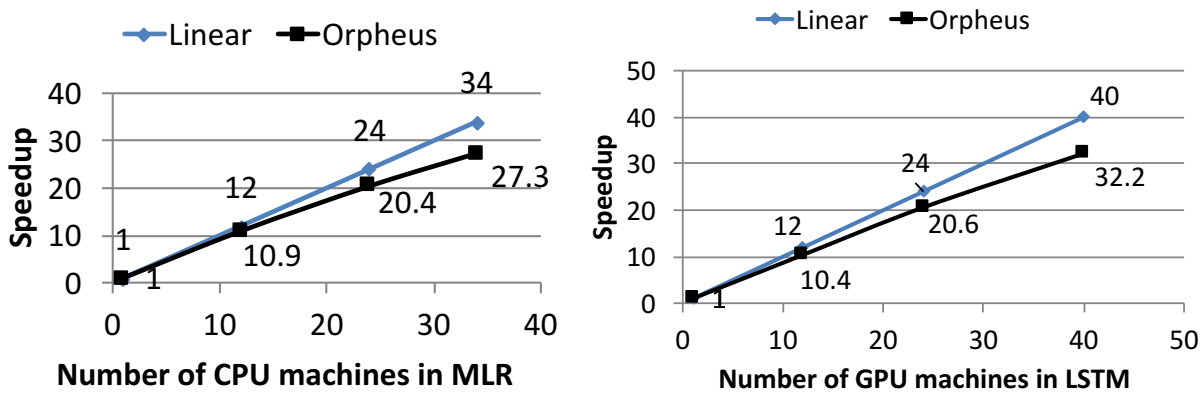

Figure 5.7: Scalability with more machines: (left) Orpheus-MLR; (right) Orpheus-LSTM.

Next, we compare Orpheus with the rest of baseline systems. Using 34 CPU machines, Orpheus is 10.3x and 7.9x faster than Spark and Gopal on MLR, and 6.3x faster than FlexiFaCT on TM. Gopal outperforms Spark possibly because it uses a better distributed-algorithm which is based on model-parallelism. However, it is slower than PS systems due to the disk IO overhead of Hadoop. So is FlexiFaCT, which is a Hadoop-based system. Spark is at least two times slower than PS systems (implemented with C++) due to the overhead incurred by resilient distributed datasets and Java virtual machine.

Scalability We evaluated how Orpheus scales up as the number of machines increases. The results on MLR and LSTM are shown in Figure 5.7. With 34 CPU machines, Orpheus achieved a 27.3x speedup on MLR. With 40 GPU machines, a 32.2x speedup is achieved on LSTM. The scalability of Orpheus is better than baseline systems, as shown in the fourth column of Table 5.2, where we measured the speedups for MLR and TM when the number of CPU/GPU machines increases from 12 to 34 and the speedups for LSTM when the number of GPU machines increases from 12 to 40. For example, in LSTM experiments with 40 GPU machines, Orpheus achieves a speedup of 2.9 compared with using 12 machines.

Evaluation of individual components

In this section, we evaluate the impact of each individual component. We compare the following systems: (1) Matrix+PS: synchronizing parameter copies by transmitting full matrices using a parameter server (PS) architecture; (2) SFB: SF broadcasting (SFB); (3) SFB+SFS: adding SF selection (SFS) to SFB; (4) SFB+SFS+RM: adding random multicast (RM); (5) SFB+SFS+RM+PCS: adding periodic centralized synchronization (PCS); (6) SFB+SFS+RM+PRR: adding parameter-replicas rotation (PRR). In these systems, no checkpointing is used. The number of machines in MLR, TM, and LSTM is set to 34, 34 and 40 respectively. Table 5.3 shows the convergence time of these systems, where we make the following observations. First, SFB is much more efficient than Matrix+PS. SFB is 2.6x, 2.4x and 2x faster than Matrix+PS on MLR, TM, and LSTM respectively. The reason is: SFB transmits small-sized vectors while Matrix+PS transmits large matrices; the communication cost of SFB is much smaller. Second, adding SFS

	MLR	TM	LSTM
Matrix+PS	7.1	23.5	16.8
SFB	2.7	9.7	8.6
SFB+SFS	2.3	7.9	6.9
SFB+SFS+RM	2.1	6.6	5.5
SFB+SFS+RM+PCS	2.0	5.9	4.9
SFB+SFS+RM+PCS+PRR	1.9	5.4	4.1

Table 5.3: Convergence time (hours) of different system configurations.

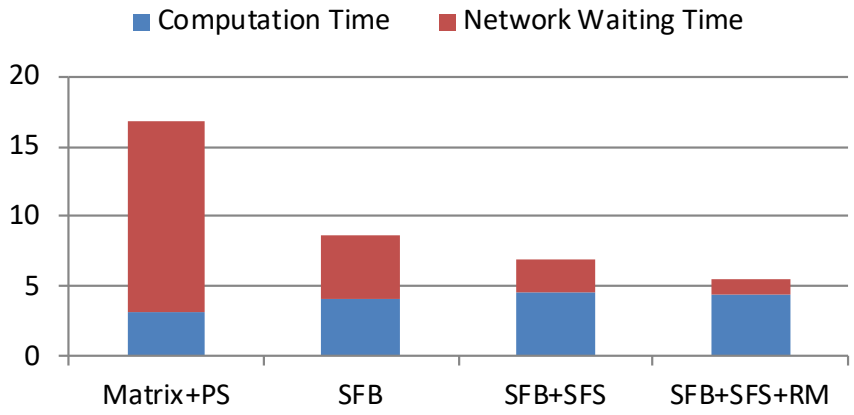

Figure 5.8: Breakdown of network waiting time (hours) and computation time (hours).

to SFB further reduces the runtime – by 15%, 19%, and 20% – on MLR, TM, and LSTM respectively. SFS selects a subset of SFGs for communication, which reduces network traffic. Third, incorporating RM reduces the runtime of SFB+SFS by 9%, 16%, and 20% on the three applications. Under RM, in each clock, each machine selects a subset of machines to send SFs to, which reduces the number of network messages. Fourth, adding PCS further speeds up convergence. Via PCS, the incoherence among different parameter copies is alleviated, which reduces noise and improves convergence quality. Fifth, comparing the last two rows of this table, we confirm the effectiveness of PRR in reducing convergence time. Under PRR, each parameter replica has the chance to explore all data shards on different machines, which facilitates symmetric update of parameters.

Figure 5.8 shows the breakdown of network waiting time and computation time for four configurations. Compared with Matrix+PS, SFB greatly reduces network waiting time by avoiding transmitting matrices. It slightly increases the computation time since the same SFG needs to be converted into an update matrix at each worker. Adding SFS further decreases network time since it reduces the number of transmitted SFs. SFS causes the increase of computation time because of the overhead of executing the JMCSS algorithm (Algorithm 3). The network time is further reduced by using RM, which decreases the number of network messages. RM has little impact on the computation time.

In the sequel, we present more detailed evaluations of several key components.

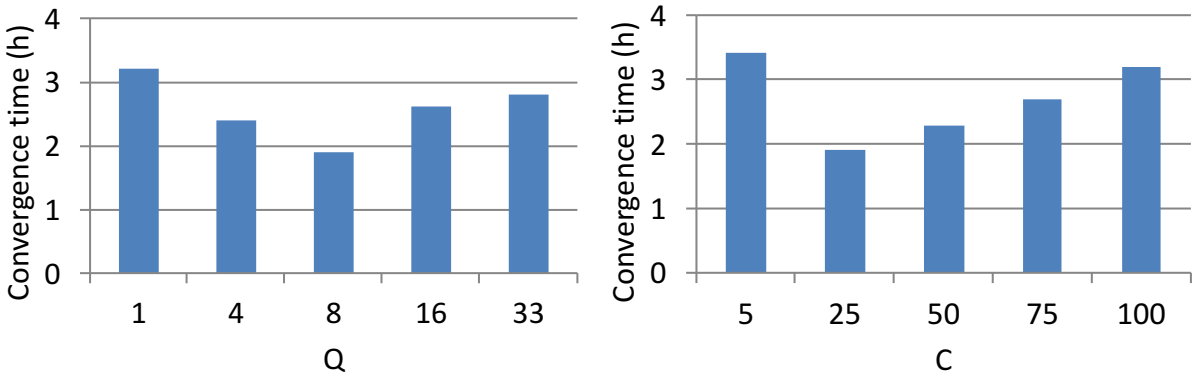

Figure 5.9: How the system parameter Q in random multicast (left) and C in SF selection (right) affect the running time of Orpheus for MLR.

Random multicast (RM) Figure 5.9 (left) shows the convergence time of MLR under varying Q – the number of destinations each machine sends messages to. As can be seen, communicating with all machines (i.e., $Q = 33$) incurs much more running time than using random multicast ($Q = 4$), which demonstrates the effectiveness of RM in improving communication efficiency. The efficiency results from RM's ability of reducing the number of network messages. However, Q cannot be too small. Otherwise, the running time increases (e.g., when $Q = 1$), due to the severe synchronization delays.

We compared RM with two multicast schemes: (1) deterministic multicast (DM) [222] where each sending machine sends messages to a fixed set of 4 receiving machines; the set of 4 receiving machines is different for each sending machine and is chosen to balance network load across the cluster and prevent network hot spots; (2) round-robin multicast (RRM) [222, 353] where every two workers communicate with each other periodically according to a deterministic circular order. Figure 5.10 (left) shows the convergence time of MLR and LSTM under DM, RRM, and RM. In both applications, RM takes less time to converge. Compared with DM, RM uses a randomly changing multicast topology to enable each pair of machines to have some chance to communicate directly, thus facilitating more symmetric (hence faster) synchronization of parameter replicas. Compared with RRM, the randomness of RM facilitates faster "mixing" [148] of parameter copies and hence speeds up convergence.

To examine the robustness of RM against network connection failures, we simulated the effect that in each clock the connections between 10% of machine pairs are "broken" randomly. Figure 5.10 (right) shows the relative increase of convergence time when failure happens. As can be seen, the relative increase under RM is much smaller than that under DM and RRM, confirming that RM is more robust, due to its random nature.

SF selection Figure 5.9 (right) shows the convergence time for MLR under varying C – the number of selected SFs. Compared with using the entire batch ($C = 100$), selecting a subset (e.g., $C = 25$) of SFs to communicate significantly speeds up convergence, thanks to the reduced network traffic. On the other hand, C cannot be too small, which otherwise incurs large approximation errors in parameter updates. For example, the convergence time under $C = 5$ is

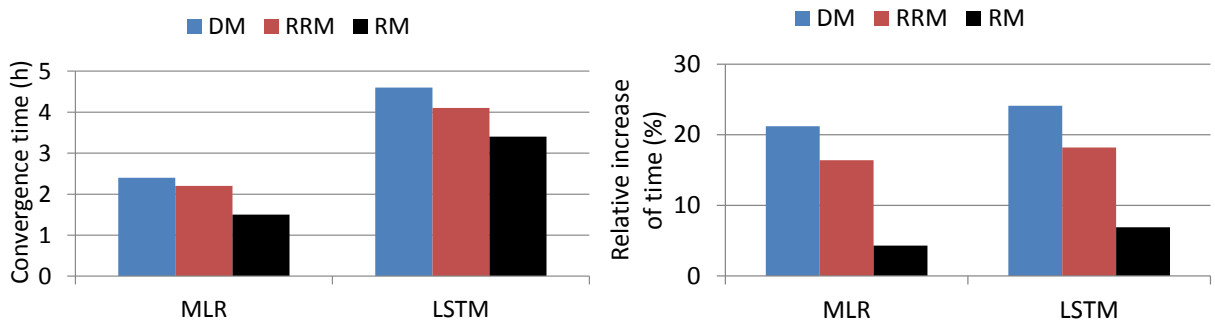

Figure 5.10: (Left) Convergence time in Orpheus under deterministic, round-robin, and random broadcast for MLR and LSTM. (Right) Relative increase of convergence time when network connection fails.

	MLR	LSTM
No checkpoint	1.9	4.1
Matrix-based checkpoint	2.4	5.2
SF-based checkpoint	1.9	4.2
Matrix-based recovery	2.9	6.7
SF-based recovery	2.3	4.8

Table 5.4: Convergence time (hours) under different configurations of fault tolerance and recovery.

worse than that under $C = 100$.

Fault tolerance and recovery We compare the following configurations: (1) no checkpoint; (2) matrix-based checkpoint: every 100 clocks[2], Orpheus saves the parameter matrix onto the disk; when saving matrices, the computation halts to ensure consistency; (3) SF-based checkpoint; (4) matrix-based recovery: we simulated the effect that in each clock, each machine fails with a probability of 0.01; when failure happens, a recovery is performed based on the checkpointed matrices; (5) SF-based recovery: machine failure is simulated in the same way as (4) and recovery is based on the saved SFs. For (2) and (3), no machine failure happens.

Table 5.4 shows the convergence time of MLR (34 machines) and LSTM (40 machines) under different configurations. From this table, we observe the following. First, compared with no-checkpoint, matrix-based checkpoint method substantially increases the convergence time while our SF-based checkpointing incurs very little increase. The reasons are twofold: (1) saving vectors consumes much less disk bandwidth than saving matrices; (2) checkpointing SFs does not halt computation, wasting no compute cycles, which is not the case in checkpointing matrices. Second, in the case where machine failure happens, matrix-based recovery causes more slowing-down of convergence than SF-based recovery. This is because in matrix-based recovery, the parameters can only be rolled back to the state that is saved every 100 clocks. If the failure happens at clock 199, the parameters are rolled back to the state saved at clock 100. The com-

[2]Choosing a number smaller than 100 would entail more disk-IO waiting.

putation from clock 101 to 198 are wasted. However, in SF-based recovery, the parameter state after every clock is preserved. It can always roll back to the latest parameter state (e.g., the state after clock 198) and no computation is wasted.

5.3 Poseidon: A Hybrid Architecture of SFB and Parameter Server

Many ML models are parameterized by multiple matrices. For example, in a convolutional neural network (CNN), the convolution layers and fully-connected layers have their own layer-specific weight matrices. Some of these matrices are of large size (in the sense that they have thousands of rows and columns at least) while others are small-sized (hundreds of rows/columns). For instance, in the first convolutional layer of AlexNet [203], the weight matrix of 96 filters has a size of 96×363 which is relatively small while that in the fully-connected (FC) layer is 4096×4096 which is much larger.

When these weight matrices are trained using stochastic gradient descent (SGD), their updates can be constructed by vectors, i.e., having the sufficient factor property. Take the $J \times D$ weight matrix $\mathbf{W}$ between two FC layers l_i and l_{i+1} as an example. In the forward pass, one data sample is fed into the network and the activations of layer l_i is produced as $\mathbf{a}_i$. During back-propagation (BP), an error message $\mathbf{e}_{i+1}$, which is a J-dimensional vector, is passed back from l_{i+1} to l_i. The gradients $\triangle\mathbf{W}$ thus can be exactly reconstructed by two vectors $\mathbf{e}_{i+1}$ and $\mathbf{a}_i$: $\triangle\mathbf{W} = e_{i+1}a_i^\top$. As a result, these weight matrices can be learned using the sufficient factor broadcasting (SFB) architecture of Orpheus.

In Section 5.2.1, we present a cost analysis of SFB and parameter server (PS) architectures [94, 226, 355]. The analysis shows that SFB outperforms PS if the matrix size is significantly larger (at least 10 times) than the mini-batch size in SGD and the number of worker machines, and PS has an advantage over SFB if otherwise. In CNN, both cases exist, which motivates us to design a hybrid communication protocol that adopts both SFB and PS, based on which a distributed deep learning system called Poseidon [411] is built.

5.3.1 Structure-aware Message Passing (SACP) Protocol

We propose the SACP [411] protocol, which hybridizes the client-server PS scheme with the peer-to-peer SFB scheme, for GPU-based distributed deep learning. In addition to PS and SFB, SACP also supports SF-based PS (SFPS) [78]. SFPS is much like a PS except that instead of transmitting update matrices from workers to the server as PS does, SFPS transmits SFs generated on the workers to the server and transform these SFs into update matrices at the server. Figure 5.11 illustrates the three communication schemes.

The SACP is structure-aware, as it intelligently determines the optimal communication method, according to the matrix size $J \times D$, the SGD batch size K, and the number of workers P. Recall that under the bulk synchronous parallel consistency model where all workers proceed at the same pace, the communication costs of PS, SFB, and SFPS are $2PJD$, $(P-1)^2K(J+D)$, $PK(J+D)+PJD$ respectively. In general, SFB and SFPS have a lower cost than PS when the

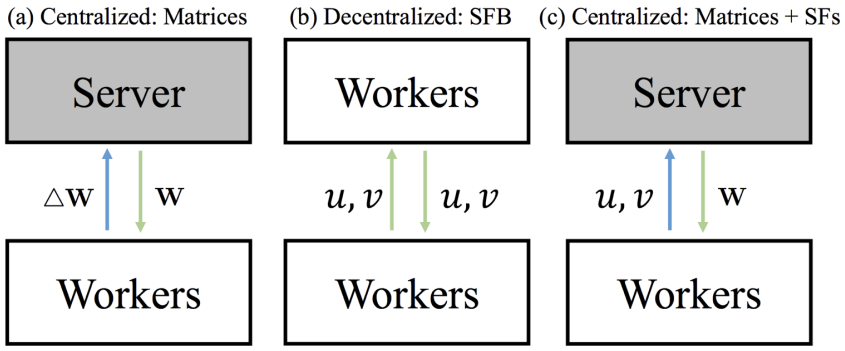

Figure 5.11: The illustration of three types of communications: (a) Full matrices communications via centralized parameter server (PS); (b) Sufficient factor broadcasting via decentralized P2P scheme; (c) SF-based PS: from workers to the server, SFs are transferred; from the server to workers, full matrices are transmitted.

matrix size is large, and the mini-batch size and the number of workers are small.

In CNN, a convolution layer has a $J \times D$ weight matrix, where J is the number of filters and the D is the size of the local receptive field. J and D are usually small. For example, in the first convolution layer of AlexNet, J and D are 96 and 363 respectively. These filters slide over a grid of locations in each image. At each location, an update matrix of the weights is generated, which can be written as the outer-product of two vectors (SFs). Let L denote the number of locations in each image, then the costs of SFB and SFPS would be $(P-1)^2KL(J+D)$, $PKL(J+D)+PJD$. The value of L could be several thousand or more (e.g., in the first convolution layer of AlexNet, L equals 3136), which renders the costs of SFB and SFPS to be larger than PS's cost that is independent of L. Therefore, we choose PS for synchronizing weight matrices in convolution layers.

For fully-connected (FC) layers, their weight matrices are in general much larger than those in convolutional layers. In AlexNet, J and D are 4096 in the FC layers. Different from the convolutional layers where multiple update matrices are generated at different locations of an image, in FC layers there is only one update matrix for each image. The mini-batch size K is usually around 100. Putting these pieces together, we conclude that in most cases the costs of SFB and SFPS are lower than that of PS. Hence, we choose either SFB or SFPS to communicate matrices in FC layers. To choose between SFB and SFPS, we directly compare their costs $(P-1)^2K(J+D)$, $PK(J+D)+PJD$, and select the one yielding lower cost. Algorithm 5 summarizes how SACP works.

5.3.2 Evaluation

We evaluated Poseidon on image classification tasks and used three datasets: CIFAR-10 [5], ILSFRC-2012 [95] which contains about one million ImageNet [95] images from 1000 classes, and ImageNet-22K which contains all ImageNet images from 22K classes. The experiments show that Poseidon significantly accelerates the training of CNNs, while guaranteeing the correct convergence. Ablation studies were performed to justify the effectiveness of SACP.

Algorithm 5: Structure-aware communication protocol (SACP).

At iteration t **on worker** p:
Input: Layer l_i, $J \times D$ gradient matrix $\triangle \mathbf{W}_i^p$, number of workers P, batch size K.
Task : Push out gradients $\triangle \mathbf{W}_i^p$ and then update $\mathbf{W}_i^p$.

```
if l_i is not an FC layer then
    Send △W_i^p to the master node.
    Synchronize updated W_i from the master node.
end
else
    Recast △W_i^p into two SFs, i.e. △W_i^p = u_i^p v_i^{p⊤}.
    if (P − 1)^2 K(J + D) ≤ PK(J + D) + PJD then
        Broadcast u_i^p, v_i^p to all other workers.
        Receive SFs u_i^j, v_i^j, j ≠ p from all other workers.
        Update W_i: W_i ← W_i + Σ_j u_i^j v_i^{j⊤}.
    end
    else
        Send u_i^p, v_i^p to the master node.
        Synchronize updated W_i from the master node.
    end
end
```

Cluster Configuration

We conducted all experiments on the PRObE Susitna cluster [235], where each node has a 4×16-core 2.1GHz AMD Opteron 6272 CPU, 128GB of RAM, and an NVIDIA Tesla K20C GPU with 4799MB memory. All cluster nodes have shared access to a network file system (NFS) with 1x Hitachi 1.0 TB HDD and 2x Hitachi 3.0 TB HDD. We used the 40GbE network. The Caffe framework [182] (the Oct 2014 version) was used as the single node baseline, and it was modified using Poseidon's client library API for distributed execution.

Image Classification

We demonstrate Poseidon's performance on three benchmark datasets.

Classification on CIFAR-10 We first evaluate Poseidon on the CIFAR-10 [5] dataset, which contains 32×32 images from 10 classes. Each class has 6K images. An official train/test split is provided where 50K images are used for training and 10K for testing.

We employed the built-in *cifar10_quick_solver* and *cifar10_quick_train_test* network structure in Caffe[3], consisting of 3 convolutional (CONV) layers and 1 fully-connected (FC) layer followed by a 10-way softmax classifier. This network has $145,578$ parameters in total. It converges to a 70% test accuracy with 4 epochs of training in a single machine without decreasing

[3] `github.com/BVLC/caffe/tree/master/examples/cifar10`.

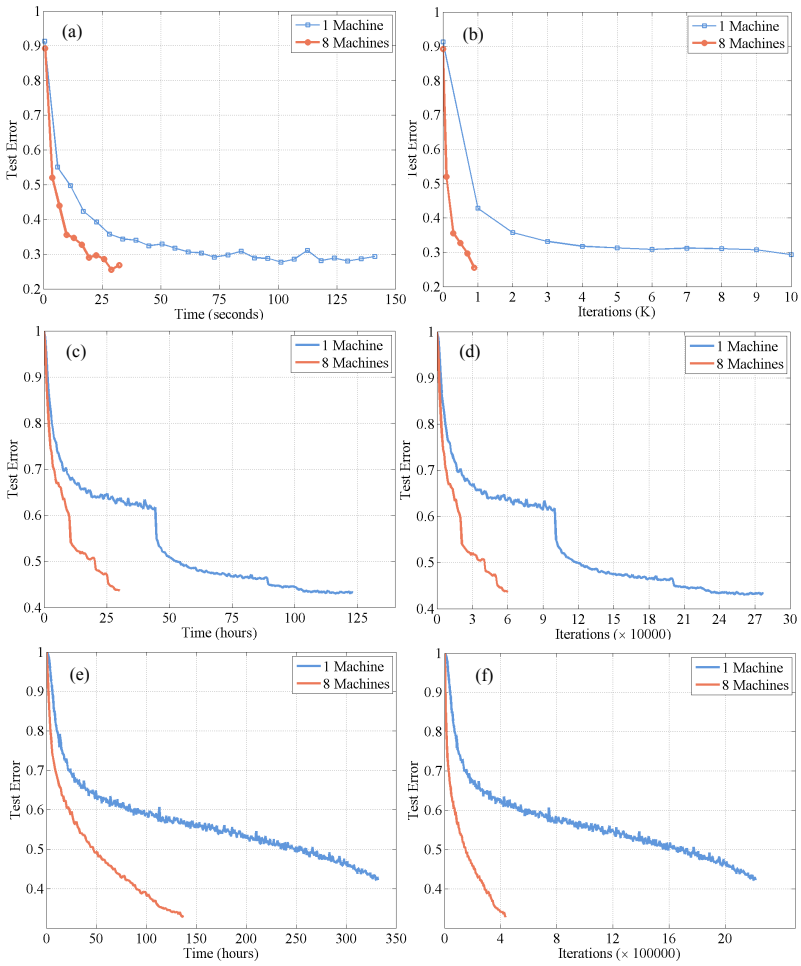

Figure 5.12: The comparison of training different CNNs to convergence between Poseidon on 8 GPU nodes and Caffe on a single node: (a)-(b) *cifar10_quick_train_test*; (c)-(d) *bvlc_alexnet*; (e)-(f) *bvlc_googlenet*. Test errors are shown with respect to (left) training time, and (right) training iterations.

the learning rate. We deployed Poseidon onto 8 Susitna nodes. Since a larger batch size usually hurts the SGD performance, we reduced the batch size from 100 to 50 and also slightly decreased the base learning rate from 0.01 to 0.007, while keeping other hyperparameter settings in *cifar10_quick_solver* unchanged. For better comparison, in the distributed setting, we used the bulk synchronous parallel consistency model.

Similar to the single machine setting, we trained the network to convergence without adjusting the learning rate. The test accuracy achieves nearly 75%. Figure 5.12(a)-(b) plot how the test error decreases along with training time and iterations for Poseidon on 8 nodes and Caffe on a single node. Under the same setting, the single-machine Caffe takes more than 4 times of training time to converge to 70% accuracy, while Poseidon quickly converges to 72% in 19 seconds and attains a higher accuracy 75% in 25 seconds with 8 GPU nodes.

Model	Speedup	Top-1 accuracy
CIFAR-10 quick	$4\times$	75%
AlexNet	$4.5\times$	56.5%
GoogLeNet	$4\times$	67.1%

Table 5.5: Speedups and converged top-1 accuracies of Poseidon by training models on 8 GPU nodes and on the CIFAR-10 and ILSFRC-2012 dataset, compared to Caffe on a single machine.

Classification on ILSFRC-2012 We then experiment on ImageNet ILSFRC-2012, consisting of 1.28 million training images and 50K validation images on 1,000 categories. We down-sampled all images to $256 \times 256 \times 3$ before feeding them into the networks, and report the top-1 accuracy on the validation set.

We evaluate Poseidon on AlexNet [203] and GoogLeNet [319]. The AlexNet has 5 CONV layers, 2 FC layers, and a 1000-class softmax classifier. It contains 61.3 million parameters in total. GoogLeNet has 22 layers and 5 million parameters. For fair comparisons, we employed the open implementations of AlexNet[4] and GoogLeNet[5] provided in Caffe, denoted as *bvlc_alexnet* and *bvlc_googlenet*. In single machine training of AlexNet, we used the standard solver in Caffe, where the batch size was 256 and the number of epochs was 70. During training, the learning rate was decreased 3 times. For the training of GoogLeNet, we employed the *quick_solver*, which uses the polynomial learning rate policy, and trains for 60 epochs with a batch size of 32. In the distributed setting, we deployed both AlexNet and GoogLeNet onto 8 GPU nodes using Poseidon, and kept the network structure and the batch size exactly the same as those in the single machine setting. Specifically, for AlexNet, we trained it on 8 nodes for about 60K iterations, with the base learning rate set to 0.005, which was decreased 5 times during the entire training process. For GoogLeNet, we used a standard step learning rate policy by setting the base learning rate to 0.005 and decreasing it 90 times during training.

Figure 5.12(c)-(d) and Figure 5.12(e)-(f) show the performance of training AlexNet and GoogLeNet using Poseidon with a GPU cluster of 8 nodes, compared to single-machine Caffe, respectively. For AlexNet, Poseidon attains 56.5% top-1 accuracy on the validation set after 27 hours of training, achieving a $4.5\times$ speedup against single machine Caffe which needs 5 days to achieve such an accuracy. For GoogLeNet, Poseidon converges to 67.1% top-1 accuracy after 130 hours of training, whereas single-machine Caffe only achieves 50% top-1 accuracy after 250 hours of training and 57% after near 350 hours of training (Poseidon only needs less than 48 hours to achieve 50% and 75 hours to achieve 57%, with a near $5\times$ speedup).

The speedups achieved by Poseidon in terms of algorithm convergence are summarized in Table 5.5. Besides, we report the speedups on throughput (i.e. number of images processed per seconds) in Figure 5.13 when training AlexNet and GoogLeNet using Poseidon on different numbers of GPU nodes, compared to single machine Caffe. The staleness synchronous parallel [162] consistency model was used and the throughput speedups are compared under different settings of the staleness value.

[4] `github.com/BVLC/caffe/tree/master/models/bvlc_alexnet`.
[5] `github.com/BVLC/caffe/tree/master/models/bvlc_googlenet`.

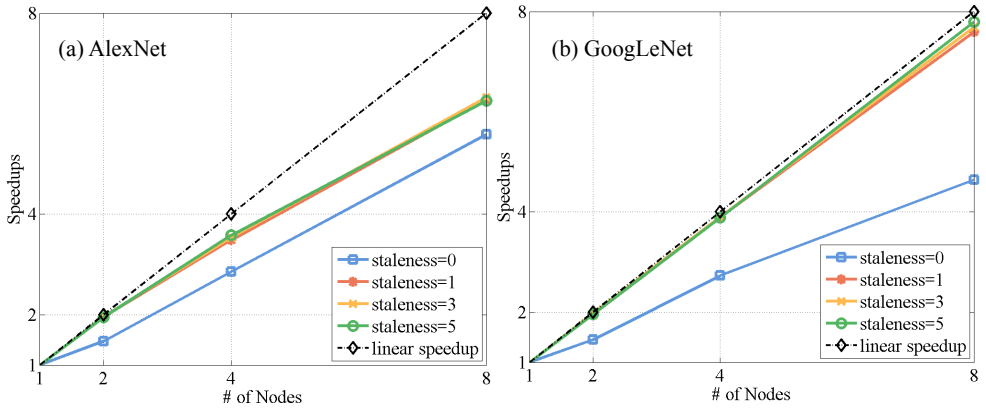

Figure 5.13: The speedups on throughput with different values of staleness, when training using Poseidon on 8 nodes, compared to Caffe on a single node. (a) AlexNet with batch size 256, and (b) GoogLeNet with batch size 32.

Framework	Data	# machines/cores	Time	Train accuracy	Test accuracy
Poseidon	7.1M ImageNet-22K images for training, 7.1M for testing	8/8 GPUs	3 days	41%	23.7%
Adam [78]	7.1M ImageNet-22K images for training, 7.1M for testing	62 machines/?	10 days	N/A	29.8%
MxNet [73]	All ImageNet-22K images for training, no testing results	1/4 GPUs	8.5 days	37.2%	N/A
Le et al. [214] w/ pretrain	7.1M ImageNet-22K and 10M unlabeled images for training, 7.1M for testing	1,000/1,6000 CPU cores	3 days	N/A	15.8%

Table 5.6: Comparisons of image classification results on ImageNet-22K.

Classification on ImageNet-22K

ImageNet-22K is the largest public dataset for image classification, including 14,197,087 labeled images from 21,841 categories, which is rarely touched by the research community due to its massive data size and complexity. We experiment on ImageNet-22K to demonstrate the scalability of Poseidon. As no official test data exists for evaluation, following previous settings in [78, 94, 214], we randomly split the whole set into two parts, and used the first 7.1 million images for training and the rest for testing. Similar to ILSFRC-2012, we resized all images to 256×256 and report the top-1 test accuracy.

We designed an AlexNet-like architecture. Specifically, the CNN takes a random 227×227 crop from the original image as input, and forwards it into 5 CONV layers and 2 FC layers before prediction. The CNN has convolution filters with sizes 7×7, 5×5, and 3×3. Similar to AlexNet, the first, second, and fifth CONV layers are followed by max pooling layers with size 3×3 and stride 2. Two FC layers with 3,000 neurons each are put at the top of the network, followed by a softmax layer for 21,841-way classification. We trained the CNN with data-parallelism by equally partitioning the training data into 8 GPU nodes. The batch size was set to 256. The network was trained using the step learning rate policy, with a base learning rate of 0.005, which is decreased 6 times during training.

Table 5.6 compares our results to those achieved by previous works including Adam [78],

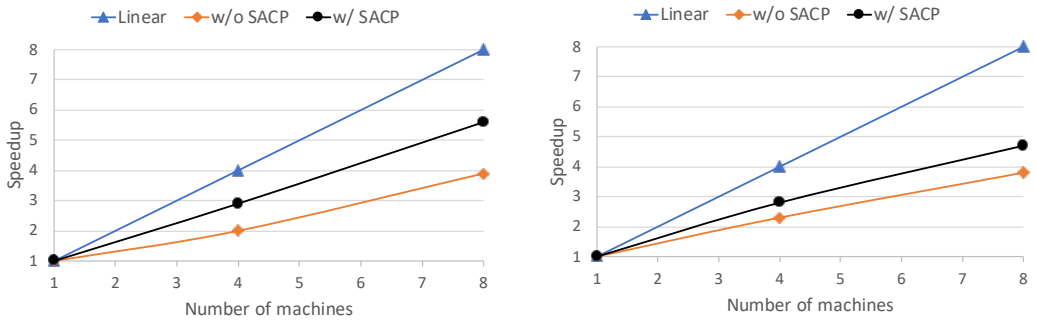

Figure 5.14: Speedups against the single-machine Caffe in terms of throughput, under different number of GPU nodes: (a) AlexNet with a batch size of 256; (b) GoogLeNet with a batch size of 32.

MXNet [73], and Le et al. [214]. Note that at this point a complete fair comparison between different frameworks is not possible, because the experiment protocol of ImageNet-22K is not standardized, the source codes are not fully available yet, and large variations exist in system configurations, models, and implementation details. However, in general Poseidon achieves a competitive accuracy 23.7% with shorter training time and less machines. Our system achieves 23.7% accuracy which is close to that achieved by Adam [78], using a model whose size is close to that of Adam. But our system takes much less training time (30% of Adam) and much fewer machines (13% of Adam). Compared with MXNet which achieves 37.2% training accuracy with 8.5 days of training on 4 GPUs, our system achieves a higher training accuracy (41%) with 3 days of training on 8 GPUs.

Internal Comparison

In this section, we conduct internal comparison to validate the effectiveness of SACP in reducing communication cost for GPU-based distributed deep learning. We measure the speedups against the single-machine Caffe in terms of throughput, which is defined as the number of images processed per second. Figure 5.14 compares the speedups for training AlexNet and GoogLeNet under the following two settings with different number of nodes: (1) `w/o SACP`: weight matrices in all layers are synchronized using PS; (2) `w/ SACP`: SACP is enabled. We used the BSP consistency model and set the batch size to 256 for AlexNet and 32 for GoogLeNet (different batch sizes will lead to slightly different speedups on throughput). With SACP enabled, the speedup on throughput is improved. Particularly, when training on 8 nodes, SACP greatly increases the speedups of AlexNet training from 4 to 6, with a 50% improvement. For GoogLeNet with fewer FC layers, SACP achieves approximately 20% improvement on the speedup.

5.4 Convergence Analysis

In this section, we analyze the convergence of algorithms executed using SFB. We first study the convergence of mini-batch SGD under full broadcasting SFB for nonconvex optimization. Since SFB is a peer-to-peer decentralized computation model, we need to show that parameter copies

on different workers converge to the same limiting point without a centralized coordination, even under delays in communication due to bounded asynchronous execution. In this respect, our analysis differs from that of centralized parameter server systems [162], which instead show convergence of global parameters on the central server. More specifically, We are interested in solving the optimization problem $\min_{\mathbf{W}} f(\mathbf{W})$, where $f(\mathbf{W})$ corresponds to the loss of a set of training samples.

Consider a distributed system with P machines. Each machine p keeps a local variable $\mathbf{W}_p$. We assume that the total loss f is distributed among the P worker machines, i.e., $f = \sum_{p=1}^{P} f_p$, and f_p denotes the loss stored in the p-th machine. Given a parameter matrix $\mathbf{W}$ and a random variable ξ, each machine p has access to a stochastic gradient oracle $G_p(\mathbf{W}, \xi)$ that satisfies $\mathbb{E}_\xi G_p(\mathbf{W}, \xi) = \nabla f_p(\mathbf{W})$. We further assume that every machine calls the stochastic oracle K times at each iteration (K is also referred to as the mini-batch size) and generates the stochastic gradient $\frac{1}{K}\sum_{j=1}^{K} G_p(\mathbf{W}_p^c, \xi_{c,j})$, where $\mathbf{W}_p^c$ denotes the local variable of machine p at iteration c.

At each iteration, machine p updates its local variable by aggregating the stochastic gradients from all machines and performing a proximal update. Specifically, the aggregated stochastic gradients on machine p at iteration c is $\mathbf{G}_p^c = \sum_{q=1}^{P} \frac{1}{K}\sum_{j=1}^{K} G_q(\mathbf{W}_q^{\tau_p^q(c)}, \xi_{\tau_p^q(c),j})$, where $\tau_p^q(c)$ is the number of iterations machine q has transmitted to machine p when machine p conducts its c-th iteration. We assume that $\tau_p^p(c) = c$ and $0 \le c - \tau_p^q(c) \le s$, i.e., machine p has access to the fresh information on itself, and receives delayed updates of machine q that are within s iterations. Denote the stepsize as $\eta > 0$, the local update rule of machine p is expressed as

$$\mathbf{W}_p^{c+1} = \mathbf{W}_p^c - \eta_c \mathbf{G}_p^c, \quad \text{where } 0 \le c - \tau_p^q(c) \le s. \tag{5.3}$$

This formulation, in which s is the maximum "staleness" allowed between any update and any worker, covers bulk synchronous parallel broadcasting ($s = 0$) and bounded-asynchronous broadcasting ($s > 0$). We also define an undelayed version of the aggregated stochastic gradient $\mathbf{G}^c = \sum_{q=1}^{P} \frac{1}{K}\sum_{j=1}^{K} \mathbf{G}_q(\mathbf{W}_q^c, \xi_{c,j})$. We adopt the following assumptions for our analysis.

Assumption 1. *(1) For all $p = 1, \ldots, P$, f_p is continuously differentiable and F is bounded from below; (2) ∇f, ∇f_p are Lipschitz continuous with constants L_f and L_p, respectively, and let $L = \sum_{p=1}^{P} L_p$; (3) There exists $B, \sigma^2 > 0$ such that for all p and c, we have $\|\mathbf{W}_p^c\|_F \le B$ and $\mathbb{E}\|\mathbf{G}^c - \sum_{p=1}^{P} \nabla f_p(\mathbf{W}_p^c)\|_F^2 \le \frac{\sigma^2}{KP}$ almost surely.*

The assumptions in item 1 and 2 are standard smoothness assumptions for gradient methods. In the case of full synchronization (i.e., $\mathbf{W}_p^c = \mathbf{W}^c$ for all p), the assumption in item 3 reduces to the standard bounded variance assumption for mini-batch SGD methods. Our analysis is based on the following auxiliary update sequence

$$\mathbf{W}^{c+1} = \mathbf{W}^c - \eta_c \mathbf{G}^c. \tag{5.4}$$

Compare to the local update in Eq.(5.3) on machine p, essentially this auxiliary update uses the undelayed aggregated stochastic gradients $\mathbf{G}^c$ generated by all machines, instead of the delayed ones $\mathbf{G}_p^c$. We show that all local machine parameter sequences $\{\mathbf{W}_p^c\}$ are asymptotically consistent with this auxiliary sequence $\{\mathbf{W}^c\}$, and their limit points are all stationary points of f.

Theorem 6. *Denote $\{\mathbf{W}_p^c\}$, $p = 1, \ldots, P$, and $\{\mathbf{W}^c\}$ as the local sequences and the auxiliary sequence generated by SFB, respectively. Let Assumption 1 hold. Then, with learning rate $\eta_c = O(\frac{KP}{(Ls+L_f)\sigma^2\sqrt{c}})$, we have*

- $\lim_{c\to\infty} \max_p \|\mathbf{W}^c - \mathbf{W}_p^c\|_F = 0$, i.e. *the maximal disagreement between all local sequences and the auxiliary sequence converges to 0;*
- *We have* $\min_{c\le C} \mathbb{E}\|\sum_{p=1}^P \nabla f_p(\mathbf{W}_p^c)\|^2 \le O\left(\sqrt{\frac{(Ls+L_f)\sigma^2}{KPC}}\right)$. *Moreover, there exists a common subsequence of* $\{\mathbf{W}_p^c\}$ *and* $\{\mathbf{W}^c\}$ *that converges almost surely to a stationary point.*

Intuitively, Theorem 6 says that, given a properly-chosen learning rate, all local worker parameters $\{\mathbf{W}_p^c\}$ eventually converge to stationary points (i.e. local minima) of the objective function F, despite the fact that SF transmission can be delayed by up to s iterations. Thus, SFB learning is robust even under bounded-asynchronous communication (such as SSP). Our analysis differs from [41] in two ways: (1) Bertsekas and Tsitsiklis [41] explicitly maintain a consensus model which would require transmitting the parameter matrix among worker machines — a communication bottleneck that we were able to avoid; (2) we allow subsampling in each worker machine. Accordingly, our theoretical guarantee is probabilistic, instead of the deterministic one in [41].

We now consider the multicast setting, where each machine updates its local variable by aggregating the stochastic gradients from a subset of the other machines. Specifically, we denote $\delta_p^q(c) \in \{0,1\}$ as whether machine p and machine q are connected at c-th iteration on machine p. The aggregated stochastic gradients on machine p at iteration c is denoted as $G_p^c(\delta) = \sum_{q=1}^P \delta_p^q(c) \frac{1}{K} \sum_{j=1}^K G_q(\mathbf{W}_q^{\tau_p^q(c)}, \xi_{\tau_p^q(c),j})$. We assume that each machine is connected to Q number of other machines at each iteration, i.e., $\sum_{q=1}^P \delta_p^q(c) = Q$ for all p and c. Denote the stepsize as $\eta > 0$, the local update rule of machine p is expressed as

$$\mathbf{W}_p^{c+1} = \mathbf{W}_p^c - \eta_c G_p^c(\delta), \quad \text{where } 0 \le c - \tau_p^q(c) \le s,\ \sum_{q=1}^P \delta_p^q(t) = Q. \tag{5.5}$$

We obtain the following result for the multicast setting.

Corollary 1. *Denote* $\{\mathbf{W}_p^c\}$, $p = 1, \dots, P$, *and* $\{\mathbf{W}^c\}$ *as the local sequences and the auxiliary sequence generated by multicast SFB, respectively, and assume that each machine aggregates the stochastic gradients from* $Q < P$ *other machines at every iteration. Let Assumption 1 hold. Then, with learning rate* $\eta_c \equiv O(\frac{1}{L(P-Q)C})$, *we have*

$$\min_{c=1,\dots,C} \mathbb{E}\|\sum_{p=1}^P \nabla f_p(\mathbf{W}_p^c)\|^2 \le O\left(L(P-Q) + \frac{(Ls+L_f)\sigma^2}{KPL(P-Q)C}\right).$$

In the multicast setting, we need to use a smaller stepzie $\eta_c = O(\frac{1}{L(P-Q)C})$ to compensate the errors caused by multicast SFB. The algorithm eventually converges to an $O(L(P-Q))$ neighbourhood of stationary point, i.e., if we broadcast the stochastic gradient updates to more machines, the variable sequence is more close to a stationary point. In the experiments, we observe that SFB under multicast converges to the same objective value as SFB under broadcast with a comparable convergence, while multicast can significantly reduce the communication cost.

5.4.1 Appendix: Proof of Theorem 6

Proof. Throughout, we denote $\mathbf{g}_c := \sum_{p=1}^{P} \nabla f_p(\mathbf{W}_p^c) = \mathbb{E}\mathbf{G}^c$. By the descent lemma [41], we have

$$\begin{aligned} f(\mathbf{W}^{c+1}) - f(\mathbf{W}^c) &\leq \langle \mathbf{W}^{c+1} - \mathbf{W}^c, \nabla f(\mathbf{W}^c)\rangle + \frac{L_f}{2}\|\mathbf{W}^{c+1} - \mathbf{W}^c\|_F^2 \\ &\overset{(i)}{=} -\eta_c \langle \mathbf{G}^c, \nabla f(\mathbf{W}^c)\rangle + \frac{L_f}{2}\eta_c^2 \|\mathbf{G}^c\|^2, \end{aligned}$$

where (i) follows from the observation that $\mathbf{W}^{c+1} - \mathbf{W}^c = -\eta_c \mathbf{G}^c$. Taking expectations on both sides, and note that $\mathbb{E}\mathbf{G}^c = \mathbf{g}_c, \mathbb{E}\|\mathbf{G}^c\|^2 \leq \|\mathbf{g}_c\|^2 + \frac{\sigma^2}{KP}$, we obtain that

$$\begin{aligned} \mathbb{E}f(\mathbf{W}^{c+1}) - \mathbb{E}f(\mathbf{W}^c) &\leq -\eta \mathbb{E}\langle \mathbf{g}_c, \nabla f(\mathbf{W}^c)\rangle + \frac{L_f \eta_c^2}{2}\mathbb{E}\|\mathbf{G}^c\|_F^2 + \frac{L_f \eta_c^2 \sigma^2}{2KP} \\ &= -\eta \mathbb{E}\|\mathbf{g}_c\|^2 - \eta \mathbb{E}\langle \mathbf{g}_c, \nabla f(\mathbf{W}^c) - \mathbf{g}_c\rangle + \frac{L_f \eta_c^2}{2}\mathbb{E}\|\mathbf{G}^c\|^2 + \frac{L_f \eta_c^2 \sigma^2}{2KP} \\ &\leq (\frac{L_f}{2}\eta_c^2 - \eta_c)\mathbb{E}\|\mathbf{g}_c\|^2 + \eta_c \mathbb{E}\|\mathbf{g}_c\| \sum_{p=1}^{P} L_p \|\mathbf{W}_p^c - \mathbf{W}^c\| + \frac{L_f \eta_c^2 \sigma^2}{2KP}. \end{aligned} \tag{5.6}$$

Next, we bound the term $\|\mathbf{W}_p^c - \mathbf{W}^c\|$. Note that $\mathbf{W}^c = \sum_{t=0}^{c-1} \eta_t \mathbf{G}^t, \mathbf{W}_p^c = \sum_{t=0}^{c-1} \eta_t \mathbf{G}_p^t$, both of which are aggregations of the stochastic gradient updates. Since $\mathbf{G}_p^t$ contains the delayed stochastic gradients with maximum staleness s, the discrepancy between $\mathbf{W}_p^c$ and $\mathbf{W}^c$ is at most the updates $\{\mathbf{G}^{c-s+1}, \ldots, \mathbf{G}^{c-1}\}$, and we obtain that

$$\|\mathbf{W}^c - \mathbf{W}_p^c\| \leq \sum_{t=c-s+1}^{c-1} \eta_t \|\mathbf{G}^t\|. \tag{5.7}$$

We note that this is only a coarse estimate for simplicity of the derivation. In general, less discrepancy may occur and does not affect the order of the final convergence rate. With Eq.(5.7), Eq.(5.6) can be further bounded as

$$\begin{aligned} &\mathbb{E}f(\mathbf{W}^{c+1}) - \mathbb{E}f(\mathbf{W}^c) \\ &\leq (\frac{L_f}{2}\eta_c^2 - \eta_c)\mathbb{E}\|\mathbf{g}_c\|^2 + L \sum_{t=c-s+1}^{c-1} \mathbb{E}\eta_c \eta_t \|\mathbf{g}_c\| \|\mathbf{G}^t\| + \frac{L_f \eta_c^2 \sigma^2}{2KP} \\ &\leq (\frac{L_f}{2}\eta_c^2 - \eta_c)\mathbb{E}\|\mathbf{g}_c\|^2 + L \sum_{t=c-s+1}^{c-1} \mathbb{E}[\eta_c^2 \|\mathbf{g}_c\|^2 + \eta_t^2 \|\mathbf{G}^t\|^2] + \frac{L_f \eta_c^2 \sigma^2}{2KP} \\ &\leq (\frac{L_f + 2Ls}{2}\eta_c^2 - \eta_c)\mathbb{E}\|\mathbf{g}_c\|^2 + L \sum_{t=c-s+1}^{c-1} \eta_t^2 [\mathbb{E}\|\mathbf{G}^t\|^2 + \frac{\sigma^2}{KP}] + \frac{L_f \eta_c^2 \sigma^2}{2KP}. \end{aligned}$$

Telescoping over c from 0 to $C-1$ and note that $\sum_{c=0}^{C-1}\sum_{t=c-s+1}^{c-1} r_t \le s\sum_{c=0}^{C-1} r_c$ for the positive sequence $\{r_t\}$, we obtain that

$$\begin{aligned}
&\inf f(\mathbf{W}) - \mathbb{E}f(\mathbf{W}^0) \\
&\le \sum_{c=0}^{C-1}(\frac{L_f+4Ls}{2}\eta_c^2 - \eta_c)\mathbb{E}\|\mathbf{g}_c\|^2 + Ls\sum_{c=0}^{C-1}\eta_c^2\frac{\sigma^2}{KP} + \sum_{c=0}^{C-1}\frac{L_f\eta_c^2\sigma^2}{2KP} \\
&\le \sum_{c=0}^{C-1}(\frac{L_f+4Ls}{2}\eta_c^2 - \eta_c)\mathbb{E}\|\mathbf{g}_c\|^2 + \sum_{c=0}^{C-1}\eta_c^2\frac{(Ls+L_f)\sigma^2}{KP}. \qquad (5.8)
\end{aligned}$$

It then follows that

$$\begin{aligned}
\min_{c=1,\ldots,C}\mathbb{E}\|\mathbf{g}_c\|^2 &\le \frac{f(\mathbf{W}^0) - \inf f(\mathbf{W}) + \frac{(Ls+L_f)\sigma^2}{KP}\sum_{c=0}^{C-1}\eta_c^2}{\sum_{c=0}^{C-1}(\eta_c - \frac{L_f+4Ls}{2}\eta_c^2)} \\
&\approx \frac{f(\mathbf{W}^0) - \inf f(\mathbf{W}) + \frac{(Ls+L_f)\sigma^2}{KP}\sum_{c=0}^{C-1}\eta_c^2}{\sum_{c=0}^{C-1}\eta_c},
\end{aligned}$$

where we ignore the higher order term in the last equation for simplicity, as we will use a diminishing stepsize $\eta_c = O(1/\sqrt{c})$ and this does not affect the order of the final estimate. Now we can apply [35, Theorem 4.2] to the above equation to conclude that

$$\min_{c=1,\ldots,C}\mathbb{E}\|\mathbf{g}_c\|^2 \le \sqrt{\frac{[f(\mathbf{W}^0) - \inf f(\mathbf{W})](Ls+L_f)\sigma^2}{KPC}},$$

with the choice of stepsize

$$\eta_c = \frac{4[f(\mathbf{W}^0) - \inf f(\mathbf{W})]KP}{(Ls+L_f)\sigma^2}\frac{1}{\sqrt{c}}. \qquad (5.9)$$

Hence we must have $\liminf_{c\to\infty}\mathbb{E}\|\mathbf{g}_c\|^2 = 0$. By our assumption, $\{\mathbf{W}_p^c\}_{p,c}$ and $\{\mathbf{W}^c\}_c$ are bounded and hence have limit points. Also note that the gradient of f_j is continuous. Thus, $\|\mathbf{G}^t\|$ is bounded. Since $\eta_c = \frac{1}{\sqrt{c}} \to 0$, Eq.(5.7) implies that $\|\mathbf{W}^c - \mathbf{W}_p^c\| \to 0$. This further implies that $\{\mathbf{W}^c\}$ and $\{\mathbf{W}_p^c\}$ share the same set of limit points. Lastly, by the fact that $\|\mathbf{W}^c - \mathbf{W}_p^c\| \to 0$ and the Lipschitz continuity of ∇f_p, we conclude that $\liminf\mathbb{E}\|\nabla f(\mathbf{W}^c)\|^2 \to 0$. Thus, there exists a common subsequence of $\{\mathbf{W}^c\}$ and $\{\mathbf{W}_p^c\}$ that converges to a stationary point almost surely.

Proof of Corollary 1

The proof strategy is similar to that of Theorem 6. Specifically, the main difference from the proof of Theorem 6 is the bound of $\|\mathbf{W}^c - \mathbf{W}_p^c\|$. In the multicast setting, we have $\mathbf{W}^c = \sum_{t=0}^{c-1}\eta_t\mathbf{G}^t, \mathbf{W}_p^c = \sum_{t=0}^{c-1}\eta_t G_p^t(\delta)$. Despite the discrepancy of gradients cause by the delay s, the multicast scheme makes $G_p^t(\delta)$ only aggregates Q stochastic gradients from other machines at

each iteration, resulting in a $P-Q$ stochastic gradient discrepancy compared to $\mathbf{G}^t$. Thus, we obtain

$$\|\mathbf{W}^c - \mathbf{W}_p^c\| \leq \sum_{t=c-s+1}^{c-1} \eta_t \|\mathbf{G}^t\| + \sum_{t=1}^{c-s} \eta_t (P-Q)R, \tag{5.10}$$

where R is an absolute constant that bounds the norm of the gradients. The rest of the proof follows that of Theorem 6. Specifically, with Eq.(5.10), Eq.(5.6) further becomes

$$\begin{aligned}
&\mathbb{E}f(\mathbf{W}^{c+1}) - \mathbb{E}f(\mathbf{W}^c) \\
&\leq (\frac{L_f}{2}\eta_c^2 - \eta_c)\mathbb{E}\|\mathbf{g}_c\|^2 + L\sum_{t=c-s+1}^{c-1} \mathbb{E}\eta_c\eta_t\|\mathbf{g}_c\|\|\mathbf{G}^t\| + L\sum_{t=1}^{c-s}\mathbb{E}\eta_c\|\mathbf{g}_c\|\eta_t(P-Q)R + \frac{L_f\eta_c^2\sigma^2}{2KP} \\
&\leq (\frac{L_f}{2}\eta_c^2 - \eta_c)\mathbb{E}\|\mathbf{g}_c\|^2 + L\sum_{t=c-s+1}^{c-1} \mathbb{E}[\eta_c^2\|\mathbf{g}_c\|^2 + \eta_t^2\|\mathbf{G}^t\|^2] + L\sum_{t=1}^{c-s}\mathbb{E}[\eta_c^2\|\mathbf{g}_c\|^2(P-Q)R + \eta_t^2(P-Q)R] \\
&\quad + \frac{L_f\eta_c^2\sigma^2}{2KP} \\
&\leq (\frac{L_f + 2Lc(P-Q)R}{2}\eta_c^2 - \eta_c)\mathbb{E}\|\mathbf{g}_c\|^2 + L\sum_{t=c-s+1}^{c-1}\eta_t^2[\mathbb{E}\|\mathbf{G}^t\|^2 + \frac{\sigma^2}{KP}] + L(P-Q)R\sum_{t=1}^{c-s}\eta_t^2 + \frac{L_f\eta_c^2\sigma^2}{2KP}.
\end{aligned}$$

Telescoping over c from 0 to $C-1$ and noting that $\sum_{c=0}^{C-1}\sum_{t=c-s+1}^{c-1} r_t \leq s\sum_{c=0}^{C-1} r_c, \sum_{c=0}^{C-1}\sum_{t=1}^{c-s} r_t \leq (c-s)\sum_{c=0}^{C-1} r_c$ for the positive sequence $\{r_t\}$, we obtain

$$\begin{aligned}
&\inf f(\mathbf{W}) - \mathbb{E}f(\mathbf{W}^0) \\
&\leq \sum_{c=0}^{C-1}(\frac{L_f + 2L(c(P-Q)R+s)}{2}\eta_c^2 - \eta_c)\mathbb{E}\|\mathbf{g}_c\|^2 + L(P-Q)R\sum_{c=1}^{C-s}\eta_c^2 + \sum_{c=0}^{C-1}\eta_c^2\frac{(Ls+L_f)\sigma^2}{KP}.
\end{aligned}$$

It then follows that

$$\begin{aligned}
\min_{c=1,\ldots,C}\mathbb{E}\|\mathbf{g}_c\|^2 &\leq \frac{f(\mathbf{W}^0) - \inf f(\mathbf{W}) + L(P-Q)R\sum_{c=1}^{C-s}\eta_t^2 + \frac{(Ls+L_f)\sigma^2}{KP}\sum_{c=0}^{C-1}\eta_c^2}{\sum_{c=0}^{C-1}(\eta_c - \frac{L_f+2L(c(P-Q)R+s)}{2}\eta_c^2)} \\
&\approx \frac{f(\mathbf{W}^0) - \inf f(\mathbf{W}) + [L(P-Q)R + \frac{(Ls+L_f)\sigma^2}{KP}]\frac{\beta^2}{C}}{\beta - \frac{\beta^2 L(P-Q)R}{2}},
\end{aligned}$$

where we have chosen the constant stepsize $\eta_c \equiv \beta/C$. Setting $\beta = \frac{1}{L(P-Q)R}$, we obtain that

$$\min_{c=1,\ldots,C}\mathbb{E}\|\mathbf{g}_c\|^2 \leq O\left(L(P-Q) + \frac{(Ls+L_f)\sigma^2}{KPL(P-Q)C}\right).$$

□

Chapter 6

Applications in Healthcare

In this chapter, we design machine learning models for several healthcare applications: (1) retrieving similar patients, (2) discovering topics from medical texts, (3) tagging pathology and radiology images, and (4) assigning ICD codes, which involve various data modalities, including texts, images, time series, and tabular data. We apply diversity-promoting learning (DPL) techniques (developed in Chapters 2-4) for the first application to better capture infrequent patterns, reduce overfitting, shrink model size without sacrificing modeling power and apply large-scale distributed learning systems (developed in Chapter 5) for the second application to improve training efficiency.

6.1 Diversity-promoting Learning for Similar-patient Retrieval

Patient similarity measurement (PSM) [315, 343], which decides whether two patients are similar or dissimilar based on their electronic health records (EHRs), is a critical task for patient cohort identification and finds wide applications in clinical decision-making. For instance, with an effective similarity measure in hand, one can perform case-based retrieval of similar patients for a target patient, who can be subsequently diagnosed and treated by synthesizing the diagnosis outcomes and treatment courses of the retrieved patients. Other applications powered by patient similarity include classification of epidemiological data on hepatic steatosis [155], patient risk prediction [261, 281], personalized treatment for hypercholesterolemia [413], personalized mortality prediction [219], near-term prognosis [106, 344], to name a few. Several approaches have applied distance metric learning (DML) [383] to learn patient-similarity measures, where physicians provide feedback on whether two patients are similar or dissimilar, and the algorithm learns a distance metric such that similar patients would have small distance while dissimilar patients are separated apart.

When using DML for patient similarity measurement, we encountered the following problems. First, it performs less well on infrequent diseases. As an example, the top and bottom plots in Figure 6.1(a) show the frequencies of eight diseases and the retrieval performance (precision@K) on individual diseases. As can be seen, the performance on infrequent diseases is much worse than that on frequent diseases. Second, in clinical decision-making, timeliness is very important. For PSM-based applications, how to retrieve similar patients efficiently is critical.

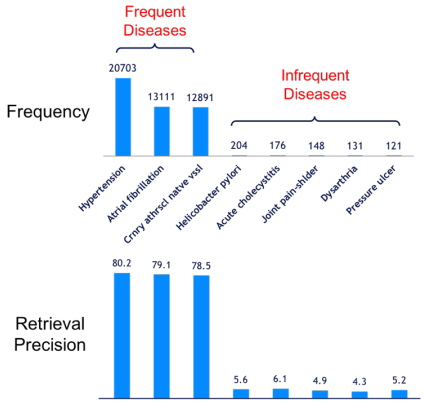

(a)

Retrieval AUC

Dataset	Train	Test
MIMIC	0.809	0.634
EICU	0.816	0.671
Reuters	0.992	0.949
News	0.852	0.757
Cars	0.863	0.714

(b)

Figure 6.1: (a) Retrieval performance on frequent and infrequent diseases. (b) Retrieval AUCs on the training and test sets.

The time complexity of retrieval increases linearly with the dimension of the latent representations learned in DML. An immediate solution for fast retrieval is to reduce the latent dimension. However, this would sacrifice the expressivity of DML and compromise retrieval performance. Third, DML generalizes less well on unseen patients. As can be seen from Figure 6.1(b), the performance on test set is much worse than that on training set.

To address these issues, we resort to diversity-promoting regularization that has been demonstrated to have the ability of better capturing infrequent patterns, reducing model size without sacrificing modeling power, and improving generalization performance (Chapter 2-4). Among the various diversity-promoting regularizers, we choose to use the convex Bregman matrix divergence regularizers (Section 2.2.2) since they guarantee to achieve the global optimal solution in optimization. Specifically, we solve the following problem:

$$\begin{aligned} &\min_{\mathbf{M}} \tfrac{1}{|\mathcal{S}|} \sum_{(\mathbf{x},\mathbf{y})\in\mathcal{S}} (\mathbf{x}-\mathbf{y})^\top \mathbf{M}(\mathbf{x}-\mathbf{y}) + \tfrac{1}{|\mathcal{D}|} \sum_{(\mathbf{x},\mathbf{y})\in\mathcal{D}} \max(0, 1-(\mathbf{x}-\mathbf{y})^\top \mathbf{M}(\mathbf{x}-\mathbf{y})) + \lambda \widehat{\Omega}_\phi(\mathbf{M}) \\ &s.t. \quad \mathbf{M} \succeq 0. \end{aligned} \tag{6.1}$$

6.1.1 Experimental Settings

The evaluation has been reported in Section 2.2.4. For readers' convenience, we re-summarize them here. Two clinical datasets are used: MIMIC-III [184] and EICU [131]. MIMIC-III contains 58K hospital admissions of patients who stayed within the intensive care units at the Beth Israel Deaconess Medical Center between 2001 and 2012. We extracted 7207-dimensional features: (1) 2 dimensions from demographics, including age and gender; (2) 5300 dimensions from clinical notes, including 5000-dimensional bag-of-words (weighted using *tf-idf*) and 300-dimensional word2vec [256]; (3) 1905-dimensions from lab tests where the zero-order, first-order, and second-order temporal features are extracted for each of the 635 lab items. In the

extraction of bag-of-words features from clinical notes, we removed stop words, then counted the document frequency (DF) of the remaining words. Then we selected the largest 5000 words to form the dictionary. Based on this dictionary, we extracted *tfidf* features. In the extraction of word2vec features, we trained a 300-dimensional embedding vector for each word using an open source word2vec tool[1]. To represent a clinical note, we averaged the embeddings of all words in this note. In lab tests, there are 635 test items in total. An item is tested at different time points for each admission. For an item, we extracted three types of temporal features: (1) *zero-order*: averaging the values of this item measured at different time points; (2) *first-order*: taking the difference of values at every two consecutive time points t and $t-1$, and averaging these differences; (3) *second-order*: for the sequence of first-order differences generated in (2), taking the difference (called second-order difference) of values at every two consecutive time points t and $t-1$, and averaging these second-order differences. If an item is missing in an admission, we set the zero-order, first-order, and second-order feature values to 0.

The EICU dataset contains hospital admissions of patients who were treated as part of the Philips eICU program across intensive care units in the United States between 2014 and 2015. There are 474 lab test items and 48 vital sign items. Each admission has a past medical history, which is a collection of diseases. There are 2644 unique past diseases. We extracted the following features: (1) age and gender; (2) zero-, first- and second- order temporal features of lab test and vital signs; (3) past medical history: we used a binary vector to encode them; if an element in the vector is 1, then the patient had the corresponding disease in the past. For both datasets, the features were normalized using min-max normalization along each dimension. We used PCA to reduce the feature dimension to 1000 to reduce the computational complexity (performing eigen-decomposition of the Mahalanobis matrix bears cubic complexity in term of feature dimension). In either dataset, each admission has a primary diagnosis (a disease). MIMIC-III and EICU have 2833 and 2175 unique diseases respectively.

Two admissions are considered as similar if they have the same primary diagnosis and dissimilar if otherwise. In similar-patient retrieval, we used each test example to query the rest of the test examples based on the learned distance metric. If the distance between $\mathbf{x}$ and $\mathbf{y}$ is smaller than a threshold s and they have the same primary diagnosis, then this is a true positive. By choosing different values of s, we obtained a receiver operating characteristic (ROC) curve. We evaluated the retrieval performance using the area under (ROC) curve (AUC) [243] which is the higher, the better. We compared the proposed convex BMD regularizers with two sets of baseline regularizers. The first set aims at promoting orthogonality, which are based on determinant of covariance (DC) [242], cosine similarity (CS) [402], determinantal point process (DPP) [204, 429], InCoherence (IC) [29], variational Gram function (VGF) [177, 420], decorrelation (DeC) [82], mutual angles (MA) [369], squared Frobenius norm (SFN) [74, 114, 122, 347], von Neumann divergence (VND), log-determinant divergence (LDD), and orthogonal constraint (OC) $\mathbf{A}\mathbf{A}^\top = \mathbf{I}$ [233, 342]. All these regularizers were applied to the non-convex *projection matrix-based DML* (PDML, Eq.(2.14) in Section 2.2.1). The other set of regularizers are not designed particularly for promoting orthogonality but are commonly used, including ℓ_2 norm, ℓ_1 norm [280], $\ell_{2,1}$ norm [399], trace norm (Tr) [234], information theoretic (IT) regularizer $-\text{logdet}(\mathbf{M}) + \text{tr}(\mathbf{M})$ [92], and dropout (Drop) [313]. All these regularizers were applied to the

[1]https://code.google.com/archive/p/word2vec/

	MIMIC			EICU		
	AUC-All	AUC-F	AUC-IF	AUC-All	AUC-F	AUC-IF
NCDML	0.634	0.654	0.608	0.671	0.690	0.637
CDML	0.641	0.659	0.617	0.677	0.693	0.652
EUC	0.559	0.558	0.562	0.583	0.584	0.581
LMNN [357]	0.628	0.643	0.609	0.662	0.678	0.633
LDML [146]	0.619	0.638	0.594	0.667	0.678	0.647
MLEC [200]	0.621	0.633	0.605	0.679	0.692	0.656
GMML [405]	0.607	0.621	0.588	0.668	0.679	0.648
ILHD [63]	0.577	0.590	0.560	0.637	0.652	0.610
ℓ_2-CDML	0.648	0.664	0.627	0.695	0.706	0.676
ℓ_1-CDML [280]	0.643	0.666	0.615	0.701	0.715	0.677
$\ell_{2,1}$-CDML [399]	0.646	0.658	0.630	0.703	0.727	0.661
Tr-CDML [234]	0.659	0.672	0.642	0.696	0.709	0.673
IT-CDML [92]	0.653	0.675	0.626	0.692	0.705	0.668
Dropout-CDML [282]	0.647	0.660	0.630	0.701	0.718	0.670
OS-CDML [116]	0.649	0.665	0.626	0.689	0.711	0.679
DCM-NCDML [242]	0.652	0.662	0.639	0.706	0.717	0.686
CS-NCDML [402]	0.661	0.676	0.641	0.712	0.736	0.670
DPP-NCDML [429]	0.659	**0.679**	0.632	0.714	0.725	0.695
IC-NCDML [29]	0.660	0.674	0.642	0.711	0.728	0.685
DC-NCDML [82]	0.648	0.666	0.625	0.698	0.711	0.675
VGF-NCDML [177]	0.657	0.673	0.634	0.718	0.730	0.697
MA-NCDML [367]	0.659	0.670	0.644	0.721	0.733	0.703
OC-NCDML [233]	0.651	0.663	0.636	0.705	0.716	0.685
OS-NCDML [116]	0.639	0.658	0.614	0.675	0.691	0.641
SFN-NCDML [74]	0.662	0.677	0.642	0.724	0.736	0.701
VND-NCDML	0.667	0.676	0.655	0.733	0.748	0.706
LDD-NCDML	0.664	0.674	0.651	0.731	0.743	0.711
CSFN-CDML	0.668	**0.679**	0.653	0.728	0.741	0.705
CVND-CDML	**0.672**	0.678	**0.664**	0.735	0.744	0.718
CLDD-CDML	0.669	0.678	0.658	**0.739**	**0.750**	**0.719**

Table 6.1: On MIMIC and EICU, we show the mean AUC (averaged on 5 random train/test splits) on all diseases (AUC-All), frequent diseases (AUC-F), and infrequent diseases (AUC-IF). On the second panel (EUC, etc.) are well established or state of the art baselines. On the third panel (ℓ_2-CDML, etc.) are CDML methods regularized by non-diversity regularizers. On the fourth panel (DCM-NCDML, etc.) are NCDML methods regularized by previously proposed diversity-promoting regularizers. On the fifth panel (VND-NCDML, etc.) are NCDML methods regularized by our proposed nonconvex BMD regularizers. On the sixth panel (CSFN-CDML, etc.) are CDML methods regularized by our proposed convex BMD regularizers.

Mahalanobis distance-based DML (MDML, Eq.(6.1) in Section 2.2.2). In addition, we compared with the vanilla Euclidean distance (EUC) and other distance learning methods including large margin nearest neighbor (LMNN) metric learning, information theoretic metric learning (ITML) [92], logistic discriminant metric learning (LDML) [146], metric learning from equivalence constraints (MLEC) [200], geometric mean metric learning (GMML) [405], and independent Laplacian hashing with diversity (ILHD) [63].

For computational efficiency, in MDML-based methods, we did not use $(\mathbf{x}-\mathbf{y})^\top\mathbf{M}(\mathbf{x}-\mathbf{y})$ to compute distance directly. Given the learned matrix $\mathbf{M}$ (which is of rank k), we can decompose it into $\mathbf{L}^\top\mathbf{L}$ where $\mathbf{L} \in \mathbb{R}^{k\times d}$. Let $\mathbf{U}\mathbf{\Lambda}\mathbf{U}^\top$ be the eigen-decomposition of $\mathbf{M}$. Let $\lambda_1, \cdots, \lambda_k$ denote the k nonzero eigenvalues and $\mathbf{u}_i, \cdots, \mathbf{u}_k$ denote the corresponding eigenvectors. Then $\mathbf{L}$ is the transpose of $[\sqrt{\sigma_1}\mathbf{u}_1, \cdots, \sqrt{\sigma_k}\mathbf{u}_k]$. Given $\mathbf{L}$, we can use it to transform each input d-dimensional feature vector $\mathbf{x}$ into a new k-dimensional vector $\mathbf{L}\mathbf{x}$, then perform retrieval on the

	MIMIC			EICU		
PDML	0.634	300	2.1	0.671	400	1.7
MDML	0.641	247	2.6	0.677	318	2.1
EUC	0.559	1000	0.6	0.583	1000	0.6
LMNN	0.628	200	3.1	0.662	400	1.7
LDML	0.619	300	2.1	0.667	400	1.7
MLEC	0.621	487	1.3	0.679	493	1.4
GMML	0.607	1000	0.6	0.668	1000	0.7
ILHD	0.577	100	5.8	0.637	100	6.4
MDML-ℓ_2	0.648	269	2.4	0.695	369	1.9
MDML-ℓ_1	0.643	341	1.9	0.701	353	2.0
MDML-$\ell_{2,1}$	0.646	196	3.3	0.703	251	2.8
MDML-Tr	0.659	148	4.5	0.696	233	3.0
MDML-IT	0.653	1000	0.7	0.692	1000	0.7
MDML-Drop	0.647	183	3.5	0.701	284	2.5
PDML-DC	0.652	100	6.5	0.706	300	2.4
PDML-CS	0.661	200	3.3	0.712	200	3.6
PDML-DPP	0.659	100	6.6	0.714	200	3.6
PDML-IC	0.660	200	3.3	0.711	200	3.6
PDML-DeC	0.648	200	3.2	0.698	300	2.3
PDML-VGF	0.657	200	3.3	0.718	200	3.6
PDML-MA	0.659	200	3.3	0.721	200	3.6
PDML-OC	0.651	100	6.5	0.705	100	7.1
PDML-SFN	0.662	100	6.6	0.724	200	3.6
PDML-VND	0.667	100	6.7	0.733	100	7.3
PDML-LDD	0.664	100	6.6	0.731	200	3.7
MDML-CSFN	0.668	143	4.7	0.728	209	3.5
MDML-CVND	**0.672**	**53**	**12.7**	0.735	**65**	**11.3**
MDML-CLDD	0.669	76	8.8	**0.739**	128	5.8

Table 6.2: Area under ROC curve (AUC), number of projection vectors (NPV), and compactness score (CS, $\times 10^{-3}$).

new vectors based on Euclidean distance. Note that only when computing Euclidean distance between $\mathbf{Lx}$ and $\mathbf{Ly}$, we have that $\|\mathbf{Lx}-\mathbf{Ly}\|_2^2$ is equivalent to $(\mathbf{x}-\mathbf{y})^\top\mathbf{M}(\mathbf{x}-\mathbf{y})$. For other distances or similarity measures between $\mathbf{Lx}$ and $\mathbf{Ly}$, such as L1 distance and cosine similarity, this does not hold. Performing retrieval based on $\|\mathbf{Lx}-\mathbf{Ly}\|_2^2$ is more efficient than that based on $(\mathbf{x}-\mathbf{y})^\top\mathbf{M}(\mathbf{x}-\mathbf{y})$ when k is smaller than d. Given m test examples, the computation complexity of $\|\mathbf{Lx}-\mathbf{Ly}\|_2^2$-based retrieval is $O(mkd+m^2k)$, while that of $(\mathbf{x}-\mathbf{y})^\top\mathbf{M}(\mathbf{x}-\mathbf{y})$-based retrieval is $O(m^2d^2)$.

6.1.2 Results

First, we verify whether CSFN, CVND, and CLDD are able to improve the performance on infrequent diseases. On MIMIC and EICU, we consider a disease as being "frequent" if it contains more than 1000 examples, and "infrequent" if otherwise. We measure AUCs on all diseases (AUC-All), infrequent diseases (AUC-IF), and frequent diseases (AUC-F). As can be seen, in most DML methods, the AUCs on infrequent diseases are worse than those on frequent diseases, showing that DML is sensitive to the imbalance of diseases' frequencies and tends to be biased towards frequent diseases and is less capable of capturing infrequent diseases. This is in accordance with the previous findings [369]. Adding our proposed CSFN, CVND, CLDD regularizers to CDML, the AUCs on infrequent diseases are greatly improved. By encouraging the components to be close to being orthogonal, our methods can reduce the redundancy among vectors. Mutually complementary vectors can achieve a broader coverage of latent features, including

	MIMIC	EICU
NCDML	0.175	0.145
CDML	0.187	0.142
LMNN [357]	0.183	0.153
LDML [146]	0.159	0.139
MLEC [200]	0.162	0.131
GMML [405]	0.197	0.157
ILHD [63]	0.164	0.162
ℓ_2-CDML	0.184	0.136
ℓ_1-CDML [280]	0.173	0.131
$\ell_{2,1}$-CDML [399]	0.181	0.129
Tr-CDML [234]	0.166	0.138
IT-CDML [92]	0.174	0.134
Dropout-CDML [282]	0.182	0.140
OS-CDML [116]	0.166	0.133
DCM-NCDML [242]	0.159	0.131
CS-NCDML [402]	0.163	0.135
DPP-NCDML [429]	0.147	0.140
IC-NCDML [29]	0.155	0.127
DC-NCDML [82]	0.164	0.123
VGF-NCDML [177]	0.158	0.136
MA-NCDML [367]	0.143	0.128
OC-NCDML [233]	0.161	0.142
OS-NCDML [116]	0.169	0.137
SFN-NCDML [74]	0.153	0.126
VND-NCDML	0.148	0.135
LDD-NCDML	0.146	0.121
CSFN-CDML	0.142	0.124
CVND-CDML	0.137	**0.115**
CLDD-CDML	**0.131**	0.118

Table 6.3: The gap of training AUC and testing AUC.

those associated with infrequent diseases. As a result, these vectors improve the performance on infrequent diseases.

Thanks to their convexity nature, our methods can achieve the global optimal solution and outperform the non-convex ones that can only achieve a local optimal and hence a sub-optimal solution. (C)VND and (C)LDD outperform (C)SFN, possibly because they measure near-orthogonality in a global way while (C)SFN conducts that in a pairwise fashion. Comparing OS-(NCDML,CDML) with the unregularized NCDML/CDML, we can see that over-sampling indeed improves performance on infrequent diseases. However, this improvement is less significant than that achieved by our methods. In general, the diversity-promoting (DP) regularizers outperform the non-DP regularizers, suggesting the effectiveness of promoting diversity. The orthogonal constraint (OC) [233, 342] imposes strict orthogonality, which may be too restrictive that hurts performance. ILHD [63] learns binary hash codes, which makes retrieval more efficient. However, it achieves lower AUCs due to the quantization errors. (CSFN,CVND,CLDD)-CDML outperform popular DML approaches including LMNN, LDML, MLEC, and GMML, demonstrating their competitive standing in the DML literature.

Table 6.2 shows the area under ROC curve (AUC) and the numbers of the projection vectors (NPVs) that achieve the AUCs. For MDML-based methods, the NPV equals the rank of the Mahalanobis matrix since $\mathbf{M} = \mathbf{A}^\top \mathbf{A}$. We define a *compactness score* (CS) which is the ratio between AUC and NPV. A higher CS indicates achieving higher AUC by using fewer projection vectors. From Table 6.2, we can see that on both datasets, MDML-(CSFN,CVND,CLDD) achieve larger CSs than the baseline methods, demonstrating their better capability in learning

compact distance metrics. CSFN, CVND, and CLDD perform better than non-convex regularizers, and CVND, CLDD perform better than CSFN. The reduction of NPV improves the efficiency of retrieval since the computational complexity grows linearly with this number.

Table 6.3 shows the difference between training AUC and testing AUC. Our methods have the smallest gap between training and testing AUCs. This indicates that our methods are better capable of reducing overfitting and improving generalization performance.

6.2 Large-scale Distributed Learning for Medical Topic Discovery

Discovering medical topics from clinical documents has many applications, such as consumer medical search [84], mining FDA drug labels [44], investigating drug repositioning opportunities [45], to name a few. In practice, the clinical text corpus can contain millions of documents and the medical dictionary is comprised of hundreds of thousands of terminologies. These large-scale documents contain rich medical topics, whose number can be tens of thousands. How to efficiently discover so many topics from such a large dataset is computationally challenging. We resort to the Orpheus system (Section 5.2) we have developed.

We begin with introducing how to learn the topics. For each document, we represent it with a bag-of-words vector $\mathbf{d} \in \mathbb{R}^V$ where V is the dictionary size. Similar to [207], we assume each document is approximately a linear combination of K topics: $\mathbf{d} \approx \mathbf{W}\boldsymbol{\theta}$. $\mathbf{W} \in \mathbb{R}^{V \times K}$ is the topic matrix, where each topic is represented with a vector $\mathbf{w} \in \mathbb{R}^V$. $w_v \geq 0$ denotes the association strength between the v-th word and this topic, and $\sum_{v=1}^{V} w_v = 1$. $\boldsymbol{\theta} \in \mathbb{R}^K$ are the linear combination weights satisfying $\theta_k \geq 0$ and $\sum_{k=1}^{K} \theta_k = 1$. θ_k denotes how relevant topic k is to this document. Given the unlabeled documents $\{\mathbf{d}_i\}_{i=1}^N$, we learn the topics by solving the following problem [207]:

$$\begin{array}{ll} \min_{\{\boldsymbol{\theta}_i\}_{i=1}^N, \mathbf{W}} & \frac{1}{2}\sum_{i=1}^{N} \|\mathbf{d}_i - \mathbf{W}\boldsymbol{\theta}_i\|_2^2 \\ \textit{s.t.} & \forall k = 1, \cdots, K, v = 1, \cdots, V, W_{kv} \geq 0, \sum_{v=1}^{V} W_{kv} = 1; \\ & \forall i = 1, \cdots, N, k = 1, \cdots, K, \theta_{ik} \geq 0, \sum_{k=1}^{K} \theta_{ik} = 1, \end{array} \tag{6.2}$$

where $\{\boldsymbol{\theta}_i\}_{i=1}^N$ denotes all the linear coefficients.

This problem can be solved by alternating between $\{\boldsymbol{\theta}_i\}_{i=1}^N$ and $\mathbf{W}$. The N sub-problems defined on $\{\boldsymbol{\theta}_i\}_{i=1}^N$ can be solved independently by each machine based on the data shard it has. No inter-machine communication is needed. For the sub-problem defined on $\mathbf{W}$, we use the Orpheus system to solve it. Each machine maintains a local copy of $\mathbf{W}$ and different copies are synchronized to ensure convergence. The projected stochastic gradient descent algorithm is applied, which iteratively performs two steps: (1) stochastic gradient descent; (2) projection onto the probability simplex. In the first step, the stochastic gradient matrix computed over one document can be written as the outer product of two vectors: $(\mathbf{W}\boldsymbol{\theta}_i - \mathbf{d}_i)\boldsymbol{\theta}_i^\top$. In other words, this problem has a sufficient factor (SF) property and fits into the sufficient factor broadcasting framework. In each iteration, each machine computes a set of SFs, sends them to other machines and uses the SFs to update its own parameter copy. On the receiver side, the received SFs are

System	Runtime (hours)
FlexiFaCT [207]	33.9
Bosen [355]	23.5
Orpheus	5.4

Table 6.4: Convergence time (hours) in Orpheus and baseline systems for topic model.

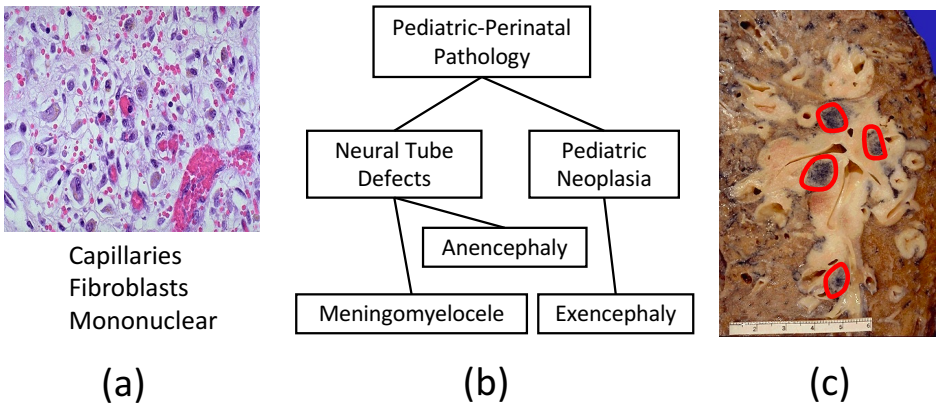

Figure 6.2: (a) A medical image has multiple tags which are correlated clinically or biologically. (b) The medical concepts are organized into a hierarchical tree. (c) The abnormal regions (marked by red contours) are small.

converted to gradient matrices which are applied to the receiver's parameter copy. A projection operation follows the gradient descent update.

We applied the Orpheus-based topic model (TM) to learn medical topics from the PubMed [9] dataset which contains 8.2M documents and ∼0.74B words. The dictionary size is 141K. The number of topics was set to 50K. The mini-batch size was set to 100. In random multicast, the number of destinations each machine sends a message to was set to 4. In SF selection, the number of selected SFs was set to 25. The consistency model was set to SSP with a staleness value of 4. Table 6.4 shows the convergence time of TM under Orpheus and two baseline systems: Bosen [355] – a parameter server framework and FlexiFaCT [207] – a Hadoop implementation of TM. As can be seen, Orpheus is much more efficient than the baselines systems. With 34 CPU machines, the training of Orpheus-TM can be finished in 5.4 hours.

6.3 Hierarchical Multi-label Tagging of Medical Images

Medical images generated from radiography, computed tomography (CT) scans, magnetic resonance imaging (MRI), ultrasound, biopsy etc. are widely used in hospitals and clinics for diagnosis, treatment, and surgery. Once read, these images are dumped into the picture archiving and communication system (PACS). Lacking accurate and rich textual labels, these images are difficult to index and search. As a result, the utilization of these images is under-explored. To

address this issue, we study the automatic tagging of medical images, where the obtained textual tags improve the accessibility of images. For example, physicians can search images that are tagged with "chest x-ray" and "pneumonia" and perform a cohort study on them.

Automatically tagging clinical images with medical concepts is challenging. First, a medical image usually contains rich information. As a result, it can be simultaneously tagged with multiple concepts. Figure 6.2a shows an example where the image is tagged with "capillary", "fibroblast", and "mononuclear". These concepts have strong clinical or biological correlations. For example, mononuclear cell and fibroblast have an interaction in scleroderma [133]. Capillaries and fibroblast have a dynamic interaction in the heart [51]. Such correlations can be explored to improve tagging accuracy. Here is an example. Since capillary is visually similar to Mallory bodies, it is difficult to distinguish these two based on image features. But Mallory bodies have little correlation with fibroblast and mononuclear cell. Leveraging the concept-correlations, we can correctly choose capillary rather than Mallory body as the label. Technically, how to capture these correlations is nontrivial.

Second, medical concepts are usually organized by physicians into a hierarchical ontology. On the top of the hierarchy are general concepts. From top to bottom, each concept is divided into more fine-grained sub-concepts. Figure 6.2b shows an example. In this concept tree, each node represents a disease, whose children represent subtypes of this disease. For instance, meningomyelocele and anencephaly are both subtypes of neural tube defects. This hierarchical structure can be leveraged to improve tagging accuracy. On one hand, if A and B are both children of C, then it is unlikely to use A and B to simultaneously tag an image. For instance, low power microscopic, middle power microscopic, and high power microscopic are children of microscopic. A pathology image can only be taken by one of these microscopic techniques. On the other hand, if the distance between A and B in the concept tree is smaller than that between A and C and we know A is the correct label, then B is more likely to be the correct label than C, since concepts with smaller distance are more relevant. For example, abscess is closer to phagocytosis than omphalocele. The former two are both under the sub-tree rooted with inflammation. As a result, if an image is tagged with abscess, it is more likely to be tagged with phagocytosis than omphalocele. How to explore the hierarchical structure among concepts for better tagging is technically demanding.

Third, in images showing abnormalities, the abnormal regions are usually very small, occupying a small proportion of the entire image. As shown in Figure 6.2c, the dark round areas (marked with red contours) show lymph nodes which are involved by the neoplasm. It is difficult to tag these abnormalities because of the smallness of the abnormal regions. How to detect these regions and properly tag them is challenging.

We aim at addressing these three challenges. To cope with the first challenge, we design an adversarial learning [134] approach where a discriminative network is used to distinguish the predicted labels from physician-provided labels while the predictive network tries to make them indistinguishable (i.e., cannot tell whether a label vector is predicted or human-provided). Such indiscernibility ensures the correlations among physician-provided labels are transferred to the predicted labels. To cope with the second challenge, we design a tree-of-sequences long short-term memory (LSTM) model which uses sequential LSTMs [163] to encode the individual concepts and uses a tree-structured LSTM [320, 368] to capture the hierarchical relationship among concepts. To address the third challenge, we design a contextual attention mechanism

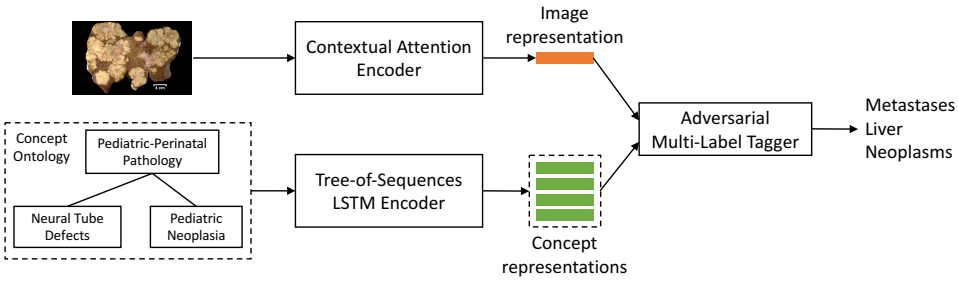

Figure 6.3: Our model consists of three major modules. Given the medical image, a contextual attention encoder is leveraged to learn a representation vector for this image. The tree-of-sequences LSTM encoder is used to learn a representation for each concept in the ontology. The image representation and concept representations are fed into the adversarial multi-label tagger to generate the tags for this image.

which calculates an importance score of each image-patch according to its contrast with the entire image. Patches with larger importance are paid more attention in predicting the tags. We demonstrate the effectiveness of our methods on two medical image datasets.

6.3.1 Methods

Figure 6.3 shows the overview of our model, where the inputs include a medical image and an ontology of medical concepts, and the outputs are multiple concepts that can be used to tag this image. In the concept ontology, only the leaf nodes are used for tagging. The model consists of three major modules: (1) a *contextual attention encoder* which takes the image as input, localizes abnormal regions which are given higher importance weights, and generates a weighted representation for this image; (2) a *tree-of-sequences LSTM encoder* which takes the concept ontology as input, uses sequential LSTMs to encode individual concepts and utilizes a bidirectional tree-structured LSTM to incorporate the hierarchical relationship among concepts into their representations; (3) an *adversarial multi-label tagger* which takes the representations of the image and the concepts as inputs, incorporates label-correlations using adversarial learning, and outputs multiple concepts to tag this image.

Adversarial Multi-label Tagging

It is often the case that a medical image can be tagged with multiple medical concepts that exhibit clinical or biological correlations. These correlations can be leveraged to distinguish concepts that are difficult to be differentiated using visual clues. In this section, we present an adversarial learning approach to capture such correlations for better multi-label tagging.

When assigning multiple concepts to an image, we need to consider two orthogonal factors: (1) *concept-image relevance* – how the content of the image is relevant to each concept; (2) *concept-concept correlation* – how strongly these concepts are correlated. To achieve (1), we build a predictive network which takes the image representation $\mathbf{x}$ (produced by the contextual attention encoder) and representation $\mathbf{c}_i$ of each concept i (produced by the tree-of-sequences

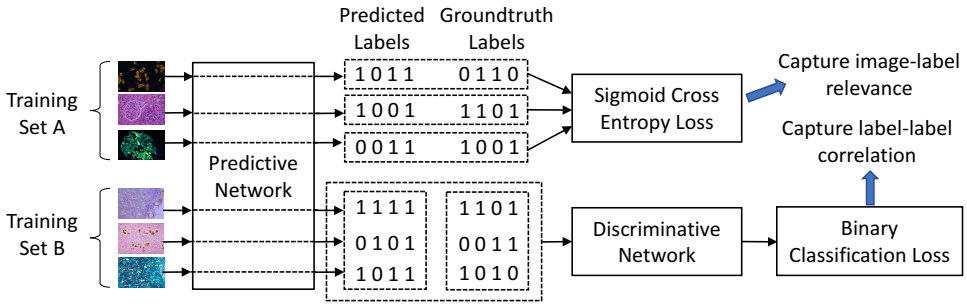

Figure 6.4: Adversarial learning for capturing correlations among concepts. The discriminative network (DN) aims at distinguishing the labels produced by the predictive network (PN) from the groundtruth labels provided by physicians. The PN tries to make the two sets of labels indistinguishable.

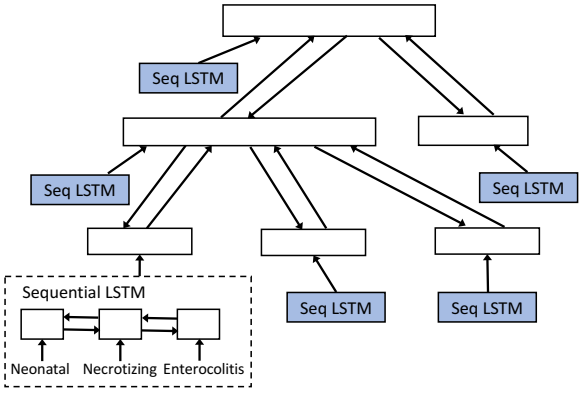

Figure 6.5: Tree-of-sequences LSTM. For each concept name, we build a sequential LSTM (SLSTM) to capture the semantics of words and the sequential structure among words. Over the concept hierarchy, we build a tree LSTM (TLSTM) to capture the hierarchical relationship among concepts. The encodings produced by the SLSTM are the inputs of the TLSTM.

LSTM encoder) as inputs and calculates a score s_i that measures how relevant this image is to this concept. To achieve (2), we leverage adversarial learning [134]. The basic idea is to use a discriminative network to tell which labels are produced by the predictive network and which are provided by the physicians. The predictive network tries to produce labels in a way that the discriminative network cannot tell whether they are predicted or human-provided. Such indiscriminability transfers the correlations manifested in human-provided labels into those predicted by the network.

Figure 6.4 illustrates the details. The training set is divided into two partitions: A and B. Partition A is used for learning the relevance between images and concepts. Partition B is used for learning the correlation among concepts. The groundtruth tagging of each image is represented by a binary vector $\mathbf{t} \in \mathbb{R}^k$ where k is the number of unique leaf concepts in the ontology and $t_i = 1$ denotes that the i-th concept is utilized by the physician to label this image. For each image

$\mathbf{x}$ in A, the predictive network (PN) predicts a score vector $\mathbf{s} = f_P(\mathbf{x}; \mathbf{W}_P)$ where $s_i \in [0, 1]$ denotes the confidence that this image should be tagged by concept i and $f_P(\cdot; \mathbf{W}_P)$ denotes the PN parameterized by weight parameters $\mathbf{W}_P$. Then a sigmoid cross entropy (SCE) loss is defined on $\mathbf{s}$ and $\mathbf{t}$ to measure the discrepancy between the prediction and the groundtruth. For each image in B, similarly the predictive network first generates the score vector $\mathbf{s}$. We use a discriminative network (DN) to differentiate the predicted score vectors $\{\mathbf{s}^{(n)}\}_{n=1}^{N_B}$ and the groundtruth label vectors $\{\mathbf{t}^{(n)}\}_{n=1}^{N_B}$, where N_B is the number of images in B. This is a binary classification task. The input to the DN (denoted by $f_D(\cdot; \mathbf{W}_D)$ where $\mathbf{W}_D$ are the weight parameters) is a k-dimensional vector and the output is the probability that the vector is predicted. As for the predictive network, it aims at making $\{\mathbf{s}^{(n)}\}_{n=1}^{N_B}$ indistinguishable from $\{\mathbf{t}^{(n)}\}_{n=1}^{N_B}$, such that the correlations reflected in $\{\mathbf{t}^{(n)}\}_{n=1}^{N_B}$ can be transferred to $\{\mathbf{s}^{(n)}\}_{n=1}^{N_B}$. Overall, we solve the following optimization problem:

$$\min_{\mathbf{W}_P} \mathcal{L}_{SCE}(\mathbf{W}_P, A) \; + \; \max_{\mathbf{W}_D} \; - \mathcal{L}_{BC}(\mathbf{W}_P, \mathbf{W}_D, B). \tag{6.3}$$

$\mathcal{L}_{SCE}(\mathbf{W}_P, A)$ is the sigmoid cross-entropy loss defined on the training set A:

$$\mathcal{L}_{SCE}(\mathbf{W}_P, A) = \sum_{n=1}^{N_A} \ell(f_P(\mathbf{x}^{(n)}; \mathbf{W}_P), \mathbf{t}^{(n)}), \tag{6.4}$$

where $\ell(\mathbf{s}, \mathbf{t}) = -\sum_{i=1}^{k} t_i \log s_i + (1 - t_i) \log(1 - s_i)$ is the SCE loss on a single image and N_A is the number of images in A. $\mathcal{L}_{BC}(\mathbf{W}_P, \mathbf{W}_D, B)$ is the binary classification loss defined on training set B:

$$\mathcal{L}_{BC}(\mathbf{W}_P, \mathbf{W}_D, B) = \textstyle\sum_{n=1}^{2N_B} \ell(f_D(\mathbf{a}^{(n)}; \mathbf{W}_D), b^{(n)}), \tag{6.5}$$

where $\mathbf{a}^{(n)}$ can be either a predicted score vector $f_P(\mathbf{x}; \mathbf{W}_P)$ or a physician-provided label vector $\mathbf{t}$. In the former case, $b = 1$. In the latter case, $b = 0$.

In the overall loss, the PN learns its weight parameters $\mathbf{W}_P$ by minimizing the SCE loss and maximizing the BC loss. The DN learns its weights parameters $\mathbf{W}_D$ by minimizing the BC loss. Note that the SCE loss and the BC loss cannot be defined on the same training image. By overfitting the training set, the SCE loss can make the predicted label vector to be the same as the groundtruth vector. In this case, it is futile to distill concept-correlations using the BC loss. In AL, designing the architecture of the prediction and discrimination networks is required. However, this is in general much easier than designing a comprehensive objective function for multi-label classification. In our experiments, we simply use common CNNs and feedforward NNs.

Previously, adversarial learning was applied for domain adaptation [119]: a discriminator is learned to judge whether an example is from the source domain or target domain; an encoder is learned so that after being encoded, a sample cannot be identified as being from the source domain or target domain. By doing this, the discrepancy between two domains are eliminated so that data from the source domain can be utilized to improve the task in the target domain. In our approach of using adversarial learning for multi-label classification, a similar idea is explored: using adversarial learning to eliminate the discrepancy between the predicted labels and ground-truth labels in terms of label-correlation patterns, so that the correlations existing in the ground-truth labels can be transferred to the predicted labels.

Tree-of-sequences LSTM Encoder

In this section, we aim at learning embedding vectors for the medical concepts. Each concept has a name (a sequence of words) that tells the semantics of this concept. We use a sequential LSTM (SLSTM) to encode this name. Meanwhile, in the hierarchical ontology, the concepts possess hierarchical relationships. To capture such relationships, on top of the encodings generated by the SLSTMs, we build a tree LSTM (TLSTM) [320] along the hierarchy, ending up with a tree-of-sequences LSTM model (Figure 6.5).

Sequential LSTM A sequential LSTM (SLSTM) [163] network is a special type of recurrent neural network that (1) learns the latent representation (which usually reflects certain semantic information) of words; (2) models the sequential structure among words. In the word sequence, each word t is allocated with an SLSTM unit, which consists of the following components: input gate $\mathbf{i}_t$, forget gate $\mathbf{f}_t$, output gate $\mathbf{o}_t$, memory cell $\mathbf{c}_t$, and hidden state $\mathbf{s}_t$. These components (vectors) are computed as follows:

$$\begin{aligned}
\mathbf{i}_t &= \sigma(\mathbf{W}^{(i)}\mathbf{s}_{t-1} + \mathbf{U}^{(i)}\mathbf{x}_t + \mathbf{b}^{(i)}) \\
\mathbf{f}_t &= \sigma(\mathbf{W}^{(f)}\mathbf{s}_{t-1} + \mathbf{U}^{(f)}\mathbf{x}_t + \mathbf{b}^{(f)}) \\
\mathbf{o}_t &= \sigma(\mathbf{W}^{(o)}\mathbf{s}_{t-1} + \mathbf{U}^{(o)}\mathbf{x}_t + \mathbf{b}^{(o)}) \\
\mathbf{c}_t &= \mathbf{i}_t \odot \tanh(\mathbf{W}^{(c)}\mathbf{s}_{t-1} + \mathbf{U}^{(c)}\mathbf{x}_t + \mathbf{b}^{(c)}) + \mathbf{f}_t \odot \mathbf{c}_{t-1} \\
\mathbf{s}_t &= \mathbf{o}_t \odot \tanh(\mathbf{c}_t),
\end{aligned} \tag{6.6}$$

where $\mathbf{x}_t$ is the embedding vector of word t. $\mathbf{W}$, $\mathbf{U}$ are component-specific weight matrices and $\mathbf{b}$ are bias vectors.

Tree-of-sequences LSTM We use a bi-directional tree LSTM (TLSTM) [320, 368] to capture the hierarchical relationships among concepts. The inputs of this LSTM include the tree structure of the concept ontology and hidden states of individual concepts produced the SLSTMs. It consists of a bottom-up TLSTM and a top-down TLSTM, which produce two hidden states $\mathbf{h}_\uparrow$ and $\mathbf{h}_\downarrow$ at each node in the tree.

In the bottom-up TLSTM, an internal node (representing a concept C, having M children) is comprised of the following components: an input gate $\mathbf{i}_\uparrow$, an output gate $\mathbf{o}_\uparrow$, a memory cell $\mathbf{c}_\uparrow$, a hidden state $\mathbf{h}_\uparrow$, and M child-specific forget gates $\{\mathbf{f}_\uparrow^{(m)}\}_{m=1}^M$ where $\mathbf{f}_\uparrow^{(m)}$ corresponds to the m-th child. The transition equations among components are:

$$\begin{aligned}
\mathbf{i}_\uparrow &= \sigma(\textstyle\sum_{m=1}^M \mathbf{W}_\uparrow^{(i,m)}\mathbf{h}_\uparrow^{(m)} + \mathbf{U}^{(i)}\mathbf{s} + \mathbf{b}_\uparrow^{(i)}) \\
\forall m, \mathbf{f}_\uparrow^{(m)} &= \sigma(\mathbf{W}_\uparrow^{(f,m)}\mathbf{h}_\uparrow^{(m)} + \mathbf{U}^{(f,m)}\mathbf{s} + \mathbf{b}_\uparrow^{(f,m)}) \\
\mathbf{o}_\uparrow &= \sigma(\textstyle\sum_{m=1}^M \mathbf{W}_\uparrow^{(o,m)}\mathbf{h}_\uparrow^{(m)} + \mathbf{U}^{(o)}\mathbf{s} + \mathbf{b}_\uparrow^{(o)}) \\
\mathbf{u}_\uparrow &= \tanh(\textstyle\sum_{m=1}^M \mathbf{W}_\uparrow^{(u,m)}\mathbf{h}_\uparrow^{(m)} + \mathbf{U}^{(u)}\mathbf{s} + \mathbf{b}_\uparrow^{(u)}) \\
\mathbf{c}_\uparrow &= \mathbf{i}_\uparrow \odot \mathbf{u}_\uparrow + \textstyle\sum_{m=1}^M \mathbf{f}_\uparrow^{(m)} \odot \mathbf{c}_\uparrow^{(m)} \\
\mathbf{h}_\uparrow &= \mathbf{o}_\uparrow \odot \tanh(\mathbf{c}_\uparrow),
\end{aligned} \tag{6.7}$$

where $\mathbf{s}$ is the SLSTM hidden state that encodes the name of the concept C. $\{\mathbf{h}_\uparrow^{(m)}\}_{m=1}^M$ and $\{\mathbf{c}_\uparrow^{(m)}\}_{m=1}^M$ are the bottom-up TLSTM hidden states and memory cells of the children. $\mathbf{W}$, $\mathbf{U}$, $\mathbf{b}$

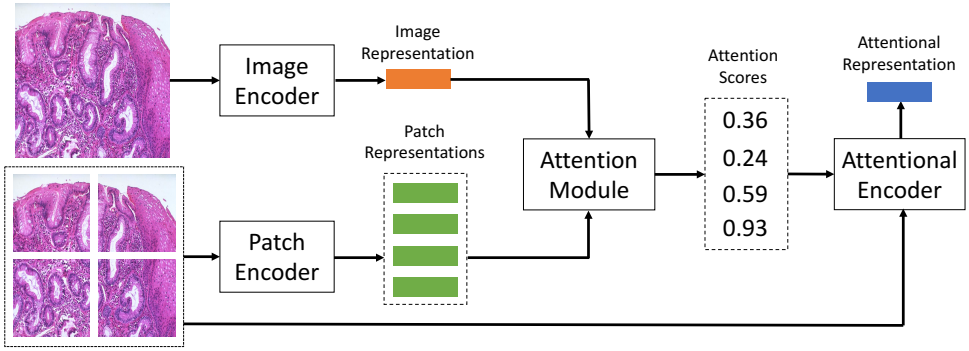

Figure 6.6: Contextual attention module. For each patch, an attention score is calculated by comparing the representation of this patch and that of the entire image. These patches are re-weighted using the corresponding attention scores to generate an attentional representation for this image.

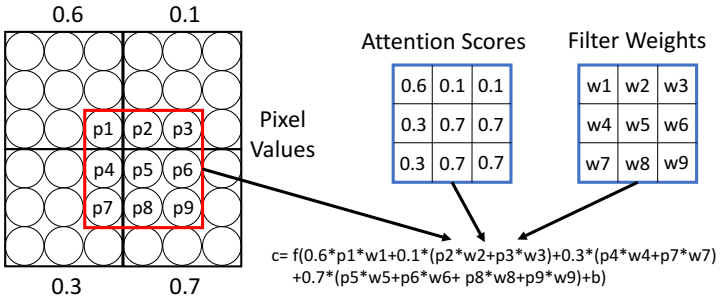

Figure 6.7: Attentional convolution. Each pixel is weighted by the attention score of the patch containing this pixel. Then the weighted pixels are convoluted with the filter weights.

are component-specific weight matrices and bias vectors. For a leaf node having no children, its only input is the SLSTM hidden state $\mathbf{s}$ and no forget gates are needed. The transition equations are:

$$\begin{aligned}
\mathbf{i}_{\uparrow} &= \sigma(\mathbf{U}^{(i)}\mathbf{s} + \mathbf{b}_{\uparrow}^{(i)}) \\
\mathbf{o}_{\uparrow} &= \sigma(\mathbf{U}^{(o)}\mathbf{s} + \mathbf{b}_{\uparrow}^{(o)}) \\
\mathbf{u}_{\uparrow} &= \tanh(\mathbf{U}^{(u)}\mathbf{s} + \mathbf{b}_{\uparrow}^{(u)}) \\
\mathbf{c}_{\uparrow} &= \mathbf{i}_{\uparrow} \odot \mathbf{u}_{\uparrow} \\
\mathbf{h}_{\uparrow} &= \mathbf{o}_{\uparrow} \odot \tanh(\mathbf{c}_{\uparrow}).
\end{aligned} \tag{6.8}$$

In the top-down TLSTM, for a non-root node, it has the following components: an input gate $\mathbf{i}_{\downarrow}$, a forget gate $\mathbf{f}_{\downarrow}$, an output gate $\mathbf{o}_{\downarrow}$, a memory cell $\mathbf{c}_{\downarrow}$, and a hidden state $\mathbf{h}_{\downarrow}$. The transition

equations are:

$$\begin{aligned}
\mathbf{i}_{\downarrow} &= \sigma(\mathbf{W}_{\downarrow}^{(i)}\mathbf{h}_{\downarrow}^{(p)} + \mathbf{b}_{\downarrow}^{(i)}) \\
\mathbf{f}_{\downarrow} &= \sigma(\mathbf{W}_{\downarrow}^{(f)}\mathbf{h}_{\downarrow}^{(p)} + \mathbf{b}_{\downarrow}^{(f)}) \\
\mathbf{o}_{\downarrow} &= \sigma(\mathbf{W}_{\downarrow}^{(o)}\mathbf{h}_{\downarrow}^{(p)} + \mathbf{b}_{\downarrow}^{(o)}) \\
\mathbf{u}_{\downarrow} &= \tanh(\mathbf{W}_{\downarrow}^{(u)}\mathbf{h}_{\downarrow}^{(p)} + \mathbf{b}_{\downarrow}^{(u)}) \\
\mathbf{c}_{\downarrow} &= \mathbf{i}_{\downarrow} \odot \mathbf{u}_{\downarrow} + \mathbf{f}_{\downarrow} \odot \mathbf{c}_{\downarrow}^{(p)} \\
\mathbf{h}_{\downarrow} &= \mathbf{o}_{\downarrow} \odot \tanh(\mathbf{c}_{\downarrow}),
\end{aligned} \tag{6.9}$$

where $\mathbf{h}_{\downarrow}^{(p)}$ and $\mathbf{c}_{\downarrow}^{(p)}$ are the top-down TLSTM hidden state and memory cell of the parent of this node. For the root node which has no parent, $\mathbf{h}_{\downarrow}$ cannot be computed using the above equations. Instead, we set $\mathbf{h}_{\downarrow}$ to $\mathbf{h}_{\uparrow}$ (the bottom-up TLSTM hidden state generated at the root node). $\mathbf{h}_{\uparrow}$ captures the semantics of all concepts in this ontology, which is then propagated downwards to each individual concept via the top-down TLSTM dynamics.

We concatenate the hidden states of the two directions to obtain the bidirectional TLSTM encoding of each concept $\mathbf{h} = [\mathbf{h}_{\uparrow}; \mathbf{h}_{\downarrow}]$. The bottom-up TLSTM composes the semantics of children (representing sub-concepts) and merges them into the current node, which hence captures child-to-parent relationship. The top-down TLSTM makes each node inherit the semantics of its parent, which captures parent-to-child relation. As a result, the hierarchical relationship among concepts is encoded in the hidden states.

Contextual Attention

When reading a medical image, the physicians care more about the regions that show abnormalities. These abnormalities are usually indicators of diseases and prompt the physicians to take treatment actions. The abnormal regions are usually small, which are difficult to detect and tag. It is important to localize these regions and encourage the tagger to pay more attention to them.

The abnormal regions can be spotted by comparing them with their context – the entire image. It is often the case that majority of an image contains normal tissues, whose visual appearance differs from the abnormalities. This observation motivates us to design a contextual attention mechanism that calculates the level of abnormality in each region by contrasting this region with the entire image.

Figure 6.6 presents an illustration. We first divide the input image into patches. For each patch, we use a *patch encoder* to extract its representation. For the entire image (which is deemed as context), an *image encoder* is used to capture the holistic information of this image. For each patch, its representation and the image representation are concatenated and fed into an *attention module* which generates a score indicating how abnormal this patch is. Then we use these attention scores to weight pixels. The weighted pixels are fed into an *attentional encoder* to generate an attentional representation for this image. For simplicity, we assume the patches are non-overlapped, hence each pixel belongs to exactly one patch. The value of a pixel is weighted by the attention score of the patch containing it. In the attentional encoder, *attentional convolution* is performed: the filters take weighted pixels as inputs to calculate the feature map. Figure 6.7 shows an example. The 6×6 image is divided into 4 patches, whose attention scores are 0.6, 0.1, 0.3, and 0.7. When a 3×3 filter (denoted by a red box) is applied, each pixel in the receptive field

is weighted using the attention score of the patch containing this pixel. Then the convolution is performed between the weighted pixels and the filter weights, by calculating the following equation $c = f\Big(\sum_{i=1}^{n} a_i p_i w_i + b\Big)$ where $\{a_i\}$ are the attention scores, $\{p_i\}$ are the pixel values, and $\{w_i\}$ are the weights of filters. Extending the method to overlapped patches is straightforward: the weight of a pixel is calculated by averaging the attention scores of overlapping patches that contain this pixel.

6.3.2 Evaluation

Datasets

We used two medical image datasets obtained from a teaching hospital. The first dataset contains 47933 pathology images which are split into a training set with 33553 images, a validation set with 7190 images, and a test set with 7190 images. The second dataset contains 39827 radiology images, which are split into train/validation/test sets with 27879, 5974, and 5974 images respectively. Labels in the first dataset are organized by doctors into a 4-level hierarchy. The number of labels in level 1-4 are 16, 38, 137, 249 respectively. The number of leaf nodes is 272. The average labels each image has is 3.7. Each label has a name. The minimum, average, and maximum number of words in the label names are 1, 5.3, 9 respectively. Labels in the second dataset are organized by doctors into a 3-level hierarchy. The number of labels in level 1-3 are 12, 51, 196 respectively. The number of leaf nodes is 211. The average labels each image has is 3.1. The minimum, average, and maximum number of words in the label names are 1, 4.4, 8 respectively. Each image is labeled by at least 3 doctors and the labels are decided using majority vote. The kappa statistics (range is [-1,1]) for measuring inter-annotator reliability is 0.83, indicating high consistency among annotators. Since it is too costly to annotate fine-grained hierarchical labels for all raw images in the PACS, we did not use all images there. The distribution of classes' frequencies is imbalanced: some classes appear in many images while others are less frequent. The number of tags that each image has follows a Gaussian distribution.

Experimental Setup

Data augmentation by cropping and rotating was applied. The images were resized to 3000×2000. Each image was divided into 16×16 overlapping patches with a stride of 8. In the contextual attentional encoder, both the image encoder and patch encoder were set to ResNet-50 [153], where the 1000-dimensional vector produced by the fully-connected layer is used as the representation of an image or a patch. The attention module was a feed-forward network with 2 hidden layers where the number of unit was 300 and 100 respectively. The activation function was set to ReLU. The attentional encoder was also set to ResNet-50. In the tree-of-sequences LSTM encoder, the hidden state size of both the sequential and tree-structured LSTM was set to 100. The size of word embedding was set to 128. In the adversarial multi-label tagger, 70% training images were used as set A to learn label-image relevance. The rest were used as set B to learn label-correlations. Both the predictive and discriminative networks were feed-forward networks with 2 hidden layers where the number of units was 300 and 100 respectively. We used AdaGrad [255] with a learning rate of 0.1 and batch size of 32 to learn model parameters. In LSTM

Methods	Pathology		Radiology	
	Sensitivity	Specificity	Sensitivity	Specificity
CRF [419]	0.30	0.34	0.48	0.50
SPEN [36]	0.32	0.34	0.46	0.48
CNN-RNN [346]	0.31	0.35	0.48	0.51
DPP [375]	0.32	0.34	0.47	0.49
No-AL	0.30	0.33	0.46	0.48
LET [38]	0.30	0.35	0.48	0.50
HD-CNN [389]	0.31	0.35	0.46	0.49
HybridNet [166]	0.32	0.36	0.45	0.49
B-CNN [425]	0.30	0.34	0.48	0.51
No-TLSTM	0.29	0.34	0.45	0.49
Bottom-up TLSTM	**0.33**	0.36	0.48	0.51
LPA [385]	0.30	0.35	**0.50**	0.51
SA [71]	0.31	0.35	0.49	0.49
No-CA	0.30	0.34	0.48	0.49
DTHMLC [337]	0.20	0.23	0.39	0.40
DenseNet-LSTM [396]	0.27	0.29	0.44	0.46
OS [171]	0.22	0.23	0.41	0.44
Our full method	**0.33**	**0.37**	**0.50**	**0.52**

Table 6.5: Average sensitivity and specificity. On the first, second, and third panel are baselines compared in the ablation study of (1) adversarial learning for multi-label tagging, (2) tree-of-sequences LSTM for capturing hierarchical relationship, and (3) contextual attention for identifying abnormalities. On the fourth panel are baselines for holistic comparison.

training, the network was unrolled for 60 iterations. For performance evaluation, we used sensitivity (true positive rate) and specificity (true negative rate), which are the most widely used evaluation metrics in clinical trial. To address the imbalance issue of classes' frequency, in the loss function in Eq.(6.4), we gave infrequent classes larger weights, where the weight of a class is proportional to the reciprocal of the frequency of this class.

Ablation Study

We perform ablation study to verify the effectiveness of each module.

Adversarial learning for multi-label tagging To evaluate the efficacy of adversarial learning (AL), we removed it from the model. In Figure 6.4, the branch associated with training set B (including the discriminative network and binary classification loss) was taken away. All the training images were put into set A to learn label-image relevance. In addition, we compared with four state of the art methods proposed for capturing label-correlation in multi-label classification, by replacing AL with each of them while keeping the other modules intact. These baselines include (1) conditional random field (CRF) [419]; (2) structured prediction energy network (SPEN) [36]; (3) CNN-RNN [346]; (4) determinantal point process (DPP) [205, 375]. In

SPEN, The local and global energy networks are chosen to be feed-forward networks consisting of two hidden layers, with 300 and 150 units in each layer. Gradient descent was applied to make predictions, where the momentum and learning rate were set to 0.95 and 0.01 respectively. In CNN-RNN, the size of hidden states in LSTM was set to 128. The network was trained using SGD with momentum 0.9, weight decay 1e-4, and dropout rate 0.5. In the DPP baseline, we feed the image representation produced by the contextual attention encoder and concept representations produced by the tree-of-sequence LSTM encoder into a conditional kernel function represented by a label-input dependency network (LIDN) and a label-correlation network (LCN). The LIDN is configured to be a fully-connected network with 2 hidden layers where the number of units in the first and second layer is 200 and 100 respectively and the activation function is ReLU. The LCN has two hidden layers as well, each having 100 and 50 units respectively.

The first panel of Table 6.5 shows the results, from which we observe the following. First, after AL is removed (denoted by No-AL), the sensitivity and specificity are significantly dropped. No-AL ignores label-correlations and selects labels purely based on their relevance to the image, hence leading to inferior performance. Second, compared with the four baselines designed for capturing label-correlations, our full method (which uses AL) achieves better performance, suggesting that AL is more effective in capturing correlations. These baselines design explicit objective functions to encode correlations. The correlations might be very complicated and diverse, which are difficult to be captured by a single objective function. Instead, our approach implicitly learns such correlation by making the predicted labels indistinguishable from the groundtruth ones. It has more flexibility and expressivity to capture various types of correlations. The advantage of DPP is that it is able to capture high-order correlations among labels while being able to perform the exact learning of model parameters (without approximation) with cubic computational complexity (in terms of the number of unique classes). Its drawback is exact inference cannot be achieved in polynomial time. Approximate inference may bear large errors. The disadvantage of CRF is both inference and parameter learning cannot be performed exactly.

Tree-of-sequences LSTM To evaluate this module, we compared with the two configurations: (1) *No TLSTM*, which removes the tree LSTM and directly uses the hidden states produced by the sequential LSTM as final representations of concepts; (2) *Bottom-up TLSTM*, which removes the hidden states generated by the top-down TLSTM. In addition, we compared with four hierarchical classification baselines including (1) hierarchical deep CNN (HD-CNN) [389], (2) HybridNet [166], (3) Branch CNN (B-CNN) [425], (4) label embedding tree (LET) [38], by using them to replace the bidirectional tree LSTM while keeping other modules untouched. The second panel of Table 6.5 shows the sensitivity and specificity achieved by these methods. We make the following observations. First, removing tree LSTM (No TLSTM) greatly degrades performance since the hierarchical relationship among labels is ignored. Second, the bottom-up tree LSTM alone performs less well than our full method that uses the bi-directional tree LSTM. This demonstrates the necessity of the top-down TLSTM, which ensures every two labels are connected by directed paths and can more expressively capture label-relations in the hierarchy. Third, our full method outperforms the four baselines. The possible reason is that our method directly builds labels' hierarchical relationship into their representations while the baselines perform representation-learning and relationship-capturing separately.

	Size	Pathology			Radiology		
		IoU	Sensitivity	Specificity	IoU	Sensitivity	Specificity
Patch	8	0.25	0.32	0.36	0.40	0.47	0.49
	16	**0.29**	**0.33**	**0.37**	0.41	0.49	0.50
	32	0.28	0.32	0.34	**0.43**	**0.50**	**0.52**
	64	0.24	0.30	0.31	0.39	0.47	0.48
Stride	4	0.28	0.30	**0.37**	0.40	0.48	0.51
	8	**0.29**	**0.33**	**0.37**	**0.43**	**0.50**	**0.52**
	16	0.27	0.31	0.36	0.42	0.47	0.50

Table 6.6: Performance versus patch sizes and stride sizes.

Contextual attention In the evaluation of this module, we compared with No-CA which removes the contextual attention (CA) module, and two other attention models: (1) label-patch attention (LPA) [69, 385, 394, 400]; (2) scale attention (SA) [71]. The third panel of Table 6.5 shows the performance scores achieved by these methods. As can be seen, the sensitivity and specificity under No-CA is lower than our full method which uses CA, which demonstrates the effectiveness of contextual attention. CA is able to localize the small abnormal regions and pays more attention to them, which leads to the successful tagging of abnormalities. Compared with other attention baselines, our full method with CA achieves better performances. This indicates that for medical images, the contextual information embodied in the entire image is very valuable for distilling "attention".

We asked doctors to label the abnormal regions in 100 pathology and 100 radiology images. We compared the abnormal regions detected by our contextual attention model with the groundtruth using Intersection over Union (IoU). We evaluated how patch size affects performance. Table 6.6 shows IoU and sensitivity/specificity of tagging under different patch sizes (the stride size is set to 8). As can be seen, a patch size in the middle ground (that best matches the scale of abnormal regions) yields the best abnormality detection and tagging performance. We also evaluated how the stride size in overlapping patches affects performance. Fixing the patch size to 16, we tried stride sizes of 4, 8, and 16 (equivalent to nonoverlap). As can be seen from the table, overlap with a stride size 8 works better than nonoverlap.

Holistic Comparison with Other Baselines

In addition to evaluating the three modules individually, we also compared the entire model with three other baselines, including (1) decision trees for hierarchical multi-label classification (DTHMLC) [337], (2) DenseNet-LSTM designed in [396] for chest x-ray classification, (3) Occlusion sensitivity (OS) used in [171] for abnormality localization in x-rays.

The fourth panel of Table 6.5 shows the comparison with these baselines. As can be seen, our approach achieves much better performances on both datasets than the baselines. DTHMLC performs less well probably because it lacks the ability to learn deep visual features. DenseNet-LSTM lacks the ability to explore concept-hierarchy. OS cannot be trained in an end-to-end fashion which leads to inferior performance.

We evaluated the effects of tagging on image search. We used the learned models to tag

images in the PACS. For either pathology or radiology images, we randomly sampled 100 tags as queries, then performed retrieval by tag matching. We compared with a baseline: retrieval by checking whether the query tag is contained in the image reports. Retrieval performance was evaluated using precision@10: among the top 10 retrieved images, how many are relevant to the query (whether being relevant is labeled by doctors). The precision@10 achieved by reports-based retrieval is 0.24 for pathology and 0.32 for radiology. Our tagging method improves the precision@10 to 0.29 for pathology and 0.40 for radiology.

On the pathology dataset, our method is significantly better than CRF, No-AL, LET, B-CNN, No-TLSTM, LPA, No-CA, DTHMLC, DenseNet-LSTM, OS with p-value < 0.01, and is significantly better than SPEN, CNN-RNN, DPP, HD-CNN, HybridNet, SA with p-value < 0.05. On the pathology dataset, our method is significantly better than SPEN, DPP, No-AL, HD-CNN, HybridNet, No-TLSTM, No-CA, DTHMLC, DenseNet-LSTM, OS with p-value < 0.01, and is significantly better than CRF, CNN-RNN, LET, B-CNN, Bottom-up TLSTM, SA with p-value < 0.05.

6.3.3 Related works

Medical image categorization Many works [107, 208, 230, 321] have been devoted to the classification of medical images related to skin cancer [107], chest x-ray [349], pathology [178], to name a few. In [396], label-correlation is considered for more accurate classification of multi-label chest x-ray images. The localization of abnormality in chest x-rays is studied in [171] using the occlusion sensitivity method [410]. The problem setting studied in our work is different from the existing ones. We simultaneously consider two important facts: (1) each image may have multiple labels; (2) the classes have a hierarchical structure. The existing works consider neither or only one of them.

Multi-label classification (MLC) In computer vision and machine learning, MLC has been widely studied [56, 57, 123, 124, 189, 190, 285, 317, 351, 351, 362, 387, 390, 415, 416]. In MLC, one fundamental problem is how to capture the correlations among labels. Many approaches have been proposed based on graphical models [36, 70, 126, 147, 151, 201, 227, 316, 322, 412], latent space projection [36, 180, 183, 221, 228, 356, 397], and class chaining [77, 289, 346]. To retain computational efficiency, these methods typically make strong assumptions, such as the order of correlation is less than three [70, 126, 151, 201, 227], the dependency relationship among labels is linear [147], the labels are independent conditioned on a latent space [36, 228, 356, 397], etc. Some of these methods [316, 322, 412] lack the flexibility to perform deep visual feature learning in an end-to-end manner.

The existing methods define explicit objective functions to encode label correlations. In reality, the correlations might be of a variety of complicated forms which are unknown to the human modelers. As a result, it is difficult to specify a comprehensive objective to capture all of them. In this paper, we propose a different approach: instead of manually defining such an objective, we use adversarial learning to implicitly transfer the correlations manifested in human-provided labels into predicted labels by making the two types of labels indistinguishable.

Hierarchical classification Leveraging the hierarchical structure among classes to improve classification accuracy has been widely studied in [38, 97, 98, 166, 247, 389]. Many methods [28, 121, 166, 231, 389, 425, 430] propose to learn coarse-to-fine classifiers or features along the class hierarchy. In [38], a method is proposed to learn label embeddings where the learning is guided by the label tree. Our work also aims at embedding labels into a latent space and uses LSTM networks to capture long-range nonlinear dependencies among labels. Several works [98, 312, 414] encode the hierarchical relationship among labels as structural constraint, Bayesian priors and potential functions in conditional random field. A variety of works [96, 140, 181, 225, 248] study how to automatically learn the tree-structure among labels. Several studies [33, 64, 65, 337] have been conducted on hierarchical multi-label classification based on decision trees, neural networks, and hierarchical support vector machines.

Visual attention Visual attention [23, 26, 69, 71, 91, 258, 297, 300, 385, 400] has been widely utilized in computer vision. In many works [69, 385, 394, 400], the attention is computed between an image patch and a label (such as a sentence, a word, an attribute) by comparing their similarity. In a video-based activity recognition task, Sharma et al. [300] use the previous frame to predict the importance of regions in the current frame. Chen et al. [71] design an attention model which takes images at different scales as inputs and predicts the importance of regions at different positions and scales.

6.4 A Neural Architecture for Automated ICD Coding

The International Classification of Diseases (ICD) is a healthcare classification system maintained by the World Health Organization [268]. It provides a hierarchy of diagnostic codes of diseases, disorders, injuries, signs, symptoms, etc. It is widely used for reporting diseases and health conditions, assisting in medical reimbursement decisions, collecting morbidity and mortality statistics, to name a few.

While ICD codes are important for making clinical and financial decisions, medical coding – which assigns proper ICD codes to a patient visit – is time-consuming, error-prone and expensive. Medical coders review the diagnosis descriptions written by physicians in the form of textual phrases and sentences and (if necessary) other information in the electronic medical record of a clinical episode, then manually attribute the appropriate ICD codes by following the coding guidelines [267]. Several types of errors frequently occur. First, the ICD codes are organized in a hierarchical structure. For a node representing a disease C, the children of this node represents the subtypes of C. In many cases, the difference between disease subtypes is very subtle. It is common that human coders select incorrect subtypes. Second, when writing diagnosis descriptions, physicians often utilize abbreviations and synonyms, which causes ambiguity and imprecision when the coders are matching ICD codes to those descriptions [302]. Third, in many cases, several diagnosis descriptions are closely related and should be mapped to a single ICD code. However, unexperienced coders may code each disease separately. Such errors are called *unbundling*. The cost incurred by coding errors and the financial investment spent on improving coding quality are estimated to be $25 billion per year in the US [109, 210].

To reduce coding errors and cost, we aim at building an ICD coding model which automatically and accurately translates the free-text diagnosis descriptions into ICD codes. To achieve this goal, several technical challenges need to be addressed. First, there exists a hierarchical structure among the ICD codes. This hierarchy can be leveraged to improve coding accuracy. On one hand, if code A and B are both children of C, then it is unlikely to simultaneously assign A and B to a patient. On the other hand, if the distance between A and B in the code tree is smaller than that between A and C and we know A is the correct code, then B is more likely to be a correct code than C, since codes with smaller distance are more clinically relevant. How to explore this hierarchical structure for better coding is technically demanding. Second, the diagnosis descriptions and the textual descriptions of ICD codes are written in quite different styles even if they refer to the same disease. In particular, the textual description of an ICD code is formally and precisely worded, while diagnosis descriptions are usually written by physicians in an informal and ungrammatical way, with telegraphic phrases, abbreviations, and typos. Third, it is required that the assigned ICD codes are ranked according to their relevance to the patient. How to correctly determine this order is technically nontrivial. Fourth, as stated earlier, there does not necessarily exist an one-to-one mapping between diagnosis descriptions and ICD codes, and human coders should consider the overall health condition when assigning codes. In many cases, two closely related diagnosis descriptions need to be mapped onto a single combination ICD code. On the other hand, physicians may write two health conditions into one diagnosis description which should be mapped onto two ICD codes under such circumstances.

In this section, we design a neural architecture to automatically perform ICD coding given the diagnosis descriptions. This architecture uses a tree-of-sequences LSTM network (Section 6.3.1) to simultaneously capture the hierarchical relationship among codes and the semantics of each code. An adversarial learning approach is utilized to reconcile the heterogeneous writing styles of diagnosis descriptions and ICD code descriptions. We use isotonic constraints to preserve the importance order among codes and develop an algorithm based on ADMM and isotonic projection to solve the constrained problem. An attentional matching mechanism is employed to perform many-to-one and one-to-many mappings between diagnosis descriptions and codes. On a clinical datasets with 59K patient visits, we demonstrate the effectiveness of the proposed methods.

6.4.1 Methods

Figure 6.8 shows the overview of our approach. The proposed ICD coding model consists of five modules. The model takes the ICD-code tree and diagnosis descriptions (DDs) of a patient as inputs and assigns a set of ICD codes to the patient. The encoder of DDs generates a latent representation vector for a DD. The encoder of ICD codes is the tree-of-sequences long short-term memory (LSTM) network introduced in Section 6.3.1. It takes the textual descriptions of the ICD codes and their hierarchical structure as inputs and produces a latent representation for each code. The representation aims at simultaneously capturing the semantics of each code and the hierarchical relationship among codes. By incorporating the code hierarchy, the model can avoid selecting codes that are subtypes of the same disease and promote the selection of codes that are clinically correlated. The writing styles of DDs and code descriptions (CDs) are largely different, which makes the matching between a DD and a CD error-prone. To address this

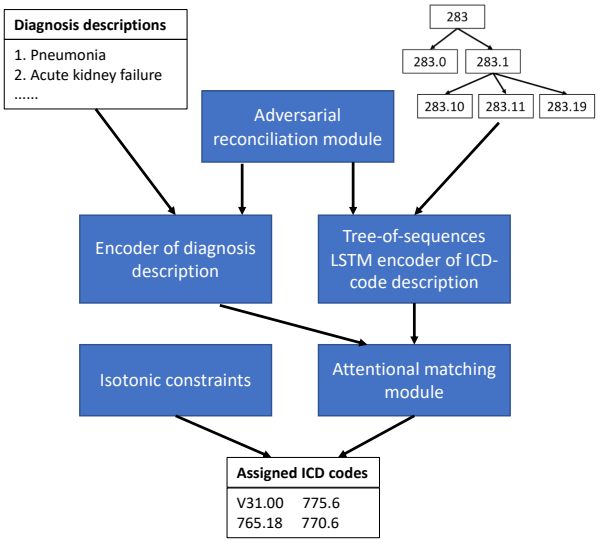

Figure 6.8: Architecture of the ICD coding model.

issue, we develop an adversarial learning approach to reconcile the writing styles. On top of the latent representation vectors of the descriptions, we build a discriminative network to distinguish which ones are DDs and which are CDs. The encoders of DDs and CDs try to make such a discrimination impossible. By doing this, the learned representations are independent of the writing styles and facilitate more accurate matching. The representations of DDs and CDs are fed into an attentional matching module to perform code assignment. This attentional mechanism allows multiple DDs to be matched to a single code and allows a single DD to be matched to multiple codes. During training, we incorporate the order of importance among codes as isotonic constraints. These constraints regulate the model's weight parameters so that codes with higher importance are given larger prediction scores.

Representation Learning

We use the tree-of-sequences LSTM network (Section 6.3.1) to encode the ICD codes. Each code has a description (a sequence of words) that tells the semantics of this code. A sequential LSTM (SLSTM) is used to encode this description. To capture the hierarchical relationship among codes, we build a tree-structured LSTM (TLSTM) [320] along the code tree. The inputs of this LSTM include the code hierarchy and the hidden states of individual codes produced by the SLSTMs. It consists of a bottom-up TLSTM and a top-down TLSTM, which produce two hidden states $\mathbf{h}_{\uparrow}$ and $\mathbf{h}_{\downarrow}$ at each node in the tree.

For the diagnosis descriptions of a patient, we use an SLSTM network to encode each description individually. The weight parameters of this SLSTM are tied with those of the SLSTM used for encoding code descriptions.

Attentional Matching

Next, we introduce how to map the DDs to codes. We denote the hidden representations of DDs and codes as $\{\mathbf{h}_m\}_{m=1}^M$ and $\{\mathbf{u}_n\}_{n=1}^N$ respectively, where M is the number of DDs of one patient and N is the total number of codes in the dataset. The mapping from DDs to codes is not one-to-one. In many cases, a code is assigned only when a certain combination of K ($1 < K \leq M$) diseases simultaneously appear within the M DDs and the value of K depends on this code. Among the K diseases, their importance of determining the assignment of this code is different. For the rest $M - K$ DDs, we can consider their importance score to be zero. We use a soft-attention mechanism [26] to calculate these importance scores. For a code $\mathbf{u}_n$, the importance of a DD $\mathbf{h}_m$ to $\mathbf{u}_n$ is calculated as $a_{nm} = \mathbf{u}_n^\top \mathbf{h}_m$. We normalize the scores $\{a_{nm}\}_{m=1}^M$ of all DDs into a probabilistic simplex using the softmax operation: $\tilde{a}_{nm} = \exp(a_{nm}) / \sum_{l=1}^M \exp(a_{nl})$. Given these normalized importance scores $\{\tilde{a}_{nm}\}_{m=1}^M$, we use them to weight the representations of DDs and get a single attentional vector of the M DDs: $\widehat{\mathbf{h}}_n = \sum_{m=1}^M \tilde{a}_{nm} \mathbf{h}_m$. Then we concatenate $\widehat{\mathbf{h}}_n$ and $\mathbf{u}_n$, and use a linear classifier to predict the probability that code n should be assigned: $p_n = \text{sigmoid}(\mathbf{w}_n^\top [\widehat{\mathbf{h}}_n; \mathbf{u}_n] + b_n)$, where the coefficients $\mathbf{w}_n$ and bias b_n are specific to code n.

We train the weight parameters Θ of the proposed model using the data of L patient visits. Θ includes the sequential LSTM weights $\mathbf{W}_s$, tree LSTM weights $\mathbf{W}_t$, and weights $\mathbf{W}_p$ in the final prediction layer. Let $c^{(l)} \in \mathbb{R}^N$ be a binary vector where $c_n^{(l)} = 1$ if the n-th code is assigned to this patient and $c_n^{(l)} = 0$ if otherwise. Θ can be learned by minimizing the following prediction loss:

$$\min_\Theta \quad \mathcal{L}_{\text{pred}}(\Theta) = \sum_{l=1}^{L} \sum_{n=1}^{N} \text{CE}(p_n^{(l)}, c_n^{(l)}), \tag{6.10}$$

where $p_n^{(l)}$ is the predicted probability that code n is assigned to patient visit l and $p_n^{(l)}$ is a function of Θ. $\text{CE}(\cdot, \cdot)$ is the cross-entropy loss.

Adversarial Reconciliation of Writing Styles

We use an adversarial learning [134] approach to reconcile the different writing styles of diagnosis descriptions (DDs) and code descriptions (CDs). The basic idea is: after encoded, if a description cannot be discerned to be a DD or a CD, then the difference in their writing styles is eliminated. We build a discriminative network which takes the encoding vector of a description as input and tries to identify it as a DD or CD. The encoders of DDs and CDs adjust their weight parameters so that such a discrimination is difficult to be achieved by the discriminative network. Consider all the descriptions $\{t_r, y_r\}_{r=1}^R$ where t_r is a description and y_r is a binary label. $y_r = 1$ if t_r is a DD and $y_r = 0$ if otherwise. Let $f(t_r; \mathbf{W}_s)$ denote the sequential LSTM (SLSTM) encoder parameterized by $\mathbf{W}_s$. This encoder is shared by the DDs and CDs. Note that for CDs, a tree LSTM is further applied on top of the encodings produced by the SLSTM. We use the SLSTM encoding vectors of CDs as the input of the discriminative network rather than using the TLSTM encodings since the latter are irrelevant to writing styles. Let $g(f(t_r; \mathbf{W}_s); \mathbf{W}_d)$ denote the discriminative network parameterized by $\mathbf{W}_d$. It takes the encoding vector $f(t_r; \mathbf{W}_s)$ as input and produces the probability that t_r is a DD. Adversarial learning is performed by solving this

problem:

$$\max_{\mathbf{W}_s} \min_{\mathbf{W}_d} \mathcal{L}_{\text{adv}} = \sum_{r=1}^{R} \text{CE}(g(f(t_r; \mathbf{W}_s); \mathbf{W}_d), y_r). \tag{6.11}$$

The discriminative network tries to differentiate DDs from CDs by minimizing this classification loss while the encoder maximizes this loss so that DDs and CDs are not distinguishable.

Isotonic Constraints

Next, we incorporate the importance order among ICD codes. For the $D^{(l)}$ codes assigned to patient l, without loss of generality, we assume the order is $1 \succ 2 \cdots \succ D^{(l)}$ (the order is given by human coders as groundtruth in the MIMIC-III dataset). We use the predicted probability p_i ($1 \leq i \leq D^{(l)}$) defined in Section 6.4.1 to characterize the importance of code i. To incorporate the order, we impose an isotonic constraint on the probabilities: $p_1^{(l)} \succ p_2^{(l)} \cdots \succ p_{D^{(l)}}^{(l)}$, and solve the following problem:

$$\begin{aligned} &\min_{\Theta} \mathcal{L}_{\text{pred}}(\Theta) + \max_{\mathbf{W}_d}(-\lambda \mathcal{L}_{\text{adv}}(\mathbf{W}_s, \mathbf{W}_d)) \\ &s.t. \quad p_1^{(l)} \succ p_2^{(l)} \cdots \succ p_{D^{(l)}}^{(l)} \\ &\qquad \forall l = 1, \cdots, L \end{aligned} \tag{6.12}$$

where the probabilities $p_i^{(l)}$ are functions of Θ and λ is a tradeoff parameter.

We develop an algorithm based on the alternating direction method of multiplier (ADMM) [52] to solve the problem defined in Eq.(6.12). Let $\mathbf{p}^{(l)}$ be a $|D^{(l)}|$-dimensional vector where the i-th element is $p_i^{(l)}$. We first write the problem into an equivalent form

$$\begin{aligned} &\min_{\Theta} \mathcal{L}_{\text{pred}}(\Theta) + \max_{\mathbf{W}_d}(-\lambda \mathcal{L}_{\text{adv}}(\mathbf{W}_s, \mathbf{W}_d)) \\ &s.t. \quad \mathbf{p}^{(l)} = \mathbf{q}^{(l)} \\ &\qquad q_1^{(l)} \succ q_2^{(l)} \cdots \succ q_{|D^{(l)}|}^{(l)} \\ &\qquad \forall l = 1, \cdots, L \end{aligned} \tag{6.13}$$

Then we write down the augmented Lagrangian

$$\begin{aligned} &\min_{\Theta, \mathbf{q}, \mathbf{v}} \mathcal{L}_{\text{pred}}(\Theta) + \max_{\mathbf{W}_d}(-\lambda \mathcal{L}_{\text{adv}}(\mathbf{W}_s, \mathbf{W}_d)) + \langle \mathbf{p}^{(l)} - \mathbf{q}^{(l)}, \mathbf{v}^{(l)} \rangle + \frac{\rho}{2} \|\mathbf{p}^{(l)} - \mathbf{q}^{(l)}\|_2^2) \\ &s.t. \quad q_1^{(l)} \succ q_2^{(l)} \cdots \succ q_{|D^{(l)}|}^{(l)} \\ &\qquad \forall l = 1, \cdots, L \end{aligned} \tag{6.14}$$

We solve this problem by alternating between $\{\mathbf{p}^{(l)}\}_{l=1}^L$, $\{\mathbf{q}^{(l)}\}_{l=1}^L$ and $\{\mathbf{v}^{(l)}\}_{l=1}^L$. The sub-problem defined over $\mathbf{q}^{(l)}$ is

$$\begin{aligned} &\min_{\mathbf{q}^{(l)}} -\langle \mathbf{q}^{(l)}, \mathbf{v}^{(l)} \rangle + \frac{\rho}{2} \|\mathbf{p}^{(l)} - \mathbf{q}^{(l)}\|_2^2 \\ &s.t. \quad q_1^{(l)} \succ q_2^{(l)} \cdots \succ q_{|D^{(l)}|}^{(l)} \end{aligned} \tag{6.15}$$

which is an isotonic projection problem and can be solved via the algorithm proposed in [403]. With $\{\mathbf{q}^{(l)}\}_{l=1}^L$ and $\{\mathbf{v}^{(l)}\}_{l=1}^L$ fixed, the sub-problem is $\min_{\Theta} \mathcal{L}_{\text{pred}}(\Theta) + \max_{\mathbf{W}_d}(-\lambda \mathcal{L}_{\text{adv}}(\mathbf{W}_s, \mathbf{W}_d))$ which can be solved using stochastic gradient descent (SGD). The update of $\mathbf{v}^{(l)}$ is simple: $\mathbf{v}^{(l)} = \mathbf{v}^{(l)} + \rho(\mathbf{p}^{(l)} - \mathbf{q}^{(l)})$.

Diagnosis Descriptions
1. Prematurity at 35 4/7 weeks gestation
2. Twin number two of twin gestation
3. Respiratory distress secondary to transient tachypnea of the newborn
4. Suspicion for sepsis ruled out
Assigned ICD Codes
1. V31.00 (Twin birth, mate liveborn, born in hospital, delivered without mention of cesarean section)
2. 765.18 (Other preterm infants, 2,000-2,499 grams)
3. 775.6 (Neonatal hypoglycemia)
4. 770.6 (Transitory tachypnea of newborn)
5. V29.0 (Observation for suspected infectious condition)
6. V05.3 (Need for prophylactic vaccination and inoculation against viral hepatitis)

Table 6.7: The diagnosis descriptions of a patient visit and the assigned ICD codes. Inside the parentheses are the descriptions of the codes. The codes are ranked according to descending importance.

6.4.2 Evaluation

In this section, we present experiment results.

Dataset

We performed the study on the publicly available MIMIC-III dataset [184], which contains de-identified electronic health records (EHRs) of 58,976 patient visits in the Beth Israel Deaconess Medical Center from 2001 to 2012. Each EHR has a clinical note called discharge summary, which contains multiple sections of information, such as 'discharge diagnosis', 'past medical history', etc. From the 'discharge diagnosis' and 'final diagnosis' sections, we extract the diagnosis descriptions (DDs) written by physicians. Each DD is a short phrase or a sentence, articulating a certain disease or condition. Medical coders perform ICD coding mainly based on DDs. Following such a practice, in this paper, we set the inputs of the automated coding model to be the DDs while acknowledging that other information in the EHRs is also valuable and is referred to by coders for code assignment. For simplicity, we leave the incorporation of non-DD information to future study.

Each patient visit is assigned with a list of ICD codes, ranked in descending order of importance and relevance. For each visit, the number of codes is usually not equal to the number of diagnosis descriptions. These groundtruth codes serve as the labels to train our coding model. The entire dataset contains 6,984 unique codes, each of which has a textual description, describing a disease, symptom, or condition. The codes are organized into a hierarchy where the top-level codes correspond to general diseases while the bottom-level ones represent specific diseases. In the code tree, children of a node represent subtypes of a disease. Table 6.7 shows the

DDs and codes of an exemplar patient.

Experimental Settings

Out of the 6,984 unique codes, we selected 2,833 codes that have the top frequencies to perform the study. We split the data into a train/validation/test dataset with 40k/7k/12k patient visits respectively. The hyperparameters were tuned on the validation set. The SLSTMs are bidirectional and dropout with 0.5 probability [313] was used. The size of hidden states in all LSTMs was set to 100. The word embeddings were trained on the fly and their dimension was set to 200. The tradeoff parameter λ was set to 0.1. The parameter ρ in the ADMM algorithm was set to 1. In the SGD algorithm for solving $\min_{\Theta} \ \mathcal{L}_{\text{pred}}(\Theta) + \max_{\mathbf{W}_d}(-\lambda \mathcal{L}_{\text{adv}}(\mathbf{W}_s, \mathbf{W}_d))$, we used the Adam [196] optimizer with an initial learning rate 0.001 and a mini-batch size 20. Sensitivity (true positive rate) and specificity (true negative rate) were used to evaluate the code assignment performance. We calculated these two scores for each individual code on the test set, then took a weighted (proportional to codes' frequencies) average across all codes. To evaluate the ranking performance of codes, we used the normalized discounted cumulative gain (NDCG) [179].

Ablation Study

We performed ablation study to verify the effectiveness of each module in our model. To evaluate module X, we remove it from the model without changing other modules and denote such a baseline by No-X. The comparisons of No-X with the full model are given in Table 6.8.

Tree-of-sequences LSTM To evaluate this module, we compared with the two configurations: (1) *No-TLSTM*, which removes the tree LSTM and directly uses the hidden states produced by the sequential LSTM as the final representations of codes; (2) *Bottom-up TLSTM*, which removes the hidden states generated by the top-down TLSTM. In addition, we compared with four hierarchical classification baselines including (1) hierarchical network (HierNet) [389], (2) HybridNet [166], (3) branch network (BranchNet) [425], (4) label embedding tree (LET) [38], by using them to replace the bidirectional tree LSTM while keeping other modules untouched. Table 6.8 shows the average sensitivity and specificity scores achieved by these methods on the test set. We make the following observations. First, removing tree LSTM largely degrades performance: the sensitivity and specificity of No-TLSTM is 0.23 and 0.28 respectively while our full model (which uses bidirectional TLSTM) achieves 0.29 and 0.33 respectively. The reason is No-TLSTM ignores the hierarchical relationship among codes. Second, the bottom-up tree LSTM alone performs less well than the bidirectional tree LSTM. This demonstrates the necessity of the top-down TLSTM, which ensures every two codes are connected by directed paths and can more expressively capture code-relations in the hierarchy. Third, our method outperforms the four baselines. The possible reason is our method directly builds codes' hierarchical relationship into their representations while the baselines learn representations and capture hierarchical relationships separately.

Next, we present some qualitative results. For a patient (admission ID 147798) having a DD 'E Coli urinary tract infection', without using tree LSTM, two sibling codes 585.2 (chronic kidney disease, stage II (mild)) – which is the groundtruth – and 585.4 (chronic kidney disease, stage

	Sensitivity	Specificity
Larkey and Croft [211]	0.15	0.17
Franz et al. [112]	0.19	0.21
Pestian et al. [274]	0.12	0.21
Kavuluru et al. [191]	0.09	0.11
Kavuluru et al. [192]	0.21	0.25
Koopman et al. [199]	0.18	0.20
LET [38]	0.23	0.29
HierNet [389]	0.26	0.30
HybridNet [166]	0.25	0.31
BranchNet [425]	0.25	0.29
No-TLSTM	0.23	0.28
Bottom-up TLSTM	0.27	0.31
No-AL	0.26	0.31
No-IC	0.24	0.29
No-AM	0.27	0.29
Our full model	**0.29**	**0.33**

Table 6.8: Weighted sensitivity and specificity on the test set. On the first panel are baselines for holistic comparison. On the second panel are baselines compared in the ablation study of tree-of-sequences LSTM for capturing hierarchical relationship. On the third panel are baselines compared in the ablation study of adversarial learning for writing-style reconciliation, isotonic constraints for ranking, and attentional matching.

IV (severe)) are simultaneously assigned possibly because their textual descriptions are very similar (only differ in the level of severity). This is incorrect because 585.2 and 585.4 are children of 585 (chronic kidney disease) and the severity level of this disease cannot simultaneously be mild and severe. After the tree LSTM is added, the false prediction of 585.4 is eliminated, which demonstrates the effectiveness of tree LSTM in incorporating one constraint induced by the code hierarchy: among the nodes sharing the same parent, only one should be selected.

For patient 197205, No-TLSTM assigns the following codes: 462 (subacute sclerosing panencephalitis), 790.29 (other abnormal glucose), 799.9 (unspecified viral infection), and 285.21 (anemia in chronic kidney disease). Among these codes, the first three are the groundtruth and the fourth one is incorrect (the groundtruth is 401.9 (unspecified essential hypertension)). Adding tree LSTM fixes this error. The average distance between 401.9 and the rest of groundtruth codes is 6.2. For the incorrectly assigned code 285.21, such a distance is 7.9. This demonstrates that tree LSTM is able to capture another constraint imposed by the hierarchy: codes with smaller tree-distance are more likely to be assigned together.

Adversarial learning To evaluate the efficacy of adversarial learning (AL), we remove it from the full model and refer to this baseline as No-AL. Specifically, in Eq.(6.12), the loss term $\max_{\mathbf{W}_d}(-\mathcal{L}_{\text{adv}}(\mathbf{W}_s, \mathbf{W}_d))$ is taken away. Table 6.8 shows the results, from which we observe that after AL is removed, the sensitivity and specificity are dropped from 0.29 and 0.33 to 0.26 and 0.31 respectively. No-AL does not reconcile different writing styles of diagnosis descriptions

Position	2	4	6	8
No-IC	0.27	0.26	0.23	0.20
IC	0.32	0.29	0.27	0.23

Table 6.9: Comparison of NDCG scores in the ablation study of isotonic constraints.

(DDs) and code descriptions (CDs). As a result, a DD and a CD that have similar semantics may be mismatched because their writing styles are different. For example, a patient (admission ID 147583) has a DD 'h/o DVT on anticoagulation', which contains abbreviation DVT (deep vein thrombosis). Due to the presence of this abbreviation, it is difficult to assign a proper code to this DD since the textual descriptions of codes do not contain abbreviations. With adversarial learning, our model can correctly map this DD to a groundtruth code: 443.9 (peripheral vascular disease, unspecified). Without AL, this code is not selected. As another example, a DD 'coronary artery disease, STEMI, s/p 2 stents placed in RCA' was given to patient 148532. This DD is written informally and ungrammatically, and contains too much detailed information, e.g., 's/p 2 stents placed in RCA'. Such a writing style is quite different from that of CDs. With AL, our model successfully matches this DD to a groundtruth code: 414.01 (coronary atherosclerosis of native coronary artery). On the contrary, No-AL fails to achieve this.

Isotonic constraint (IC) To evaluate this ingredient, we remove the ICs from Eq.(6.12) during training and denote this baseline as No-IC. We used NDCG to measure the ranking performance, which is calculated in the following way. Consider a testing patient-visit l where the groundtruth ICD codes are $\mathcal{M}^{(l)}$. For any code c, we define the relevance score of c to l as 0 if $c \notin \mathcal{M}^{(l)}$ and as $|\mathcal{M}^{(l)}| - r(c)$ if otherwise, where $r(c)$ is the groundtruth rank of c in $\mathcal{M}^{(l)}$. We rank codes in descending order of their corresponding prediction probabilities and obtain the predicted rank for each code. We calculated the NDCG scores at position 2, 4, 6, 8 based on the relevance scores and predicted ranks, which are shown in Table 6.9. As can be seen, using IC achieves much higher NDCG than No-IC, which demonstrates the effectiveness of IC in capturing the importance order among codes.

We also evaluated how IC affects the sensitivity and specificity of code assignment. As can be seen from Table 6.8, No-IC degrades the two scores from 0.29 and 0.33 to 0.24 and 0.29 respectively, which indicates that IC is helpful in training a model that can more correctly assign codes. This is because IC encourages codes that are highly relevant to the patients to be ranked at top positions, which prevents the selection of irrelevant codes.

Attentional matching (AM) In the evaluation of this module, we compared with a baseline – No-AM, which performs an unweighted average of the M DDs: $\widehat{\mathbf{h}}_n = \frac{1}{M}\sum_{m=1}^{M}\mathbf{h}_m$, concatenates $\widehat{\mathbf{h}}_n$ with $\mathbf{u}_n$, and feeds the concatenated vector into the final prediction layer. From Table 6.8, we can see our full model (with AM) outperforms No-AM, which demonstrates the effectiveness of attentional matching. In determining whether a code should be assigned, different DDs have different importance weights. No-AM ignores such weights, therefore performing less well.

AM can correctly perform the many-to-one mapping from multiple DDs to a CD. For exam-

ple, patient 190236 was given two DDs: 'renal insufficiency' and 'acute renal failure'. AM maps them to a combined ICD code: 403.91 (hypertensive chronic kidney disease, unspecified, with chronic kidney disease stage V or end stage renal disease), which is in the groundtruth provided by medical coders. On the contrary, No-AM fails to assign this code. On the other hand, AM is able to correctly map a DD to multiple CDs. For example, a DD 'congestive heart failure, diastolic' was given to patient 140851. AM successfully maps this DD to two codes: (1) 428.0 (congestive heart failure, unspecified); (2) 428.30 (diastolic heart failure, unspecified). Without AM, this DD is mapped only to 428.0.

Holistic comparison with other baselines

In addition to evaluating the four modules individually, we also compared our full model with four other baselines proposed by [112, 191, 192, 199, 211, 274] for ICD coding. Table 6.8 shows the results. As can be seen, our approach achieves much better sensitivity and specificity scores. The reason that our model works better is two-fold. First, our model is based on deep neural networks, which has arguably better modeling power than linear methods used in the baselines. Second, our model is able to capture the hierarchical relationship and importance order among codes, can alleviate the discrepancy in writing styles, and allows flexible many-to-one and one-to-many mappings from DDs to CDs. These merits are not possessed by the baselines.

6.4.3 Related Works

Larkey and Croft [211] studied the automatic assignment of ICD-9 codes to dictated inpatient discharge summaries, using a combination of three classifiers: k-nearest neighbors, relevance feedback, and Bayesian independence classifiers. This method assigns a single code to each patient visit. However, in clinical practice, each patient is usually assigned with multiple codes. Franz et al. [112] investigated the automated coding of German-language free-text diagnosis phrases. This approach performs one-to-one mapping between diagnosis descriptions and ICD codes. This is not in accordance with the coding practice where one-to-many and many-to-one mappings widely exist [267]. Pestian et al. [274] studied the assignment of ICD-9 codes to radiology reports. Kavuluru et al. [191] proposed an unsupervised ensemble approach to automatically perform ICD-9 coding based on textual narratives in electronic health records (EHRs) Kavuluru et al. [192] developed multi-label classification, feature selection, and learning to rank approaches for ICD-9 code assignment of in-patient visits based on EHRs. Koopman et al. [199] explored the automatic ICD-10 classification of cancers from free-text death certificates. These methods did not consider the hierarchical relationship or importance order among codes.

The tree LSTM network was first proposed by [320] to model the constituent or dependency parse trees of sentences. Teng and Zhang [330] extended the unidirectional tree LSTM to a bidirectional one. Xie and Xing [368] proposed a sequence-of-trees LSTM network to model a passage. In this network, a sequential LSTM is used to compose a sequence of tree LSTMs. The tree LSTMs are built on the constituent parse trees of individual sentences and the sequential LSTM is built on the sequence of sentences. Our proposed tree-of-sequences LSTM network differs from the previous works in two-fold. First, it is applied to a code tree to capture the

hierarchical relationship among codes. Second, it uses a tree LSTM to compose a hierarchy of sequential LSTMs.

Adversarial learning [134] has been widely applied to image generation [134], domain adaptation [118], feature learning [104], text generation [401], to name a few. In this paper, we use adversarial learning for mitigating the discrepancy among the writing styles of a pair of sentences.

The attention mechanism was widely used in machine translation [26], image captioning [385], reading comprehension [295], text classification [395], etc. In this work, we compute attention scores between sentences to perform many-to-one and one-to-many mappings.

Chapter 7

Conclusions and Future Directions

In this thesis, we focused on developing diversity-promoting learning methods and large-scale distributed learning systems for automatic smart data-driven medical predictions, recommendations, and decision-making, to assist physicians and hospitals to improve the quality and efficiency of healthcare.

7.1 Contributions

We recapitulate the key contributions.

Diversity-promoting Learning

- In frequentist learning, we proposed a number of diversity-promoting regularizers, including uniform-eigenvalue regularizer (UER), nonconvex and convex Bregman matrix divergence (BMD) regularizers, angular constraints (ACs), and nonoverlap-promoting regularization. We discussed their advantages, disadvantages, and inter-connections. We validated their effectiveness in a wide spectrum of ML models including distance metric learning (DML), long short-term memory network (LSTM), convolutional neural network (CNN), feedforward neural network (FNN), sparse coding (SC), and multiclass logistic regression (MLR). We extended the study of diversity-promoting regularization (DPR) from finite-dimensional vector space to infinite-dimensional reproducing kernel Hilbert space and investigated the nonoverlap-promoting effect of DPR when jointly used with sparsity-promoting regularization.
- In Bayesian learning, we proposed diversity-promoting priors, including the mutual angular process (MAP) and infinite MAP. We validated their effectiveness on two models: Bayesian mixture of experts model (BMEM) and infinite latent feature model (ILFM).
- In theoretical analysis, we formally justified why promoting diversity can better capture infrequent patterns, using nonconvex BMD regularizers as study cases. To understand why DPR can improve generalization performance, we conducted analysis to show that (1) angular constraints can exploit the tradeoff between estimation error and approximation

error, and (2) reducing the nonconvex and convex BMD regularizers can reduce estimation errors.

- In algorithm development, we derived efficient optimization and Bayesian inference methods, based on projected gradient descent, proximal gradient descent, functional gradient descent, coordinate ascent, ADMM, KKT conditions, variational inference, and MCMC sampling, to solve the problems regularized or biased by diversity-promoting regularizers or priors.

Large-scale Distributed Learning

- We proposed a sufficient factor broadcasting (SFB) computation model by exploring the sufficient factor property of a large family of ML models. SFB can greatly reduce communication cost. We also proposed a hybrid computation model that leverages the best of SFB and parameter-server architectures.
- We provided theoretical guarantee on the convergence of algorithms executed using SFB. The analysis was extended to partial SFB where each machine communicates with a subset of neighbors.
- Based on SFB, we built a distributed system that provides efficient communication, light weight fault tolerance, and easy-to-use programming interface. We validated its efficiency and scalability on three large-scale ML models containing billions of parameters.

Applications in Healthcare

- In terms of problems, we studied similar patient retrieval, medical topic discovery, medical image tagging, and automated ICD coding.
- In terms of methods, we applied the diversity-promoting and distributed learning techniques for two applications. For the other two applications we proposed tree-of-sequences encoding for hierarchy modeling, adversarial learning for multi-label classification, contextual attention for abnormality localization, adversarial learning for writing-style reconciliation, isotonic constraints for order preservation, etc.
- In terms of evaluation, we validated the effectiveness of our methods on various clinical datasets including electronic health records from ICU, radiology and pathology images, medical literature, to name a few.

7.2 Conclusions

We have the following conclusions.

- Promoting diversity can effectively capture infrequent patterns. This is justified both empirically and theoretically. The experiments on (1) DML regularized by UER, nonconvex and convex BMD, (2) BMEM biased by MAP, and (3) ILFM biased by infinite MAP demonstrate that promoting diversity improve the performance on infrequent patterns. In

theory, we proved that decreasing the nonconvex BMD regularizers can reduce an imbalance factor (IF) in DML and a smaller IF indicates better capturing of infrequent patterns.

- Promoting diversity can improve generalization performance, as validated in experiments and theory. In each section of Chapter 2 and 3, the evaluation shows that adding diversity-promoting regularizers or priors improves the performance on test data. In theory, our analysis showed that: (1) a stronger angular constraint yields smaller estimation error and larger approximation error, which hence can explore the tradeoff between these two types of errors and seeks the optimal generalization error; (2) decreasing the nonconvex and convex BMD regularizers can reduce the estimation error.
- Promoting diversity can improve interpretability. It is demonstrated that by encouraging diversity using the LDD-L1 regularizer and the infinite MAP prior, the basis vectors in sparse coding and the latent features in the infinite latent feature model are more mutually distinct and have less overlap, making them easier to interpret.
- Promoting diversity can reduce model size without sacrificing modeling power. In the following experiments: UER-regularized DML, nonconvex/convex BMD regularized DML, BMD-regularized kernel DML, MAP-biased BMEM, infinite MAP biased ILFM, it is shown that with diversity-promoting regularization, an ML model can achieve better performance with fewer components.
- System-algorithm co-design is essential for building efficient distributed ML systems, as evidenced in the Orpheus system. On one hand, we leveraged an algorithmic insight – sufficient factor property – to drive the design of efficient communication and light-weight fault tolerance. On the other hand, we designed new algorithms (e.g., joint matrix column subset selection) to support the realization of system designs (e.g., sufficient factor selection). Empirical evaluation on various large-scale applications demonstrate the benefits of system-algorithm co-design.
- When applied to healthcare applications, the proposed diversity-promoting and distributed learning techniques demonstrate great effectiveness in solving the problems mentioned in the introduction chapter.
- The additionally proposed ML techniques for healthcare applications are effective, as demonstrated in extensive evaluations. The tree-of-sequences LSTM model can effectively capture the hierarchical relationship among classes. Adversarial learning is successful applied to capture correlations among classes and reconcile the discrepancy between writing styles. Contextual attention shows great efficacy in identifying abnormal regions in medical images. Isotonic constraints effectively improve ranking performance.

7.3 Future Directions

We identify the following directions for future work.

Diversity-promoting Learning

- **Promoting structured diversity** The diversity-promoting regularizers/priors developed in this thesis do not consider the structural relationships among components. In many ML models, the components admit a certain structure, such as multiview, grouping, and hierarchy. For example, in cross-modal distance metric learning [283], each feature modality has a separate set of components. In clustered multi-task learning [175], the tasks (components) are partitioned into latent groups. In hierarchical topic models [144], the topics (components) are organized into a tree. In the presence of such structures, how to promote diversity deserves investigation.
- **Provably consistent parameter estimation** Most diversity-promoting regularizers developed in this thesis are nonconvex, rendering the regularized problems to be nonconvex and therefore vulnerable to local optima. Further, they are difficult, if possible, to be convexified. It is intriguing to study whether the global optima of these nonconvex problems can be achieved. We plan to investigate methods of moments and spectral algorithms [168], which were demonstrated to be computationally efficient and provably consistent estimators in a number of nonconvex problems [20, 66, 269].
- **Posterior contraction analysis** In Bayesian models, it is interesting to analyze how diversity-promoting priors affect the contraction rate of components' posterior. Inspired by [262], we plan to study how fast the convex hull G of the estimated components contracts to the convex hull G_0 of the "true" components, where the "closeness" between G and G_0 can be measured by the "minimum-matching" Euclidean distance or Hausdorff metric. In the mutual angular process, the concentration parameter κ represents the level of diversity. Our goal is to establish a relationship between κ and the contraction rate.
- **Information geometry analysis** In probabilistic models, there are two types of manifolds. First, these models essentially define distributions over the observed data and these distributions have a manifold structure [215] which is studied by information geometry [19]. Second, the components in ML models also lie in a manifold. We are interested in how diversity-promoting regularizers/priors affect the component manifold and further how they affect the distribution manifold (indirectly via the component manifold).

Large-scale Distributed Learning

- **Model parallelism** In this thesis, we assume the parameter matrix (PM) can fit into the memory of each machine, which may not hold when the PM is excessively large. One way to address this issue is to divide the PM into sub-matrices so that each of which can fit into the memory of one machine. Multiple machines collaboratively update a single PM via model parallelism. On the other hand, we retain the parallelism on data by adopting a hierarchical architecture. The machines are divided into groups. Each group holds one replica of the PM and one data shard. Machines within the same group hold different sub-matrices of the PM replica. Data parallelism is executed between machine groups and model parallelism is conducted within each group.

Applications in Healthcare

- **Never-ending construction of medical knowledge graph** Medical knowledge graph (MKG) which consists of medical entities (e.g., symptoms, diseases, medications) and their relationships (e.g., medication A can treat disease B, medication A and C have adverse interactions) is a fundamental asset that empowers many clinical applications, such as medical named entity recognition, symptom checking, medication-prescription safety alert, to name a few. Manually building an MKG is time-consuming and not scalable. There have been efforts to automatically construct MKGs by analyzing literature and clinical notes [292]. However, they lack the mechanism to continuously grow the MKGs from medical texts that are newly generated every day. We plan to build a reinforcement learning system that constantly digests the new medical texts and ceaselessly expands and refines the MKG.
- **Discharge summary generation** When discharging patients, physicians need to collect a large amount of information accumulated during inpatient stay (e.g., hospital course, problem list, medications, test results) and consolidate them into a discharge summary. This process is very time-consuming. It would be helpful to build an ML software that automatically pulls data from different sources, extracts key information from the raw data, and summarizes these information into a highly precise and readable discharge note.

Bibliography

[1] 20-Newsgroups dataset. *http://www.daviddlewis.com/resources/testcollections/reuters21578/*. 2.2.4, 2.5.3, 3.2.4

[2] GPUDirect RDMA. *http://docs.nvidia.com/cuda/gpudirect-rdma/#axzz4eWBuf9Rj*. 5.2.4

[3] Pytorch word language model. *https://github.com/pytorch/examples/tree/master/word_language_model*. 2.5.3

[4] TDT dataset. *http://www.itl.nist.gov/iad/mig/tests/tdt/2004/*. 3.2.4

[5] CIFAR-10 dataset. *https://www.cs.toronto.edu/~kriz/cifar.html*. 2.3.3, 2.5.3, 5.3.2, 5.3.2

[6] InfiniBand. *http://www.infinibandta.com*. 5.2.4

[7] MAGMA matrix algebra on GPU. In *http://icl.cs.utk.edu/magma/*. 2.1.3, 2.2.3, 2.2.4

[8] MPI. *https://www.mpich.org/*. 5.2.4

[9] PubMed. *https://catalog.data.gov/dataset/pubmed*. 5.2.5, 6.2

[10] Reuters dataset. *http://www.daviddlewis.com/resources/testcollections/reuters21578/*. 2.2.4, 2.5.3, 3.2.4

[11] TIMIT dataset. *https://catalog.ldc.upenn.edu/LDC93S1*. 2.3.3

[12] Emergency department pulse report 2010: Patient perspectives on american health care. 2010. 1.1

[13] Martín Abadi, Paul Barham, Jianmin Chen, Zhifeng Chen, Andy Davis, Jeffrey Dean, Matthieu Devin, Sanjay Ghemawat, Geoffrey Irving, Michael Isard, et al. TensorFlow: A system for large-scale machine learning. In *USENIX Symposium on Operating Systems Design and Implementation*, 2016. 1.3.2, 5, 5.2, 5.2.2, 5.2.3, 5.2.5

[14] Ossama Abdel-Hamid, Li Deng, Dong Yu, and Hui Jiang. Deep segmental neural networks for speech recognition. *Interspeech*, 2013. 2.3.3

[15] Sachin Abeywardana. Expectation and covariance of von Mises-Fisher distribution. In *https://sachinruk.github.io/blog/von-Mises-Fisher/*, 2015. 3.1.6

[16] Raja Hafiz Affandi, Emily Fox, and Ben Taskar. Approximate inference in continuous determinantal processes. In *Advances in Neural Information Processing Systems*, 2013.

3, 3.1.5

[17] Saurabh Agarwal, Rahul Garg, Meeta S Gupta, and Jose E Moreira. Adaptive incremental checkpointing for massively parallel systems. In *Proceedings of the 18th annual international conference on Supercomputing*, pages 277–286. ACM, 2004. 5.2.2

[18] David J Aldous. *Exchangeability and related topics*. Springer, 1985. 3.2

[19] Shun-ichi Amari and Hiroshi Nagaoka. *Methods of information geometry*, volume 191. American Mathematical Soc., 2007. 7.3

[20] Animashree Anandkumar, Rong Ge, Daniel Hsu, Sham M Kakade, and Matus Telgarsky. Tensor decompositions for learning latent variable models. *The Journal of Machine Learning Research*, 15(1):2773–2832, 2014. 7.3

[21] Davide Anguita, Alessandro Ghio, Luca Oneto, Xavier Parra, and Jorge L Reyes-Ortiz. Human activity recognition on smartphones using a multiclass hardware-friendly support vector machine. In *Ambient assisted living and home care*. 2012. 2.2.4

[22] Jimmy Ba and Rich Caruana. Do deep nets really need to be deep? In *Advances in neural information processing systems*, 2014. 2.3.3

[23] Jimmy Ba, Volodymyr Mnih, and Koray Kavukcuoglu. Multiple object recognition with visual attention. *International Conference on Learning Representations*, 2015. 6.3.3

[24] Francis R Bach. Exploring large feature spaces with hierarchical multiple kernel learning. In *Advances in neural information processing systems*, pages 105–112, 2009. 2.5

[25] Francis R Bach and Michael I Jordan. Kernel independent component analysis. *Journal of machine Learning research*, 2002. 2.4, 2.4.1

[26] Dzmitry Bahdanau, Kyunghyun Cho, and Yoshua Bengio. Neural machine translation by jointly learning to align and translate. In *International Conference on Learning Representations*, 2014. 6.3.3, 6.4.1, 6.4.3

[27] Robert E Banfield, Lawrence O Hall, Kevin W Bowyer, and W Philip Kegelmeyer. Ensemble diversity measures and their application to thinning. *Information Fusion*, 2005. 1.3.1

[28] Hichem Bannour and Céline Hudelot. Hierarchical image annotation using semantic hierarchies. In *Proceedings of the 21st ACM international conference on Information and knowledge management*, pages 2431–2434. ACM, 2012. 6.3.3

[29] Yebo Bao, Hui Jiang, Lirong Dai, and Cong Liu. Incoherent training of deep neural networks to de-correlate bottleneck features for speech recognition. In *IEEE International Conference on Acoustics, Speech and Signal Processing*, pages 6980–6984. IEEE, 2013. 1.3.1, 1.3.1, 2.1, 2.1.1, 2.1.4, 2.1.4, 2.1.4, 2.1.4, 2.1.4, 2.1.4, 2.2.4, 2.3.2, 2.3.3, 2.5.3, 2.2.4, 2.2.4, 2.2.4, 2.2.4, 2.3.3, 2.3.3, 2.3.3, 2.3.3, 2.5.3, 6.1.1, 6.1.2

[30] Rémi Bardenet and Michalis Titsias. Inference for determinantal point processes without spectral knowledge. In *Advances in Neural Information Processing Systems*, pages 3393–3401, 2015. 3.1

[31] Andrew R Barron. Universal approximation bounds for superpositions of a sigmoidal

function. *IEEE Transactions on Information Theory*, 1993. 4.2.1, 4.2.1, 4.3.3, 15, 4.3.3

[32] Peter L Bartlett and Shahar Mendelson. Rademacher and gaussian complexities: Risk bounds and structural results. *Journal of Machine Learning Research*, 3:463–482, 2003. 4.2.1, 4.2.1, 4.3.2, 4.3.2, 4.3.2, 4.3.4, 4.3.4, 4.3.5, 4.3.5

[33] Zafer Barutcuoglu, Robert E Schapire, and Olga G Troyanskaya. Hierarchical multi-label prediction of gene function. *Bioinformatics*, 22(7):830–836, 2006. 6.3.3

[34] Frédéric Bastien, Pascal Lamblin, Razvan Pascanu, James Bergstra, Ian Goodfellow, Arnaud Bergeron, Nicolas Bouchard, David Warde-Farley, and Yoshua Bengio. Theano: new features and speed improvements. *NIPS Workshop on Deep Learning and Unsupervised Feature Learning*, 2012. 5.2.3

[35] Amir Beck and Marc Teboulle. Mirror descent and nonlinear projected subgradient methods for convex optimization. *Operations Research Letters*, 2003. 5.4.1

[36] David Belanger and Andrew McCallum. Structured prediction energy networks. In *International Conference on Machine Learning*, 2016. 6.3.2, 6.3.2, 6.3.3

[37] A. Bellet and A. Habrard. Robustness and generalization for metric learning. *Neurocomputing*, 2015. 4.2.2, 4.2.3

[38] Samy Bengio, Jason Weston, and David Grangier. Label embedding trees for large multi-class tasks. In *Advances in Neural Information Processing Systems*, pages 163–171, 2010. 6.3.2, 6.3.2, 6.3.3, 6.4.2

[39] Ingemar Bengtsson and Karol Zyczkowski. *Geometry of quantum states: an introduction to quantum entanglement*. Cambridge University Press, 2007. 2.1.1

[40] Dimitri P Bertsekas. *Nonlinear programming*. Athena scientific Belmont, 1999. 5.1

[41] Dimitri P. Bertsekas and John N. Tsitsiklis. *Parallel and Distributed Computation: Numerical Methods*. Prentice-Hall, 1989. 5.4, 5.4.1

[42] Kanishka Bhaduri, Ran Wolff, Chris Giannella, and Hillol Kargupta. Distributed decision-tree induction in peer-to-peer systems. *Statistical Analysis and Data Mining: The ASA Data Science Journal*, 2008. 5.2

[43] Christian H Bischof, Paul D Hovland, and Boyana Norris. On the implementation of automatic differentiation tools. *Higher-Order and Symbolic Computation*, 2008. 5.2.3

[44] Halil Bisgin, Zhichao Liu, Hong Fang, Xiaowei Xu, and Weida Tong. Mining fda drug labels using an unsupervised learning technique-topic modeling. In *BMC bioinformatics*, volume 12, page S11. BioMed Central, 2011. 6.2

[45] Halil Bisgin, Zhichao Liu, Reagan Kelly, Hong Fang, Xiaowei Xu, and Weida Tong. Investigating drug repositioning opportunities in fda drug labels through topic modeling. 13 (15):S6, 2012. 6.2

[46] Christopher M Bishop and Michael E Tipping. Bayesian regression and classification. *Nato Science Series sub Series III Computer And Systems Sciences*, 2003. 3

[47] David Blei and John Lafferty. Correlated topic models. In *Advances in neural information processing systems*, 2006. 3.1.1

[48] David M Blei and Michael I Jordan. Variational inference for Dirichlet process mixtures. *Bayesian analysis*, 2006. 3.2

[49] David M Blei, Andrew Y Ng, and Michael I Jordan. Latent dirichlet allocation. *Journal of machine Learning research*, 2003. 1.1, 1.3.1, 2.5, 5, 5.2.5

[50] Guillaume Bouchard. Efficient bounds for the softmax function, applications to inference in hybrid models. 2007. 3.1.2, 3.1.2, 3.1.6

[51] Stephanie LK Bowers, Thomas K Borg, and Troy A Baudino. The dynamics of fibroblast–myocyte–capillary interactions in the heart. *Annals of the New York Academy of Sciences*, 1188(1):143–152, 2010. 6.3

[52] S. Boyd, N. Parikh, E. Chu, B. Peleato, and J. Eckstein. Distributed optimization and statistical learning via alternating direction method of multipliers. *Foundations and Trends® in Machine Learning*, 2011. 1.2.1, 2.3, 2.4, 2.4.2, 6.4.1

[53] Stephen Boyd and Lieven Vandenberghe. *Convex optimization*. Cambridge university press, 2004. 2.1.3, 2.1.3, 2.2.2, 2.3.2, 2.3.2, 2.3.2

[54] John S Breese, David Heckerman, and Carl Kadie. Empirical analysis of predictive algorithms for collaborative filtering. In *Proceedings of the Fourteenth conference on Uncertainty in artificial intelligence*, pages 43–52. Morgan Kaufmann Publishers Inc., 1998. 5

[55] Leo Breiman. Random forests. *Machine Learning*, 2001. 3.1.5, 3.1.5

[56] Serhat S Bucak, Pavan Kumar Mallapragada, Rong Jin, and Anil K Jain. Efficient multi-label ranking for multi-class learning: application to object recognition. In *The IEEE International Conference on Computer Vision*, 2009. 6.3.3

[57] Serhat Selcuk Bucak, Rong Jin, and Anil K Jain. Multi-label learning with incomplete class assignments. In *IEEE Conference on Computer Vision and Pattern Recognition*, 2011. 6.3.3

[58] Christopher JC Burges. A tutorial on support vector machines for pattern recognition. *Data mining and knowledge discovery*, 1998. 3.1.5, 3.1.5

[59] Simon Byrne and Mark Girolami. Geodesic monte carlo on embedded manifolds. *Scandinavian Journal of Statistics*, 2013. 3.2.3, 3.2.3, 3.2.4

[60] Deng Cai and Xiaofei He. Manifold adaptive experimental design for text categorization. *IEEE Transactions on Knowledge and Data Engineering*, 2012. 2.5.3

[61] Deng Cai, Xiaofei He, and Jiawei Han. Document clustering using locality preserving indexing. *IEEE Transactions on Knowledge and Data Engineering*, 2005. 3.2.4

[62] Emmanuel Candes and Benjamin Recht. Exact matrix completion via convex optimization. *Communications of the ACM*, 2012. 2.1.1, 2.2.2

[63] Miguel A Carreira-Perpinán and Ramin Raziperchikolaei. An ensemble diversity approach to supervised binary hashing. In *Advances in Neural Information Processing Systems*, 2016. 2.2.4, 2.2.4, 2.2.4, 2.2.4, 2.2.4, 2.2.4, 6.1.1, 6.1.2

[64] Ricardo Cerri, Rodrigo C Barros, and André CPLF De Carvalho. Hierarchical multi-label

classification using local neural networks. *Journal of Computer and System Sciences*, 80 (1):39–56, 2014. 6.3.3

[65] Ricardo Cerri, Rodrigo C Barros, André CPLF de Carvalho, and Yaochu Jin. Reduction strategies for hierarchical multi-label classification in protein function prediction. *BMC bioinformatics*, 17(1):373, 2016. 6.3.3

[66] Arun Tejasvi Chaganty and Percy Liang. Spectral experts for estimating mixtures of linear regressions. In *International Conference on Machine Learning*, pages 1040–1048, 2013. 7.3

[67] Ciprian Chelba, Tomas Mikolov, Mike Schuster, Qi Ge, Thorsten Brants, Phillipp Koehn, and Tony Robinson. One billion word benchmark for measuring progress in statistical language modeling. *Conference of the International Speech Communication Association*, 2014. 5.2.5

[68] Danqi Chen, Jason Bolton, and Christopher D Manning. A thorough examination of the CNN/Daily mail reading comprehension task. *Annual Meeting of the Association for Computational Linguistics*, 2016. 2.1.4, 2.3.3

[69] Kan Chen, Jiang Wang, Liang-Chieh Chen, Haoyuan Gao, Wei Xu, and Ram Nevatia. ABC-CNN: An attention based convolutional neural network for visual question answering. *arXiv preprint arXiv:1511.05960*, 2015. 6.3.2, 6.3.3

[70] Liang-Chieh Chen, George Papandreou, Iasonas Kokkinos, Kevin Murphy, and Alan L Yuille. Semantic image segmentation with deep convolutional nets and fully connected CRFs. *International Conference on Learning Representations*, 2014. 6.3.3

[71] Liang-Chieh Chen, Yi Yang, Jiang Wang, Wei Xu, and Alan L Yuille. Attention to scale: Scale-aware semantic image segmentation. In *Proceedings of the IEEE Conference on Computer Vision and Pattern Recognition*, pages 3640–3649, 2016. 6.3.2, 6.3.2, 6.3.3

[72] Robert Chen, Hang Su, Mohammed Khalilia, Sizhe Lin, Yue Peng, Tod Davis, Daniel A Hirsh, Elizabeth Searles, Javier Tejedor-Sojo, Michael Thompson, et al. Cloud-based predictive modeling system and its application to asthma readmission prediction. In *AMIA Annual Symposium Proceedings*, 2015. 1.3.3

[73] Tianqi Chen, Mu Li, Yutian Li, Min Lin, Naiyan Wang, Minjie Wang, Tianjun Xiao, Bing Xu, Chiyuan Zhang, and Zheng Zhang. Mxnet: A flexible and efficient machine learning library for heterogeneous distributed systems. *NIPS 2015 Workshop*, 2015. 1.3.2, 5.2.5, 5.2.5, 5.3.2, 5.3.2

[74] Yong Chen, Hui Zhang, Yongxin Tong, and Ming Lu. Diversity regularized latent semantic match for hashing. *Neurocomputing*, 2017. 2.2, 2.2.4, 2.2.4, 2.2.4, 2.2.4, 2.2.4, 6.1.1, 6.1.2

[75] Yukun Chen, Hongxin Cao, Qiaozhu Mei, Kai Zheng, and Hua Xu. Applying active learning to supervised word sense disambiguation in MEDLINE. *Journal of the American Medical Informatics Association*, 2013. 1.3.3, 1.3.3

[76] Wei-Chen Cheng, Stanley Kok, Hoai Vu Pham, Hai Leong Chieu, and Kian Ming A Chai. Language modeling with sum-product networks. In *Fifteenth Annual Conference of the International Speech Communication Association*, 2014. 2.5.3

[77] Weiwei Cheng, Eyke Hüllermeier, and Krzysztof J Dembczynski. Bayes optimal multilabel classification via probabilistic classifier chains. In *International Conference on Machine Learning*, 2010. 6.3.3

[78] Trishul Chilimbi, Yutaka Suzue, Johnson Apacible, and Karthik Kalyanaraman. Project Adam: building an efficient and scalable deep learning training system. In *USENIX Symposium on Operating Systems Design and Implementation*, 2014. 1.3.2, 5, 5.1, 5.2, 5.2.1, 5.2.1, 5.3.1, 5.3.2, 5.3.2, 5.3.2

[79] Edward Choi, Mohammad Taha Bahadori, and Jimeng Sun. Doctor AI: Predicting clinical events via recurrent neural networks. *Machine Learning for Healthcare Conference*, 2015. 1.3.3

[80] Jan K Chorowski, Dzmitry Bahdanau, Dmitriy Serdyuk, Kyunghyun Cho, and Yoshua Bengio. Attention-based models for speech recognition. In *Advances in Neural Information Processing Systems*, 2015. 2.3.3

[81] Djork-Arné Clevert, Thomas Unterthiner, and Sepp Hochreiter. Fast and accurate deep network learning by exponential linear units (ELUs). *International Conference on Learning Representations*, 2016. 2.3.3, 2.5.3

[82] M. Cogswell, F. Ahmed, R. Girshick, L. Zitnick, and D. Batra. Reducing overfitting in deep networks by decorrelating representations. *International Conference on Learning Representations*, 2015. 1.3.1, 1.3.1, 2.1, 2.1.1, 2.1.4, 2.1.4, 2.1.4, 2.1.4, 2.1.4, 2.1.4, 2.2.4, 2.3.3, 2.5.3, 2.2.4, 2.2.4, 2.2.4, 2.2.4, 2.3.3, 2.3.3, 2.3.3, 2.5.3, 6.1.1, 6.1.2

[83] Thomas M Cover and Joy A Thomas. *Elements of information theory*. John Wiley & Sons, 2012. 2.1, 2.1.1, 2.1.1

[84] Steven P Crain, Shuang-Hong Yang, Hongyuan Zha, and Yu Jiao. Dialect topic modeling for improved consumer medical search. In *AMIA Annual Symposium Proceedings*, volume 2010, page 132. American Medical Informatics Association, 2010. 6.2

[85] Henggang Cui, Hao Zhang, Gregory R Ganger, Phillip B Gibbons, and Eric P Xing. Geeps: Scalable deep learning on distributed GPUs with a GPU-specialized parameter server. In *European Conference on Computer Systems*, 2016. 1.3.2, 5.2, 5.2.1

[86] Yiming Cui, Zhipeng Chen, Si Wei, Shijin Wang, Ting Liu, and Guoping Hu. Attention-over-attention neural networks for reading comprehension. *Annual Meeting of the Association for Computational Linguistics*, 2017. 2.1.4, 2.3.3

[87] Brianna A Da Silva and Mahesh Krishnamurthy. The alarming reality of medication error: a patient case and review of pennsylvania and national data. *Journal of community hospital internal medicine perspectives*, 6(4):31758, 2016. 1.1

[88] George Dahl, Abdel-rahman Mohamed, Geoffrey E Hinton, et al. Phone recognition with the mean-covariance restricted Boltzmann machine. In *Advances in neural information processing systems*, 2010. 2.3.3

[89] Bo Dai, Bo Xie, Niao He, Yingyu Liang, Anant Raj, Maria-Florina F Balcan, and Le Song. Scalable kernel methods via doubly stochastic gradients. In *Neural Information Processing Systems*, 2014. 1.2.1, 2.4, 2.4.2

[90] Michael Daniel and Martin A Makary. Medical errorthe third leading cause of death in the us. *Bmj*, 353(i2139):476636183, 2016. 1.1

[91] Abhishek Das, Harsh Agrawal, Larry Zitnick, Devi Parikh, and Dhruv Batra. Human attention in visual question answering: Do humans and deep networks look at the same regions? *Computer Vision and Image Understanding*, 2017. 6.3.3

[92] Jason V Davis, Brian Kulis, Prateek Jain, Suvrit Sra, and Inderjit S Dhillon. Information-theoretic metric learning. In *Proceedings of the 24th international conference on Machine learning*, 2007. 2.1.2, 2.1.4, 2.1.4, 2.1.4, 2.2.2, 2.2.4, 2.4.3, 2.5.1, 2.2.4, 2.2.4, 2.2.4, 2.2.4, 2.4.3, 6.1.1, 6.1.2

[93] Jeffrey Dean and Sanjay Ghemawat. MapReduce: simplified data processing on large clusters. *Communications of the ACM*, 2008. 1.3.2, 5

[94] Jeffrey Dean, Greg Corrado, Rajat Monga, Kai Chen, Matthieu Devin, Mark Mao, Andrew Senior, Paul Tucker, Ke Yang, Quoc V Le, et al. Large scale distributed deep networks. In *Advances in Neural Information Processing Systems*, 2012. 1.3.2, 5, 5.1, 5.2, 5.2.1, 1, 5.2.1, 5.3, 5.3.2

[95] Jia Deng, Wei Dong, Richard Socher, Li-Jia Li, Kai Li, and Li Fei-Fei. Imagenet: A large-scale hierarchical image database. In *IEEE Conference on Computer Vision and Pattern Recognition*. IEEE, 2009. 2.1.4, 2.4.3, 5, 5.3.2

[96] Jia Deng, Sanjeev Satheesh, Alexander C Berg, and Fei Li. Fast and balanced: Efficient label tree learning for large scale object recognition. In *Advances in Neural Information Processing Systems*, pages 567–575, 2011. 6.3.3

[97] Jia Deng, Jonathan Krause, Alexander C Berg, and Li Fei-Fei. Hedging your bets: Optimizing accuracy-specificity trade-offs in large scale visual recognition. In *IEEE Conference on Computer Vision and Pattern Recognition*, pages 3450–3457. IEEE, 2012. 6.3.3

[98] Jia Deng, Nan Ding, Yangqing Jia, Andrea Frome, Kevin Murphy, Samy Bengio, Yuan Li, Hartmut Neven, and Hartwig Adam. Large-scale object classification using label relation graphs. In *European Conference on Computer Vision*, pages 48–64. Springer, 2014. 6.3.3

[99] Amit Deshpande and Santosh Vempala. Adaptive sampling and fast low-rank matrix approximation. In *Approximation, Randomization, and Combinatorial Optimization. Algorithms and Techniques*, pages 292–303. Springer, 2006. 5.2.1

[100] Inderjit S Dhillon and Joel A Tropp. Matrix nearness problems with bregman divergences. *SIAM Journal on Matrix Analysis and Applications*, 29(4):1120–1146, 2007. 1.2.1, 2.2.1, 2.4

[101] Bhuwan Dhingra, Hanxiao Liu, William W Cohen, and Ruslan Salakhutdinov. Gated-attention readers for text comprehension. *Annual Meeting of the Association for Computational Linguistics*, 2017. 2.1.4, 2.3.3

[102] Bhuwan Dhingra, Zhilin Yang, William W Cohen, and Ruslan Salakhutdinov. Linguistic knowledge as memory for recurrent neural networks. *arXiv preprint arXiv:1703.02620*, 2017. 2.1.4, 2.3.3

[103] Son Doan, Ko-Wei Lin, Mike Conway, Lucila Ohno-Machado, Alex Hsieh,

Stephanie Feudjio Feupe, Asher Garland, Mindy K Ross, Xiaoqian Jiang, Seena Farzaneh, et al. PhenDisco: phenotype discovery system for the database of genotypes and phenotypes. *Journal of the American Medical Informatics Association*, 2014. 1.3.3

[104] Jeff Donahue, Philipp Krähenbühl, and Trevor Darrell. Adversarial feature learning. *arXiv preprint arXiv:1605.09782*, 2016. 6.4.3

[105] Finale Doshi-Velez and Zoubin Ghahramani. Accelerated sampling for the Indian buffet process. In *International conference on machine learning*, 2009. 3.2.4

[106] Shahram Ebadollahi, Jimeng Sun, David Gotz, Jianying Hu, Daby Sow, Chalapathy Neti, et al. Predicting patients trajectory of physiological data using temporal trends in similar patients: A system for near-term prognostics. In *AMIA Annual Symposium*, 2010. 1.3.3, 6.1

[107] Andre Esteva, Brett Kuprel, Roberto A Novoa, Justin Ko, Susan M Swetter, Helen M Blau, and Sebastian Thrun. Dermatologist-level classification of skin cancer with deep neural networks. *Nature*, 542(7639):115–118, 2017. 6.3.3

[108] Konstantinos P Exarchos, Themis P Exarchos, Christos V Bourantas, Michail I Papafaklis, Katerina K Naka, Lampros K Michalis, Oberdan Parodi, and Dimitrios I Fotiadis. Prediction of coronary atherosclerosis progression using dynamic Bayesian networks. In *International Conference of the IEEE Engineering in Medicine and Biology Society*, 2013. 1.3.3

[109] Richárd Farkas and György Szarvas. Automatic construction of rule-based ICD-9-CM coding systems. *BMC bioinformatics*, 2008. 6.4

[110] Li Fei-Fei, Rob Fergus, and Pietro Perona. Learning generative visual models from few training examples: An incremental bayesian approach tested on 101 object categories. *Computer vision and Image understanding*, 2007. 3.2.4

[111] Thomas S Ferguson. A bayesian analysis of some nonparametric problems. *The annals of statistics*, pages 209–230, 1973. 1.2.1, 3, 3.2, 3.2

[112] Pius Franz, Albrecht Zaiss, Stefan Schulz, Udo Hahn, and Rüdiger Klar. Automated coding of diagnoses–three methods compared. In *Proceedings of the AMIA Symposium*, page 250. American Medical Informatics Association, 2000. 6.4.2, 6.4.2, 6.4.3

[113] Jerome Friedman, Trevor Hastie, and Robert Tibshirani. Sparse inverse covariance estimation with the graphical lasso. *Biostatistics*, 9(3):432–441, 2008. 2.5

[114] Xiping Fu, Brendan McCane, Steven Mills, and Michael Albert. Nokmeans: Non-orthogonal k-means hashing. In *Asian Conference on Computer Vision*, 2014. 2.2.4, 6.1.1

[115] Yarin Gal and Zoubin Ghahramani. A theoretically grounded application of dropout in recurrent neural networks. In *Advances in Neural Information Processing Systems*, pages 1019–1027, 2016. 2.5.3

[116] Mikel Galar, Alberto Fernandez, Edurne Barrenechea, Humberto Bustince, and Francisco Herrera. A review on ensembles for the class imbalance problem: bagging-, boosting-, and hybrid-based approaches. *IEEE Transactions on Systems, Man, and Cybernetics, Part*

C (Applications and Reviews), 2012. 2.2.4, 2.2.4, 2.2.4, 2.2.4, 6.1.1, 6.1.2

[117] Mark JF Gales. Maximum likelihood linear transformations for HMM-based speech recognition. *Computer speech & language*, 12(2):75–98, 1998. 2.3.3

[118] Yaroslav Ganin and Victor Lempitsky. Unsupervised domain adaptation by backpropagation. In *International Conference on Machine Learning*, pages 1180–1189, 2015. 6.4.3

[119] Yaroslav Ganin, Evgeniya Ustinova, Hana Ajakan, Pascal Germain, Hugo Larochelle, François Laviolette, Mario Marchand, and Victor Lempitsky. Domain-adversarial training of neural networks. *The Journal of Machine Learning Research*, 17(1):2096–2030, 2016. 6.3.1

[120] Shenghua Gao, Ivor Wai-Hung Tsang, and Liang-Tien Chia. Kernel sparse representation for image classification and face recognition. In *European Conference on Computer Vision*, 2010. 1.2.1, 2.4, 2.4.1, 2.4.1, 2.4.3, 2.4.3

[121] Tianshi Gao and Daphne Koller. Discriminative learning of relaxed hierarchy for large-scale visual recognition. In *The IEEE International Conference on Computer Vision*, pages 2072–2079. IEEE, 2011. 6.3.3

[122] Tiezheng Ge, Kaiming He, and Jian Sun. Graph cuts for supervised binary coding. In *European Conference on Computer Vision*, 2014. 2.2, 2.2.4, 6.1.1

[123] Xin Geng and Longrun Luo. Multilabel ranking with inconsistent rankers. In *IEEE Conference on Computer Vision and Pattern Recognition*, 2014. 6.3.3

[124] Marian George and Christian Floerkemeier. Recognizing products: A per-exemplar multi-label image classification approach. In *European Conference on Computer Vision*, 2014. 6.3.3

[125] Athinodoros S. Georghiades, Peter N. Belhumeur, and David J. Kriegman. From few to many: Illumination cone models for face recognition under variable lighting and pose. *IEEE transactions on pattern analysis and machine intelligence*, 23(6):643–660, 2001. 3.2.4

[126] Nadia Ghamrawi and Andrew McCallum. Collective multi-label classification. In *ACM International Conference on Information and Knowledge Management*, 2005. 6.3.3

[127] Walter R Gilks. *Markov chain Monte Carlo*. Wiley Online Library, 2005. 1.2.1, 3, 3.1, 3.1.2, 3.1.6

[128] Walter R Gilks and Pascal Wild. Adaptive rejection sampling for Gibbs sampling. *Applied Statistics*, 1992. 3.2.3

[129] Mark Girolami and Ben Calderhead. Riemann manifold langevin and hamiltonian monte carlo methods. *Journal of the Royal Statistical Society: Series B (Statistical Methodology)*, 2011. 1.2.1, 3.2, 3.2.3, 3.2.3

[130] Glenn T Gobbel, Jennifer Garvin, Ruth Reeves, Robert M Cronin, Julia Heavirland, Jenifer Williams, Allison Weaver, Shrimalini Jayaramaraja, Dario Giuse, Theodore Speroff, et al. Assisted annotation of medical free text using RapTAT. *Journal of the American Medical Informatics Association*, 2014. 1.3.3

[131] Ary L Goldberger, Luis AN Amaral, Leon Glass, Jeffrey M Hausdorff, Plamen Ch Ivanov, Roger G Mark, Joseph E Mietus, George B Moody, Chung-Kang Peng, and H Eugene Stanley. Physiobank, physiotoolkit, and physionet. *Circulation*, 2000. 2.2.4, 6.1.1

[132] Joseph E Gonzalez, Yucheng Low, Haijie Gu, Danny Bickson, and Carlos Guestrin. Powergraph: Distributed graph-parallel computation on natural graphs. In *USENIX Symposium on Operating Systems Design and Implementation*, 2012. 1.3.2, 5

[133] Roberto Gonzalez-Amaro, Donato Alarcon-Segovia, Jorge Alcocer-Varela, Lino Diaz De Leon, and Yvonne Rosenstein. Mononuclear cell-fibroblast interactions in scleroderma. *Clinical immunology and immunopathology*, 46(3):412–420, 1988. 6.3

[134] Ian Goodfellow, Jean Pouget-Abadie, Mehdi Mirza, Bing Xu, David Warde-Farley, Sherjil Ozair, Aaron Courville, and Yoshua Bengio. Generative adversarial nets. In *Advances in neural information processing systems*, pages 2672–2680, 2014. 1.2.3, 6.3, 6.3.1, 6.4.1, 6.4.3

[135] Ian J Goodfellow, David Warde-Farley, Mehdi Mirza, Aaron Courville, and Yoshua Bengio. Maxout networks. *Proceedings of the 30th International Conference on Machine Learning*, 2013. 2.3.3, 2.5.3

[136] Siddharth Gopal and Yiming Yang. Distributed training of large-scale logistic models. In *International Conference on Machine Learning*, 2013. 5, 5.2.5

[137] Rudolf Gorenflo, Yuri Luchko, and Francesco Mainardi. Analytical properties and applications of the Wright function. *Fractional Calculus and Applied Analysis*, 1999. 2.2.3, 2.4.2, 2.4.4

[138] Benjamin Graham. Fractional max-pooling. *arXiv preprint arXiv:1412.6071*, 2014. 2.3.3, 2.5.3

[139] Alex Graves, Abdel-rahman Mohamed, and Geoffrey Hinton. Speech recognition with deep recurrent neural networks. In *Ieee international conference on Acoustics, speech and signal processing*, 2013. 2.3.3, 2.3.3

[140] Gregory Griffin and Pietro Perona. Learning and using taxonomies for fast visual categorization. In *IEEE Conference on Computer Vision and Pattern Recognition*, pages 1–8. IEEE, 2008. 6.3.3

[141] Gregory Griffin, Alex Holub, and Pietro Perona. Caltech-256 object category dataset. 2007. 2.3.3, 2.4.3

[142] Thomas Griffiths and Zoubin Ghahramani. Infinite latent feature models and the Indian buffet process. In *Advances in Neural Information Processing Systems*, 2005. 3.2, 3.2, 3.2.2, 3.2.3, 3.2.3, 3.2.4, 3.2.4, 3.2.4

[143] Thomas L Griffiths and Zoubin Ghahramani. The indian buffet process: An introduction and review. *Journal of Machine Learning Research*, 12(Apr):1185–1224, 2011. 1.2.1, 3.2, 3.2.2, 3.2.3

[144] Thomas L Griffiths, Michael I Jordan, Joshua B Tenenbaum, and David M Blei. Hierarchical topic models and the nested chinese restaurant process. In *Advances in neural information processing systems*, pages 17–24, 2004. 7.3

[145] William Gropp, Ewing Lusk, Nathan Doss, and Anthony Skjellum. A high-performance, portable implementation of the MPI message passing interface standard. *Parallel computing*, 1996. 5.2.4

[146] Matthieu Guillaumin, Jakob Verbeek, and Cordelia Schmid. Is that you? metric learning approaches for face identification. In *IEEE International Conference on Computer Vision*. IEEE, 2009. 2.1.2, 2.1.4, 2.1.4, 2.1.4, 2.2.4, 2.4.1, 2.4.3, 2.5.1, 2.2.4, 2.2.4, 2.2.4, 2.2.4, 2.4.3, 6.1.1, 6.1.2

[147] Yuhong Guo and Suicheng Gu. Multi-label classification using conditional dependency networks. In *International Joint Conference on Artificial Intelligence*, 2011. 6.3.3

[148] Bernhard Haeupler. Simple, fast and deterministic gossip and rumor spreading. *Journal of the ACM*, 62(6):47, 2015. 5.2.5

[149] Yoni Halpern, Steven Horng, Youngduck Choi, and David Sontag. Electronic medical record phenotyping using the anchor and learn framework. *Journal of the American Medical Informatics Association*, 2016. 1.3.3

[150] Yoni Halpern, Steven Horng, and David Sontag. Clinical tagging with joint probabilistic models. *Machine Learning for Healthcare Conference*, 2016. 1.3.3

[151] Bharath Hariharan, Lihi Zelnik-Manor, Manik Varma, and Svn Vishwanathan. Large scale max-margin multi-label classification with priors. In *International Conference on Machine Learning*, 2010. 6.3.3

[152] W Keith Hastings. Monte carlo sampling methods using markov chains and their applications. *Biometrika*, 1970. 3.2.3

[153] Kaiming He, Xiangyu Zhang, Shaoqing Ren, and Jian Sun. Deep residual learning for image recognition. In *Proceedings of the IEEE Conference on Computer Vision and Pattern Recognition*, pages 770–778, 2016. 2.3.3, 2.5.3, 6.3.2

[154] Karl Moritz Hermann, Tomas Kocisky, Edward Grefenstette, Lasse Espeholt, Will Kay, Mustafa Suleyman, and Phil Blunsom. Teaching machines to read and comprehend. In *Advances in Neural Information Processing Systems*, 2015. 2.1.2, 2.1.4, 2.3.3, 2.3.3, 2.3.3

[155] Tommy Hielscher, Myra Spiliopoulou, Henry Völzke, and Jens-Peter Kühn. Using participant similarity for the classification of epidemiological data on hepatic steatosis. In *IEEE 27th International Symposium on Computer-Based Medical Systems*, pages 1–7. IEEE, 2014. 6.1

[156] Nicholas J Higham and Hyun-Min Kim. Solving a quadratic matrix equation by Newton's method with exact line searches. *SIAM Journal on Matrix Analysis and Applications*, 2001. 2.4.4

[157] Felix Hill, Antoine Bordes, Sumit Chopra, and Jason Weston. The Goldilocks principle: Reading children's books with explicit memory representations. *International Conference on Learning Representations*, 2015. 2.3.3

[158] Anika L Hines, Marguerite L Barrett, H Joanna Jiang, and Claudia A Steiner. Conditions with the largest number of adult hospital readmissions by payer, 2011: statistical brief# 172. 2014. 1.1

[159] Geoffrey Hinton, Li Deng, Dong Yu, George E Dahl, Abdel-rahman Mohamed, Navdeep Jaitly, Andrew Senior, Vincent Vanhoucke, Patrick Nguyen, Tara N Sainath, et al. Deep neural networks for acoustic modeling in speech recognition: The shared views of four research groups. *IEEE Signal Processing Magazine*, 2012. 2.3.3

[160] Geoffrey E Hinton and Ruslan R Salakhutdinov. Reducing the dimensionality of data with neural networks. *Science*, 2006. 3.1.5, 3.1.5

[161] Joyce C Ho, Joydeep Ghosh, Steve R Steinhubl, Walter F Stewart, Joshua C Denny, Bradley A Malin, and Jimeng Sun. Limestone: High-throughput candidate phenotype generation via tensor factorization. *Journal of biomedical informatics*, 2014. 1.3.3

[162] Qirong Ho, James Cipar, Henggang Cui, Seunghak Lee, Jin Kyu Kim, Phillip B Gibbons, Garth A Gibson, Greg Ganger, and Eric Xing. More effective distributed ML via a stale synchronous parallel parameter server. In *Advances in Neural Information Processing Systems*, 2013. 1.3.2, 5, 5.1, 5.2, 5.3.2, 5.4

[163] Sepp Hochreiter and Jürgen Schmidhuber. Long short-term memory. *Neural computation*, 9(8):1735–1780, 1997. 1.2.1, 1.3.3, 2.1, 2.1.2, 2.1.2, 2.3.3, 2.5.1, 2.5.3, 5.2.5, 6.3, 6.3.1

[164] Matthew D Hoffman, David M Blei, Chong Wang, and John Paisley. Stochastic variational inference. *Journal of Machine Learning Research*, 2013. 3.1.2

[165] Ulrich Hoffmann, Jean-Marc Vesin, Touradj Ebrahimi, and Karin Diserens. An efficient p300-based brain–computer interface for disabled subjects. *Journal of Neuroscience methods*, 167(1):115–125, 2008. 3.2.4

[166] Saihui Hou, Yushan Feng, and Zilei Wang. VegFru: A domain-specific dataset for fine-grained visual categorization. In *Proceedings of the IEEE Conference on Computer Vision and Pattern Recognition*, pages 541–549, 2017. 6.3.2, 6.3.2, 6.3.3, 6.4.2

[167] Cho-Jui Hsieh, Kai-Wei Chang, Chih-Jen Lin, S Sathiya Keerthi, and Sellamanickam Sundararajan. A dual coordinate descent method for large-scale linear SVM. In *International conference on machine learning*, 2008. 5, 5.1

[168] Daniel Hsu, Sham M Kakade, and Tong Zhang. A spectral algorithm for learning hidden markov models. *Journal of Computer and System Sciences*, 78(5):1460–1480, 2012. 7.3

[169] Gao Huang, Zhuang Liu, Kilian Q Weinberger, and Laurens van der Maaten. Densely connected convolutional networks. *IEEE Conference on Computer Vision and Pattern Recognition*, 2017. 2.3.3, 2.5.3

[170] Hakan Inan, Khashayar Khosravi, and Richard Socher. Tying word vectors and word classifiers: A loss framework for language modeling. *International Conference on Learning Representations*, 2017. 2.5.3

[171] Mohammad Tariqul Islam, Md Abdul Aowal, Ahmed Tahseen Minhaz, and Khalid Ashraf. Abnormality detection and localization in chest x-rays using deep convolutional neural networks. *arXiv preprint arXiv:1705.09850*, 2017. 6.3.2, 6.3.2, 6.3.3

[172] T Jaakkola and Michael I Jordan. A variational approach to Bayesian logistic regression models and their extensions. In *Sixth International Workshop on Artificial Intelligence and Statistics*, 1997. 3

[173] Christopher H Jackson, Linda D Sharples, Simon G Thompson, Stephen W Duffy, and Elisabeth Couto. Multistate Markov models for disease progression with classification error. *Journal of the Royal Statistical Society: Series D (The Statistician)*, 2003. 1.3.3

[174] Laurent Jacob, Guillaume Obozinski, and Jean-Philippe Vert. Group lasso with overlap and graph lasso. In *Proceedings of the 26th international conference on machine learning*, pages 433–440, 2009. 2.5

[175] Laurent Jacob, Jean-philippe Vert, and Francis R Bach. Clustered multi-task learning: A convex formulation. In *Advances in neural information processing systems*, pages 745–752, 2009. 7.3

[176] P. Jain, B. Kulis, J. Davis, and I. Dhillon. Metric and kernel learning using a linear transformation. *Journal of machine Learning research*, 2012. 2.4, 2.4.1, 2.4.1, 2.4.3, 2.4.3

[177] Amin Jalali, Lin Xiao, and Maryam Fazel. Variational Gram functions: Convex analysis and optimization. *Siam Journal on Optimization*, 2017. 1.3.1, 2.2.4, 2.2.4, 2.2.4, 2.2.4, 2.2.4, 6.1.1, 6.1.2

[178] Andrew Janowczyk and Anant Madabhushi. Deep learning for digital pathology image analysis: A comprehensive tutorial with selected use cases. *Journal of pathology informatics*, 7, 2016. 6.3.3

[179] Kalervo Järvelin and Jaana Kekäläinen. Cumulated gain-based evaluation of ir techniques. *ACM Transactions on Information Systems*, 20(4):422–446, 2002. 6.4.2

[180] Shuiwang Ji, Lei Tang, Shipeng Yu, and Jieping Ye. Extracting shared subspace for multi-label classification. In *ACM SIGKDD International Conference on Knowledge Discovery and Data Mining*, 2008. 6.3.3

[181] Yangqing Jia, Joshua T Abbott, Joseph L Austerweil, Thomas Griffiths, and Trevor Darrell. Visual concept learning: Combining machine vision and bayesian generalization on concept hierarchies. In *Advances in Neural Information Processing Systems*, pages 1842–1850, 2013. 6.3.3

[182] Yangqing Jia, Evan Shelhamer, Jeff Donahue, Sergey Karayev, Jonathan Long, Ross Girshick, Sergio Guadarrama, and Trevor Darrell. Caffe: Convolutional architecture for fast feature embedding. In *Proceedings of the 22nd ACM international conference on Multimedia*, pages 675–678. ACM, 2014. 5.3.2

[183] Liping Jing, Liu Yang, Jian Yu, and Michael K Ng. Semi-supervised low-rank mapping learning for multi-label classification. In *IEEE Conference on Computer Vision and Pattern Recognition*, 2015. 6.3.3

[184] A. Johnson, T. Pollard, L. Shen, L. Lehman, M. Feng, M. Ghassemi, B. Moody, P. Szolovits, L. Celi, and R. Mark. Mimic-iii, a freely accessible critical care database. *Scientific data*, 3, 2016. 2.1.4, 2.2.4, 2.4.3, 6.1.1, 6.4.2

[185] Ian Jolliffe. *Principal component analysis*. Wiley Online Library, 2002. 2.1, 2.1.1

[186] Michael I Jordan and Robert A Jacobs. Hierarchical mixtures of experts and the EM algorithm. *Neural computation*, 1994. 3.1.4

[187] Shalmali Joshi, Suriya Gunasekar, David Sontag, and Joydeep Ghosh. Identifiable pheno-

typing using constrained non-negative matrix factorization. *Machine Learning for Healthcare Conference*, 2016. 1.3.3

[188] Rudolf Kadlec, Martin Schmid, Ondrej Bajgar, and Jan Kleindienst. Text understanding with the attention sum reader network. *Annual Meeting of the Association for Computational Linguistics*, 2016. 2.1.4, 2.3.3

[189] Atsushi Kanehira and Tatsuya Harada. Multi-label ranking from positive and unlabeled data. In *IEEE Conference on Computer Vision and Pattern Recognition*, 2016. 6.3.3

[190] Feng Kang, Rong Jin, and Rahul Sukthankar. Correlated label propagation with application to multi-label learning. In *IEEE Conference on Computer Vision and Pattern Recognition*, 2006. 6.3.3

[191] Ramakanth Kavuluru, Sifei Han, and Daniel Harris. Unsupervised extraction of diagnosis codes from emrs using knowledge-based and extractive text summarization techniques. In *Canadian conference on artificial intelligence*, pages 77–88. Springer, 2013. 6.4.2, 6.4.2, 6.4.3

[192] Ramakanth Kavuluru, Anthony Rios, and Yuan Lu. An empirical evaluation of supervised learning approaches in assigning diagnosis codes to electronic medical records. *Artificial intelligence in medicine*, 65(2):155–166, 2015. 6.4.2, 6.4.2, 6.4.3

[193] Seyoung Kim and Eric P Xing. Tree-guided group lasso for multi-response regression with structured sparsity, with an application to eqtl mapping. *Annals of Applied Statistics*, 6(3):1095–1117, 2012. 2.5.3

[194] Yoon Kim, Yacine Jernite, David Sontag, and Alexander M Rush. Character-aware neural language models. In *Thirtieth AAAI Conference on Artificial Intelligence*, 2016. 2.5.3

[195] Ross Kindermann, James Laurie Snell, et al. *Markov random fields and their applications*. American Mathematical Society Providence, 1980. 3.1.1

[196] Diederik Kingma and Jimmy Ba. Adam: A method for stochastic optimization. *International Conference for Learning Representations*, 2015. 6.4.2

[197] Sosuke Kobayashi, Ran Tian, Naoaki Okazaki, and Kentaro Inui. Dynamic entity representation with max-pooling improves machine reading. In *Annual Conference of the North American Chapter of the Association for Computational Linguistics: Human Language Technologies*, 2016. 2.1.4, 2.3.3

[198] Daphne Koller and Nir Friedman. *Probabilistic graphical models: principles and techniques*. MIT press, 2009. 3.1, 3.1.1, 3.2.1, 3.2.1

[199] Bevan Koopman, Guido Zuccon, Anthony Nguyen, Anton Bergheim, and Narelle Grayson. Automatic icd-10 classification of cancers from free-text death certificates. *International journal of medical informatics*, 84(11):956–965, 2015. 6.4.2, 6.4.2, 6.4.3

[200] M Kostinger, Martin Hirzer, Paul Wohlhart, Peter M Roth, and Horst Bischof. Large scale metric learning from equivalence constraints. In *IEEE Conference on Computer Vision and Pattern Recognition*, 2012. 2.2.4, 2.2.4, 2.2.4, 2.2.4, 2.2.4, 6.1.1, 6.1.2

[201] Philipp Krähenbühl and Vladlen Koltun. Efficient inference in fully connected CRFs with gaussian edge potentials. In *Advances in Neural Information Processing Systems*, pages

109–117, 2011. 6.3.3

[202] Jonathan Krause, Michael Stark, Jia Deng, and Li Fei-Fei. 3d object representations for fine-grained categorization. In *ICCV Workshops*, 2013. 2.1.4, 2.2.4, 2.4.3

[203] Alex Krizhevsky, Ilya Sutskever, and Geoffrey E Hinton. Imagenet classification with deep convolutional neural networks. In *Advances in neural information processing systems*, pages 1097–1105, 2012. 1.2.2, 2.3.3, 5.3, 5.3.2

[204] Alex Kulesza and Ben Taskar. Determinantal point processes for machine learning. *Foundations and Trends in Machine Learning*, 2012. 1.3.1, 1.3.1, 2.1, 2.1.4, 2.2.1, 2.2.4, 2.3.3, 3, 3.1, 3.1.5, 3.2.1, 6.1.1

[205] Alex Kulesza and Ben Taskar. Learning determinantal point processes. *The Conference on Uncertainty in Artificial Intelligence*, 2012. 6.3.2

[206] Brian Kulis, Mátyás A Sustik, and Inderjit S Dhillon. Low-rank kernel learning with bregman matrix divergences. *Journal of Machine Learning Research*, 10:341–376, 2009. 2.1.1, 2.2, 2.2.1

[207] Abhimanu Kumar, Alex Beutel, Qirong Ho, and Eric P Xing. Fugue: Slow-worker-agnostic distributed learning for big models on big data. In *International Conference on Artificial Intelligence and Statistics*, 2014. 1.2.3, 5.2.5, 5.2.5, 6.2, 6.2, 6.2

[208] Ashnil Kumar, Jinman Kim, David Lyndon, Michael Fulham, and Dagan Feng. An ensemble of fine-tuned convolutional neural networks for medical image classification. *IEEE journal of biomedical and health informatics*, 21(1):31–40, 2017. 6.3.3

[209] Ludmila I Kuncheva and Christopher J Whitaker. Measures of diversity in classifier ensembles and their relationship with the ensemble accuracy. *Machine learning*, 2003. 1.3.1

[210] Dee Lang. Consultant report-natural language processing in the health care industry. *Cincinnati Children's Hospital Medical Center, Winter*, 2007. 6.4

[211] Leah S Larkey and W Bruce Croft. Combining classifiers in text categorization. In *Proceedings of the 19th annual international ACM SIGIR conference on Research and development in information retrieval*, pages 289–297. ACM, 1996. 6.4.2, 6.4.2, 6.4.3

[212] Svetlana Lazebnik, Cordelia Schmid, and Jean Ponce. Beyond bags of features: Spatial pyramid matching for recognizing natural scene categories. In *IEEE Conference on Computer Vision and Pattern Recognition*, volume 2, pages 2169–2178, 2006. 2.3.3, 2.4.3, 2.4.3, 3.2.4

[213] Quoc V Le, Jiquan Ngiam, Zhenghao Chen, Daniel Chia, Pang Wei Koh, and Andrew Y Ng. Tiled convolutional neural networks. In *Neural Information Processing Systems*, 2010. 2.3.2, 2.3.3

[214] Quoc V Le, Marc'Aurelio Ranzato, Rajat Monga, Matthieu Devin, Kai Chen, Greg S Corrado, Jeff Dean, and Andrew Y Ng. Building high-level features using large scale unsupervised learning. In *Proceedings of the 29th International Conference on Machine Learning*, pages 507–514, 2012. 5.2.1, 5.3.2, 5.3.2, 5.3.2

[215] Guy Lebanon. *Riemannian geometry and statistical machine learning*. 7.3

[216] Michel Ledoux and Michel Talagrand. *Probability in Banach Spaces*. Springer, 1991. 4.3.2

[217] Chen-Yu Lee, Saining Xie, Patrick Gallagher, Zhengyou Zhang, and Zhuowen Tu. Deeply-supervised nets. In *Artificial Intelligence and Statistics*, pages 562–570, 2015. 2.3.3, 2.5.3

[218] Daniel D Lee and H Sebastian Seung. Learning the parts of objects by non-negative matrix factorization. *Nature*, 1999. 5, 5.1

[219] Joon Lee, David M Maslove, and Joel A Dubin. Personalized mortality prediction driven by electronic medical data and a patient similarity metric. *PloS one*, 10(5), 2015. 6.1

[220] David D Lewis, Yiming Yang, Tony G Rose, and Fan Li. Rcv1: A new benchmark collection for text categorization research. *Journal of Machine Learning Research*, 2004. 3.1.5

[221] Cheng Li, Bingyu Wang, Virgil Pavlu, and Javed Aslam. Conditional Bernoulli mixtures for multi-label classification. In *International Conference on Machine Learning*, 2016. 6.3.3

[222] Hao Li, Asim Kadav, Erik Kruus, and Cristian Ungureanu. MALT: distributed data-parallelism for existing ML applications. In *European Conference on Computer Systems*, 2015. 1.3.2, 5, 5.1, 5.2.1, 5.2.5

[223] Jianxin Li, Haoyi Zhou, Pengtao Xie, and Yingchun Zhang. Improving the generalization performance of multi-class SVM via angular regularization. *International Joint Conference on Artificial Intelligence*, 2017. 1.1

[224] Li-Jia Li and Li Fei-Fei. What, where and who? classifying events by scene recognition. In *International Conference on Computer Vision*, 2007. 2.3.3, 2.4.3

[225] Li-Jia Li, Chong Wang, Yongwhan Lim, David M Blei, and Li Fei-Fei. Building and using a semantivisual image hierarchy. In *IEEE Conference on Computer Vision and Pattern Recognition*, pages 3336–3343. IEEE, 2010. 6.3.3

[226] Mu Li, David G Andersen, Jun Woo Park, Alexander J Smola, Amr Ahmed, Vanja Josifovski, James Long, Eugene J Shekita, and Bor-Yiing Su. Scaling distributed machine learning with the parameter server. In *USENIX Symposium on Operating Systems Design and Implementation*, 2014. 1.2.2, 1.3.2, 5, 5.2, 5.2.1, 1, 5.2.1, 5.2.5, 5.3

[227] Qiang Li, Maoying Qiao, Wei Bian, and Dacheng Tao. Conditional graphical lasso for multi-label image classification. In *IEEE Conference on Computer Vision and Pattern Recognition*, 2016. 6.3.3

[228] Xin Li, Feipeng Zhao, and Yuhong Guo. Conditional restricted Boltzmann machines for multi-label learning with incomplete labels. In *International Conference on Artificial Intelligence and Statistics*, 2015. 6.3.3

[229] Min Lin, Qiang Chen, and Shuicheng Yan. Network in network. *International Conference on Learning Representations*, 2014. 2.3.3, 2.5.3

[230] Geert Litjens, Thijs Kooi, Babak Ehteshami Bejnordi, Arnaud Arindra Adiyoso Setio, Francesco Ciompi, Mohsen Ghafoorian, Jeroen AWM van der Laak, Bram van Ginneken,

and Clara I Sánchez. A survey on deep learning in medical image analysis. *Medical Image Analysis*, 2017. 6.3.3

[231] Baoyuan Liu, Fereshteh Sadeghi, Marshall Tappen, Ohad Shamir, and Ce Liu. Probabilistic label trees for efficient large scale image classification. In *Proceedings of the IEEE conference on computer vision and pattern recognition*, pages 843–850, 2013. 6.3.3

[232] Jiuxing Liu, Amith R Mamidala, and Dhabaleswar K Panda. Fast and scalable MPI-level broadcast using InfiniBand's hardware multicast support. In *Parallel and Distributed Processing Symposium*, 2004. 5.2.4

[233] Wei Liu, Steven Hoi, and Jianzhuang Liu. Output regularized metric learning with side information. *European conference on computer vision*, 2008. 2.2.4, 2.2.4, 2.2.4, 2.2.4, 2.2.4, 2.2.4, 6.1.1, 6.1.2

[234] Wei Liu, Cun Mu, Rongrong Ji, Shiqian Ma, John R Smith, and Shih-Fu Chang. Low-rank similarity metric learning in high dimensions. In *AAAI Conference on Artificial Intelligence*, 2015. 2.2.4, 2.2.4, 2.2.4, 2.2.4, 2.2.4, 6.1.1, 6.1.2

[235] Wyatt Lloyd, Michael J. Freedman, Michael Kaminsky, and David G. Andersen. Stronger semantics for low-latency geo-replicated storage. In *the 10th USENIX Symposium on Networked Systems Design and Implementation*, pages 313–328. USENIX, 2013. 5.3.2

[236] David G Lowe. Object recognition from local scale-invariant features. In *The proceedings of the seventh IEEE international conference on Computer vision*, volume 2, pages 1150–1157. Ieee, 1999. 3.1.5

[237] David G Lowe. Distinctive image features from scale-invariant keypoints. *International Journal of Computer Vision*, 2004. 2.3.3, 2.4.3, 3.2.4

[238] Liang Lu, Lingpeng Kong, Chris Dyer, Noah A Smith, and Steve Renals. Segmental recurrent neural networks for end-to-end speech recognition. *Interspeech*, 2016. 2.3.3

[239] Liang Lu, Lingpeng Kong, Chris Dyer, and Noah A Smith. Multi-task learning with CTC and segmental CRF for speech recognition. *Interspeech*, 2017. 2.3.3

[240] Anne E Magurran. *Measuring biological diversity*. John Wiley & Sons, 2013. 2.1

[241] Grzegorz Malewicz, Matthew H Austern, Aart JC Bik, James C Dehnert, Ilan Horn, Naty Leiser, and Grzegorz Czajkowski. Pregel: a system for large-scale graph processing. In *ACM SIGMOD International Conference on Management of data*, 2010. 1.3.2

[242] Jonathan Malkin and Jeff Bilmes. Ratio semi-definite classifiers. In *IEEE International Conference on Acoustics, Speech and Signal Processing*, pages 4113–4116. IEEE, 2008. 1.3.1, 1.3.1, 2.1, 2.1.1, 2.1.4, 2.1.4, 2.1.4, 2.1.4, 2.1.4, 2.1.4, 2.2.4, 2.3.3, 2.2.4, 2.2.4, 2.2.4, 2.2.4, 6.1.1, 6.1.2

[243] Christopher D Manning, Prabhakar Raghavan, Hinrich Schütze, et al. *Introduction to information retrieval*, volume 1. 2008. 2.2.4, 6.1.1

[244] Mitchell P Marcus, Mary Ann Marcinkiewicz, and Beatrice Santorini. Building a large annotated corpus of english: The penn treebank. *Computational linguistics*, 19(2):313–330, 1993. 2.5.3

[245] Kanti V Mardia and Peter E Jupp. *Directional statistics*, volume 494. John Wiley & Sons, 2009. 3.1, 3.1.1, 3.1.2

[246] Zelda Mariet and Suvrit Sra. Diversity networks. *International Conference on Learning Representations*, 2015. 1.3.1

[247] Marcin Marszalek and Cordelia Schmid. Semantic hierarchies for visual object recognition. In *IEEE Conference on Computer Vision and Pattern Recognition*, pages 1–7. IEEE, 2007. 6.3.3

[248] Marcin Marszałek and Cordelia Schmid. Constructing category hierarchies for visual recognition. In *European Conference on Computer Vision*, pages 479–491. Springer, 2008. 6.3.3

[249] Aleix M Martínez and Avinash C Kak. Pca versus lda. *IEEE transactions on pattern analysis and machine intelligence*, 23(2):228–233, 2001. 3.2.4

[250] Stephen Merity, Caiming Xiong, James Bradbury, and Richard Socher. Pointer sentinel mixture models. *International Conference on Learning Representations*, 2017. 2.5.3

[251] Charles A Micchelli and Massimiliano Pontil. Learning the kernel function via regularization. *Journal of machine Learning research*, 2005. 2.4

[252] A. Mignon and F. Jurie. PCCA: A new approach for distance learning from sparse pairwise constraints. In *IEEE Conference on Computer Vision and Pattern Recognition*, 2012. 2.4.3, 2.4.3

[253] Tomas Mikolov and Geoffrey Zweig. Context dependent recurrent neural network language model. *IEEE Spoken Language Technology conference*, 12:234–239, 2012. 2.5.3

[254] Tomáš Mikolov, Martin Karafiát, Lukáš Burget, Jan Černockỳ, and Sanjeev Khudanpur. Recurrent neural network based language model. In *Eleventh Annual Conference of the International Speech Communication Association*, 2010. 2.5.3

[255] Tomas Mikolov, Kai Chen, Greg Corrado, and Jeffrey Dean. Efficient estimation of word representations in vector space. *International Conference on Learning Representations Workshop*, 2013. 6.3.2

[256] Tomas Mikolov, Ilya Sutskever, Kai Chen, Greg S Corrado, and Jeff Dean. Distributed representations of words and phrases and their compositionality. In *Advances in Neural Information Processing Systems*, 2013. 2.1.4, 2.4.3, 6.1.1

[257] Dmytro Mishkin and Jiri Matas. All you need is a good init. *International Conference on Learning Representations*, 2015. 2.3.3, 2.5.3

[258] Volodymyr Mnih, Nicolas Heess, Alex Graves, et al. Recurrent models of visual attention. In *Advances in neural information processing systems*, pages 2204–2212, 2014. 6.3.3

[259] Taesup Moon, Heeyoul Choi, Hoshik Lee, and Inchul Song. Rnndrop: A novel dropout for RNNs in ASR. In *IEEE Automatic Speech Recognition and Understanding Workshop*, 2015. 2.3.3

[260] Radford M Neal. *Bayesian learning for neural networks*. Springer Science & Business Media, 2012. 3

[261] Kenney Ng, Jimeng Sun, Jianying Hu, and Fei Wang. Personalized predictive modeling and risk factor identification using patient similarity. *AMIA Summits on Translational Science Proceedings*, page 132, 2015. 1.3.3, 6.1

[262] XuanLong Nguyen et al. Posterior contraction of the population polytope in finite admixture models. *Bernoulli*, 21(1):618–646, 2015. 7.3

[263] Bogdan Nicolae and Franck Cappello. Ai-ckpt: leveraging memory access patterns for adaptive asynchronous incremental checkpointing. In *Proceedings of the 22nd international symposium on High-performance parallel and distributed computing*, pages 155–166. ACM, 2013. 5.2.2

[264] Michael A Nielsen and Isaac L Chuang. *Quantum computation and Quantum information*. 2.2.2

[265] G. Niu, B. Dai, M. Yamada, and M. Sugiyama. Information-theoretic semisupervised metric learning via entropy regularization. *Neural Computation*, 2012. 2.4.3, 2.4.3

[266] Bruno A Olshausen and David J Field. Sparse coding with an overcomplete basis set: A strategy employed by v1? *Vision research*, 1997. 1.2.1, 2.3.1, 2.4.3, 2.5.3, 5, 5.1

[267] Kimberly J O'malley, Karon F Cook, Matt D Price, Kimberly Raiford Wildes, John F Hurdle, and Carol M Ashton. Measuring diagnoses: Icd code accuracy. *Health services research*, 2005. 6.4, 6.4.3

[268] World Health Organization et al. International classification of diseases:[9th] ninth revision, basic tabulation list with alphabetic index. *World Health Organization*, 1978. 6.4

[269] Ankur P Parikh, Le Song, and Eric P Xing. A spectral algorithm for latent tree graphical models. In *Proceedings of the 28th International Conference on Machine Learning*, pages 1065–1072, 2011. 7.3

[270] Neal Parikh and Stephen Boyd. Proximal algorithms. *Foundations and Trends in Optimization*, 1(3):127–239, 2014. 1.2.1, 2.2, 2.2.3, 2.5.2, 2.5.2

[271] Ioannis Partalas, Grigorios Tsoumakas, and Ioannis P Vlahavas. Focused ensemble selection: A diversity-based method for greedy ensemble selection. In *European Conference on Artificial Intelligence*, 2008. 1.3.1

[272] Ioannis Partalas, Aris Kosmopoulos, Nicolas Baskiotis, Thierry Artieres, George Paliouras, Eric Gaussier, Ion Androutsopoulos, Massih-Reza Amini, and Patrick Galinari. LSHTC: A benchmark for large-scale text classification. *arXiv preprint arXiv:1503.08581*, 2015. 5, 5.2.5

[273] Razvan Pascanu, Caglar Gulcehre, Kyunghyun Cho, and Yoshua Bengio. How to construct deep recurrent neural networks. *International Conference on Learning Representations*, 2014. 2.5.3

[274] John P Pestian, Christopher Brew, Paweł Matykiewicz, Dj J Hovermale, Neil Johnson, K Bretonnel Cohen, and Włodzisław Duch. A shared task involving multi-label classification of clinical free text. In *Proceedings of the Workshop on BioNLP 2007: Biological, Translational, and Clinical Language Processing*, pages 97–104. Association for Computational Linguistics, 2007. 6.4.2, 6.4.2, 6.4.3

[275] John Platt et al. Fast training of support vector machines using sequential minimal optimization. *Advances in Kernel Methods Support Vector Learning*, 3, 1999. 3.1.5

[276] Graham E Poliner and Daniel PW Ellis. A discriminative model for polyphonic piano transcription. *EURASIP Journal on Applied Signal Processing*, (1):154–154, 2007. 3.2.4

[277] Daniel Povey, Arnab Ghoshal, Gilles Boulianne, Lukas Burget, Ondrej Glembek, Nagendra Goel, Mirko Hannemann, Petr Motlicek, Yanmin Qian, Petr Schwarz, et al. The Kaldi speech recognition toolkit. In *IEEE 2011 workshop on automatic speech recognition and understanding*. IEEE Signal Processing Society, 2011. 2.3.3, 2.3.3

[278] Rohit Prabhavalkar, Tara N Sainath, David Nahamoo, Bhuvana Ramabhadran, and Dimitri Kanevsky. An evaluation of posterior modeling techniques for phonetic recognition. In *IEEE International Conference on Acoustics, Speech and Signal Processing*, 2013. 2.3.3

[279] Ofir Press and Lior Wolf. Using the output embedding to improve language models. In *Proceedings of the 15th Conference of the European Chapter of the Association for Computational Linguistics*, volume 2, pages 157–163, 2017. 2.5.3

[280] Guo-Jun Qi, Jinhui Tang, Zheng-Jun Zha, Tat-Seng Chua, and Hong-Jiang Zhang. An efficient sparse metric learning in high-dimensional space via l1-penalized log-determinant regularization. In *International Conference on Machine Learning*, 2009. 2.2.2, 2.2.4, 2.2.4, 2.2.4, 2.2.4, 2.2.4, 6.1.1, 6.1.2

[281] Buyue Qian, Xiang Wang, Nan Cao, Hongfei Li, and Yu-Gang Jiang. A relative similarity based method for interactive patient risk prediction. *Data Mining and Knowledge Discovery*, 29(4):1070–1093, 2015. 6.1

[282] Qi Qian, Juhua Hu, Rong Jin, Jian Pei, and Shenghuo Zhu. Distance metric learning using dropout: a structured regularization approach. In *ACM SIGKDD international conference on Knowledge discovery and data mining*, 2014. 2.1.4, 2.1.4, 2.1.4, 2.1.4, 2.2.4, 2.2.4, 2.2.4, 2.2.4, 6.1.1, 6.1.2

[283] Novi Quadrianto and Christoph Lampert. Learning multi-view neighborhood preserving projections. In *Proceedings of the 28 th International Conference on Machine Learning*, pages 425–432, 2011. 7.3

[284] Ali Rahimi and Ben Recht. Random features for large-scale kernel machines. In *Neural Information Processing Systems*, 2007. 2.4.2

[285] Viresh Ranjan, Nikhil Rasiwasia, and CV Jawahar. Multi-label cross-modal retrieval. In *The IEEE International Conference on Computer Vision*, 2015. 6.3.3

[286] Carl Edward Rasmussen. The infinite Gaussian mixture model. In *Advances in neural information processing systems*, 1999. 3.2

[287] Narges Razavian, Saul Blecker, Ann Marie Schmidt, Aaron Smith-McLallen, Somesh Nigam, and David Sontag. Population-level prediction of type 2 diabetes from claims data and analysis of risk factors. *Big Data*, 2015. 1.3.3

[288] Narges Razavian, Jake Marcus, and David Sontag. Multi-task prediction of disease onsets from longitudinal lab tests. *Machine Learning for Healthcare Conference*, 2016. 1.3.3

[289] Jesse Read, Bernhard Pfahringer, Geoff Holmes, and Eibe Frank. Classifier chains for

multi-label classification. *Machine learning*, 2011. 6.3.3

[290] Benjamin Recht, Maryam Fazel, and Pablo A Parrilo. Guaranteed minimum-rank solutions of linear matrix equations via nuclear norm minimization. *SIAM review*, 52(3): 471–501, 2010. 2.1.4, 2.1.4, 2.1.4, 2.1.4

[291] Pau Rodríguez, Jordi Gonzàlez, Guillem Cucurull, Josep M Gonfaus, and Xavier Roca. Regularizing cnns with locally constrained decorrelations. *International Conference on Learning Representations*, 2017. 2.3.3, 2.5.3, 2.3.3, 2.3.3

[292] Maya Rotmensch, Yoni Halpern, Abdulhakim Tlimat, Steven Horng, and David Sontag. Learning a health knowledge graph from electronic medical records. *Scientific Reports*, 2017. 7.3

[293] B. Schölkopf, A. Smola, and K. Müller. Kernel principal component analysis. In *International Conference on Artificial Neural Networks*, 1997. 2.4, 2.4.1

[294] Bernhard Schölkopf and Alexander J Smola. *Learning with kernels: Support vector machines, regularization, optimization, and beyond*. MIT press, 2002. 2.2.4, 2.4, 2.4.2, 2.4.2, 2.4.3, 2.4.3, 2.4.3, 2.4.3

[295] Minjoon Seo, Aniruddha Kembhavi, Ali Farhadi, and Hannaneh Hajishirzi. Bidirectional attention flow for machine comprehension. *arXiv preprint arXiv:1611.01603*, 2016. 6.4.3

[296] Minjoon Seo, Aniruddha Kembhavi, Ali Farhadi, and Hannaneh Hajishirzi. Bidirectional attention flow for machine comprehension. *International Conference on Learning Representations*, 2017. 2.1.4, 2.1.4, 2.1.4, 2.3.3, 2.3.3, 2.3.3

[297] Pierre Sermanet, Andrea Frome, and Esteban Real. Attention for fine-grained categorization. *arXiv preprint arXiv:1412.7054*, 2014. 6.3.3

[298] Shai Shalev-Shwartz and Shai Ben-David. *Understanding Machine Learning: From Theory to Algorithms*. Cambridge University Press, 2014. 12, 4.3.2, 4.3.2

[299] Shai Shalev-Shwartz and Tong Zhang. Stochastic dual coordinate ascent methods for regularized loss. *Journal of Machine Learning Research*, 2013. 5, 5.1

[300] Shikhar Sharma, Ryan Kiros, and Ruslan Salakhutdinov. Action recognition using visual attention. *International Conference on Learning Representations*, 2015. 6.3.3

[301] Yelong Shen, Po-Sen Huang, Jianfeng Gao, and Weizhu Chen. Reasonet: Learning to stop reading in machine comprehension. *ACM SIGKDD International Conference on Knowledge Discovery and Data Mining*, 2017. 2.1.4, 2.3.3

[302] Joanna E Sheppard, Laura CE Weidner, Saher Zakai, Simon Fountain-Polley, and Judith Williams. Ambiguous abbreviations: an audit of abbreviations in paediatric note keeping. *Archives of disease in childhood*, 2008. 6.4

[303] Karen Simonyan and Andrew Zisserman. Very deep convolutional networks for large-scale image recognition. *International Conference on Learning Representations*, 2015. 2.1.4, 2.4.3

[304] Vikas Sindhwani and Amol Ghoting. Large-scale distributed non-negative sparse coding and sparse dictionary learning. In *ACM SIGKDD International Conference on Knowledge*

Discovery and Data Mining, 2012. 5

[305] Hardeep Singh, Ashley ND Meyer, and Eric J Thomas. The frequency of diagnostic errors in outpatient care: estimations from three large observational studies involving us adult populations. *BMJ Qual Saf*, pages bmjqs–2013, 2014. 1.1

[306] Christine Sinsky, Lacey Colligan, Ling Li, Mirela Prgomet, Sam Reynolds, Lindsey Goeders, Johanna Westbrook, Michael Tutty, and George Blike. Allocation of physician time in ambulatory practice: a time and motion study in 4 specialties. *Annals of internal medicine*, 165(11):753–760, 2016. 1.1

[307] Leslie N Smith and Nicholay Topin. Deep convolutional neural network design patterns. *IEEE Conference on Computer Vision and Pattern Recognition*, 2017. 2.3.3, 2.5.3

[308] Mark Smith, Robert Saunders, Leigh Stuckhardt, J Michael McGinnis, et al. *Best care at lower cost*. 1.1

[309] Alessandro Sordoni, Philip Bachman, Adam Trischler, and Yoshua Bengio. Iterative alternating neural attention for machine reading. *arXiv preprint arXiv:1606.02245*, 2016. 2.1.4, 2.3.3

[310] Jost Tobias Springenberg, Alexey Dosovitskiy, Thomas Brox, and Martin Riedmiller. Striving for simplicity: The all convolutional net. *International Conference on Learning Representations*, 2014. 2.3.3, 2.5.3

[311] Nathan Srebro and Adi Shraibman. Rank, trace-norm and max-norm. In *International Conference on Computational Learning Theory*, 2005. 2.2.2

[312] Nitish Srivastava and Ruslan R Salakhutdinov. Discriminative transfer learning with tree-based priors. In *Advances in Neural Information Processing Systems*, pages 2094–2102, 2013. 6.3.3

[313] Nitish Srivastava, Geoffrey E Hinton, Alex Krizhevsky, Ilya Sutskever, and Ruslan Salakhutdinov. Dropout: a simple way to prevent neural networks from overfitting. *Journal of Machine Learning Research*, 15(1):1929–1958, 2014. 2.1.4, 2.1.4, 2.2.4, 2.3.3, 2.3.3, 6.1.1, 6.4.2

[314] Rupesh Kumar Srivastava, Klaus Greff, and Jürgen Schmidhuber. Highway networks. *arXiv preprint arXiv:1505.00387*, 2015. 2.3.3, 2.5.3

[315] Jimeng Sun, Fei Wang, Jianying Hu, and Shahram Edabollahi. Supervised patient similarity measure of heterogeneous patient records. *ACM SIGKDD Explorations Newsletter*, 2012. 1.3.3, 6.1

[316] Liang Sun, Shuiwang Ji, and Jieping Ye. Hypergraph spectral learning for multi-label classification. In *ACM SIGKDD International Conference on Knowledge Discovery and Data Mining*, 2008. 6.3.3

[317] Ganesh Sundaramoorthi and Byung-Woo Hong. Fast label: Easy and efficient solution of joint multi-label and estimation problems. In *IEEE Conference on Computer Vision and Pattern Recognition*, 2014. 6.3.3

[318] Sayantan Sur, Uday Kumar Reddy Bondhugula, Amith Mamidala, H-W Jin, and Dhabaleswar K Panda. High performance RDMA based all-to-all broadcast for InfiniBand

clusters. In *International Conference on High-Performance Computing*, 2005. 5.2.4

[319] Christian Szegedy, Wei Liu, Yangqing Jia, Pierre Sermanet, Scott Reed, Dragomir Anguelov, Dumitru Erhan, Vincent Vanhoucke, Andrew Rabinovich, Jen-Hao Rick Chang, et al. Going deeper with convolutions. In *The IEEE Conference on Computer Vision and Pattern Recognition*, 2014. 5.3.2

[320] Kai Sheng Tai, Richard Socher, and Christopher D Manning. Improved semantic representations from tree-structured long short-term memory networks. *Annual Meeting of the Association for Computational Linguistics*, 2015. 6.3, 6.3.1, 6.3.1, 6.4.1, 6.4.3

[321] Nima Tajbakhsh, Jae Y Shin, Suryakanth R Gurudu, R Todd Hurst, Christopher B Kendall, Michael B Gotway, and Jianming Liang. Convolutional neural networks for medical image analysis: Full training or fine tuning? *IEEE transactions on medical imaging*, 35(5):1299–1312, 2016. 6.3.3

[322] Mingkui Tan, Qinfeng Shi, Anton van den Hengel, Chunhua Shen, Junbin Gao, Fuyuan Hu, and Zhen Zhang. Learning graph structure for multi-label image classification via clique generation. In *IEEE Conference on Computer Vision and Pattern Recognition*, 2015. 6.3.3

[323] Buzhou Tang, Hongxin Cao, Yonghui Wu, Min Jiang, and Hua Xu. Recognizing clinical entities in hospital discharge summaries using structural support vector machines with word representation features. *BMC medical informatics and decision making*, 2013. 1.3.3

[324] Buzhou Tang, Yonghui Wu, Min Jiang, Yukun Chen, Joshua C Denny, and Hua Xu. A hybrid system for temporal information extraction from clinical text. *Journal of the American Medical Informatics Association*, 2013. 1.3.3

[325] Buzhou Tang, Hongxin Cao, Xiaolong Wang, Qingcai Chen, and Hua Xu. Evaluating word representation features in biomedical named entity recognition tasks. *BioMed research international*, 2014. 1.3.3

[326] Hao Tang, Weiran Wang, Kevin Gimpel, and Karen Livescu. Discriminative segmental cascades for feature-rich phone recognition. In *IEEE Automatic Speech Recognition and Understanding Workshop*, 2015. 2.3.3

[327] Yee W Teh and Dilan Gorur. Indian buffet processes with power-law behavior. In *Advances in neural information processing systems*, 2009. 3.2.4, 3.2.4

[328] Yee Whye Teh and Zoubin Ghahramani. Stick-breaking construction for the Indian buffet process. 2007. 1.2.1

[329] Yee Whye Teh and Zoubin Ghahramani. Stick-breaking construction for the Indian buffet process. 2007. 3.2, 3.2.2, 3.2.3, 3.2.4

[330] Zhiyang Teng and Yue Zhang. Bidirectional tree-structured lstm with head lexicalization. *arXiv preprint arXiv:1611.06788*, 2016. 6.4.3

[331] Robert Tibshirani. Regression shrinkage and selection via the lasso. *Journal of the Royal Statistical Society. Series B (Methodological)*, pages 267–288, 1996. 2.4.4, 2.5, 2.5, 2.5.3, 2.5.3, 2.5.3, 2.5.3

[332] László Tóth. Phone recognition with deep sparse rectifier neural networks. In *IEEE*

International Conference on Acoustics, Speech and Signal Processing, 2013. 2.3.3

[333] László Tóth. Combining time-and frequency-domain convolution in convolutional neural network-based phone recognition. In *IEEE International Conference on Acoustics, Speech and Signal Processing*, 2014. 2.3.3

[334] Adam Trischler, Zheng Ye, Xingdi Yuan, and Kaheer Suleman. Natural language comprehension with the epireader. *Conference on Empirical Methods in Natural Language Processing*, 2016. 2.1.4, 2.3.3

[335] Ivor W Tsang, James T Kwok, C Bay, and H Kong. Distance metric learning with kernels. In *International Conference on Artificial Neural Networks*, 2003. 1.2.1, 2.4, 2.4.1, 2.4.1, 2.4.3, 2.4.3

[336] Koji Tsuda, Gunnar Rätsch, and Manfred K Warmuth. Matrix exponentiated gradient updates for on-line learning and Bregman projection. *Journal of Machine Learning Research*, 2005. 2.2.1

[337] Celine Vens, Jan Struyf, Leander Schietgat, Sašo Džeroski, and Hendrik Blockeel. Decision trees for hierarchical multi-label classification. *Machine Learning*, 2008. 6.3.2, 6.3.2, 6.3.3

[338] Nakul Verma and Kristin Branson. Sample complexity of learning mahalanobis distance metrics. In *Advances in Neural Information Processing Systems*, pages 2584–2592, 2015. 4.2.2, 4.2.3, 4.2.3

[339] Oriol Vinyals, Charles Blundell, Tim Lillicrap, Daan Wierstra, et al. Matching networks for one shot learning. In *Advances in Neural Information Processing Systems*, pages 3630–3638, 2016. 2.1.2

[340] Martin J Wainwright, Michael I Jordan, et al. Graphical models, exponential families, and variational inference. *Foundations and Trends® in Machine Learning*, 2008. 1.2.1, 3, 3.1, 3.1.2

[341] Chong Wang and David M Blei. Variational inference in nonconjugate models. *Journal of Machine Learning Research*, 2013. 3.1.1

[342] Daixin Wang, Peng Cui, Mingdong Ou, and Wenwu Zhu. Deep multimodal hashing with orthogonal regularization. In *International Joint Conference on Artificial Intelligence*, 2015. 2.2, 2.2.4, 2.2.4, 6.1.1, 6.1.2

[343] Fei Wang, Jimeng Sun, and Shahram Ebadollahi. Integrating distance metrics learned from multiple experts and its application in patient similarity assessment. In *SIAM data mining conference*, 2011. 1.3.3, 6.1

[344] Fei Wang, Jianying Hu, and Jimeng Sun. Medical prognosis based on patient similarity and expert feedback. In *International Conference on Pattern Recognition*, 2012. 1.3.3, 6.1

[345] J. Wang, H. Do, A. Woznica, and A. Kalousis. Metric learning with multiple kernels. In *Neural Information Processing Systems*, 2011. 2.4.3, 2.4.3

[346] Jiang Wang, Yi Yang, Junhua Mao, Zhiheng Huang, Chang Huang, and Wei Xu. CNN-RNN: A unified framework for multi-label image classification. In *IEEE Conference on*

Computer Vision and Pattern Recognition, 2016. 6.3.2, 6.3.2, 6.3.3

[347] Jun Wang, Sanjiv Kumar, and Shih-Fu Chang. Semi-supervised hashing for large-scale search. *IEEE Transactions on Pattern Analysis and Machine Intelligence*, 2012. 2.2, 2.2.4, 6.1.1

[348] Xiang Wang, David Sontag, and Fei Wang. Unsupervised learning of disease progression models. In *ACM SIGKDD international conference on Knowledge discovery and data mining*, 2014. 1.3.3

[349] Xiaosong Wang, Yifan Peng, Le Lu, Zhiyong Lu, Mohammadhadi Bagheri, and Ronald M Summers. Chestx-ray8: Hospital-scale chest x-ray database and benchmarks on weakly-supervised classification and localization of common thorax diseases. *Computer Vision and Pattern Recognition*, 2017. 6.3.3

[350] Yichen Wang, Robert Chen, Joydeep Ghosh, Joshua C Denny, Abel Kho, You Chen, Bradley A Malin, and Jimeng Sun. Rubik: Knowledge guided tensor factorization and completion for health data analytics. In *ACM SIGKDD International Conference on Knowledge Discovery and Data Mining*, 2015. 1.1, 1.3.3

[351] Zengmao Wang, Bo Du, Lefei Zhang, Liangpei Zhang, Meng Fang, and Dacheng Tao. Multi-label active learning based on maximum correntropy criterion: Towards robust and discriminative labeling. In *European Conference on Computer Vision*, 2016. 6.3.3

[352] Larry Wasserman. *All of statistics: a concise course in statistical inference*. Springer Science & Business Media, 2013. 3, 3.1.1

[353] Pijika Watcharapichat, Victoria Lopez Morales, Raul Castro Fernandez, and Peter Pietzuch. Ako: Decentralised deep learning with partial gradient exchange. In *ACM Symposium on Cloud Computing*, 2016. 1.3.2, 5.2.5

[354] Steve Waterhouse, David MacKay, Tony Robinson, et al. Bayesian methods for mixtures of experts. *Advances in Neural Information Processing Systems*, 1996. 1.2.1, 3.1, 3.1.4, 3.1.4

[355] Jinliang Wei, Wei Dai, Aurick Qiao, Qirong Ho, Henggang Cui, Gregory R Ganger, Phillip B Gibbons, Garth A Gibson, and Eric P Xing. Managed communication and consistency for fast data-parallel iterative analytics. In *ACM Symposium on Cloud Computing*, 2015. 1.2.2, 1.2.3, 1.3.2, 5, 5.2, 5.2.1, 5.2.1, 5.2.5, 5.2.5, 5.3, 6.2, 6.2

[356] Yunchao Wei, Wei Xia, Junshi Huang, Bingbing Ni, Jian Dong, Yao Zhao, and Shuicheng Yan. CNN: Single-label to multi-label. *arXiv preprint arXiv:1406.5726*, 2014. 6.3.3

[357] Kilian Q Weinberger, John Blitzer, and Lawrence K Saul. Distance metric learning for large margin nearest neighbor classification. In *Advances in neural information processing systems*, 2005. 2.1.2, 2.2.4, 2.5.1, 2.2.4, 2.2.4, 2.2.4, 2.2.4, 6.1.1, 6.1.2

[358] P. Welinder, S. Branson, T. Mita, C. Wah, F. Schroff, S. Belongie, and P Perona. Caltech-ucsd birds. 2010. 2.1.4, 2.2.4, 2.4.3

[359] Zaiwen Wen and Wotao Yin. A feasible method for optimization with orthogonality constraints. *Mathematical Programming*, 2013. 2.2.4

[360] Darren Wilkinson. Metropolis hastings mcmc when the proposal and target have differing

support. In *https://darrenjw.wordpress.com/2012/06/04/metropolis-hastings-mcmc-when-the-proposal-and-target-have-differing-support/*, 2015. 3.1.6

[361] Frank Wood and Thomas L Griffiths. Particle filtering for nonparametric bayesian matrix factorization. *Advances in Neural Information Processing Systems*, 19:1513, 2007. 3.2.4

[362] Baoyuan Wu, Siwei Lyu, and Bernard Ghanem. ML-MG: multi-label learning with missing labels using a mixed graph. In *The IEEE International Conference on Computer Vision*, 2015. 6.3.3

[363] Wei Wu, Eugene Bleecker, Wendy Moore, William W Busse, Mario Castro, Kian Fan Chung, William J Calhoun, Serpil Erzurum, Benjamin Gaston, Elliot Israel, et al. Unsupervised phenotyping of severe asthma research program participants using expanded lung data. *Journal of Allergy and Clinical Immunology*, 133(5):1280–1288, 2014. 1.1

[364] Jianxiong Xiao, James Hays, Krista Ehinger, Aude Oliva, Antonio Torralba, et al. SUN database: Large-scale scene recognition from abbey to zoo. In *IEEE Conference on Computer Vision and Pattern Recognition*, 2010. 3.1.5

[365] Bo Xie, Yingyu Liang, and Le Song. Diversity leads to generalization in neural networks. *International Conference on Artificial Intelligence and Statistics*, 2017. 1.3.1, 1.3.1

[366] Fangzheng Xie and Yanxun Xu. Bayesian repulsive gaussian mixture model. *arXiv preprint arXiv:1703.09061*, 2017. 3.2

[367] Pengtao Xie. Learning compact and effective distance metrics with diversity regularization. In *European Conference on Machine Learning*, 2015. 1.1, 2.1.2, 2.1.4, 2.1.4, 2.1.4, 2.1.4, 2.1.4, 2.2, 2.2.4, 2.2.4, 2.2.4, 2.2.4, 2.2.4, 6.1.1, 6.1.2

[368] Pengtao Xie and Eric Xing. A constituent-centric neural architecture for reading comprehension. In *Proceedings of the 55th Annual Meeting of the Association for Computational Linguistics*, volume 1, pages 1405–1414, 2017. 6.3, 6.3.1, 6.4.3

[369] Pengtao Xie, Yuntian Deng, and Eric Xing. Diversifying restricted boltzmann machine for document modeling. In *Proceedings of the 21th ACM SIGKDD International Conference on Knowledge Discovery and Data Mining*, pages 1315–1324. ACM, 2015. 1.1, 1.3.1, 1.3.1, 2.1, 2.1.1, 2.1.4, 2.1.4, 2.2.4, 2.2.4, 2.3.3, 2.4.3, 2.5.3, 2.3.3, 2.3.3, 2.3.3, 2.3.3, 2.4.3, 2.4.3, 2.4.3, 2.5.3, 3.1, 3.1.1, 3.1.3, 3.1.3, 3.1.5, 3.1.5, 3.1.5, 3.1.6, 6.1.1, 6.1.2

[370] Pengtao Xie, Jin Kyu Kim, Yi Zhou, Qirong Ho, Abhimanu Kumar, Yaoliang Yu, and Eric Xing. Distributed machine learning via sufficient factor broadcasting. In *Conference on Uncertainty in artificial intelligence*, 2016. 1.1, 1.2.2, 1.3.2, 5

[371] Pengtao Xie, Jun Zhu, and Eric Xing. Diversity-promoting Bayesian learning of latent variable models. In *International Conference on Machine Learning*, 2016. 1.1, 1.1, 3, 3.1

[372] Pengtao Xie, Yuntian Deng, Yi Zhou, Abhimanu Kumar, Yaoliang Yu, James Zou, and Eric P. Xing. Learning latent space models with angular constraints. In *Proceedings of the 34th International Conference on Machine Learning*, pages 3799–3810, 2017. 1.1, 1.2.1, 1.2.1, 2, 2.3, 4.2.1

[373] Pengtao Xie, Barnabas Poczos, and Eric P Xing. Near-orthogonality regularization in kernel methods. In *Conference on Uncertainty in Artificial Intelligence*, 2017. 1.1, 2

[374] Pengtao Xie, Barnabas Poczos, and Eric P Xing. Near-orthogonality regularization in kernel methods. 2017. 1.2.1, 1.2.1, 2.4

[375] Pengtao Xie, Ruslan Salakhutdinov, Luntian Mou, and Eric P. Xing. Deep determinantal point process for large-scale multi-label classification. In *The IEEE International Conference on Computer Vision*, 2017. 6.3.2, 6.3.2

[376] Pengtao Xie, Aarti Singh, and Eric P. Xing. Uncorrelation and evenness: a new diversity-promoting regularizer. In *Proceedings of the 34th International Conference on Machine Learning*, pages 3811–3820, 2017. 1.1, 1.1, 1.1, 1.2.1, 2, 2.1

[377] Pengtao Xie, Jin Kyu Kim, Qirong Ho, Yaoliang Yu, and Eric P. Xing. Orpheus: Efficient distributed machine learning via system and algorithm co-design. *Symposium of Cloud Computing*, 2018. 1.1, 1.2.2, 1.2.3, 5

[378] Pengtao Xie, Haoran Shi, Ming Zhang, and Eric P. Xing. A neural architecture for automated icd coding. *The 56th Annual Meeting of the Association for Computational Linguistics*, 2018. 1.1, 1.2.3

[379] Pengtao Xie, Wei Wu, Yichen Zhu, and Eric P. Xing. Orthogonality-promoting distance metric learning: Convex relaxation and theoretical analysis. *International Conference on Machine Learning*, 2018. 1.1, 1.2.1, 1.2.1, 1.2.3, 2, 2.2, 2.2.1, 4.1, 4.2.2, 4.2.3

[380] Pengtao Xie, Hongbao Zhang, and Eric P. Xing. Nonoverlap-promoting variable selection. *International Conference on Machine Learning*, 2018. 1.1, 1.2.1, 1.2.1, 2, 2.5

[381] Pengtao Xie, Jun Zhu, and Eric P. Xing. Diversity-promoting bayesian learning of latent variable models. *Journal of Machine Learning Research*, 2018. 1.1, 1.2.1, 3

[382] Saining Xie, Ross Girshick, Piotr Dollár, Zhuowen Tu, and Kaiming He. Aggregated residual transformations for deep neural networks. *IEEE Conference on Computer Vision and Pattern Recognition*, 2017. 2.3.3, 2.5.3

[383] Eric P Xing, Michael I Jordan, Stuart Russell, and Andrew Y Ng. Distance metric learning with application to clustering with side-information. In *Advances in neural information processing systems*, 2002. 1.2.1, 2.1, 2.1.2, 2.1.2, 2.2, 2.2.3, 2.5.1, 5, 5.1, 6.1

[384] Eric P Xing, Qirong Ho, Wei Dai, Jin-Kyu Kim, Jinliang Wei, Seunghak Lee, Xun Zheng, Pengtao Xie, Abhimanu Kumar, and Yaoliang Yu. Petuum: A new platform for distributed machine learning on big data. In *ACM SIGKDD International Conference on Knowledge Discovery and Data Mining*, 2015. 1.1

[385] Kelvin Xu, Jimmy Ba, Ryan Kiros, Kyunghyun Cho, Aaron Courville, Ruslan Salakhudinov, Rich Zemel, and Yoshua Bengio. Show, attend and tell: Neural image caption generation with visual attention. In *International Conference on Machine Learning*, 2015. 6.3.2, 6.3.2, 6.3.3, 6.4.3

[386] Yanxun Xu, Peter Müller, and Donatello Telesca. Bayesian inference for latent biologic structure with determinantal point processes (dpp). *Biometrics*, 72(3):955–964, 2016. 3.2

[387] Xiangyang Xue, Wei Zhang, Jie Zhang, Bin Wu, Jianping Fan, and Yao Lu. Correlative multi-label multi-instance image annotation. In *The IEEE International Conference on Computer Vision*, 2011. 6.3.3

[388] Yoshihiro Yamada, Masakazu Iwamura, and Koichi Kise. Deep pyramidal residual networks with separated stochastic depth. *arXiv preprint arXiv:1612.01230*, 2016. 2.3.3, 2.5.3

[389] Zhicheng Yan, Hao Zhang, Robinson Piramuthu, Vignesh Jagadeesh, Dennis DeCoste, Wei Di, and Yizhou Yu. HD-CNN: hierarchical deep convolutional neural networks for large scale visual recognition. In *Proceedings of the IEEE International Conference on Computer Vision*, pages 2740–2748, 2015. 6.3.2, 6.3.2, 6.3.3, 6.4.2

[390] Hao Yang, Joey Tianyi Zhou, and Jianfei Cai. Improving multi-label learning with missing labels by structured semantic correlations. In *European Conference on Computer Vision*, 2016. 6.3.3

[391] J Yang, Anton Ragni, Mark JF Gales, and Kate M Knill. Log-linear system combination using structured support vector machines. In *Interspeech*, 2016. 2.3.3

[392] Jianchao Yang, Kai Yu, Yihong Gong, and Thomas Huang. Linear spatial pyramid matching using sparse coding for image classification. In *IEEE Conference on Computer Vision and Pattern Recognition*, 2009. 2.3.3, 2.4.3

[393] Yuan Yang, Pengtao Xie, Xin Gao, Carol Cheng, Christy Li, Zhang Hongbao, and Eric P. Xing. Predicting discharge medications at admission time based on deep learning. *arXiv preprint arXiv:1711.01386*, 2017. 1.1

[394] Zichao Yang, Xiaodong He, Jianfeng Gao, Li Deng, and Alex Smola. Stacked attention networks for image question answering. In *Proceedings of the IEEE Conference on Computer Vision and Pattern Recognition*, pages 21–29, 2016. 6.3.2, 6.3.3

[395] Zichao Yang, Diyi Yang, Chris Dyer, Xiaodong He, Alex Smola, and Eduard Hovy. Hierarchical attention networks for document classification. In *Proceedings of the 2016 Conference of the North American Chapter of the Association for Computational Linguistics: Human Language Technologies*, pages 1480–1489, 2016. 6.4.3

[396] Li Yao, Eric Poblenz, Dmitry Dagunts, Ben Covington, Devon Bernard, and Kevin Lyman. Learning to diagnose from scratch by exploiting dependencies among labels. *arXiv preprint arXiv:1710.10501*, 2017. 6.3.2, 6.3.2, 6.3.3

[397] Chih-Kuan Yeh, Wei-Chieh Wu, Wei-Jen Ko, and Yu-Chiang Frank Wang. Learning deep latent spaces for multi-label classification. 2017. 6.3.3

[398] Yiming Ying and Peng Li. Distance metric learning with eigenvalue optimization. *Journal of machine Learning research*, 2012. 2.4.3, 2.4.3

[399] Yiming Ying, Kaizhu Huang, and Colin Campbell. Sparse metric learning via smooth optimization. In *Advances in neural information processing systems*, 2009. 2.2.4, 2.2.4, 2.2.4, 2.2.4, 2.2.4, 6.1.1, 6.1.2

[400] Quanzeng You, Hailin Jin, Zhaowen Wang, Chen Fang, and Jiebo Luo. Image captioning with semantic attention. In *IEEE Conference on Computer Vision and Pattern Recognition*, 2016. 6.3.2, 6.3.3

[401] Lantao Yu, Weinan Zhang, Jun Wang, and Yong Yu. Seqgan: Sequence generative adversarial nets with policy gradient. In *AAAI*, 2017. 6.4.3

[402] Yang Yu, Yu-Feng Li, and Zhi-Hua Zhou. Diversity regularized machine. In *International Joint Conference on Artificial Intelligence*, 2011. 1.3.1, 1.3.1, 2.1, 2.1.1, 2.1.4, 2.1.4, 2.1.4, 2.1.4, 2.1.4, 2.2.4, 2.3.3, 2.5.3, 2.2.4, 2.2.4, 2.2.4, 2.2.4, 2.3.3, 2.3.3, 2.3.3, 2.3.3, 2.5.3, 6.1.1, 6.1.2

[403] Yao-Liang Yu and Eric P Xing. Exact algorithms for isotonic regression and related. In *Journal of Physics: Conference Series*, volume 699, page 012016. IOP Publishing, 2016. 6.4.1

[404] Ming Yuan and Yi Lin. Model selection and estimation in regression with grouped variables. *Journal of the Royal Statistical Society: Series B (Statistical Methodology)*, 68(1): 49–67, 2006. 2.5, 2.5

[405] Pourya Habib Zadeh, Reshad Hosseini, and Suvrit Sra. Geometric mean metric learning. 2016. 2.1.4, 2.1.4, 2.1.4, 2.2.4, 2.4.3, 2.2.4, 2.2.4, 2.2.4, 2.2.4, 2.4.3, 6.1.1, 6.1.2

[406] Sergey Zagoruyko. Wide residual networks. *British Machine Vision Conference*, 2016. 2.3.3, 2.5.3, 2.3.3

[407] Matei Zaharia, Mosharaf Chowdhury, Tathagata Das, Ankur Dave, Justin Ma, Murphy McCauley, Michael J Franklin, Scott Shenker, and Ion Stoica. Resilient distributed datasets: A fault-tolerant abstraction for in-memory cluster computing. In *USENIX Symposium on Networked Systems Design and Implementation*, 2012. 1.3.2, 5, 5.2, 5.2.2

[408] Wojciech Zaremba, Ilya Sutskever, and Oriol Vinyals. Recurrent neural network regularization. *arXiv preprint arXiv:1409.2329*, 2014. 2.5.3

[409] Matthew D Zeiler. Adadelta: an adaptive learning rate method. *arXiv preprint arXiv:1212.5701*, 2012. 2.1.4, 2.3.3

[410] Matthew D Zeiler and Rob Fergus. Visualizing and understanding convolutional networks. In *European conference on computer vision*, pages 818–833. Springer, 2014. 6.3.3

[411] Hao Zhang, Zeyu Zheng, Shizhen Xu, Wei Dai, Qirong Ho, Xiaodan Liang, Zhiting Hu, Jinliang Wei, Pengtao Xie, and Eric P Xing. Poseidon: An efficient communication architecture for distributed deep learning on GPU clusters. *USENIX Annual Technical Conference*, 2017. 1.1, 1.2.2, 1.3.2, 5.3, 5.3.1

[412] Min-Ling Zhang and Kun Zhang. Multi-label learning by exploiting label dependency. In *ACM SIGKDD International Conference on Knowledge Discovery and Data Mining*, 2010. 6.3.3

[413] Ping Zhang, Fei Wang, Jianying Hu, and Robert Sorrentino. Towards personalized medicine: leveraging patient similarity and drug similarity analytics. *AMIA Joint Summits on Translational Science*, 2014. 6.1

[414] Bin Zhao, Fei Li, and Eric P Xing. Large-scale category structure aware image categorization. In *Advances in Neural Information Processing Systems*, pages 1251–1259, 2011. 6.3.3

[415] Fang Zhao, Yongzhen Huang, Liang Wang, and Tieniu Tan. Deep semantic ranking based hashing for multi-label image retrieval. In *IEEE Conference on Computer Vision and Pattern Recognition*, 2015. 6.3.3

[416] Kaili Zhao, Wen-Sheng Chu, and Honggang Zhang. Deep region and multi-label learning for facial action unit detection. In *IEEE Conference on Computer Vision and Pattern Recognition*, 2016. 6.3.3

[417] Peng Zhao and Bin Yu. On model selection consistency of lasso. *Journal of Machine learning research*, 7:2541–2563, 2006. 2.5

[418] Peng Zhao, Guilherme Rocha, and Bin Yu. The composite absolute penalties family for grouped and hierarchical variable selection. *The Annals of Statistics*, pages 3468–3497, 2009. 2.5

[419] Shuai Zheng, Sadeep Jayasumana, Bernardino Romera-Paredes, Vibhav Vineet, Zhizhong Su, Dalong Du, Chang Huang, and Philip HS Torr. Conditional random fields as recurrent neural networks. In *Proceedings of the IEEE International Conference on Computer Vision*, pages 1529–1537, 2015. 6.3.2, 6.3.2

[420] Dengyong Zhou, Lin Xiao, and Mingrui Wu. Hierarchical classification via orthogonal transfer. *International Conference on Machine Learning*, 2011. 1.3.1, 2.2.4, 6.1.1

[421] Jiayu Zhou, Jun Liu, Vaibhav A Narayan, and Jieping Ye. Modeling disease progression via fused sparse group lasso. In *ACM SIGKDD international conference on Knowledge discovery and data mining*, 2012. 1.3.3

[422] Jiayu Zhou, Jimeng Sun, Yashu Liu, Jianying Hu, and Jieping Ye. Patient risk prediction model via top-k stability selection. In *SIAM Conference on Data Mining*, 2013. 1.3.3

[423] Jun Zhu, Ning Chen, and Eric P Xing. Infinite SVM: a Dirichlet process mixture of large-margin kernel machines. In *International Conference on Machine Learning*, 2011. 3.1.5, 3.1.5

[424] Jun Zhu, Ning Chen, and Eric P Xing. Bayesian inference with posterior regularization and applications to infinite latent SVMs. *Journal of Machine Learning Research*, 2014. 3.1, 3.1.3

[425] Xinqi Zhu and Michael Bain. B-CNN: Branch convolutional neural network for hierarchical classification. *arXiv preprint arXiv:1709.09890*, 2017. 6.3.2, 6.3.2, 6.3.3, 6.4.2

[426] Julian Georg Zilly, Rupesh Kumar Srivastava, Jan Koutník, and Jürgen Schmidhuber. Recurrent highway networks. *International Conference on Machine Learning*, 2016. 2.5.3

[427] Barret Zoph and Quoc V Le. Neural architecture search with reinforcement learning. *International Conference on Learning Representations*, 2017. 2.5.3

[428] Hui Zou and Trevor Hastie. Regularization and variable selection via the elastic net. *Journal of the Royal Statistical Society: Series B (Statistical Methodology)*, 67(2):301–320, 2005. 2.5, 2.5, 2.5.3

[429] James Y Zou and Ryan P Adams. Priors for diversity in generative latent variable models. In *Advances in Neural Information Processing Systems*, 2012. 1.3.1, 1.3.1, 2.1, 2.1.1, 2.1.4, 2.1.4, 2.1.4, 2.1.4, 2.1.4, 2.1.4, 2.2.4, 2.3.3, 2.4.3, 2.2.4, 2.2.4, 2.2.4, 2.2.4, 2.4.3, 2.4.3, 2.4.3, 3.1.5, 3.1.5, 3.1.5, 6.1.1, 6.1.2

[430] Alon Zweig and Daphna Weinshall. Exploiting object hierarchy: Combining models from different category levels. In *The IEEE International Conference on Computer Vision*,

pages 1–8. IEEE, 2007. 6.3.3

[431] Matt Zwolenski, Lee Weatherill, et al. The digital universe: Rich data and the increasing value of the internet of things. *Australian Journal of Telecommunications and the Digital Economy*, 2(3):47, 2014. 1.1